THEORETICAL AND EXPERIMENTAL STUDY OF MICROSTRIP DISCONTINUITIES IN MILLIMETER WAVE INTEGRATED CIRCUITS

by
Pisti B. Katehi

Radiation Laboratory
Department of Electrical Engineering and Computer Science
The University of Michigan
Ann Arbor, MI 48109-2122

September 1988

PREFACE

This program started as a combined effort by the University of Michigan and Hughes Aircraft Co., Torrance in August 1986. At the time the contract was awarded, Hughes had agreed and committed itself (see enclosed letter in the original proposal) to develop de-embedding techniques for up to 40GHz and conduct all the necessary measurements for verification of the theory that the University was going to develop. This plan worked really well during the first year. Hughes developed de-embedding procedures and conducted measurements on open microstrip filters for up to 12 GHz.

In the summer of 1987, Hughes went through many changes in its structure and priorities were redefined. This project was de-emphasized and Hughes contribution reduced dramatically. As a result, all the experiments during the second year were performed at the University. Because of the state-of-the-art equipment in our facilities and the experienced personell the experiments were conducted successfully and resulted in excellent agreement with the theory.

For the third year we plan to move along the same lines. Because we recognize the importance of experiments in this project, we want to take, also, the responsibility for the experimental part of the proposed work. All the experiments necessary for the verification of the theory will be conducted at our facilities and the University will cover the cost.

PROGRESS REPORT

1. NSF Proposal Number: ECS-8602530

2. Period Covered By Report: August 1, 1987 - July 31, 1988

3. Title of Proposal: Theoretical and Experimental Study of Microstrip Discontinuities in Millimeter Wave Integrated Circuits.

4. Contract Number: ECS-8602530

5. Name of Institution: University of Michigan

6. Authors of Report: Pisti B. Katehi

7. Listing of Interim Reports and Manuscripts Submitted or Published Under Full or Partial NSF Sponsorship During This Reporting Period:

(1) L.P. Dunleavy and P.B. Katehi, " A Generalized Method for Analyzing Shielded Thin Microstrip Discontinuities". To appear in the IEEE Trans. on Microwave Theory and Techniques in Dec. 1988.

(2) L.P. Dunleavy and P.B. Katehi, "Shielding Effects in Microstrip Discontinuities". To appear in the IEEE Trans. on Microwave Theory and Techniques in Dec. 1988.

(3) L.P. Dunleavy and P.B. Katehi, "A New Method For Discontinuity Analysis in Shielded Microstrip", Digest of the 1988 IEEE MTT-S International Symposium, New York, New York, May 1988, pp. 701-704.

(4) L.P. Dunleavy and P.B. Katehi, "A New Method for Discontinuity Analysis in Shielded Microstrip: Theoretical and Computational Considerations", Digest of the 1988 URSI Radio Science Meeting, Syracuse, June 1988, pp. 313.

(5) T. Weller and P.B. Katehi, "The Effect of Semi-Insulating, Semi-Conducting Materials on the Propagation Characteristics of Dielectric Loaded Waveguides", Technical Report NSF-023827-3-T, EECS Department, University of Michigan, Ann Arbor, April 1988.

(6) W. Harokopus and P.B. Katehi, "High-Frequency Characterization of Open Microstrip Junctions", Technical Report NSF-023827-5-T, EECS Department, University of Michigan, Ann Arbor, June 1988.

(7) T.G. Livernois and P.B. Katehi, "High-Frequency Characterization of Interconnects on Multilayer Substrates", Technical Report NSF-023827-4-T, EECS Department, University of Michigan, Ann Arbor, June 1988.

8. Scientific Personnel Supported By This Project:

Faculty

P. B. Katehi

Graduate Students

L.P. Dunleavy
W. Harokopus
T.G. Livernois

Undergraduate Students

T. Weller

APPENDICES

Appendix A	"A Generalized Method for Analyzing Shielded Thin Microstrip Discontinuities" L.P. Dunleavy and P.B. Katehi
Appendix B	"Discontinuity Characterization in Shielded Microstrip: A Theoretical and Experimental Study" L.P. Dunleavy
Appendix C	"A New Method for Discontinuity Analysis in Shielded Microstrips" L.P. Dunleavy and P.B. Katehi
Appendix D	"Shielding Effects in Microstrip Discontinuities" L.P. Dunleavy and P.B. Katehi
Appendix E	"High Frequency Characterization of Open Microstrip Junctions" W. Harokopus and P.B. Katehi
Appendix F	"High-Frequency Characterization of Interconnects on Multilayer Substrates: The Green's Function" T.G. Livernois and P.B. Katehi
Appendix G	"The Effect of Semi-Insulating, Semi-Conducting Materials on the Propagation Characteristics of Dielectric Loaded Waveguides" T. Weller and P.B. Katehi

RESEARCH TASKS

Title	**Personel Involved with the Research**
1.Theoretical Study of Thin-Strip Discontinuities in Shielded Microstrip.	P.B. Katehi L.P. Dunleavy
2.Improvement of De-embedding Procedures.	L.P. Dunleavy
3.Wide-Strip Discontinuities in Open Microstrip.	P.B. Katehi W. Harokopus
4.Wide-Strip Shielded Discontinuities and Interconnects on Multilayer Structures.	P.B. Katehi T.G. Livernois
5.The Effect of Semiconducting Substrates on the Propagating Characteristics of Dielectric Loaded Waveguides.	P.B. Katehi T. Weller

1. THEORETICAL STUDY OF THIN-STRIP DISCONTINUITIES IN SHIELDED MICROSTRIP.

Faculty Supervisor: P.B. Katehi

Graduate Student Participant: L.P. Dunleavy

Period: August 1, 1987 - July 31, 1988

Work Performed:

An integral equation method has been developed for the accurate evaluation of shielding effects on the propagation properties of shielded microstrip lines. The integral equation has been derived by applying reciprocity theorem and then is solved by the method of moments [1],[2] (Appendix A). The cases of an open end, a gap, and parallel coupled-line filters have been studied extensively and results are presented in [3],[4],[5] (Appendices B,C,D). In addition, these results are compared to experimental data for verification of the theory. The agreement is excellent.

Program for the third year:

For the third year we plan to extend the study of shielding effects to wide microstrip discontinuities on multilayer substrates.

Publications and Reports:

[1] L.P. Dunleavy and P.B. Katehi, "A New Method for Discontinuity Analysis in Shielded Microstrip: Theoretical and Computational Considerations", Digest of the 1988 URSI Radio Science Meeting, Syracuse, June 1988, pp. 313.

[2] L.P. Dunleavy and P.B. Katehi, " A Generalized Method for Analyzing Shielded Thin Microstrip Discontinuities". To appear in the IEEE Trans. on Microwave Theory and Techniques in Dec. 1988.

[3] L.P. Dunleavy, "Discontinuity Characterization in Shielded Microstrip: A Theoretical and Experimental Study", Ph.D. dissertation, EECS Department, The University of Michigan, Ann Arbor, April 1988.

[4] L.P. Dunleavy and P.B. Katehi, "A New Method For Discontinuity Analysis in Shielded Microstrip", Digest of the 1988 IEEE MTT-S International Symposium, New York, New York, May 1988, pp. 701-704.

[5] L.P. Dunleavy and P.B. Katehi, "Shielding Effects in Microstrip Discontinuities". To appear in the IEEE Trans. on Microwave Theory and Techniques in Dec. 1988.

2. IMPROVEMENT OF DE-EMBEDDING PROCEDURES (2-20GHz).

Faculty Supervisors: P.B. Katehi

Graduate Student Participant: L.P. Dunleavy

Period: August 1, 1987 - July 31, 1988.

Work Performed:

The improvement of De-embedding procedures, as it has been described in [1], has been completed and results are presented in [2] (see Appendix B). The purpose of this part of the research has been the experimental characterization of shielded thin-strip discontinuities for verification of the theory. The fabrication of the test fixturing and the test circuits was performed at the facilities of the University of Michigan. The measured data were in excellent agreement with the theoretical predictions [2].

Program for the Third Year:

During the third year the above study on de-embedding procedures will be repeated for the (20-40GHz) frequency range. Measurements will be performed on wide strip discontinuities at the University of Michigan Solid State Lab facilities. Theoretical results will be compared to these experimental ones for verification purposes.

Publications and Reports:

[1] P.B. Katehi, " A Theoretical and Experimental Study of Microstrip Discontinuities in Millimeter Wave Integrated Circuits", NSF Annual Report, NSF-023872-1-F, September 1987.

[2] L.P. Dunleavy, "Discontinuity Characterization in Shielded Microstrip: A Theoretical and Experimental Study", Ph.D. dissertation, Radiation Laboratory, The University of Michigan, Ann Arbor, April 1988.

3. WIDE-STRIP DISCONTINUITIES IN OPEN MICROSTRIP.

Faculty Supervisor: P.B. Katehi

Graduate Student Participant: W. Harokopus

Period: August 1, 1987 - July 31, 1988.

Work Performed:

The analysis for wide-strip open-microstrip discontinuities has been completed. In addition, the programs which evaluate the current on the conducting strips have been written and checked thoroughly. At this point, these programs have been used to find the currents on specific discontinuities and results are presented in [1] (see Appendix E).

Program for the Third Year:

Using the programs that we have developed so far, we will analyze various discontinuities such as bends, T- and X- junctions and the theoretical results , in the form of scattering parameters, will be compared to available experimental data. Also, the radiation properties of these discontinuities will be studied extensively. Specifically, we will try to evaluate the radiated power in the air and dielectric and the surface wave pattern. This is going to be of great help to the designer for laying out circuits.

Publications and Reports:

[1] W. Harokopus and P.B. Katehi, "High-Frequency Characterization of Open Microstrip Junctions", Technical Report NSF-023827-5-T, EECS Department, University of Michigan, Ann Arbor, June 1988.

4. WIDE-STRIP SHIELDED DISCONTINUITIES AND INTERCONNECTS ON MULTILAYER STRUCTURES.

Faculty Supervisor: P.B. Katehi

Graduate Student Participant: T.G. Livernois

Period: August 1, 1987 - July 31, 1988

Work Performed:

The analysis of shielded microstrip discontinuities started in fall 1987 and has already been completed. As a first step to studying these discontinuities, we tried to analyze and design microstrip lines on multilayer substrates which included semiconducting materials. As it is explained in [1] (see Appendix F), we were able to derive, using full-wave analysis, a simple equation which can be solved numerically on a PC to give the complex propagation constant of all microstrip modes. Theoretical results for the case of slow-wave structures have been checked against measurements and show excellent agreement [2]. The superiority of this technique over the other existing ones is that it combines accuracy with simplicity and therefore it can result in a very efficient design procedure.

Program for the third year:

During the third year, the developed method will be extended to more complicated structures such as bends, filters and directional couplers printed on multi-layer dielectrics. The theoretical results will be compared to available experimental data for verification.

Publications and Reports:

[1] T.G. Livernois and P.B. Katehi, "High-Frequency Characterization of Interconnects on Multilayer Substrates: The Green's Function", Technical Report NSF-023827-4-T, EECS Department, University of Michigan, Ann Arbor, June 1988.

[2] T.G. Livernois and P.B. Katehi, " A New Method for Analysis and Design of Slow Wave Structures". To be submitted for publication to the IEEE Trans. on Microwave Theory and Techniques.

5. THE EFFECT OF SEMICONDUCTING SUBSTRATES ON THE PROPAGATING CHARACTERISTICS OF DIELECTRIC LOADED WAVEGUIDES.

Faculty Supervisor: P.B. Katehi

Graduate Student Participant: T. Weller

Period: January 1, 1987 - July 30, 1988.

Work Performed:

In order to study the effect of semiconducting layers on the propagation characteristics of a dielectric loaded waveguide, we considered a single semi-conducting layer with a doping density varying from 10^{14} to 10^{16}. With N_D varying in this range of values, we evaluated the cut-off frequencies of the first few waveguide modes. Conclusions drawn from this study are presented in [1] (see Appendix G) and show a very interesting behavior in the propagation characteristics of the waveguide modes. These conclusions may be extended to the case of a shielded microstrip.

Program for the second year:

A similar study will be performed in the case of shielded lines on multi-layered semiconducting substrates. Specifically, the complex propagation constant and wave impedance for each microstrip mode will be studied as functions of the doping densities of the dielectric layers.

Publications and Reports:

[1] T. Weller and P.B. Katehi, "The effect of Semi-Insulating, Semi-Conducting Materials on the Propagation Characteristics of Dielectric Loaded Waveguides", Technical Report NSF-023827-3-T, EECS Department, University of Michigan, Ann Arbor, April 1988.

A Generalized Method for Analyzing Shielded Thin Microstrip Discontinuities

Submitted to IEEE Trans. on Microwave Theory and Tech. - April 1988

L.P. Dunleavy* and P.B. Katehi
Radiation Laboratory
Dept. of Electrical Engineering and Computer Science
The University of Michigan
1301 Beal Avenue
Ann Arbor, MI 48109-2122

Abstract-. A new integral equation method is described for the accurate full-wave analysis of shielded thin microstrip discontinuities. The integral equation is derived by applying the reciprocity theorem, then solved by the method of moments. In this derivation, a coaxial aperture is modeled with an equivalent magnetic current, and is used as the excitation mechanism for generating the microstrip currents. Computational aspects of the method have been explored extensively. A summary of some of the more interesting conclusions is included.

* L.P. Dunleavy is now with Hughes Aircraft Company.

I. INTRODUCTION

The need for more accurate microstrip circuit simulations has become increasingly apparent with the advent of monolithic microwave integrated circuits (MMICs), as well as the increased interest in millimeter-wave and near-millimeter-wave frequencies. The development of more accurate microstrip discontinuity models, based on full-wave analyses, is key to improving high frequency circuit simulations and reducing lengthy design cycle costs. Further, in most applications the microstrip circuit is enclosed in a shielding cavity (or housing) as shown in Figure 1. There are two main conditions where shielding effects are significant: 1) when the frequency approaches or is above the cutoff frequency f_c for higher order modes and 2) when the metal enclosure is physically close to the circuitry. A full-wave analysis is required to accurately model these effects.

Although shielding effects have been studied to some extent in the past (e.g. [1]), the treatment has been incomplete, particularly for more complicated structures such as a coupled line filter. Further, shielding effects are not accurately accounted for in the discontinuity models of most available microwave CAD software. To address these inadequacies, this paper develops an accurate method for the analysis of thin strip discontinuities in shielded microstrip. The method presented is based on an integral equation approach. The integral equation is derived by an application of reciprocity theorem, then solved by the method of moments.

To derive a realistically based formulation, a coaxial excitation mechanism is used. To date, all full-wave analyses of microstrip discontinuities use either a gap generator excitation method [2,3,4], or a cavity resonance technique [5,6]. Both of these techniques are purely mathematical tools. The former has no physical basis relative to an actual circuit. The latter is also abstract, since in any practical circuit some form of excitation is present. In fact, one of the most common excitations in practice comes from a coaxial feed (Figure 1). A magnetic current model for such a feed is used in the present treatment as the excitation.

In addition to developing the theory, computational aspects of the solution are explored extensively. This is an important area that has been largely neglected in the presentation of numerical solutions of this nature. Most significantly, it is shown that an optimum sampling range may be specified that dictates how to divide the conducting strip for best computational accuracy. The method developed in this paper has been applied to study the effect of shielding on the characteristics of discontinuities of the type shown in Figure 2. Numerical results from this study are presented in a companion paper [7] and are seen to be in excellent agreement with measured data.

II. THEORETICAL FORMULATION

The details of the theoretical derivation for the present method are given in [8]. Hence, only a summary of the key steps is described below.

A. Integral Equation

In the theoretical formulation, a few simplifying assumptions are made to reduce unnecessary complexity and excessive computer time. Throughout the analysis, it is assumed that the width of the conducting strips is small compared to the microstrip wavelength λ_g (the "thin-strip" approximation). In this case, the transverse component of the current may be neglected. While substrate losses are accounted for, it is assumed that the strip conductors and the walls of the shielding box are lossless, and that the strip has infinitesimal thickness. These assumptions are valid for the high frequency analysis of the microstrip structures of Figure 2, provided good conductors are used in the metalized areas.

Consider the geometry of Figure 1. In most cases the coaxial feed, or "launcher", is designed to allow only transverse electromagnetic (TEM) propagation, and the feed's center conductor is small compared to a wavelength ($kr_a \ll 1$). In these cases, the radial electric field will be dominant in the aperture and we can replace the feed by an equivalent magnetic surface current $\bar{M}_s$ [9]. This current is sometimes called a "frill" current. The source $\bar{M}_s$ induces the current distribution $\bar{J}_s$ on the conducting strip and produces the total electric field $\bar{E}^{tot}$ and the total magnetic field $\bar{H}^{tot}$ inside the cavity as indicated in Figure 1.

Now consider a cavity geometry similar to Figure 1, with the strip conductors as well as the coaxial input and output removed. Assume a test current $\bar{J}_q$ existing on a small subsection of the area which was occupied by the strip. The fields inside this new geometry are denoted by $\bar{E}_q$, and $\bar{H}_q$. Using the reciprocity theorem, the two sets of sources ($\bar{M}_s$, $\bar{J}_s$; and $\bar{J}_q$) are related according to

$$\int\int\int_V \left(\bar{J}_s \cdot \bar{E}_q - \bar{H}_q \cdot \bar{M}_s\right) dv = \int\int\int_V \bar{J}_q \cdot \bar{E}^{tot} dv \tag{1}$$

where V represents the volume of the interior of the cavity.

Note that reciprocity theorem has been widely used for developing integral equations similar to (1) for application to antenna and scattering problems [10, 11,12]. Since $\bar{J}_q \cdot \bar{E}^{tot}$ is zero everywhere inside the cavity, the right hand side of (1) vanishes. Reducing the remaining volume integrals in (1) to surface integrals results in

$$\int\int_{S_{strip}} \bar{E}_q(z = h) \cdot \bar{J}_s ds = \int\int_{S_f} \bar{H}_q(x = 0) \cdot \bar{M}_s ds \tag{2}$$

where S_{strip} is the surface of the conducting strip and S_f is the surface of the coaxial aperture(s). For one-port discontinuities, S_f represents the surface of the feed on the left hand side of Figure 1, while for two-port discontinuities, S_f represents both feed surfaces. An integral equation similar to (2) can be derived for the case of gap generator excitation by setting $\bar{M}_s = 0$ and assuming that E_x is non-zero at one point on the strip [8].

In order to solve the integral equation (2), the current distribution $\bar{J}_s$ is expanded into a series of orthonormal functions as follows [1]:

$$\bar{J}_s = \psi(y) \sum_{p=1}^{N_s} I_p \alpha_p(x) \hat{x} \tag{3}$$

[1] The assumed time dependence is $e^{j\omega t}$.

where I_p are unknown current coefficients and N_s is the number of sections considered on the strip (Figure 3). The function $\psi(y)$ describes the transverse variation of the current and is given by [2,13]

$$\psi(y) = \begin{cases} \dfrac{\frac{2}{\pi W}}{\sqrt{1-\left[\frac{2(y-Y_0)}{W}\right]^2}} & Y_0 - W/2 \le y \le Y_0 + W/2 \\ 0 & \text{otherwise} \end{cases} \tag{4}$$

where W is the width of the microstrip line and Y_0 is the y-coordinate of the center of the strip with respect to the origin in Figure 1.

The basis functions $\alpha_p(x)$ are described by

$$\alpha_p(x) = \begin{cases} \frac{\sin[K(x_{p+1}-x)]}{\sin(Kl_x)} & x_p \le x \le x_{p+1} \\ \frac{\sin[K(x-x_{p-1})]}{\sin(Kl_x)} & x_{p-1} \le x \le x_p \\ 0 & \text{otherwise} \end{cases} \tag{5}$$

for $p \neq 1$, and

$$\alpha_1(x) = \begin{cases} \frac{\sin[K(l_x-x)]}{\sin(Kl_x)} & 0 \le x \le l_x \\ 0 & \text{otherwise} \end{cases} \tag{6}$$

for $p = 1$, where

K is a scaling factor, taken to be equal to the wave number in the dielectric

x_p is the x-coordinate of the pth subsection $(= (p-1)l_x)$

l_x is the subsection length $(l_x = x_{p+1} - x_p)$.

For computation, all of the geometrical parameters are normalized with respect to the dielectric wavelength (λ_d); hence the normalized scaling factor is equal to 2π.

The integral equation (2) can now be transformed into a matrix equation by substituting the expansion of (3) for the current $\bar{J}_s$. The result may be put in the form

$$[\mathbf{Z}]\,[\mathbf{I}] = [\mathbf{V}]\ . \tag{7}$$

In the above, [Z] is an $N_s \times N_s$ impedance matrix, [I] is a vector comprised of the unknown current coefficients I_p, and [V] is the excitation vector. The individual elements of the impedance matrix are given by

$$Z_{qp} = \int\int_{S_p} \bar{E}_q(z = h) \cdot \hat{x}\psi(y)\,\alpha_p(x)\,ds\ . \tag{8}$$

where S_p is the area of the two subsections on either side of the point x_p. The elements of the excitation vector are found according to

$$V_q = \int\int_{S_f} \bar{H}_q \cdot \bar{M}_s ds\ . \tag{9}$$

Once the elements of the impedance matrix and excitation vector have been computed, the current distribution is found by solving (7) as follows:

$$[\mathbf{I}] = [\mathbf{Z}]^{-1}\,[\mathbf{V}]\ . \tag{10}$$

B. Evaluation of impedance matrix elements

Before evaluating the elements of the impedance matrix, the Green's function associated with the electric current $\bar{J}_q$ is derived. To do this the cavity is divided into two regions: region 1 consists of the volume contained within the substrate ($z < h$), while region 2 is the volume above the substrate surface ($z > h$).

The integral form of the electric field is given in terms of the Green's function, by

$$\bar{E}_q^{\,i} = -j\omega\mu_0 \int\int\int_V \left[\left(\bar{\bar{I}} + \frac{1}{k_i^2}\bar{\nabla}\bar{\nabla}\right) \cdot (\bar{\bar{G}}^i)^T\right] \cdot \bar{J} dv' \tag{11}$$

where $k_i^2 = \omega^2 \mu_0 \epsilon_i$. The index i indicates that the above holds in each region (i.e. for $i = 1, 2$).

In (11), $\bar{\bar{G}}^i$ is a dyadic Green's function [14] satisfying the following equation

$$\nabla^2 \bar{\bar{G}}^i + k_i^2 \bar{\bar{G}}^i = -\bar{\bar{I}} \delta(\bar{r} - \bar{r}') \ . \tag{12}$$

where $\bar{\bar{I}}$ is the unit dyadic ($= \hat{x}\hat{x} + \hat{y}\hat{y} + \hat{z}\hat{z}$), $\bar{r}$ is the position vector of a field point anywhere inside the cavity, and $\bar{r}'$ is the position vector of an infinitesimal current source.

Because of the existence of an air/dielectric interface, and the assumption of a unidirectional current, the dyadic Green's function will have the form

$$\bar{\bar{G}}^i = G_{xx}^i \hat{x}\hat{x} + G_{xz}^i \hat{x}\hat{z} \ . \tag{13}$$

The dyadic components of (13) are found by applying appropriate boundary conditions at the walls: $x = 0$, and a ; $y = 0$, and b ; and $z = 0$, c ; and at the air-dielectric interface [8]. These components may be expressed as

$$G_{xx}^{(1)} = \sum_{m=1}^{\infty} \sum_{n=0}^{\infty} A_{mn}^{(1)} \cos k_x x \sin k_y y \sin k_z^{(1)} z \tag{14}$$

$$G_{xz}^{(1)} = \sum_{m=1}^{\infty} \sum_{n=0}^{\infty} B_{mn}^{(1)} \sin k_x x \sin k_y y \cos k_z^{(1)} z \tag{15}$$

$$G_{xx}^{(2)} = \sum_{m=1}^{\infty} \sum_{n=0}^{\infty} A_{mn}^{(2)} \cos k_x x \sin k_y y \sin k_z^{(2)} (z - c) \tag{16}$$

$$G_{xz}^{(2)} = \sum_{m=1}^{\infty} \sum_{n=0}^{\infty} B_{mn}^{(2)} \sin k_x x \sin k_y y \cos k_z^{(2)} (z - c) \tag{17}$$

where

$$k_x = n\pi/a \tag{18}$$

$$k_y = m\pi/b \tag{19}$$

$$k_z^{(1)} = \sqrt{k_1^2 - k_x^2 - k_y^2} \tag{20}$$

$$k_z^{(2)} = \sqrt{k_0^2 - k_x^2 - k_y^2} \tag{21}$$

$$k_1 = \omega\sqrt{\mu_0 \epsilon_1} \tag{22}$$

$$k_0 = \omega\sqrt{\mu_0 \epsilon_0}\,, \tag{23}$$

and

$$A_{mn}^{(1)} = \frac{-\varphi_n \cos k_x x' \sin k_y y' \tan k_z^{(2)}(h-c)}{abd_{1mn} \cos k_z^{(1)} h} \tag{24}$$

$$A_{mn}^{(2)} = \frac{-\varphi_n \cos k_x x' \sin k_y y' \tan k_z^{(1)} h}{abd_{1mn} \cos k_z^{(2)}(h-c)} \tag{25}$$

$$B_{mn}^{(1)} = \frac{-\varphi_n (1-\epsilon_r^*) k_x \cos k_x x' \sin k_y y' \tan k_z^{(1)} h \tan k_z^{(2)}(h-c)}{abd_{1mn} d_{2mn} \cos k_z^{(1)} h} \tag{26}$$

$$B_{mn}^{(2)} = \frac{-\varphi_n (1-\epsilon_r^*) k_x \cos k_x x' \sin k_y y' \tan k_z^{(1)} h \tan k_z^{(2)}(h-c)}{abd_{1mn} d_{2mn} \cos k_z^{(2)}(h-c)} \tag{27}$$

In (24)-(27), ϵ_r^* is the complex dielectric constant of the substrate and

$$\varphi_n = \begin{cases} 2 & \text{for } n = 0 \\ 4 & \text{for } n \neq 0 \end{cases} \tag{28}$$

$$d_{1mn} = k_z^{(2)} \tan k_z^{(1)} h - k_z^{(1)} \tan k_z^{(2)}(h-c) \tag{29}$$

$$d_{2mn} = k_z^{(2)} \epsilon_r^* \tan k_z^{(2)}(h-c) - k_z^{(1)} \tan k_z^{(1)} h\,. \tag{30}$$

In view of (11)-(30), the elements of the impedance matrix may be put in the following form [2]:

$$Z_{qp} = \frac{j\omega\mu_0 K^2 l_x^4}{16ab\sin^2 K l_x} \zeta_q \zeta_p \sum_{n=0}^{NSTOP} \varphi_n \cos k_x x_q \cos k_x x_p \cdot [\,\mathrm{Sinc}\left[\frac{1}{2}(k_x + K) l_x\right] \mathrm{Sinc}\left[\frac{1}{2}(k_x - K) l_x\right]]^2 \, LN(n) \tag{31}$$

[2] The expression given here for the impedance matrix elements, and that given shortly for the excitation vector elements apply to the case of an open-end or series gap. Slight modifications are necessary for analysis of parallel coupled line filters.

with $LN(n)$ given by the series

$$LN(n) = \sum_{m=1}^{MSTOP} L_{mn} \,. \tag{32}$$

The series elements L_{mn} are given by

$$\begin{aligned} L_{mn} &= \frac{\varphi_n[\sin(k_y Y_0) J_0\left(\frac{k_y W}{2}\right)]^2 \tan k_z^{(1)}h \tan k_z^{(2)}(h-c)}{\left[k_z^{(2)} \tan k_z^{(1)}h - k_z^{(1)} \tan k_z^{(2)}(h-c)\right]} \\ &\cdot \frac{\left[k_z^{(2)}\epsilon_r^* \left(1 - \frac{k_z^2}{k_1^2}\right) \tan k_z^{(2)}(h-c) - k_z^{(1)}\left(1 - \frac{k_z^2}{k_0^2}\right) \tan k_z^{(1)}h\right]}{\left[k_z^{(2)}\epsilon_r^* \tan k_z^{(2)}(h-c) - k_z^{(1)} \tan k_z^{(1)}h\right]} , \end{aligned} \tag{33}$$

where Y_0 is the y-coordinate of of the center of the strip, and

$$\mathrm{Sinc}(t) = \begin{cases} \frac{\sin t}{t} & \text{for } t \neq 0 \\ 1 & \text{for } t = 0 \end{cases} \tag{34}$$

$$\zeta_q = \begin{cases} 2 & \text{for } q = 1 \\ 4 & \text{otherwise} \end{cases} \tag{35}$$

$$R_{1n} = \frac{1}{2}(k + k_x)l_x \tag{36}$$

$$R_{2n} = \frac{1}{2}(k - k_x)l_x \,. \tag{37}$$

C. Evaluation of the Excitation Vector Elements

The formulation for the excitation vector elements for the one-port case will now be carried out. The case for two-port excitation is a straightforward extension [8].

To evaluate the excitation vector elements according to (9), we need to find the magnetic field $\bar{H}_q$ and the frill current $\bar{M}_s = M_\phi \hat{\phi}$. An approximate expression for the frill current is given by [9]

$$\bar{M}_s = -\frac{V_0}{\rho \ln\left(\frac{r_b}{r_a}\right)} \hat{\phi} \tag{38}$$

where

V_0 is the complex voltage applied by the coaxial line at the feed point

r_b is the radius of the coaxial feed's outer conductor

r_a is the radius of the coaxial feed's inner conductor

ρ, ϕ are cylindrical coordinates referenced to the feed's center.

Substituting from (38) into (9) yields (with $ds = \rho d\rho d\phi$)

$$\begin{aligned} V_q &= -\frac{V_0}{\ln\left(\frac{r_b}{r_a}\right)} \int\int_{S_f} H^i_{q\phi}(x=0) d\rho d\phi \\ &= -\frac{V_0}{\ln\left(\frac{r_b}{r_a}\right)} \left[\int\int_{S_f^{(1)}} H^{(1)}_{q\phi}(x=0) d\rho d\phi + \int\int_{S_f^{(2)}} H^{(2)}_{q\phi}(x=0) d\rho d\phi\right] \end{aligned} \quad (39)$$

where

$S_f^{(1)}$ is the portion of the feed surface below the substrate/air interface ($z'' = \rho \sin\phi \leq -t$)

$S_f^{(2)}$ is the portion of the feed surface above the substrate ($z'' = \rho \sin\phi \geq -t$)

$H^{(1)}_{q\phi}(x=0)$ and $H^{(2)}_{q\phi}(x=0)$ are the $\hat{\phi}$ components of the magnetic field, in regions 1 and 2 respectively, evaluated on the plane of the aperture.

After solving for the magnetic fields $H^i_{q\phi}(x=0)$ and substituting the resulting expressions into (39), the following formulation is produced for excitation vector elements:

$$\begin{aligned} V_q &= \frac{-V_0 \zeta_q K l_x^2}{\ln\left(\frac{r_b}{r_a}\right) 4ab \sin K l_x} \sum_{n=0}^{NSTOP} \cos k_x x_q \\ &\quad \cdot \mathrm{Sinc}\left[\frac{1}{2}(k_x + K) l_x\right] \mathrm{Sinc}\left[\frac{1}{2}(k_x - K) l_x\right] [MN(n)] \end{aligned} \quad (40)$$

where $MN(n)$ is expressed in terms of the series given by

$$MN(n) = \sum_{m=1}^{MSTOP} M_{mn} \,. \tag{41}$$

The series elements M_{mn} are given by the following integral

$$\begin{aligned} M_{mn} &= \int\int_{S_f} \mathcal{M}^i_{mn}\, d\rho\, d\phi \\ &= \int\int_{S_f^{(1)}} \mathcal{M}^{(1)}_{mn}\, d\rho\, d\phi + \int\int_{S_f^{(2)}} \mathcal{M}^{(2)}_{mn}\, d\rho\, d\phi \,. \end{aligned} \tag{42}$$

The above integrations are performed numerically, with the integrands $\mathcal{M}^i_{mn}$ given by

$$\begin{aligned} \mathcal{M}^{(1)}_{mn} &= \cos\phi\, c^{(1)}_{zmn} \cos k_y(\rho\cos\phi + Y_c) \sin k_z^{(1)}(\rho\sin\phi + h_c) \\ &\quad - \sin\phi\, c^{(1)}_{ymn} \sin k_y(\rho\cos\phi + Y_c) \cos k_z^{(1)}(\rho\sin\phi + h_c) \end{aligned} \tag{43}$$

for ρ and ϕ in region 1, and

$$\begin{aligned} \mathcal{M}^{(2)}_{mn} &= \cos\phi\, c^{(2)}_{zmn} \cos k_y(\rho\cos\phi + Y_c) \sin k_z^{(2)}(\rho\sin\phi - c + h_c) \\ &\quad - \sin\phi\, c^{(2)}_{ymn} \sin k_y(\rho\cos\phi + Y_c) \cos k_z^{(2)}(\rho\sin\phi - c + h_c) \,. \end{aligned} \tag{44}$$

for ρ and ϕ in region 2. In (43), and (44) Y_c, and h_c are the the y and z coordinates of the coaxial feed, and

$$\begin{aligned} c^{(1)}_{ymn} &= \frac{c^{(1)}_{zmn}}{k_y d_{2mn}} \Big\{ k_z^{(1)} k_z^{(2)} \epsilon_r^* \tan k_z^{(2)}(h-c) \\ &\quad - \Big[(k_z^{(1)})^2 + k_x^2(1-\epsilon_r^*) \Big] \tan k_z^{(1)} h \Big\} \end{aligned} \tag{45}$$

$$c^{(1)}_{zmn} = \frac{\varphi_n k_y \tan k_z^{(2)}(h-c)}{d_{1mn} \cos k_z^{(1)} h} \sin k_y Y_0\, J_0(k_y \frac{W}{2}) \tag{46}$$

$$\begin{aligned} c^{(2)}_{ymn} &= \frac{c^{(2)}_{zmn}}{k_y d_{2mn}} \Big\{ k_z^{(1)} k_z^{(2)} \tan k_z^{(1)} h \\ &\quad - \Big[(k_z^{(2)})^2 \epsilon_r^* - k_x^2(1-\epsilon_r^*) \Big] \tan k_z^{(2)}(h-c) \Big\} \end{aligned} \tag{47}$$

$$c^{(2)}_{zmn} = \frac{\varphi_n k_y \tan k_z^{(1)} h}{d_{1mn} \cos k_z^{(2)}(h-c)} \sin k_y Y_0\, J_0(k_y \frac{W}{2}) \,. \tag{48}$$

The above outlines the theory for computing the current distribution on the conducting strips of shielded microstrip discontinuities. The next step is to use the current distribution to derive the network parameters of the discontinuity under consideration. However, since the methods used to derive network parameters are described elsewhere [2,8,15], only a brief summary is given in Appendix I.

The theoretical method developed above has been implemented in a Fortran program. The remainder of the paper addresses computational aspects of the solution for the current distribution and discontinuity network parameters.

III. COMPUTATION OF CURRENT DISTRIBUTION

To gain insight into the nature of the computations, we will now examine plots of a typical impedance matrix, excitation vector, and current distribution for an open-ended microstrip line.

Figure 5 shows the amplitude distribution of a typical impedance matrix. It is seen that the amplitude of the diagonal elements is the greatest and it tapers off uniformly as one moves away from the diagonal. Another observation is that the matrix is symmetric such that $Z_{qp} = Z_{pq}$ for any p and q, which is expected from (31). When the impedance matrix of Figure 5 is inverted, the amplitude distribution is as shown in Figure 6. The inverted impedance matrix shows a sinusoidal shape for any given row or column.

Figure 7 shows the amplitude distribution for the excitation vector. The amplitude is highest over the subsection closest to the feed then tapers off smoothly. In contrast, the excitation vector for the gap generator method has only one non-zero value, at the position of the source.

Multiplying the inverted impedance matrix by the excitation vector of Figure 7 yields the current distribution of Figure 8. It can be seen that the shape of the current is similar to that exhibited by the first column of the inverted impedance matrix. This is not surprising given the shape of the excitation vector.

IV. CONVERGENCE OF Z_{qp} AND V_q

In the expressions of (31), and (40) for the impedance matrix and excitation vector elements, the summations over m and n are theoretically infinite. The number of elements included in these series depends on the convergence behavior of Z_{qp} and V_q with the summation indices.

As seen from (31), the convergence of the impedance matrix is described mainly by the convergence of $LN(n)$. Figure 9 shows the typical variation of $LN(n)$ with m and n. Most of the contributions from $LN(n)$ to the impedance matrix are concentrated in the first several n values. The convergence over m is good, and it appears that performing the computations out to $m = 200$ may be sufficient. Note, however, that the allowable truncation points for the summations over m and n vary with the geometry. The values quoted here are for illustration purposes only.

The computation of Z_{qp} over n is illustrated for a typical impedance matrix in Figure 10. Shown is the convergence behavior for one row ($q = 32$) of the 64 x 64 element impedance matrix of Figure 5. This behavior is representative of that for any row. After only a few terms the diagonal element ($p = q = 32$) rises above the others, and after adding 100 terms the amplitude distribution is well formed.

Similar conclusions can be drawn for the convergence of the excitation vector elements with respect to the summation indices m and n.

V. CONVERGENCE OF NETWORK PARAMETERS

The convergence behavior of the elements of the impedance matrix and excitation vector is important to examine, yet the more relevant question remains: how are the final results affected by various convergence related parameters?

To answer this question, a series of numerical experiments were carried out, and the main results are presented here. As illustrated in Figure 4, an open end discontinuity can be represented by either an effective length extension L_{eff} or an equivalent capacitance c_{op}. The microstrip effective dielectric constant ϵ_{eff} is calculated from the distance between two adjacent maxima of the open-end current distribution (Figure 8).

The experiments investigated the convergence behavior of L_{eff} and ϵ_{eff} with respect to the sampling rate N_x $(= 1/l_x)$, and the truncation points $NSTOP$, $MSTOP$ for the summations over n and m respectively. These numerical experiments have been grouped into three separate categories each exploring a different aspect of the convergence behavior [3].

[3] The parameters used for the plots shown in this section are the following: $\epsilon_r = 9.7, W = h = .025'', a = 3.5'', b = c = .25'', f = 18\text{GHz}$.

A. Effect of K-value

Using the program mentioned above, data was generated to plot L_{eff} and ϵ_{eff} versus N_x for several different values of the normalized scaling factor K of (5) and (6). Figure 11a shows the convergence behavior of L_{eff} for a typical case. It is seen that a relatively flat convergence region exists for all the K-values between about 40 and 100 samples per wavelength. Outside this region the convergence behavior depends on K.

At first glance, it appears that the best convergence is achieved for higher K-values (e.g. $K = 8\pi$); however, quite the opposite conclusion results from examining the ϵ_{eff} computation. As can be seen from Figure 11b, the best convergence for ϵ_{eff} is obtained for low K-values.

Based on these and other observations [8], it was determined that a value of $K = 2\pi$ gives the best overall convergence behavior for the L_{eff} and ϵ_{eff} computations.

B. L_{eff}, ϵ_{eff} Convergence on n and m

To investigate the convergence of the network parameter computations with the summation index n, several program runs were executed for different values of $NSTOP$, with $MSTOP$ fixed at 1000. Data was generated to plot L_{eff} and ϵ_{eff} versus n for several l_x values. Figure 12a shows that for all the l_x values, good convergence on n is achieved after 500 terms. The same can be said for the convergence of ϵ_{eff}.

In examining the convergence behavior with n it was found that, for a given subsection length l_x, cavity length a, and truncation point $NSTOP$, a maximum sampling limit exists beyond which the computed current becomes completely erratic. This is called the erratic current condition and is given by the following simple relationship:

$$NSTOP * l_x < a \quad \text{or} \quad N_x > \frac{NSTOP}{a}. \tag{49}$$

Outside of the region defined by (49), the numerical solution appears to be completely stable. To investigate the convergence behavior with respect to the summation index m, $NSTOP$ was fixed at 500, and the program was run for different values of $MSTOP$. Figure 12b shows that L_{eff} converges well on m after about 500 terms. The convergence behavior of ϵ_{eff} on m, was found to be similar to that for L_{eff}.

C. Optimum Sampling Range

In this last numerical experiment, the effect of varying l_x on the numerical accuracy of the matrix solution was examined. This was done by studying the variation of the matrix condition number [16], with respect to l_x for a fixed matrix size . After studying several cases it was found that an optimum sampling range, may be defined by the following choice of subsection length l_x

$$\frac{1.5a}{NSTOP} \leq l_x \leq \frac{4a}{NSTOP}. \tag{50}$$

Sampling within this range automatically avoids the erratic current condition and provides the best accuracy in the matrix solution, and also in the solution for network parameters.

To support this last claim, consider the plot of Figure 13. It is seen that the optimum sampling region specified by (50) coincides directly with the flat convergence region for the L_{eff} calculation. This consistency between the optimum sampling region and the flat convergence region for the L_{eff} calculation was observed in all the cases examined [8].

VI. SUMMARY

In the theoretical part of the presented research, a method of moments formulation for the shielded microstrip problem was derived based on a more realistic excitation model than used with previous techniques. The formulation follows from the reciprocity theorem, with the use of a frill current model for the coaxial feed.

Computational considerations for implementing the theoretical solution were studied extensively. Several numerical experiments were presented that explored the convergence and the stability of the solution. Most significantly, it was found that an erratic current condition and an optimum sampling range exist; both of these are given by very simple relationships.

APPENDIX I

A. One-Port Network Parameters (Open-End Discontinuity)

The effective length extension (Figure 4) for an open-end discontinuity is given by

$$L_{eff} = \frac{\lambda_g}{4} - d_{max} \, . \tag{51}$$

where d_{max} is the distance from the end of the line to a current maximum.

The normalized equivalent capacitance (Figure 4) can be expressed as

$$c_{op} = \frac{\sin 2\beta_g d_{max}}{\omega(1 - \cos 2\beta_g d_{max})} = \frac{\sin 2\beta_g L_{eff}}{\omega(1 + \cos 2\beta_g L_{eff})} \, . \tag{52}$$

In the above, β_g is the phase constant of microstrip transmission line.

B. Two-Port Network Parameters (Gap discontinuity, Coupled Line Filters)

For the computation of two-port network parameters, the strip geometry is assumed to be physically symmetric with respect to the center of the cavity (in both the x and y directions of Figure 1). The network parameters are determined by analyzing the currents from the even and odd mode excitations as discussed in [2,8,15].

The normalized impedance parameters are given by according to

$$z_{11} = \frac{z_{IN}^e + z_{IN}^o}{2} \tag{53}$$

$$z_{12} = \frac{z_{IN}^o - z_{IN}^e}{2} \, . \tag{54}$$

where z_{IN}^e and z_{IN}^o are the input impedances of the even and odd mode networks. The scattering parameters for the network may be derived using the following relations:

$$S_{11} = S_{22} = \frac{z_{11}^2 - 1 - z_{12}^2}{D} \quad (55)$$

$$S_{12} = S_{21} = \frac{2z_{12}}{D} \quad (56)$$

where

$$D = z_{11}^2 + 2z_{11} - z_{12}^2 \quad (57)$$

ACKNOWLEDGEMENTS

The authors thank Mr. Ed Watkins, Mr. Jim Schellenberg, and Mr. Marcel Tutt for their contributions to this work. This work was primarily sponsored by The National Science Foundation (Contract. No. ECS -8602530). Partial sponsorship was also provided by the Army Research Office (Contract No. DAAL03-87-K-0088) and the Microwave Products Division of Hughes Aircraft Co.

References

[1] R.H. Jansen and N.H.L. Koster, "Accurate Results on the End Effect of Single and Coupled Lines for Use in Microwave Circuit Design", *A.E.U.*, vol. 34, pp 453-459, 1980.

[2] P.B. Katehi and N.G. Alexopoulos,"Frequency-Dependent Characteristics of Microstrip Discontinuities in Millimeter-wave Integrated Circuits", *IEEE*

Trans. Microwave Theory Tech., vol. MTT-33 No. 10, pp. 1029-1035, Oct. 1985.

[3] R.H. Jansen, and W. Wertgen, "Modular Source-Type 3D Analysis of Scattering Parameters for General Discontinuities, Components and Coupling Effects in (M)MICs", *Proc.* 17^{th} *Eur. Microwave Conf.(Rome) 1987*, pp. 427-432.

[4] J.C. Rautio, "An Electromagnetic Time-Harmonic Analysis of Shielded Microstrip Circuits", *IEEE Trans. Microwave Theory Tech.*, vol. MTT-35, pp726-729, 1987.

[5] R.H. Jansen, "Hybrid Mode Analysis of End Effects of Planar Microwave and Millimeter-Wave Transmission Lines", *Proc. Inst. Elec. Eng.*, vol 128, pp. 77-86, Apr. 1981.

[6] T. Itoh,"Analysis of Microstrip Resonators", *IEEE Trans. Microwave Theory Tech.*, vol MTT-22, pp 946-951, 1974.

[7] L.P. Dunleavy and P.B. Katehi, "Shielding Effects in Microstrip Discontinuities", Accepted for publication in *IEEE Trans. Microwave Theory Tech.*

[8] L.P. Dunleavy, "Discontinuity Characterization in Shielded Microstrip: A Theoretical and Experimental Study", Ph.D. dissertation, University of Michigan, April 1988.

[9] R.F. Harrington, *Time-Harmonic Electromagnetic Fields*, McGraw Hill 1961, pp.111-112.

[10] C. Chi and N.G. Alexopoulos, "Radiation by a Probe Through a Substrate", *IEEE Trans. Antennas Propagat.*, vol. AP-34, Sept. 1986, pp 1080-1091.

[11] N.N. Wang, J.H. Richmond and M.C. Gilreath "Sinusoidal Reaction Formulation for Radiation and Scattering from Conducting Surfaces", *IEEE Trans. Antennas Propagat.*, vol. AP-23, May 1975, pp 376-382.

[12] E.H. Newman and D.H. Pozar, "Electromagnetic Modeling of Composite Wire and Surface Geometries", *IEEE Trans. Antennas Propagat.*, vol. AP-26, Nov. 1978, pp 784-789.

[13] J.C. Maxwell, *A Treatise on Electricity and Magnetism* 3rd. ed., vol. 1,New York: Dover 1954 pp 296-297.

[14] C.T. Tai, *Dyadic Green's Functions in Electromagnetic Theory* , Intext Educational Publishers 1971.

[15] P.B. Katehi, "Radiation Losses in MM-Wave Open Microstrip Filters," *Electromagnetics* 7, pp137-152, 1987.

[16] G.H. Golub and C.F. Van Loan, *Matrix Computations*, John Hopkins University Press, 1983, pp26-27.

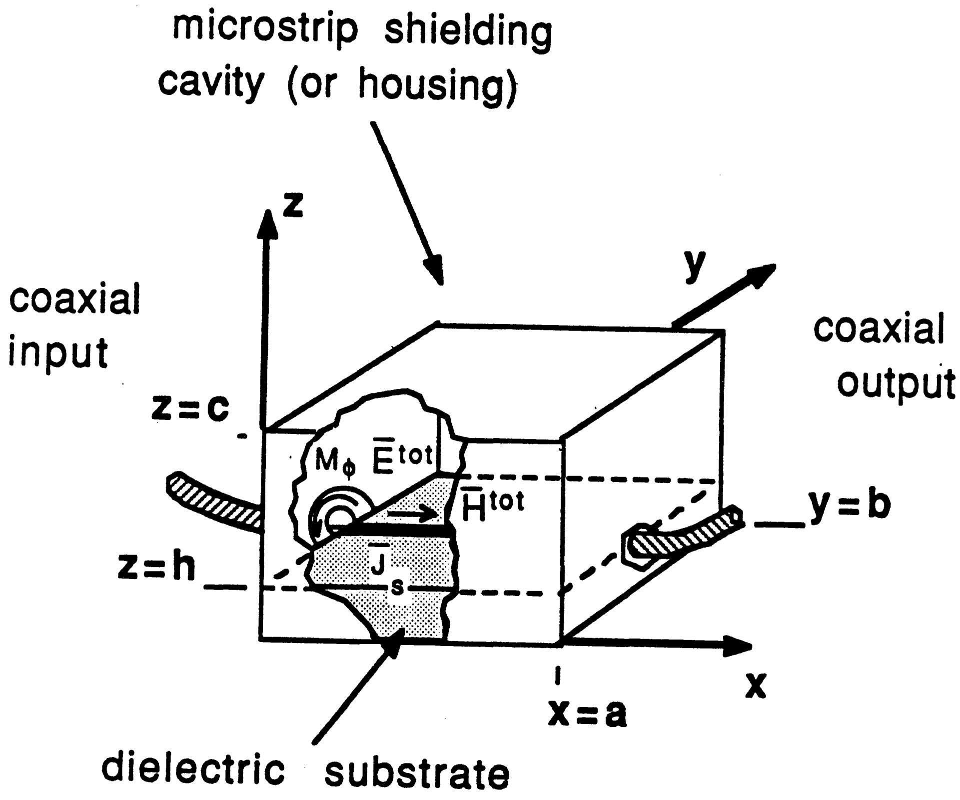

Figure 1: Basic shielded microstrip geometry.

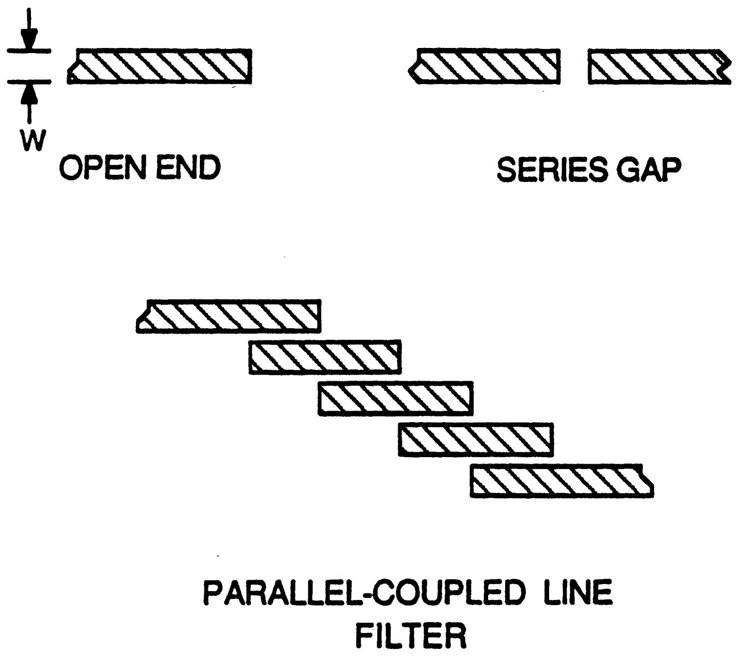

Figure 2: Discontinuity structures addressed in the present research.

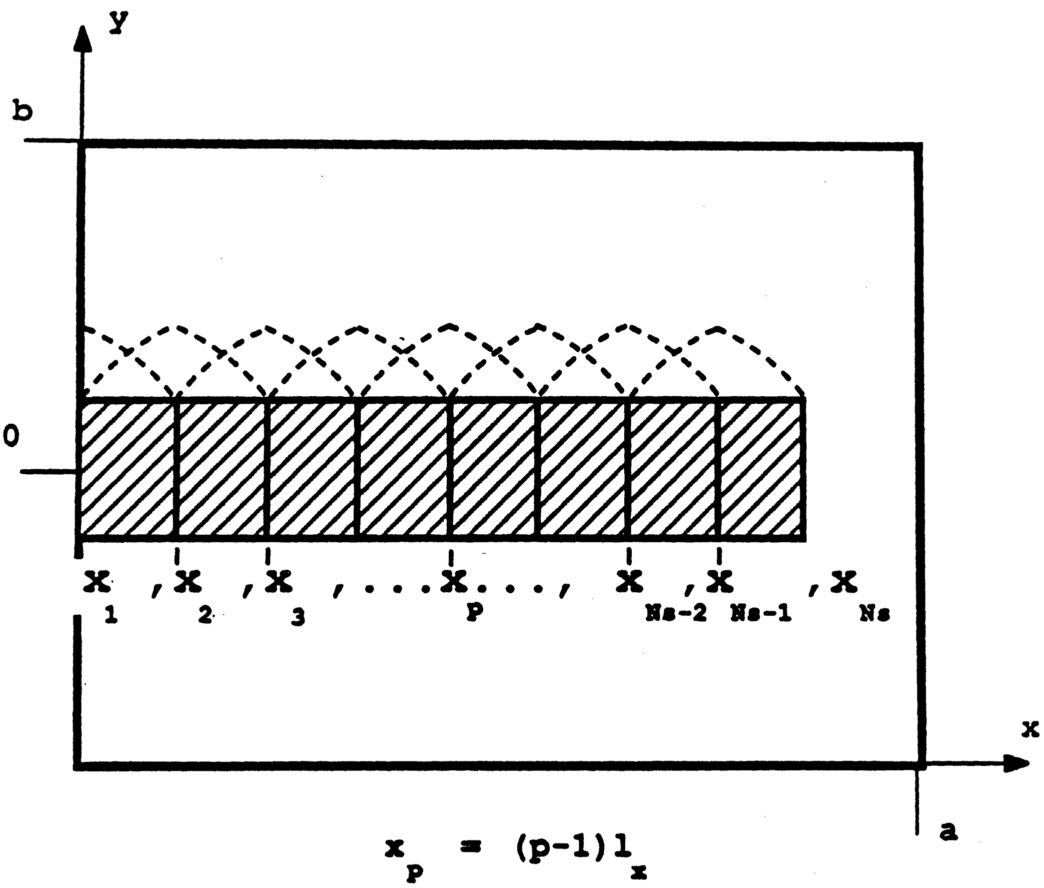

Figure 3: Strip geometry for expansion of longitudinal current into overlapping sinusoidal basis functions.

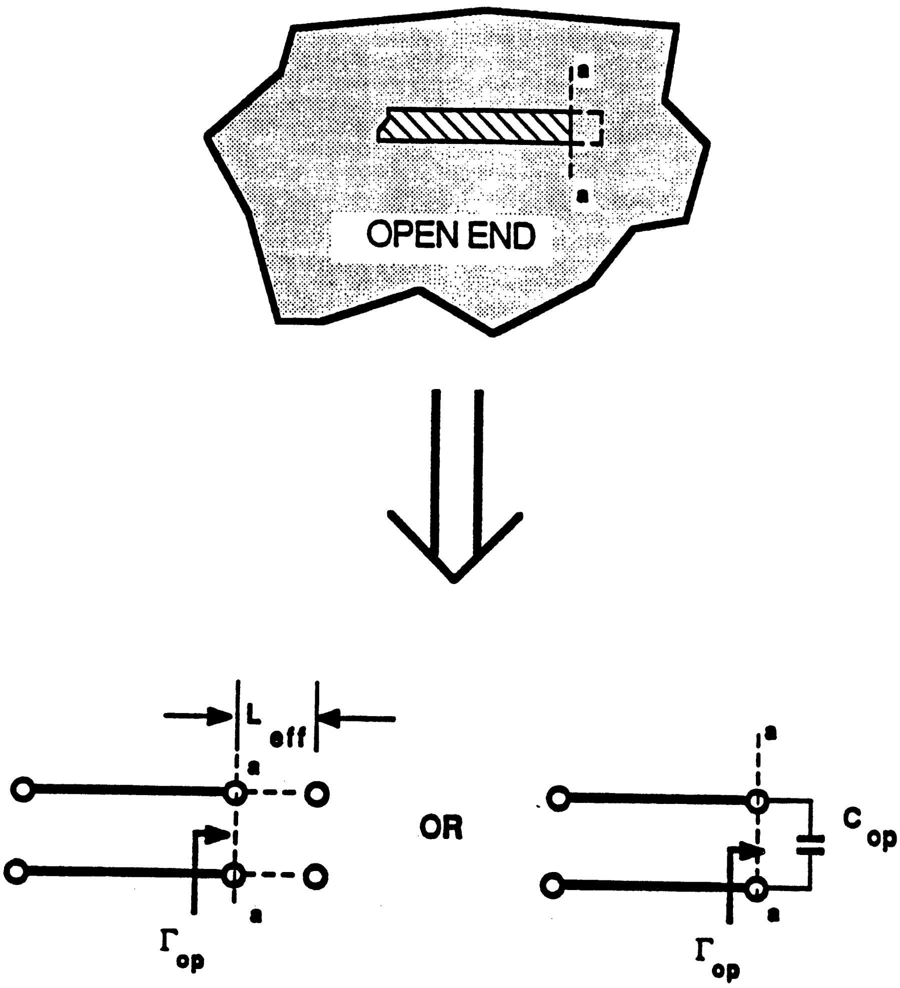

Figure 4: Representation of a shielded microstrip open-end.

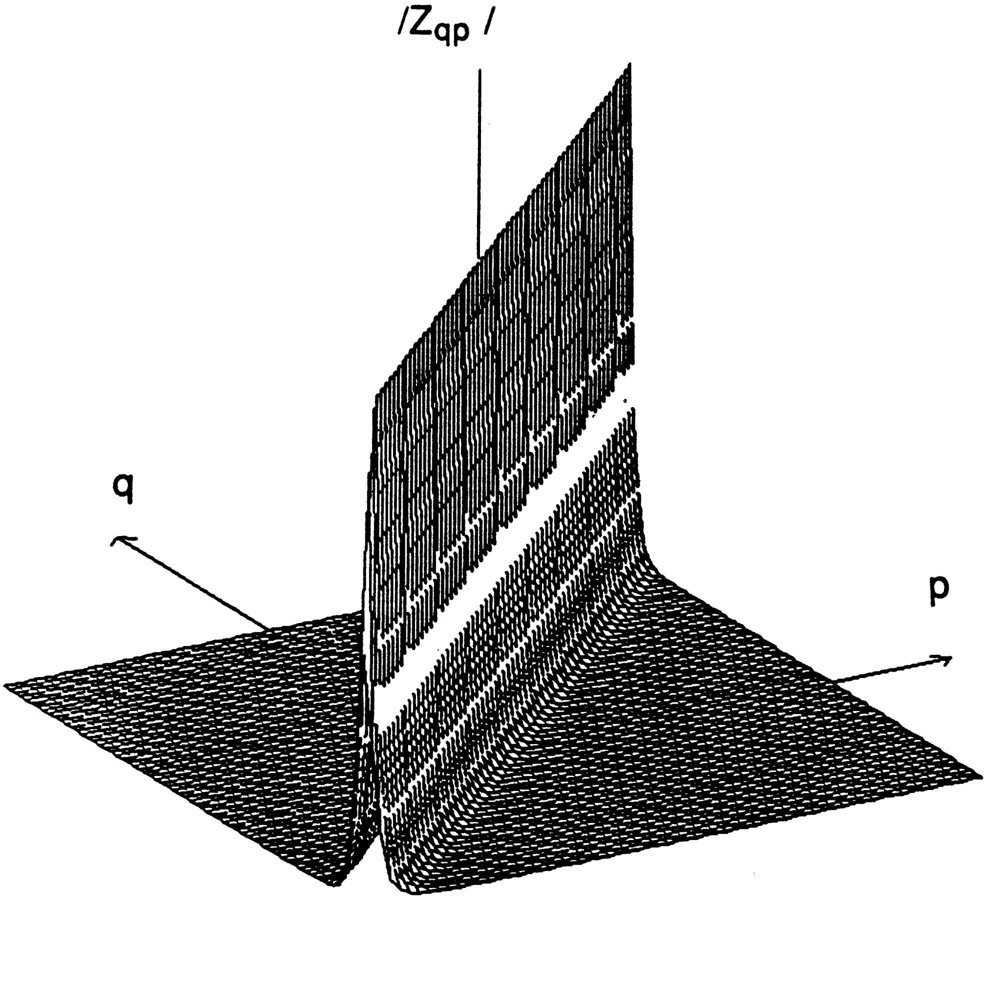

Figure 5: Impedance matrix for an open-end.

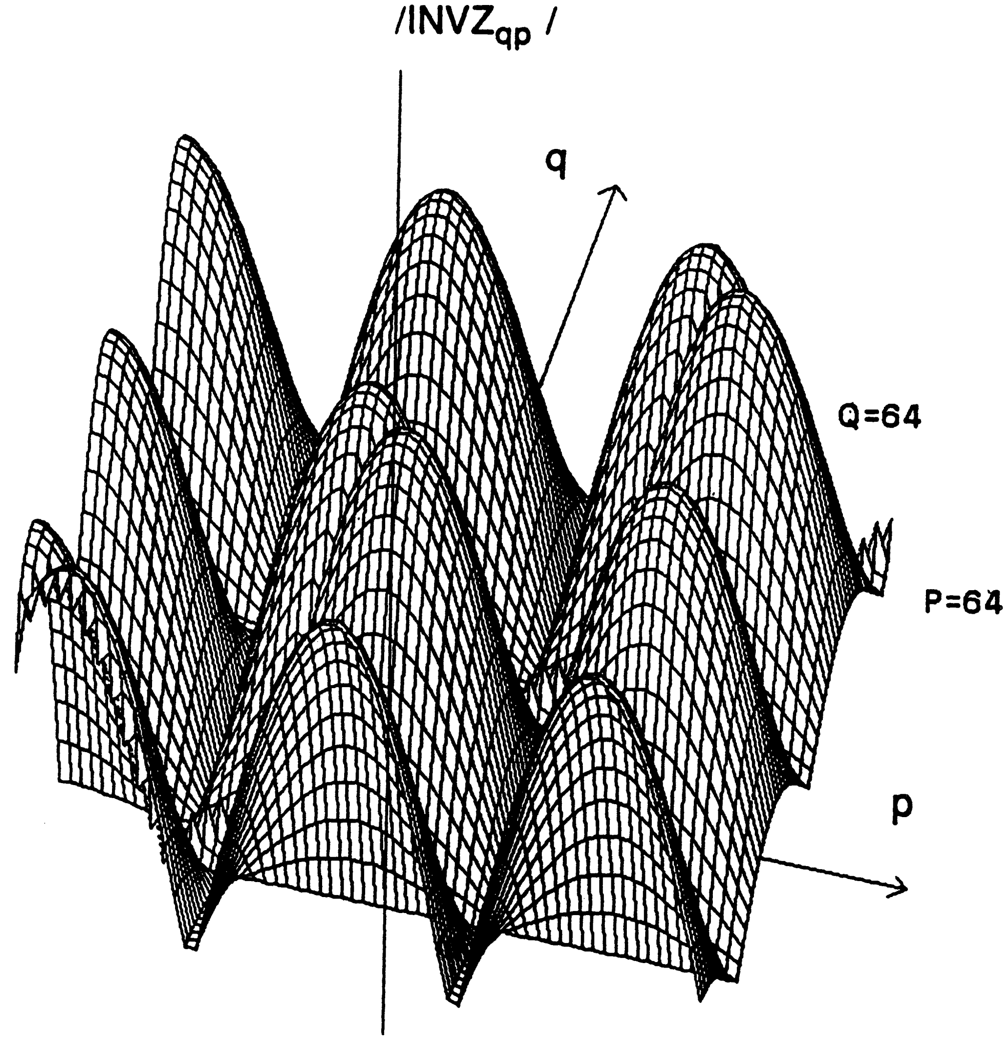

Figure 6: Inverted impedance matrix for an open-end. The sinusoidal shape of any row or column corresponds to the shape of the current distribution.

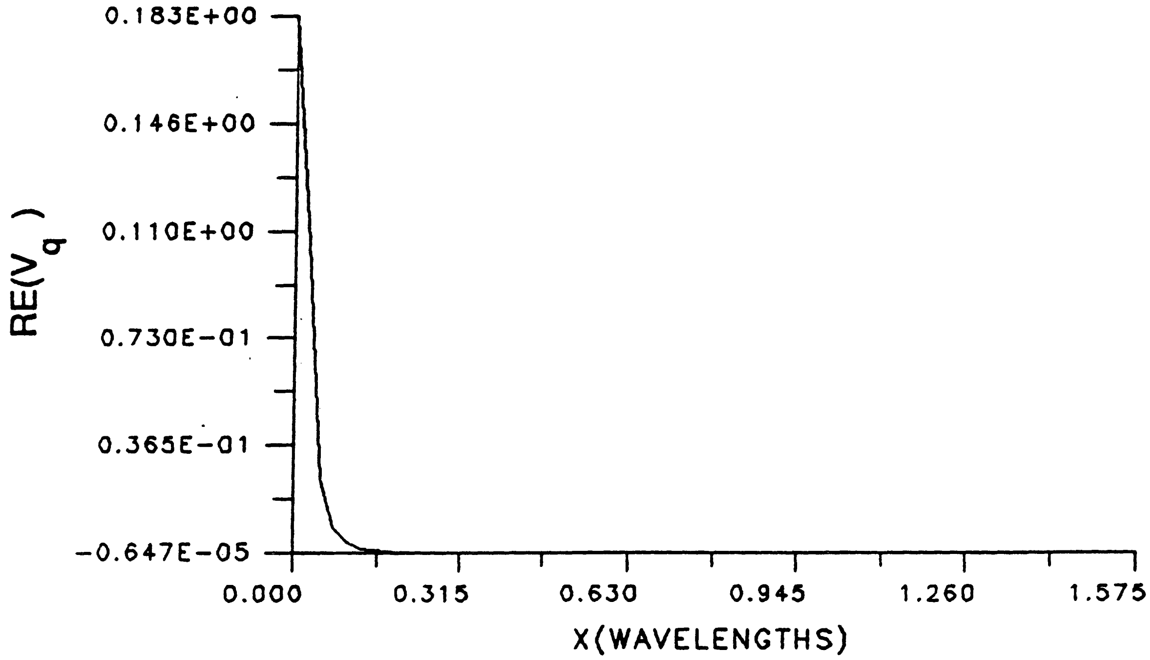

Figure 7: Amplitude distribution of the excitation vector.

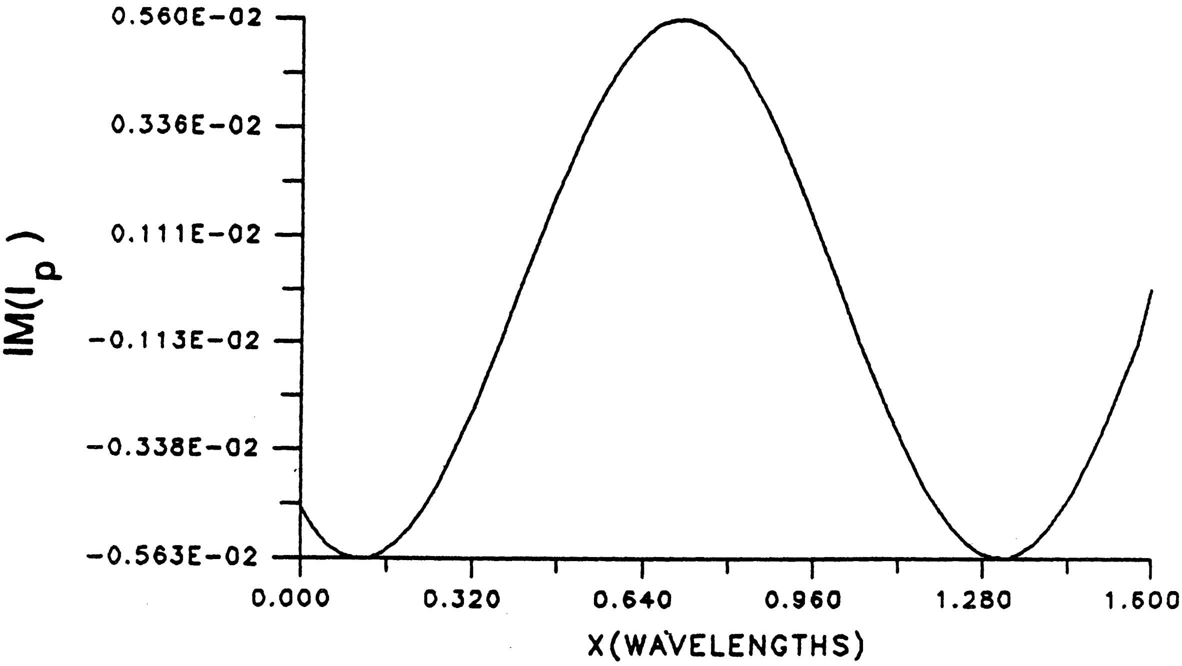

Figure 8: Imaginary part of the current distribution for an open-ended line.

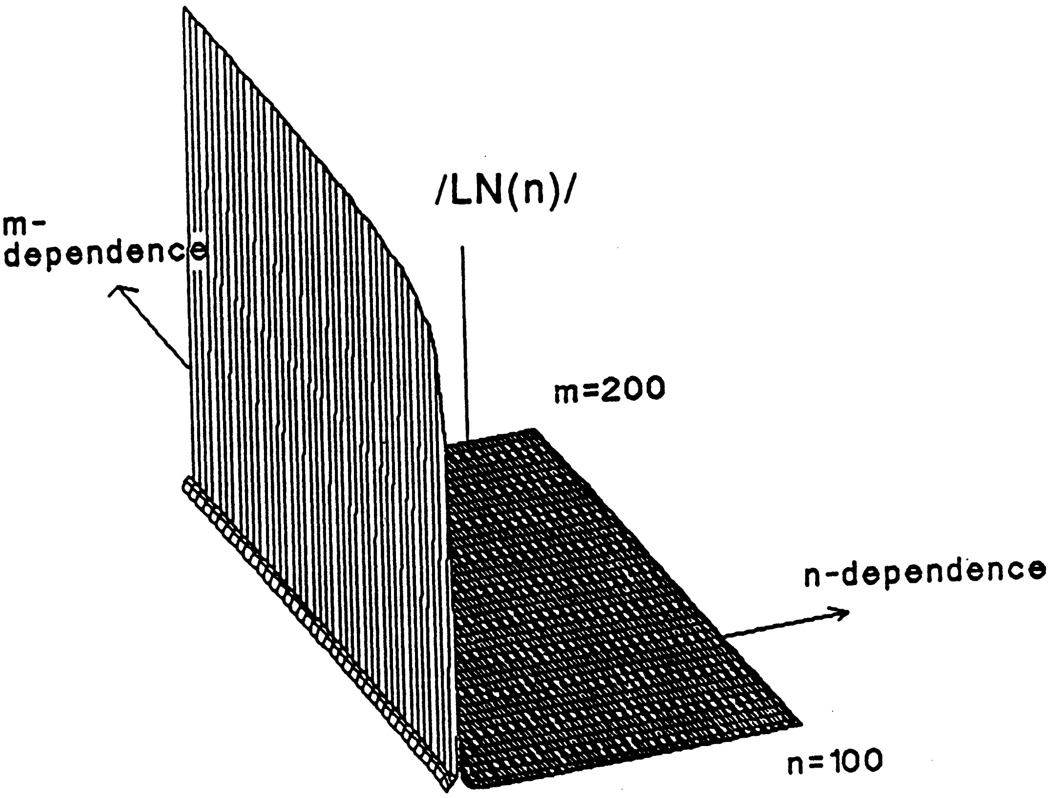

Figure 9: Three dimensional plot of $LN(n)$ versus summation indices.

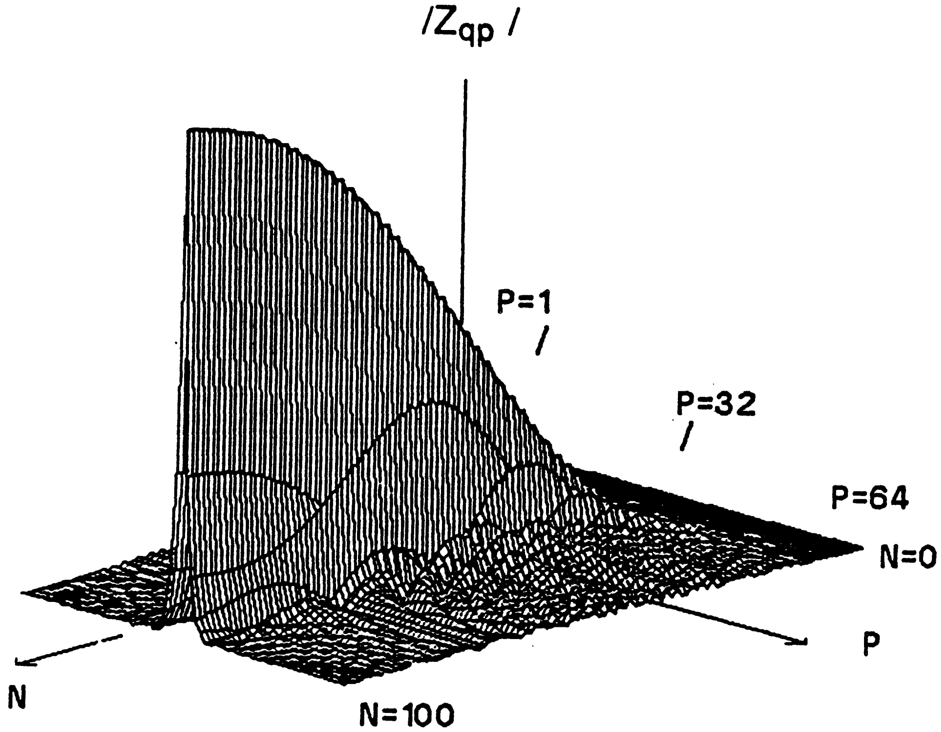

Figure 10: Convergence of impedance matrix elements. A row (q = 32) of the matrix is seen to be well formed after adding 100 terms on n.

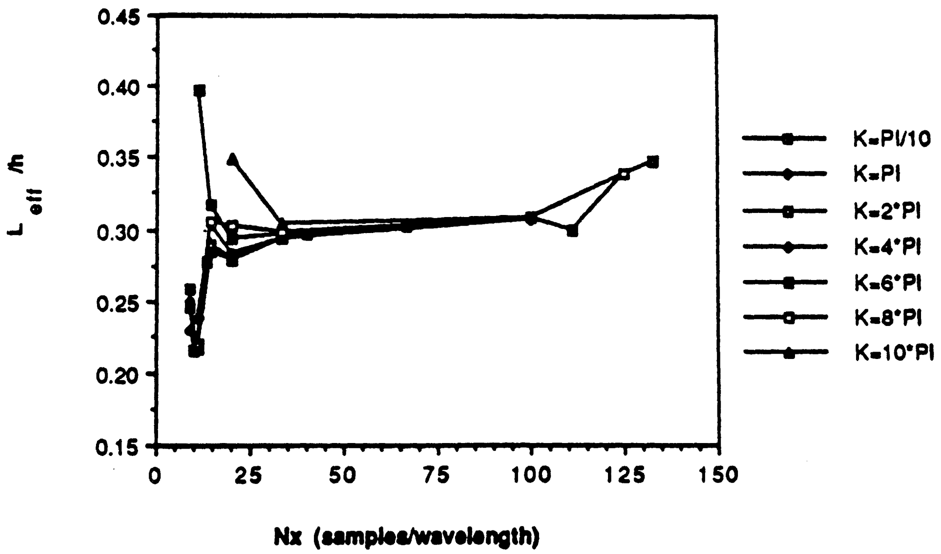

a. L_{eff} versus sampling. A flat convergence region exists for all values of K considered.

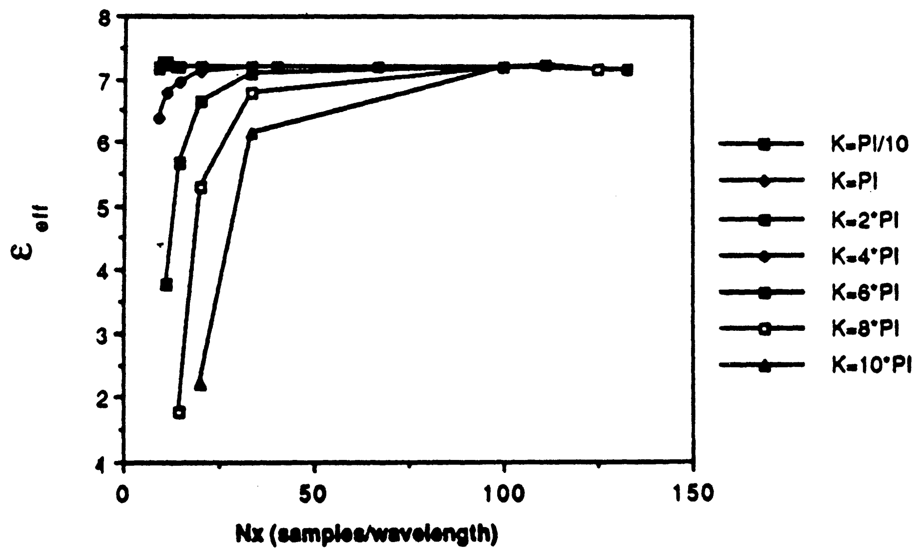

b. ϵ_{eff} versus sampling. Convergence is better for low K-values.

Figure 11: Convergence of L_{eff} and ϵ_{eff} versus sampling.

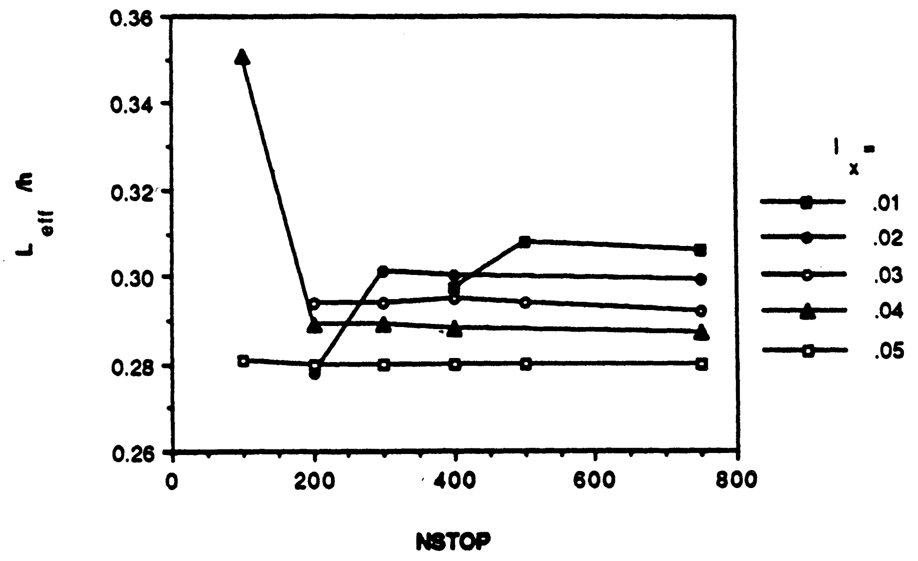

a. Convergence of L_{eff} on n.

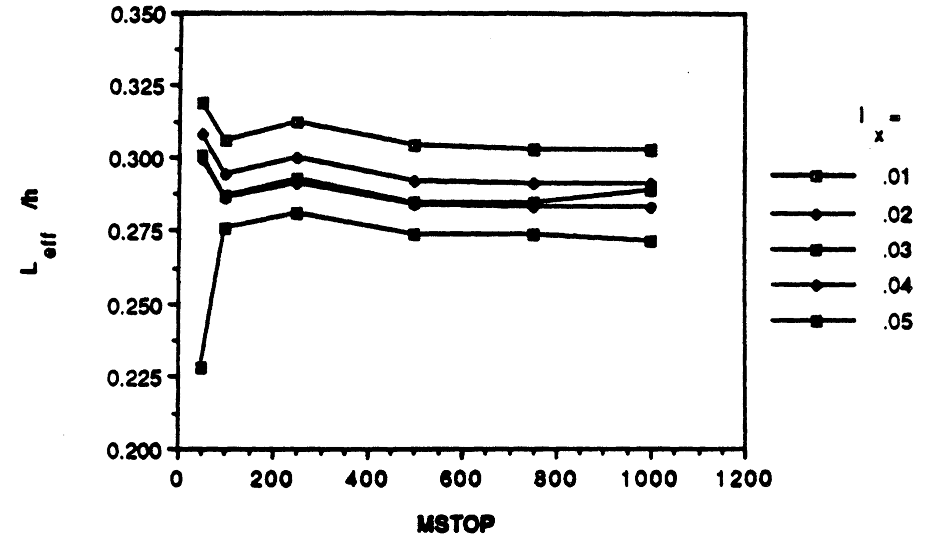

b. Convergence of L_{eff} on m.

Figure 12: Convergence of L_{eff} on n and m.

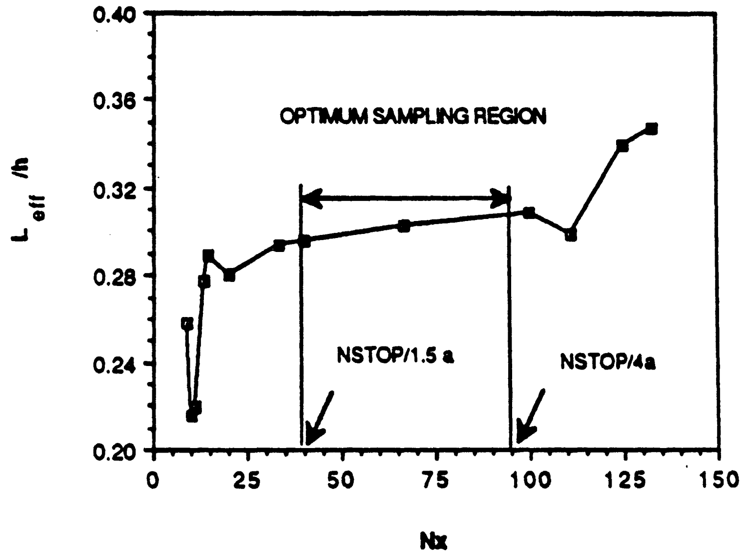

Figure 13: Illustration of optimum sampling range which is seen to correspond directly with the flat convergence region for the L_{eff} computation.

DISCONTINUITY CHARACTERIZATION IN SHIELDED MICROSTRIP: A THEORETICAL AND EXPERIMENTAL STUDY

by

Lawrence Patrick Dunleavy

A dissertation submitted in partial fulfillment
of the requirements for the degree of
Doctor of Philosophy
(Electrical Engineering)
in The University of Michigan
1988

Doctoral Committee:

Assistant Professor Pisti B. Katehi, Chairperson
Professor George I. Haddad
Associate Professor William R. Martin
Professor Dimitris Pavlidis
Associate Research Scientist Jack R. East

ABSTRACT

DISCONTINUITY CHARACTERIZATION IN SHIELDED MICROSTRIP: A THEORETICAL AND EXPERIMENTAL STUDY

by
Lawrence Patrick Dunleavy

Chairperson: Pisti B. Katehi

The need for more accurate modeling of microstrip discontinuity structures has become apparent with the advent of Monolithic Microwave Integrated Circuits (MMICs) as well as the push to higher millimeter-wave frequencies. The development of accurate microstrip discontinuity models, based on full-wave analyses, is key to improving circuit simulations and reducing lengthy design cycle costs. In most applications, radiation and electromagnetic interference are avoided by enclosing microstrip circuitry in a shielding cavity (or housing). The effects of the shielding can be significant, even when the top of the cavity is several substrate heights above the circuitry. Shielding effects are not adequately accounted for in the discontinuity models used in most microwave CAD software.

A new integral equation method is described for the full-wave analysis of shielded microstrip discontinuities. The integral equation is derived by an application of the reciprocity theorem and then solved by the method of moments. Two types of circuit excitation are considered: a coaxial excitation method developed here, and the widely used gap generator method. Several numerical experiments are presented that lead to very useful relationships governing the convergence and stability of the method of moments analysis of this problem. Most significantly, an optimum sampling range is defined that provides the most accuracy in the matrix solution.

Numerical and measured results are presented for microstrip effective dielectric constants, and the network parameters of open-end and series gap discontinuities, and two coupled line filters. For the effective dielectric constant, as the size of the shielding cavity is reduced, the difference between the numerical and CAD package results becomes significant. Conversely, for an open-end discontinuity, choosing a smaller shielding cavity extends the frequency range over which the equivalent capacitance is relatively constant. The numerical results are in excellent agreement with measured data obtained using a variation of the thru-short-delay de-embedding technique. A case in point is that of a four resonator coupled line filter. The numerical results accurately predict the filter performance in every way, whereas discrepancies are observed in the CAD model predictions. It is demonstrated that these discrepancies are mainly due to shielding effects.

May the road rise
to meet you.
May the wind be always
at your back.
May the sun shine warm
upon your face,
And the rains fall soft
upon your fields.
And until we meet again
May God hold you
in the palm of his hand.

An old Irish benediction

To my parents and to the memory of my brother Michael

ACKNOWLEDGEMENTS

I have many to thank for helping me along the Ph.D. journey. First I thank my advisor, her constant optimism and good nature greatly eased the difficult times. I also extend my sincere gratitude to the other members of my dissertation committee for their time and their consideration.

There are several other professors whose inspiration and advice have left their mark on my career. Among these are Dr. T.B.A. Senior, Dr. Chen-To Tai (my favorite tennis rival), Dr. Val Liepa, and Dr. Emmett Leith. I also thank Dr. W.A. Fordon and Dr. Jon Soper of Michigan Technological University.

I am indebted to my friends and colleagues who contributed in various ways to this work especially Mlle. Emilie van Deventer, Mr. Tim Peters , Mr. Marcel Tutt, Mr. Mike Dunn, Ms. Jeanette Vecchio, and Mr. Jim Morgan. The insightful conversations held with Dr. Tom Willis, Mr. Norm VandenBerg, and Mr. Tom Livernois helped form some of the ideas presented. I also thank Mr. Jim Schellenberg, Mr. Ed Watkins and Mr. Doug Dunn of Hughes Aircraft Company for their inputs to the experimental part of this work.

Finally, I thank my family. Though they openly feared I would be a professional student for life, my parents, brothers, sisters, and other relatives always gave love, support, and encouragement. For this, I also extend my appreciation to my friends The Buschellmans, The van Deventers, The Heeremas, and The Linquists.

This work was sponsored in part through a Howard Hughes Doctoral Fellowship. Additional support was provided by The National Science Foundation (Contract. No. ECS-8602530) and the Army Research Office (Contract No. DAAL03-87-K-0088).

TABLE OF CONTENTS

LIST OF FIGURES

Figure

LIST OF TABLES

Table

LIST OF APPENDICES

LIST OF SYMBOLS

a = Dimension of cavity along longitudinal (x) direction of microstrip

$\bar{A}^i$ = Magnetic vector potential

$A_{mn}^{(i)}$ = Complex coefficients for series representation for $G_{xx}^{(i)}$

b = Dimension of cavity along transverse (y) direction of microstrip

$B_{mn}^{(i)}$ = Complex coefficients for series representation for $G_{zz}^{(i)}$

c = Dimension of cavity along direction perpendicular to substrate (z-direction)

c'' = Distance from the center of the feed to the top of the cavity ($c'' = c - h_c$)

c_{nq} = Variable multiplier function of n and q used to simplify expressions for magnetic field $\bar{H}_q$ at coaxial aperture

c_{op} = Normalized equivalent capacitance for open end discontinuity

$c_{ymn}^{(i)}$ = Complex coefficients associated with the y-component of the magnetic field $\bar{H}_q^{(i)}$

$c_{zmn}^{(i)}$ = Complex coefficients associated with the z-component of the magnetic field $\bar{H}_q^{(i)}$

d_{1mn} = First denominator function of complex Green's function coefficients

d_{2mn} = Second denominator function of complex Green's function coefficients

$\bar{E}^i$ = Electric field in the i^{th} region of the cavity

$\bar{E}_q$ = Electric field associated with the test current $\bar{J}_q$

E_{qx} = x-component of the electric field due to the test source $\bar{J}_q$ evaluated at the substrate/air interface

$\bar{E}^{tot}$ = Total electric field inside shielding cavity

f = Frequency of operation (Hz)

f = Cut-off frequency for non-evanescent waveguide modes (GHz)

f_{mn} = Numerator function used in expression for Γ_{xx}

$\bar{\bar{G}}^i$ = Dyadic Green's function of i^{th} region

$G^{(i)}_{xx}$ = xx- component of dyadic Green's in region i

$G^{(i)}_{xz}$ = xz- component of dyadic Green's in region i

h = Thickness of microstrip substrate

h_c = z-coordinate of center of coaxial feed

$\bar{H}^i$ = Magnetic field in i^{th} region of cavity

$\bar{H}_q$ = Magnetic field associated with the test current $\bar{J}_q$

H_{q0} = Common variable multiplier function of q used to simplify expressions for magnetic field $\bar{H}_q$ at coaxial aperture.

$\bar{H}_{qt}$ = Projection of magnetic field onto the plane of the feed aperture

$[\mathbf{I}]$ = Unknown current vector comprised of complex coefficients for current

$[\mathbf{I}_d]$ = Unknown current vector for general dual excitation

$[\mathbf{I}_e]$ = Unknown current vector for even excitation

$[\mathbf{I}_o]$ = Unknown current vector for odd excitation

I_p = Complex coefficients current expansion into series of basis functions (= components of I).

$\mathcal{I}_{qmn}$ = Surface integral encountered in the evaluation of E_{qx}

$\bar{J}$ = Electric current distribution in cavity

$\bar{J}_q$ = Test current source (weighting function in method of moments)

$\bar{J}_s$ = Surface current distribution on microstrip conductors

k_i = Complex wave number in region i

k_x = Eigenvalues for the x-variation of the Green's function ($= \frac{n\pi}{a}$)

k_y = Eigenvalues for the y-variation of the Green's function ($= \frac{m\pi}{b}$)

$k_z^{(i)}$ = Eigenvalues for the z-variation of the Green's function in region i

K = Wave number used in the sinusoidal subsectional expansion of the current (equal to the real part of the wave number in the dielectric region)

l_x = Length of each subsection

L_1 = Length of input uniform line section section for series gap or filter

L_{eff} = Effective length extension for open end discontinuity

L_{in} = Length of the microstrip line in inches (for an open end or thru line).

L' = Normalized length of the microstip line ($=L_{in}/\lambda_d$)

L_{mn} = mn^{th} term of series used to compute $LN(n)$

$LN(n)$ = Storage vector used in computation of the impedance matrix

M_{mn} = mn^{th} term of series used to compute $MN(n)$

$\mathcal{M}^{i}_{mn}$ = Integrand for numerical integration performed to compute M_{mn}

$MN(n)$ = Storage vector used in computation of the impedance matrix

$\bar{M}_s$ = Magnetic frill current existing over aperture of coaxial feed

$\bar{M}_{sl}$ = Magnetic frill current existing over aperture of coaxial feed on left, for case of dual excitation

$\bar{M}_{sr}$ = Magnetic frill current existing over aperture of coaxial feed on right, for case of dual excitation

$\bar{M}_\phi$ = Component of magnetic frill current in the $\hat{\phi}$ direction

$MSTOP$ = Index for truncation of m-series used to compute $LN(n)$, and $MN(n)$

$\bar{M}_s$ = Equivalent magnetic surface current distribution at coaxial aperture

$NSTOP$ = Index for truncation of n-series used to compute Z_{qp} and V_q

N_s = Number of subsections that strip is divided

N_x = Number of samples per dielectric wavelength ($= 1/l_x$)

$\bar{r}$ = Position vector anywhere inside cavity

$\bar{r}'$ = Position vector of assumed infinitesimal current source

r_a = Radius of inner conductor of coaxial feed

r_b = Radius of outer conductor of coaxial feed

RC = Reciprocal matrix condition number

R_{1n} = Argument of first Sinc function of expression for $\mathcal{I}_{qmn}$ $(= \left[\frac{1}{2}(k_x + K)l_x\right])$

R_{2n} = Argument of second Sinc function of expression for $\mathcal{I}_{qmn}$ $(= \left[\frac{1}{2}(k_x - K)l_x\right])$

s = Estimated standard deviation (used for experimental data analysis)

S_{ij} = Scattering parameters $(i, j = 1, 2)$

S_f = Surface of coaxial aperture

$S_f^{(i)}$ = Portion of coaxial aperture surface lying in region i

S_{lf} = Surface of coaxial aperture for feed on left hand side ($x = 0$ side) of cavity

S_q = Surface of the q^{th} strip subsection

S_{rf} = Surface of coaxial aperture for feed on right hand side ($x = a$ side) of cavity

S_{strip} = Surface of conducting strip

SWR = Standing wave ratio on microstrip line

$\tan \delta_d$ = Loss tangent of substrate material $(= \frac{\sigma}{\omega \epsilon_{r1} \epsilon_0})$

V = Volume of shielding cavity

V_0 = Complex voltage present in the coaxial line at the feeding point

[V] = Excitation vector used in method of moments solution

$[\mathbf{V_l}]$ = Excitation vector associated with left hand feed

$[\mathbf{V_r}]$ = Excitation vector associated with right hand feed

$[\mathbf{V}_d]$ = Combined excitation vector for dual excitation

$[\mathbf{V}_e]$ = Even excitation vector

$[\mathbf{V}_o]$ = Odd excitation vector

V_q = q^{th} element of the excitation vector

V_{ql} = q^{th} element of the excitation vector corresponding to left hand feed for case of dual excitation

V_{qr} = q^{th} element of the excitation vector corresponding to right hand feed for case of dual excitation

W = Width of microstrip line

x_p = Position vector giving x-coordinate of the p^{th} subsection

Y_0 = y-coordinate of the center of the strip with respect to the origin

Y_c = y-coordinate of center of coaxial feed

y_{ij} = Normalized admittance parameters $(i, j = 1, 2)$

$z(x)$= Input impedance at position x looking toward the discontinuity

z_{ij} = Normalized impedance parameters $(i, j = 1, 2)$

$[\mathbf{Z}]$= Impedance matrix used in method of moments solution

Z_{qp} = The $q - p$ element of the impedance matrix

α_g = Loss factor of microstrip transmission line

α_p = Subsectional sinusoidal basis functions used for series expansion of current in the longitudinal (x) direction

β_g = Phase constant of microstrip transmission line

γ_g = Complex propagation constant of microstrip transmission line

$\bar{\bar{\Gamma}}^i$ = Modified dyadic Green's function in region i

$\Gamma(x)$= Input voltage reflection coefficient at position x looking toward the discontinuity

Γ_{xx} = xx-component of modified dyadic Green's function in either region evaluated at substrate/air interface ($z = h$)

ϵ_0 = Free space permittivity ($= 8.854 \times 10^{-12}$ F/cm)

ϵ_i = Complex permittivity of material in i^{th} region of cavity

ϵ_r^* = Complex relative dielectric constant of substrate material ($= \frac{\epsilon_i}{\epsilon_0}$)

ϵ_{r1} = Real part of ϵ_r^*

ζ_q = Variable multiplier used in expression for $\mathcal{I}_{qmn}$

θ_{op}= Angle of reflection coefficient for open-end discontinuity

λ_0 = Wavelength in air ($\epsilon_r = 1$)

λ_d = Wavelength in dielectric ($\epsilon_r = \epsilon_r 1$)

λ_g = Microstrip wavelength ($\epsilon_r = \epsilon_{eff}$)

μ_i = Permeability of material in i^{th} region of cavity

μ_0 = Free space permeability ($= 4\pi \times 10^{-7}$ H/m)

ρ = Volume charge density in cavity

σ= Conductivity of substrate material

φ_n = Variable multiplier for complex Green's function coefficients

ψ = Function describing variation of microstrip current in the transverse(y) direction

ω = Radian frequency ($= 2\pi f$)

CHAPTER I

INTRODUCTION

1.1 Motivation

Millimeter-wave integrated circuits are important for a variety of scientific and military applications, and a wide range of solid state circuitry has been developed in both hybrid and monolithic form. However, the inability to accurately predict the electrical characteristics of various circuit components is a serious barrier to the widespread and cost effective application of these technologies. In fact, even at microwave frequencies, computer simulations of Monolithic Microwave Integrated Circuit (MMIC) components are often inadequate leading to lengthy design cycles with many costly circuit design iterations. The development of more accurate microstrip discontinuity models, based on full-wave analyses, is key to improving microwave and millimeter-wave circuit simulations and reducing lengthy design cycle costs.

Typical microwave and millimeter-wave IC's contain various active and passive elements interconnected by microstrip transmission lines as illustrated in Figure 1.1. In the vicinity of transmission line junctions and other discontinuities, parasitic effects occur that can significantly modify circuit operation. These discontinuity effects can be modeled by the use of lumped equivalent circuits or by

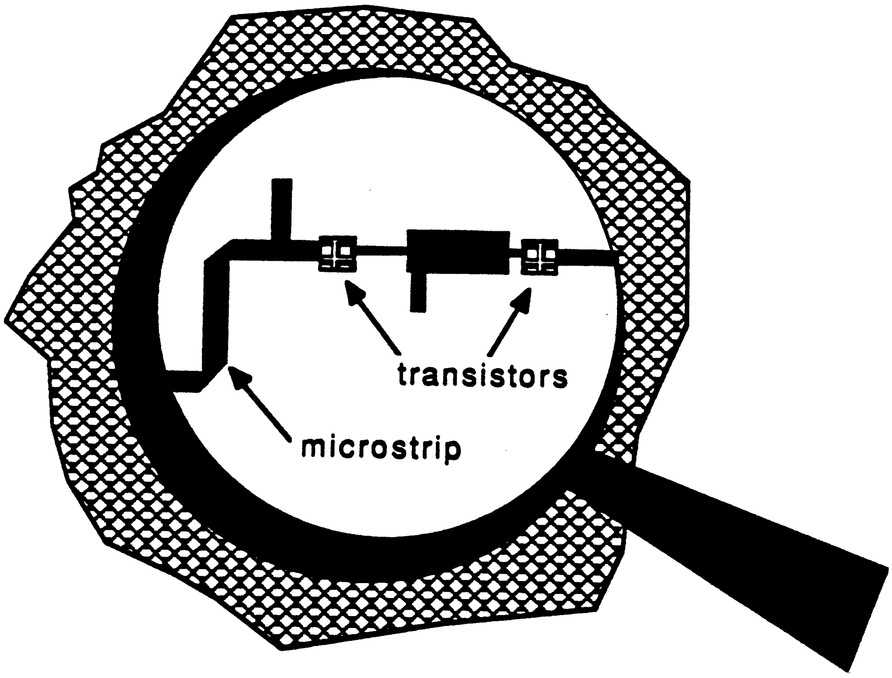

Figure 1.1: Typical millimeter-wave integrated circuit structure. Accurate modeling of discontinuities is key to cost effective designs.

generalized matrix representations; however, the models are only as accurate as the analysis technique used to derive them. Several techniques have been applied, and approximate models exist for most common discontinuities. However, for MMICs and for both hybrid and Monolithic Millimeter-wave Integrated Circuits (M^3ICs), additional theoretical and experimental research is needed to establish the accuracy of these models and to develop improved models where needed.

One area where this is true is for shielded microstrip discontinuities. As shown in Figure 1.2, there are three basic classes of microstrip. In open microstrip the top of the substrate is left open to the air. In this case, surface waves and radiation from circuit elements is unavoidable. In covered microstrip, a conducting cover is present, but no side walls are present, and in shielded microstrip the circuitry is enclosed in a rectangular waveguide.

This last category, shielded microstrip, is the most common for practical applications. In fact, usually the microstrip circuit is completely enclosed in a shielding cavity (or housing) as shown in Figure 1.3. This prevents radiation and electromagnetic interference and it also supresses surface wave modes.

The effect of the shielding on discontinuity behavior can be significant, and requires accurate modeling, at high frequencies. There are two main conditions where this is true. The first occurs when the frequency approaches or is above the cutoff frequency above which higher order modes can propagate within the shielded structure. The second occurs when the metal enclosure is physically close to the circuitry. A full-wave analysis is required to accurately model shielding effects. These effects are not adequately accounted for in the discontinuity models used in most available CAD packages. The theoretical part of this thesis addresses this area.

There is also a great need for experimental data. Published experimental data on microstrip discontinuites is very limited, especially for high microwave (above X-band) and millimeter-wave frequencies. Such measurements are not trivial, but are essential to verifying the accuracy or at least the reasonableness of theoretical results. This was the motivation for the experimental part of this work.

1.2 Thesis Objectives

The overall goal of this research is to use full-wave analysis techniques combined with experimental data to study some relatively basic shielded microstrip discontinuities. This research is intended to aid in the development of an accurate data base for all kinds of microstrip discontinuities. Such a data base has several uses: 1) existing CAD models can be checked against it to determine their regions of validity, 2) it can be used to develop new and more accurate, C.A.D. models , and 3) it can be used to improve experimental methodology. For example, it can

a) Open microstrip

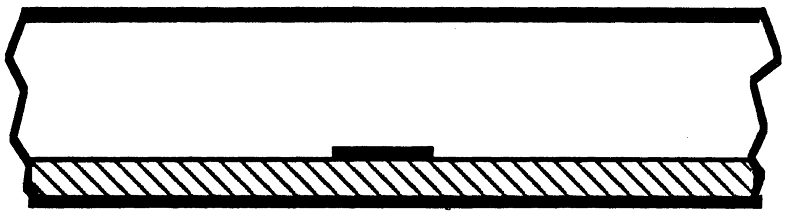

b) Covered microstrip

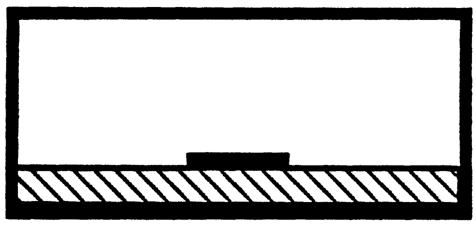

c) Shielded microstrip

Figure 1.2: Three basic classes of microstrip.

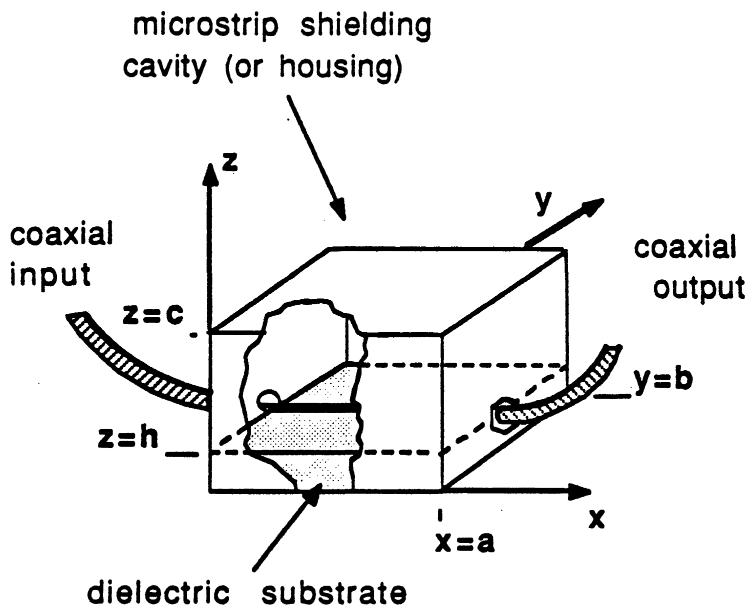

Figure 1.3: Basic geometry for the shielded microstrip cavity problem.

be used to help characterize microstrip standards for measurement calibration and verification.

The specific objectives of the present research may be summarized as follows:

- Develop a new theoretical method for computational analysis of shielded microstrip discontinuities
- Explore the use of a practical excitation mechanism
- Investigate high frequency microstrip measurement techniques
- Conduct an experimental study in close correlation with the theoretical work

The primary objective is to develop an accurate and computer efficient method for full-wave analysis of discontinuities in shielded microstrip. This method is to be demonstrated by obtaining numerical results for practical discontinuity structures for which the thin-strip approximation [1] applies.

Another objective is to investigate ways to use practical circuit excitation mechanisms in the theoretical solution. To date, all full-wave analyses of microstrip discontinuities use either a gap generator excitation method [5,11], or use a cavity resonance technique (without actually exciting the circuit)[8,10] to determine discontinuity parameters. Both of these techniques are purely mathematical tools. The former has no physical basis relative to an actual circuit. The latter is also abstract, since in any practical circuit some form of excitation is present. To derive a more realistically based formulation, the use of a coaxial excitation mechanism is to be explored and compared to the gap generator method.

A final objective is to conduct an experimental study to aid in the verification of the theory. As part of this study, a number of techniques are to be assessed qualitatively as to their suitability for high frequency (X-band and higher) measurements. Limitations on measurement accuracy are also to be addressed.

1.3 Accomplishments

In this thesis, the research objectives outlined above are accomplished as follows. A new method is developed for the analysis of discontinuities in shielded microstrip. In the analysis one of two different types of excitation can be used: the first is a coaxial excitation method, and the second is the gap generator approach discussed above. It is shown that with gap generator excitation, the current is disrupted over the region surrounding it; while with coaxial excitation, the current is undisturbed and uniform along the length of the strip. However, for the evaluation of discontinuity parasitics, the final results appear to be unaffected by the method of excitation. The validity of the thin-strip approximation for the

[1] The thin-strip approximation assumes that the width of the conducting strips is small compared to a wavelength.

structures considered in this thesis is also examined.

To demonstrate the method, numerical results are presented for open-end and series gap discontinuities, and a four resonator coupled line filter. These results are compared to other full-wave analyses, to data from *Super Compact* and *Touchstone* [2], and to measurements. The measurements were performed by the author using a variation of the TSD de-embedding technique [44].

The contribution of this thesis is in three areas: theoretical, computational, and experimental. The theoretical contribution is in the derivation of the method of moments solution for the problem of Figure 1.3. This derivation is based on modeling the coaxial feed with a magnetic frill current (Chapter 2). To the author's knowledge, this is the first time that the frill current approach has been applied to the shielded microstrip problem. From a computational point of view, extensive numerical convergence experiments were performed that lead to some surprisingly simple relationships governing the convergence and stability behavior of the method of moments solution for this problem (Chapter 3). Finally, as part of the experimental study, a novel perturbation analysis was applied to study the effect of connection repeatability errors on microstrip de-embedding accuracy (Chapter 4). The experimental results demonstrate the accuracy and usefulness of the theory developed here and also suggest some areas where improvements can be made (Chapter 5).

1.4 Brief Review of Theoretical Approaches

As mentioned above, several approximate techniques exist for microstrip discontinuity analysis. The published literature on this subject is voluminous. However, a few comments are in order before discussing full-wave solutions.

---

[2] *Super Compact* and *Touchstone* are microwave CAD software packages available from Compact Software and EESOF respectively.

1.4.1 Quasi-Static Techniques

Quasi-static techniques are well established and described in standard texts [1]-[3]. With these techniques, equivalent circuits are derived in terms of static capacitances and low frequency inductances. Convenient analytical formulas for discontinuity parasitics are possible, yet their accuracy is questionable for frequencies above a few GHz. Also, most existing models based on these techniques ignore shielding effects.

1.4.2 Planar Waveguide Models

Planar waveguide models provide a frequency dependent solution. In this approach, an equivalent planar waveguide geometry is proposed for the microstrip problem. The transformed problem is then solved using an appropriate analytical technique, such as mode matching [4]. Models derived from this technique are generally considered accurate to higher frequencies than those derived from quasi-static models.

However, the method does not provide an adequate model for shielded microstrip. As discussed in Chapter 5, the higher order modes in shielded microstrip are essentially rectangular waveguide modes. The mode behavior of a planar waveguide is quite different than for rectangular waveguide. Its applicability even for the dominant microstrip mode is questionable, since the dominant mode in shielded microstrip is the result of an infinite summation of evanescent waveguide modes. This is not to say that reasonable predictions are not possible with this method, only that its application for the shielded microstrip problem is not rigorous.

1.4.3 Rigorous Full-Wave Solutions

As described above, for many applications, the limitations of the above two techniques cannot be tolerated, and a more accurate solution is required.

A full-wave solution[3] that meets this requirement was developed by Katehi to treat discontinuites in open microstrip [5,6]. This technique has so far been applied to solve for various discontinuities in open microstrip. The new analytical methodology presented here is an extension of the approach of Katehi to shielded microstrip configurations.

While rigorous solutions to shielded discontinuities have been advanced by others, their is a need for further research in this area. The most extensive work has been performed by Jansen et al. [7]-[9]. Although reasonable results have been demonstrated for several microstrip structures, there has been little accompanying experimental verification, and only limited comparisons to other rigorous numerical solutions. The primary reasons for this have most likely been the difficulties of performing the measurements, as discussed herein, and the existence of only a few other rigorous solutions ([10]-[12]). Further, the only published results from the other rigorous solutions that the author is aware of is for the open-end discontinuity.

1.5 Description of Theoretical Methods

The theoretical method developed here is addressed to the shielded microstrip geometry shown in Figure 1.3. The shielding box forms a rectangular cavity, which –for most practical uses– is cutoff for the highest frequency of operation. That is, the cavity dimensions are usually such that the coupling of microstrip

[3] A full-wave solution, refers to the application of a rigorous electromagnetic analysis to the microstrip geometry, making as few assumptions as possible.

modes into higher order waveguide modes is avoided. However, as far as the the current distribution is concerned, the solution presented here is accurate whether the cavity is cutoff or not. Above this cutoff frequency the onset of higher order modes distort the current distribution and the definition of circuit behavior in the usual way, by a transmission line model, becomes ambiguous.

The theoretical method is based on Galerkin's implementation of the method of moments. A flow chart illustrating the method is shown in Figure 1.4. First, the required matrix equation is derived. In this derivation, the coaxial feed is represented by an equivalent magnetic current source. The reciprocity theorem is then applied to establish an integral equation that relates this magnetic current source and the electric current on the conducting strips to the electromagnetic fields inside the cavity. By expanding the electric current into a series of sinusoidal subsectional basis functions, the integral equation is transformed into a matrix equation. In a similar way, the reciprocity theorem is applied for the case of gap generator, and an identical form results for the elements of the impedance matrix.

Next, the Green's function is derived and used to evaluate the electric and magnetic fields within the cavity. The Green's function is derived by applying boundary conditions to the problem of Figure 1.3 with the conducting strips replaced by an infinitesimal current source on the substrate/air interface. This is a common approach in solving boundary conditions of this type [16].

Finally, the matrix equation is solved to compute the current distribution. Based on the current, either an equivalent circuit or scattering parameters are derived to characterize the discontinuity being considered.

1.6 Description of Experimental Study

To obtain verification data for the theoretical method of this thesis, an ex-

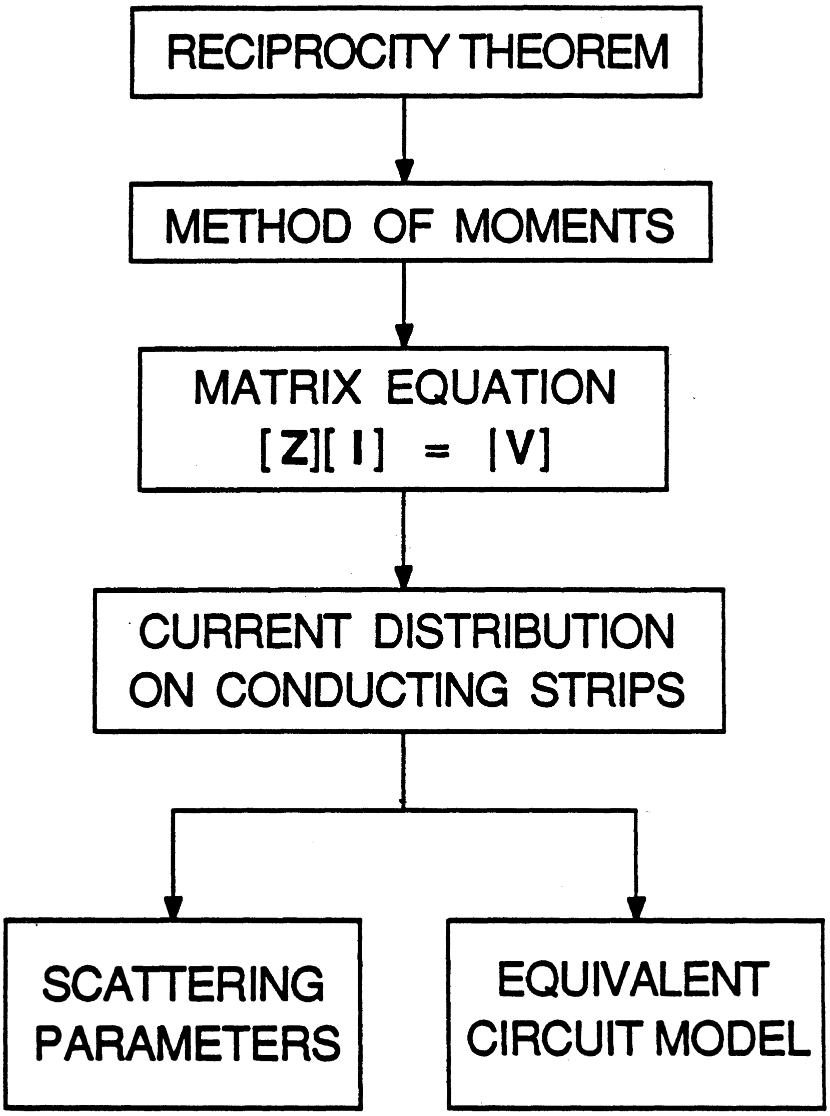

Figure 1.4: Flow chart illustrating theoretical approach for characterizing microstrip discontinuities.

perimental study was conducted in cooperation with Hughes Aircraft Company [4]. As discussed in Chapter 4, the lack of experimental data on microstrip discontinuities is mainly due to the difficulties with removing test fixture parasitics from the measurements (called de-embedding), and the non-repeatability of microstrip connections. To address these issues, a study of de-embedding techniques was conducted, from which it has been concluded that the most suitable technique for the measurements of this thesis is the thru-short-delay (TSD) method. Also, a connection repeatability study was carried out [14,15], and the results were used to decide on how to best implement TSD de-embedding, and they were used to approximate the associated uncertainty in de-embedding accuracy. S-parameter measurements were then obtained for an open-end discontinuity, three series gap discontinuities with different gap widths, and two coupled line band pass filter structures.

---

[4] Hughes Aircraft Company, Microwave Products Division, Torrance, California.

CHAPTER II

THEORETICAL METHODOLOGY

2.1 Assumptions

In this solution, a few simplifying assumptions are made to reduce unnecessary complexity, and excessive computer time. Throughout the analysis, it is assumed that the width of the conducting strips is small compared to the microstrip wavelength λ_g. In this case, unidirectional currents may be assumed with negligible loss in accuracy. While substrate losses are accounted for, it is assumed that the strip conductors and the walls of the shielding box are lossless, and that the strip thickness is negligible. For the computation of two-port network parameters (Section 2.7.2), the strip geometry is assumed to be physically symmetric with respect to the center of the cavity (in both the x and y directions of Figure 1.3). Also, to simplify notation, the assumed time dependence is $e^{j\omega t}$, and it is suppressed throughout the dissertation.

The above assumptions are valid for the high frequency analysis of the microstrip structures of Figure 2.1, provided good conductors are used in the metalized areas. The first three structures of Figure 2.1, the open-end, the series gap and the coupled lines are discontinuity structures. The last one, the thru-line,

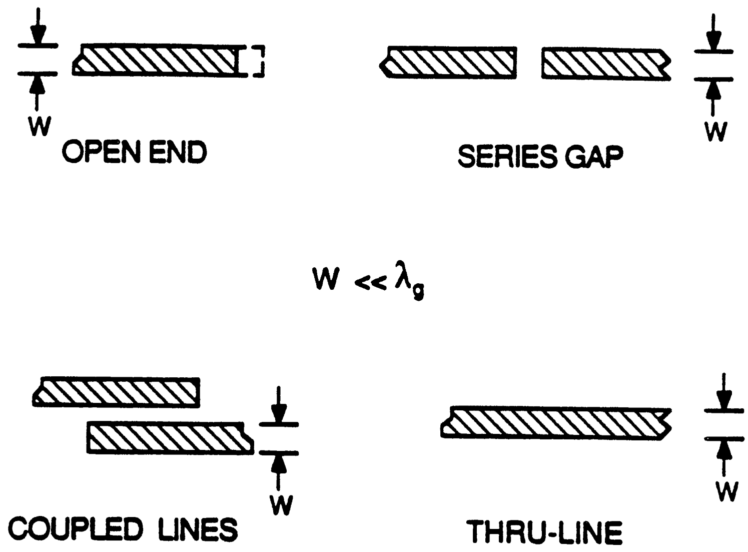

Figure 2.1: Microstrip structures for which thin-strip approximation is valid.

is not. The thru-line is included since it is a useful test case, and it is used to determine the microstrip propagation constant γ_g.

2.2 Method of Moments Formulation

The method of moments is a well established numerical technique for solving electromagnetic problems [17],[18]. A review of the basic approach is given in Appendix A. This section makes use of the method of moments to set up a matrix equation that provides for a computer solution to shielded microstrip discontinuity problems.

For the most part, the theory presented applies to the use of a coaxial excitation mechanism, based on the frill current model. A few comments are made, however, to indicate how the theory differs for the use of a gap generator excitation model. In the matrix equation, the only significant difference is the excitation vector used.

2.2.1 Application of Reciprocity Theorem

Reciprocity Theorem for Coaxial Excitation

Consider the geometry of Figure 1.3. In most cases the coaxial feed, or "launcher", is designed to allow only transverse electromagnetic (TEM) propagation, and the feed's center conductor is small compared to a wavelength. In these cases, the radial electric field will be dominant on the aperture and we can replace the feed by an equivalent magnetic surface current, sometimes called a "frill" current, whose only component is in the $\hat{\phi}$ direction (i.e.$\bar{M}_s = M_\phi \hat{\phi}$) [1]. This method of modeling the feed with a magnetic current source will be discussed further in Section 2.5. The magnetic current source is coupled with the current distribution $\bar{J}_s$ on the conducting strip to produce the total electric field $\bar{E}^{tot}$ and the total magnetic field $\bar{H}^{tot}$ inside the cavity as indicated in Figure 2.3.

We now propose an independent test current source $\bar{J}_q$ existing only on a small subsection of the conducting strip as shown in Figure 2.4. Using the reciprocity theorem, the two sets of current sources are related according to

$$\int\int\int_V \left(\bar{J}_s \cdot \bar{E}_q - \bar{H}_q \cdot \bar{M}_s\right) dv = \int\int\int_V \bar{J}_q \cdot \bar{E}^{tot} dv \qquad (2.1)$$

where the volume V is the interior of the cavity.

Since $\bar{J}_q$ is x-directed and zero everywhere except over one subsection of the conducting strip, the right hand side of (2.1) reduces to

$$\int\int\int_V \bar{J}_q \cdot \bar{E}^{tot} dv = \int\int_{S_q} \left|\bar{J}_q\right| E_x^{tot}(z = h) ds = 0 \qquad (2.2)$$

---

[1] $\hat{\phi}$ refers to the cylindrical coordinate referenced to the center of the feeding aperture (see Figure 2.2.)

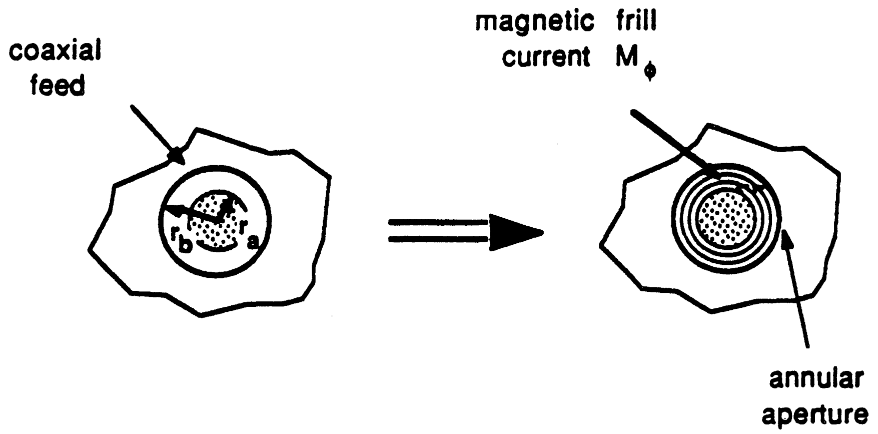

Figure 2.2: Representation of coaxial feed by a circular aperture with magnetic frill current M_ϕ.

where S_q is the surface of an arbitrary subsection and $E_x^{tot}(z = h)$ is the x-component of the total electric field which must vanish on the surface of the conductors ($z = h$) since they are assumed to be perfectly conducting.

Reducing the remaining volume integrals in (2.1) to surface integrals results in

$$\int\int_{S_{strip}} \bar{E}_q(z = h) \cdot \bar{J}_s ds = \int\int_{S_f} \bar{H}_q(x = 0) \cdot \bar{M}_s ds \tag{2.3}$$

where S_{strip} is the surface of the conducting strip and S_f is the surface of the coaxial aperture. Note that this equation is not explicitly in the form of the operator equation of (A.1). This is because in using the reciprocity theorem formulation we have inherently placed it in the inner product form of (A.3).

Reciprocity Theorem for Gap Generator Excitation

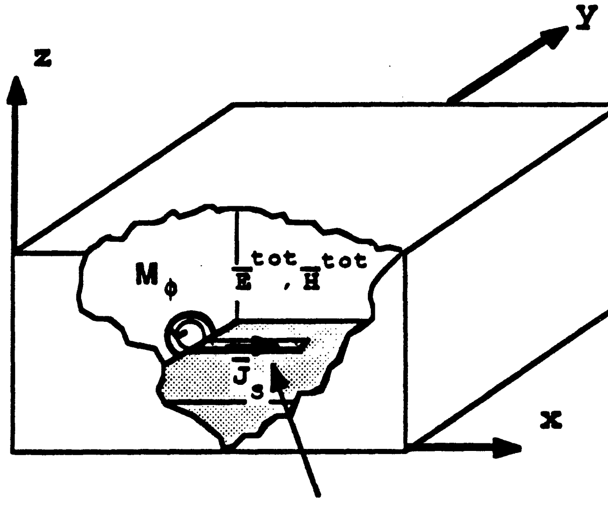

Figure 2.3: Total fields $\bar{E}^{tot}$, $\bar{H}^{tot}$ inside cavity are produced by magnetic current source M_ϕ at aperture and electric current distribution $\bar{J}_s$ on the conducting strip.

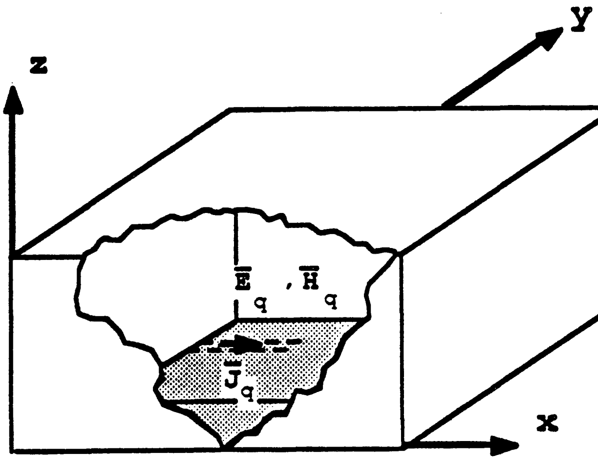

Figure 2.4: Test current $\bar{J}_q$ on conducting strip and associated fields $\bar{E}_q$, $\bar{H}_q$ inside the cavity.

The formulation for the case of gap generator excitation can also be derived from reciprocity theorem. In this case, it is assumed that E_x is non-zero at one point (x_g) on the strip, between two subsections. Setting $\bar{M}_s = 0$ in 2.1, and reducing the resulting volume integrals to surface integrals yields

$$\int\int_{S_{strip}} \bar{E}_q(z=h)\cdot \bar{J}_s ds = \int\int_{S_q} \left|\bar{J}_q\right| E_x^{tot}(z=h) ds \tag{2.4}$$

Since $E_x = 0$ everywhere except x_g, the right hand side of 2.4 vanishes everywhere except over the the subsectional surface containing x_g. This surface integral we arbitrarily set equal to unity. That is

$$\int\int_{S_q} \left|\bar{J}_q\right| E_x^{tot}(z=h) ds = \begin{cases} 1 & \text{for } q = g \\ 0 & \text{else} \end{cases} \tag{2.5}$$

where g is the index corresponding to the position of the gap generator.

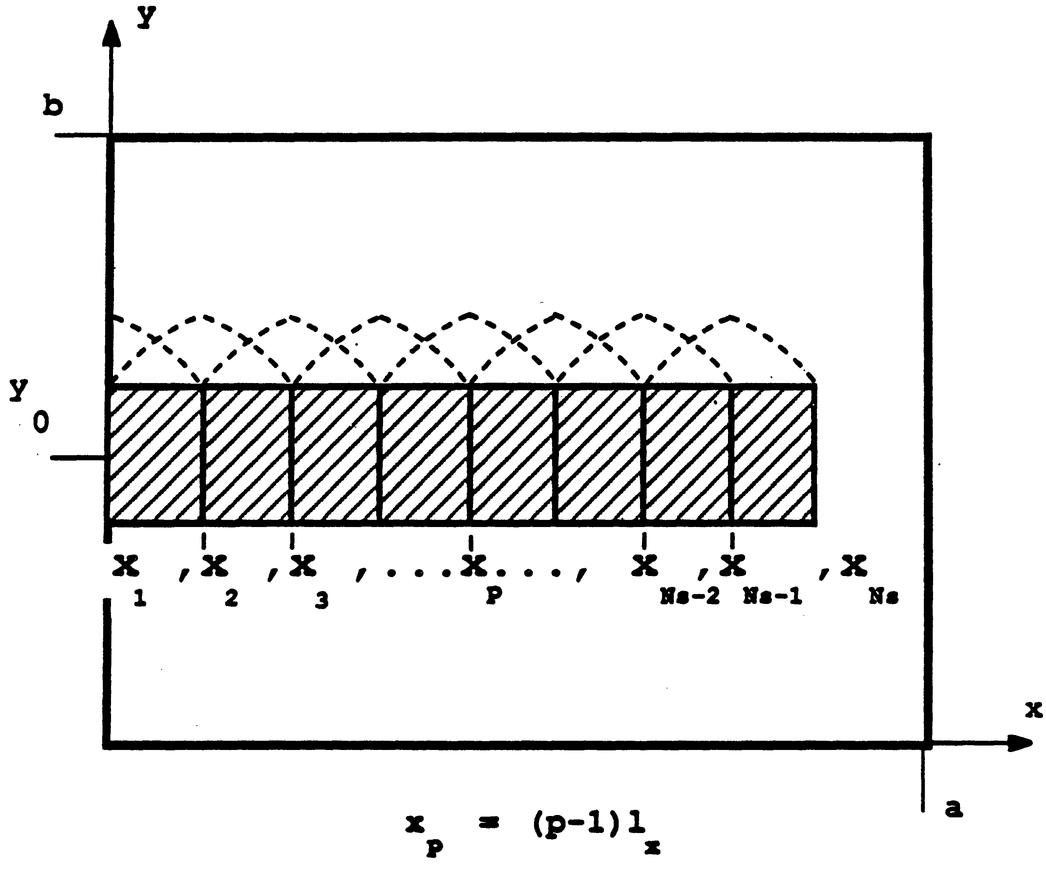

Figure 2.5: Strip geometry for use in basis function expansion of current for the case of an open-ended line.

2.2.2 Expansion of Current with Sinusoidal Basis Functions

In order to solve the integral equation (2.3), the current distribution $\bar{J}_s$ is expanded into a series of orthogonal functions as follows. Consider the strip geometry shown in Figure 2.5, let

$$\bar{J}_s = \psi(y) \sum_{p=1}^{N_s} I_p \alpha_p(x)\,\hat{x} \tag{2.6}$$

where I_p are unknown current coefficients. The function $\psi(y)$ describes the variation of the current in the transverse direction and is given by

$$\psi(y) = \begin{cases} \dfrac{\frac{2}{\pi W}}{\sqrt{1-\left[\frac{2(y-Y_0)}{W}\right]^2}} & Y_0 - W/2 \le y \le Y_0 + W/2 \\ 0 & \text{else} \end{cases} \tag{2.7}$$

This variation was chosen to agree with that derived by Maxwell for the charge density distribution on an isolated conducting strip [20], and it has been used successfully by others to describe the transverse variation of microstrip currents [5,21,22].

The basis functions $\alpha_p(x)$ comprise an orthonormal set and are described by

$$\alpha_p(x) = \begin{cases} \frac{\sin[K(x_{p+1}-x)]}{\sin(Kl_x)} & x_p \le x \le x_{p+1} \\ \frac{\sin[K(x-x_{p-1})]}{\sin(Kl_x)} & x_{p-1} \le x \le x_p \\ 0 & \text{else} \end{cases} \tag{2.8}$$

for $p \neq 1$, and

$$\alpha_1(x) = \begin{cases} \frac{\sin[K(l_x-x)]}{\sin(Kl_x)} & 0 \le x \le l_x \\ 0 & \text{else} \end{cases} \tag{2.9}$$

for $p = 1$, where

$K = \omega\sqrt{\mu_o \epsilon_{r1} \epsilon_0}$ is the real part of the wave number in the dielectric region

W is the width of the microstrip line

Y_0 is the y-coordinate of the center of the strip with respect to the origin in Figure 1.3

x_p is the x-coordinate of the pth subsection ($= (p-1)l_x$)

l_x is the subsection length ($l_x = x_{p+1} - x_p$) .

2.2.3 Transformation of Integral Equation into a Matrix Equation

The integral equation (2.3) can now be transformed into a matrix equation by substituting the expansion of (2.6) for the current $\bar{J}_s$. This results in the following:

$$\sum_{p=1}^{N_s} \left[\int\int_{S_p} \bar{E}_q(z=h) \cdot \psi(y)\, \alpha_p(x)\, \hat{x} ds \right] I_p = \int\int_{S_f} \bar{H}_q \cdot M_s ds \qquad (2.10)$$

where S_p is the surface area of the p^{th} subsection, and N_s is the number of sections that the strip is divided into for computation.

We may now express (2.10) as

$$[\mathbf{Z}]\,[\mathbf{I}] = [\mathbf{V}] \; . \qquad (2.11)$$

In the above, [Z] is called the impedance matrix, and has the form

$$[\mathbf{Z}] = \begin{bmatrix} Z_{11} & Z_{12} & \cdots & Z_{1N_s} \\ Z_{21} & Z_{22} & & Z_{2N_s} \\ \vdots & & \ddots & \vdots \\ Z_{N_s1} & Z_{N_s2} & \cdots & Z_{N_sN_s} \end{bmatrix} \qquad (2.12)$$

[V] is called the excitation vector and may be expressed as

$$[\mathbf{V}] = \begin{bmatrix} V_1 & V_2 & \cdots & V_{N_s} \end{bmatrix}^T . \qquad (2.13)$$

[I] is the current vector comprised of the unknown current coefficients as follows:

$$[\mathbf{I}] = \begin{bmatrix} I_1 & I_2 & \cdots & I_{N_s} \end{bmatrix}^T . \qquad (2.14)$$

The individual elements of the impedance matrix are given by

$$Z_{qp} = \int\int_{S_p} \bar{E}_q(z=h) \cdot \psi(y)\, \alpha_p(x)\, \hat{x} ds \; . \qquad (2.15)$$

The elements of the excitation vector (coaxial excitation) are given by

$$V_q = \int\int_{S_f} \bar{H}_q \cdot \bar{M}_s ds \; . \qquad (2.16)$$

We can now solve for the current vector by matrix inversion and multiplication according to

$$[\mathbf{I}] = [\mathbf{Z}]^{-1}[\mathbf{V}] \; . \qquad (2.17)$$

For gap generator excitation, the impedance matrix elements are also given by (2.15); however, the elements of the excitation vector are given by the right hand side of (2.5).

2.3 Derivation of the Green's Function

To compute the elements of the impedance matrix, we must derive the Green's function associated with the electric and magnetic fields $\bar{E}_q$, $\bar{H}_q$. We will first define the problem geometry and outline the electromagnetic theory to be used. Then, the boundary value problem will be solved for the Green's function.

2.3.1 Geometry and Electromagnetic Theory

The geometry used in the Green's function derivation is shown in Figure 2.6. The cavity is divided into two regions: Region 1 consists of the volume contained within the substrate ($z < h$), while region 2 is the volume above the substrate surface ($z > h$). Notice, as discussed in Section 1.5, the conducting strips have been replaced by an infinitesimal current source $\bar{J}$.

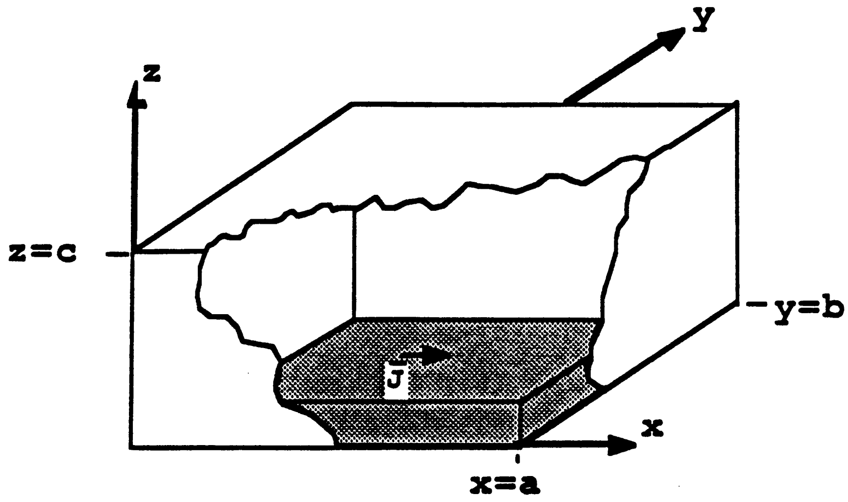

a) Cutaway view

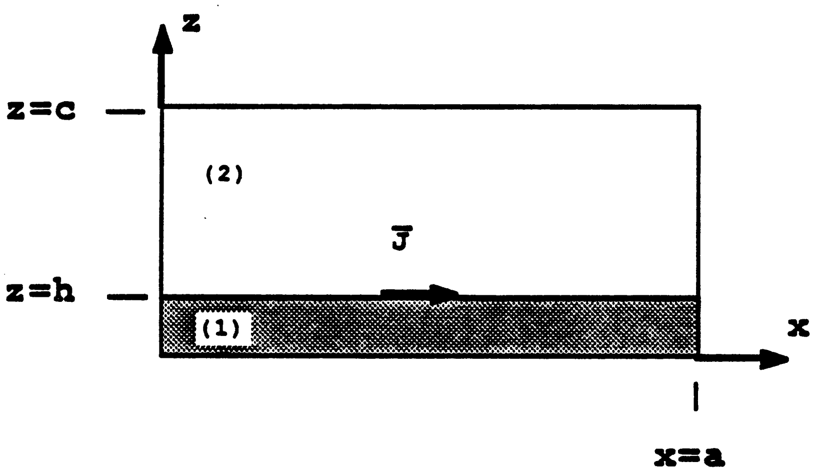

b) Cross section in x-z plane

Figure 2.6: Geometry used in derivation of the Green's function.

The Green's function will be defined as the electric field due to an infinitesimal current source located on the substrate surface of Figure 2.6. After deriving the Green's function, the fields associated with the test source $\bar{J}_q$ will be evaluated by integrating over the surface of the q^{th} subsection.

The test source $\bar{J}_q$ and the associated fields within the cavity ($\bar{E}_q$,$\bar{H}_q$) are related through Maxwell's equations, which may be put in the following form:

$$\bar{\nabla} \times \bar{E}^i = -j\omega\mu_i\bar{H}^i \tag{2.18}$$

$$\bar{\nabla} \times \bar{H}^i = j\omega\epsilon_i\bar{E}^i + \bar{J} \tag{2.19}$$

$$\bar{\nabla} \cdot \bar{J} = -j\omega\rho \tag{2.20}$$

$$\bar{\nabla} \cdot \left(\epsilon_i\bar{E}^i\right) = \rho \tag{2.21}$$

$$\bar{\nabla} \cdot \left(\mu_i\bar{H}^i\right) = 0\,. \tag{2.22}$$

In the above, $i = 1,2$ indicates that these equations hold in each of the regions respectively. Also, to simplify the notation of this subsection, the subscript q is suppressed with the understanding that all the field quantities discussed here are associated with the test source $\bar{J}_q$ (i.e. $\bar{E}^i = \bar{E}^i_q$ etc.). Further, since it is assumed that both regions are non-magnetic and that region 2 is air, we have

$$\mu_1 = \mu_2 = \mu_0 \tag{2.23}$$

$$\epsilon_i = \begin{cases} \epsilon_r^*\epsilon_0 & for\ i = 1 \\ \epsilon_0 & for\ i = 2 \end{cases} \tag{2.24}$$

where

$$\epsilon_r^* = \epsilon_{r1} - j\frac{\sigma}{\omega\epsilon_0} = \epsilon_{r1}\left(1 - j\tan\delta_d\right)\,. \tag{2.25}$$

In the above, $\tan\delta_d = \frac{\sigma}{\omega\epsilon_{r1}\epsilon_0}$ is referred to as the dielectric loss tangent of the dielectric region, δ_d is called the dissipation angle.

2.3.2 Solution to Boundary Value Problem for the Green's Function

We now introduce the vector potentials $\bar{A}^i$ such that

$$\bar{H}^i = \frac{1}{\mu_o}\bar{\nabla} \times \bar{A}^i \,. \tag{2.26}$$

In view of (2.26), the electric field may be written as (B.13)

$$\bar{E}^i = -j\omega\left(1 + \frac{1}{k_i^2}\bar{\nabla}\bar{\nabla}\cdot\right)\bar{A}^i \tag{2.27}$$

where $\bar{A}^i$ satisfies the inhomogeneous wave equation

$$\nabla^2 \bar{A}^i + k_i^2 \bar{A}^i = -\mu_0 \bar{J} \,. \tag{2.28}$$

The integral form of the electric field is derived in Appendix B, and is given by (B.21)

$$\bar{E}^i = -j\omega\mu_0 \int\int\int_V \left[\left(1 + \frac{1}{k_i^2}\bar{\nabla}\bar{\nabla}\cdot\right)(\bar{\bar{G}}^i)^T\right] \cdot \bar{J} dv' \tag{2.29}$$

where $k_i^2 = \omega^2\mu_0\epsilon_i$, and $\bar{\bar{G}}^i$ is a dyadic Green's function [23] satisfying the following equation

$$\nabla^2 \bar{\bar{G}}^i + k_i^2 \bar{\bar{G}}^i = -\bar{\bar{I}}\delta(\bar{r} - \bar{r}') \,. \tag{2.30}$$

In (2.30), $\bar{\bar{I}}$ is the unit dyadic given by $\hat{x}\hat{x} + \hat{y}\hat{y} + \hat{z}\hat{z}$.

Because of the air/dielectric interface, a two component vector potential is necessary to satisfy the boundary conditions [24]. Accordingly, let

$$\bar{A}^i = A_x^i \hat{x} + A_z^i \hat{z} \,. \tag{2.31}$$

From (B.17) $\bar{A}^i$ is related to $\bar{\bar{G}}^i$ by the following volume integral:

$$\bar{A}^i = \mu \int\int\int_V \bar{J} \cdot \bar{\bar{G}}^i dv' \,. \tag{2.32}$$

$\bar{\bar{G}}^i$ may be expressed in most general form as follows:

$$\bar{\bar{G}}^i = \begin{pmatrix} G_{xx}^i\hat{x}\hat{x} & + & G_{xy}^i\hat{x}\hat{y} & + & G_{xz}^i\hat{x}\hat{z} \\ + G_{yx}^i\hat{y}\hat{x} & + & G_{yy}^i\hat{y}\hat{y} & + & G_{yz}^i\hat{y}\hat{z} \\ + G_{zx}^i\hat{z}\hat{x} & + & G_{zy}^i\hat{z}\hat{y} & + & G_{zz}^i\hat{z}\hat{z} \end{pmatrix} \,. \tag{2.33}$$

Assuming an infinitesimal x-directed current source given by

$$\bar{J} = \delta(\bar{r} - \bar{r}')\,\hat{x} \tag{2.34}$$

in (2.32) allows for reducing $\bar{\bar{G}}^i$ to

$$\bar{\bar{G}}^i = G^i_{xx}\hat{x}\hat{x} + G^i_{xz}\hat{x}\hat{z}\,. \tag{2.35}$$

The dyadic components of (2.35) are found by applying appropriate boundary conditions at the walls: $x = 0$, and a ; $y = 0$, and b ; and $z = 0$, and c. As detailed in Appendix C, these components may be expressed as

$$G^{(1)}_{xx} = \sum_{m=1}^{\infty}\sum_{n=0}^{\infty} A^{(1)}_{mn} \cos k_x x \sin k_y y \sin k^{(1)}_z z \tag{2.36}$$

$$G^{(1)}_{xz} = \sum_{m=1}^{\infty}\sum_{n=0}^{\infty} B^{(1)}_{mn} \sin k_x x \sin k_y y \cos k^{(1)}_z z \tag{2.37}$$

$$G^{(2)}_{xx} = \sum_{m=1}^{\infty}\sum_{n=0}^{\infty} A^{(2)}_{mn} \cos k_x x \sin k_y y \sin k^{(2)}_z (z - c) \tag{2.38}$$

$$G^{(2)}_{xz} = \sum_{m=1}^{\infty}\sum_{n=0}^{\infty} B^{(2)}_{mn} \sin k_x x \sin k_y y \cos k^{(2)}_z (z - c) \tag{2.39}$$

where

$$k_x = n\pi/a \tag{2.40}$$

$$k_y = m\pi/b \tag{2.41}$$

$$k^{(1)}_z = \sqrt{k_1^2 - k_x^2 - k_y^2} \tag{2.42}$$

$$k^{(2)}_z = \sqrt{k_0^2 - k_x^2 - k_y^2} \tag{2.43}$$

$$k_1 = \omega\sqrt{\mu_0\epsilon_1} \tag{2.44}$$

$$k_0 = \omega\sqrt{\mu_0\epsilon_0}\,. \tag{2.45}$$

The coefficients $A^{(1)}_{mn}$, $A^{(2)}_{mn}$, $B^{(1)}_{mn}$, and $B^{(2)}_{mn}$ are found by applying boundary conditions at the air/dielectric interface. The details of this analysis can be found in Appendix D. The results are:

$$A^{(1)}_{mn} = \frac{-\varphi_n \cos k_x x' \sin k_y y' \tan k^{(2)}_z (h - c)}{abd_{1mn} \cos k^{(1)}_z h} \tag{2.46}$$

$$A_{mn}^{(2)} = \frac{-\varphi_n \cos k_x x' \sin k_y y' \tan k_z^{(1)} h}{abd_{1mn} \cos k_z^{(2)}(h-c)} \tag{2.47}$$

$$B_{mn}^{(1)} = \frac{-\varphi_n(1-\epsilon_r^*)k_x \cos k_x x' \sin k_y y' \tan k_z^{(1)} h \tan k_z^{(2)}(h-c)}{abd_{1mn}d_{2mn} \cos k_z^{(1)} h} \tag{2.48}$$

$$B_{mn}^{(2)} = \frac{-\varphi_n(1-\epsilon_r^*)k_x \cos k_x x' \sin k_y y' \tan k_z^{(1)} h \tan k_z^{(2)}(h-c)}{abd_{1mn}d_{2mn} \cos k_z^{(2)}(h-c)} \tag{2.49}$$

where

$$\varphi_n = \begin{cases} 2 & \text{for } n = 0 \\ 4 & \text{for } n \neq 0 \end{cases} \tag{2.50}$$

$$d_{1mn} = k_z^{(2)} \tan k_z^{(1)} h - k_z^{(1)} \tan k_z^{(2)}(h-c) \tag{2.51}$$

$$d_{2mn} = k_z^{(2)} \epsilon_r^* \tan k_z^{(2)}(h-c) - k_z^{(1)} \tan k_z^{(1)} h \,. \tag{2.52}$$

Having derived the Green's function, we are now ready to proceed to the formulation for the elements of the impedance matrix and excitation vector.

2.4 Impedance Matrix Formulation

The elements of the impedance matrix are given by (2.15)

$$Z_{qp} = \int\int_{S_p} \bar{E}_q(z=h) \cdot \psi(y')\, \alpha_p(x')\, \hat{x} ds' \tag{2.53}$$

which reduces to

$$Z_{qp} = \int\int_{S_p} E_{qx}(z=h) \psi(y')\, \alpha_p(x')\, ds' \,. \tag{2.54}$$

To evaluate the impedance matrix elements we need only $E_{qx}(z=h)$; that is, the x-component of the electric field due to the test currents $\bar{J}_q$ at the air/dielectric interface.

2.4.1 Evaluation of the Electric Field Due to the Test Currents

Since $\bar{J}_q$ is a surface current distribution, the volume integral in (2.29) is reduced to the following surface integral:

$$\bar{E}_q{}^i = -j\omega\mu_0 \int\int_{S_q} \left[\left(1 + \frac{1}{k_i^2} \bar{\nabla}\bar{\nabla}\cdot \right) (\bar{\bar{G}}^i)^T \right] \cdot \bar{J}_q dx'dy' \qquad (2.55)$$

where S_q is the surface of the q^{th} subsection.

For best accuracy in applying the method of moments, the test currents $\bar{J}_q$ are expressed in terms of functions which are identical to the basis functions (Galerkin's method)

$$\bar{J}_q = \psi(y')\alpha_q(x')\hat{x} \qquad (2.56)$$

where $\psi(y')$ is given by (2.7) with y replaced by y', and $\alpha_q(x')$ is given by (2.8) and (2.9) with p replaced by q and x replaced by x'.

We now substitute from (2.56) for $\bar{J}_q$ in (2.55) to yield

$$\bar{E}_q{}^i = -j\omega\mu_0 \int\int_{S_q} \left[\left(1 + \frac{1}{k_i^2} \bar{\nabla}\bar{\nabla}\cdot \right) (\bar{\bar{G}}^i)^T \right] \cdot \psi(y')\alpha_q(x')\hat{x}dx'dy' \qquad (2.57)$$

Let us define a *modified dyadic Green's function* $\bar{\bar{\Gamma}}^i$ by

$$\bar{\bar{\Gamma}}^i = -j\omega\mu_0 \left[\left(1 + \frac{1}{k_i^2} \bar{\nabla}\bar{\nabla}\cdot \right) (\bar{\bar{G}}^i)^T \right] . \qquad (2.58)$$

Then, $\bar{E}_q^i$ can be expressed as

$$\bar{E}_q^i = \int\int_{S_q} \bar{\bar{\Gamma}}^i \cdot \psi(y')\alpha_q(x')\hat{x}dx'dy' . \qquad (2.59)$$

The dyadic transpose of (2.35) yields

$$(\bar{\bar{G}}^i)^T = G_{xx}^i \hat{x}\hat{x} + G_{xz}^i \hat{z}\hat{x} . \qquad (2.60)$$

When this expression is substituted in (2.58) and the divergence and gradient operations are performed we can express $\bar{\bar{\Gamma}}^i$ as (see Appendix E, (E.3))

$$\bar{\bar{\Gamma}}^i = \Gamma_{xx}^i \hat{x}\hat{x} + \Gamma_{yx}^i \hat{y}\hat{x} + \Gamma_{zx}^i \hat{z}\hat{x} \qquad (2.61)$$

where

$$\Gamma^i_{xx} = G^i_{xx} + \frac{1}{k_i^2}\frac{\partial}{\partial x}\left(\frac{\partial G^i_{xx}}{\partial x} + \frac{\partial G^i_{zz}}{\partial z}\right) \quad (2.62)$$

$$\Gamma^i_{yx} = \frac{1}{k_i^2}\frac{\partial}{\partial y}\left(\frac{\partial G^i_{xx}}{\partial x} + \frac{\partial G^i_{zz}}{\partial z}\right) \quad (2.63)$$

$$\Gamma^i_{zx} = G^i_{xz} + \frac{1}{k_i^2}\frac{\partial}{\partial z}\left(\frac{\partial G^i_{xx}}{\partial x} + \frac{\partial G^i_{xz}}{\partial z}\right) . \quad (2.64)$$

Substituting this expression into (2.59) gives

$$\begin{aligned}\bar{E}^i_q &= \int\int_{S_q} \Gamma^i_{xx}\psi(y')\alpha_q(x')dx'dy'\,\hat{x} \\ &+ \int\int_{S_q} \Gamma^i_{yx}\psi(y')\alpha_q(x')dx'dy'\,\hat{y} \\ &+ \int\int_{S_q} \Gamma^i_{zx}\psi(y')\alpha_q(x')dx'dy'\,\hat{z}\,. \end{aligned} \quad (2.65)$$

Recall that we only need the x-component of this field which is given by

$$E^i_{qx} = \int\int_{S_q} \Gamma^i_{xx}\psi(y')\alpha_q(x')dx'dy'\,. \quad (2.66)$$

Furthermore, at $z = h$, boundary conditions require that $E^{(1)}_{qx}(z = h)$ and $E^{(2)}_{qx}(z = h)$ be identical. From the above equation it is obvious that this implies

$$\Gamma^{(1)}_{xx}(z = h) = \Gamma^{(2)}_{xx}(z = h) = \Gamma_{xx}(z = h). \quad (2.67)$$

This equality is verified in Appendix E, and the result of (E.7) may be put in the form

$$\Gamma_{xx}(z = h) = j\omega\mu_0 \sum_{m=1}^{\infty}\sum_{n=0}^{\infty} \frac{f_{mn}}{abd_{1mn}d_{2mn}} [\cos k_x x \,\sin k_y y\, \cos k_x x' \,\sin k_y y'] \quad (2.68)$$

where

$$\begin{aligned} f_{mn} &= \varphi_n \tan k_z^{(1)}h \tan k_z^{(2)}(h-c)\left[k_z^{(2)}\epsilon_r^*\left(1 - \frac{k_x^2}{k_1^2}\right)\tan k_z^{(2)}(h-c)\right. \\ &\left. -k_z^{(1)}\left(1-\frac{k_x^2}{k_0^2}\right)\tan k_z^{(1)}h\right] . \end{aligned} \quad (2.69)$$

If we place (2.68) into (2.66) we obtain

$$\begin{aligned} E_{qx}^{(1)}(z=h) &= E_{qx}^{(2)}(z=h) = \\ E_{qx}(z=h) &= j\omega\mu_0 \sum_{m=1}^{\infty}\sum_{n=0}^{\infty} \frac{f_{mn}}{abd_{1mn}d_{2mn}} \cos k_x x \ \sin k_y y \ \mathcal{I}_{qmn} \, . \end{aligned} \tag{2.70}$$

where

$$\mathcal{I}_{qmn} = \int\int_{S_q} \cos k_x x' \ \sin k_y y' \psi(y') \alpha_q(x') dx' dy' \, . \tag{2.71}$$

This surface integration is evaluated in closed form in Appendix F; the result is

$$\begin{aligned} \mathcal{I}_{qmn} &= -\frac{\zeta_q K l_x^2 \cos k_x x_q}{4 \sin K l_x} \text{Sinc}\left[\frac{1}{2}(k_x + K) l_x\right] \text{Sinc}\left[\frac{1}{2}(k_x - K) l_x\right] \\ & \sin k_y Y_0 \ J_0(k_y \frac{W}{2}) \, . \end{aligned} \tag{2.72}$$

where

$$\text{Sinc}(t) = \begin{cases} \frac{\sin t}{t} & \text{for } t \neq 0 \\ 1 & \text{for } t = 0 \, . \end{cases} \tag{2.73}$$

$$\zeta_q = \begin{cases} 2 & \text{for } q = 1 \\ 4 & \text{else} \end{cases} \tag{2.74}$$

$$K = \omega\sqrt{\mu_0 \epsilon_0 \epsilon_{r1}} \tag{2.75}$$

$$R_{1n} = \frac{1}{2}(k + k_x) l_x \tag{2.76}$$

$$R_{2n} = \frac{1}{2}(k - k_x) l_x \, . \tag{2.77}$$

The position vector x_q gives the x-coordinate of the q^{th} strip subsection. As will be outlined in Section 3.1.3, the functional dependence of this vector varies with the type of structure being analyzed.

We are now ready to evaluate the impedance elements.

2.4.2 Evaluation of the Impedance Matrix Elements

From (2.70) and (2.54) we have

$$Z_{qp} = j\omega\mu_0 \sum_{m=1}^{\infty}\sum_{n=0}^{\infty} \frac{f_{mn}\mathcal{I}_{qmn}}{abd_{1mn}d_{2mn}} \mathcal{I}_{pmn} \tag{2.78}$$

where

$$\mathcal{I}_{pmn} = \int\int_{S_p} \cos k_x x \, \sin k_y y \, \psi(y) \alpha_p(x) dx dy \ . \tag{2.79}$$

Since (2.79) is the same integral as (2.71), we can obtain the expression for $\mathcal{I}_{pmn}$ by substituting p for q in (2.72). From (2.78), the entire expression for Z_{qp} may be written as follows:

$$Z_{qp} = \frac{j\omega\mu_0 K^2 l_x^4}{16ab\sin^2 K l_x} \zeta_q \zeta_p \sum_{m=1}^{\infty} \sum_{n=0}^{\infty} \varphi_n \cos k_x x_q \cos k_x x_p [\,\mathrm{Sinc} R_{1n}\,\mathrm{Sinc} R_{2n}]^2$$
$$\cdot \frac{[\sin(k_y Y_0) J_0\left(\frac{k_y W}{2}\right)]^2 \tan k_z^{(1)} h \tan k_z^{(2)}(h-c)}{\left[k_z^{(2)} \tan k_z^{(1)} h - k_z^{(1)} \tan k_z^{(2)}(h-c)\right]}$$
$$\cdot \frac{\left[k_z^{(2)}\epsilon_r^* \left(1 - \frac{k_z^2}{k_1^2}\right) \tan k_z^{(2)}(h-c) - k_z^{(1)} \left(1 - \frac{k_z^2}{k_0^2}\right) \tan k_z^{(1)} h\right]}{\left[k_z^{(2)}\epsilon_r^* \tan k_z^{(2)}(h-c) - k_z^{(1)} \tan k_z^{(1)} h\right]} \tag{2.80}$$

With the theory for the computation of the impedance matrix complete, we turn to the theory for the excitation vector

<u>2.5 Excitation Vector Formulation</u>

In this section, a surface integral will be set up that provides for evaluating the elements of the excitation vector according to (2.16). This equation may be re-written as

$$V_q = \int\int_{S_f} \bar{H}_q(x=0) \cdot M_\phi \hat{\phi} \rho d\rho d\phi \tag{2.81}$$

where ρ, and ϕ are cylindrical coordinates referenced to the center of the feeding aperture, as shown in Figure 2.7.

An expression for M_ϕ will be presented first. Then, the magnetic field components parallel to the plane of the aperture (i.e. the $y - z$ plane) will be derived based on the Green's function of Section 2.3. The actual integration of (2.81) is performed numerically, and this is described in Section 3.1.

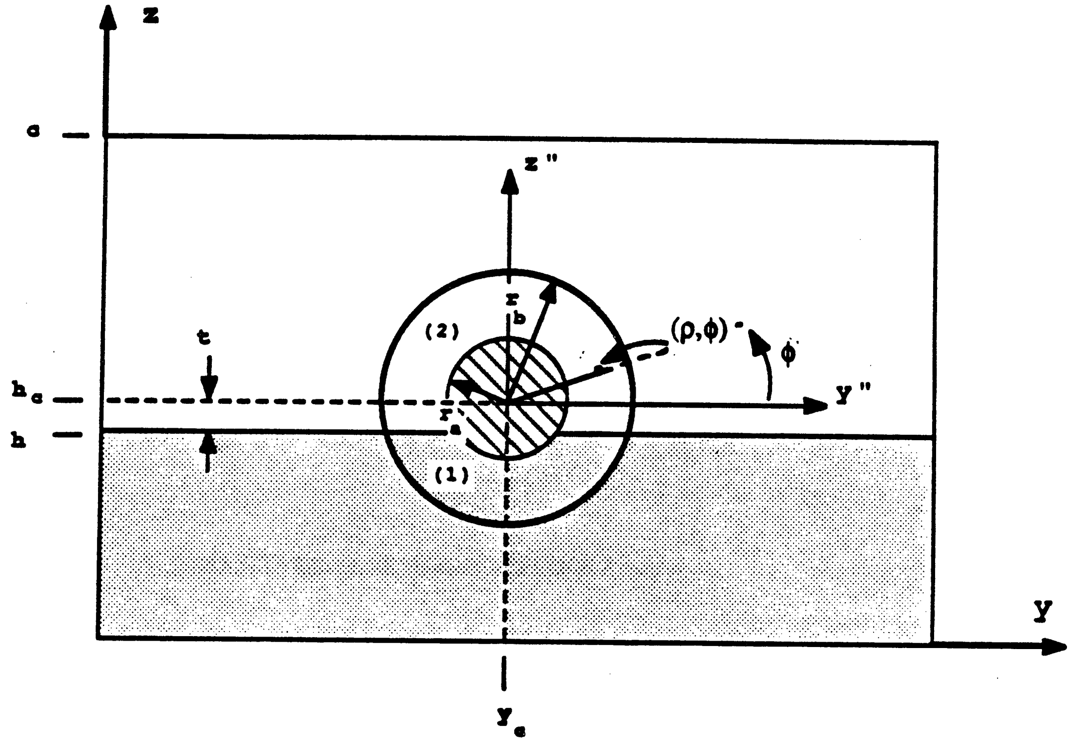

Figure 2.7: Geometry used to set up surface integral for excitation vector.

2.5.1 Coaxial Feed Modeling by an Equivalent Magnetic Current

If the radius of the coaxial feed's inner conductor is assumed to be much smaller than the wavelength ($kr_a \ll 1$), and the coaxial feed line is designed to allow only transverse magnetic (TEM) propagation, we can represent the aperture by an equivalent magnetic frill current given by [25,18]

$$\bar{M}_s = -\frac{V_0}{\rho \ln\left(\frac{r_b}{r_a}\right)}\hat{\phi} \tag{2.82}$$

where

V_0 is the complex voltage present in the coaxial line at the feeding point

r_b is the radius of the coaxial feed's outer conductor

r_a is the radius of the coaxial feed's inner conductor

ρ, ϕ are cylindrical coordinates referenced to the feed's center

Substituting from (2.82) into (2.81) yields (with $ds = \rho d\rho d\phi$)

$$V_q = -\frac{V_0}{\ln\left(\frac{r_b}{r_a}\right)}\int\int_{S_f} H^i_{q\phi}(x=0)d\rho d\phi \tag{2.83}$$

where the cylindrical coordinates ρ and ϕ are defined in Figure 2.7, and $H^i_{q\phi}$ is the $\hat{\phi}$ component of the magnetic field evaluated in the plane of the aperture ($x = 0$).

One factor that complicates the integration of (2.83) is that it must be performed in two regions whose boundaries depend on the feed position as can be seen in Figure 2.7. The integration can be broken up as follows:

$$\begin{aligned} V_q &= -\frac{V_0}{\ln\left(\frac{r_b}{r_a}\right)}\int\int_{S_f} H^i_{q\phi} d\rho d\phi \\ &= -\frac{V_0}{\ln\left(\frac{r_b}{r_a}\right)}\left[\int\int_{S_f^{(1)}} H^{(1)}_{q\phi} d\rho d\phi + \int\int_{S_f^{(2)}} H^{(2)}_{q\phi} d\rho d\phi\right] \end{aligned} \tag{2.84}$$

where

$S_f^{(1)}$ is the portion of the feed surface lying below the substrate ($z'' = \rho \sin\phi \leq -t$)

$S_f^{(2)}$ is the portion of the feed surface lying above the substrate ($z'' = \rho \sin\phi \geq -t$)

The evaluation of the magnetic field components $H_{q\phi}^{(1)}$ and $H_{q\phi}^{(2)}$ is described next. Once these have been evaluated, the integration of (2.84) is carried out numerically as discussed in Section 3.1.

2.5.2 Evaluation of the Magnetic Field at the Aperture

To evaluate the magnetic field component $H_{q\phi}$, we will first determine the $\hat{y}$ and $\hat{z}$ components, and then perform a coordinate transformation to the cylindrical coordinates ρ and ϕ.

Determination of $\hat{y}$ and $\hat{z}$ components of $\bar{H}_q$.— The magnetic field $\bar{H}_q$ anywhere inside the cavity is given by (2.26)

$$\bar{H}_q^i = \frac{1}{\mu_o}\bar{\nabla} \times \bar{A}_q^i \,.$$

The $\hat{y}$ and $\hat{z}$ components are given by

$$H_{qy}^i = \frac{1}{\mu_0}\left(\frac{\partial A_{qx}^i}{\partial z} - \frac{\partial A_{qz}^i}{\partial x}\right) \tag{2.85}$$

$$H_{qz}^i = -\frac{1}{\mu_0}\frac{\partial A_{qx}^i}{\partial y} \tag{2.86}$$

where, from (2.32) and (2.56),

$$A_{qx}^i = \mu_0 \int\int_{S_q} \psi(y')\alpha_q(x')G_{xx}^i ds' \tag{2.87}$$

$$A_{qz}^i = \mu_0 \int\int_{S_q} \psi(y')\alpha_q(x')G_{zx}^i ds' \,. \tag{2.88}$$

Combining the last four equations, we have

$$H_{qy}^i = \int\int_{S_q}\left(\frac{\partial G_{xx}^i}{\partial z} - \frac{\partial G_{zx}^i}{\partial x}\right)\psi(y')\alpha_q(x')ds' \tag{2.89}$$

$$H_{qz}^i = -\int\int_{S_q}\frac{\partial G_{xx}^i}{\partial y}\psi(y')\alpha_q(x')ds' \,. \tag{2.90}$$

These components are evaluated in Appendix G (for $i = 1,2$). Setting $x = 0$ in the resulting expressions yields:

$$H_{qy}^{(1)}(x=0) = H_{q0} \sum_{m=1}^{\infty}\sum_{n=0}^{\infty} c_{nq} c_{ymn}^{(1)} \sin k_y y \, \cos k_z^{(1)} z \tag{2.91}$$

$$H_{qz}^{(1)}(x=0) = H_{q0} \sum_{m=1}^{\infty}\sum_{n=0}^{\infty} c_{nq} c_{zmn}^{(1)} \cos k_y y \, \sin k_z^{(1)} z \tag{2.92}$$

$$H_{qy}^{(2)}(x=0) = H_{q0} \sum_{m=1}^{\infty}\sum_{n=0}^{\infty} c_{nq} c_{ymn}^{(2)} \sin k_y y \, \cos k_z^{(2)} (z-c) \tag{2.93}$$

$$H_{qz}^{(2)}(x=0) = H_{q0} \sum_{m=1}^{\infty}\sum_{n=0}^{\infty} c_{nq} c_{zmn}^{(2)} \cos k_y y \, \sin k_z^{(2)} (z-c) \tag{2.94}$$

where

$$H_{q0} = \frac{\zeta_q K l_x^2}{4ab \sin K l_x}$$

$$c_{nq} = \cos k_x x_q \,\mathrm{Sinc}\left[\frac{1}{2}(k_x + K) l_x\right] \mathrm{Sinc}\left[\frac{1}{2}(k_x - K) l_x\right]$$

and

$$c_{ymn}^{(1)} = \frac{c_{zmn}^{(1)}}{k_y d_{2mn}} \Big\{ k_z^{(1)} k_z^{(2)} \epsilon_r^* \tan k_z^{(2)}(h-c) - \left[(k_z^{(1)})^2 + k_x^2 (1-\epsilon_r^*) \right] \tan k_z^{(1)} h \Big\} \tag{2.95}$$

$$c_{zmn}^{(1)} = \frac{\varphi_n k_y \tan k_z^{(2)}(h-c)}{d_{1mn} \cos k_z^{(1)} h} \sin k_y Y_0 \, J_0(k_y \frac{W}{2}) \tag{2.96}$$

$$c_{ymn}^{(2)} = \frac{c_{zmn}^{(2)}}{k_y d_{2mn}} \Big\{ k_z^{(1)} k_z^{(2)} \tan k_z^{(1)} h - \left[(k_z^{(2)})^2 \epsilon_r^* - k_x^2 (1-\epsilon_r^*) \right] \tan k_z^{(2)}(h-c) \Big\} \tag{2.97}$$

$$c_{zmn}^{(2)} = \frac{\varphi_n k_y \tan k_z^{(1)} h}{d_{1mn} \cos k_z^{(2)}(h-c)} \sin k_y Y_0 \, J_0(k_y \frac{W}{2}) \,. \tag{2.98}$$

<u>Coordinate transformation and evaluation of $H_{q\phi}$</u> .— Equations (2.91)-(2.94) give the $\hat{y}$ and $\hat{z}$ components of the magnetic field anywhere inside the cavity. To find the $\hat{\phi}$ component we will perform the necessary coordinate transformation in two steps:

1. move the origin from the corner of the cavity (Figure 1.3) to the center of the coaxial feeding aperture.

Table 2.1: COORDINATE TRANSFORMATION VARIABLES

VARIABLE RELATIONS	UNIT VECTOR RELATIONS
$x'' = x$	$\hat{x}'' = \hat{x}$
$y'' = y - Y_c = \rho\cos\phi$	$\hat{y}'' = \hat{y} = \cos\phi\hat{\rho} - \sin\phi\hat{\phi}$
$z'' = z - h_c = \rho\cos\phi$	$\hat{z}'' = \hat{z} = \sin\phi\hat{\rho} + \cos\phi\hat{\phi}$

2. perform a cartesian to cylindrical coordinate transformation.

Referring to Figure 2.7, let us denote a new coordinate system by (x'', y'', z'') whose origin is at the feed's center $(x, y, z) = (0, Y_c, h_c)$. The relationship between the new and old coordinates are outlined in Table 2.1.

Using these relations, we will make the following substitutions in (2.91)-(2.94) to move the origin to the feed's center, and transform to cylindrical coordinates:

$$\begin{aligned} y \to y'' + Y_c &= \rho\cos\phi + Y_c \\ z \to z'' + h_c &= \rho\sin\phi + Y_c \end{aligned}$$

Now, let $\bar{H}^i_{qt}$ represent the projection of $\bar{H}^i_q$ onto the plane of the aperture such that

$$\bar{H}^i_{qt} = H^i_{qy}\hat{y} + H^i_{qz}\hat{z} = H^i_{q\phi}\hat{\phi} + H^i_{q\rho}\hat{\rho} \tag{2.99}$$

where $H^i_{q\rho}$ and $H^i_{q\phi}$ are the $\hat{\rho}$ and $\hat{\phi}$ components respectively.

Using the relations of Table 2.1, we readily obtain

$$H^i_{q\phi} = -\sin\phi H^i_{qy} + \cos\phi H^i_{qz}\,. \tag{2.100}$$

If we substitute from (2.91)-(2.94) into the above, and transform to cylindrical coordinates we obtain

$$H^{(1)}_{q\phi}(x = 0) =$$

$$H_{q0}\left[-\sin\phi\sum_{m=1}^{\infty}\sum_{n=0}^{\infty}c_{nq}c_{ymn}^{(1)}\sin k_y(\rho\cos\phi+Y_c)\cos k_z^{(1)}(\rho\sin\phi+h_c)\right.$$
$$\left.+\cos\phi\sum_{m=1}^{\infty}\sum_{n=0}^{\infty}c_{nq}c_{zmn}^{(1)}\cos k_y(\rho\cos\phi+Y_c)\sin k_z^{(1)}(\rho\sin\phi+h_c)\right] \quad (2.101)$$

$$H_{q\phi}^{(2)}(x=0)=$$
$$H_{q0}\left[-\sin\phi\sum_{m=1}^{\infty}\sum_{n=0}^{\infty}c_{nq}c_{ymn}^{(2)}\sin k_y(\rho\cos\phi+Y_c)\cos k_z^{(2)}(\rho\sin\phi-c'')\right.$$
$$\left.+\cos\phi\sum_{m=1}^{\infty}\sum_{n=0}^{\infty}c_{nq}c_{zmn}^{(2)}\cos k_y(\rho\cos\phi+Y_c)\sin k_z^{(2)}(\rho\sin\phi-c'')\right] \quad (2.102)$$

where

$$c''=c-h_c\,. \quad (2.103)$$

2.6 Current Computation for Two-Port Structures

In the preceeding sections, the theory has been advanced for computing the impedance matrix and excitation vector associated with a one-port discontinuity, such as an open-ended transmission line. This section will present the modifications necessary to extend the theory for treatment of two-port structures. Our approach for computing the network parameters (scattering parameters etc.) of two-ports, requires simultaneous excitation of the strip conductors from both sides of the cavity. We will refer to this as "dual excitation".

2.6.1 Application of Reciprocity Theorem for Dual Excitation

In section 2.2.1 an integral equation (2.3) was derived by applying the reciprocity theorem to the one-port network of Figure 2.5. In an analogous fashion, we will now apply the reciprocity theorem to the two-port network of Figure 2.8.

In Figure 2.8, both magnetic current sources $M_{\phi l}$ and $M_{\phi r}$ are coupled with the electric current source $\bar{J}_s$ on the conducting strips to produce the total fields

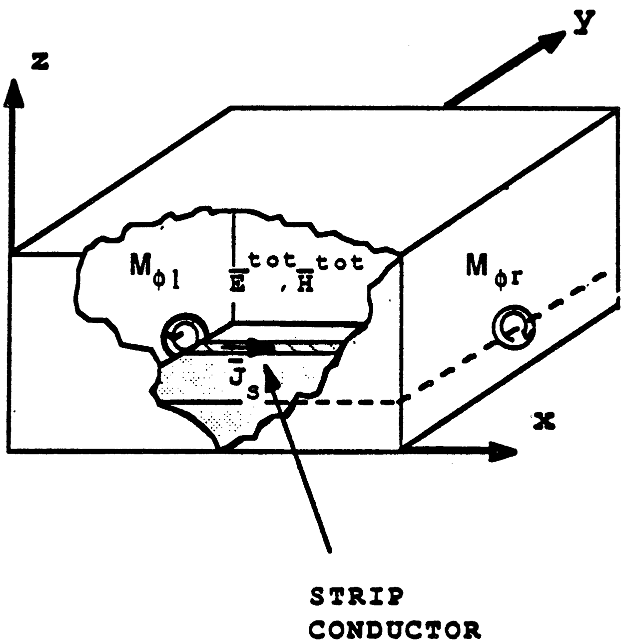

Figure 2.8: In the case of dual excitation, the total fields $\bar{E}^{tot}$, $\bar{H}^{tot}$ inside the cavity are produced by magnetic currents $M_{\phi l}$, $M_{\phi r}$, and the electric current $\bar{J}_s$.

$\bar{E}^{tot}$, $\bar{H}^{tot}$ inside the cavity. As before, we consider an independent test source $\bar{J}_q$, and associated fields $\bar{E}_q$ and $\bar{H}_q$ as shown in Figure 2.4.

Applying reciprocity theorem between these two sets of sources yields

$$\begin{aligned} \int\int\int_V \left(\bar{J}_s \cdot \bar{E}_q - \bar{H}_q \cdot \bar{M}_{sl} - \bar{H}_q \cdot \bar{M}_{sr}\right) dv &= \int\int\int_V \bar{J}_q \cdot \bar{E}^{tot} dv \\ &= 0 \end{aligned} \tag{2.104}$$

where the volume V is the interior of the cavity and

$$\bar{M}_{sl} = M_{\phi l}\hat{\phi} \tag{2.105}$$

$$\bar{M}_{sr} = M_{\phi r}\hat{\phi}. \tag{2.106}$$

The right hand side of (2.104) vanishes as described by (2.2). Reducing the remaining volume integrals of (2.104) to the appropriate surface integrals gives

$$\begin{aligned} \int\int_{S_{strip}} \bar{E}_q(z = h) \cdot \bar{J}_s ds &= \int\int_{S_{lf}} \bar{H}_q(x = 0) \cdot \bar{M}_{sl} ds \\ &+ \int\int_{S_{rf}} \bar{H}_q(x = a) \cdot \bar{M}_{sr} ds. \end{aligned} \tag{2.107}$$

In the above,

S_{lf} = Surface of coaxial aperture on left hand side ($x = 0$ side) of cavity

S_{rf} = Surface of coaxial aperture on right hand side ($x = a$ side) of cavity.

By comparison with (2.3), (2.107) can be seen as a natural extension to the theory for the case of single excitation.

2.6.2 Expansion of Current and Modified Matrix Equation

The current $\bar{J}_s$ is again expanded according to (2.6)

$$\bar{J}_s = \psi(y) \sum_{p=1}^{N_s} I_p \alpha_p(x) \hat{x}$$

The only difference is that we now must consider the basis function for the x-dependence on the last subsection (i.e. closest to the right-most feed) as a special case. This is necessary since at each end of the cavity only a half sinusoidal basis function is required as illustrated in Figure 2.9. Hence, for the right-most subsection we let

$$\alpha_{N_s}(x) = \begin{cases} \frac{\sin[K(x-a)]}{\sin(Kl_x)} & x_{N_s-1} \leq x \leq a \\ 0 & \text{else} \end{cases} \tag{2.108}$$

where the quantities K and l_x are as defined in Section 2.2.2, and N_s represents the index for the right-most subsection. The rest of the basis function expansion is the same as given by (2.7)-(2.9).

Substitution of (2.6) into (2.107) yields

$$\sum_{p=1}^{N_s}\left[\int\int_{S_p} \bar{E}_q(x=h)\cdot\psi(y)\,\alpha_p(x)\,\hat{x}ds\right] I_p = \int\int_{S_{lf}} \bar{H}_q(x=0)\cdot\bar{M}_{sl}ds + \int\int_{S_{rf}} \bar{H}_q(x=a)\cdot\bar{M}_{sr}ds \tag{2.109}$$

which can be expressed as

$$[\mathbf{Z}]\,[\mathbf{I}_d] = [\mathbf{V}_l] + [\mathbf{V}_r] = [\mathbf{V}_d] \tag{2.110}$$

where

$[\mathbf{I}_d]$ is the vector containing the current coefficients for the case of dual excitation

$[\mathbf{V}_l]$ is the excitation vector of the feed on the left ($N_s \times 1$)

$[\mathbf{V}_r]$ is the excitation vector of the feed on the right ($N_s \times 1$)

$[\mathbf{V}_d]$ is the combined excitation vector for dual excitation.

The elements of the excitation vectors $[\mathbf{V}_l]$, and $[\mathbf{V}_r]$ are given by

$$V_{ql} = \int\int_{S_{lf}} \bar{H}_q(x=0)\cdot\bar{M}_{sl}ds \tag{2.111}$$

$$V_{qr} = \int\int_{S_{rf}} \bar{H}_q(x=a)\cdot\bar{M}_{sr}ds \tag{2.112}$$

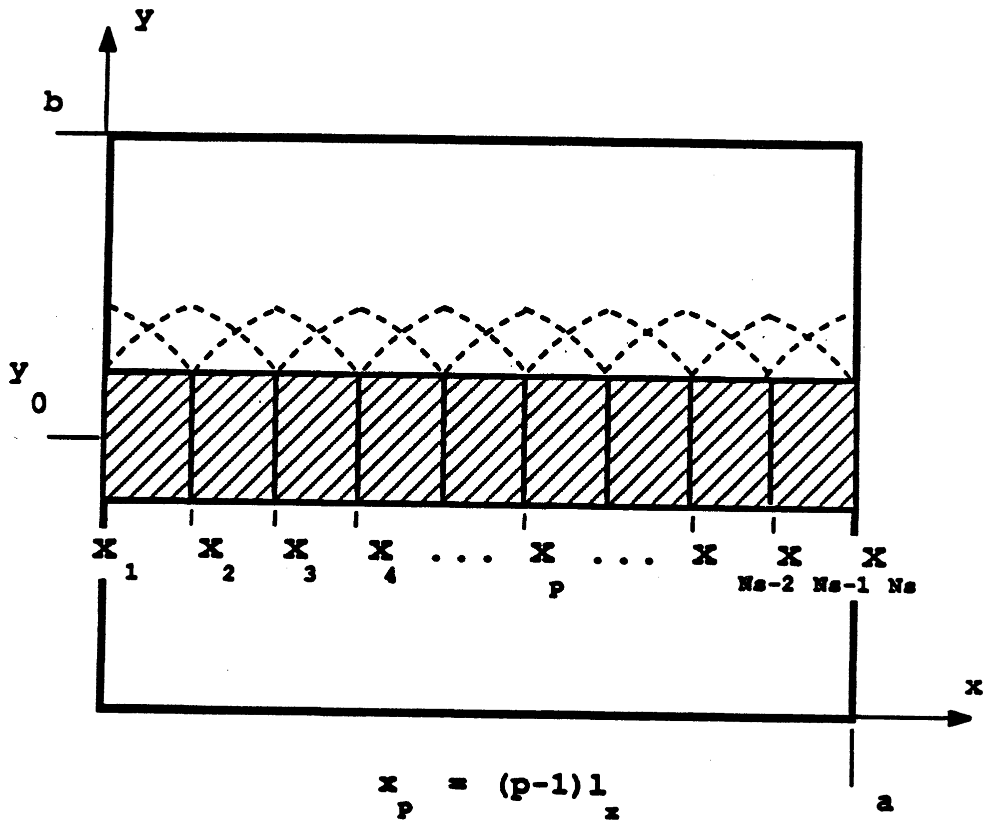

Figure 2.9: Strip geometry for basis function expansion with dual excitation. The case shown corresponds to a thru-line.

We can solve for the current vector by matrix inversion and multiplication according to

$$[\mathbf{I}] = [\mathbf{Z}]^{-1}[\mathbf{V}_d] \tag{2.113}$$

2.6.3 Modifications to Impedance Matrix

The elements of the impedance matrix for the case of dual excitation are given by the same integral equation as for the one port case, namely (2.15). The difference is in the integration over the last subsection ($p = N_s$) where $\alpha_p(x)$ is now given by (2.108). The integration for E_{qx} given by (2.70) is also modified for the last subsection ($q = N_s$) in a similar way. It can readily be shown that the surface integration over the last subsection (i.e. closest to the feed on the right) is equivalent to the integration over the first subsection (i.e. closest to the feed on the left). Hence, the elements of the impedance matrix are again given by (2.80) the only change being that ζ_q is as redefined below rather than by (2.74)

$$\zeta_q = \begin{cases} 2 & \text{for } q = 1 \text{ or } q = N_s \\ 4 & \text{else} \end{cases} \tag{2.114}$$

and ζ_p for the dual excitation case is given from (2.114) with q replaced by p.

2.6.4 Modifications to Excitation Vector

We now consider the integrations of (2.111), and (2.112). By analogy with (2.82) we may express the two magnetic currents as follows:

$$\bar{M}_{sl} = -\frac{V_{0l}}{\ln\left(\frac{r_b}{r_a}\right)\rho}\hat{\phi} \tag{2.115}$$

$$\bar{M}_{sr} = +\frac{V_{0r}}{\ln\left(\frac{r_b}{r_a}\right)\rho}\hat{\phi} \tag{2.116}$$

where the positive sign in the second current source indicates that it is taken to be in the opposite sense (Figure 2.8). In the above two equations, V_{0l} is the complex voltage in the coaxial line at the left-hand feed, and V_{0r} is the complex voltage in the coaxial line at the right-hand feed.

Substituting from (2.115) into (2.111) yields

$$V_{ql} = -\frac{V_{0l}}{\ln\left(\frac{r_h}{r_a}\right)} \int\int_{S_f} H_{q\phi}(x=0) d\rho d\phi \,. \tag{2.117}$$

Similarly, from (2.116) and (2.112),

$$V_{qr} = \frac{V_{0r}}{\ln\left(\frac{r_h}{r_a}\right)} \int\int_{S_f} H_{q\phi}(x=a) d\rho d\phi \,. \tag{2.118}$$

Now, the integration required for V_{ql} is identical to that carried out in Section 2.5 for V_q (single excitation case). The computation of V_{qr} is only slightly modified as we need to shift the origin to $(x', y', z') = (a, Y_c, h_c)$ instead of to $(0, Y_c, h_c)$. After examining the x-dependence of $\bar{H}_q$ given in Appendix G, it becomes obvious that we need only multiply the result for V_{ql} by $\cos n\pi$ to get the result for V_{qr}. That is

$$V_{qr} = -\frac{V_{0l}}{V_{0r}} \cos n\pi \; V_{ql}. \tag{2.119}$$

Let V_{qd} represent the elements of $[\;\mathbf{V}_d]$ given by

$$V_{qd} = V_{ql} + V_{qr} \,.$$

Then,

$$V_{qd} = \left(1 - \frac{V_{0l}}{V_{0r}} \cos n\pi\right) V_q \tag{2.120}$$

where V_q represents the excitation vector of Section 2.5 with V_0 set equal to unity.

As discussed in Section 2.7, two-port scattering parameters are found by applying even and odd mode excitations to the circuit. The next step here is to find the excitation vectors for these two cases.

For the even mode excitation, we let $V_{0l} = V_{0r} = 1$. In this case, from (2.120) we have

$$V_{qe} = V_q (1 - \cos n\pi)$$

$$= \begin{cases} 0 & \text{for n even} \\ 2V_q & \text{for n odd .} \end{cases} \tag{2.121}$$

For the odd mode excitation, we let $V_{0l} = -V_{0r} = 1$. Now, using (2.120)

$$\begin{aligned} V_{qo} &= V_q(1 + \cos n\pi) \\ &= \begin{cases} 2V_q & \text{for n even} \\ 0 & \text{for n odd} \end{cases} \end{aligned} \tag{2.122}$$

where

V_{qe} represents the elements of the even excitation vector $[\mathbf{V}_e]$

V_{qo} represents the elements of the odd excitation vector $[\mathbf{V}_o]$.

Using these two excitations, we can compute both the even and odd mode current distributions using the following matrix equations:

$$[\mathbf{I}_e] = [\mathbf{Z}]^{-1}[\mathbf{V}_e] \tag{2.123}$$

$$[\mathbf{I}_o] = [\mathbf{Z}]^{-1}[\mathbf{V}_o] \tag{2.124}$$

where

$[\mathbf{I}_e]$ represents the current vector for even excitation

$[\mathbf{I}_o]$ represents the current vector for odd excitation.

2.7 Determination of Network Parameters

The preceeding sections presented the theoretical methods for computing the current distributions for one- and two-port shielded microstrip discontinuities. The next step is to use these currents to determine the associated network parameters that can be used to represent them.

The relevant network parameters include the parameters of uniform microstrip line sections, and the parameters associated with discontinuity structures. The parameters for the uniform line sections are the complex propagation constant (γ_g), and the characteristic impedance (Z_0). For the discontinuity structures, the relevant parameters are one or more of the following:

- input impedance
- reflection coefficient
- scattering parameters
- impedance parameters
- admittance parameters
- equivalent circuit parameters.

Since the aim of this thesis is to concentrate on discontinuity effects, the characteristic impedance is not considered. For a microstrip line Z_0 cannot be strictly defined, and there has been considerable controversy over the most appropriate definition to use [27]-[31]. To avoid potential ambiguities caused by comparing results which may have been normalized to a different Z_0, the author has chosen to work with normalized network parameters where possible. In comparing scattering parameters, the normalizing impedance is whatever impedance corresponds to the microstrip line width in use (i.e. it does not need to be calculated to compare scattering parameters). This is true for both the measurements and the numerical results of the present research, although it may not be true for the results presented from CAD packages.

2.7.1 Network Parameters for One-Port Discontinuities

The simplest one-port discontinuity is an open-ended microstrip line. We will use the open-end as an example to illustrate the methodology for determining one-port network parameters. These include the propagation constant of the line, the reflection coefficient, and the input impedance at various points on the line.

Calculation of the Propagation Constant

In general, the complex propagation constant γ_g is given by

$$\gamma_g = \alpha_g + j\,\beta_g \tag{2.125}$$

For the computation of the current distribution, the theory for which is described in the preceeding sections,

In the development of the preceeding sections, which describes the theory for computation of the current distribution, the dielectric material was assumed to be lossy in general. However, for the discontinuity structures treated in this thesis, only the lossless case is considered for the computation of network parameters. The network parameter theory for the lossy case is a relatively straightforward extension, hence the theory of this section can easily be generalized to handle the lossy case.

In the lossless case $\gamma_g = j\beta_g$, where the phase constant β_g is given by

$$\beta_g = \frac{2\pi}{\lambda_g} \tag{2.126}$$

and λ_g is the microstrip wavelength. This can be determined by calculating the distance between adjacent current maximums. Another parameter that is often used to describe microstrip propagation characteristics is the effective dielectric constant ϵ_{eff}. This may be found from λ_g according to

$$\epsilon_{eff} = \left(\frac{\lambda_0}{\lambda_g}\right)^2 \tag{2.127}$$

where λ_0 is the free space wavelength.

Determination of the Input Reflection Coefficient and Impedance

To determine the input reflection coefficient we first need to establish a reference plane at some point on the line. Two convenient points are just to the right of the coaxial input ($x = 0$) and at the point where the discontinuity begins. Choosing the reference plane at $x = 0$, the voltage reflection coefficient (looking towards the discontinuity) anywhere on the transmission line is given by [5]

$$\Gamma(x) = \frac{SWR - 1}{SWR + 1} e^{-j\pi} e^{-j2\beta_g(x_{max} - x)} \tag{2.128}$$

where x_{max} is the position of a current maximum. SWR denotes the standing wave ratio, which is given by the ratio of the maximum current amplitude $|I_{max}|$ to the minimum current amplitude $|I_{min}|$. That is,

$$SWR = \frac{|I_{max}|}{|I_{min}|} . \tag{2.129}$$

The $e^{-j\pi}$ term in (2.128) arises since, on a lossless line, a current maximum corresponds to a short circuit (i.e. $\Gamma(x_{max}) = e^{-j\pi}$).

From (2.128), the reflection coefficient at the end of the line($x = L_{in}$) is given by

$$\Gamma(L_{in}) = \frac{SWR - 1}{SWR + 1} e^{-j\pi} e^{j2\beta_g d_{max}} \tag{2.130}$$

where

$$d_{max} = l - x_{max}$$

is the distance from the end of the line to a maximum.

The normalized input impedance at any point on the line may be found from the reflection coefficient according to

$$z(x) = \frac{1+\Gamma(x)}{1-\Gamma(x)} \,. \tag{2.131}$$

Equivalent Circuit for an Open-End Discontinuity

An open-end discontinuity in microstrip can be represented as either an effective length extension L_{eff} or by an equivalent capacitance c_{op} as shown in Figure 2.10.

Effective length extension for open-end discontinuity.— The effective length extension represents the length of ideal open circuited transmission line which, if as a continuation of the strip, would present the same reflection coefficient at $x = L_{in}$ as the open-end discontinuity (Figure 2.10). This length is deduced from the fact that the current on an ideal open circuit would go to zero at a distance $\frac{\lambda_g}{4}$ from the last current maximum. Hence, the effective length extension is given by

$$L_{eff} = \frac{\lambda_g}{4} - d_{max} \,. \tag{2.132}$$

This representation gives an intuitive feel for the magnitude of the end effect. On the other hand, the equivalent capacitance representation is better for circuit design purposes.

Equivalent capacitance for open-end discontinuity.— For an open-end in a lossless microstrip environment, the standing wave ratio is infinite ($SWR \rightarrow \infty$); hence, from (2.130)

$$\Gamma_{op} = \Gamma_{op} = e^{j\theta_{op}} \tag{2.133}$$

where

$$\theta_{op} = 2\beta_g d_{max} - \pi \,. \tag{2.134}$$

The associated normalized equivalent capacitance (Figure 2.10) can be expressed as

$$c_{op} = \frac{\sin 2\beta_g d_{max}}{\omega(1 - \cos 2\beta_g d_{max})} = \frac{\sin 2\beta_g L_{eff}}{\omega(1 + \cos 2\beta_g L_{eff})} \,. \tag{2.135}$$

An algorithm for calculating one-port network parameters from the microstrip current, computed numerically, is discussed in the following chapter.

2.7.2 Network Parameters for Two-Port Structures

The network parameters for two-port structures determined by analyzing the currents from the even and odd mode excitations discussed in Section 2.6, and illustrated in Section 3.2.4.

General Representation by Equivalent T-network

In general, a passive symmetric two-port structure can be represented by the T-network equivalent circuit of Figure 2.11. The T-network parameters are given in terms of the normalized impedance parameters according to

$$\begin{bmatrix} V_1 \\ V_2 \end{bmatrix} = \begin{bmatrix} z_{11} & z_{12} \\ z_{21} & z_{22} \end{bmatrix} \begin{bmatrix} I_1 \\ I_2 \end{bmatrix} \,. \tag{2.136}$$

Since we have assumed that the two-port structure is passive, reciprocal, and symmetric $z_{11} = z_{22}$ and $z_{12} = z_{21}$.

These impedance parameters are found from the input impedances of the even and odd current distributions. The even mode excitation ($V_{g1} = V_{g2} = V_0$) corresponds to placing an electric wall in the center of the circuit as shown in Figure 2.12a. The odd mode excitation ($V_{g1} = -V_{g2} = V_0$) corresponds to placing a magnetic wall in the center of the circuit as shown in Figure 2.12. The normalized input impedances z_{IN}^e and z_{IN}^o, for these two cases are found by analyzing the two separate current distributions as described in Section 4.2 for one-port analysis.

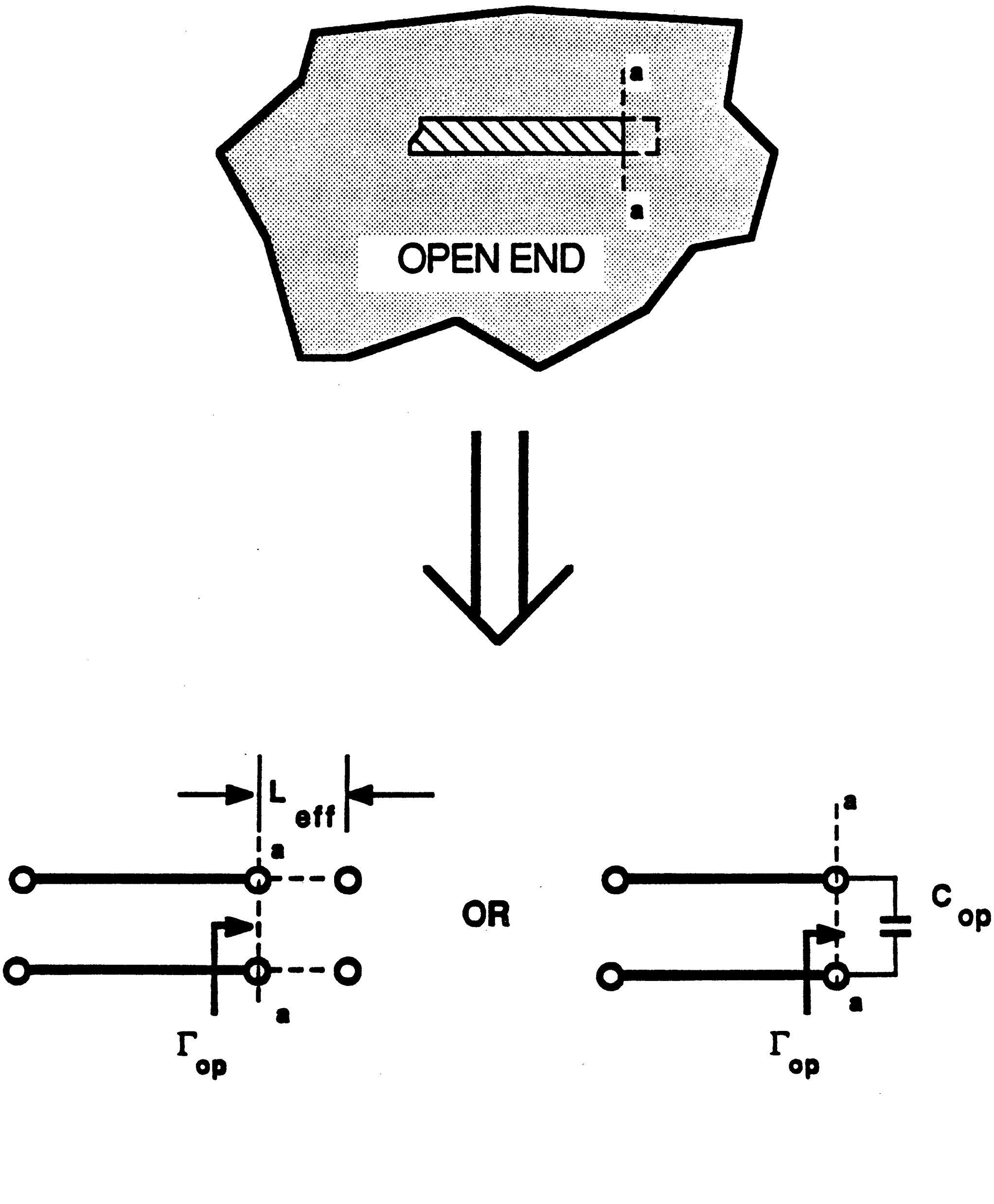

Figure 2.10: Representation for microstrip open end discontinuity.

Once these impedances have been determined, the impedance parameters are found according to

$$z_{11} = \frac{z_{IN}^{e} + z_{IN}^{o}}{2} \quad (2.137)$$

$$z_{12} = \frac{z_{IN}^{o} - z_{IN}^{e}}{2} . \quad (2.138)$$

Derivation of Scattering and Admittance Parameters

The scattering parameters may be derived from the normalized z-parameters by using the following relations

$$S_{11} = S_{22} = \frac{z_{11}^2 - 1 - z_{12}^2}{D} \quad (2.139)$$

$$S_{12} = S_{21} = \frac{2z_{12}}{D} \quad (2.140)$$

where

$$D = z_{11}^2 + 2z_{11} - z_{12}^2 \quad (2.141)$$

Furthermore, it may also be desirable to compute the normalized y-parameters for the network. These may be derived from the scattering parameters using the following relations:

$$y_{11} = y_{22} = \frac{1 - S_{11}^2 - S_{12}^2}{(1 + S_{11})^2 - S_{12}^2} \quad (2.142)$$

$$y_{12} = y_{21} = \frac{2S_{11}S_{12}}{(1 + S_{11})^2 - S_{12}^2} \quad (2.143)$$

2.8 Summary of Theoretical Methodology

In this chapter, the theoretical approach used to compute network parameters for shielded microstrip discontinuities has been described. A combination of reciprocity theorem and the method of moments is used to derive a matrix equation

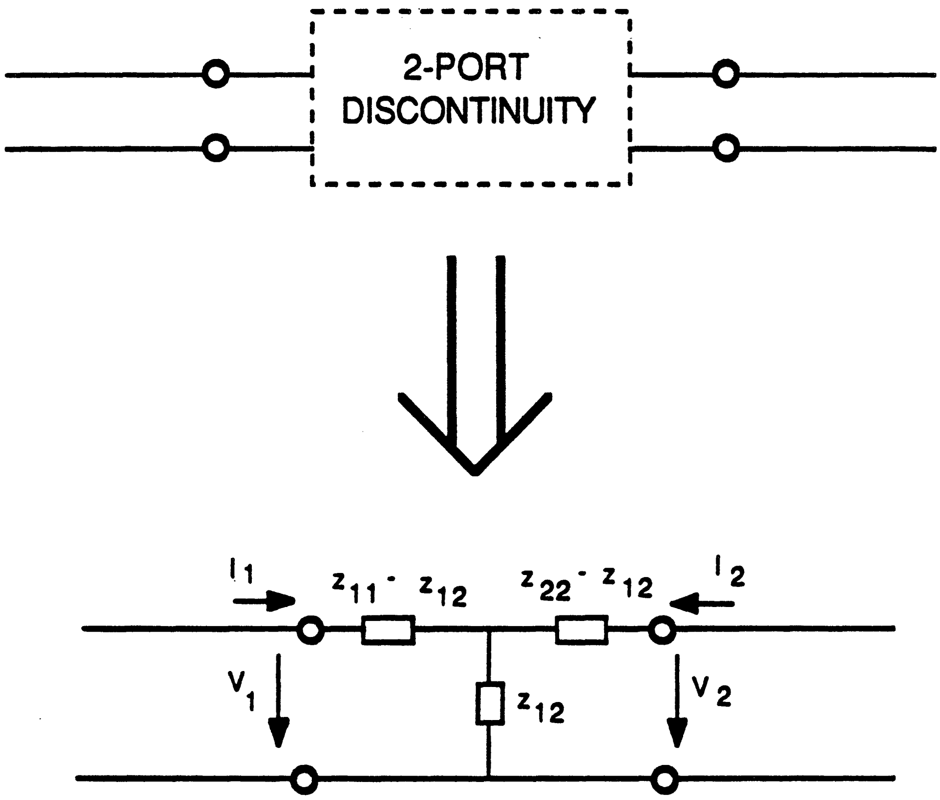

Figure 2.11: Equivalent network representation for generalized 2-port discontinuity.

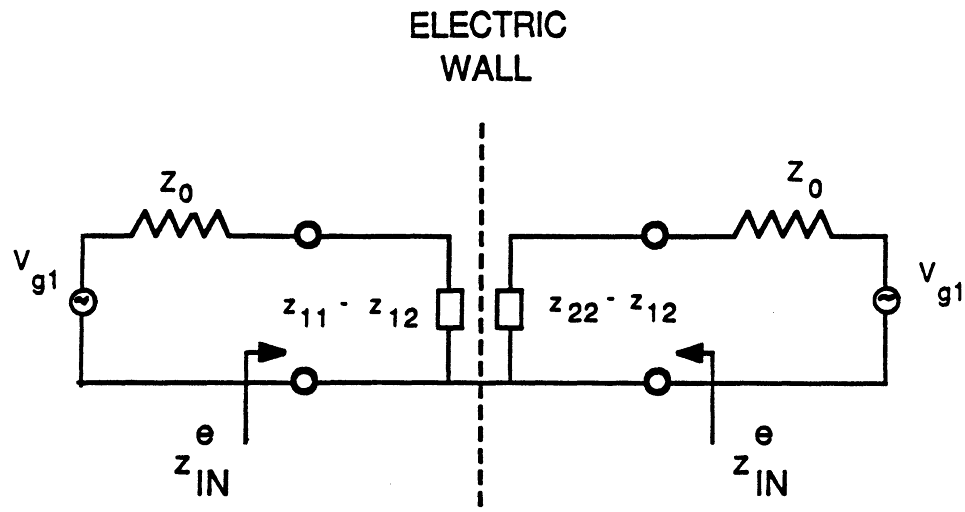

a) Case for even excitation.

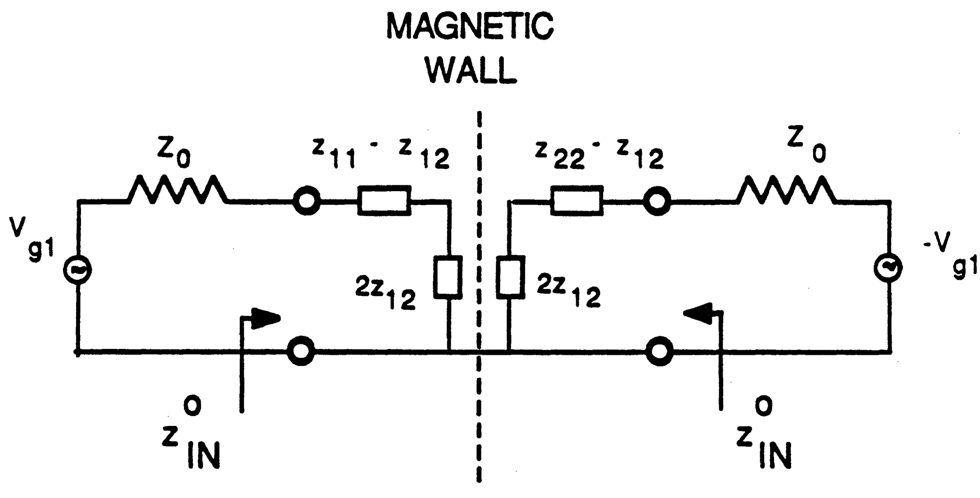

b) Case for odd excitation.

Figure 2.12: The even and odd mode excitations correspond to placing electric and magnetic walls in the center of the two-port structure.

that consists of an impedance matrix, an unknown current vector and an excitation vector. Two types of circuit excitation mechanisms are considered: 1) a coaxial excitation method, and 2) a gap generator method. The matrix equation is solved to compute the current distribution on the conducting strips. Based on this current distribution, the network parameters for one- and two-port discontinuities are calculated.

CHAPTER III

COMPUTATIONAL CONSIDERATIONS

This chapter is divided into two main parts. The first part describes the software design for implementing the theory developed in Chapter 2. First, the formulation used to compute the current distribution is re-arranged to facilitate computer solution. Next, the computer algorithm is discussed, and the computation of the current distribution is described. Algorithms for computing one- and two-port network parameters are also included.

The second part of the chapter focuses on numerical convergence considerations. First, the convergence of the elements of the impedance matrix and excitation vectors is considered. Then a series of numerical experiments are described which are designed to test the stability and convergence of the final results.

3.1 Formulation for Computer Solution

To compute the current distribution given by (2.17) we must first compute the elements of the impedance matrix Z_{qp} and the elements of the excitation vector V_q. The formulations for these elements, given in Chapter 2 are put in a form more convenient for programming below.

3.1.1 Formulation to Compute Impedance Matrix [Z]

The elements of the impedance matrix are given by (2.80). This equation may be re-written in the following form

$$\begin{aligned} Z_{qp} &= \frac{j\omega\mu_0 K^2 l_x^4}{16ab\sin^2 Kl_x}\zeta_q\zeta_p \sum_{n=0}^{NSTOP} \varphi_n \cos k_x x_q \cos k_x x_p \\ &\cdot [\,\mathrm{Sinc}\left[\frac{1}{2}(k_x+K)l_x\right] \mathrm{Sinc}\left[\frac{1}{2}(k_x-K)l_x\right]]^2\ [LN(n)] \end{aligned} \quad (3.1)$$

where the vector $LN(n)$ is given by the series

$$LN(n) = \sum_{m=1}^{MSTOP} L_{mn} \quad (3.2)$$

with the series elements L_{mn} given by

$$\begin{aligned} L_{mn} &= \frac{\varphi_n[\sin(k_y Y_0) J_0\left(\frac{k_y W}{2}\right)]^2 \tan k_z^{(1)}h \tan k_z^{(2)}(h-c)}{\left[k_z^{(2)} \tan k_z^{(1)}h - k_z^{(1)} \tan k_z^{(2)}(h-c)\right]} \\ &\cdot \frac{\left[k_z^{(2)}\epsilon_r^* \left(1-\frac{k_x^2}{k_1^2}\right) \tan k_z^{(2)}(h-c) - k_z^{(1)}\left(1-\frac{k_x^2}{k_0^2}\right) \tan k_z^{(1)}h\right]}{\left[k_z^{(2)}\epsilon_r^* \tan k_z^{(2)}(h-c) - k_z^{(1)} \tan k_z^{(1)}h\right]}\,. \end{aligned} \quad (3.3)$$

All of the other parameters are as defined in Chapter 2.

3.1.2 Formulation to Compute Excitation Vector [V]

Excitation vector for coaxial (frill current) excitation

Formulation.— The elements of the excitation vector for the coaxial excitation mechanism (2.84) may be written as

$$\begin{aligned} V_q &= \frac{-V_0\zeta_q K l_x^2}{\ln\left(\frac{r_b}{r_a}\right) 4ab\sin Kl_x} \sum_{n=0}^{NSTOP} \cos k_x x_q \\ &\cdot \mathrm{Sinc}\left[\frac{1}{2}(k_x+K)l_x\right] \mathrm{Sinc}\left[\frac{1}{2}(k_x-K)l_x\right] [MN(n)] \end{aligned} \quad (3.4)$$

where the vector $MN(n)$ is expressed in terms of the series given by

$$MN(n) = \sum_{m=1}^{MSTOP} M_{mn}\,. \quad (3.5)$$

The series elements M_{mn} are given by the following integral

$$\begin{aligned} M_{mn} &= \int\int_{S_f} \mathcal{M}^i_{mn}\, d\rho\, d\phi \\ &= \int\int_{S_f^{(1)}} \mathcal{M}^{(1)}_{mn}\, d\rho\, d\phi + \int\int_{S_f^{(2)}} \mathcal{M}^{(2)}_{mn}\, d\rho\, d\phi \end{aligned} \tag{3.6}$$

In the above, $S_f^{(1)}$ is the portion of the coaxial aperture surface lying above the substrate (region 2) and $S_f^{(2)}$ is the portion of the coaxial aperture surface lying within the substrate (region 1). The integrands $\mathcal{M}^i_{mn}$ of (3.6) are given by

$$\begin{aligned} \mathcal{M}^{(1)}_{mn} &= \cos\phi\, c^{(1)}_{zmn} \cos k_y(\rho\cos\phi + Y_c) \sin k_z^{(1)}(\rho\sin\phi + h_c) \\ &\quad - \sin\phi\, c^{(1)}_{ymn} \sin k_y(\rho\cos\phi + Y_c) \cos k_z^{(1)}(\rho\sin\phi + h_c) \end{aligned} \tag{3.7}$$

for ρ and ϕ in region 1, and

$$\begin{aligned} \mathcal{M}^{(2)}_{mn} &= \cos\phi\, c^{(2)}_{zmn} \cos k_y(\rho\cos\phi + Y_c) \sin k_z^{(2)}(\rho\sin\phi - c'') \\ &\quad - \sin\phi\, c^{(2)}_{ymn} \sin k_y(\rho\cos\phi + Y_c) \cos k_z^{(2)}(\rho\sin\phi - c'')\ . \end{aligned} \tag{3.8}$$

for ρ and ϕ in region 2. Note that the coefficients $c^{(1)}_{ymn}, c^{(1)}_{zmn}, c^{(2)}_{ymn}$, and $c^{(2)}_{zmn}$, which are given by (2.95)-(2.98), are independent of the integration variables ρ and ϕ.

Numerical Integration.— The elements M_{mn} of the series $MN(n)$ needed to compute the excitation vector for the coaxial (frill current) method are calculated numerically using a 16 point Product Gauss formula approximation [33].

Let us define a pair of dummy variables s and u and a function $\mathcal{F}(s,u)$ such that

$$\int_{\phi_{min}=0}^{\phi_{max}=2\pi} \int_{\rho_{min}=r_a}^{\rho_{max}=r_b} \mathcal{M}^i_{mn} d\rho d\phi = \int_{s_{min}=-1}^{s_{max}=1} \int_{u_{min}=-1}^{u_{max}=1} \mathcal{F}(s,u) ds \tag{3.9}$$

where the correspondence between (u,s) and (ρ,ϕ) is given by the following relations

$$u = \frac{2\rho - (\rho_{max} + \rho_{min})}{\rho_{max} - \rho_{min}} = \frac{2\rho - (r_b - r_a)}{r_b - r_a} \tag{3.10}$$

$$\rho = \frac{1}{2}[u(r_b - r_a) + (r_b + r_a)] \tag{3.11}$$

$$s = \frac{2\phi - (\phi_{max} + \phi_{min})}{\phi_{max} - \phi_{min}} = \phi/\pi - 1 \tag{3.12}$$

$$\phi = \pi(s+1)\ . \tag{3.13}$$

The numerical integration can be carried out by generating a set of 16 pairs of points (u_j, s_j) and adding up their contributions according to

$$\int_{\phi_{min}=0}^{\phi_{max}=2\pi} \int_{\rho_{min}=r_a}^{\rho_{max}=r_b} \mathcal{M}_{mn}^{i} d\rho d\phi \doteq \sum_{j=1}^{16} B_j \mathcal{F}(u_j, s_j) \tag{3.14}$$

where

(u_j, s_j) is the j^{th} pair of integration points

B_j is the weighting factor associated with the j^{th} pair of integration points, and

$\mathcal{F}(s_j, u_j)$ is the transformed integrand found by performing a coordinate transformation on $\mathcal{M}_{mn}$.

Alternatively, once we have chosen the 16 points (s_j, u_j), we can find the corresponding values of ρ and ϕ by (3.11) and (3.13) and obtain the same result. That is

$$\int_{\phi_{min}=0}^{\phi_{max}=2\pi} \int_{\rho_{min}=r_a}^{\rho_{max}=r_b} \mathcal{M}_{mn}^{i} d\rho d\phi = \sum_{j=1}^{16} B_j \mathcal{M}_{mn}(\rho_j, \phi_j) \tag{3.15}$$

where

$$\begin{aligned} \rho_j &= \frac{1}{2}[u_j(r_b - r_a) + (r_b + r_a)] \\ \phi_j &= \pi(s_j + 1) \end{aligned}$$

and

$$\mathcal{M}_{mn}^{i}(\rho_j, \phi_j) = \begin{cases} \mathcal{M}_{mn}^{(1)}(\rho_j, \phi_j) & \text{for } -h_c \le \rho_j \sin\phi_j \le -t \\ \mathcal{M}_{mn}^{(2)}(\rho_j, \phi_j) & \text{for } -t \le \rho_j \sin\phi_j \le c'' = c - h_c \\ \text{error condition} & \text{else .} \end{cases} \tag{3.16}$$

Gap generator excitation

For the excitation vector, all of the elements of the impedance matrix are set to zero except one, which is given a value of unity. That is,

$$[\mathbf{V}] = \begin{bmatrix} 0 & 0 & \cdots & 1 & \cdots & 0 & 0 & 0 \end{bmatrix}^T . \tag{3.17}$$

Hence, the elements of the excitation vector for this case are given by

$$V_q = \delta_{qg} = \begin{cases} 1 & \text{for } x_q = x_g \\ 0 & \text{else} \end{cases} \tag{3.18}$$

where $x = x_g$ is the position of the gap generator.

3.1.3 Defining the Strip Geometry

The formulations derived above for the computation of the current is general. That is, the same formulation can be used for all of the discontinuities considered in this thesis. However, the strip geometry differs between the cases. The strip geometry is specified by the position vector x_q (or x_p) and the number of sections N_s. The following discussion illustrates how these parameters are determined for various structures.

For an open-ended line (Figure 2.5) and a thru-line (Figure 2.9) the position vector is given by

$$x_p = (p-1)l_x . \tag{3.19}$$

The only difference between the two cases is the number of subsections N_s.

The strip geometry for a series gap discontinuity is shown in Figure 3.1. Let N_a be the number of subsections required to compute the current on the left hand strip, with N_s being the total number of subsections. The position vector may be written as

$$x_p = \begin{cases} (p-1)l_x & p \le N_a \\ pl_x + G & p > N_a . \end{cases} \tag{3.20}$$

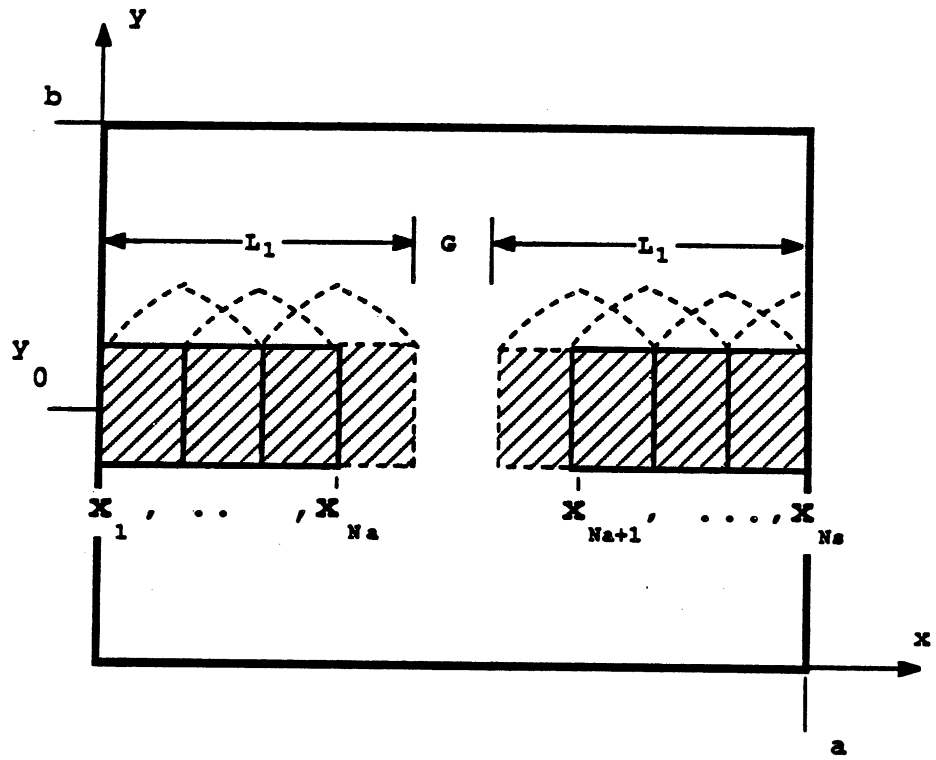

Figure 3.1: Determination of the computational parameters for a series gap is somewhat more complicated than for an open-end or a thru-line.

where G is the length of the gap space.

The strip geometry definition for coupled line structures is only slightly more complicated, than those discussed above. Further details have been omitted.

3.2 Algorithm for Current Computation

The method of moments solution for the current distribution was implemented in a Fortran program named *SHDISC*. The various computation steps are outlined in the flow chart of Figure 3.2 and are summarized below.

3.2.1 Input Data File

A data file is set up first to input the analysis frequencies and the geometrical parameters of the problem to be solved. Also, in this data file several flags may be set or cleared to direct the program flow, and file names are assigned to output files that will contain the results of the computations.

One important flag indicates whether or not the $LN(n)$ and $MN(n)$ vectors are to be calculated or read in from a storage file. These vectors are independent of the subsection length l_x and the strip geometry in the x-direction described by x_p. Hence, once they have been calculated they need not be re-calculated unless the cavity geometry or the frequency has changed. For example, the same $LN(n)$, $MN(n)$ vectors may be used to calculate the current distributions for an open-end discontinuity, a thru-line, and series gap discontinuities with different gap spacings. This is important because approximately 50% to 90% of the computation time (depending on the size of the impedance matrix) is spent on evaluating the vectors $LN(n)$ and $MN(n)$ vectors.

There is also a flag to choose between gap generator and coaxial excitation.

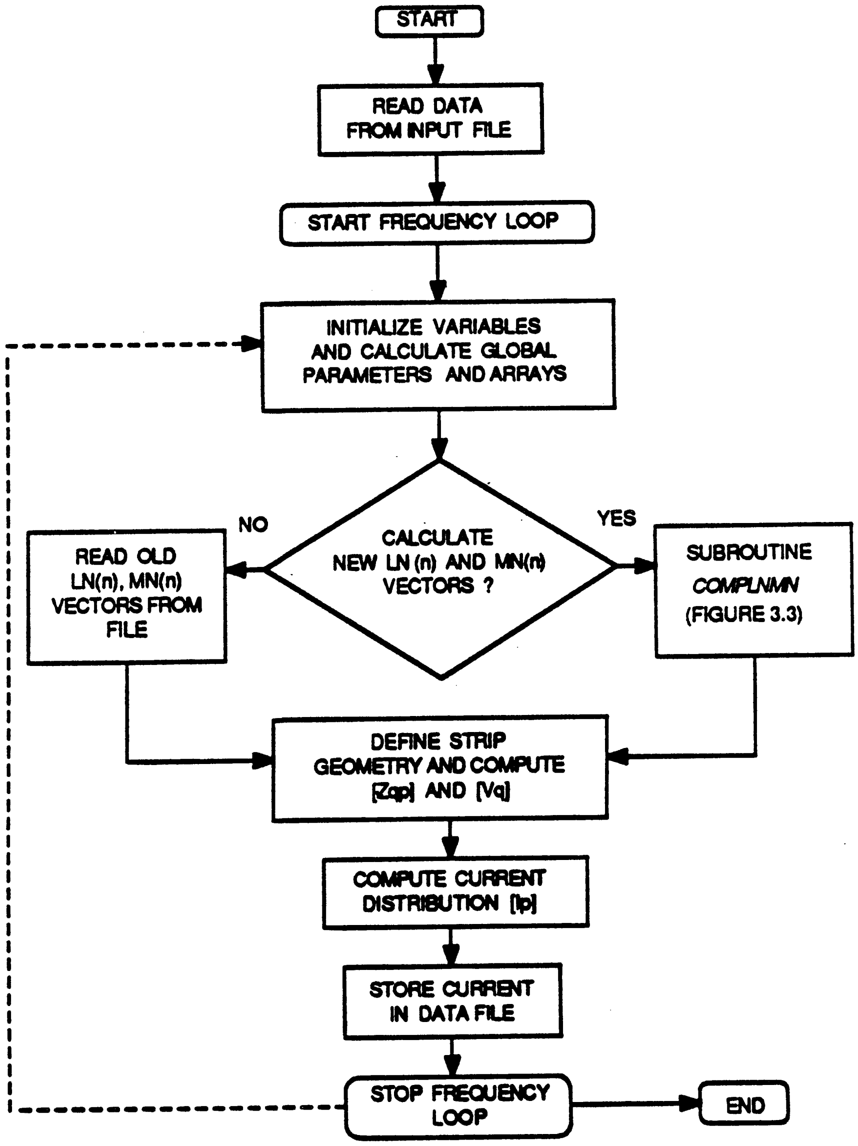

Figure 3.2: Flow chart for program *SHDISC* to compute current distribution.

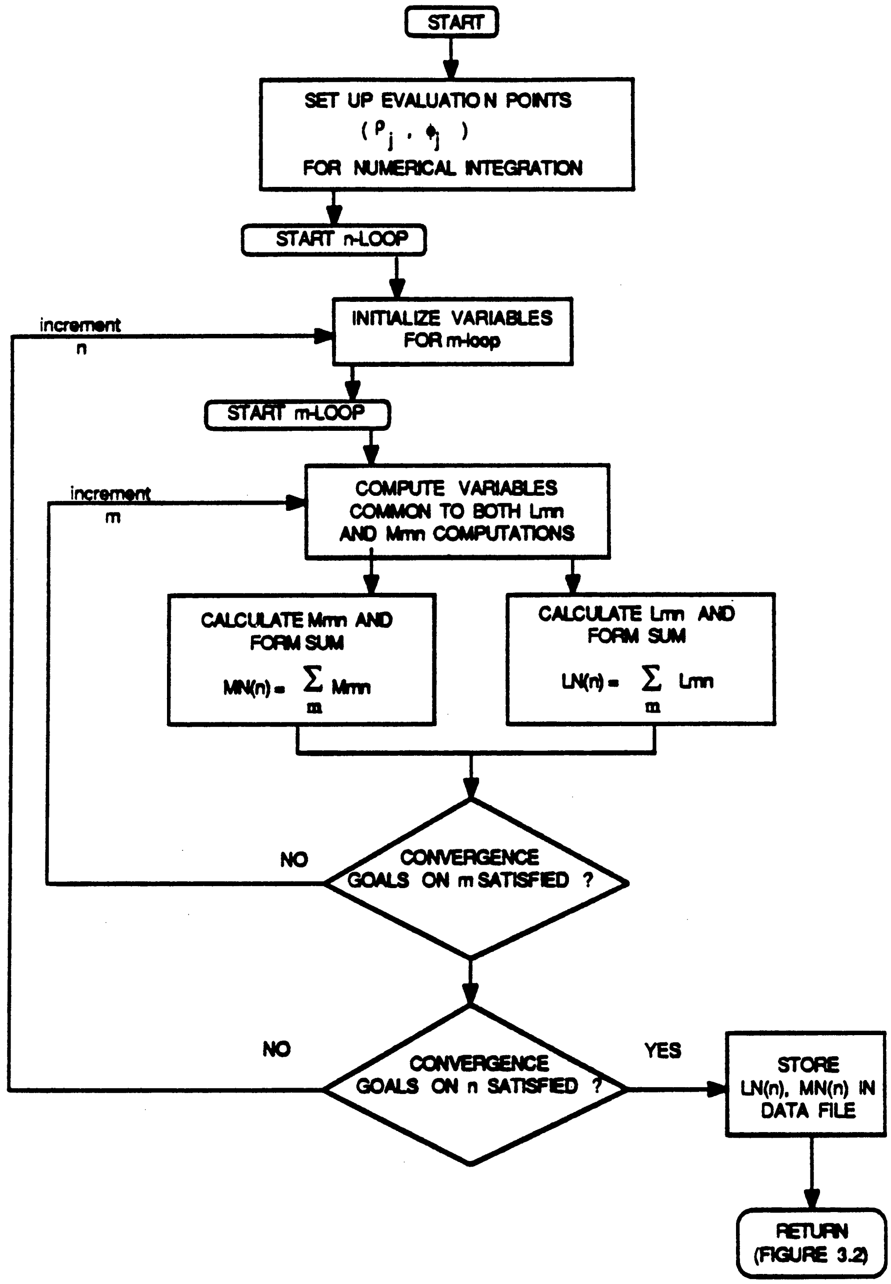

Figure 3.3: Flow chart for subroutine that computes vectors $LN(n)$, and $MN(n)$.

3.2.2 Computation of $LN(n)$ and $MN(n)$ Vectors

After the input data file is read and the global parameters and arrays have been calculated, the program flow is directed to the subroutine "COMPLNMN", if the $LN(n)$ and $MN(n)$ vectors have not been previously computed. A flow chart for this subroutine is given in Figure 3.3. The first step is to set up the integration points ρ_j and ϕ_j to be used in the numerical integration for computing M_{mn} as discussed in Section 3.1.2. After this, the computation of $LN(n)$ and $MN(n)$ for each n is carried out by adding up the L_{mn}'s and M_{mn}'s over the summation index m.

The summations over m are terminated in one of two ways. The first is to test error functions which describe the fractional change in $LN(n)$ and $MN(n)$ with the addition of the last L_{mn} and M_{mn} respectively. The other way that the summations over m are terminated is if the specified maximum index value $MSTOP$ is reached before the error goals have been satisfied. The truncation of the computations over the n-index is determined in a similar way. This time, however, the error functions describe the fractional change in the summation of $LN(n)$ and $MN(n)$ over n. As in the summation over m, the computation is also terminated if the maximum n-index $NSTOP$ is reached before the error goal has been reached. For the convergence experiments which are described shortly, the error goals are set to very low values so that the computations on m and n are carried out to $MSTOP$ and $NSTOP$ respectively.

3.2.3 Computation of the Impedance Matrix and Excitation Vectors

After the $LN(n)$ and $MN(n)$ vectors have either been calculated or read in from a storage file, the strip geometry is defined. This is done based on the type of discontinuity to be analyzed and the geometry specified in the input file, as discussed in Section 3.1.3. Next, the elements of the impedance matrix and excitation vector are computed. To gain insight into the nature of these matrices, we will examine plots of a typical impedance matrix and typical one- and two-port excitation vectors.

Typical impedance matrix.— Figure 3.4 shows the amplitude distribution of a typical impedance matrix. It is seen that the amplitude of the diagonal elements is the greatest and the amplitude tapers off uniformly as one moves away from the diagonal. Another observation is that the matrix is symmetric such that $Z_{qp} = Z_{pq}$ for any p and q, and the amplitude for any row or column displays the same distribution with respect to the diagonal element.

Typical excitation vectors.— Figure 3.5 shows the amplitude distribution for the excitation vector for a typical one-port (open-end) structure. It is seen that the amplitude is highest over the first subsection, which is closest to the feed. The amplitude then tapers off rapidly over the subsequent subsections.

The even and odd excitation vectors for a typical two-port (thru-line) structure is shown in Figure 3.6. The amplitude distribution is symmetric around the center of the cavity for the even case, and asymmetric for the odd case. Next to each feed (i.e. near $x = 0$ and $x = a$) the amplitude distribution has the same shape as for the one-port case, which is expected from (2.120).

3.2.4 Computation of the Current Distribution

In the matrix equation (2.17), which describes the solution for the current distribution, matrix inversion and multiplication is implied. While this is correct mathematically, it is not efficient numerically. There are several approaches for solving systems of equations without matrix inversion. Most of these are readily

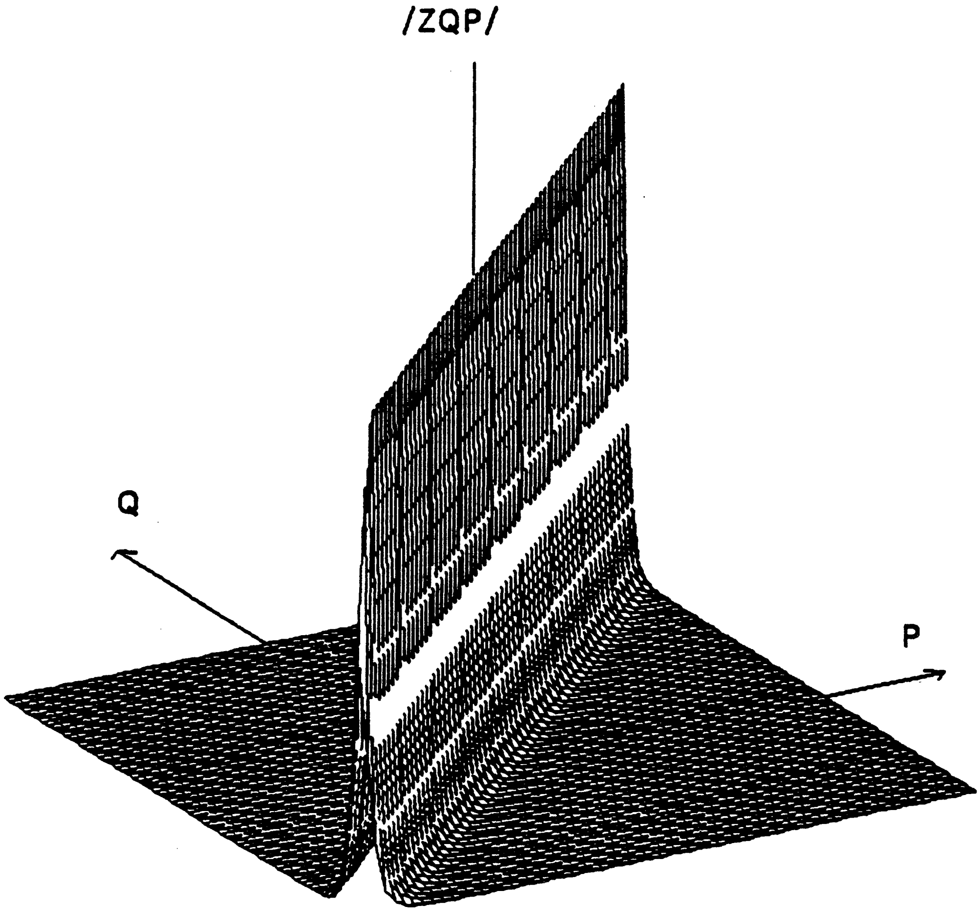

Figure 3.4: A plot 3-dimensional plot of the impedance matrix for a typical open-end shows that it is diagonally dominant and well behaved.

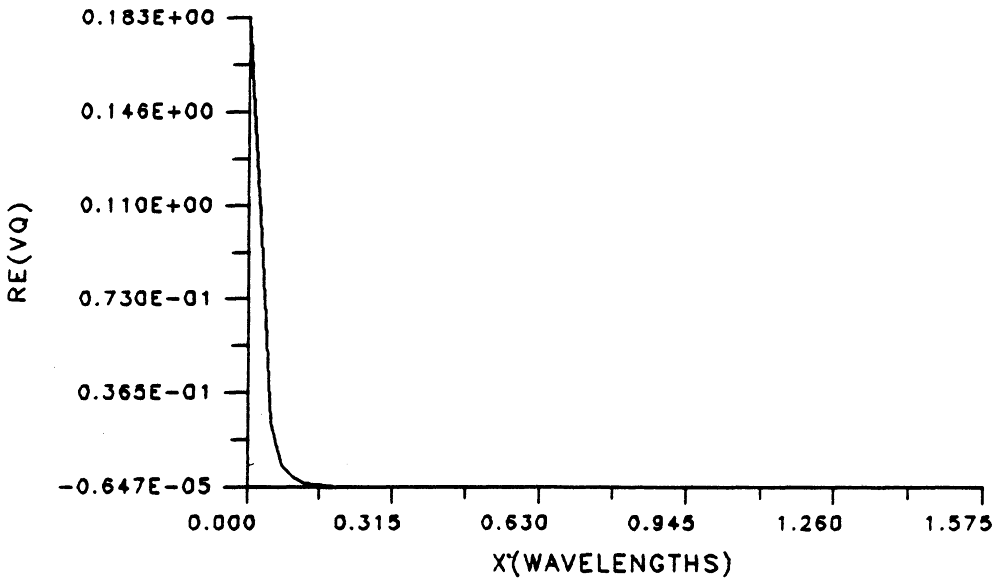

Figure 3.5: The amplitude distribution for the excitation vector is highest for Q=1, which corresponds to the position of the feed.

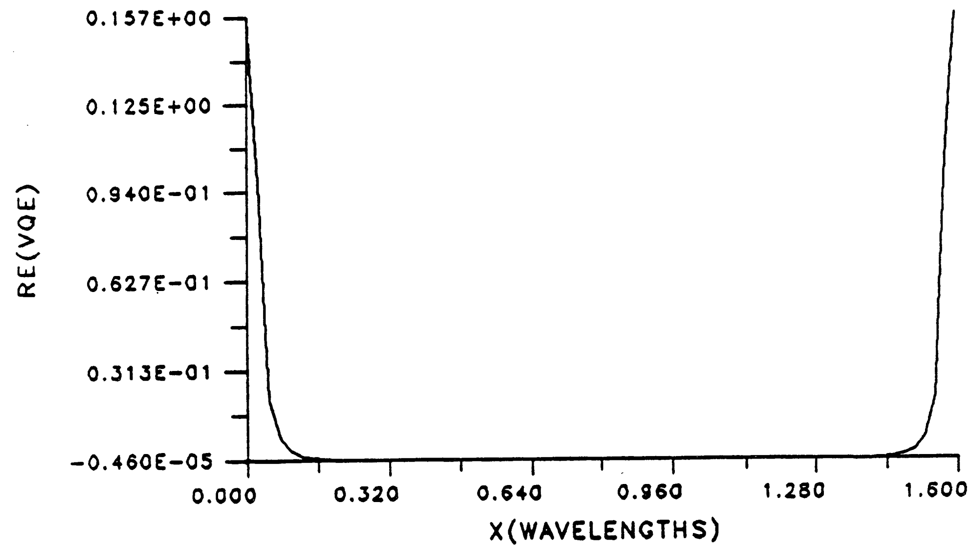

a. The amplitude distribution for the even case is symmetric

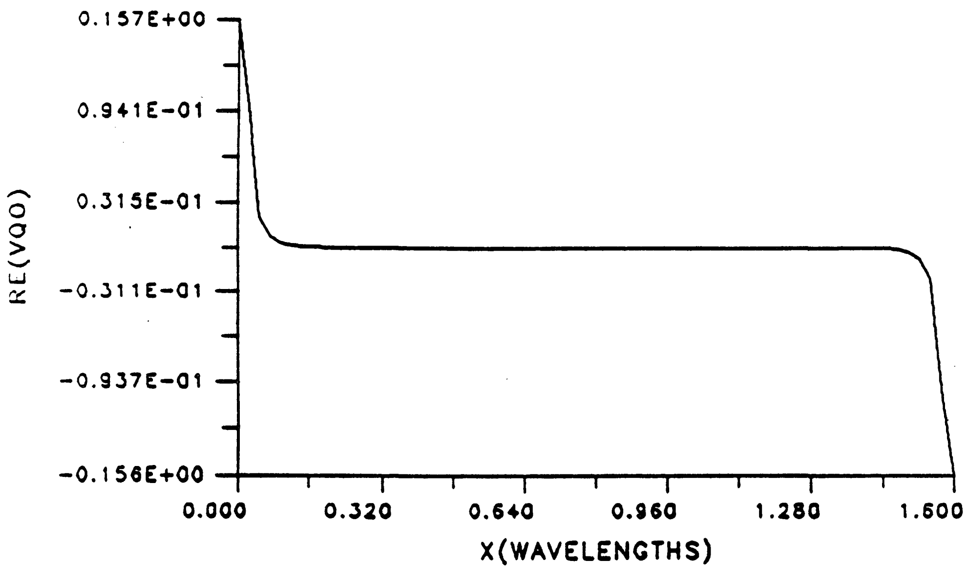

b. The amplitude distribution for the odd case is asymmetric

Figure 3.6: Excitation vector for two port coaxial excitation.

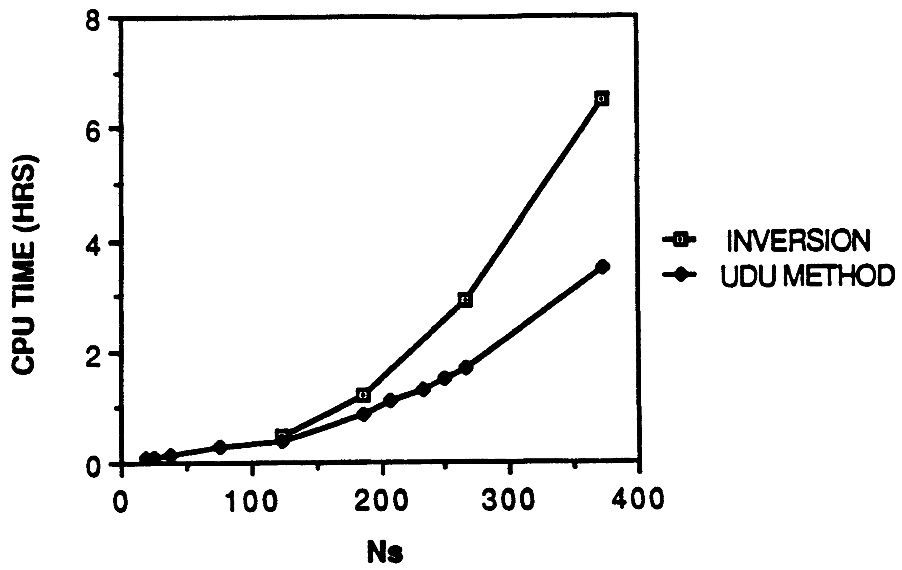

Figure 3.7: A comparison of computation times for two different methods of matrix equation solution shows the advantage of using alternatives to matrix inversion .

available as subroutines in standardized libraries (e.g. Numerical Analysis and Applications Software -NAAS).

For this work, a subroutine was employed that uses UDU factorization and back substitution. This method (also called LDL in some texts) takes advantage of the symmetry of the impedance matrix to speed computations. Figure 3.7 shows a comparison of computing times observed for a typical problem using matrix inversion versus the UDU factorization method. These computations were performed on an Apollo DN3000 work station. The speed advantage of the latter method becomes increasingly significant after a matrix size of about 150×150. Matrix sizes for problems studied in this thesis typically vary between about 50×50 and 250×250.

Typical open-end current distribution.— When the impedance matrix of Figure 3.4 is inverted, the amplitude distribution is as shown in Figure 3.8. Multiplying by the excitation vector of Figure 3.5 yields the current distribution of

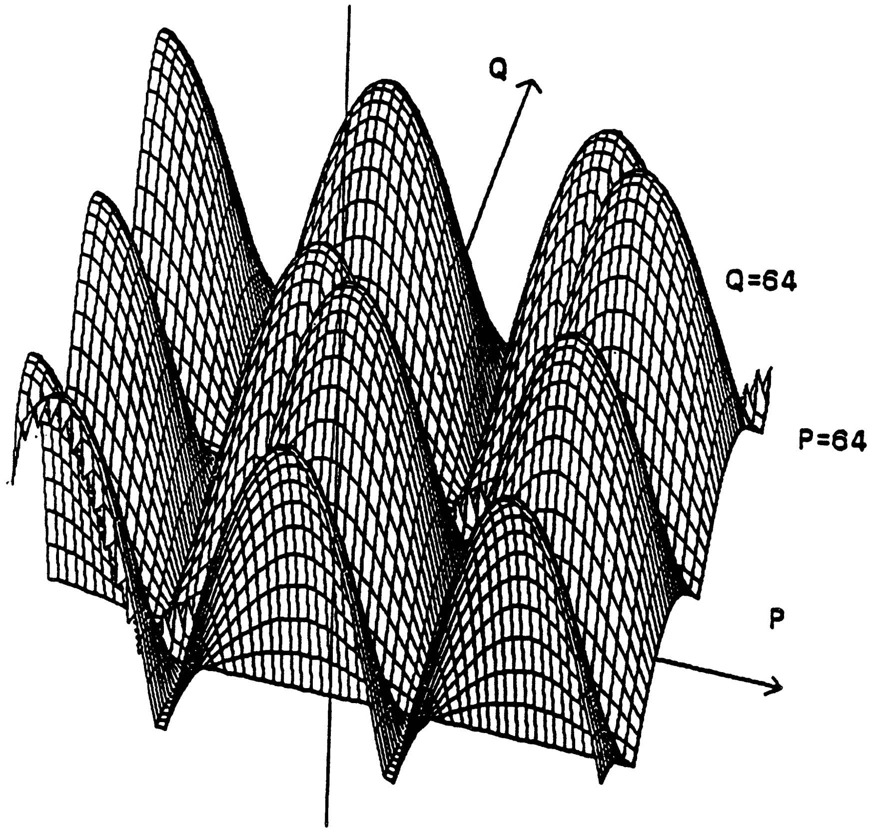

Figure 3.8: This 3-dimensional plot of the magnitude of the elements of the inverted impedance matrix shows that each row and column has a sinusoidal shape.

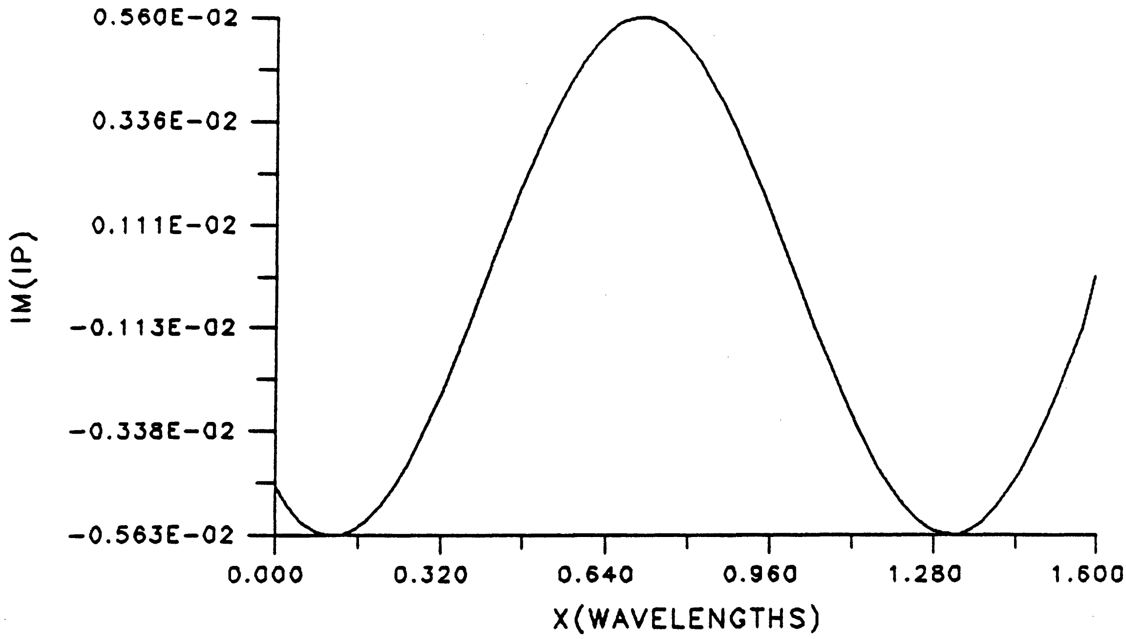

Figure 3.9: The imaginary part of current distribution for an open-end discontinuity displays a sinusoidal behavior.

Figure 3.9. It can be seen that the sinusoidal shape of the current has the same general shape exhibited by the first column of the impedance matrix. This is not surprising given the shape of the excitation vector. The multiplication can be thought of as a weighted summation of the first few rows of the inverted impedance matrix.

A typical current for gap generator excitation is shown in Figure 3.10. For this computation the gap generator was located at a short distance ($\sim .3\lambda_d$)from the wall. The current is seen to be discontinuous around the region of the gap generator, however, is otherwise well behaved. The effect of this discontinuity can be minimized by locating the gap generator source at the beginning at the beginning of the first subsection ($q = 1$).

<u>Typical two-port current distributions.</u>— The current computation for two-port structures is similar. In this case, even and odd currents are computed using excitation vectors shaped like those of Figure 3.6. The current distributions for a

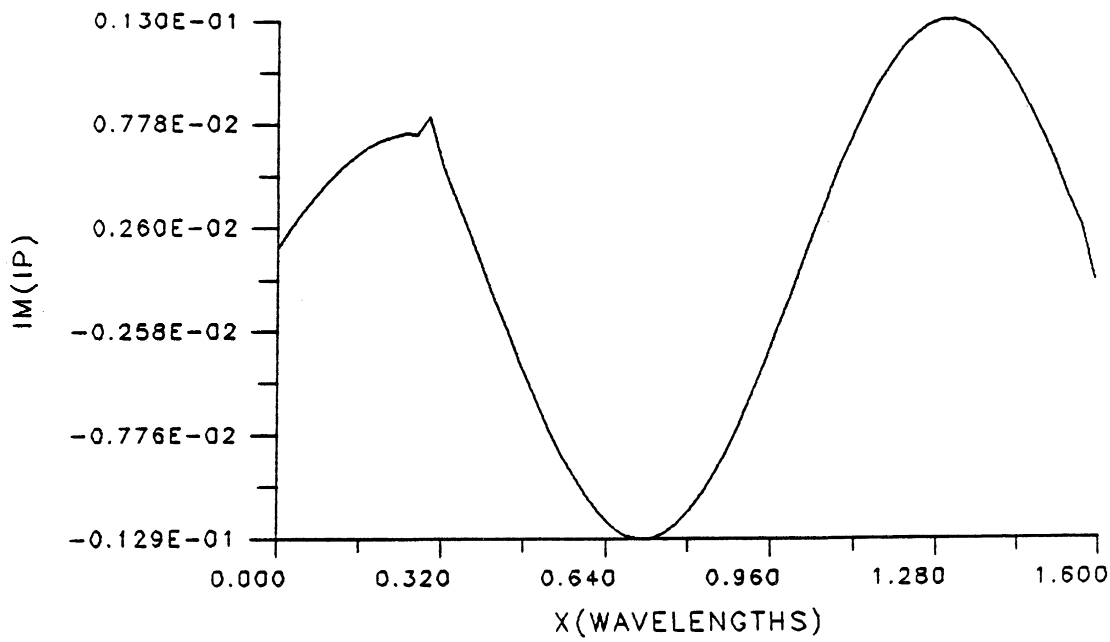

Figure 3.10: The current for gap generator excitation is discontinuous around the position of the source, but is otherwise well behaved.

series gap are shown in Figure 3.11. Due to the symmetry of the structure, the even current is symmetric, and the odd current is asymmetric around the middle of the cavity.

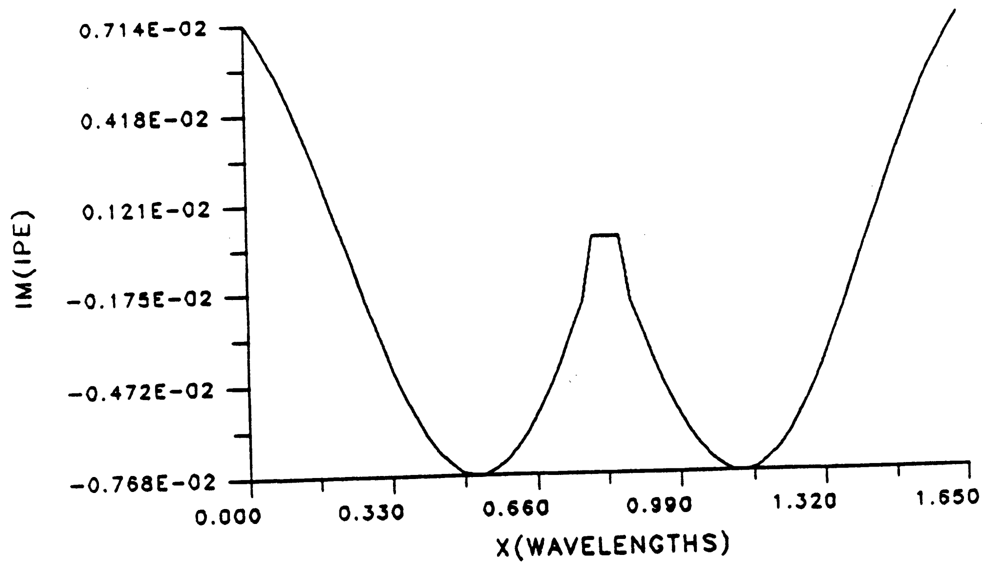

a. Even current

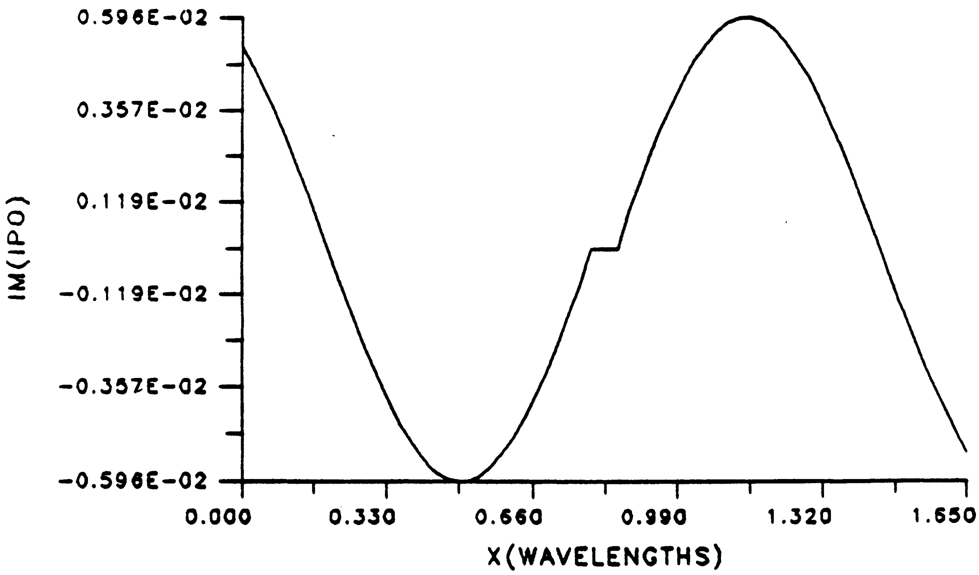

b. Odd current

Figure 3.11: Current distributions for a typical series gap discontinuity

3.3 Algorithms for Computing Network Parameters

3.3.1 Algorithm to Compute One-port Network Parameters

A Fortran program was written to compute one-port network parameters as discussed above [1]. A flow chart for the program *ONENET* is shown in Figure 3.12. The program first reads in the current distribution from a storage file created with *SHDISC*.

The next step is to perform a cubic spline fit to the current. This is necessary to accurately determine the positions of the minimum and maximum current values. The subroutine used to perform this spline fit is a modification of a program appearing in [34]. In a cubic spline fit, each interval between two points is represented by a different cubic equation of the form

$$I(x) = a_p(x - x_p)^3 + b_p(x - x_p)^2 + c_p(x - x_p) + d_p \tag{3.21}$$

Once the spline fit coefficients a_p, b_p, c_p, and d_p have been found, determining the positions of the current minima and maxima is straightforward. First, the two points surrounding an extremum are found by searching for a sign change in the slope of the current ($I'(x_p) = c_p$) evaluated at successive points. Next, the actual position of the extremum is found to within the accuracy of the curve fit. This is done by finding the root of $I'(x) = 0$ which lies within the interval $(x_p \leq x \leq x_{p+1})$.

The microstrip wavelength (λ_g) is then computed as the average distance between each pair of current minima and maxima. With the knowledge of the wavelength, the effective dielectric constant ϵ_{eff}, and the phase constant β_g can be calculated according to (2.127) and (2.126).

---

[1] In this thesis the only one-port structure considered is the open-end discontinuity.

Finally, the equivalent circuit parameters for the open-end are computed. To do this, the reflection coefficient Γ_{op} and impedance z_{op} are calculated. Then, the effective length extension and equivalent capacitance are computed from (2.132) and (2.135) respectively.

3.3.2 Algorithm to Compute Two-port Network Parameters

The program for computing two-port network parameters *TWONET* is very similar to that for one-port parameters. A flow chart is given in Figure 3.13. The first step is to read in the even and odd current distributions. These are analyzed separately. The analysis is performed in the subroutine *SPLIMP* following the same steps as in the one port case to compute λ_g, β_g, ϵ_{eff}, $\Gamma(L_1)$, and $z(L_1)$ for each of the distributions. Next, the impedance, scattering, and admittance parameters are calculated using the relations of Section 2.7. This whole process is repeated for each of the analysis frequencies.

3.4 Convergence Considerations Z_{qp} and V_q

In this section, the convergence of the elements of the impedance matrix Z_{qp} and the excitation vector V_q are discussed. The series involved in the computation of these elements are functions of two summation indices m and n. In theory, the summations are infinite; however, for computation we must truncate them at some point where the error due to this truncation is negligible.

3.4.1 Convergence of Impedance Matrix Elements Z_{qp}

We will now consider the convergence behavior of the matrix with respect to the summation indices m and n.

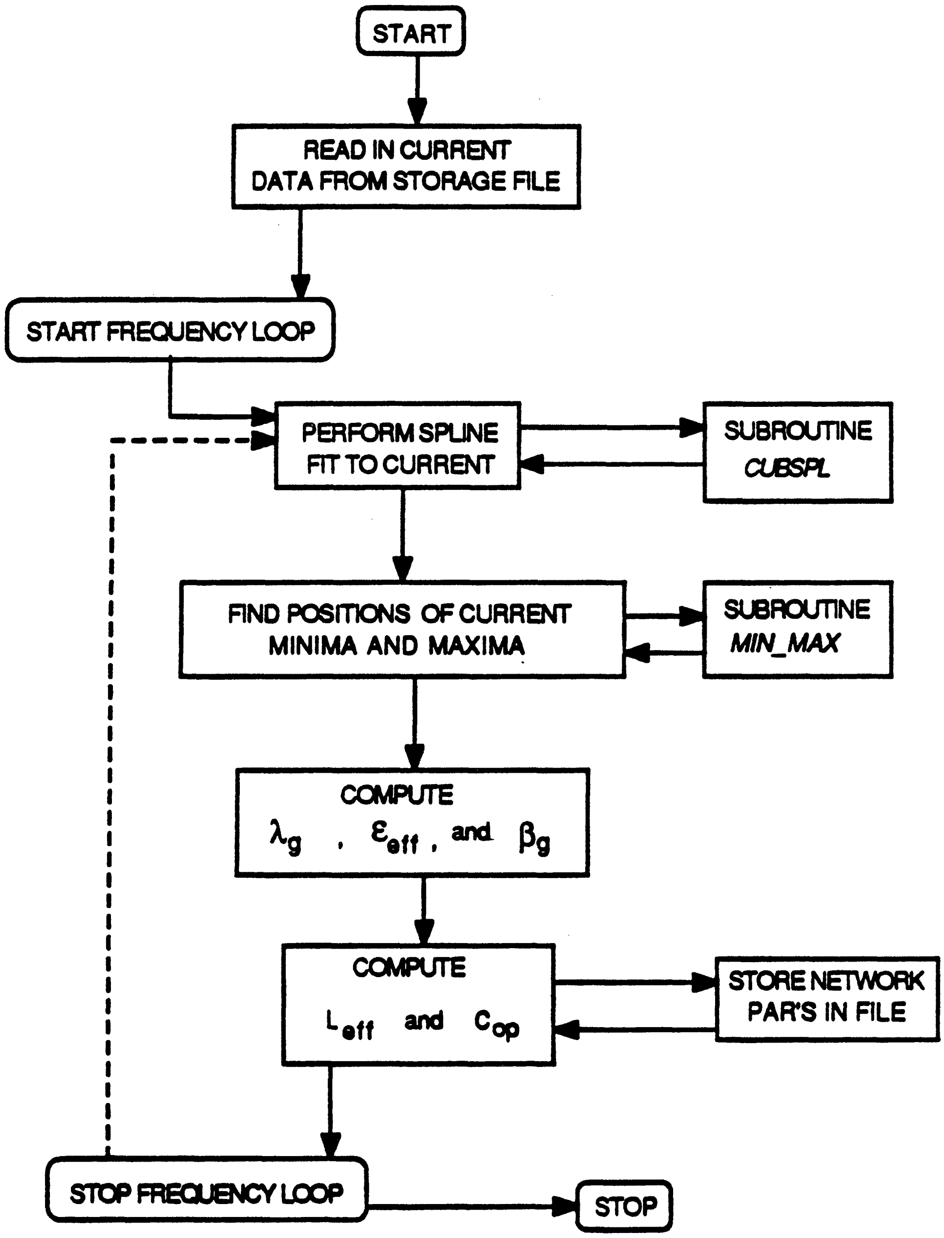

Figure 3.12: Flow chart for computation of one-port network parameters

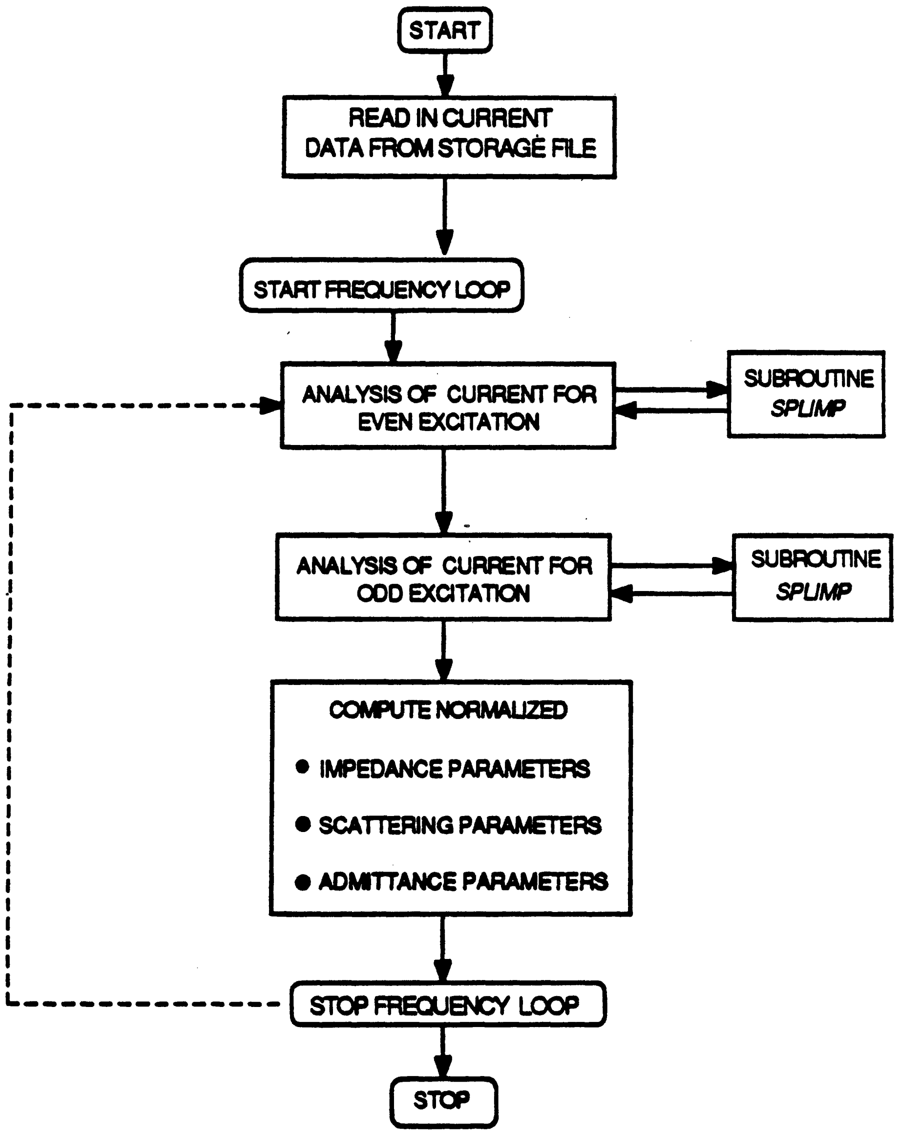

Figure 3.13: Flow chart for computation of two-port network parameters

Convergence of Z_{qp} with m.— As can be seen from (3.1), the convergence of the impedance matrix with respect to m is described by the convergence of $LN(n)$ with m. Recall that $LN(n)$ is given in terms of the series of (3.2)

$$LN(n) = \sum_{m=1}^{MSTOP} L_{mn} \,. \tag{3.22}$$

Figure 3.14 shows the typical variation of $LN(n)$ with m and n. Most of the contributions from $LN(n)$ to the impedance matrix are concentrated in the first several n values. The convergence over m is good. Further analysis, for this case shows that the change in $LN(n)$ appears to be negligible after about $m = 500$.

Convergence of Z_{qp} with n.—

This computation of Z_{qp} over n is illustrated for a typical impedance matrix in Figure 3.15. This figure shows the convergence behavior for one row (the 32^{nd}) of the 64 x 64 element impedance matrix of Figure 3.4. This behavior is representative of that for any row. After only a few terms the diagonal element ($p = q = 32$) rises above the others, and after adding 100 terms the amplitude distribution is well formed.

3.4.2 Convergence of Excitation Vector Elements V_q

We now turn our attention to the convergence of the excitation vector. In the following discussion, we consider only the one-port excitation vector since the two-port excitation vectors are derived from the one-port case (Section 2.6.4).

Convergence of V_q with m.—

As can be seen from examining (3.4), the convergence of V_q with respect to m is described by the convergence of $MN(n)$ with respect to m. $MN(n)$ is given by (3.5)

$$MN(n) = \sum_{m=1}^{MSTOP} M_{mn} \,. \tag{3.23}$$

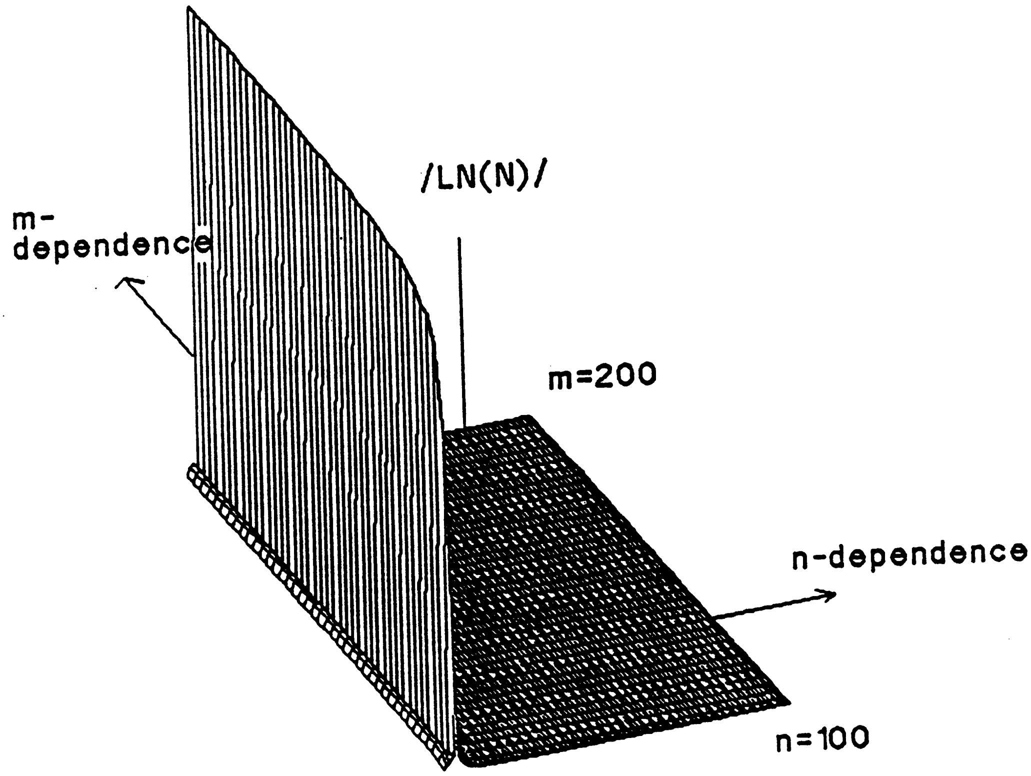

Figure 3.14: 3-dimensional plot illustrating computation of $LN(n)$ over m and n.

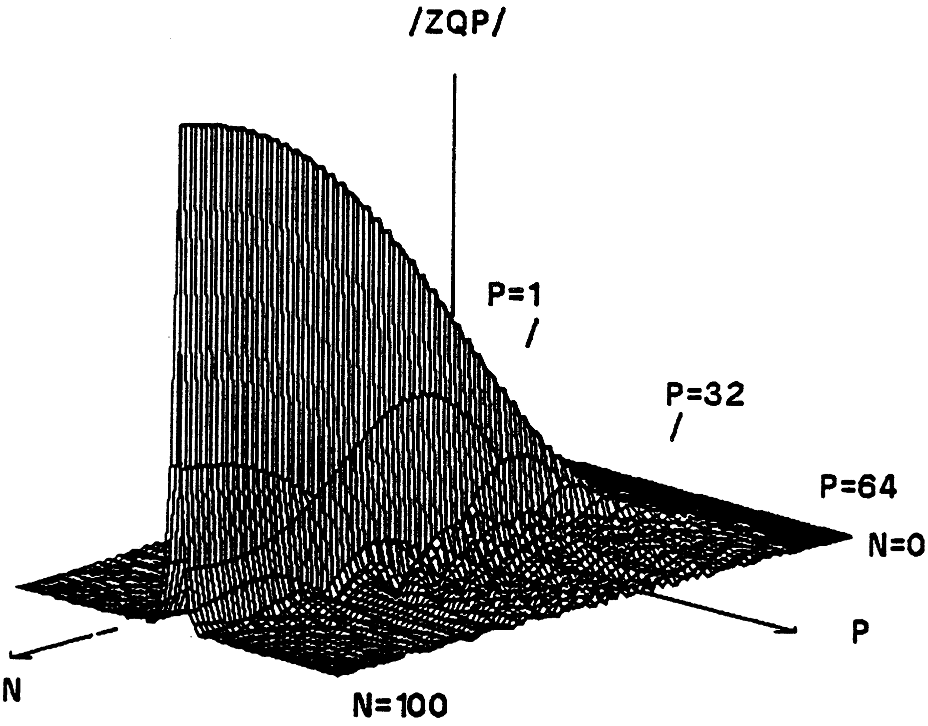

Figure 3.15: The formation of an impedance matrix for one row ($Q = 32$) versus the summation index n.

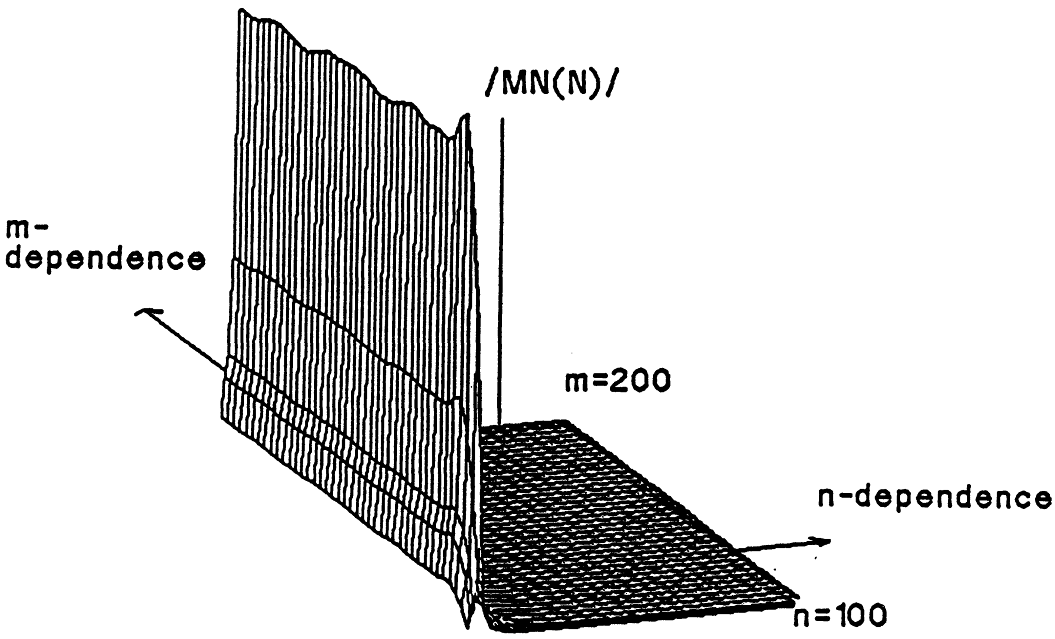

Figure 3.16: 3-dimensional plot illustrating computation of $MN(n)$ over m and n.

A plot of $MN(n)$ with m and n, shown in Figure 3.16, shows that the convergence of MN(n) on m is not as good as that for $LN(n)$. The series exhibits a damped oscillation around the convergent value, which may take more than 1000 terms to determine. However, good results for network parameters are obtained by stopping at $m = 500$. This is discussed further in the section 3.5.

Convergence of V_q with n.— Figure 3.17 illustrates the computation of the elements of V_q as a function of the summation index n. As in the case of the impedance matrix, the amplitude distribution for the excitation vector has been well defined after adding the first 100 terms.

3.5 Convergence of Network Parameters

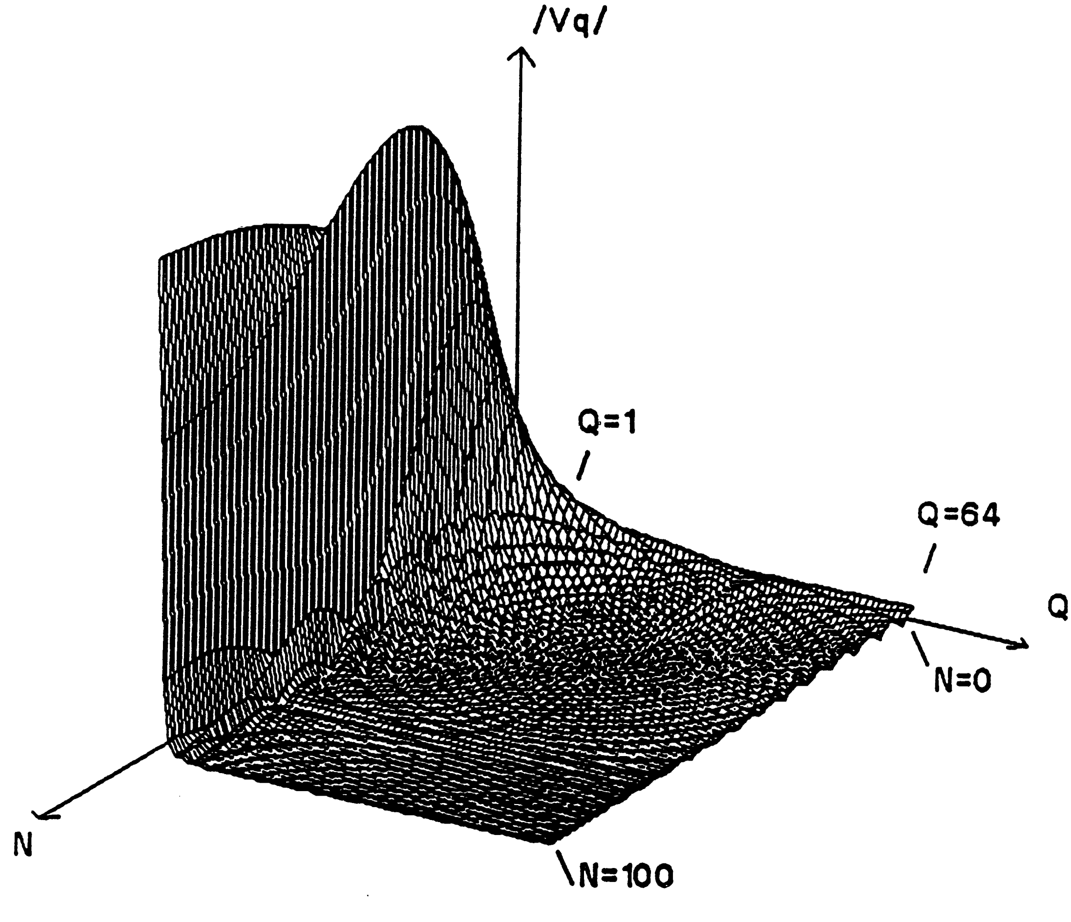

Figure 3.17: The formation of an excitation vector versus the summation index n.

The previous section described how the elements of the impedance matrix and excitation vectors converge on the summation indices m and n. This convergence is important to examine; yet the question remains: how are the final results affected by various convergence related parameters?

To answer this question, a series of numerical experiments were carried out. These experiments investigate the convergence behavior of the network parameters for an open-end discontinuity with respect to the number of samples per wavelength N_x ($= 1/l_x$), and the truncation points $NSTOP$, $MSTOP$ for the summations over n and m respectively. From an efficiency point of view, we would like to minimize both the sampling rate and the truncation points. To examine these issues, of numerical experiments were performed at different frequencies and for different geometries, and a summary is given here.

In this summary, the numerical experiments have been grouped into three separate categories which are named Experiment A, Experiment B, and Experiment C. Each of these explores a different aspect of the convergence behavior [2].

3.5.1 Numerical Experiment A: Effect of K-value

Objective

In the first experiment, the objective was to investigate how the value for K (K-value) used in the basis functions (2.8) and (2.9) affects the convergence on N_x of the L_{eff} and ϵ_{eff} computations.

Procedures and results

[2] Unless otherwise noted, the parameters used for the plots shown in this section are the following: $\epsilon_r = 9.7, W = h = .025'', a = 3.5'', b = c = .25'', f = 18$GHz.

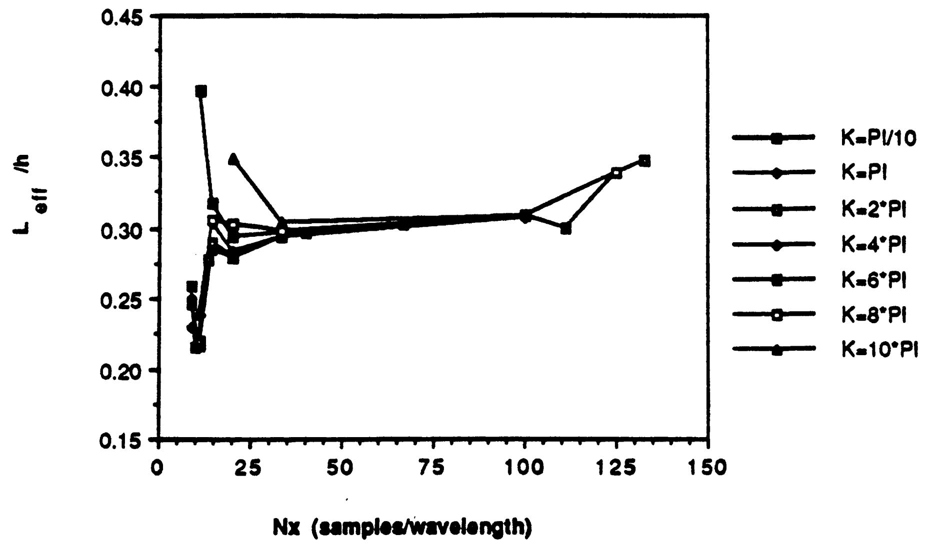

Figure 3.18: Convergence of L_{eff} versus sampling for several different K-values.

Using the programs discussed previously, data was generated to plot L_{eff} and ϵ_{eff} versus N_x for several different K-values. Figure 3.18 shows the convergence behavior of L_{eff} for a typical case. It is seen that a relatively flat convergence region exists for all the K-values between about 40 and 100 samples per wavelength (λ_d). Outside this region the solution behaves differently for different K-values.

At first glance, it appears that the best convergence is achieved for higher K-values (e.g. $K = 8\pi$); however, quite the opposite conclusion results from examining the ϵ_{eff} computation. As can be seen from Figure 3.19, the best convergence for ϵ_{eff} is obtained for low K-values.

Based on these observations, it was theorized that it may be possible to improve the L_{eff} computation by choosing a larger K-value at the end of the line, while keeping the K-value over the rest of the line at a low value. This was investigated by modifying the program *SHDISC* to use $K = 2\pi$ for all the subsections except

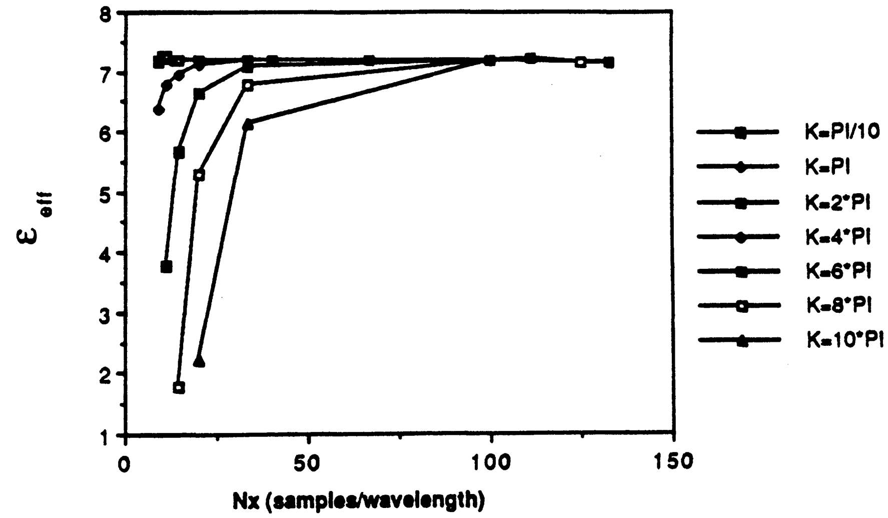

Figure 3.19: Convergence of ϵ_{eff} versus sampling for several different K-values.

the last $\lambda_d/8$ portion of the strip. Over the last $\lambda_d/8$ portion, the K-value was varied to examine its effect on the L_{eff} and ϵ_{eff} computations. It was found that a constant value of $K = 2\pi$ over all the subsections yields the best convergence behavior for L_{eff}. As expected, changing the K-value just at the end of the strip had very little effect on the ϵ_{eff} result.

Some comments will now be made on the L_{eff} convergence behavior for low and high sampling rates. Referring back to Figure 3.18, it was found that a minimum sampling limit was observed that varies with the K-value. This limit may be expressed by the following

Observation III.1 *For the sinusoidal basis functions of (2.8) and (2.9), there exists a lower sampling limit which depends on K and l_x as follows*

$$Kl_x < \frac{\pi}{2} \tag{3.24}$$

or

$$N_x > \frac{2K}{\pi}. \tag{3.25}$$

If the sampling rate is lower than this limit, obvious errors in the current distribution and the network parameters (e.g. negative L_{eff}) result.

This limit has a physical basis in that if it is violated, more than one quarter of a sinusoid is represented by each half basis function. This means that the basis function tries to peak before it reaches the end of the section.

Before examining the convergence behavior for high sampling rates, it will be useful to define the matrix condition number. The matrix condition number gives a measure of the relative sensitivity of the errors in the matrix solution to a change in the matrix elements. It may be defined as [35]

$$\text{Cond}\,(\mathbf{Z}) = ||\mathbf{Z}|| * ||\mathbf{Z}^{-1}|| \,. \tag{3.26}$$

Matrices with low condition numbers are said to be *well conditioned*; matrices with high condition numbers are said to be *ill conditioned.* In general the condition number, and therefore the accuracy of the matrix solution, degrades as the matrix size increases.

This degradation in the condition number is responsible for the non-convergent behavior exhibited in Figure 3.18 for high sampling rates. Figure 3.20 shows how the reciprocal condition number (RC = 1/Cond(**Z**)) is degraded as Nx increases. As N_x increases, the matrix order (N_s) also increases for a fixed physical length of line. Hence, the gradual degradation in the condition number observed out to about $N_x = 130$ was expected.

Not expected was the large jump in RC which occurs at about 140 samples per wavelength. This jump indicates that the matrix suddenly becomes ill conditioned and, the associated current distribution is completely erratic. This erratic current condition was found to be independent of K, however, as discussed in the next section it is directly related to the length of the cavity a, and the number of terms added in the summation over n ($NSTOP$).

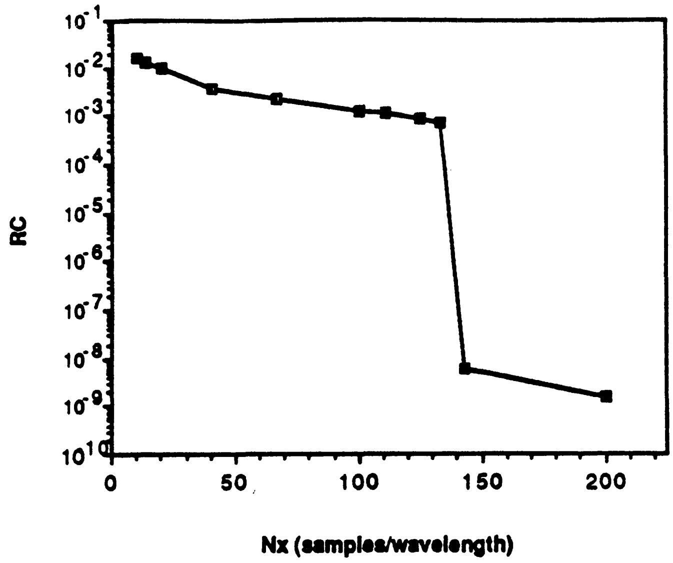

Figure 3.20: Reciprocal matrix condition number versus sampling.

3.5.2 Numerical Experiment B: L_{eff}, ϵ_{eff} Convergence on n and m

Objective

The objective of this next experiment was to determine the appropriate truncation points $NSTOP$ and $MSTOP$ for the double summations involved with computing the impedance matrix and excitation vector elements.

Procedures and Results

First, several program runs were executed for different values of $NSTOP$, with $MSTOP$ fixed at 1000. Data was generated to plot L_{eff} and ϵ_{eff} versus n for several l_x values. Figure 3.21 shows that for all the l_x values $NSTOP = 500$, gives good convergence. The same can be said for the convergence of ϵ_{eff} with n

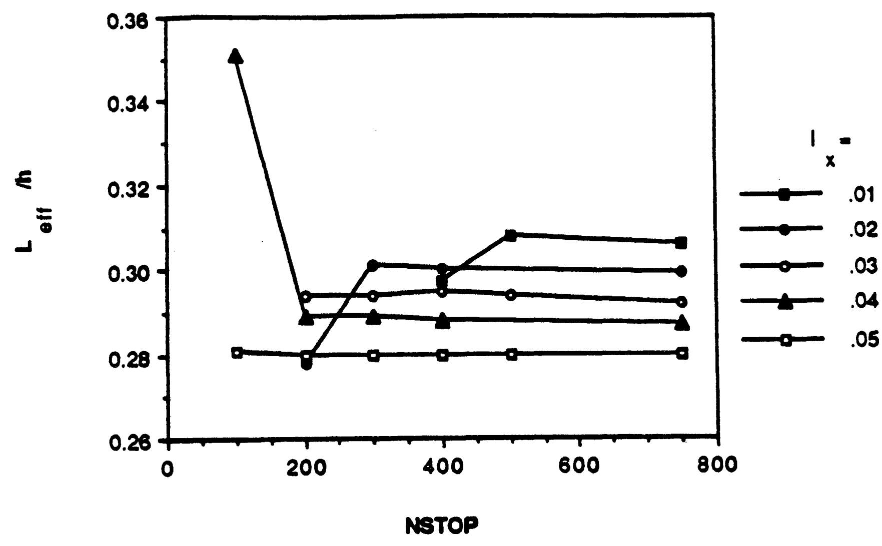

Figure 3.21: The convergence of L_{eff} on n was found to depend on l_x, but is satisfied in all cases after 500 terms have been added.

(Figure 3.22).

To investigate the convergence behavior with respect to the summation index m, $NSTOP$ was fixed at 500, and the program was run for different values of $MSTOP$. Figure 3.23 shows that L_{eff} converges well on m also after about 500 terms. Unlike the convergence on n behavior, the convergence on m does not depend on l_x. The convergence behavior of ϵ_{eff} (not shown) on m, was found to be similar to that for L_{eff}.

The dependence of the n convergence on l_x observed in Figures 3.21 and 3.22 warrants further consideration. It is seen that for large l_x values the solution converges faster on n. This variation of the convergence behavior with different l_x values is also reflected in the reciprocal condition number as seen in Figure 3.24. It is also seen that the condition for erratic current, discussed in Section 3.5.1, is a function of both $NSTOP$ and l_x. Further experimentation with different geometries and frequencies, lead to the formulation of the following observation:

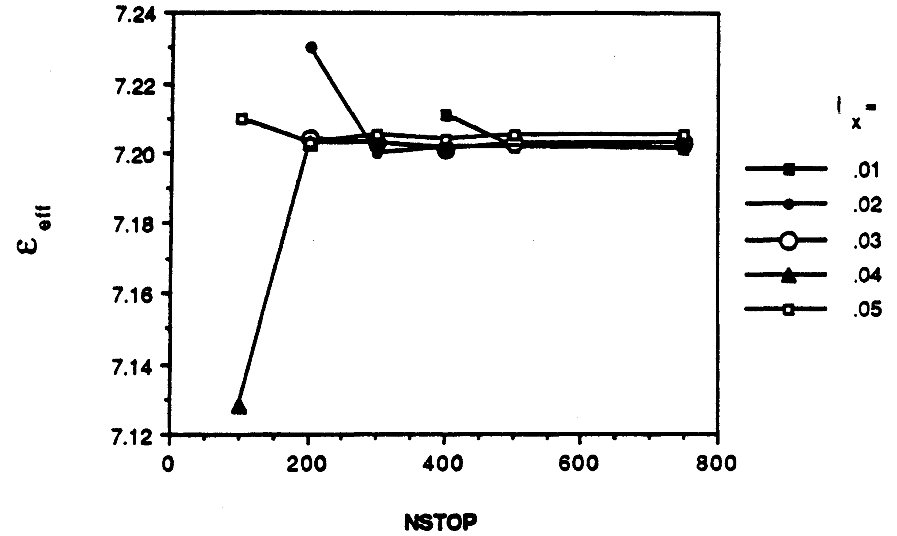

Figure 3.22: The convergence of ϵ_{eff} on n shows similar behavior as that for L_{eff}, and is satisfied in all cases after 500 terms have been added.

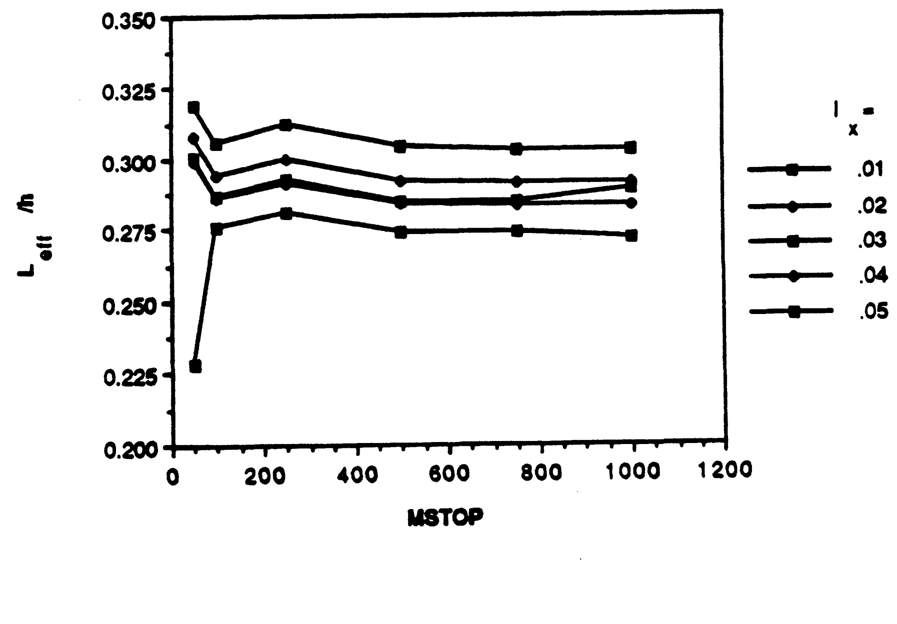

Figure 3.23: The convergence of L_{eff} on m is also satisfied after 500 terms.

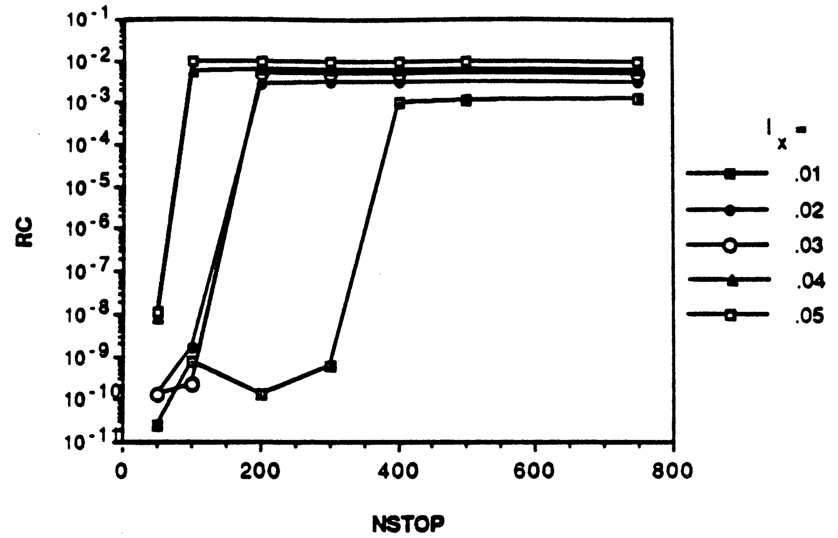

Figure 3.24: A plot of the reciprocal condition number versus NSTOP shows that the condition for erratic current depends on both $NSTOP$ and l_x .

Observation III.2 *The condition for erratic current is given by a simple relation between the cavity length a, the truncation point* $NSTOP$*, and the subsection length* l_x *which may be expressed as*

$$NSTOP * l_x < a \tag{3.27}$$

or

$$\frac{NSTOP}{N_x} < a \tag{3.28}$$

This will be referred to as the **erratic current condition.** *This condition places an upper limit on* N_x *and, correspondingly, a lower limit on the* l_x *value that can be used to generate useful current results.*

The erratic current condition was tested against several cases where erratic currents were observed, and it appears to give an exact prediction.

3.5.3 Numerical Experiment C: Optimum Sampling Range

Objectives

The objective in this last experiment was to examine the effect of varying l_x on the reciprocal matrix condition number, while keeping the matrix size constant. It was hoped that an optimum value, or range of values, for l_x could be found for which the matrix condition number is maximized.

Procedures and Results

To keep the matrix size constant, the number of sections N_s was fixed at 100, and the length of the open-ended line ($L' = L_{in}/\lambda_d$) was allowed to vary such that

$$L' = 100 * l_x$$

for all cases. Data was then generated to plot RC versus l_x as shown in Figure 3.25. As suspected, an optimum sampling range was found, outside of which the matrix is ill conditioned. The experiment was repeated at three different frequencies and for several different shielding geometries. In all cases, an optimum sampling range was found, but it was different for each of them.

To examine this sampling range further the following postulate was advanced, based on the erratic current condition of Experiment B.

Postulate III.1 Postulate:.— *Let N_{x1} and N_{x2} correspond to the minimum and maximum desired sampling rates. These rates are defined as those values between which the reciprocal condition number is greater than 10^{-4} for a fixed matrix size*

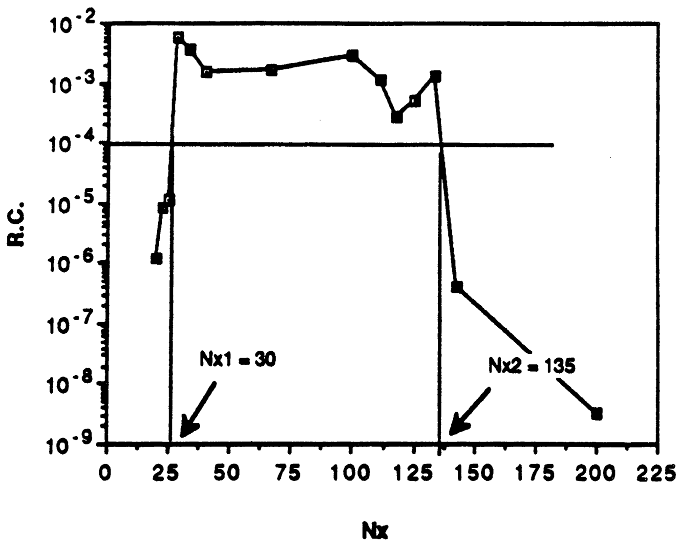

Figure 3.25: The effect on the reciprocal condition number of varying only l_x indicates the existence of an optimum sampling range

of 100×100. [3]

Let l_{x1} and l_{x2} be the subsection lengths corresponding to N_{x1} and N_{x2} respectively. That is

$$l_{x1} = 1/N_{x1} \tag{3.29}$$

$$l_{x2} = 1/N_{x2}\,. \tag{3.30}$$

We now postulate the existence of two constants r_1 and r_2 such that

$$l_{x1} = \frac{r_1 a}{NSTOP} \tag{3.31}$$

$$l_{x2} = \frac{r_2 a}{NSTOP}\,. \tag{3.32}$$

The definition of the sampling range is illustrated in Figure 3.25. This postulate

---

[3] Based on observation, a value of RC $= 10^{-4}$ appeared to be a good value to use as a lower limit.

Table 3.1: RESULTS FOR OPTIMUM SAMPLING RANGE EXPERIMENT

f (GHz)	a	l_{x2}	l_{x1}	l_{xavg}	r_2	r_1	r_{avg}
2	1.58	.0035	.0125	.008	1.1	4.0	2.5
8	6.33	.017	.07	.043	1.3	5.5	3.4
8	1.0	.0029	.0125	.008	1.5	6.3	3.9
18	3.5	.0074	.033	.020	1.1	4.7	2.9
18	1.0	.0023	.0125	.0074	1.2	6.3	3.7
min.	-	-	-	-	1.1	4.0	2.5
max.	-	-	-	-	1.5	6.3	3.9
avg.	-	-	-	-	1.2	5.4	3.3

was applied to the observations from several test runs and the results for the sampling range parameters are summarized in Table 3.1.

The data of Table 3.1 shows that, although Postulate 3.1 is only approximately true, an optimum sampling range can be specified in terms of the multipliers r_1 and r_2. This range is formulated in the observation below. In selecting the multiplier r_2, the maximum observed value from Table 3.1 is used, and in selecting the multiplier r_1 the minimum observed value is used. This is done to define a range for which condition number for the cases of Table 3.1 is always greater than 10^{-4}.

Observation III.3 *An optimum sampling range (or criteria) may be defined by the following choice of subsection length* l_x

$$\frac{1.5a}{NSTOP} \leq l_x \leq \frac{4a}{NSTOP}. \tag{3.33}$$

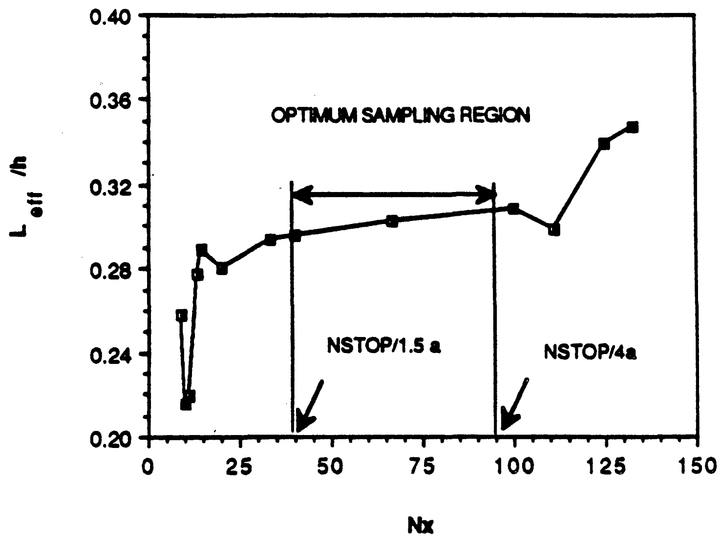

Figure 3.26: The optimum sampling range is seen to correspond directly with the flat convergence region for the L_{eff} computation.

A good average value to use is

$$l_x = \frac{3a}{NSTOP} \tag{3.34}$$

The above observation is very significant. Based on the knowledge of only two parameters, a and $NSTOP$, an optimum sampling range (or range of subsection lengths) can be determined. The erratic current condition is automatically avoided by sampling within this range, and the best accuracy in the matrix solution should be guaranteed.

To support this last claim, consider the plot of Figure 3.26. It is seen that the optimum sampling region specified by 3.33 coincides directly with the flat convergence region for the L_{eff} calculation! This consistency between the optimum sampling region and the flat convergence region for the L_{eff} calculation was observed in all the cases of Table 3.1.

3.6 Summary of Computational Considerations

In this chapter, the software design for the computation of the current distribution, and the network parameters for discontinuities has been described. The programming language used is Fortran. The convergence of the solution with respect to the relevant parameters has been explored extensively by performing a series of numerical convergence experiments. The results from these experiments lead to some simple, but very useful relationships governing the convergence and stability of the solution. A summary of the main findings is given in Chapter 6.

CHAPTER IV

EXPERIMENTAL METHODOLOGY

As part of this research an experimental study of microstrip discontinuities was performed. In conducting this study, the author spent fifteen months at Hughes Aircraft Company[1]. Hence, parts of the study were performed at Hughes; the rest was performed at the University of Michigan.

The chapter gives a description of the study and the procedures used to obtain measured data. First, a general discussion of the experimental approach is given. This consists of the use of Automatic Network Analyzer (ANA) techniques in conjunction with a method for de-embedding (or removing) the effects of the test fixture from the measurements. Next, a comparison of various de-embedding methods is presented. It is concluded that the method most suitable for the measurements of this thesis is the thru-short-delay (TSD) method. The implementation of this method for use with the present research is then explained. Finally, the procedures used to obtain measurements of effective dielectric constant, open-end and series gap discontinuities, and coupled line filter structures are explained. A complete error analysis for these measurements is beyond the scope of this thesis, however, an attempt is made to give a reasonable estimate of measurement uncertainties. To this end a perturbation analysis approach is developed and applied to approximate the effect of connection repeatability errors on de-embedding accuracy.

---

[1] Hughes Aircraft Company, Microwave Products Division, Torrance, CA

4.1 Discussion of Experimental Approach

4.1.1 ANA Error Correction

A basic ANA provides for two-port, error corrected S-parameter measurements in a coaxial or waveguide environment. Error correction is achieved by using a set of standards whose electrical characteristics can be determined to a high degree of certainty. For example, the standards used in a typical coaxial calibration are a 50 ohm load, a short circuit, an open circuit (whose fringing capacitance has been determined apriori), and a thru connection. Measurements on these standards are used to construct an error model for the ANA system which accounts for various system imperfections such as finite coupler directivities, connector mismatches, unflat frequency responses, and source and load impedance mismatches [36].

4.1.2 Difficulties with Microstrip Measurements

Measured data on microstrip discontinuities is very limited, particularly at higher frequencies (above 10GHz). This is due to the many difficulties involved with performing accurate microstrip measurements. The key difficulties associated with these measurements are summarized in Table 4.1. These difficulties are not unique to microstrip and apply to measurements in other planar transmission media as well.

The main difficulty is that in order to measure a microstrip circuit, it is generally mounted in a test fixture with either coaxial-to-microstrip or waveguide-to-microstrip transitions (also called launchers). Figure 4.1 shows the basic configuration for test fixture measurements. The transitions invariably introduce unwanted

Table 4.1: DIFFICULTIES WITH MICROSTRIP MEASUREMENTS

• Separation of microstrip test fixture parasitics from measurements
• Inadequate microstrip calibration standards
• Non-repeatability of microstrip connections
• Effect of variations in substrate material properties
• Effect of variations of metallization dimensions and substrate thickness
• Effect of substrate mounting techniques

parasitics and a reference plane shift to the measurements. These effects must be accurately accounted for and removed from the measurements, or incorporated into the ANA system error model.

One alternative to the use of a test fixture is to employ coplanar wafer probing [37]. However, to measure microstrip structures with coplanar probes requires the use of coplanar-to-microstrip transitions. Since the issues with removing the effect of these transitions are the same as for the other transitions mentioned above, the term "test fixture" as used below will be assumed to include the case of coplanar probing.

Another main difficulty with the measurements is the inadequacy of microstrip calibration standards. Conventional calibration standards are much more difficult to realize in microstrip than in waveguide and coax. Perfect short circuits are complicated by the non-uniform nature of the fringing fields in microstrip, thin-film resistors do not provide the same quality of 50 ohm terminations as in conventional media, and the open-end capacitance is not known to a high enough degree of accuracy for it to be used directly as a calibration piece [2]. Hence, conventional ANA

[2] A rigorous numerical solution, such as that developed here may provide

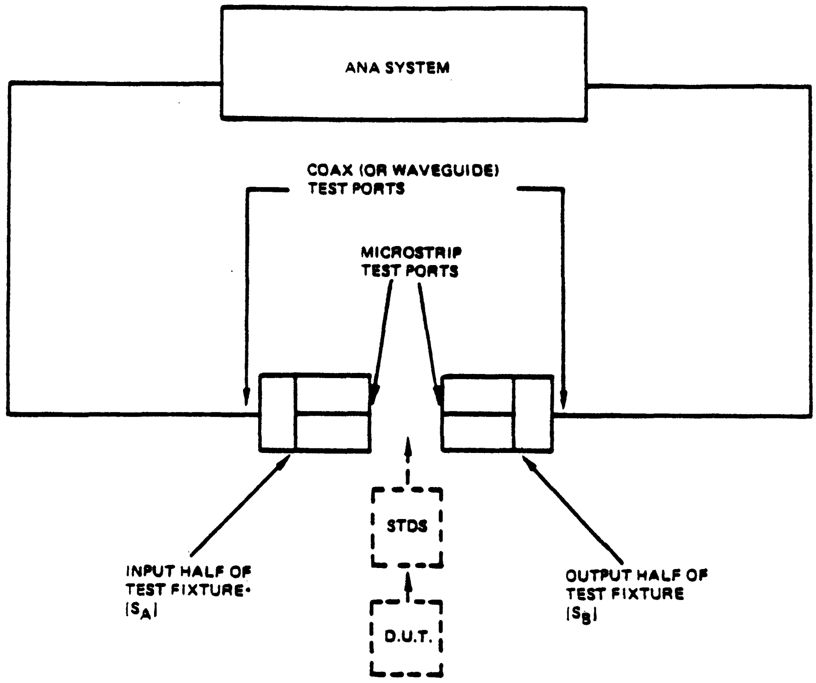

Figure 4.1: Microstrip test fixture approach for de-embedded measurements.

calibration (Section 4.1.1) in microstrip is not easily performed. This difficulty is overcome through the use of de-embedding techniques as discussed below.

The third factor complicating these measurements is the non-repeatability of microstrip connections. Microstrip connections are much harder to make, and much less repeatable than connections in coax and waveguide. This is a key limiting factor to the accuracy of microstrip measurements at higher frequencies. To address this issue, a microstrip connection repeatability study was carried out [14,15]. Details of this study are included in Appendix H, and the results are summarized in Section 4.3 below.

The remaining factors of Table 4.1 can also be important. These factors include the effect of variations in substrate material properties, variations in metalization and substrate thickness dimensions, and substrate mounting techniques. The ef-

---

the required accuracy to alleviate this problem.

fects of these factors on measurements is considered further in Section 4.3, and some consideration is also given in the repeatability study (Appendix H). Their effect can be minimized by paying careful attention during material selection, and during the fabrication and mounting of test circuits.

Before discussing de-embedding methods, a few comments will be made on resonator techniques, since they have been widely used for microstrip measurements.

4.1.3 Resonator Techniques

One way of minimizing transition effects is to incorporate the transition into a resonant circuit which is lightly coupled to a source and detection system [1]. The majority of existing experimental microstrip data have been obtained using such resonator techniques [38]-[41]. The main advantage of this approach is that unwanted transition effects, such as poor VSWR or contact repeatability have minimal effect on measurement accuracy. Also, useful measured data can be obtained without the use of an ANA.

However, the coupling necessary for adequate sensitivity is sufficient to provide some reactive loading of the resonant system which is not easily accounted for. In addition, the measurement procedure is tedious and is not practical for measurements over a broad range of frequencies.

4.1.4 The De-embedding Approach

The preferred approach to removing test fixture effects is called de-embedding. De-embedding refers to the process by which test fixture effects are removed from the measurements. With the exception of time-domain de-embedding, which will be discussed in Section 4.2.2, the de-embedding process consists of two steps:

1. Test fixture (or error) characterization

2. Error extraction.

A microstrip test fixture can be characterized either by an equivalent circuit model (this is generally valid only at low frequencies) or by performing measurements with a number of planar standards inserted within the fixture. The electrical parameters of the fixture, for example the S-parameters for each fixture half, are then used to mathematically move the effective calibration reference planes from the coax or waveguide test ports to the desired microstrip test ports (Figure 4.1).

4.2 Comparison of De-embedding Methods

In this section, several de-embedding methods are compared in terms of their applicability for our measurement requirements. Specifically, the method used must:

- be usable at high frequencies (10GHZ and higher)
- allow the de-embedding of arbitrary transition effects
- allow the connection of any standards used to be similar to those made to the discontinuity structures
- use standards whose electrical characteristics are "known" to a reasonable degree of certainty.

Also, the electrical characteristics of any standards used must be They must be well established theoretically, or determined from independent measurements.

4.2.1 Fixture Equivalent Circuit Modeling

One method of fixture characterization is to propose an equivalent circuit model for the fixture. The simplest model uses a section of ideal transmission line to model each half of the test fixture. In this case, launcher parasitics are completely neglected and de-embedding is performed by simple transmission line rotations around the Smith chart.

Launcher parasitics can be at least partially taken into account by using more complicated equivalent circuit for the fixture whose parameters are fitted to a set of measurements on a reference circuit (e.g. a straight section of transmission line [42]). This approach while an improvement over simple transmission line rotations, lacks generality. It also tends to be unreliable for high frequency use, since fixture parasitics become more difficult to model as frequency increases.

4.2.2 Time Domain De-embedding

Another method of de-embedding makes use of transformations back and forth between the frequency and time domains. This method, which follows from Hines and Stinehelfer [50], involves the use of a Fourier transform to obtain a time domain response from frequency-domain data. In concept, fixture effects can be eliminated by isolating (or gating) the time response of the desired circuit and then transforming back to the frequency domain to obtain the de-embedded frequency response. However, for adequate resolution, it is necessary to use long input and output lines and collect data over a broad range of frequencies. Even then, although useful for many applications ,such as fixture development, this technique is not as accurate as full matrix de-embedding in the frequency domain [51].

4.2.3 Full Matrix De-embedding

The remaining de-embedding methods to be discussed fall into the category of full matrix de-embedding. In full matrix de-embedding, each half of the test fixture is characterized by matrix parameters (e.g. scattering matrix $[S]$, or transmission matrix $[T]$) as a "black box". This is done by measuring planar standards for which the network parameters are known, or can be determined to a reasonable degree of certainty. Examples of such standards are microstrip delay lines, offset microstrip open-ends, and varactor diodes Once the fixture has been characterized, inverse matrix operations can be used to deduce the electrical parameters of the unknown device or circuit.

These matrix operations vary little between full matrix de-embedding methods; conversely, the fixture characterization process differs considerably depending on the type of standards used. Most methods use one of the following combinations of standards:

1. Delay line and reflection standards [44]-[47]

2. 1-port offset reflection standards [52]

3. Varactor diode standards [53]-[55]

The relative merits of different fixture characterization approaches based on the use of these standards are compared in Table 4.2. Based on this comparison, the use of delay line and reflection standards, and in particular, a method based on the thru-short-delay (TSD) approach was adopted for this thesis. A discussion of this choice is given below.

In the TSD method (Figure 4.2), two-port measurements made on a thru (zero length delay) line, a "short" circuit, and a delay line provide enough information to characterize the fixture. As byproducts of the procedure, calculations of the propagation constant γ_g, and the reflection coefficient Γ_s are provided.

Since the original paper [44], it has been pointed out that the "short" implied

Table 4.2: FULL MATRIX DE-EMBEDDING METHODS

APPROACH	TSD (TRL, LRL etc.)	S.C. + 4 O.C.'S	VARACTOR DIODE
AUTHORS	Franzen and Speciale, Bianco et. al., Engen and Hoer, Maury et. al.	da Silva and McPhun	Bauer and Penfield, Peck and Peterson
CONCEPT	o Thru, delay and reflection stds. o Network par's of stds. theoretically known or not critical o Fixture network parameters computed from 1- and 2-port meas.	o Offset reflection stds. o Short used to establish reference plane. o Fixture network parameters computed from 1-port meas.	o Reverse bias varactor diodes used as variable capacitance stds. o Stds. characterized by independent measurements o Fixture network parameters computed from 1-port meas.
ADVANTAGES	o Stds. easy to realize in microstrip o Connections to stds. same as connections to mstrip discontinuities o Provides calculation of propagation constant γ_g o Provides calculation of reflection coefficient Γ_s	o Open circuit stds. easy to realize o Connections to stds. same as connections to mstrip discontinuities o Provides calculation of propagation constant γ_g	o Multiple known loads possible with a single connection o Connections to stds. similar to connections to active devices
DRAWBACKS	o Connection repeatability important for accuracy	o Perfect short circuit difficult to realize o Connection repeatability important for accuracy	o Connections to diodes dissimilar to mstrip discontinuities. o Characterization of stds. tends to be complicated

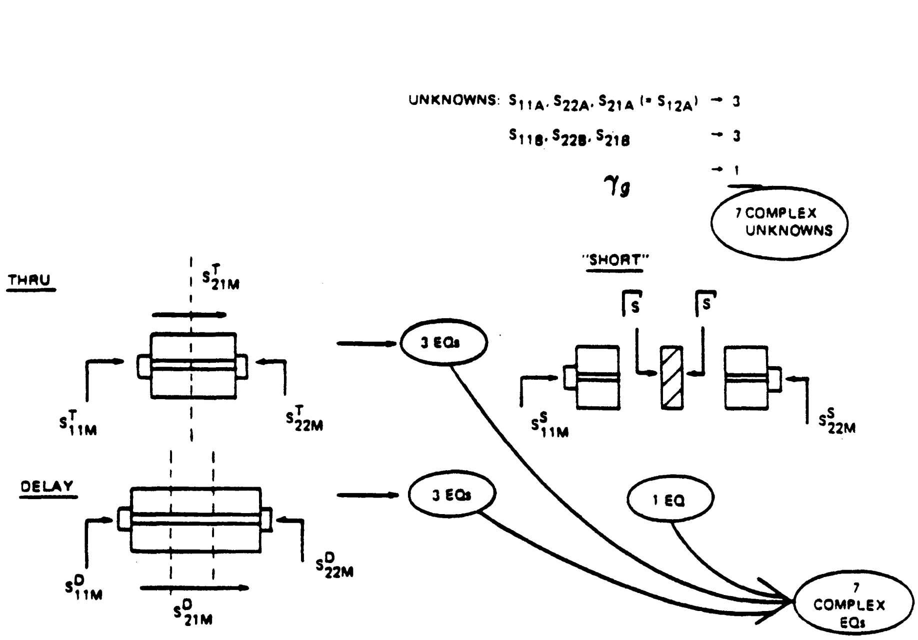

Figure 4.2: Fixture characterization by the TSD technique (Note: the "short" can be any highly reflecting standard).

in TSD, need not be perfect. In fact, any highly reflecting standard may be used in its place [45,46]. The only requirement is that the same reflection coefficient Γ_s must be presented to both microstrip test ports. This is important since, as discussed above, a perfect short is difficult to achieve in microstrip. This variation of the TSD method, that uses an arbitrary reflection standard, has been called the thru-reflect-line (TRL) method. Another variation, called the line-reflect-line method (LRL) [47], allows the use of a non-zero length thru line. Since both of these variations are derived from TSD, the overall approach will be referred to as TSD in this thesis. The understanding will be that the "short" is non-critical.

The main advantage of the TSD approach over the alternatives of Table 4.2 is that the TSD standards are easiest to realize in microstrip. da Silva and McPhun, suggest the use of 4 microstrip open circuits, and a short circuit. As far as this author can determine a perfect short is required to accurately establish the reference plane. To use varactor diode standards a rather complicated modeling procedure must be carried out to characterize the diodes prior to use.

In addition, the fixture hardware may be designed so that the connections made to the TSD standards are made in the same way as the connections to the microstrip discontinuity test circuits. This is not the case with varactor diode standards as the introduction of the diode mounting structure adds parasitics during fixture characterization that, in general, are not present when measuring discontinuity circuits.

One drawback to the TSD method is that good microstrip connection repeatability, and microstrip circuit fabrication repeatability are important for accuracy. This is also true (probably to a greater degree since more standards are required) for da Silva and McPhun's approach. In this area, the varactor diode approach is attractive since several different capacitances can be realized by varying the diode's reverse bias voltage. However, this advantage may be partially offset by the nonrepeatability of returning to the exact same bias voltage during calibration that was used during the characterization of the diodes.

One-tier vs. Two-tier De-embedding.— As discussed by Lane [43], full matrix de-embedding can be performed using either a one-tier or a two-tier approach. The choice between these two options is controversial, and it depends on the application and fixture hardware.

Referring to Figure 4.1, one-tier de-embedding involves making a direct calibration at the microstrip test ports. In this approach, fixture effects are included in the error model used to represent the ANA system imperfections. This approach has been used in coplanar waveguide [37], and also in microstrip [56]. One-tier de-embedding is more straight forward and in some ways easier to implement than two-tier de-embedding. Also, with the speed of current ANAs, the one-tier approach can display de-embedded measurements in essentially real time.

In contrast, two-tier de-embedding involves calibrating first at the coaxial or waveguide terminals. Measurements are then made on various microstrip standards to determine the S-parameters of each half of the test fixture. These are stored and later used to mathematically transform the measurements to the microstrip test ports.

One advantage of two-tier de-embedding for the present application is that it provides for better monitoring of the de-embedding process. Measurements can be made with several different connections made to each of the standards used for fixture characterization. These measurements can be stored in files and then compared in order to screen out bad connections. The remaining connection trials can then be averaged to reduce connection repeatability errors. For this reason the TSD method was implemented as a two-tier procedure, as described next.

4.3 Implementation of TSD De-embedding

4.3.1 Software and Hardware Considerations

Computer programs for performing TSD fixture characterization and de-embedding were provided by Hughes. As part of this work, modifications were made to these programs to customize them for the present application. The mathematics used are described in detail elsewhere [48,49].

A flow chart for the measurement procedure used is shown in Figure 4.3. The programs used to carry out this measurement procedure are set up to process several measurement frequencies simultaneously. First, ANA system calibration is performed with coaxial standards. The S-parameters of each of the TSD standards are then measured and stored in data files. To reduce connection repeatability errors, repeated measurements are performed with two to five connections made to each of the standards. These measurements are then used to obtain an average set of S-parameters for each fixture measurement.

The averaged S-parameters of the standards and the physical length of the delay line are then input to the fixture characterization program. This program performs calculations to provide measured values for $\epsilon_{eff}, \Gamma_s(= \Gamma_{op})$, and the S-parameters $[S_a]$, $[S_b]$ for each half of the test fixture.

Finally, measurements are made with the D.U.T. (i.e. the desired discontinuity circuit) connected within the fixture. Again, repeated measurements are made to reduce connection errors. The averaged D.U.T. S-parameters are then processed along with the fixture characterization data to obtain the de-embedded measurement. If necessary, the reference planes established by the de-embedding (in the middle of the thru line) are moved by performing simple transmission line rotations. The phase constant used for these rotations is based on the measured effective dielectric constant.

The instrumentation used for the measurements of this thesis was almost exclusively HP8510 ANAs which were available to the author at both the University and at Hughes. The only exception is that an HP8409 ANA with a high frequency waveguide extension was used to perform connection repeatability measurements in the 26.5-40GHz frequency range.

The test fixture that was used for the discontinuity measurements was also provided by Hughes. A picture of the test fixture is shown in Figure 4.4. The fixture employs a pair of 7mm coaxial "Eisenhart" launchers [57] and is usable to 18GHz. The shielding is provided by placing U-shaped covers on top of the microstrip carriers. This forms a cavity similar to Figure 1.3.

Another fixture, usable to 40GHz was also developed by the author for use with this thesis. This fixture was used in the connection repeatability study (Appendix H), but not for discontinuity measurements. The reason for this was logis-

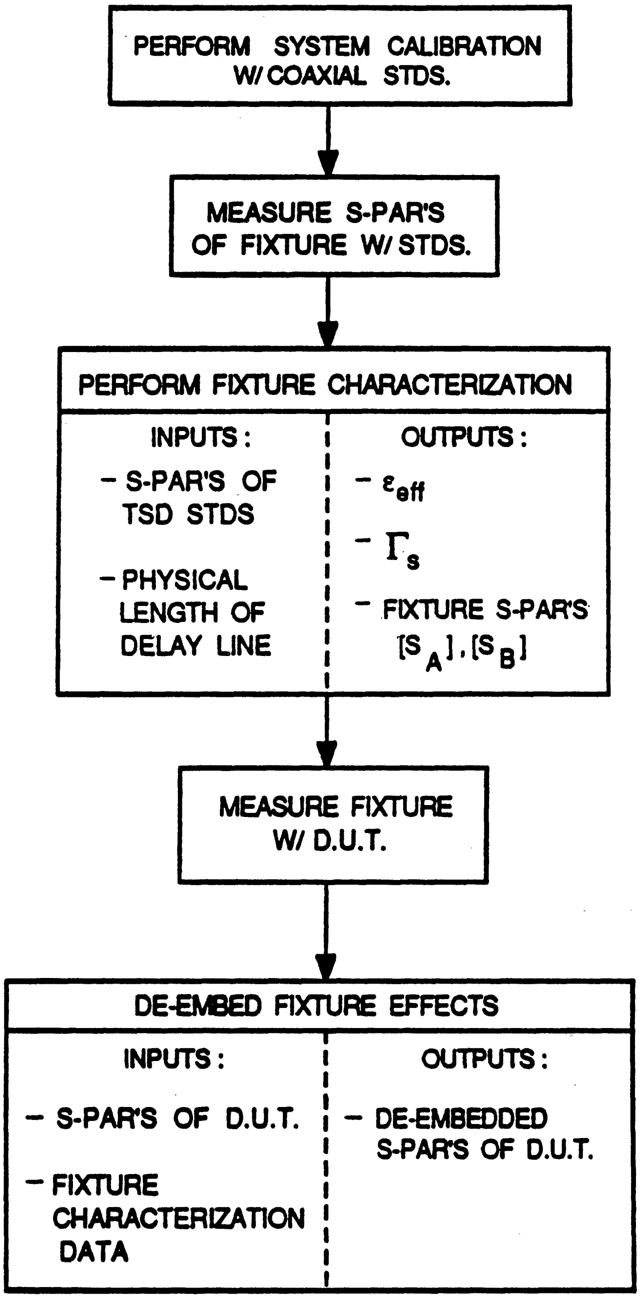

Figure 4.3: Procedure used in this work for measurement and de-embedding.

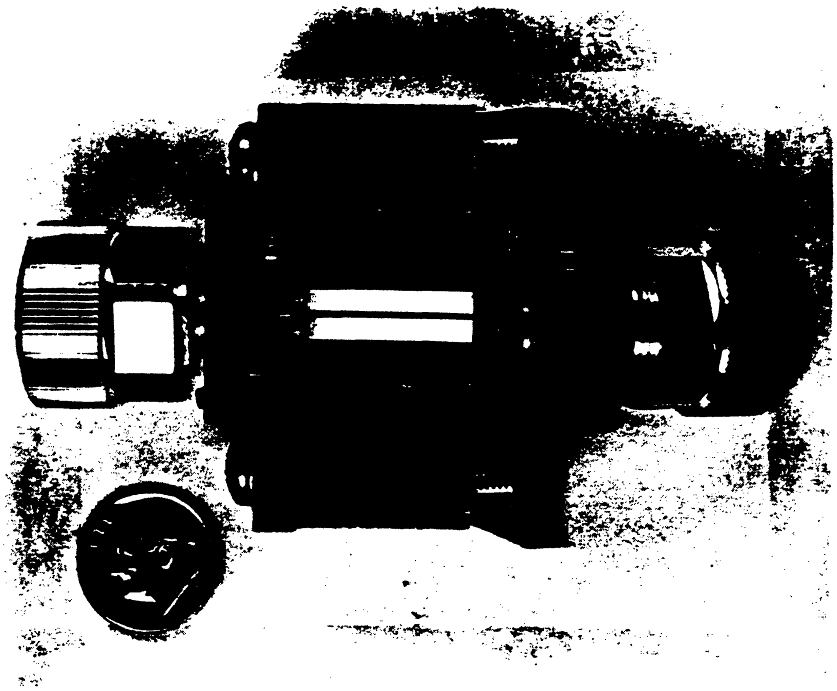

Figure 4.4: 7mm coaxial/microstrip test fixture (partially disassembled).

tical and not technical. All of the discontinuity measurements were performed at the University, and at the time these experiments were planned (substrates ordered etc.), facilities were not available to make measurements above 18GHz. Hence, the 7mm fixture was used for all the discontinuity measurements.

4.3.2 Connection Approaches For TSD De-embedding

There are three basic connection alternatives for TSD characterization of a coaxial fixture. Each of these must rely on at least one of the following assumptions:

1. repeatability of connections made from the coaxial-to-microstrip transition (launcher) to the microstrip line (i.e. coax/microstrip connection repeatability)

2. repeatability of microstrip/microstrip interconnects

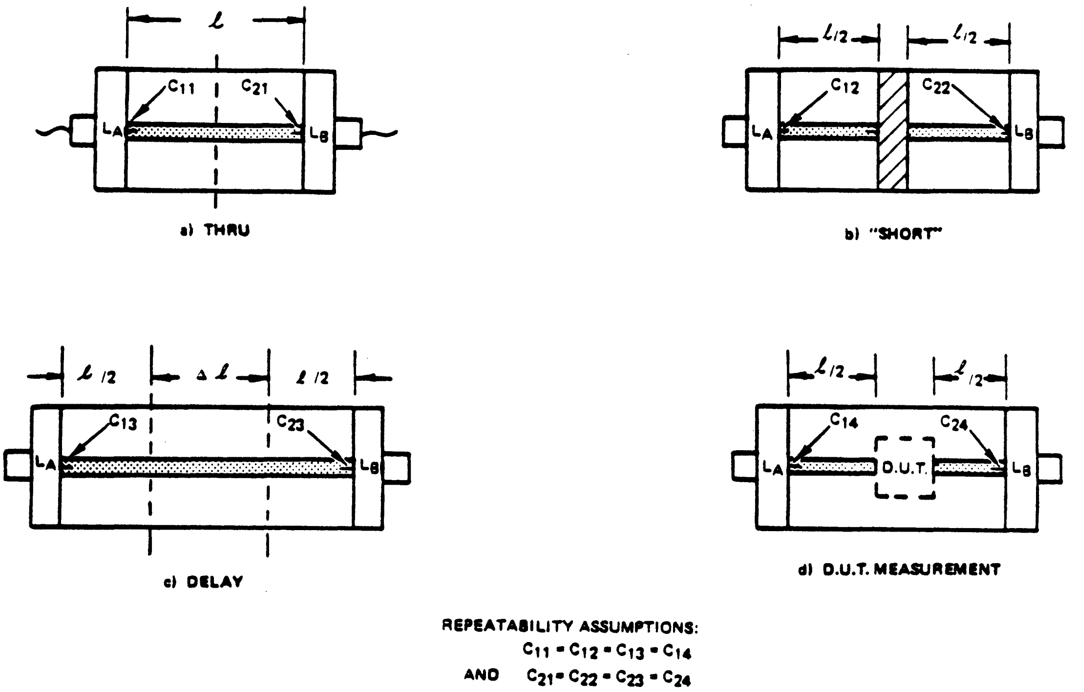

Figure 4.5: The TSD Connection approach used for the present work, relies on repeatable coax/microstrip connections.

3. uniformity of electrical characteristics between different transitions (launcher-to-launcher uniformity).

In the first connection approach (Figure 4.5), continuous substrates are used to realize the three standards, which are connected between the same pair of launchers (L_a, L_b). In the second method (Figure 4.6), the TSD standards, and the D.U.T., are connected between the same two launcher/microstrip assemblies using microstrip-to-microstrip interconnects (e.g. ribbon bonds). In the third approach, each of the standards would be constructed complete with their own intact launchers. While this has practical advantages, such as improving the durability of the standards, launcher-to-launcher uniformity is not generally a good assumption for microwave de-embedding (Appendix H).

In all of the above approaches, it is important to have good uniformity between various microstrip line sections as mounted in the fixture hardware. If the fixture must be removed from the coaxial measurement ports to insert either the stan-

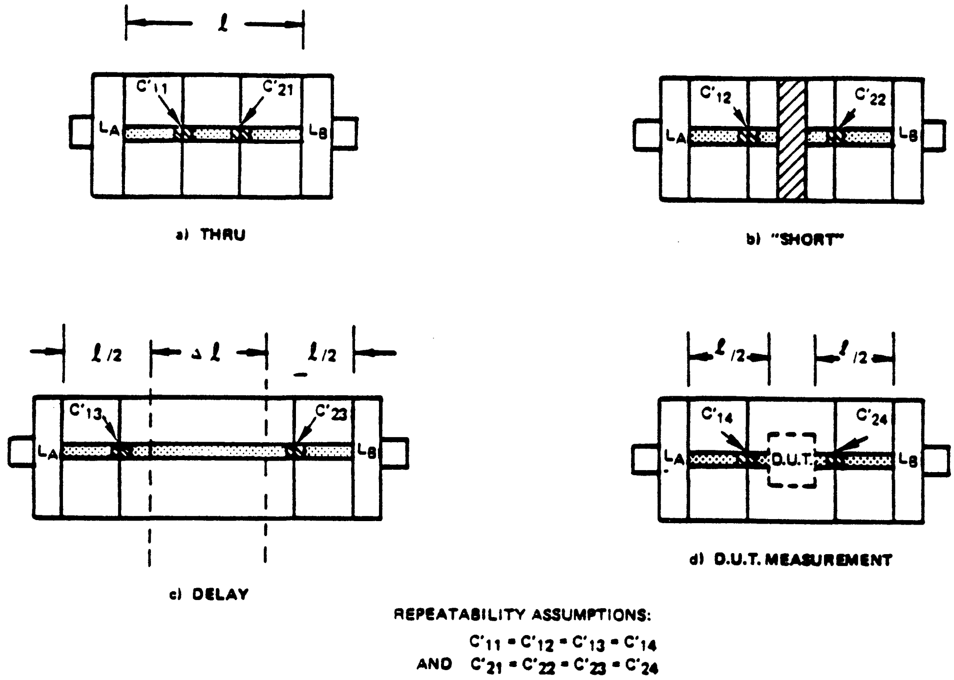

Figure 4.6: TSD Connection approach relying on repeatable microstrip/microstrip connections.

dards or the D.U.T., de-embedding accuracy is also subject to uncertainties due to repeated coax/coax connections. However, the study results suggest that these uncertainties are negligible compared to other errors.

The results of the repeatability study (Appendix H) clearly favor the connection approach of Figure 4.5 relying on repeatable coax/microstrip connections, and this was the approach adopted for the present work.

4.3.3 Measurement of Effective Dielectric Constant

As mentioned previously, one of the byproducts of the TSD method is the calculation of the propagation constant $\gamma_g(= \alpha_g + j\beta_g)$. For the alumina substrates used, the loss factor α was found to be too small to measure by this method, or conversely the measurement sensitivity is not great enough. Using Super Compact this loss (combined dielectric and conductor losses) is estimated to be .05dB/cm at 10GHz. For the delay length used here this translates to a total loss of .01dB which is less than the error due to connection repeatability.

The phase constant β is measurable, and may be used to calculate the effective dielectric constant ϵ_{eff} by the following relation:

$$\epsilon_{eff} = \left(\frac{\beta c}{\omega}\right)^2 \tag{4.1}$$

where c is the velocity of light and ω is the radian frequency.

The value of ϵ_{eff} calculated from the TSD procedure relies mainly on the delay line length Δl, and the difference in measured transmission phase between the thru and delay line standards.

Figure 4.8 shows a typical ϵ_{eff} measurement resulting from a single TSD fixture characterization procedure. A sketch of the standards used is given in Figure 4.7. The "raw" measurement shown is the actual measurement, and the "fitted" result was obtained by performing a least squares polynomial curve fit to the measurements. As supported by the theoretical results of Chapter 5, the actual ϵ_{eff} should follow a smooth curve. Hence, deviations from the fitted curve indicate imperfections in the measurement. In this work, the fitted curve is generally used for any post de-embedding transmission line rotations.

4.3.3 Measurement of Open-end Discontinuity

A measurement of the reflection coefficient and related capacitance of a microstrip open-end discontinuity was obtained based on using an open-ended microstrip line as the reflection standard in place of the "short" of Figure 4.2. A measurement of the reflection coefficient $\Gamma_s(= /\Gamma_{op}/e^{j\theta_{op}})$ results from the fixture characterization procedure. Figure 4.9 shows a representative plot of the measured (de-embedded) reflection coefficient of the open-end standard of Figure 4.7. The phase angle shows an increasingly negative phase shift with frequency, as expected.

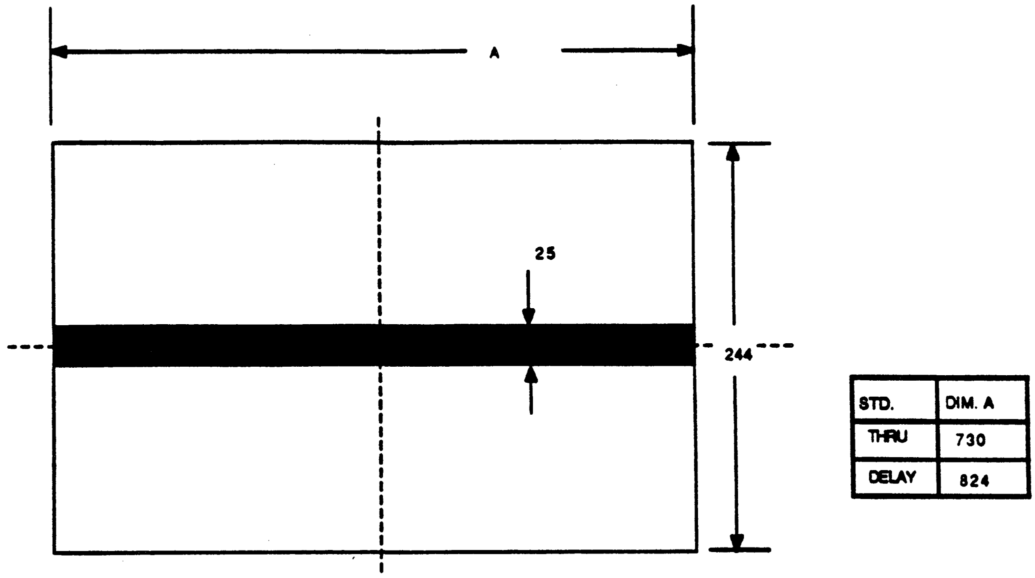

a) Thru and delay line standard

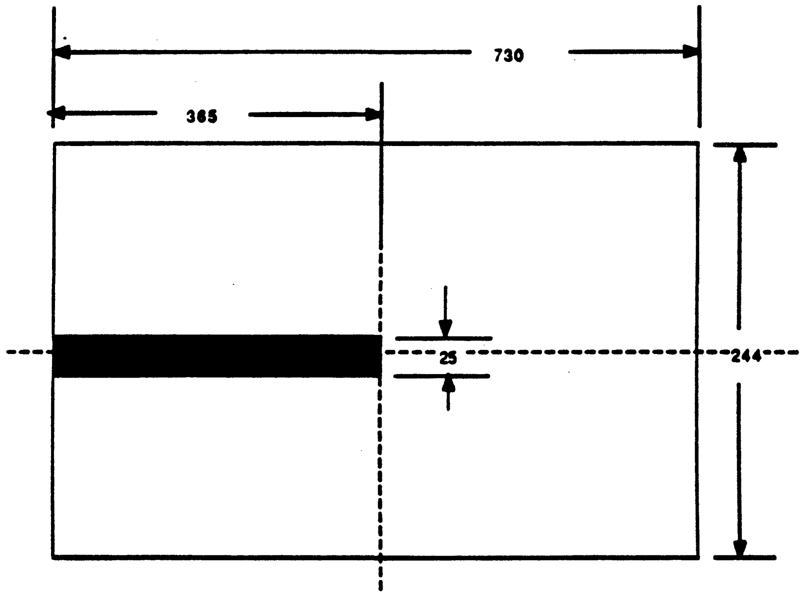

b) Open-end standard

Figure 4.7: Sketch of TSD standards used for measurements of ϵ_{eff}, and open-end and series gap discontinuity circuit. Note: all dimensions of Figure are in mils (1 mil=.001″), h = .025″, $\epsilon_r = 9.7$.

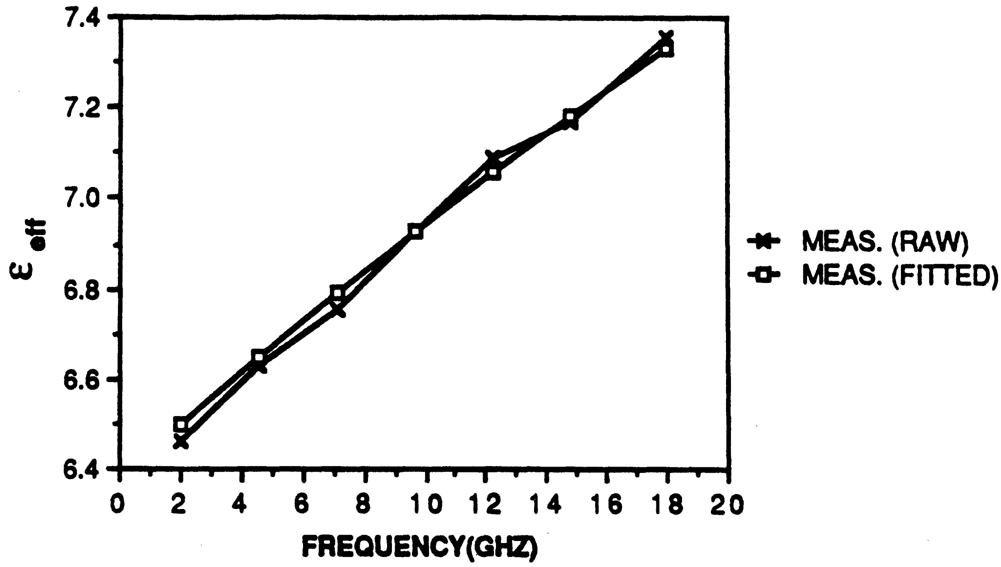

Figure 4.8: Typical effective dielectric constant measurement resulting from TSD fixture characterization. (Shielding dimensions: $b = c = .25''$)..

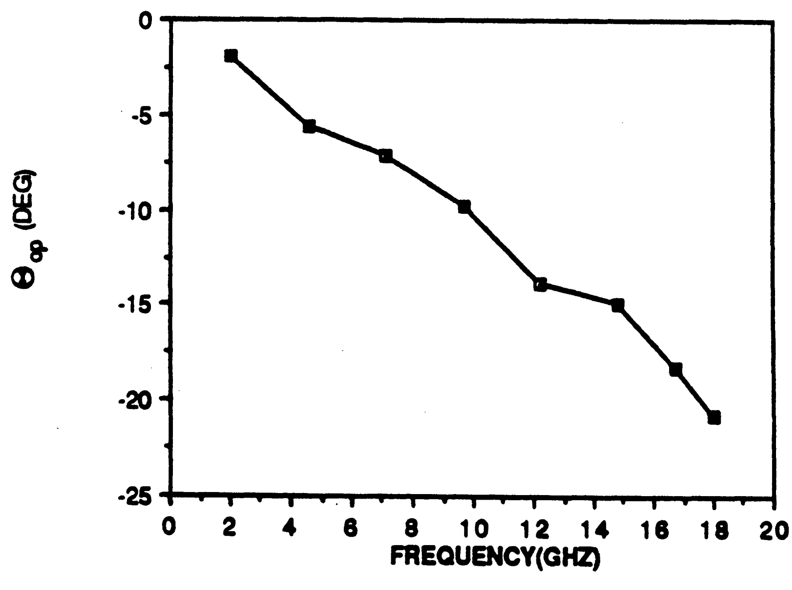

Figure 4.9: Angle of open-end reflection coefficient resulting from a typical fixture characterization procedure.

The reflection coefficient angle θ_{op} is related to the normalized capacitance by the relation given by (2.135)

$$c_{op} = \frac{-\sin\theta_{op}}{\omega(1+\cos\theta_{op})} \,. \tag{4.2}$$

A calculation of c_{op} based on measurements is shown compared to numerical results in Chapter 5.

4.3.4 Measurement of Series Gap Discontinuities

Measurements were performed on three series gap test circuits of different gap widths 15mil, 9mil, and 5mil. A sketch of the test circuit layout is shown in Figure 4.10. The TSD standards of Figure 4.7 were used for fixture characterization. Because the length of the input/output lines L_1 and L_2, to the left and right of the series gap respectively, are shorter than half the thru line of Figure 4.7, the reference planes established by the de-embedding are not at the desired positions of a-a and b-b (Figure 4.10). A transmission line rotation is used, in each case, to move the reference planes to the desired positions. The phase constant used for this rotation is calculated from the fitted effective dielectric constant discussed in Section 4.3.2. The length of rotation is given by the difference in physical length between L_1, L_2, and half the thru line length. The measured results are discussed in Chapter 5.

4.3.5 Measurement of Coupled Line Filters

The last measurements to be described were made on two different coupled line band pass filters. The first filter is the two resonator coupled line filter depicted in the sketch of Figure 4.11. The TSD standards used for this measurement are

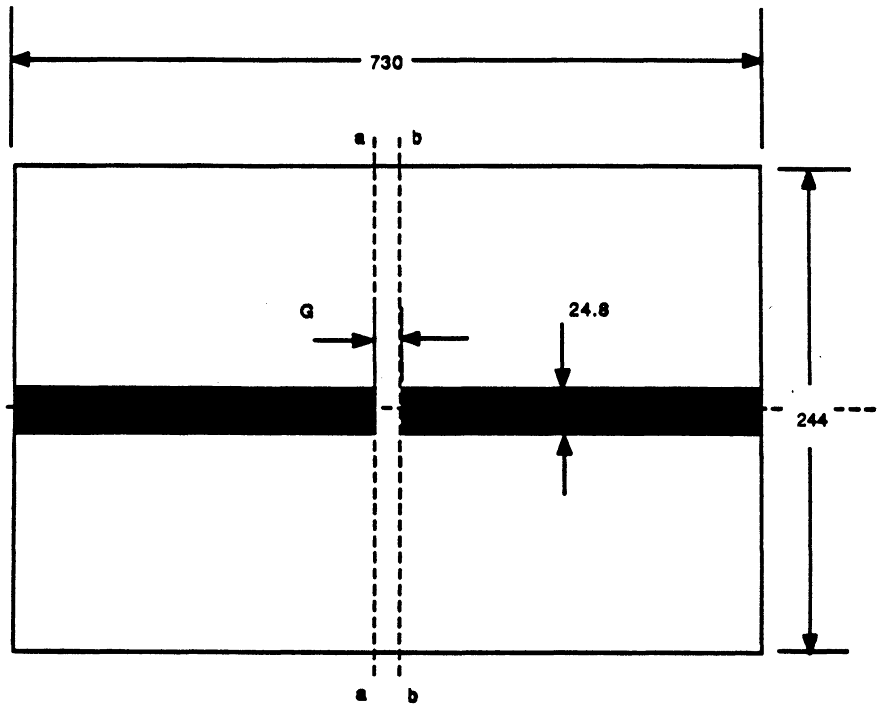

TEST CKT.	DIM. G
A	15
B	9
C	5

Figure 4.10: Sketch of series gap discontinuity test circuit. Note: all dimensions in mils, $h = 25, \epsilon_r = 9.7$. (Shielding dimensions: $b = c = .25''$).

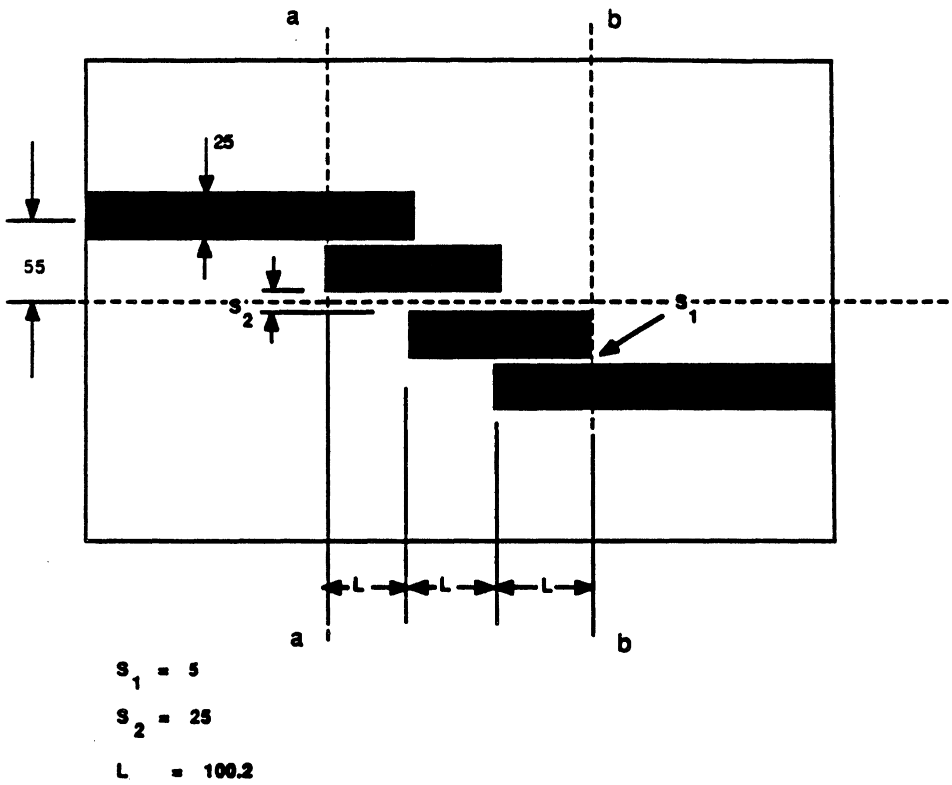

Figure 4.11: Sketch of two resonator coupled line filter. Note: all dimensions in mils, $h = 25, \epsilon_r = 9.7$. (Shielding dimensions: $b = .4'', c = .25''$).

shown in Figure 4.12. As in the case of the series gap measurement, a transmission line rotation was required after de-embedding to adjust the reference planes to the desired positions a-a and b-b of Figure 4.11.

The other filter measured is the four resonator filter of Figure 4.13. In this filter, the line widths of the filter structure are 11.9 mils (.302mm) which corresponds to about a 65 ohm impedance level. Since the ANA provides for measurements in a 50 ohm environment, a quarter wave transformer was designed to transform from this 65 ohm impedance level to approximately 50 ohms at the coax/microstrip connection points. By including the same transformer on the input and output portions of the TSD standards (Figure 4.14), its effects can be effectively removed through the de-embedding process.

The result is that microstrip calibration reference planes are established at the

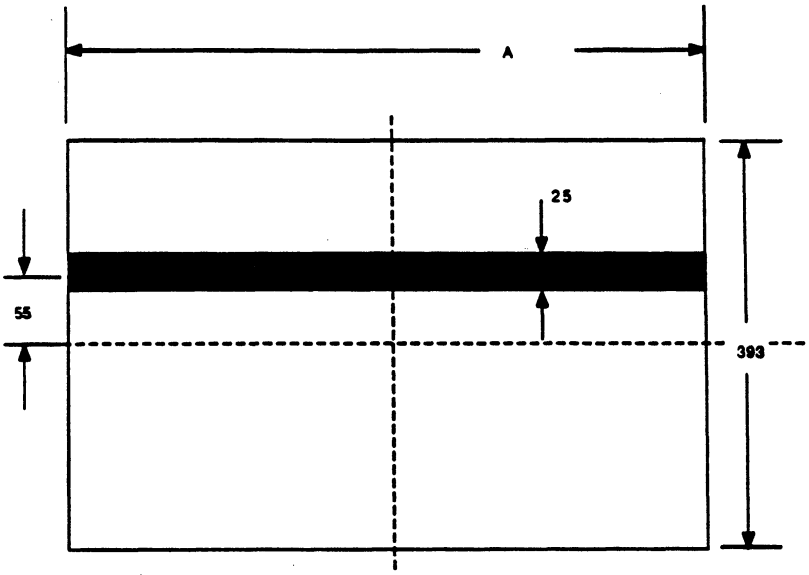

STD.	DIM. A
THRU	730
DELAY	824

a. Thru and delay line standards

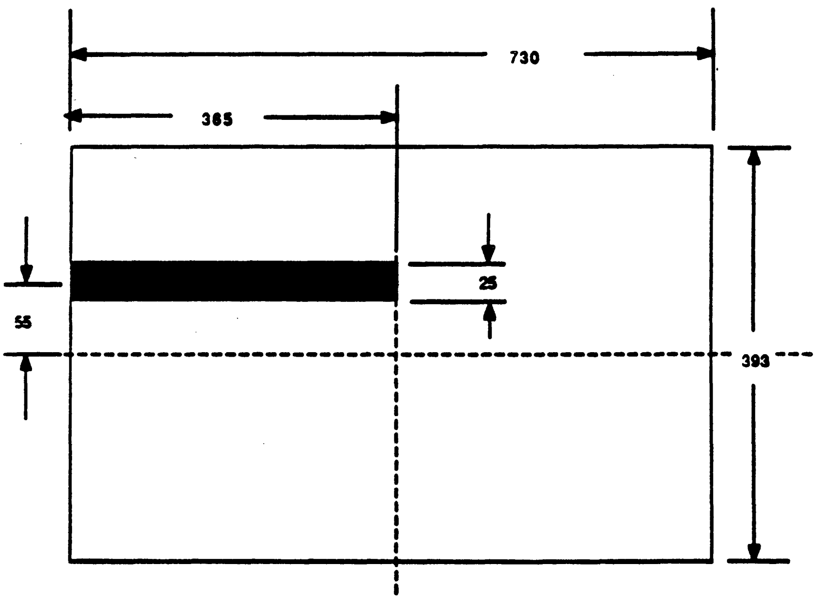

b. Open end standard.

Figure 4.12: Sketch of TSD standards for two resonator filter measurement. Note: all dimensions in mils, $h = .025'', \epsilon_r = 9.7$.

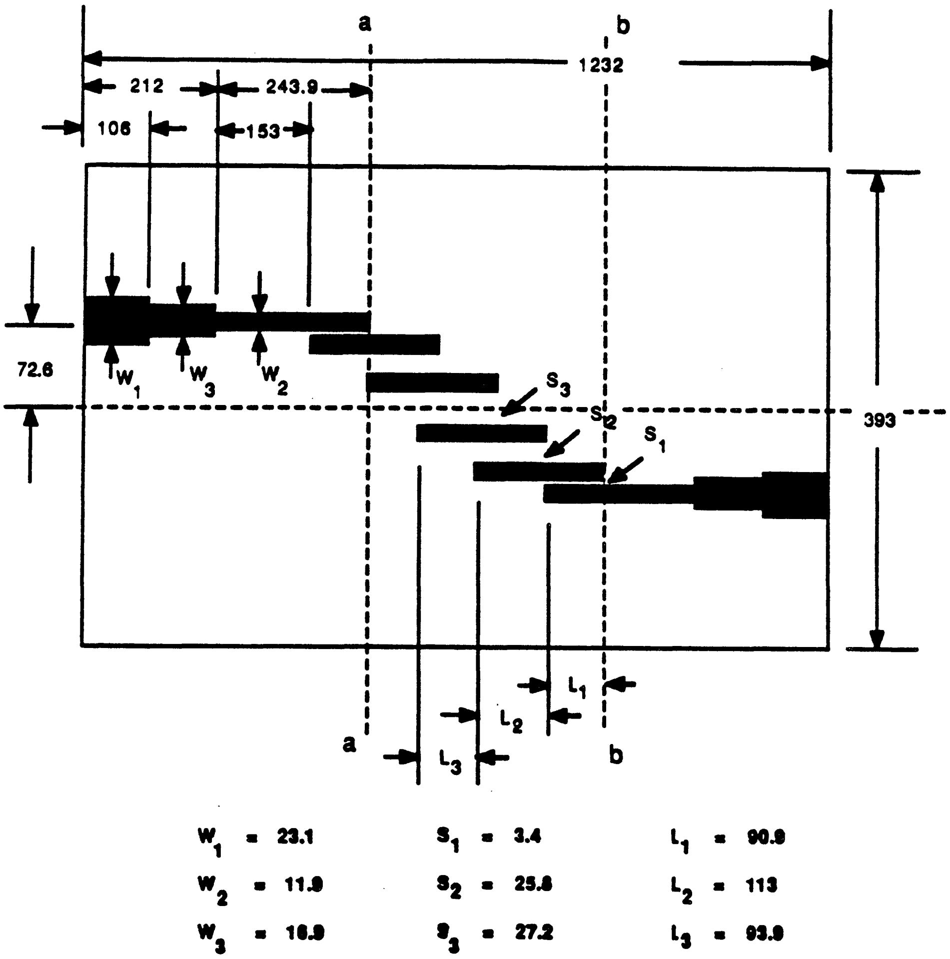

Figure 4.13: Sketch of four resonator coupled line filter. Note: all dimensions in mils, $h = .025'', \epsilon_r = 9.7$. (Shielding dimensions: $b = .4'', c = .25''$).

planes a-a and b-b of Figure 4.13. The de-embedded scattering parameters are referenced to approximately 65 ohms. Note that no transmission line rotations are required to adjust the reference planes for this measurement since the input and output line sections L_1 and L_2 are the same length as half the thru line.

The measured results for both of these filters is discussed in the next chapter.

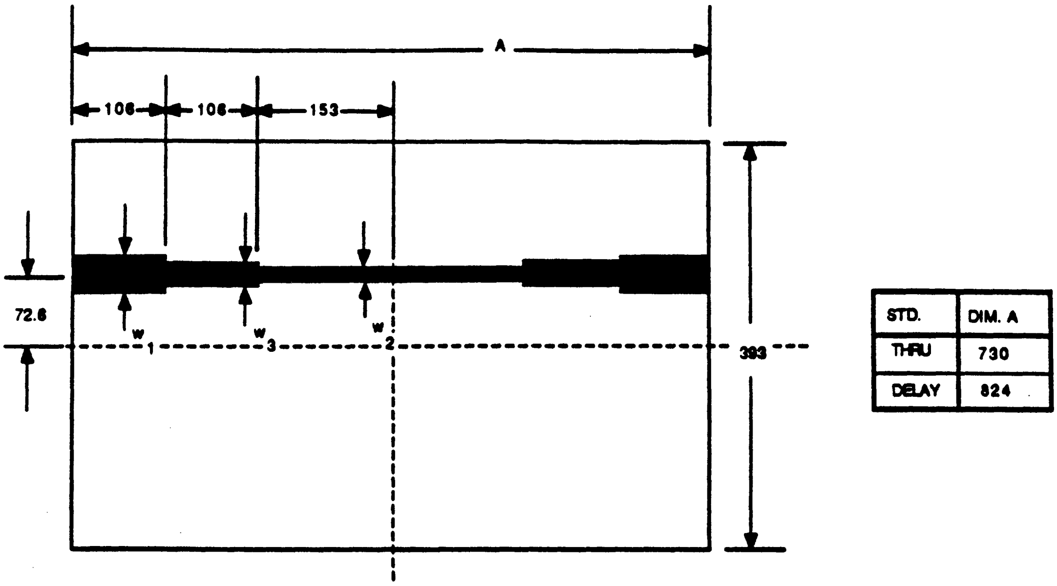

a. Thru and delay line standards.

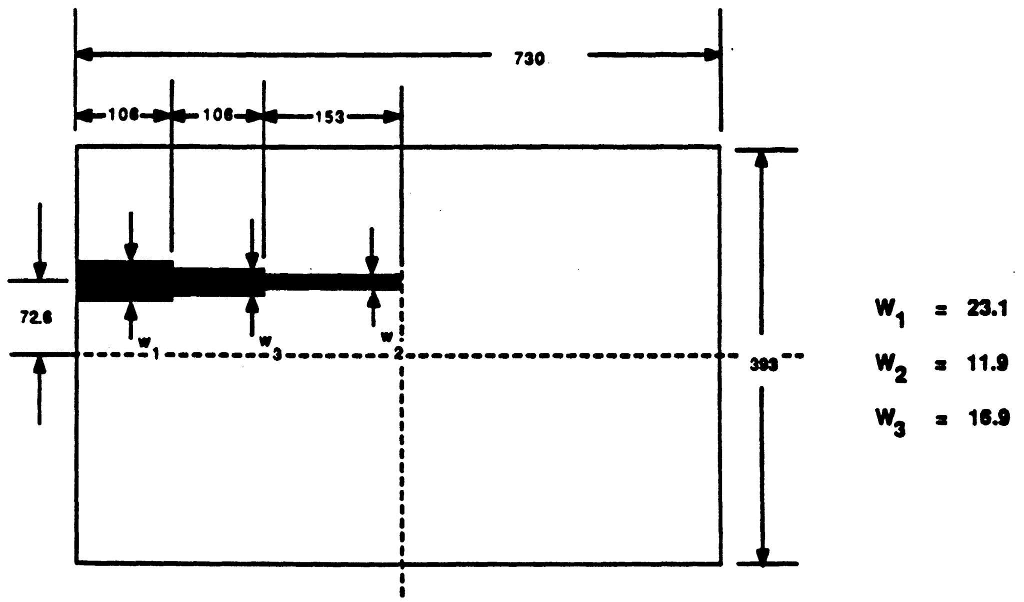

b. Open end standard.

Figure 4.14: Sketch of TSD standards for four resonator filter measurement. Note: all dimensions in mils, $h = .025'', \epsilon_r = 9.7$.

4.4 A Perturbation Analysis of Connection Errors in TSD De-embedding

As part of this thesis, an approach was developed to analyze the uncertainties in TSD de-embedding results arising from connection repeatability errors. The analysis consists of perturbing the S-parameters of the TSD standards and the D.U.T. with a set of error vectors that are representative of the variations of each S-parameter (S_{11}, S_{12} etc.) measurement with repeated connections. Software was written to allow processing the perturbed S-parameter data in the same way as the measurement data is processed (Figure 4.3). This perturbation analysis, allows for an approximation of how connection errors —which are inevitable— propagate through the TSD mathematics and limit the precision of the final results.

The *precision* of a measurement process is not the same as accuracy. *Accuracy* refers to how close the result of an experiment comes to the true value. Since the true value is usually unknown, as it is for the present measurements, true measurement accuracy is often impossible to evaluate. *Precision* on the other hand is a measure of how reproducible a result is. Measurement reproducibility is something for which a reasonable estimate can usually be made, and this is the purpose of the following discussion.

An examination of the measurement procedure (Figure 4.3) shows that any variations in the final results are due to uncertainties in the fixture measurements of the standards and the D.U.T.. The precision of these fixture measurements is affected by two factors. First is the non-repeatability of the fixture connections, which for the present measurements includes both coax/coax and coax/microstrip connections. The second factor affecting the precision is random errors due to ANA instrumentation or the non-repeatability of the system calibration procedure, which is believed to be negligible compared to other error sources. For convenience, the following definition is advanced:

Definition IV.1 *The combined effect of the random errors in the ANA instrumentation and the errors due to connection non-repeatability will be referred to as* **connection errors.**

The repeatability experiments presented in Appendix H explore the errors in microstrip fixture measurements caused by non-repeatable microstrip connections. In these measurements, the resulting spread of the data in each case includes both random ANA errors, and those due to coax/coax connection non-repeatability in addition to the repeatability issue being studied. Hence, the results presented actually represent the total connection errors associated with each repeatability issue.

These connection errors are present during the measurement of each of the three TSD standards (Figure 4.2) and also during the measurement of the D.U.T., which in the present application is a discontinuity structure.

4.4.1 Basic Approach to Perturbation Analysis

The perturbation approach developed to analyze the effect of these connection errors is outlined in Figure 4.15. First, an analysis frequency is chosen. The analysis is performed at a single frequency to prevent the data processing from becoming too cumbersome. In this work a frequency of 10GHz was chosen since it is about in the middle of the frequency range used for the discontinuity measurements.

After the analysis frequency has been chosen, the next step is to derive a representative set of error vectors for the type of connection used. Figure H.4 shows one way of looking at the coax/microstrip connection repeatability data. There, the average set of S-parameters are used to normalize the S-parameters from each of the connection trials by way of vector division. Another way to look at this data is to perform a vector subtraction between the S-parameters from each

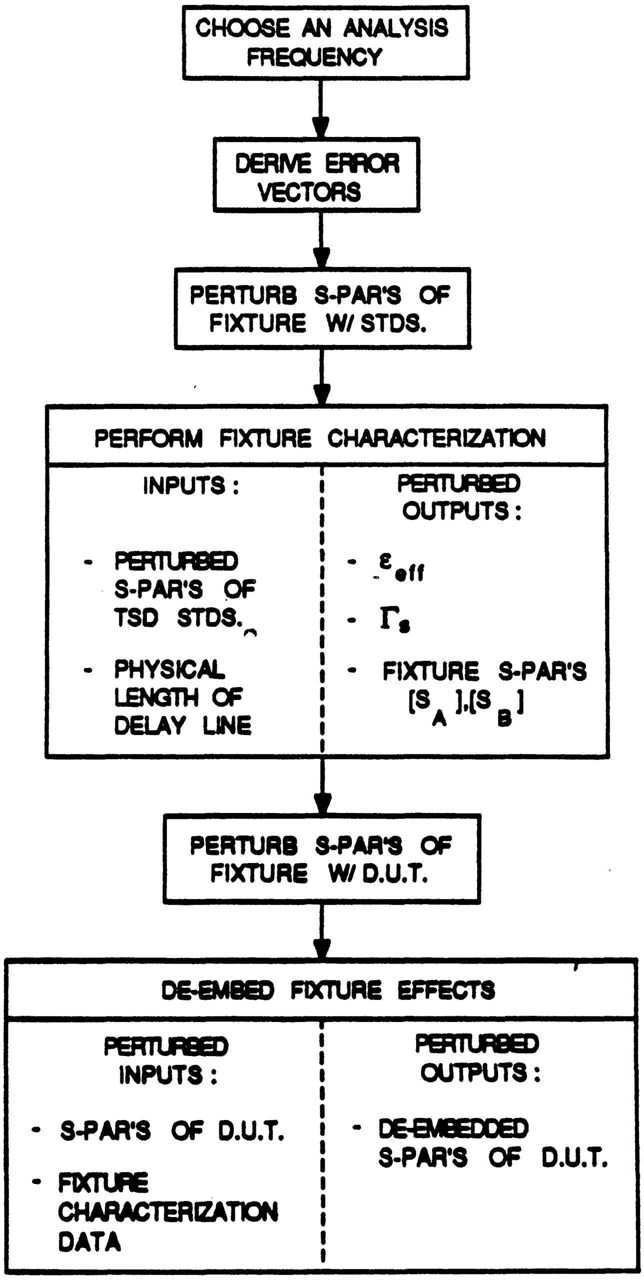

Figure 4.15: Flow chart illustrating approach for perturbation analysis of connection errors.

of the connection trials and the average S-parameters. In this case the result is a set of error vectors that represents the vector perturbation of each of the S-parameter measurements from the average.

This idea is illustrated in Figure 4.16. This figure shows a typical set of S_{11} and S_{12} measurements resulting from 10 connections on a thru line[3]. The error vector ΔS_{11} shown is given by

$$\Delta S_{11} = S_{11m} - S_{11avg} \tag{4.3}$$

where S_{11m} is the measurement for a single connection trial and S_{11avg} is the average of 10 connections. The error vectors ΔS_{12}, ΔS_{21}, and ΔS_{22} are defined analogously. Thus, for each connection trial we may define four error vectors.

Error vectors so derived, are used in the analysis to perturb the S-parameters for each of the TSD standards and the D.U.T.. To do this, a nominal (or average) set of S-parameters are obtained from measured data. The different error vectors are then added to the nominal S-parameters in an order determined by setting up a permutation table similar to that shown in Table 4.3.

To understand how this permutation table is used, consider the following example. Assume that each fixture connection can be made in one of ten possible ways and let these connections be numbered 1 through 10. Associated with each connection is a set of four error vectors may be derived as discussed above. For this example, assume that the same set of error vectors can be used for all fixture measurements. The final de-embedded result will depend on which of the 10 possible connections was made to each of the standards during fixture characterization and to the D.U.T. before measurement and de-embedding. For 4 fixture measurements, and 10 possible connections for each, there are 10^4 permutations of different con-

[3] Note: In Figure 4.16 and the other polar representations that follow, the Smith chart lines drawn only have meaning when the scale is 1.0. When magnified scales are indicated (e.g. SCALE=0.1), only the relative magnitudes and phases of the points plotted are important.

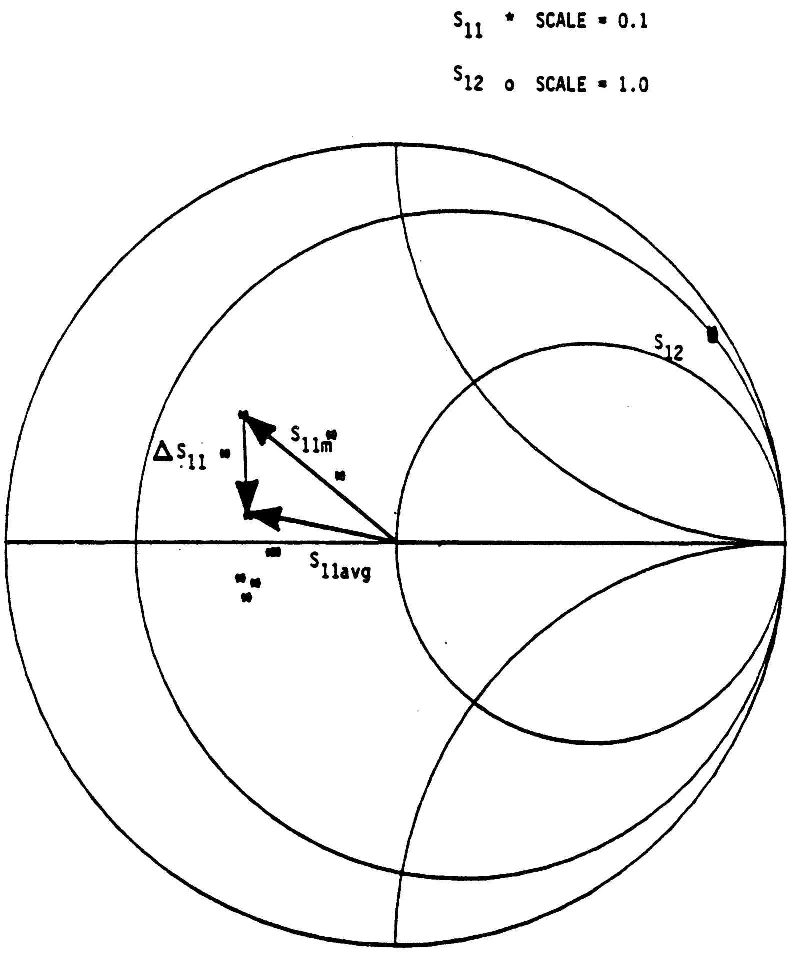

Figure 4.16: Variation of S_{11} and S_{12} for 10 connections made to a typical thru (or delay line) standard. Error vectors may be defined as the vector perturbation of each of the measurements from the average.

Table 4.3: CONNECTION PERMUTATION TABLE EXAMPLE

CONNECTION COMB. NO.	THRU	"SHORT" (OPEN)	DELAY	D.U.T.
1	1	2	5	5
2	6	5	1	9
3	1	6	10	10
4	3	3	7	4
5	7	5	6	4

nection combinations. Table 4.3 only shows 5 of these permutations. Each of the connection combinations is assigned a number, and each row of the table describes the corresponding connections for each of the fixture measurements. The order of the connections is chosen randomly by using a a pseudo-random number generator to set up each column of the table. In this way a large number of repeated de-embedding procedures can be synthesized with a relatively small set of measured data.

Once the perturbed sets of S-parameter data on the standards and the D.U.T. have been obtained, the fixture characterization and de-embedding operations are the same as those of Figure 4.3. The only difference is that instead of processing measured data for different frequencies, the software is used to process perturbed S-parameters for different connection combinations.

4.4.2 Perturbation Analysis and Results

The above gives a brief description of the basic approach used to analyze connection errors. A critical step in the analysis is the selection of a representative set of error vectors for the connection errors of a given microstrip fixture measurement. To be statistically rigorous, a different set of error vectors is required for each different fixture measurement that is made, since the error vectors may differ with the device or circuit being measured. In addition, these error vectors should be derived from a large number of connections in each case.

Obtaining this extensive of a data set would be a formidable task. One problem is that the measurements themselves, and the associated data processing is very time consuming. Second, there is a limit on the number of connections that can be made between a particular set of connectors and a particular microstrip test line. As the number of connections is increased, the wear on the fixture hardware (and the experimenter) gradually degrades the performance of the connection and from a statistical point of view the population average μ will not be a constant.

Because of these difficulties, some simplifying assumptions are made to allow an approximate analysis to be carried out. In doing this, the author has attempted to make the best use of the available connection repeatability data to derive error vectors for each of the fixture measurements. These error vectors are described below. The main assumption made is that the error vectors used represent a random sample of the possible connection errors. Within the limits of this assumption, the resulting analysis gives a reasonable approximation to the related uncertainties.

In the analysis which follows an analysis is carried out to estimate the precision of the measurements made of ϵ_{eff}, and the open-end and series gap discontinuities. An approximation of the precision of the coupled line filter structures is not included because the repeatability data currently available is not sufficient to derive error vectors for these measurements.

Error Vectors used for Delay Lines, and Filters

Based on the repeatability measurements for a microstrip thru line presented in Figure H.4, a set of error vectors were derived in the manner described above. These are shown plotted in Figure 4.17.

The difference observed in this Figure between the S_{12} and S_{21} error vectors (Figure 4.17b) may concern some readers, since for a passive two port structure we would expect the S_{12} and S_{21} measurement to be identical. However, The difference is very small and not considered significant. They are due to a residual systematic error in the ANA that is not removed by the calibration. In the de-embedding algorithm (Figure 4.3) the two measurements are averaged and set equal. However, to avoid amiguities in the perturbation analysis to follow only the S_{12} data is processed.

Also, in the perturbation analysis it will be assumed that the error vectors of Figure 4.17 are representative of the connection errors in the measurement of both the thru and the delay line standards of Figure 4.7. The only difference between these standards and the thru line that was measured for the connection repeatability study is the length of the line. Otherwise, the type of connection used for each is the same. The vector subtraction performed in deriving the error vectors essentially normalizes them to the average (though in a different way than a vector division does). Because of this it is reasonable to assume that the error vectors do not vary greatly between different fixture measurements, provided the magnitudes of the average S-parameters are similar. This is true for both the thru

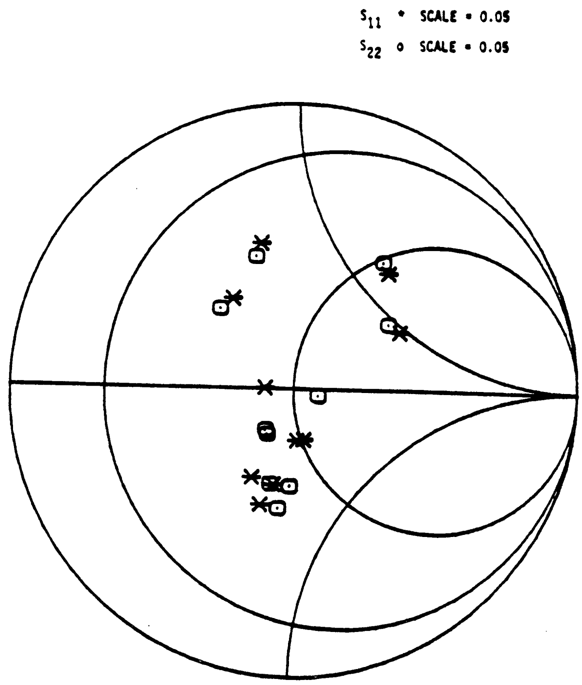

a. Error vectors for S_{11} and S_{22} measurement.

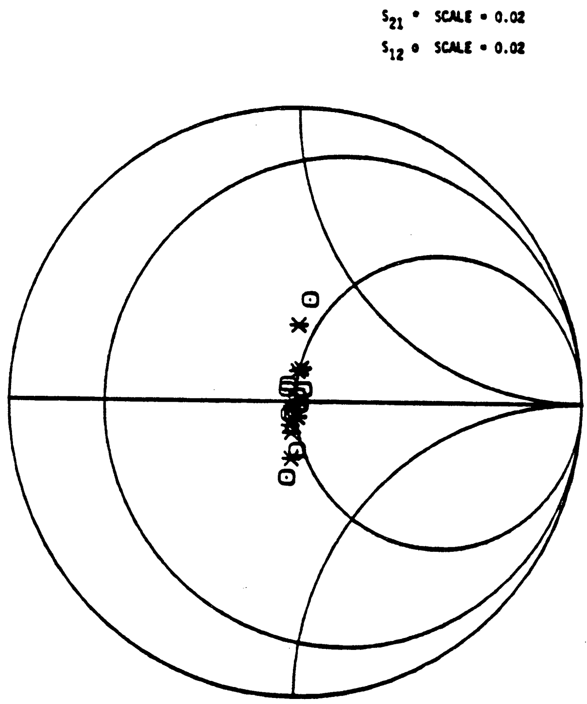

b. Error vectors for S_{12} and S_{21} measurement.

Figure 4.17: Error vectors for thru or delay line standards. These were also used to perturb the S-parameters of the two and four resonator filter structures.

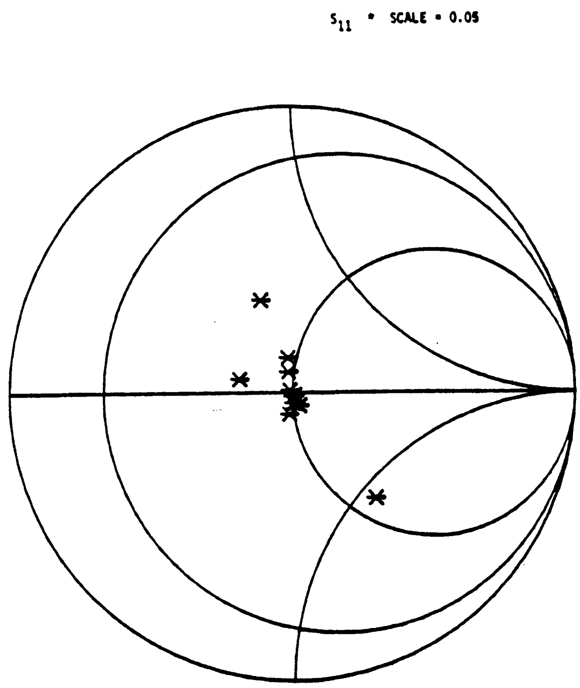

Figure 4.18: Error vectors for measurement of open-end reflection standard.

and delay line standards. Error Vectors For Open-End Standard

In contrast, the reflection coefficient measurement for an open-end is not similar to that for a thru line and a different set of error vectors is needed. Hence, a new set of error vectors were derived from measurements of 11 repeated connections made to the open-end standard and these are shown in Figure 4.18. Since the magnitude of S_{11} and S_{22} are about the same, it is assumed that the same error vectors can be used to perturb both of these measurements.

Error Vectors For Series Gap Measurements.

For the series gap measurements, repeatability data was obtained for four connections on two of the gap circuits, and five connections on the third. Error vectors were derived separately for each of the gaps and compared. It was seen that the magnitude of the error vectors did not differ significantly between the three sets. These error vector sets were then combined to form a larger set of error vectors representing 13 possible connections. These are shown in Figure 4.19.

4.4.3 Connection Errors in ϵ_{eff} and Open-end Measurement

Using the method described above, a perturbation analysis was carried out to analyze the effects of connection errors on the ϵ_{eff}, Γ_{op}, and c_{op} measurements which are calculated as part of the TSD procedure as described previously.

To do this, nominal S-parameter measurements were taken from measurements on the standards of Figure 4.7 at $f = 10$ GHz. The error vectors discussed above were used to perturb these nominal parameters according to two different permutation tables, one with 20 connection permutations and the other with 100 permutations. These permutation tables are similar to Table 4.3, except that a different set of error vectors are used for the open-end standard. Also, the connection combinations for the S_{11} and S_{22} measurements were allowed to vary independently so that the permutation tables had 5 columns instead of 4.

The statistical data are calculated for each parameter based on the observed results for the different connection combinations. The average is calculated by summing up the results for each of the different combination numbers and dividing by the number of permutations. The estimated standard deviation s for the data is given by

$$s = \text{Std.Deviation} = \sqrt{\frac{\sum x_i^2 - \frac{(\sum x_i)^2}{N}}{N-1}} \tag{4.4}$$

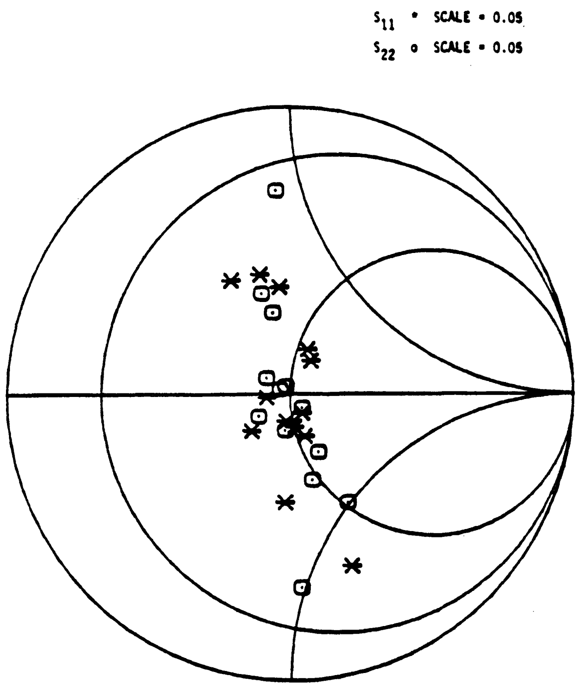

a. Error vectors for S_{11} and S_{22} measurement.

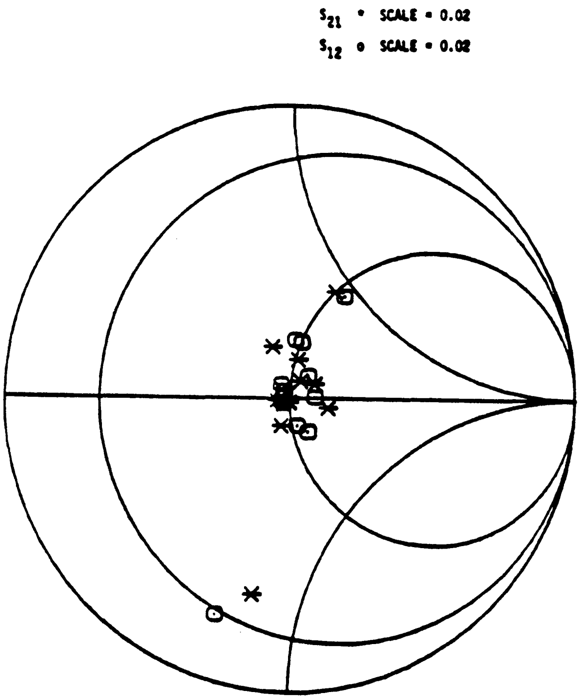

b. Error vectors for S_{12} and S_{21} measurement.

Figure 4.19: Combined error vectors for series gap measurements.

where

N = number of trials

x_i = observed result for the parameter of interest for connection combination i

The results of the perturbation analysis are summarized in Table 4.4. It is seen that the results for 100 connection permutations are not significantly different than those for 20 permutations. The range of observed values increase slightly for each of the parameters. This is reasonable since more worst case connection combinations are possible with a greater number of permutations. On the other hand, the standard deviation values are seen to change by a much smaller amount. It appears that 100 is a sufficient number of permutations from which to base the statistical observations.

The results of the analysis indicate that the uncertainty in ϵ_{eff} and the open-end parameters due to connection errors can be appreciable. The standard deviations for these parameters is about .5% (of the average) for ϵ_{eff}, and about 8% for the open-end parameters. These standard deviation values were used to derive error bars for the measurements of ϵ_{eff} and the open-end parameters presented in the next chapter.

Table 4.4: PERTURBATION ANALYSIS RESULTS FOR ϵ_{eff} and OPEN-END MEASUREMENTS

PARAMETER	PERMU-TATIONS	MIN VALUE	MAX VALUE	AVG VALUE	RANGE	STD. DEV.
ϵ_{eff}	20	6.851	6.978	6.922	.127	.0302
	100	6.850	6.998	6.922	.147	.0312
θ_{op}	20	-11.8	-9.2	-10.3	2.6	.799
(DEG)	100	-12.0	-8.7	-10.2	3.3	.837
c_{op}	20	1.285	1.650	1.440	.365	.110
(pF-Ohm)	100	1.210	1.670	1.420	.465	.115

4.4.5 Connection Errors in Measurement of Series Gap Discontinuities

Next, the perturbation analysis was carried through the de-embedding of the three series gap discontinuity circuits measured for this thesis. For this part, nominal S-parameters were taken from each of the series gap measurements at $f = 10$GHz. The error vectors of Figure 4.19 were then used to perturb this data, and both 20 and 100 connection permutations were synthesized.

Figure 4.20 illustrates the information that can be gained from this perturbation analysis. Shown is the spread in final de-embedded S_{11} and S_{12} data for gap circuit C ($G = 5mil$) caused by connection errors. The perturbation analysis results (100 permutations) for all three gap circuits are summarized in Table 4.5. From these results it is seen that the S_{11} data shows relatively constant behavior with respect to the statistical parameters, while the change in the S_{12} data is significant. This is because in each case the amplitude of the S_{11} measurement is relatively large compared to the corresponding error vectors (Figure 4.19).

One important observation is that for large gap widths the uncertainty in the phase of S_{12} can be appreciable. This is because the magnitude of the nominal S_{12} value begins to approach the magnitude of the connection error. At first glance it appears that the uncertainty in the magnitude of the S_{12} measurement increases as the gap width is reduced. This is not the case since if the range and standard deviation values are divided by the average to calculate these parameters on a percentage basis, the opposite is true. Hence, the measurement uncertainty caused by connection errors increases as the magnitude of the S-parameter being measured decreases.

The standard deviation data from this analysis is used in constructing error bars for the series gap measurements presented in Chapter 5.

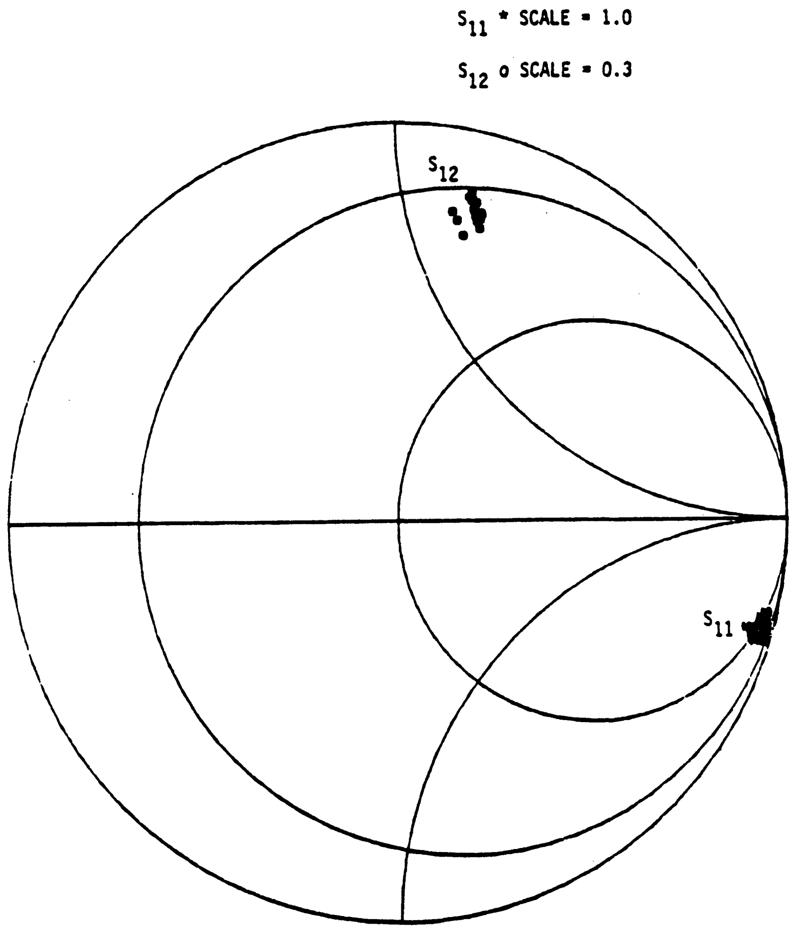

Figure 4.20: This plot of the final de-embedded result for a 5 mil series gap discontinuity illustrates the information obtained through the perturbation analysis (f=10GHz, 20 connection permutations).

Table 4.5: PERTURBATION ANALYSIS RESULTS FOR SERIES GAP MEASUREMENTS

TEST CKT.	PARAMETER	MIN VALUE	MAX VALUE	AVG VALUE	RANGE	STD. DEV.
A (G=15mil)	$\|S_{11}\|$	.964	1.02	.991	.056	.014
	$\angle S_{11}$	-8.2	-2.5	-4.7	5.7	1.33
	$\|S_{12}\|$	.07	.088	.081	.019	.004
	$\angle S_{12}$	76.9	95.1	83.5	18.2	3.2
B (G=9mil)	$\|S_{11}\|$	.963	1.00	.982	.041	.011
	$\angle S_{11}$	-14.2	-7.7	-11.1	6.5	1.29
	$\|S_{12}\|$	.117	.141	.132	.023	.005
	$\angle S_{12}$	77.1	88.8	81.3	11.7	2.0
C (G=5mil)	$\|S_{11}\|$	.940	.983	.962	.043	.011
	$\angle S_{11}$	-20.1	-14.2	-16.7	5.9	1.28
	$\|S_{12}\|$	.220	.254	.240	.034	.007
	$\angle S_{12}$	72.7	78.9	75.2	6.2	1.1

4.5 Summary of Experimental Methodology

The experimental methods used in this thesis are summarized below.

- The TSD method is used to de-embed the test fixture effects from the measurements. An open-end is used in place of the "short" circuit as the reflection standard
- The measurements of ϵ_{eff} and Γ_{op} are obtained as by products of the TSD procedure
- A perturbation analysis approach is used to help approximate measurement uncertainties

CHAPTER V

NUMERICAL AND EXPERIMENTAL RESULTS

In this chapter numerical and experimental results obtained through the present research are presented for the network parameters of shielded microstrip discontinuities. Included here are results for the effective dielectric constant , open-end and series gap discontinuities, and coupled line filters. Where possible comparisons are made to available data from other theoretical solutions. One case for an open-end is compared to to other full-wave solutions. However, since the emphasis in this study is to compare with measured data, extensive comparisons are made to available CAD models since this data is easier to generate for an arbitrary test case. Also, it is useful to include data from these CAD models in the study since they are widely applied to design shielded microstrip circuits.

The CAD models of *Super Compact* and *Touchstone* are based on a combination of different theoretical techniques, most often embodied in simplified closed form solutions, curve fit expressions or look-up tables [1]. These models do not provide a means to account for the effects of the shielding box of Figure 1.3. In the case of *Touchstone*, no shielding effects are included, and for *Super Compact* only a cover height is provided for, and this does not apply to the open-end or series

---

[1] In the manuals for these programs, references are listed for each discontinuity model, the reader is referred to these manuals for further information about the theoretical basis for the CAD models.

gap discontinuities. It is generally believed that as long as the dimensions of the shielding are large relative to the substrate thickness that the shielding will have a negligible effect. To simulate a complicated circuit containing many discontinuities, the discontinuities are assumed to be independent of one another and their respective models are used to generate a matrix representation for each discontinuity. The overall circuit performance is predicted by mathematically cascading the matrices together.

In contrast, the full-wave solution presented here accurately treats the entire geometry of the shielded microstrip circuit as a boundary value problem. Any interactions between, for example, the fringing fields on an open-ended line and an adjacent conducting strip are automatically included in the analysis. Because of this, the method is expected to provide better accuracy than CAD model predictions. Still, as will be seen shortly, the CAD models give quite reasonable results in many cases. However, in other cases, particularly where shielding effects become significant, the accuracy of the CAD models is questionable.

One case where shielding effects are noticeable is when the frequency approaches the cutoff frequency for the onset of higher order modes. As will be discussed next, as the size of the shielding box increases the cutoff frequency for the onset of higher order modes decreases.

5.1 Cutoff Frequency for Higher Order Modes

Higher order modes occur in open microstrip in the form of surface waves and radiation modes. Surface wave modes may be minimized by keeping the substrate electrically thin at the operating frequency. However, the first surface wave mode has a cutoff frequency of zero.

This is not the case for shielded microstrip, where the nature of higher order modes are quite different. The shielding forms a waveguide structure that eliminates radiation and surface waves. Instead, the higher order modes take the form of waveguide modes. As a consequence, below the waveguide cutoff frequency, only the dominant microstrip mode can exist.

For the present problem of Figure 1.3, the cutoff frequency for higher order modes may be approximated by analyzing the infinite dielectric-loaded waveguide of Figure 5.1. The closeness of the solution for the propagating modes of the dielectric-loaded waveguide to the solution for shielded microstrip has been observed in the past, both analytically [58], and numerically [59]. The solution for the propagation characteristics of the dielectric-loaded waveguide takes the form of trancendental equations [26,60] that must be solved either numerically or graphically. The analysis is carried out with LSE and LSM modes which are TE and TM respectively relative to the normal to the air-dielectric interface ($\hat{z}$). The cutoff frequency for the first propagating mode within the structure depends on the geometry. The following definition will help clarify what is meant by cutoff frequency as used in this thesis.

Definition V.1 *For the purposes of this thesis the* **cutoff frequency** f_c *will be defined as the first frequency where non-evanescent waveguide modes can exist inside the cavity. It will correspond to either an LSM or an LSE mode depending on which has the lowest cutoff frequency.*

A numerical solution to the dielectric-loaded waveguide problem was formulated by a student at the University [61]. This program has been used to analyze the cutoff frequencies for several of the shielding geometries considered in this thesis. The plot of Figure 5.2 shows the variation of the cutoff frequencies with shielding sized for a square waveguide three different substrates enclosed. It is seen that for the alumina ($\epsilon_r = 9.7$) substrate, the highest achievable cutoff frequency is limited to about 50GHz , while for a given shielding size, much higher cutoff frequencies are possible with the use of the thinner quartz ($\epsilon_r = 3.8$), or GaAs ($\epsilon_r = 12.7$)

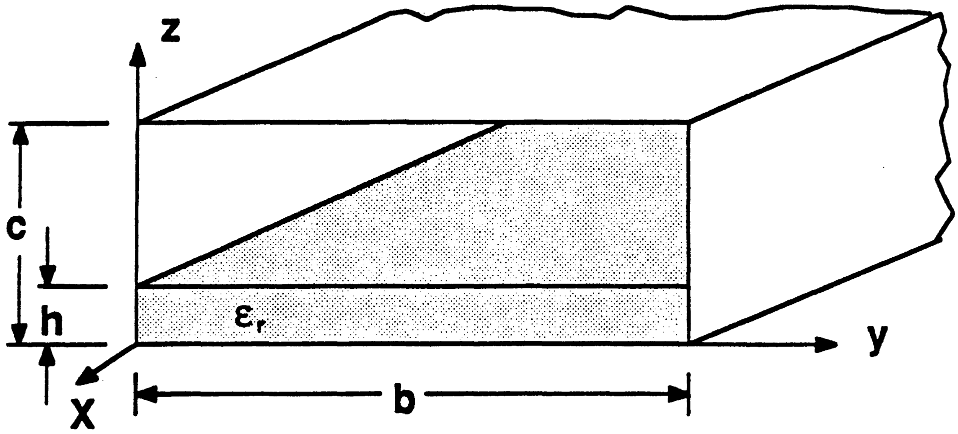

Figure 5.1: The cutoff frequency for higher order modes in shielded microstrip may be approximated by analyzing an infinite dielectric-loaded waveguide.

substrates.

These cutoff frequencies have been found to give a good prediction of the onset of higher order effects observed in the current distributions computed with the new method. As an example, Figure 5.3 shows the current distribution on an open-ended line operating below the cutoff frequency. For the indicated geometry, f_c is about 17.9 GHz. As the frequency is raised above the cutoff frequency, the current becomes more and more distorted as shown in Figure 5.4.

This distortion may be explained as follows. Above cutoff, the microstrip current excites a waveguide mode which travels down the cavity until it reaches the wall at $x = a$, it is then reflected back and forth inside the cavity and interacts with the microstrip current. This waveguide behavior can take place, even though the cavity is not at resonance, because the microstrip current has an external energy source via the coaxial excitation.

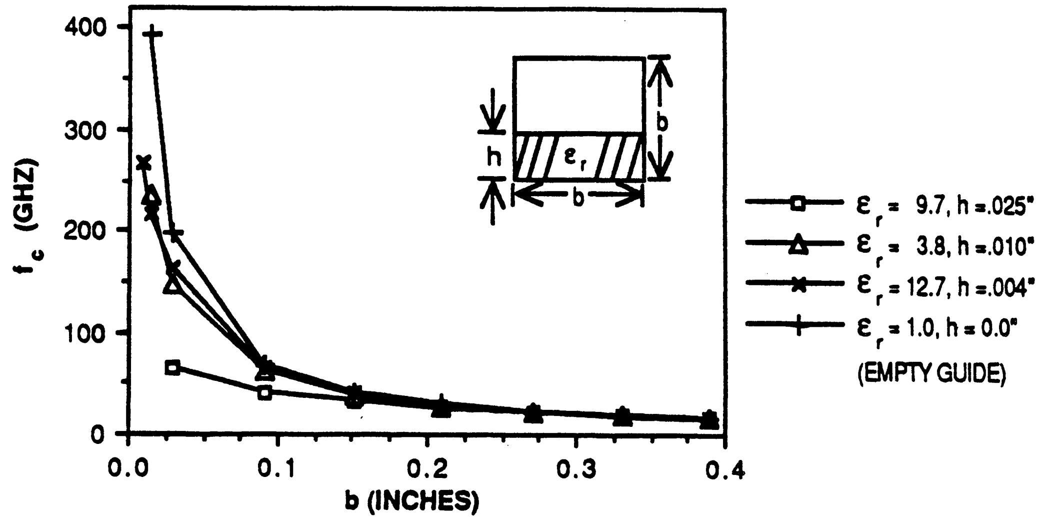

Figure 5.2: Variation of cutoff frequencies with shielding for three commonly used substrates enclosed in a square waveguide ($b = c$). Also shown is empty guide case ($\epsilon_r = 1, h = 0$).

5.2 Effective Dielectric Constant Results

Effective dielectric constant results are presented in this section for 50 ohm lines on three common substrates: alumina, quartz and gallium arsenide (GaAs). As discussed in Section 2.7, the microstrip effective dielectric constant ϵ_{eff} is computed from the current distribution. The current can be associated either with a thru line or an open-ended line. Although a calculation of the effective dielectric constant was not among the primary objectives of this work, its determination is an integral part of the solution for discontinuity effects, and the comparisons which follow also lend insight into the relationship between substrate geometry and shielding effects.

Effective Dielectric Constant Results for an Alumina Substrate

Figure 5.5 shows ϵ_{eff} for a 25 mil thick alumina substrate. The numerical re-

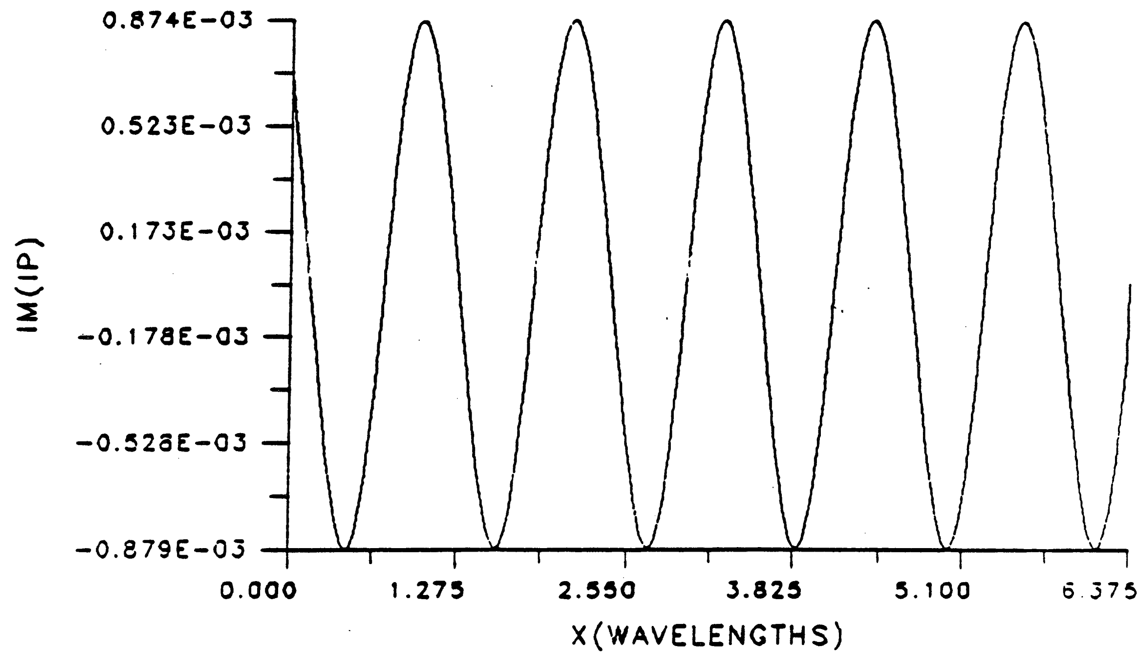

Figure 5.3: Below the cutoff frequency f_c, the microstrip current on an open-ended line forms a uniform standing wave pattern (f = 16GHz, ϵ_r = 9.7, W/h = 1.57, h = .025", b = c = .275").

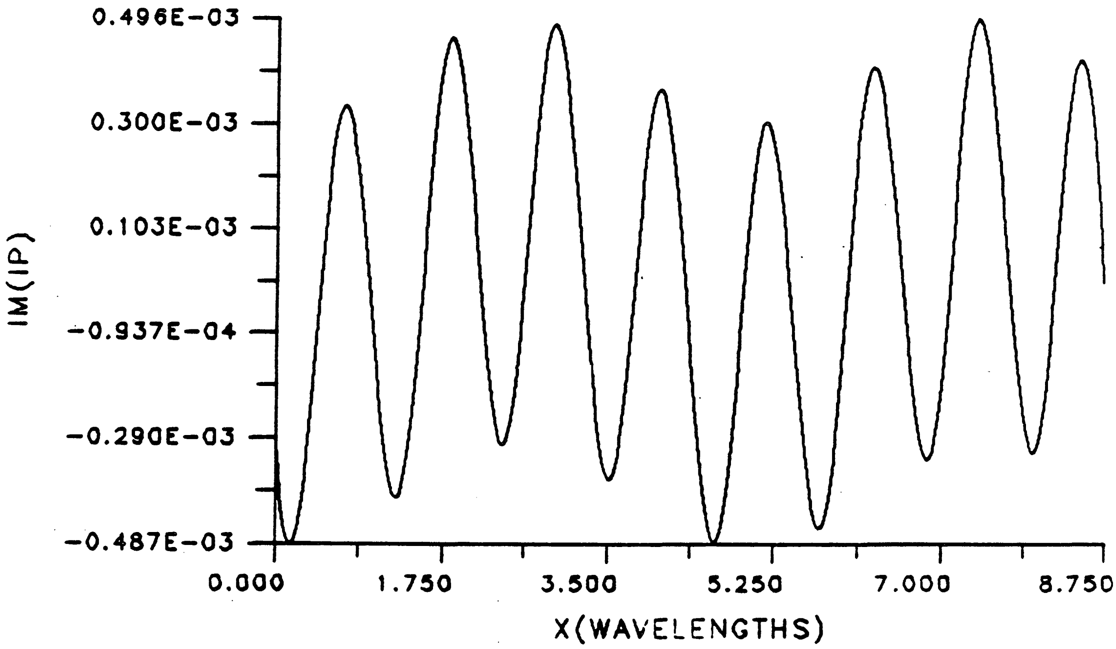

Figure 5.4: As the frequency is increased above f_c, more and more distortion is observed in the open-end current distribution (f = 22GHz, $\epsilon_r = 9.7, W/h = 1.57, h = .025", b = c = .275''$).

sults are compared to measurements, and to CAD package results. Note that *Super Compact* allows only the cover height to be varied while the calculation provided by *Touchstone* neglects shielding effects. For the shielding geometry used here, it is seen that the difference between the numerical and CAD package results are within experimental error. However, interestingly enough, better agreement between the CAD results and the numerical results is observed at higher frequencies. This may be due to the fact that the side walls, which are not included in the *Super Compact* analysis, are electrically closer to the strip at low frequencies.

The measured data is obtained as a byproduct of the TSD fixture characterization procedure (Section 4.3). The data shown represents the average of ten separate procedures. These procedures were conducted over a period of about four years at both Hughes (not all by the author) and at the University. At least three or four different sets of TSD standards were used over this period, however, the mechanical dimensions and substrate parameters are designed to be identical. The error bars shown in Figure 5.5 represent the standard deviation ($\pm s$) of the different measurements.

This data is shown here in lieu of the result from a single measurement, since it gives a more representative view of the involved measurement uncertainty. In this case the error bars shown represent the combined effect of connection errors, variations in ϵ_r, differences in substrate mounting, and errors in specifying the physical difference between the length of the thru and delay line standards. The major error source is believed to be the variations in ϵ_r which can be significant for alumina substrates [62,63].

To see how ϵ_{eff} varies with shielding, consider the plot of Figure 5.6. This plot compares numerical and *Super Compact* results for three different shielding geometries. The notation used to describe different shielding and substrate geometries is explained in Table 5.1. The case for cavity CA is the same as that of

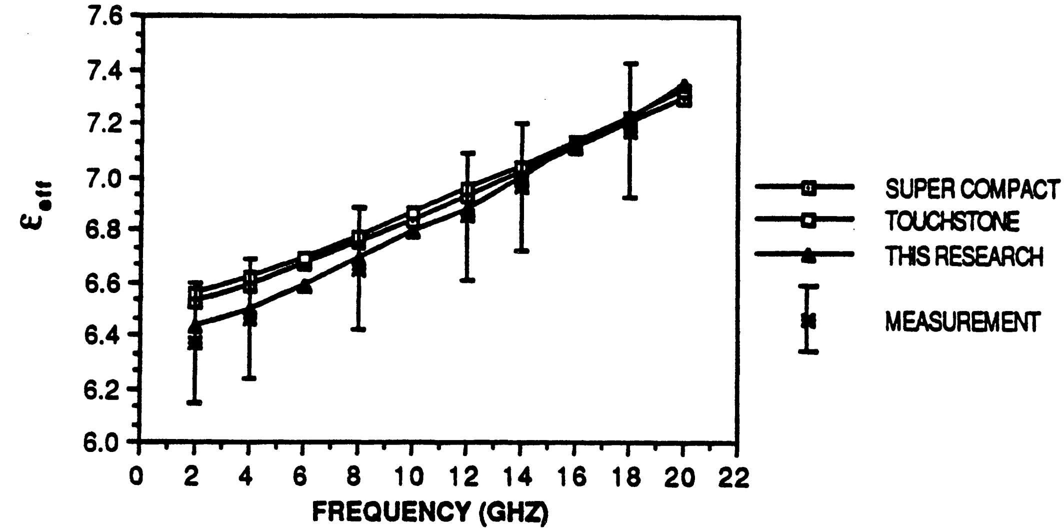

Figure 5.5: Effective dielectric constant comparison for an alumina substrate compared to measurements and CAD package results ($\epsilon_r = 9.7, h = .025'', b = c = .25''$).

Figure 5.5. For the other two cases, where the shielding is closer to the microstrip, the agreement is not as good.

Effective Dielectric Constant for a Quartz Substrate

The effect of shielding on ϵ_{eff} for a quartz substrate is displayed in Figure 5.7. In this case the *Super Compact* analysis is seen to give good results for both of the two larger shielding geometries . However, the numerical results again show a reduced value as the size of the shielding is reduced further.

The reduction of the effective dielectric constant, relative to *Super Compact*, can be explained as follows. For a larger shielding geometry, the field distribution on the microstrip more closely resembles the open microstrip case, with most of the electric field concentrated in the substrate. In this case, most of the electric field lines originate on the microstrip conductors and terminate on the ground plane

Table 5.1: CAVITY NOTATION USED TO DENOTE DIFFERENT GEOMETRY AND SUBSTRATE PARAMETERS

CAVITY	ϵ_r	W (in)	h (in)	b (in)	c (in)	f_c (GHz)
CA	9.7	.025	.025	.250	.250	21.8
CC	9.7	.025	.025	.100	.100	37.5
CF	9.7	.025	.025	.075	.075	41.7
QCB	3.82	.0157	.010	.122	.080	45.8
QCE	3.82	.0157	.010	.100	.100	73.0
QCG	3.82	.0157	.010	.050	.05	102.5

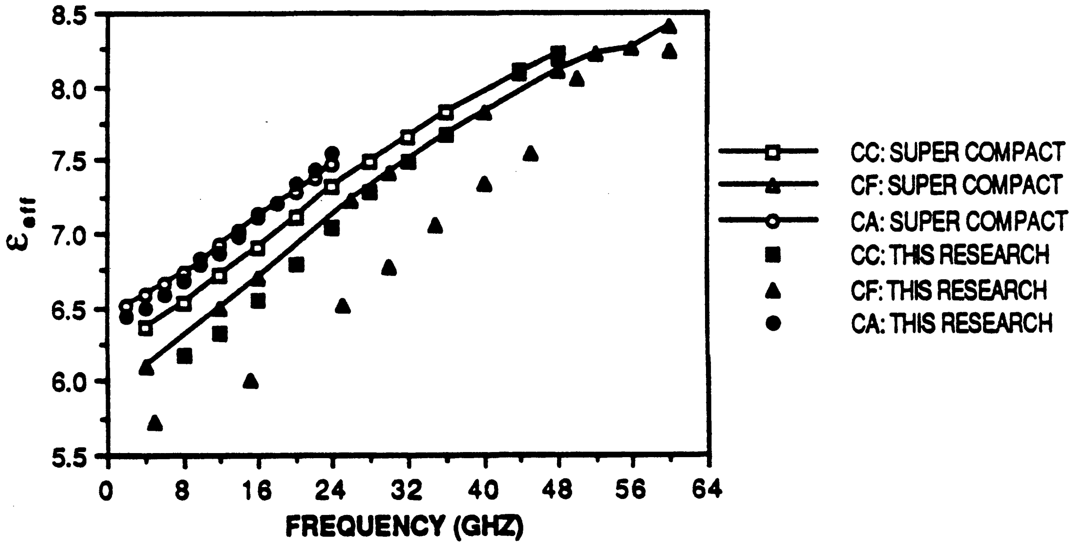

Figure 5.6: The effects of shielding on ϵ_{eff} are apparent as the size of the shielding cavity is reduced (see Table 5.1 for geometry.)

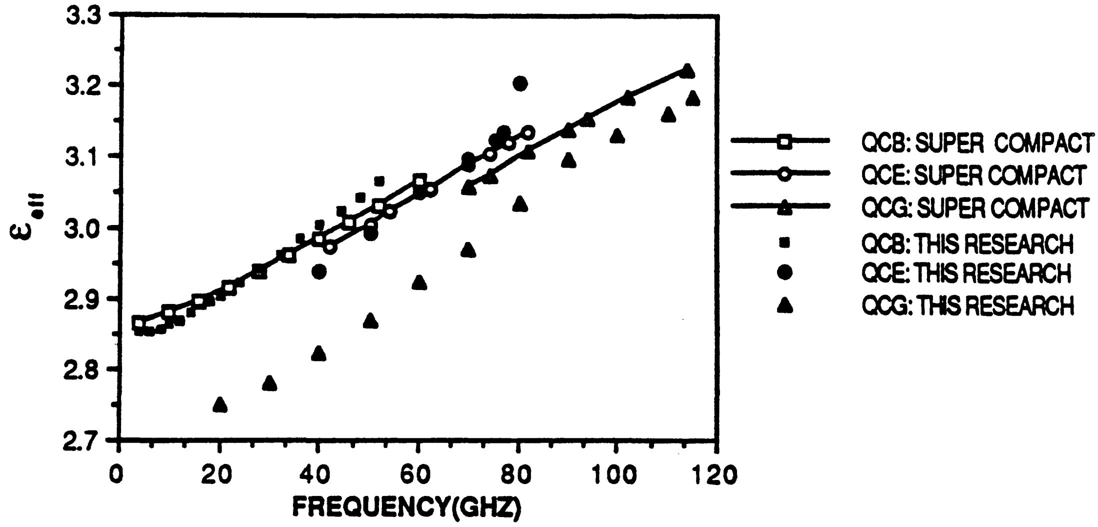

Figure 5.7: Shielding effects are also significant for the quartz substrate shown here (see Table 5.1 for geometry).

below. As the cavity size is reduced, the ground planes of the top and side-walls are brought closer to the microstrip lines. The electric field distribution is now less concentrated in the substrate, as more field lines can terminate on the top and side walls. As a result, a proportionally larger percentage of the energy propagating down the line does so in the air region, and the dielectric constant is reduced.

<u>Effective Dielectric Constant for a GaAs Substrate</u>

Figure 5.8 shows a comparison of the effective dielectric constant for a 4 mil thick GaAs substrate. This is a typical substrate geometry used for MMIC purposes. The agreement between the numerical and CAD model predictions this case is excellent. The differences observed in the case of the other two substrates was not seen for the GaAs substrate of Figure 5.8. because of how thin the substrate is relative to the size of the cavity.

Hence, all of the effective dielectric constant results presented above demon-

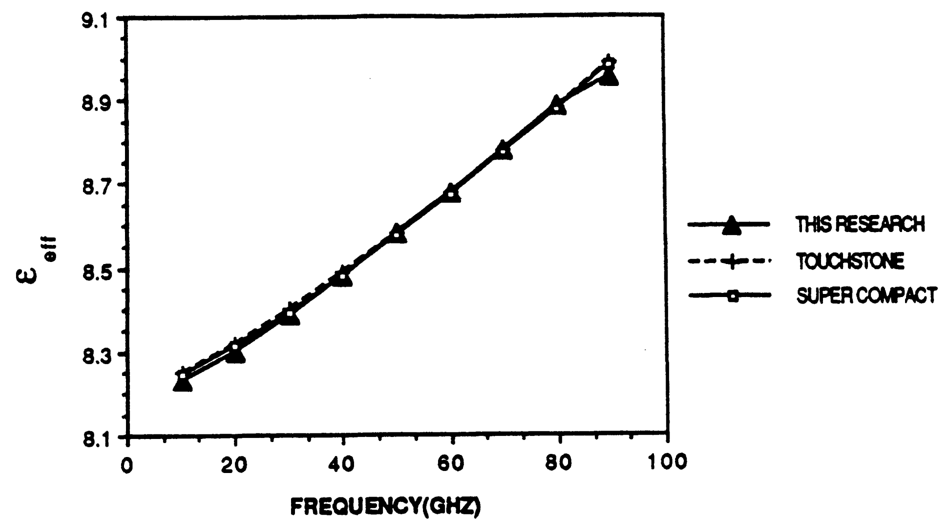

Figure 5.8: The numerical and CAD package results display excellent agreement for the case of a thin GaAs substrate ($\epsilon_r = 12.7, h = .004'', b = c = .07'', f_c = 81\text{GHz}$).

strate that the CAD package predictions are valid when two conditions are met: 1) the shielding is large with respect to the substrate height, and 2) the frequency is below the cutoff frequency. When the dimensions of the shielding becomes comparable to the substrate height, the CAD results are no longer accurate. This suggests the need for an improved CAD formulation valid for small as well as large shielding geometries. The present method could be used as the basis for deriving such a formulation.

5.3 Results for Open-end Discontinuity

As discussed in Section 2.7, an open-end discontinuity can be represented by an effective length extension L_{eff}, by a shunt capacitance c_{op}, or by the associated reflection coefficient Γ_{op} ($= S_{11}$). Each of these three representations will be used in this section.

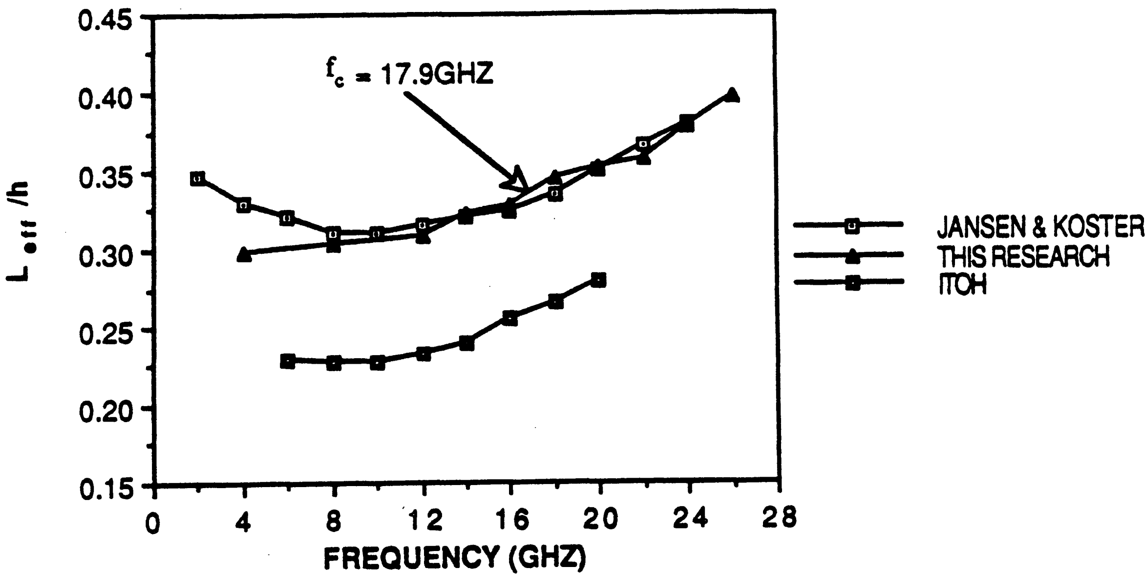

Figure 5.9: Effective length extension of a microstrip open-end discontinuity, as compared to results from other full-wave analyses (ϵ_r = 9.6, W/h = 1.57, b = .305″, c = .2″, h = .025″).

The plot of Figure 5.9 compares L_{eff} results to those of Jansen et al. [64] and Itoh [10]. The results from this research are almost identical to those obtained by Jansen et al. for frequencies above 8 GHz, but show a reduced value for lower frequencies. Jansen et al. speculate that the large difference in the results obtained by Itoh are due to an inadequate choice of basis functions.

The case of Figure 5.9 was chosen to compare the coaxial and gap generator excitation methods used in the method of moments solution [2]. Table 5.2 shows that the results computed for this case by the two methods are equivalent. This equivalence is also observed for the computations of two-port scattering parameters for the structures considered herein. Hence, as far as computing network parameters is concerned either method gives good results. Since the coaxial method is more

[2] The inner and outer radii of the coax feed was taken to be .007″ and .016″ respectively.

Table 5.2: COMPARISON OF L_{eff}/h COMPUTATION FOR THE TWO TYPES OF EXCITATION METHODS

f (GHz)	4	8	12	14	16	18	20
GAP GENERATOR	.298	.305	.309	.321	.324	.344	.353
COAXIAL EXCITATION	.299	.304	.309	.322	.327	.344	.352

realistically based, this conclusion lends validity to the use of the gap generator method.

The results shown in Figure 5.10 illustrate the effect of the shielding on the open-end discontinuity. The normalized open-end capacitance c_{op} is plotted for three different cavity sizes. The results show that reducing the cavity size raises f_c (as expected), and it lowers the value of c_{op}. For comparison, data obtained from *Super Compact* and *Touchstone* and measurements (see Section 4.3) are included. The errors bars on the measurements represent the estimated standard deviation ($\pm s$) of the connection errors for this measurement from Table 4.4.

Similar shielding effects are observed for an open-end on a a quartz substrate as shown in Figure 5.11. In this case it is seen that the *Super Compact* result gives a good value for low frequencies, and where the frequency is well below the cutoff frequency for a given shielding size. Or stated another way, the shielding effects are less severe for a smaller shielding cavity! This conclusion defies common sense, but is strongly supported by the numerical results. Note that Jansen's results (Figure 5.9) show a similar rise in the open-end effect as the cutoff frequency is approached.

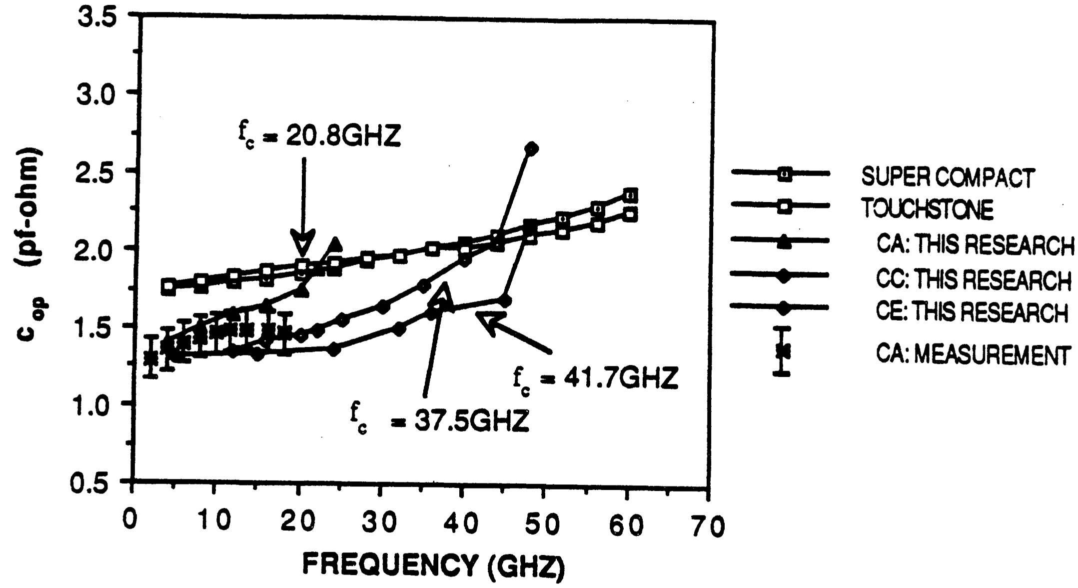

Figure 5.10: A comparison of the normalized open-end capacitance for three different cavity sizes shows that shielding effects are significant at high frequencies (see Table 5.1 for cavity geometries).

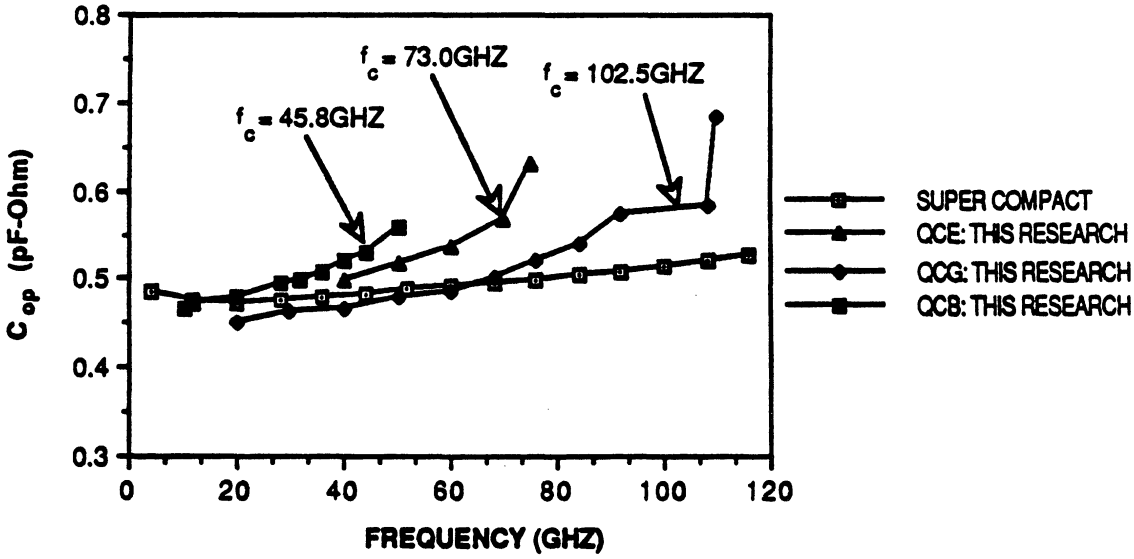

Figure 5.11: Nomalized open-end capacitance for three different cavity sizes for a quartz substrate. This data also shows an increase in the capacitance as the cutoff frequency is approached (see Table 5.1 for cavity geometries).

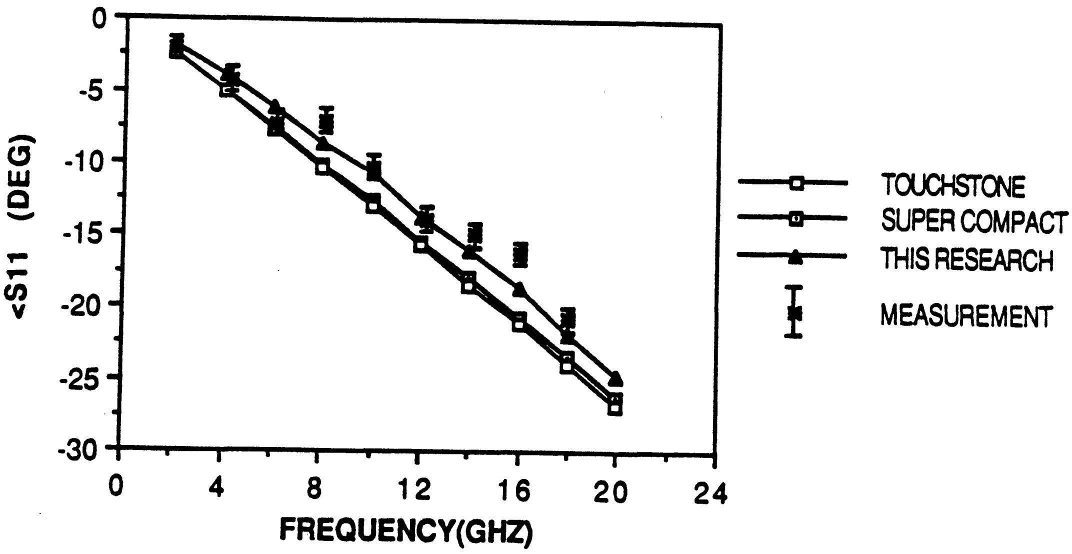

Figure 5.12: Numerical and measured results show good agreement for the angle of S11 of an open circuit ($\epsilon_r = 9.7$, W = h =.025″, b = c =.25″).

As a last example of the open-end effect, Figure 5.12 shows results for the angle of S_{11} of an open-end compared to measurements (see Chapter 4). The measurement is seen to favor the numerical results, although the differences observed are not overly significant for this shielding geometry. The error bars the approximate standard deviation of the connection errors associated with this measurement (Table 4.4).

5.4 Results for Series Gap Discontinuities

Numerical and experimental results have been obtained for series gap discontinuities with three different gap spacings (G) 15 mil (i.e. .015″), 9 mil, and 5 mil. The test circuits and the shielding dimensions used for the measurements are those of Figure 5.12.

Numerical results for the magnitude of S_{21} for these gaps are shown plotted in Figures 5.13- 5.15. For comparison, results obtained using *Super Compact*, and *Touchstone* are also shown plotted along with measured data. The error bars associated with the standard deviation of connection errors (Table 4.5), are on the order of ±.5dB and are too small to show on the plots.

With one exception, the measured data best follows the results of this research. In contrast, the *Touchstone* analysis had the least agreement with the measurements. This may in part be due to the fact that *Touchstone* does not include any shielding effects either the side walls or the shielding cover into account. However, the *Super Compact* model for the series gap does not appear to include the effect of the cover.

The one exception where the numerical result appears to be slightly off from the measurement is in the plot of the magnitude of S_{21} of the 5 mil gap. Based on numerical investigation it appears that by using a smaller subsection length in the method of moments computations, the value for S_{21} can be improved (i.e. it approaches the measurement). However, as discussed in section 3.5, the subsection length cannot be decreased arbitrarily as other implications must be considered. The best approach may be to minimize the size of the matrix by using a small subsection length around the region of the gap and a larger subsection length over the uniform line sections.

Results for the angle of S_{21} and S_{11} for the 15 mil series gap are shown in Figures 5.16 and 5.17. The error bars in these charts represent the estimated standard deviation from the perturbation analysis (Table 4.4). Although the measurements tend to favor the numerical results, the differences are not too significant. The phase of the S-parameters for the other two series gaps behave in a similar way as

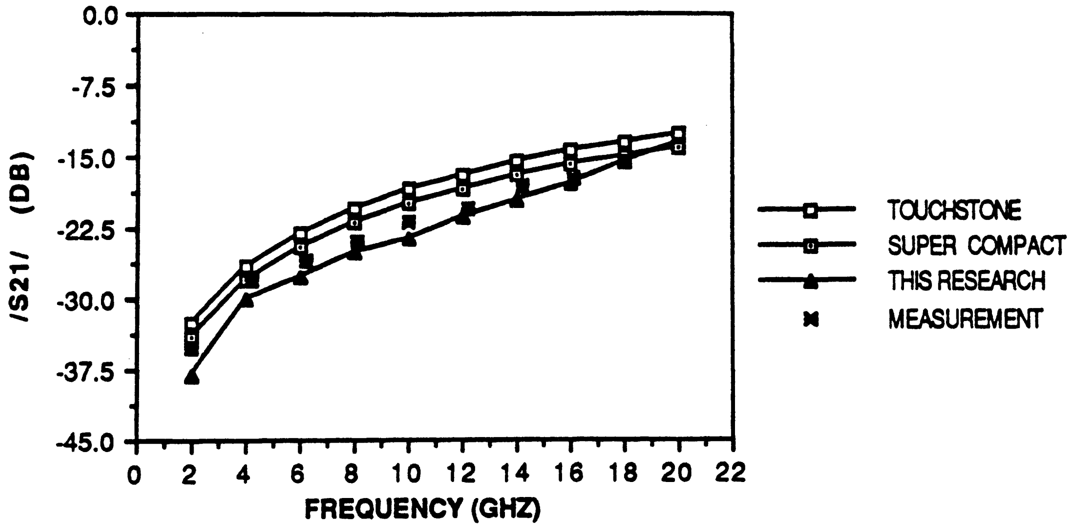

Figure 5.13: Magnitude of S_{21} for series gap circuit A (G = 15 mil).

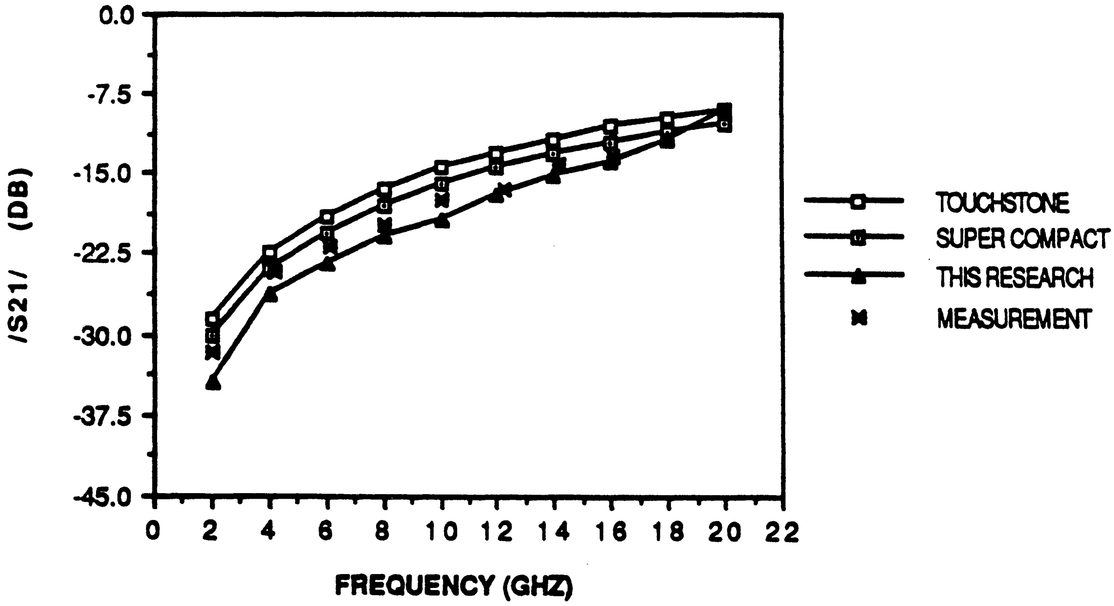

Figure 5.14: Magnitude of S_{21} for series gap circuit B (G = 9 mil).

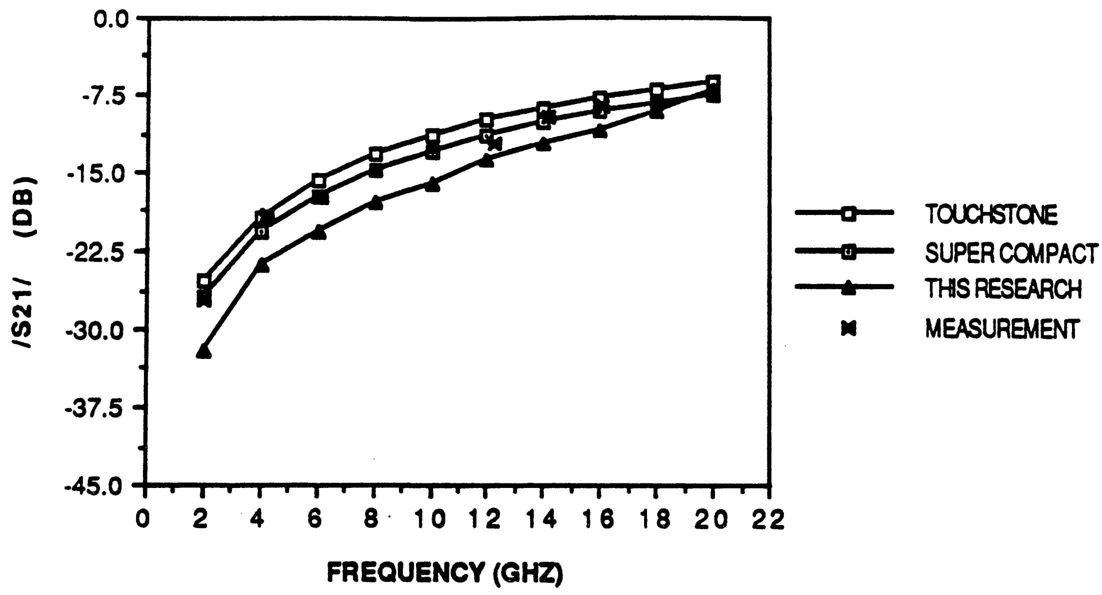

Figure 5.15: Magnitude of S_{21} for series gap circuit C (G = 5 mil).

that for the 15 mil gap and have been omitted from this treatment.

The measurements made on the series gap discontinuities are seen to further verify that the theory developed here gives good results. For the large shielding dimensions used for the measurements ($b, c \gg h$) the CAD models are seen to give reasonable results. The behavior of series gaps for small shielding dimensions was not studied, instead emphasis was placed on obtaining results for coupled line filters since their behavior is more complicated and therefore more interesting.

5.5 Results for Coupled Line Filters

The last results to be discussed were obtained for the two and four resonator filters discussed in Section 4.3. For brevity only the amplitude and phase of the transmission coefficient S_{21} will be discussed. Note that for the shielding geometry of both filters, the cutoff frequency f_c. is approximately 13.9GHz. Above this, the

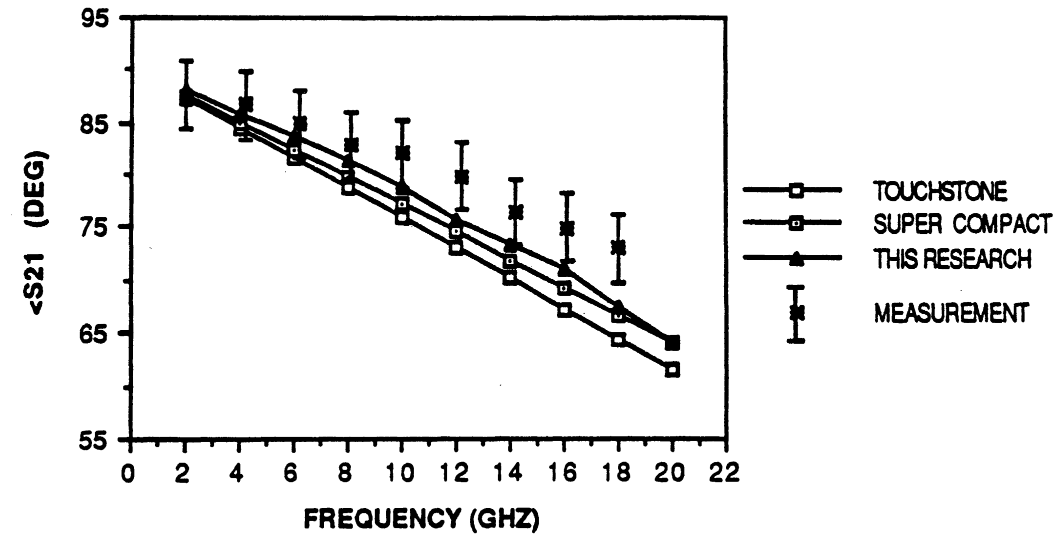

Figure 5.16: Angle of S_{21} for series gap circuit A (G = 15 mil).

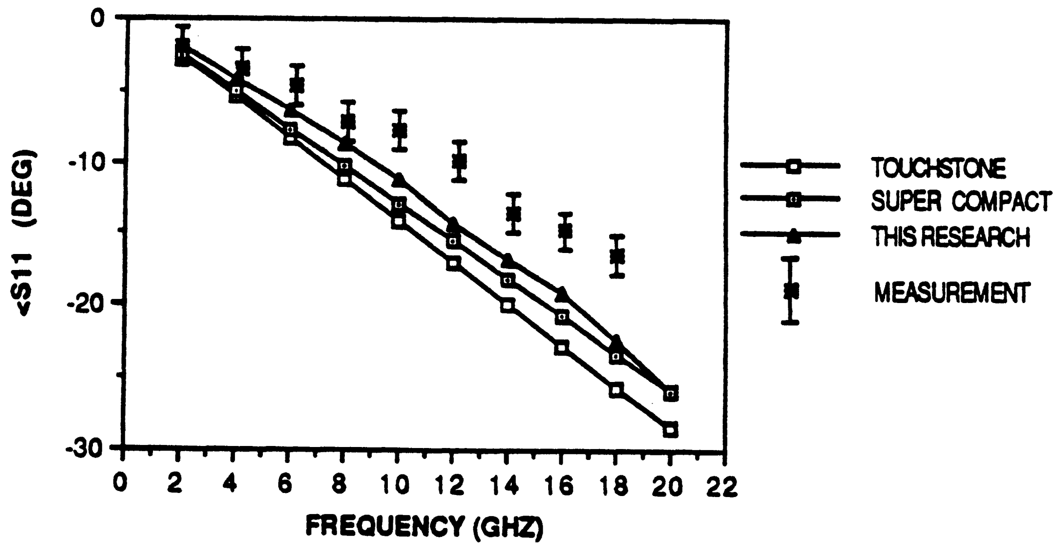

Figure 5.17: Angle of S_{11} for series gap circuit A (G = 15 mil).

filter measurements are distorted due to waveguide moding within the test fixture [3].

The measured and numerical results of this research are compared to CAD model predictions. The CAD package analysis for coupled line filters is performed by cascading two different types of discontinuity elements together: coupled microstrip lines, and open-end discontinuities. As mentioned previously, neither of the packages studied here account for shielding in the open-end discontinuity, however, *Super Compact* does include the effect of the cover height in the model for coupled lines.

Two Resonator Filter

Figure 5.18 shows a comparison of the measured and predicted response of the two resonator filter. From this plot, it is seen that the analysis from both the numerical and the CAD packages give a very good prediction of the response of the filter in the pass band. Outside the pass band the amplitude response is seen to more closely follow the numerical results.

Close examination of the phase plot (Figure 5.18b) shows that the the numerical results are shifted up in frequency by a small amount as compared to the measurements. It is believed that this discrepancy, though small, is related to the thin-strip approximation used for the current distribution. In the theoretical solution, the current is assumed to be uni-directional and to have a symmetric variation in the transverse direction as described by (2.7). In the coupling region

---

[3] Because energy can propagate in a waveguide mode, significant coupling occurs between the two coaxial feeds of the fixture, and the resulting measurement uncertainty is large. Hence, for all the filter results presented, the measurements are only good up to $f_c = 13.9$ GHz.

of the filter the close proximity of the adjacent strip conductors will cause the current to become non-symmetric and may require a more general definition of the current as the strip becomes wide.

However, note that the thin-strip approximation used here already gives a very good result. If in the magnitude plot of Figure 5.18, the response for the numerical results of this research are shifted down slightly, the agreement with the measurement will practically be exact.

Four Resonator Filter

The results for the four resonator filter are shown in Figure 5.19. In this case, numerical results for S_{21}, demonstrate excellent agreement with measurements up to the cutoff frequency. Note that for this filter the strip widths are about half as wide as those in the two resonator filter. Hence, the error due to the thin strip approximation is reduced. As in the case of the two resonator filter, the CAD models fail to predict the filter response in the rejection band, whereas the numerical results follow the measurements closely. For the four resonator filter, this is true for both the phase as well as the magnitude of S_{21}.

In the phase response, the CAD models display a large error compared to measurements between about 6 and 8.5GHz, while the numerical results track the measured phase very well. Below about 5.5GHz, the measured phase is seen to be different from the predictions of both the CAD models and the numerical results. This is most likely due to a phase error in the measurements. In the TSD technique, the delay line for the measurements should ideally be $\frac{\lambda_g}{4}$ at the measurement frequency. When the electrical length becomes either too short or too close to a multiple of $\frac{\lambda_g}{2}$ phase ambiguities can result. A good rule of thumb is for the delay line to be between $\frac{\lambda_g}{8}$ and $\frac{3\lambda_g}{8}$ [4]. At 5.5GHz the delay line used for the measurements is slightly less than $\frac{\lambda_g}{8}$; hence, this is most likely the source of the phase error.

We will now examine what happens as the top cover is brought closer to the circuitry. The results of Figure 5.19 show that even for large shielding dimensions the CAD models do not adequately predict the filter response in the rejection band. Figure 5.20a shows *Super Compact* predictions for the four resonator filter with two different cover heights. These predictions indicate that lowering the cover height should significantly narrow the pass band, and reduce the amplitude in the rejection band.

A significantly different prediction is observed in the numerical results for this case presented in Figure 5.20b. A narrowing of the pass band response is also observed in the numerical predictions, but not by nearly as much as in the *Super Compact* prediction. More importantly, the amplitude in the rejection band is seen to increase instead of decrease!

To prove that the numerical prediction is indeed the correct one, an additional measurement was made of the filter for the low cover height case. As can be seen from Figure 5.20b the measured data falls practically on top of the numerical predictions for both cover heights.

5.6 Summary of Numerical and Experimental Results

In this chapter results were presented for the effective dielectric constant of uniform microstrip lines, and the network parameters for open-end and series gap

[4] Multiple lines are needed for broadband measurements.

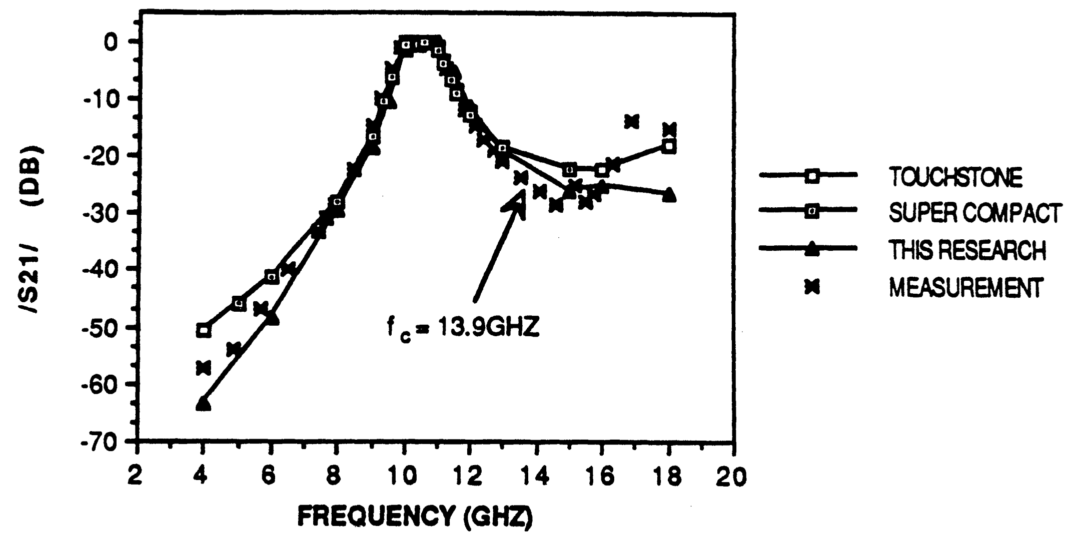

a. Amplitude of S_{21}

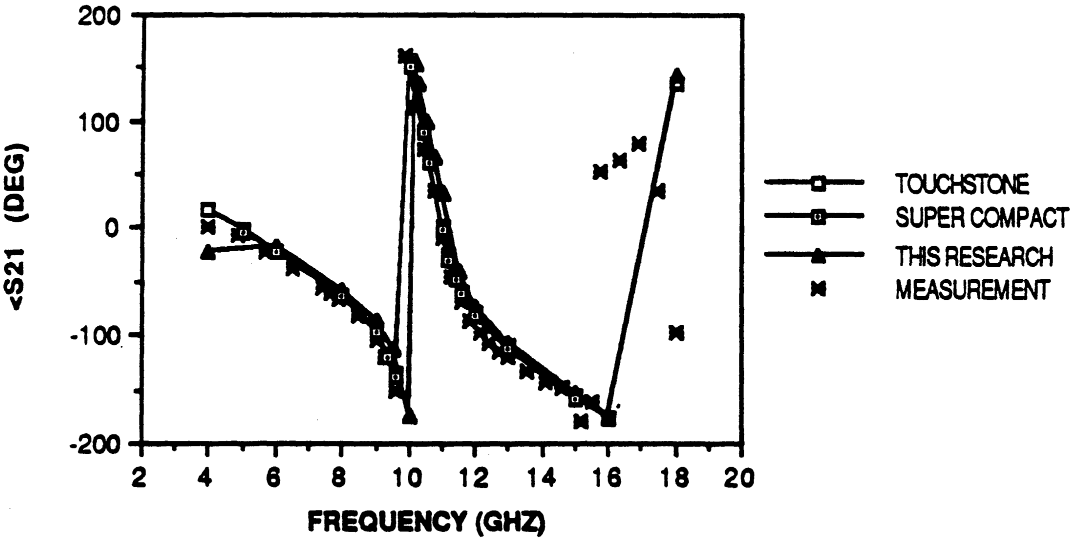

b. Phase of S_{21}

Figure 5.18: Results for transmission coefficient S_{21} of two resonator filter ($\epsilon_r = 9.7, W = h = .025"; b = .4'', c = .25''$).

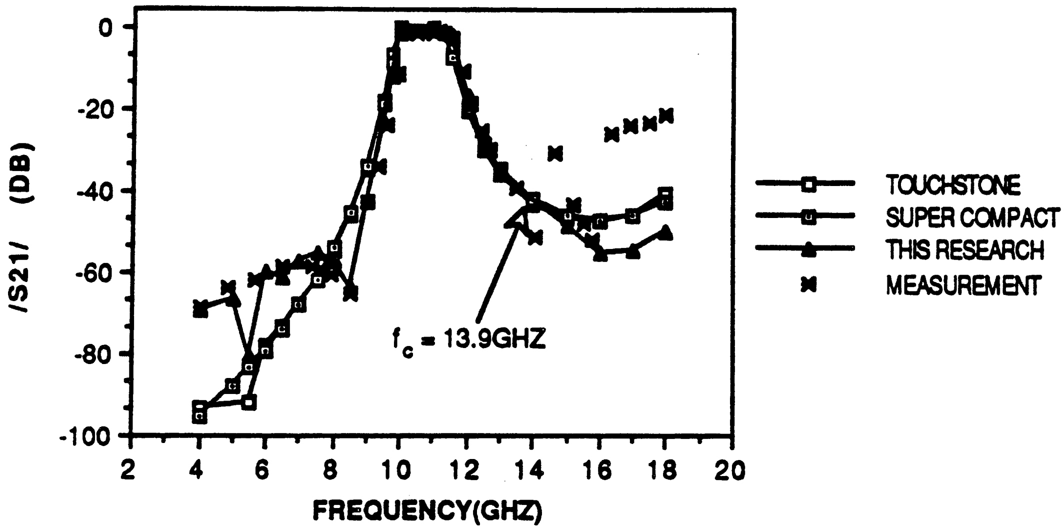

a. Amplitude of S_{21}

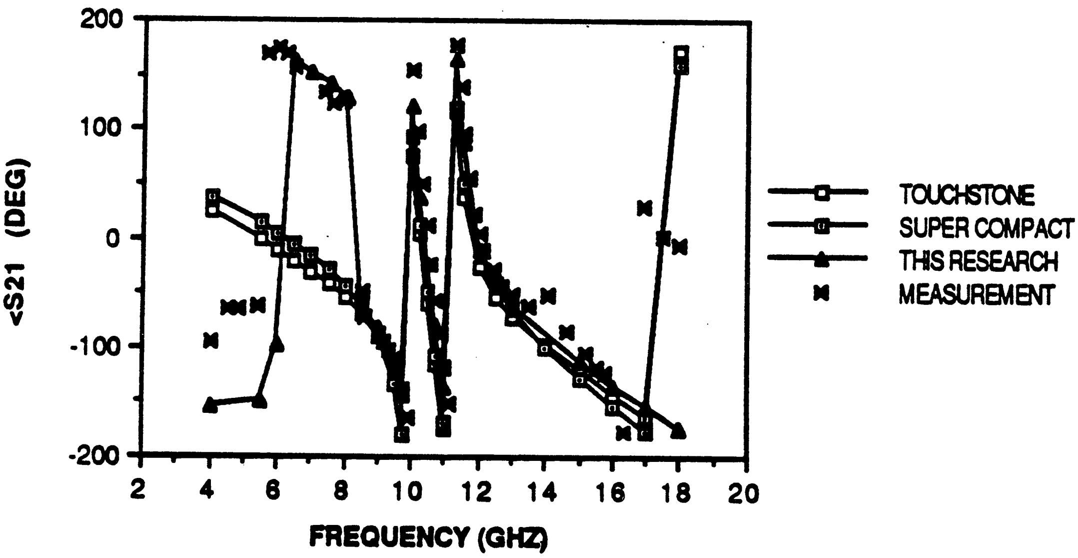

b. Phase of S_{21}

Figure 5.19: Results for transmission coefficient S_{21} of four resonator filter ($\epsilon_r = 9.7, W = .012'', h = .025''; b = .4'', c = .25''$).

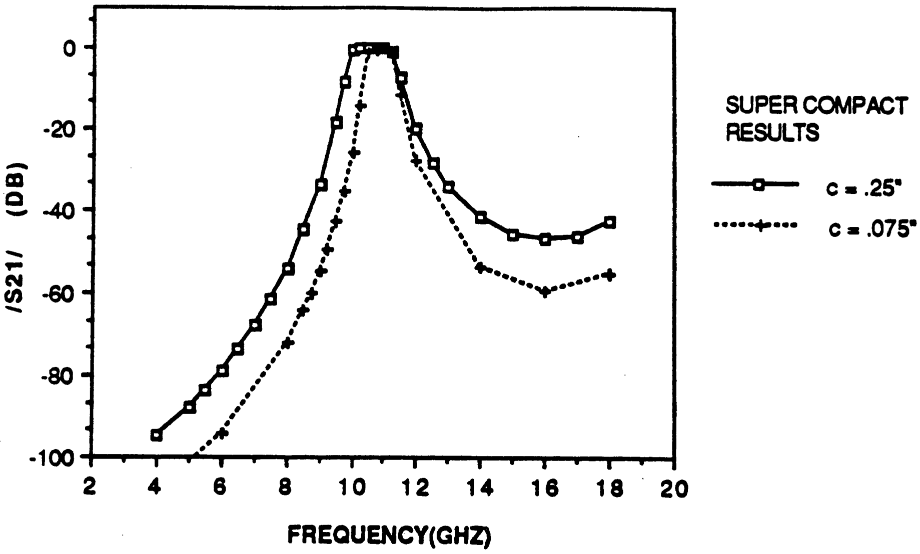

a. Super Compact predictions

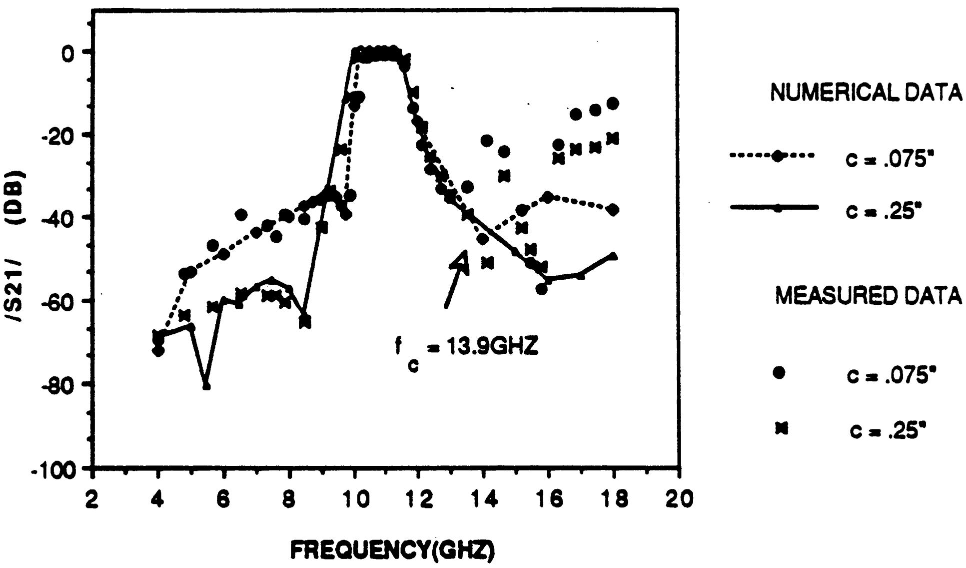

b. Numerical results of this research compared to measurements

Figure 5.20: Results for lowering the shielding cover on the amplitude response of four resonator filter ($\epsilon_r = 9.7, W = .012'', h = .025''; b = .4''$).

discontinuity and for two coupled line filters. The higher order modes in shielded microstrip are described to be essentially waveguide modes. In fact, the cutoff frequency f_c for a partially filled rectangular waveguide gives a good prediction of the onset of higher order mode behavior in the computed microstrip current distribution. A wealth of numerical and experimental data is presented for the above mentioned structures, and comparisons are made to other full-wave analysis and to commercially available CAD packages. Conclusions based on these comparisons are summarized in the next chapter.

CHAPTER VI

CONCLUSIONS AND RECOMMENDATIONS

The results from the research presented in this thesis lead to several conclusions regarding different aspects of shielded microstrip discontinuity characterization. These conclusions have been separated into appropriate categories as addressed herein.

6.1 Conclusions from Theoretical Work

In the theoretical work (Chapter 2) a method of moments formulation for the shielded microstrip problem is derived based on a more realistic excitation model than used with previous techniques. This result follows directly from the reciprocity theorem, with the use of a frill current model for the coaxial feed. The reciprocity theorem is applied in a similar way for the case of gap generator excitation. The impedance matrix formulation for gap generator excitation is seen to be identical to that for the coaxial excitation method developed here. The difference between the two methods is therefore only in the excitation vector used on the right hand side of the matrix equation. In solving for the impedance matrix elements, all of the required integrations are solved in closed form. Conversely, for the excitation vector of the coaxial excitation method, numerical integration is required.

6.2 Conclusions from Computational Work

Computational considerations for implementing the theoretical solution are explored extensively (Chapter 3). A graphical presentation is given that illustrates the different steps in the computation of microstrip currents. The current for the coaxial excitation method is shown to be uniform along the strip, while a discontinuity in the current is evident in the current for the gap generator method. The effect of this discontinuity is minimized by positioning the gap generator at the beginning of the first strip subsection. The gap generator method is more computationally efficient than the coaxial excitation method since numerical integration is not required.

Several numerical experiments are presented (Chapter 3) that explore the convergence and the stability of the solution. The parameters explored are the subsection length l_x, the sampling rate $N_x(= 1/l_x)$, the value for K used in the basis functions, the summation truncation points $NSTOP$ and $MSTOP$, and the cavity length a. A value of $K = 2\pi$ appears to be the best choice. The main conclusions drawn from these experiments may be summarized as follows:

- A value of $K = 2\pi$ is a good value to use in the sinusoidal basis functions.
- A minimum sampling limit exists such that the condition $Kl_x < \frac{\pi}{2}$ must be satisfied in order to obtain useful current results. For a value of $K = 2\pi$, $l_x = .25$ is the largest subsection length that can be used.
- Good convergence on n and m is achieved after 500 terms have been added on each.
- A maximum sampling limit exists in the form of an erratic current condition which may be defined by the simple formula $NSTOP{*}l_x < a$. ($NSTOP{*}l_x \geq a$ must hold for useful results.)

- An optimum sampling range may be specified that automatically avoids the erratic current condition, and guarantees the best accuracy in the matrix solution. This range is given approximately by $\frac{1.5a}{NSTOP} \leq l_x \leq \frac{4a}{NSTOP}$.
- The optimum sampling range was found to correspond directly with the flat convergence region for the L_{eff} and ϵ_{eff} computations.

6.3 Conclusions from Experimental Study

From the experimental study (Chapter 4), a comparison of various measurement techniques lead to the choice of the TSD de-embedding method for the measurements of this thesis. Various microstrip connection repeatability issues are explored experimentally (Appendix I). The results indicate that, for the hardware tested, the best connection approach is to make the required fixture connections at the coax/microstrip connection points, rather than relying on the repeatability of microstrip/microstrip interconnects. Still, connection errors remain an important consideration for the measurements. To examine this, a perturbation analysis is developed that allows for an approximation to be made of the effects of connection errors on the precision of the final de-embedded results. It is seen that connection errors affect the phase of the S-parameter measurements most, and the amount of resulting measurement uncertainty increases as the magnitude of the parameter being measured decreases.

6.4 Conclusions Based on the Results

Numerical and experimental results are presented for several microstrip structures (Chapter 5). Conclusions based on these results are described below.

The effect of higher order modes on the current distribution is demonstrated. As the frequency is increased above the cutoff frequency, the current becomes increasingly distorted due to higher order modes. On the other hand, as long as the cavity size is such that the frequency is below the cutoff frequency, the current is uniform and undistorted regardless of how thick the substrate is. This is in contrast to the case of open microstrip, where the first surface wave mode has a zero cutoff frequency and the onset of higher order modes depends strongly on the substrate thickness. The cavity resonance technique, mentioned in Chapter 1, does not allow for the current distribution to be studied.

A comparison of effective dielectric constant results shows good agreement between the CAD package results, the numerical results from this research, and measurements for large shielding dimensions ($b, c \gg h$). The effects of shielding on the effective dielectric constant are examined. Only one of the packages studied takes shielding into account for the effective dielectric constant calculation, and then only cover effects are considered. A comparison of the CAD package results with numerical results show that good agreement is obtained when the shielding dimensions are large with respect to the substrate thickness, while for small shielding dimensions, the difference between the CAD package results and numerical results becomes significant.

For the open-end discontinuity, good agreement with other full-wave solutions and with measurements is demonstrated. A comparison of open-end capacitance for different cavity sizes shows that, as the cutoff frequency is approached, the capacitance increases in each case. Choosing a small cavity with a high cut-off frequency extends the region where the capacitance is relatively constant. The open-end models used in the two CAD packages studied here do not include shielding and cannot show this effect.

A comparison of numerical and measured results for series gap discontinuities portrays good agreement for all three gap widths studied. The agreement with measurements is very good for the two larger gap widths, but for the smallest gap width it is seen that one of the CAD models give a slightly better prediction of the behavior of the magnitude of S_{21} than the numerical results. The effects of shielding on the behavior of series gaps is not explored extensively.

Good agreement is also demonstrated for the two and four resonator coupled line filters. For both filters, the numerical results of this research give a better prediction of the overall filter response than provided by the CAD models. This is especially true in the rejection bands of the filters. For the two resonator filter, a slight frequency shift is observed in the numerical results compared to the measurements. This is most likely due to the thin-strip approximation used for the current distribution, and is not a limitation of the method itself.

In contrast, for the four resonator filter, which has thinner strip widths, the present method gave an excellent prediction of the filter performance in every way, whereas discrepancies are observed in the CAD model predictions. Reducing the cover height is seen to narrow the pass band response and raise the amplitude of the filter's rejection band response. The numerical results of this research give an excellent prediction of this effect, and this is proven by measured data.

6.5 Recommendations

The data comparisons performed here have demonstrated the validity of the theoretical methods. However, there are a few areas where improvements can be made to the theory.

Further numerical investigation for series gap discontinuities indicates that as the gap width becomes small, a smaller subsection length is required for accurate computation of the scattering parameters. However, the improvement in the result is limited because a smaller subsection length increases the matrix size and degrades the condition number (Section 3.5). One way to extend this limit would be to use a variable subsection length in the computations. That is, use a small subsection length close to the discontinuity where the current is disturbed, and use a larger subsection length over the uniform sections of strip. In this way the size of the matrix would be maximized for a given problem.

The thin strip approximation as used here provides an accurate solution for the discontinuity structures studied. In one case, that of the two resonator filter, it appears that a more general current distribution may improve the solution. The thin strip approximation uses a unidirectional current. The method presented here may be generalized in a straight forward way to allow for two component current distributions. This will also allow for more complicated structures to be considered, yet it will be more computation intensive. It may be possible to improve the filter analysis by changing the formulation to allow the transverse variation of the longitudinal component of the current to be non-symmetrical without actually adding a transverse current component. To be able to discern which approximations are most appropriate for a given problem detailed comparisons should be made between results obtained with a more general current distribution and those obtained with the present method.

The experimental work has shown that good measured data on microstrip discontinuities can be obtained with the TSD technique. On the other hand it is shown that the measurement uncertainties due to connection errors, and other repeatability issues can be appreciable. In applying the technique for millimeter-wave measurements close attention is required to minimize the associated uncertainties: The following suggests some guidelines for doing so:

1. Connection repeatability errors can be reduced by first selecting the best available fixture and connection technique, and then by averaging measurements from repeated connections made for each fixture measurement.

2. Variations in ϵ_r can be minimized by fabricating the standards. and the discontinuity circuits from the same substrate, or by using substrates from

the same "lot", or manufacturing run.

3. Variations in substrate and line width geometry, though not a major error source, should be monitored carefully during all steps of fabrication. This can be done by performing careful measurements of the fabrication masks, the substrates to be used, and the surface metalization geometry after etching.

4. In the area of substrate mounting, care must be taken to use the exact same technique in bonding the substrates onto carriers.

5. Finally, if the physical delay line length is used in the fixture characterization procedure, it should be carefully measured and input to the program for each set of standards that are used.

Because of its susceptibility to connection repeatability errors, the TSD technique is not necessarily the best technique for high frequency measurements, and research into improved de-embedding methods should continue. In considering the trade-offs between alternative approaches that already exist, the sensitivity of each technique to the unavoidable measurement repeatability issues discussed here should be analyzed and compared. Ultimately, the best de-embedding method for a particular application depends on the required accuracy, the type of test fixture, and the nature of the device or circuit being tested.

APPENDICES

APPENDIX A

REVIEW OF METHOD OF MOMENTS

The general steps involved for in the computation of surface currents using the method of moments can be summarized as follows:

1. Formulate an integral equation for the electric or magnetic field in terms of the surface current density $\bar{J}_s$ on the conductors. It is generally possible to put this equation in the form

$$L_{op}\left(\bar{J}_s\right) = \bar{g}\begin{pmatrix} \bar{E} \\ \bar{H} \end{pmatrix} \tag{A.1}$$

where L_{op} is an integral operator, and $\bar{g}$ is a vector function of either the electric field $\bar{E}$ or magnetic field $\bar{H}$ associated with $\bar{J}_s$.

2. Expand $\bar{J}_s$ into a series of basis functions $\bar{J}_p$ so that

$$\bar{J}_s = \sum_{p=1}^{N_s} I_p \bar{J}_p \tag{A.2}$$

where the I_p's are complex coefficients and N_s is the number of sections the conductor is divided into.

3. Determine a suitable inner product and define a set of test (or weighting) functions $\bar{W}_q$. The result may be expressed as

$$\sum_{p=1}^{N_s} I_p \left\langle \bar{W}_q, L_{op}\left(\bar{J}_p\right)\right\rangle = \left\langle \bar{W}_q, \bar{g}\right\rangle \tag{A.3}$$

where the inner product is defined as

$$\left\langle \bar{a}, \bar{b} \right\rangle = \int_S \int \bar{a} \cdot \bar{b} ds \,.$$

In Galerkin's method, the weighting functions are taken to be test currents $\bar{J}_q$ which are identical in form to the basis functions $\bar{J}_p$.

4. Solve the inner product equation (A.3) and form a matrix equation of the form

$$[\mathbf{Z}]\,[\mathbf{I}] = [\mathbf{V}] \tag{A.4}$$

where [Z] is termed the impedance matrix, and [V] is called the excitation vector.

5. Solve for the current coefficient vector by matrix inversion and multiplication according to

$$[\mathbf{I}] = [\mathbf{Z}]^{-1}\,[\mathbf{V}]\,. \tag{A.5}$$

APPENDIX B

DERIVATION OF INTEGRAL EQUATION FOR ELECTRIC FIELD

Starting with Maxwell's equations

$$\bar{\nabla} \times \bar{E} = -j\omega\mu\bar{H} \tag{B.1}$$

$$\bar{\nabla} \times \bar{H} = j\omega\epsilon\bar{E} + \bar{J} \tag{B.2}$$

$$\bar{\nabla} \cdot \bar{J} = -j\omega\rho \tag{B.3}$$

$$\bar{\nabla} \cdot \left(\epsilon\bar{E}\right) = \rho \tag{B.4}$$

$$\bar{\nabla} \cdot \left(\mu\bar{H}\right) = 0 \,, \tag{B.5}$$

We define $\bar{A}$ such that

$$\bar{H} = \frac{1}{\mu}\bar{\nabla} \times \bar{A} \,. \tag{B.6}$$

Substituting (B.6) into (B.1) yields

$$\bar{\nabla} \times (\bar{E} + j\omega\bar{A}) = 0 \,. \tag{B.7}$$

Since $\bar{\nabla} \times \bar{\nabla}\phi = 0$ for an arbitrary vector function ϕ, we let

$$\bar{E} + j\omega\bar{A} = -\bar{\nabla}\phi \,. \tag{B.8}$$

Making use of (B.6) and (B.8) in (B.2) yields

$$\bar{\nabla} \times \frac{1}{\mu}\bar{\nabla} \times \bar{A} = -j\omega\epsilon(j\omega\bar{A} + \bar{\nabla}\phi) + \bar{J} \tag{B.9}$$

or

$$-\nabla^2\bar{A}+\bar{\nabla}(\bar{\nabla}\cdot\bar{A})=\omega^2\mu\epsilon\bar{A}-j\omega\mu\epsilon\bar{\nabla}\phi+\mu\bar{J}\,. \tag{B.10}$$

We use the Lorentz condition

$$\bar{\nabla}(\bar{\nabla}\cdot\bar{A})=-j\omega\mu\epsilon\bar{\nabla}\phi \tag{B.11}$$

in (B.10) to obtain

$$\nabla^2\bar{A}+k^2\bar{A}=-\mu\bar{J} \tag{B.12}$$

where $k^2=\omega^2\mu\epsilon$. From (B.9) and (B.11) the electric field may be expressed as

$$\begin{aligned}\bar{E} &= -j\omega\bar{A}+\frac{1}{j\omega\mu\epsilon}\bar{\nabla}(\bar{\nabla}\cdot\bar{A})\\ &= -j\omega(1+\frac{1}{k^2}\bar{\nabla}\bar{\nabla}\cdot)\bar{A}\,.\end{aligned} \tag{B.13}$$

We now define a dyadic Green's function $\bar{\bar{G}}$ to be a solution of

$$\nabla^2\bar{\bar{G}}+k^2\bar{\bar{G}}=-\bar{\bar{I}}\delta(\bar{r}-\bar{r}')\,. \tag{B.14}$$

To relate $\bar{\bar{G}}$ to $\bar{A}$, we will derive a vector-dyadic extension of Green's theorem. The vector Green's theorem is given by [23,19]

$$\begin{aligned}&\iiint_V\left\{\bar{Q}\cdot[\bar{\nabla}\times\bar{\nabla}\times\bar{P}]-\bar{P}\cdot[\bar{\nabla}\times\bar{\nabla}\times\bar{Q}]\right\}dv=\\ &\qquad\iint_{S_w+S_s}\hat{n}\cdot[\bar{P}\times(\bar{\nabla}\times\bar{Q})-\bar{Q}\times(\bar{\nabla}\times\bar{P})]ds\end{aligned} \tag{B.15}$$

For the shielded microstrip cavity problem of Figure 2.4, the volume V is the interior of the cavity, and S_w and S_s are the surface of the cavity walls, and the surface of a small volume enclosing the source region ($\bar{J}$) respectively. The unit normal vector $\hat{n}$ is directed outward from V, and we will denote $\hat{n}'=-\hat{n}$ to be the inward directed normal vector. $\bar{P}$ and $\bar{Q}$ are arbitrary vector fields.

After applying a few vector identities, (B.15) may be re-written as follows:

$$\begin{aligned}&\iiint_V\left\{\bar{P}\cdot[\bar{\nabla}\times\bar{\nabla}\times\bar{Q}]-[\bar{\nabla}\times\bar{\nabla}\times\bar{P}]\cdot\bar{Q}\right\}dv=\\ &\qquad\iint_{S_w+S_s}\left[(\hat{n}'\times\bar{P})\cdot(\bar{\nabla}\times\bar{Q})+\hat{n}'\times(\bar{\nabla}\times\bar{P})\cdot\bar{Q}\right]ds\end{aligned} \tag{B.16}$$

With the equation in this form, we can replace $\bar{Q}$ by a dyadic function $\bar{\bar{T}}$. The result is the vector-dyadic Green's theorem given by

$$\begin{aligned}\iiint_V \left\{\bar{P}\cdot[\bar{\nabla}\times\bar{\nabla}\times\bar{\bar{T}}]-[\bar{\nabla}\times\bar{\nabla}\times\bar{P}]\cdot\bar{\bar{T}}\right\}dv = \\ \iint_{S_w+S_s}\left[(\hat{n}'\times\bar{P})\cdot(\bar{\nabla}\times\bar{\bar{T}})+\hat{n}'\times(\bar{\nabla}\times\bar{P})\cdot\bar{\bar{T}}\right]ds\,. \qquad \text{(B.17)}\end{aligned}$$

We may now replace $\bar{P}$ with $\bar{A}$ and $\bar{\bar{T}}$ with $\bar{\bar{G}}$ and make use of vector-dyadic identities to yield

$$\begin{aligned}\iiint_V (\nabla^2\bar{A}\cdot\bar{\bar{G}}-\bar{A}\cdot\nabla^2\bar{\bar{G}})dv = \\ \iint_{S_w+S_s}\Big\{(\hat{n}'\times\bar{A})\cdot\bar{\nabla}\times\bar{\bar{G}}+(\hat{n}'\times\bar{\nabla}\times\bar{A})\cdot\bar{\bar{G}} \\ +\hat{n}'\cdot\left[\bar{A}(\bar{\nabla}\cdot\bar{\bar{G}})\right]-\hat{n}'\cdot\left[(\bar{\nabla}\cdot\bar{A})\bar{\bar{G}}\right]\Big\}ds\,. \qquad \text{(B.18)}\end{aligned}$$

If we require that the components of $\bar{A}$ and $\bar{\bar{G}}$ satisfy the same boundary conditions on S_w and S_s, it can be shown that the entire surface integral on the right hand side of (B.18) vanishes. Substitution from (B.11) and (B.14) for $\nabla^2\bar{A}$ and $\nabla^2\bar{\bar{G}}$ we obtain

$$\begin{aligned}\iiint_V (\nabla^2\bar{A}\cdot\bar{\bar{G}}-\bar{A}\cdot\nabla^2\bar{\bar{G}})dv &= \iiint_V \Big\{(-\mu\bar{J}-k^2\bar{A})\cdot\bar{\bar{G}} \\ &\quad -\bar{A}\cdot\left[-\bar{\bar{I}}\delta(\bar{r}-\bar{r}')-k^2\cdot\bar{\bar{G}}\right]\Big\}dv \\ &= -\mu\iiint_V \bar{J}\cdot\bar{\bar{G}}dv+\bar{A}(\bar{r}) \\ &= 0\,. \qquad \text{(B.19)}\end{aligned}$$

Hence,

$$\bar{A}=\mu\iiint_V \bar{J}\cdot\bar{\bar{G}}dv\,. \qquad \text{(B.20)}$$

Finally, substituting from (B.20) into (B.13) produces the following integral equation for the electric field

$$\begin{aligned}\bar{E} &= -j\omega\mu(1+\frac{1}{k^2}\bar{\nabla}\bar{\nabla}\cdot)\iiint_V \bar{J}\cdot\bar{\bar{G}}dv \\ &= -j\omega\mu\iiint_V \left[(1+\frac{1}{k^2}\bar{\nabla}\bar{\nabla}\cdot)(\bar{\bar{G}})^T\right]\cdot\bar{J}dv \qquad \text{(B.21)}\end{aligned}$$

where $(\bar{\bar{G}})^T$ represents the transpose of $\bar{\bar{G}}$.

APPENDIX C

EIGENFUNCTION SOLUTION FOR GREEN'S FUNCTION

The boundary conditions on the cavity walls are applied here in order to derive the functional form of the Green's function. First, the general solution to the homogeneous differential equations for the components of the Green's function is presented. Then, the boundary conditions on the walls are used to arrive at an eigenfunction expansion for each of the Green's function components. The particular solution for the Green's function is found by integrating the inhomogeneous differential equation across the source region.

GENERAL SOLUTION TO HOMOGENEOUS D.E.'s FOR GREEN'S FUNCTION

Consider the homogeneous forms of equations (2.28) and (2.30)

$$\nabla^2 \bar{A}^i + k_i^2 \bar{A}^i = 0 \tag{C.1}$$

$$\nabla^2 \bar{\bar{G}}^i + k_i^2 \bar{\bar{G}}^i = 0 \tag{C.2}$$

where $i = 1, 2$ denotes that these equations hold in each region respectively.

The relationship between $\bar{A}^i$ and $\bar{\bar{G}}^i$ is given by (B.20) which reduces to

$$\frac{1}{\mu_0} \bar{A}^i = \hat{x} \cdot \bar{\bar{G}}^i , \tag{C.3}$$

since we consider an infinitesimal current source $\bar{J}$ for the Green's function derivation. The components of $\bar{A}^i$ and $\bar{\bar{G}}^i$ are related as follows:

$$A_x^i = \mu_0 G_{xx}^i \tag{C.4}$$

$$A_z^i = \mu_0 G_{xz}^i \, . \tag{C.5}$$

With $\bar{\bar{G}}^i$ given by (2.35), it can readily be shown that (C.2) implies

$$\nabla^2 G_{xx}^i + k_i^2 G_{xx}^i = 0 \tag{C.6}$$

$$\nabla^2 G_{xz}^i + k_i^2 G_{xz}^i = 0 \, . \tag{C.7}$$

We apply the method of separation of variables with

$$G_{xx}^i = X_x^i(x) Y_x^i(y) Z_x^i(z) \tag{C.8}$$

$$G_{xz}^i = X_z^i(x) Y_z^i(y) Z_z^i(z) \, . \tag{C.9}$$

The well known general solution of each of the above differential equations may be put in the form

$$\psi = A_1 \cos k_t^i t + A_2 \sin k_t^i t \tag{C.10}$$

where $t = x, y$, or $z; \psi = X_s^i, Y_s^i$, orZ_s^i (where $s = x$ or z) and k_t^i is complex in general. The eigenvalues are related by

$$k_i^2 = k_x^{i2} + k_y^{i2} + k_z^{i2} \, . \tag{C.11}$$

APPLICATION OF BOUNDARY CONDITIONS ON THE CAVITY WALLS

In applying the vector-dyadic Green's theorem of (B.18), it was imposed that $\bar{A}^i$ and $\bar{\bar{G}}^i$ satisfy the same boundary conditions. Hence, A_x^i and G_{xx}^i must satisfy the same boundary conditions on the waveguide walls and on the substrate/air interface and, must have the same functional form in terms of spatial variation. The same holds true for A_z^i and G_{xz}^i.

In order to establish what conditions $\bar{A}^i$ (and correspondingly $\bar{\bar{G}}^i$) must satisfy at the walls, we need first to establish more explicit relations between $\bar{A}^i$ and $\bar{E}^i$. From (B.13)

$$\bar{E}^i = -j\omega\bar{A}^i + \frac{1}{j\omega\epsilon\mu}\bar{\nabla}(\bar{\nabla}\cdot\bar{A}^i)\,. \tag{C.12}$$

The vector potential $\bar{A}^i$ may be expressed as (2.31)

$$\bar{A}^i = A_x^i\hat{x} + A_z^i\hat{z}\,. \tag{C.13}$$

The use of (C.13) in (C.12) yields the following expressions for the electric field components:

$$\begin{aligned} E_x^i &= -j\omega\left[A_x^i + \frac{1}{k_i^2}\frac{\partial}{\partial x}(\bar{\nabla}\cdot\bar{A}^i)\right] \\ &= -j\omega\left[A_x^i + \frac{1}{k_i^2}\frac{\partial}{\partial x}(\frac{\partial A_x^i}{\partial x} + \frac{\partial A_z^i}{\partial z})\right] \end{aligned} \tag{C.14}$$

$$E_y^i = \frac{-j\omega}{k_i^2}\frac{\partial}{\partial y}(\frac{\partial A_x^i}{\partial x} + \frac{\partial A_z^i}{\partial z}) \tag{C.15}$$

$$E_z^i = -j\omega\left[A_z^i + \frac{1}{k_i^2}\frac{\partial}{\partial z}(\frac{\partial A_x^i}{\partial x} + \frac{\partial A_z^i}{\partial z})\right]\,. \tag{C.16}$$

We now will consider the boundary conditions at each of the cavity walls.

Boundary Conditions at $x = 0,\ a$

Since the cavity walls are assumed to be perfectly conducting, the tangential components of the electric field must vanish at the walls. We have

$$E_y^i(x = 0, a) = 0 \tag{C.17}$$

$$E_z^i(x = 0, a) = 0\,. \tag{C.18}$$

In view of these two equations, (C.14) and (C.16) lead to

$$E_y^i(x=0,a) \;=\; \left[\frac{\partial}{\partial y}\left(\frac{\partial A_x^i}{\partial x}+\frac{\partial A_z^i}{\partial z}\right)\right]\Bigg|_{x=0,a} = 0\,. \tag{C.19}$$

$$E_z^i(x=0,a) \;=\; -j\omega\left[A_z^i+\frac{1}{k_i^2}\frac{\partial}{\partial z}\left(\frac{\partial A_x^i}{\partial x}+\frac{\partial A_z^i}{\partial z}\right)\right]\Bigg|_{x=0,a} = 0\,. \tag{C.20}$$

(C.19) is satisfied if the following condition is imposed:

$$\left(\frac{\partial A_x^i}{\partial x}+\frac{\partial A_z^i}{\partial z}\right)\Bigg|_{x=0,a} = 0 \tag{C.21}$$

in which case (C.20) leads to

$$A_z^i(x=0,a) = 0\,. \tag{C.22}$$

If (C.22) is placed into (C.21) it is seen that

$$\frac{\partial A_x^i}{\partial x}\Bigg|_{x=0,a} = 0\,. \tag{C.23}$$

The boundary conditions of (C.22) and (C.23) can be satisfied by choosing the following eigenfunction solutions for the x-dependence:

$$X_x^i \;=\; \cos k_x^i x \tag{C.24}$$

$$X_z^i \;=\; \sin k_x^i x\,. \tag{C.25}$$

for $i = 1, 2$, where

$$k_x^{(1)} = k_x^{(2)} = k_x = \tfrac{n\pi}{a} \qquad \text{for } n = 0, 1, 2, \ldots\;. \tag{C.26}$$

Boundary Conditions at $y = 0,\ b$

The tangential component of the electric field must vanish on the walls $y = 0$ and b; hence,

$$E_x^i(y=0,b) \;=\; 0 \tag{C.27}$$

$$E_z^i(y=0,b) \;=\; 0\,. \tag{C.28}$$

From (C.14) and (C.15)

$$E_x^i(y=0,b) = -j\omega\left[A_x^i + \frac{1}{k_i^2}\frac{\partial}{\partial x}(\frac{\partial A_x^i}{\partial x} + \frac{\partial A_z^i}{\partial z})\right]|_{y=0,b} = 0 \qquad (C.29)$$

$$E_z^i(y=0,b) = -j\omega\left[A_z^i + \frac{1}{k_i^2}\frac{\partial}{\partial z}(\frac{\partial A_x^i}{\partial x} + \frac{\partial A_z^i}{\partial z})\right]|_{y=0,b} = 0\ . \qquad (C.30)$$

It follows from the above two equations that the eigenfunction solution for the y-dependence is given by

$$Y_x^i = \sin k_y^i y \qquad (C.31)$$

$$Y_z^i = \sin k_y^i y \qquad (C.32)$$

(for $i = 1, 2$), where

$$k_y^{(1)} = k_y^{(2)} = k_y = \tfrac{m\pi}{b} \qquad for\ m = 1, 2, 3, \ldots\ . \qquad (C.33)$$

Note that it is easily shown that $m = 0$ leads to a trivial solution for the y-dependence of both components.

<u>**Boundary Conditions at $z = 0, c$**</u>

Similarly at the walls $z = 0$ and c we have

$$E_x^i(z=0,c) = 0 \qquad (C.34)$$

$$E_y^i(z=0,c) = 0\ . \qquad (C.35)$$

Making use of (C.14) and (C.15) yields

$$E_x^i(z=0,c) = -j\omega\left[A_x^i + \frac{1}{k_i^2}\frac{\partial}{\partial x}(\frac{\partial A_x^i}{\partial x} + \frac{\partial A_z^i}{\partial z})\right]|_{z=0,c} = 0 \qquad (C.36)$$

$$E_y^i(z=0,c) = \left[\frac{-j\omega}{k_i^2}\frac{\partial}{\partial y}(\frac{\partial A_x^i}{\partial x} + \frac{\partial A_z^i}{\partial z})\right]|_{z=0,c} = 0\ . \qquad (C.37)$$

It can readily be shown that the eigenfunction solution for the z-dependence can be written as

$$Z_x^{(1)} = \sin k_z^{(1)} z \qquad (C.38)$$

$$Z_z^{(1)} = \cos k_z^{(1)} z \tag{C.39}$$

$$Z_z^{(2)} = \sin k_z^{(2)}(z-c) \tag{C.40}$$

$$Z_z^{(2)} = \cos k_z^{(2)}(z-c) \tag{C.41}$$

where, from (C.11), (C.26), and (C.33), $k_z^{(1)}$ and $k_z^{(2)}$ are given explicitly by

$$k_z^{(1)} = \sqrt{k_1^2 - (\frac{n\pi}{a})^2 - (\frac{m\pi}{b})^2} \tag{C.42}$$

$$k_z^{(2)} = \sqrt{k_0^2 - (\frac{n\pi}{a})^2 - (\frac{m\pi}{b})^2}\,. \tag{C.43}$$

k_1 and k_0 are the wave numbers in region 1 and 2 respectively, and are given by

$$k_1 = \omega\sqrt{\mu\epsilon_1} \tag{C.44}$$

$$k_0 = \omega\sqrt{\mu\epsilon_0}\,. \tag{C.45}$$

REPRESENTATION OF GREEN'S FUNCTION BY EIGENFUNCTION SERIES

We now combine the results obtained above, so that the Green's function may be written in series expansion form. Substituting from (C.24), (C.31),(C.38), and (C.40) into (C.8) and taking the summation over all the possible modes, results in the following for G_{xx}^i:

$$G_{xx}^{(1)} = \sum_{m=1}^{\infty}\sum_{n=0}^{\infty} A_{mn}^{(1)} \cos k_x x \, \sin k_y y \, \sin k_z^{(1)} z \tag{C.46}$$

$$G_{xx}^{(2)} = \sum_{m=1}^{\infty}\sum_{n=0}^{\infty} A_{mn}^{(2)} \cos k_x x \, \sin k_y y \, \sin k_z^{(2)}(z-c)\,. \tag{C.47}$$

Similarly, if we substitute from (C.25),(C.32),(C.39), and (C.41) into (C.9) we obtain the following for G_{xz}^i

$$G_{xz}^{(1)} = \sum_{m=1}^{\infty}\sum_{n=0}^{\infty} B_{mn}^{(1)} \sin k_x x \, \sin k_y y \, \cos k_z^{(1)} z \tag{C.48}$$

$$G_{xz}^{(2)} = \sum_{m=1}^{\infty}\sum_{n=0}^{\infty} B_{mn}^{(2)} \sin k_x x \, \sin k_y y \, \cos k_z^{(2)}(z-c)\,. \tag{C.49}$$

The complex coefficients A_{mn}^i and B_{mn}^i $(i = 1,2)$ are determined in Appendix D by the application of boundary conditions at the substrate/air interface $(z = h)$.

APPENDIX D

BOUNDARY CONDITIONS AT SUBSTRATE/AIR INTERFACE

The complex coefficients A^i_{mn}, and B^i_{mn} (for $i = 1, 2$) for the Green's function components given by (2.36)-(2.39) are found here by applying boundary conditions at the substrate/air interface ($z = h$).

Figure D.1 shows a cross section of the cavity in the x–z plane. The application of boundary conditions at the interface is made difficult by the presence of the infinitesimal current source on the substrate surface. We will avoid this difficulty by first solving a similar problem with the current source raised a distance Δh above the substrate. After solving for the boundary conditions at $z = h$ and $z = h + \Delta h$, the equations required to determine the coefficients A^i_{mn}, and B^i_{mn} are obtained by letting Δh go to zero.

FORMULATION

From the consideration of the boundary conditions on the waveguide walls the components of the Green's function are given as

$$G^{(1)}_{xx} = \sum_{m=1}^{\infty}\sum_{n=0}^{\infty} A^{(1)}_{mn} \cos k_x x \, \sin k_y y \, \sin k^{(1)}_z z \tag{D.1}$$

$$G^{(1)}_{zx} = \sum_{m=1}^{\infty}\sum_{n=0}^{\infty} B^{(1)}_{mn} \sin k_x x \, \sin k_y y \, \cos k^{(1)}_z z \tag{D.2}$$

$$G^{(2)}_{xx} = \sum_{m=1}^{\infty}\sum_{n=0}^{\infty} A^{(2)}_{mn} \cos k_x x \, \sin k_y y \, \sin k^{(2)}_z (z - c) \tag{D.3}$$

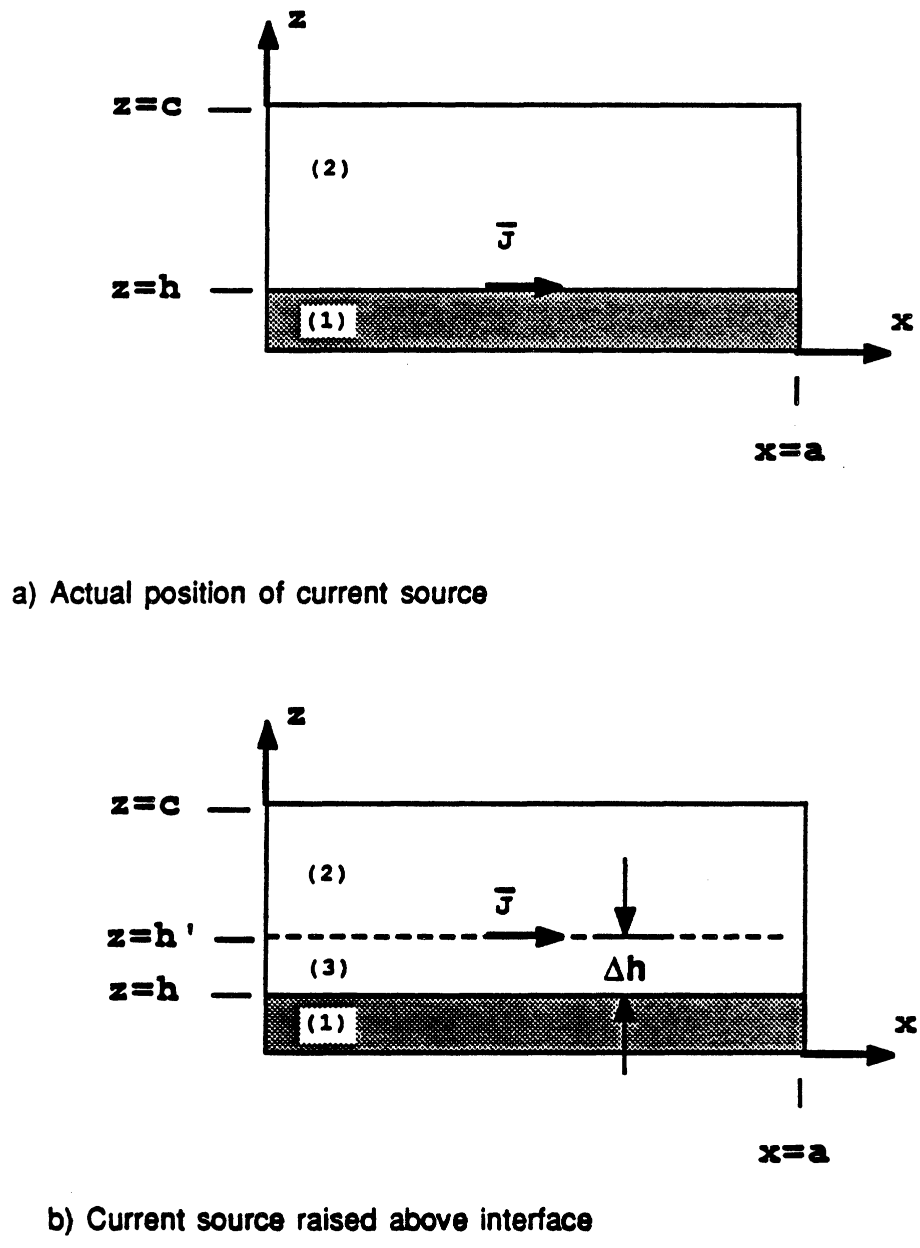

Figure D.1: The current source is raised above the substrate/air interface to apply boundary conditions.

$$G_{zz}^{(2)} = \sum_{m=1}^{\infty}\sum_{n=0}^{\infty} B_{mn}^{(2)} \sin k_x x \sin k_y y \cos k_z^{(2)}(z-c)\,. \tag{D.4}$$

For region 3, the Green's function must satisfy the same differential equation (2.30) as in the other two regions. We will use the form of the general solution given by

$$G_{xx}^{(3)} = \sum_{m=1}^{\infty}\sum_{n=0}^{\infty} \cos k_x x \sin k_y y \left[A_{mn}^{(3)} e^{jk_z^{(3)}z} + B_{mn}^{(3)} e^{-jk_z^{(3)}z}\right] \tag{D.5}$$

$$G_{zz}^{(3)} = \sum_{m=1}^{\infty}\sum_{n=0}^{\infty} \sin k_x x \sin k_y y \left[C_{mn}^{(3)} e^{jk_z^{(3)}z} + D_{mn}^{(3)} e^{-jk_z^{(3)}z}\right] \tag{D.6}$$

where

$$k_x = n\pi/a \tag{D.7}$$

$$k_y = m\pi/b \tag{D.8}$$

$$k_z^{(1)} = \sqrt{k_1^2 - k_x^2 - k_y^2} \tag{D.9}$$

$$k_z^{(2)} = \sqrt{k_0^2 - k_x^2 - k_y^2} \tag{D.10}$$

$$k_z^{(3)} = k_z^{(2)} \tag{D.11}$$

$$k = \omega\sqrt{\mu_0\epsilon_1} \tag{D.12}$$

$$k_0 = \omega\sqrt{\mu_0\epsilon_0}\,. \tag{D.13}$$

Recall, the electric field solution in terms of the vector potential components (C.14)-(C.16)

$$E_x^i = -j\omega\left[A_x^i + \frac{1}{k_i^2}\frac{\partial}{\partial x}\left(\frac{\partial A_x^i}{\partial x} + \frac{\partial A_z^i}{\partial z}\right)\right] \tag{D.14}$$

$$E_y^i = \frac{-j\omega}{k_i^2}\frac{\partial}{\partial y}\left(\frac{\partial A_x^i}{\partial x} + \frac{\partial A_z^i}{\partial z}\right) \tag{D.15}$$

$$E_z^i = -j\omega\left[A_z^i + \frac{1}{k_i^2}\frac{\partial}{\partial z}\left(\frac{\partial A_x^i}{\partial x} + \frac{\partial A_z^i}{\partial z}\right)\right]\,. \tag{D.16}$$

These equations hold in each region respectively (i.e. for $i = 1, 2, 3$).

The solution for the magnetic field can be written using (2.26) and (2.31) as follows:

$$\bar{H}^i = \frac{1}{\mu_o}\bar{\nabla}\times\bar{A}^i = \frac{1}{\mu_o}[\bar{\nabla}\times(A_x^i\hat{x} + A_z^i\hat{z})]\,. \tag{D.17}$$

Separating this into x, y, and z components gives

$$H_x^i = \frac{1}{\mu_0}\frac{\partial A_z^i}{\partial y} \quad \text{(D.18)}$$

$$H_y^i = \frac{1}{\mu_0}\left(\frac{\partial A_x^i}{\partial z} - \frac{\partial A_z^i}{\partial x}\right) \quad \text{(D.19)}$$

$$H_z^i = -\frac{1}{\mu_0}\frac{\partial A_x^i}{\partial y}\,. \quad \text{(D.20)}$$

APPLICATION OF BOUNDARY CONDITIONS

Boundary Conditions at $z = h$

At $z = h$, the following boundary conditions apply:

$$E_x^{(1)} = E_x^{(3)} \quad \text{(D.21)}$$

$$E_y^{(1)} = E_y^{(3)} \quad \text{(D.22)}$$

$$H_x^{(1)} = H_x^{(3)} \quad \text{(D.23)}$$

$$H_y^{(1)} = H_y^{(3)} \quad \text{(D.24)}$$

$$\mu_0 H_z^{(1)} = \mu_0 H_z^{(3)} \Longrightarrow H_z^{(1)} = H_z^{(3)} \quad \text{(D.25)}$$

$$\epsilon_1 E_z^{(1)} = \epsilon_0 E_z^{(3)}\,. \quad \text{(D.26)}$$

We will make use of (D.22)-(D.25) to formulate four of the eight equations needed to solve for the complex coefficients in (D.1)-(D.6). We start with (D.25), then substitute from (D.20), and recall the correspondences of (C.3) to obtain

$$\frac{\partial G_{xx}^{(1)}}{\partial y}\Big|_{z=h} = \frac{\partial G_{xx}^{(3)}}{\partial y}\Big|_{z=h}\,. \quad \text{(D.27)}$$

When (D.1)and (D.5) are used the above, and orthogonality is applied, the following is obtained

$$A_{mn}^{(1)} \sin k_z^{(1)} h = A_{mn}^{(3)} e^{jk_z^{(2)} h} + B_{mn}^{(3)} e^{-jk_z^{(2)} h} \quad \text{(D.28)}$$

where $k_z^{(2)}$ has been substituted for $k_z^{(3)}$ in accordance with (D.11).

Next, from (D.23),(D.18), and (C.3)

$$\frac{\partial G_{xz}^{(1)}}{\partial y} = \frac{\partial G_{xz}^{(3)}}{\partial y} . \tag{D.29}$$

From (D.2),(D.6) and the above

$$B_{mn}^{(1)} \cos k_z^{(1)} h = C_{mn}^{(3)} e^{jk_z^{(2)} h} + D_{mn}^{(3)} e^{-jk_z^{(2)} h} . \tag{D.30}$$

The combination of (D.24), (D.19) and (C.3) yields

$$\left(\frac{\partial G_{xx}^{(1)}}{\partial z} - \frac{\partial G_{xz}^{(1)}}{\partial x} \right) |_{z=h} = \left(\frac{\partial G_{xx}^{(3)}}{\partial z} - \frac{\partial G_{xz}^{(3)}}{\partial x} \right) |_{z=h} . \tag{D.31}$$

Making substitutions from (D.1),(D.2),(D.5) and (D.6) into this expression and using (D.30) leads to

$$A_{mn}^{(1)} k_z^{(1)} \cos k_z^{(1)} h = j k_z^{(2)} \left[A_{mn}^{(3)} e^{jk_z^{(2)} h} - B_{mn}^{(3)} e^{-jk_z^{(2)} h} \right] . \tag{D.32}$$

Now consider (D.22). From (D.15) and (C.3)

$$\frac{1}{\epsilon_r^*} \frac{\partial}{\partial y} \left(\frac{\partial G_{xx}^{(1)}}{\partial x} + \frac{\partial G_{xz}^{(1)}}{\partial z} \right) |_{z=h} = \frac{\partial}{\partial y} \left(\frac{\partial G_{xx}^{(3)}}{\partial x} + \frac{\partial G_{xz}^{(3)}}{\partial z} \right) |_{z=h} . \tag{D.33}$$

After appropriate substitutions and some algebra, the following equation is obtained

$$\begin{aligned} A_{mn}^{(1)} (1 - \epsilon_r^*) k_x \sin k_z^{(1)} h + B_{mn}^{(1)} k_z^{(1)} \sin k_z^{(1)} h = \\ -j k_z^{(2)} \epsilon_r^* \left[C_{mn}^{(3)} e^{jk_z^{(2)} h} - D_{mn}^{(3)} e^{-jk_z^{(2)} h} \right] . \end{aligned} \tag{D.34}$$

Equations (D.28), (D.30), (D.32), and (D.34) represent 4 of the 8 equations we need.

Boundary Conditions at $z = h'$

We now proceed to the boundary conditions at $z = h'$ (see Figure D.1) we have

$$E_x^{(2)} = E_x^{(3)} \tag{D.35}$$

$$E_y^{(2)} = E_y^{(3)} \tag{D.36}$$

$$E_z^{(2)} - E_z^{(3)} = \sigma_s \tag{D.37}$$

$$H_z^{(2)} = H_z^{(3)} \tag{D.38}$$

$$\hat{z} \times (\bar{H}^{(2)} - \bar{H}^{(3)}) = J_s \hat{x} \Longrightarrow$$

$$H_x^{(2)} = H_x^{(3)} \tag{D.39}$$

$$-(H_y^{(2)} - H_y^{(3)}) = J_s \, . \tag{D.40}$$

Of the above, we will use (D.35), (D.38), and (D.39) to derive three more equations for the complex coefficients.

We start with (D.39) and use (D.18) and (C.3) to obtain

$$\frac{\partial G_{xz}^{(2)}}{\partial y}|_{z=h'} = \frac{\partial G_{xz}^{(3)}}{\partial y}|_{z=h'} \tag{D.41}$$

which yields after substituting from (D.4) and (D.6)

$$B_{mn}^{(2)} \cos k_z^{(2)}(h' - c) = C_{mn}^{(3)} e^{jk_z^{(2)}h'} + D_{mn}^{(3)} e^{-jk_z^{(2)}h'} \, . \tag{D.42}$$

Next, consider the boundary condition of (D.38). This leads to

$$\frac{\partial G_{xx}^{(2)}}{\partial y}|_{z=h'} = \frac{\partial G_{xx}^{(3)}}{\partial y}|_{z=h'} \tag{D.43}$$

Substitution from (D.3) and (D.5) yields

$$A_{mn}^{(2)} \sin k_z^{(2)}(h' - c) = A_{mn}^{(3)} e^{jk_z^{(2)}h'} + B_{mn}^{(3)} e^{-jk_z^{(2)}h'} \, . \tag{D.44}$$

This equation, when combined with (D.3) and (D.5) , shows that

$$G_{xx}^{(2)}(z = h') = G_{xx}^{(3)}(z = h') \, . \tag{D.45}$$

With the above equality, we can substitute from (D.14) into the boundary condition of (D.35), and make use of (C.3) to produce

$$\frac{\partial}{\partial x}(\frac{\partial G_{xx}^{(2)}}{\partial x} + \frac{\partial G_{xz}^{(2)}}{\partial z}) = \frac{\partial}{\partial x}(\frac{\partial G_{xx}^{(3)}}{\partial x} + \frac{\partial G_{xz}^{(3)}}{\partial z}) \, . \tag{D.46}$$

Suffering through the details again we obtain

$$B_{mn}^{(2)} \sin k_z^{(2)}(h' - c) = -j\left[C_{mn}^{(3)} e^{jk_z^{(2)}h'} - D_{mn}^{(3)} e^{-jk_z^{(2)}h'}\right] . \tag{D.47}$$

At this point we have 7 independent equations —(D.28), (D.30),(D.32), (D.34),-(D.42),(D.44), and (D.47)— and we have 8 unknown complex coefficients. The other required equation is obtained by integrating the differential equation of (2.30) across the boundary at $z = h'$.

Integration Across the Source Region at $z = h'$

From (2.30) we have

$$\nabla^2 \bar{\bar{G}}^i + k_i^2 \bar{\bar{G}}^i = -\bar{\bar{I}}\delta(\bar{r} - \bar{r}') . \tag{D.48}$$

Substitution from (2.35) for $\bar{\bar{G}}^i$ yields

$$(\nabla^2 + k_i^2)\left(G_{xx}^i \hat{x}\hat{x} + G_{zx}^i \hat{x}\hat{z}\right) = -\delta(\bar{r} - \bar{r}')\hat{x}\hat{x} . \tag{D.49}$$

Hence,

$$(\nabla^2 + k_i^2) G_{xx}^i = -\delta(\bar{r} - \bar{r}') = -\delta(x - x')\delta(y - y')\delta(z - z') . \tag{D.50}$$

We now integrate both sides of this equation over a line passing through the source point $\bar{r}'$, and then take the limit as the length of this line vanishes

$$\lim_{\alpha \to 0} \int_{h'-\alpha}^{h'+\alpha} (\nabla^2 + k_i^2) G_{xx}^i dz = -\delta(x - x')\delta(y - y') . \tag{D.51}$$

This may be written as

$$\lim_{\alpha \to 0}\left[\left(\frac{\partial^2}{\partial x^2} + \frac{\partial^2}{\partial y^2} + k_i^2\right)\int_{h'-\alpha}^{h'+\alpha} G_{xx}^i dz + \int_{h'-\alpha}^{h'+\alpha} \frac{\partial^2}{\partial z^2} G_{xx}^i dz\right] = -\delta(x - x')\delta(y - y') \tag{D.52}$$

If we make use of (D.3) and (D.5), we can show that the first integral vanishes as follows:

$$\begin{aligned}
\lim_{\alpha\to 0}\int_{h'-\alpha}^{h'+\alpha} G^{i}_{xx}dz &= \lim_{\alpha\to 0}\left[\int_{h'-\alpha}^{h'} G^{(3)}_{xx}dz + \int_{h'}^{h'+\alpha} G^{(2)}_{xx}dz\right] \\
&= \lim_{\alpha\to 0}\left[\sum_{m=1}^{\infty}\sum_{n=0}^{\infty}\left(\frac{1}{jk_z^{(2)}}\right)\cos k_x x\,\sin k_y y\left(A^{(3)}_{mn}e^{jk_z^{(2)}z} - B^{(3)}_{mn}e^{-jk_z^{(2)}z}\right)\right]\Big|_{z=h'-\alpha}^{z=h'} \\
&\quad + \lim_{\alpha\to 0}\left[\sum_{m=1}^{\infty}\sum_{n=0}^{\infty}\left(\frac{-1}{k_z^{(2)}}\right)A^{(2)}_{mn}\cos k_x x\,\sin k_y y\,\cos k_z^{(2)}(z-c)\right]\Big|_{z=h'}^{z=h'+\alpha} \\
&= 0
\end{aligned} \tag{D.53}$$

(since each of the limits on the right hand side of the second equality vanishes individually.)

Therefore, (D.52) can be reduced to

$$\lim_{\alpha\to 0}\int_{h'-\alpha}^{h'+\alpha}\frac{\partial^2}{\partial z^2}G^{i}_{xx}dz = -\delta(x-x')\delta(y-y') \tag{D.54}$$

From which we obtain

$$\lim_{\alpha\to 0}\frac{\partial G^{i}_{xx}}{\partial z}\Big|_{h'-\alpha}^{h'+\alpha} = -\delta(x-x')\delta(y-y'), \tag{D.55}$$

or

$$\left(\frac{\partial G^{(2)}_{xx}}{\partial z} - \frac{\partial G^{(3)}_{xx}}{\partial z}\right)\Bigg|_{z=h'} = -\delta(x-x')\delta(y-y'). \tag{D.56}$$

Substitution in the above from (D.3) and (D.5), and simplifying yields

$$\begin{aligned}
\frac{ab}{\varphi_n}\left\{A^{(2)}_{mn}k_z^{(2)}\cos k_z^{(2)}(h'-c)\right. &- \left. jk_z^{(2)}(A^{(3)}_{mn}e^{jk_z^{(2)}z} - B^{(3)}_{mn}e^{-jk_z^{(2)}z})\right\} \\
&= -\cos k_x x'\sin k_y y'
\end{aligned} \tag{D.57}$$

where

$$\varphi_n = \begin{cases} 2 & \text{for } n = 0 \\ 4 & \text{for } n \neq 0 \end{cases} \tag{D.58}$$

The above represents the final equation needed to evaluate the complex coefficients.

EVALUATION OF THE COMPLEX COEFFICIENTS OF THE GREEN'S FUNCTION

To evaluate the complex coefficients, we will make use of the equations derived above involving A^{i}_{mn}, B^{i}_{mn} $(i = 1,3)$, and $C^{(3)}_{mn}$ and $D^{(3)}_{mn}$. Since we are only interested in $A^{(1)}_{mn}$, $B^{(1)}_{mn}$, $A^{(2)}_{mn}$, and $B^{(2)}_{mn}$ these will be evaluated by eliminating the other complex coefficients.

Now, recall that $h' = h + \Delta h$. If $\Delta h \to 0$ then $h' \to h$ in equations (D.42), (D.44), (D.47), and (D.57).

Starting with (D.42) with $h' \to h$ we can substitute from (D.30) to obtain

$$B^{(1)}_{mn} \cos k_z^{(1)} h = B^{(2)}_{mn} \cos k_z^{(2)}(h - c)\,. \tag{D.59}$$

Similarly, (D.28) and (D.44) yield

$$A^{(2)}_{mn} \sin k_z^{(2)}(h - c) = A^{(1)}_{mn} \sin k_z^{(1)} h\,. \tag{D.60}$$

From (D.34) and (D.47) we get

$$B^{(2)}_{mn} \sin k_z^{(2)}(h - c) = \frac{1}{k_z^{(2)}}\left[A^{(1)}_{mn}\left(\frac{1}{\epsilon_r^*} - 1\right) k_x \sin k_z^{(1)} h + \frac{B^{(1)}_{mn} k_z^{(1)}}{\epsilon_r^*} \sin k_z^{(1)} h\right]. \tag{D.61}$$

From (D.32) and (D.57)

$$\frac{ab}{\varphi_n}\left[A^{(2)}_{mn} k_z^{(2)} \cos k_z^{(2)}(h' - c) - A^{(1)}_{mn} k_z^{(1)} \cos k_z^{(1)} h\right] = -\cos k_x x' \sin k_y y'\,. \tag{D.62}$$

The combination of (D.60) and (D.62) yields

$$\frac{ab}{\varphi_n}\left[\frac{A^{(1)}_{mn} \sin k_z^{(1)} h}{\sin k_z^{(2)}(h - c)} k_z^{(2)} \cos k_z^{(2)}(h - c) - A^{(1)}_{mn} k_z^{(1)} \cos k_z^{(1)} h\right] = -\cos k_x x' \sin k_y y'\,. \tag{D.63}$$

Solving for $A^{(1)}_{mn}$

$$A^{(1)}_{mn} = \frac{-\varphi_n \cos k_x x' \sin k_y y' \tan k_z^{(2)}(h - c)}{ab\, d_{1mn} \cos k_z^{(1)} h} \tag{D.64}$$

where

$$d_{1mn} = k_z^{(2)} \tan k_z^{(1)} h - k_z^{(1)} \tan k_z^{(2)}(h-c) \tag{D.65}$$

and φ_n is given by (D.58). $A_{mn}^{(2)}$ is found by substitution from (D.64) into (D.60)

$$A_{mn}^{(2)} = \frac{-\varphi_n \cos k_x x' \sin k_y y' \tan k_z^{(1)} h}{ab\, d_{1mn} \cos k_z^{(2)}(h-c)} \,. \tag{D.66}$$

Next, we combine (D.59) and (D.61) to get

$$\begin{aligned} \frac{B_{mn}^{(1)} \cos k_z^{(1)} h \sin k_z^{(2)}(h-c)}{\cos k_z^{(2)}(h-c)} &= \frac{1}{k_z^{(2)}} \left[A_{mn}^{(1)} \left(\frac{1}{\epsilon_r^*} - 1 \right) k_x \sin k_z^{(1)} h \right. \\ &\quad \left. + \frac{B_{mn}^{(1)} k_z^{(1)}}{\epsilon_r^*} \sin k_z^{(1)} h \right] \,. \end{aligned} \tag{D.67}$$

By substituting for $A_{mn}^{(1)}$ from (D.64), the above can be rearranged to find $B_{mn}^{(1)}$ as

$$B_{mn}^{(1)} = \frac{-\varphi_n (1-\epsilon_r^*) k_x \cos k_x x' \sin k_y y' \tan k_z^{(1)} h \tan k_z^{(2)}(h-c)}{ab\, d_{1mn} d_{2mn} \cos k_z^{(1)} h} \tag{D.68}$$

where

$$d_{2mn} = k_z^{(2)} \epsilon_r^* \tan k_z^{(2)}(h-c) - k_z^{(1)} \tan k_z^{(1)} h \,. \tag{D.69}$$

Finally, if we place (D.68) in (D.59), $B_{mn}^{(2)}$ can be expressed as:

$$B_{mn}^{(2)} = \frac{-\varphi_n (1-\epsilon_r^*) k_x \cos k_x x' \sin k_y y' \tan k_z^{(1)} h \tan k_z^{(2)}(h-c)}{ab\, d_{1mn} d_{2mn} \cos k_z^{(2)}(h-c)} \,. \tag{D.70}$$

We now have derived explicit relations for the desired complex coefficients $A_{mn}^{(1)}$, $A_{mn}^{(2)}$, $B_{mn}^{(1)}$, $B_{mn}^{(2)}$. It can be shown that the same relations can be obtained by moving the current source of Figure D.1 into the dielectric region and then bringing it back to the substrate surface.

APPENDIX E

EVALUATION OF MODIFIED DYADIC GREENS FUNCTION

For the purposes of evaluating the electric field (2.66), only the xx component of the modified dyadic Green's function $\bar{\bar{\Gamma}}^i$ is needed. In this appendix, expressions for $\Gamma_{xx}^{(1)}$, and $\Gamma_{xx}^{(2)}$ are derived. Then, each of these are evaluated at the air/dielectric interface ($z = h$) and shown to be equal.

The modified dyadic Greens function was defined in (2.58) as

$$\bar{\bar{\Gamma}}^i = -j\omega\mu_0 \left[\left(1 + \frac{1}{k_i^2} \bar{\nabla}\bar{\nabla}\cdot \right) (\bar{\bar{G}}^i)^T \right] . \tag{E.1}$$

From (2.35)

$$\bar{\bar{G}}^i = G_{xx}^i \hat{x}\hat{x} + G_{xz}^i \hat{x}\hat{z} .$$

The dyadic transpose is

$$(\bar{\bar{G}}^i)^T = G_{xx}^i \hat{x}\hat{x} + G_{xz}^i \hat{z}\hat{x} \tag{E.2}$$

Using (E.2) into (E.1) yields

$$\begin{aligned} \bar{\bar{\Gamma}}^i \quad = \quad & -j\omega\mu_0 \left\{ \left[G_{xx}^i + \frac{1}{k_i^2} \frac{\partial}{\partial x} \left(\frac{\partial G_{xx}^i}{\partial x} + \frac{\partial G_{xz}^i}{\partial z} \right) \right] \hat{x}\hat{x} \right. \\ & + \left[\frac{1}{k_i^2} \frac{\partial}{\partial y} \left(\frac{\partial G_{xx}^i}{\partial x} + \frac{\partial G_{xz}^i}{\partial z} \right) \right] \hat{y}\hat{x} \\ & \left. + \left[G_{xz}^i + \frac{1}{k_i^2} \frac{\partial}{\partial z} \left(\frac{\partial G_{xx}^i}{\partial x} + \frac{\partial G_{xz}^i}{\partial z} \right) \right] \hat{z}\hat{x} \right\} . \end{aligned} \tag{E.3}$$

Hence, the xx component of the modified Green's function is given by

$$\Gamma_{xx}^i = -j\omega\mu_0 \left[G_{xx}^i + \frac{1}{k_i^2} \frac{\partial}{\partial x} \left(\frac{\partial G_{xx}^i}{\partial x} + \frac{\partial G_{xz}^i}{\partial z} \right) \right] . \tag{E.4}$$

Substitution from (2.36) and (2.37) into (E.4) results in

$$\Gamma_{xx}^{(1)} = -j\omega\mu_0 \sum_{m=1}^{\infty}\sum_{n=0}^{\infty} \cos k_x x \sin k_y y \sin k_z^{(1)} z \left[A_{mn}^{(1)}\left(1-\frac{k_x^2}{k_1^2}\right) - \frac{k_x k_z^{(1)}}{k_1^2} B_{mn}^{(1)}\right]$$

If we use the expressions for $A_{mn}^{(1)}$ and $B_{mn}^{(1)}$ from (2.46) and (2.48) we may write

$$\begin{aligned}\Gamma_{xx}^{(1)} = {} & j\omega\mu_0 \sum_{m=1}^{\infty}\sum_{n=0}^{\infty}\Bigg\{\frac{\varphi_n}{abd_{1mn}d_{2mn}\cos k_z^{(1)}h} \\ & \cdot\left[\cos k_x x \sin k_y y \sin k_z^{(1)} z \cos k_x x' \sin k_y y' \tan k_z^{(2)}(h-c)\right] \\ & \cdot\Bigg[k_z^{(2)}\epsilon_r^*\left(1-\frac{k_x^2}{k_1^2}\right)\tan k_z^{(2)}(h-c) \\ & -k_z^{(1)}\left(1-\frac{\epsilon_r^* k_x^2}{k_1^2}\right)\tan k_z^{(1)}h\Bigg]\Bigg\}\end{aligned} \quad \text{(E.5)}$$

where the expression for d_{2mn} from (D.69) is used to combine terms. Evaluation of (E.5) at $z = h$ gives

$$\begin{aligned}\Gamma_{xx}^{(1)}(z=h) = {} & j\omega\mu_0 \sum_{m=1}^{\infty}\sum_{n=0}^{\infty}\Bigg\{\left(\frac{\varphi_n}{abd_{1mn}d_{2mn}}\right) \\ & \cdot\left[\cos k_x x \sin k_y y \cos k_x x' \sin k_y y' \tan k_z^{(1)}h \tan k_z^{(2)}(h-c)\right] \\ & \cdot\Bigg[k_z^{(2)}\epsilon_r^*\left(1-\frac{k_x^2}{k_1^2}\right)\tan k_z^{(2)}(h-c) \\ & -k_z^{(1)}\left(1-\frac{\epsilon_r^* k_x^2}{k_1^2}\right)\tan k_z^{(1)}h\Bigg]\Bigg\}.\end{aligned} \quad \text{(E.6)}$$

Proceeding in a similar fashion for region 2, it can be shown that

$$\begin{aligned}\Gamma_{xx}^{(2)} = {} & -j\omega\mu_0 \sum_{m=1}^{\infty}\sum_{n=0}^{\infty} \cos k_x x \sin k_y y \sin k_z^{(2)}(z-c) \\ & \cdot\Bigg\{\left[\frac{-\varphi_n \cos k_x x' \sin k_y y' \tan k_z^{(1)}h}{abd_{1mn}\cos k_z^{(2)}(h-c)}\right]\left(1-\frac{k_x^2}{k_0^2}\right) - \frac{k_x k_z^{(2)}}{k_0^2} \\ & \cdot\left[\frac{-\varphi_n(1-\epsilon_r^*)k_x \cos k_x x' \sin k_y y' \tan k_z^{(1)}h \tan k_z^{(2)}(h-c)}{abd_{1mn}d_{2mn}\cos k_z^{(2)}(h-c)}\right]\Bigg\}.\end{aligned}$$

Evaluation of this expression at z=h and rearranging the result produces

$$\Gamma_{xx}^{(2)}(z=h) = j\omega\mu_0 \sum_{m=1}^{\infty}\sum_{n=0}^{\infty}\Bigg\{\left(\frac{\varphi_n}{abd_{1mn}d_{2mn}}\right)$$

$$\cdot [\cos k_x x \, \sin k_y y \, \cos k_x x' \, \sin k_y y' \, \tan k_z^{(1)} h \, \tan k_z^{(2)} (h-c)]$$
$$\cdot \left[k_z^{(2)} \epsilon_r^* \left(1 - \frac{k_x^2}{k_1^2}\right) \tan k_z^{(2)} (h-c) \right.$$
$$\left. \left. - k_z^{(1)} \left(1 - \frac{\epsilon_r^* k_x^2}{k_1^2}\right) \tan k_z^{(1)} h \right] \right\} . \tag{E.7}$$

Upon comparison of (E.7) with (E.6) we can readily see that

$$\Gamma_{xx}^{(1)}(z=h) = \Gamma_{xx}^{(2)}(z=h) = \Gamma_{xx}(z=h) . \tag{E.8}$$

APPENDIX F

INTEGRATION OVER SUBSECTIONAL SURFACES

Consider the surface integral given by (2.71)

$$\mathcal{I}_{qmn} = \int\int_{S_q} \cos k_x x' \sin k_y y' \,\psi(y')\alpha_q(x')\, dx'dy' . \tag{F.1}$$

where from (2.7)

$$\psi(y') = \begin{cases} \dfrac{\frac{2}{\pi W}}{\sqrt{1-\left[\frac{2(y'-Y_0)}{W}\right]^2}} & Y_0 - \frac{W}{2} \le y' \le Y_0 + \frac{W}{2} \\ 0 & \text{else} . \end{cases} \tag{F.2}$$

From (2.8), for $q \neq 1$

$$\alpha_q(x') = \begin{cases} \frac{\sin[K(x_{q+1}-x')]}{\sin(Kl_x)} & x_q \le x' \le x_{q+1} \\ \frac{\sin[K(x'-x_{q-1})]}{\sin(Kl_x)} & x_{q-1} \le x' \le x_q \\ 0 & \text{else} , \end{cases} \tag{F.3}$$

and from (2.9), for $q = 1$

$$\alpha_1(x') = \begin{cases} \frac{\sin[K(l_x-x')]}{\sin(Kl_x)} & 0 \le x' \le l_x \\ 0 & \text{else} . \end{cases} \tag{F.4}$$

In the above,

$$l_x = x_{q+1} - x_q = x_q - x_{q-1}$$

and, for our purposes here[1] , we let

$$x_q = (q-1)l_x .$$

---

[1] Note that for strip geometries other than an open-end and a thru line, the position function x_q will be more complicated in general (see Section 3.1.4).

Figure F.1 illustrates the strip geometry used to determine the integration limits in equation (F.1). The boundaries of the q^{th} subsection depend on q as follows:

$$S_q = \begin{cases} 0 \le x' \le l_x \\ Y_0 - \frac{W}{2} \le y' \le Y_0 + \frac{W}{2} \quad \text{for } q = 1 \\ \\ x_{q-1} \le x' \le x_{q+1} \\ Y_0 - \frac{W}{2} \le y' \le Y_0 + \frac{W}{2} \quad \text{else}. \end{cases} \tag{F.5}$$

With these subsection boundaries, $\mathcal{I}_{qmn}$ may be expressed as

$$\mathcal{I}_{qmn} = \mathcal{I}^{y'} \mathcal{I}_q^{x'} \tag{F.6}$$

where

$$\mathcal{I}^{y'} = \int_{Y_0-W/2}^{Y_0+W/2} \psi(y') \sin k_y y' \, dy' \tag{F.7}$$

$$\mathcal{I}_q^{x'} = \begin{cases} \int_0^{l_x} \cos k_x x' \, \alpha_q(x') dx' & \text{for } q = 1 \\ \int_{x_{q-1}}^{x_{q+1}} \cos k_x x' \alpha_q(x') dx' & \text{for } q \ne 1 . \end{cases} \tag{F.8}$$

INTEGRATION OVER y'

From (F.7) and (F.2) we have

$$\mathcal{I}^{y'} = \frac{2}{\pi W} \int_{Y_0-W/2}^{Y_0+W/2} \frac{\sin k_y y'}{\sqrt{1 - \left[\frac{2(y'-Y_0)}{W}\right]^2}} dy' . \tag{F.9}$$

Now, let

$$\begin{aligned} \sin\phi &= \frac{2(y'-Y_0)}{W} &\Longrightarrow \quad \cos\phi \, d\phi &= \frac{2}{W} dy' \\ y' &= \frac{W}{2}\sin\phi + Y_0 &\Longrightarrow \quad dy' &= \frac{W}{2}\cos\phi \, d\phi \end{aligned} \tag{F.10}$$

with these substitutions

$$\mathcal{I}^{y'} = \frac{1}{\pi} \int_{-\frac{\pi}{2}}^{\frac{\pi}{2}} \sin\left[k_y(\frac{W}{2}\sin\phi + Y_0)\right] d\phi . \tag{F.11}$$

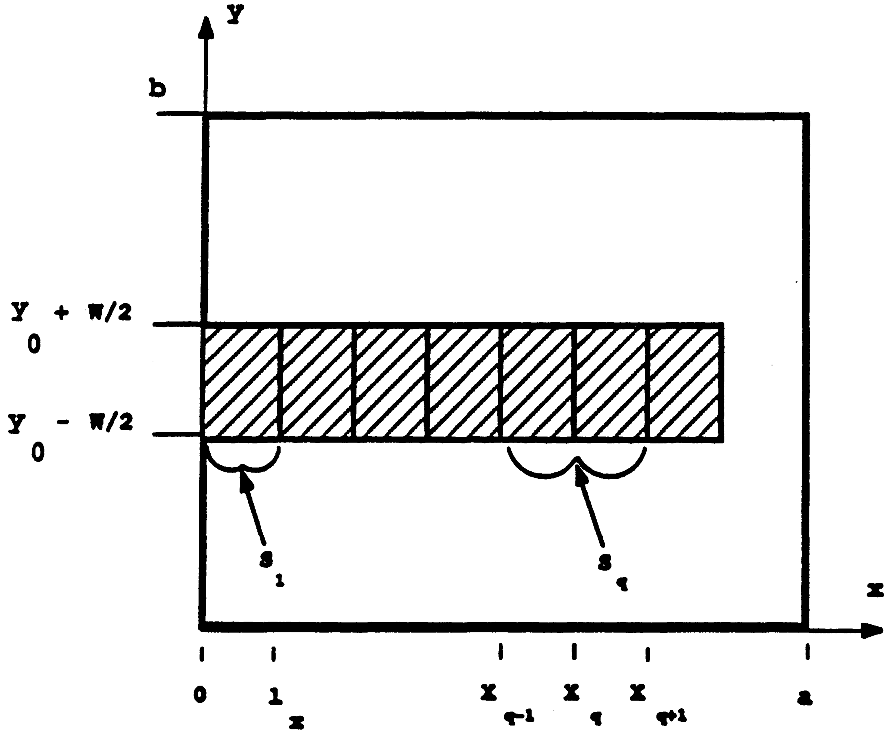

Figure F.1: Strip geometry used in evaluation of surface integrals

The above may be rewritten as

$$
\begin{aligned}
\mathcal{I}^{y'} &= \frac{1}{\pi}\left[\int_{-\frac{\pi}{2}}^{\frac{\pi}{2}} \sin(k_y \frac{W}{2} \sin\phi) \cos k_y Y_0 \, d\phi \right. \\
&\quad \left. + \int_{-\frac{\pi}{2}}^{\frac{\pi}{2}} \cos(k_y \frac{W}{2} \sin\phi) \sin k_y Y_0 \, d\phi \right] \\
&= \int^{(1)y'} + \int^{(2)y'} . \qquad \text{(F.12)}
\end{aligned}
$$

Consider the first term of (F.12):

$$
\begin{aligned}
\int^{(1)y'} &= \frac{1}{\pi} \cos k_y Y_0 \int_{-\frac{\pi}{2}}^{\frac{\pi}{2}} \sin(k_y \frac{W}{2} \sin\phi)\, d\phi \\
&= \frac{1}{\pi} \cos k_y Y_0 \left[\int_{-\frac{\pi}{2}}^{0} \sin(k_y \frac{W}{2} \sin\phi)\, d\phi + \int_{0}^{\frac{\pi}{2}} \sin(k_y \frac{W}{2} \sin\phi)\, d\phi \right] .
\end{aligned}
$$

If, in the second integral above, we let

$$\phi' = -\phi \;\; ; \;\; d\phi' = -d\phi$$

then

$$
\begin{aligned}
\int^{(1)y'} &= \frac{1}{\pi} \cos k_y Y_0 \left[\int_{-\frac{\pi}{2}}^{0} \sin(k_y \frac{W}{2} \sin\phi)\, d\phi + \int_{0}^{-\frac{\pi}{2}} \sin(-k_y \frac{W}{2} \sin\phi)(-d\phi) \right] \\
&= 0 .
\end{aligned}
$$

Hence, (F.12) becomes

$$
\begin{aligned}
\mathcal{I}^{y'} &= \int^{(2)y'} = \frac{1}{\pi} \sin k_y Y_0 \int_{-\frac{\pi}{2}}^{\frac{\pi}{2}} \cos(k_y \frac{W}{2} \sin\phi)\, d\phi \\
&= \frac{1}{\pi} \sin k_y Y_0 \left[\int_{-\frac{\pi}{2}}^{0} \cos(k_y \frac{W}{2} \sin\phi)\, d\phi \right. \\
&\quad \left. + \int_{0}^{\frac{\pi}{2}} \cos(k_y \frac{W}{2} \sin\phi)\, d\phi \right] . \qquad \text{(F.13)}
\end{aligned}
$$

If, in the first integral of (F.13), we let

$$\phi' = -\phi \;\; ; \;\; d\phi' = -d\phi$$

we obtain

$$\mathcal{I}^{y'} = \frac{2}{\pi} \sin k_y Y_0 \int_0^{\frac{\pi}{2}} \cos(k_y \frac{W}{2} \sin\phi)\, d\phi \, . \qquad (F.14)$$

By comparison of the Bessel function of the 2η order given by [65]

$$J_{2\eta}(z) = \frac{2}{\pi} \int_0^{\frac{\pi}{2}} \cos 2\eta\theta \cos(z \sin\theta)\, d\theta$$

with (F.14) we may readily see that

$$\mathcal{I}^{y'} = \sin k_y Y_0 \, J_0 \left(k_y \frac{W}{2} \right) \qquad (F.15)$$

This completes the y'-portion of the integration.

INTEGRATION OVER x'

From (F.8),

$$\mathcal{I}_q^{x'} = \int_{x_{q-1}}^{x_{q+1}} \cos k_x x' \alpha_q(x') dx' \qquad (F.16)$$

First we consider the case for $q \neq 1$. Substitution from (F.3) in the above yields

$$\begin{aligned} \mathcal{I}_q^{x'} &= \frac{1}{\sin K l_x} \left[\int_{x_{q-1}}^{x_q} \sin K(x' - x_{q-1}) \cos k_x x'\, dx' \right. \\ &\quad \left. + \int_{x_q}^{x_{q+1}} \sin K(x' + x_{q-1}) \cos k_x x'\, dx' \right] \\ &= \frac{1}{\sin K l_x} \left[\mathcal{I}_q^{(1)x'} + \mathcal{I}_q^{(2)x'} \right] \qquad (q \neq 1) \, . \end{aligned} \qquad (F.17)$$

For the first integral we have

$$\begin{aligned} \mathcal{I}_q^{(1)x'} &= \int_{x_{q-1}}^{x_q} \sin K(x' - x_{q-1}) \cos k_x x' dx' \\ &= \frac{1}{2} \int_{x_{q-1}}^{x_q} \{ \sin[(K + k_x)x' - K x_{q-1}] + \sin[(K - k_x)x' - K x_{q-1}] \} \, dx' \\ &= -\frac{1}{2} \left\{ \frac{1}{K + k_x} [\cos(K l_x + k_x x_q) - \cos k_x x_{q-1}] \right. \\ &\quad \left. + \frac{1}{K - k_x} [\cos(K l_x - k_x x_q) - \cos k_x x_{q-1}] \right\} \, . \end{aligned} \qquad (F.18)$$

We can solve for $\mathcal{I}_q^{(2)x'}$ in a similar fashion to yield

$$\begin{aligned}\mathcal{I}_q^{(2)x'} &= \int_{x_q}^{x_{q+1}} \sin\left[K(x_{q+1}-x')\right]\cos k_x x' dx' \\ &= \frac{1}{2}\left\{\frac{1}{K-k_x}\left[\cos k_x x_{q+1} - \cos(Kl_x + k_x x_q)\right]\right. \\ &\quad \left.+\frac{1}{K+k_x}\left[\cos k_x x_{q+1} - \cos(Kl_x - k_x x_q)\right]\right\} . \end{aligned} \tag{F.19}$$

Substitution from (F.18) and (F.19) back into (F.17) yields

$$\begin{aligned}\mathcal{I}_q^{x'} &= \frac{1}{\sin Kl_x}\left(\frac{1}{K+k_x}+\frac{1}{K-k_x}\right) \\ &\quad \cdot\left[\frac{1}{2}\left(\cos k_x x_{q+1} + \cos k_x x_{q-1}\right) - \cos Kl_x \cos k_x x_q\right] . \end{aligned} \tag{F.20}$$

After some manipulation, this expression may be put in the following form

$$\begin{aligned}\mathcal{I}_q^{x'} &= \frac{-4K\cos k_x x_q \sin\left[\frac{1}{2}(k_x+K)l_x\right]\sin\left[\frac{1}{2}(k_x-K)l_x\right]}{\sin Kl_x\ (K+k_x)\ (K-k_x)} \\ &= -\frac{Kl_x^2\cos k_x x_q}{\sin Kl_x}\operatorname{Sinc}\left[\frac{1}{2}(k_x+K)l_x\right]\operatorname{Sinc}\left[\frac{1}{2}(k_x-K)l_x\right] \end{aligned} \tag{F.21}$$

where

$$\operatorname{Sinc}(t) = \begin{cases} \frac{\sin t}{t} & t \neq 0 \\ 1 & t = 0 . \end{cases} \tag{F.22}$$

Recall now the integral for the case $q = 1$ from (F.8)

$$\mathcal{I}_1^{x'} = \int_0^{l_x} \cos k_x x' \alpha_1(x') dx' .$$

Substitution from (F.4) for $\alpha_1(x)$

$$\mathcal{I}_1^{x'} = \frac{1}{\sin Kl_x}\int_0^{l_x} \cos k_x x' \sin(l_x - x') dx' . \tag{F.23}$$

Comparison of this expression to the integral of (F.19) shows that if we let $x_q \to 0$ and $x_{q+1} \to l_x$ in (F.19) we can obtain the solution for the integral in (F.23). The result is

$$\begin{aligned}\mathcal{I}_1^{x'} &= \frac{1}{2\sin Kl_x}\left\{\frac{1}{K-k_x}\left[\cos k_x l_x - \cos Kl_x\right] + \frac{1}{K+k_x}\left[\cos k_x l_x - \cos Kl_x\right]\right\} \\ &= \frac{1}{2\sin Kl_x}\left(\frac{1}{K-k_x}+\frac{1}{K+k_x}\right)\left[\cos k_x l_x - \cos Kl_x\right] . \end{aligned}$$

The above can be rearranged to give

$$\mathcal{I}_1^{x'} = \frac{-Kl_x^2}{2\sin Kl_x}\,\mathrm{Sinc}\left[\frac{1}{2}(k_x+K)l_x\right]\,\mathrm{Sinc}\left[\frac{1}{2}(k_x-K)l_x\right] \quad (\text{for } q=1)\,. \tag{F.24}$$

Combination of this with (F.21) yields

$$\mathcal{I}_q^{x'} = -\frac{\zeta_q K l_x^2 \cos k_x x_q}{4\sin Kl_x}\,\mathrm{Sinc}\left[\frac{1}{2}(k_x+K)l_x\right]\,\mathrm{Sinc}\left[\frac{1}{2}(k_x-K)l_x\right] \quad (\text{for any } q) \tag{F.25}$$

where

$$\zeta_q = \begin{cases} 2 & \text{for } \; q=1 \\ 4 & \text{for } \; q\neq 1\,. \end{cases} \tag{F.26}$$

Finally, substitution from (F.15) and (F.25) back into (F.6) yields

$$\begin{aligned} \mathcal{I}_{qmn} &= \int\!\!\int_{S_q} \cos k_x x' \sin k_y y' \psi(y')\alpha_q(x')dx'dy' \\ &= -\frac{\zeta_q K l_x^2 \cos k_x x_q}{\sin Kl_x}\,\mathrm{Sinc}\left[\frac{1}{2}(k_x+K)l_x\right]\,\mathrm{Sinc}\left[\frac{1}{2}(k_x-K)l_x\right] \\ &\quad \cdot \sin k_y Y_0 \; J_0(k_y\frac{W}{2})\,. \end{aligned} \tag{F.27}$$

APPENDIX G

EVALUATION OF MAGNETIC FIELD COMPONENTS

The magnetic field components anywhere inside the cavity are given by the surface integrals of (2.89) and (2.90)

$$H^i_{qy} = \int\int_{S_q} \left(\frac{\partial G^i_{xx}}{\partial z} - \frac{\partial G^i_{xz}}{\partial x} \right) \psi(y')\alpha_q(x')ds' \tag{G.1}$$

$$H^i_{qz} = -\int\int_{S_q} \frac{\partial G^i_{xx}}{\partial y} \psi(y')\alpha_q(x')ds' . \tag{G.2}$$

We will evaluate H^i_{qy} first.

EVALUATION OF THE $y-$ COMPONENT OF THE MAGNETIC FIELD

From (2.36) and (2.37)

$$\begin{aligned} \frac{\partial G^{(1)}_{xx}}{\partial z} - \frac{\partial G^{(1)}_{xz}}{\partial x} &= \sum_{m=1}^{\infty}\sum_{n=0}^{\infty} k^{(1)}_z A^{(1)}_{mn} \cos k_x x \sin k_y y \cos k^{(1)}_z z \\ &- \sum_{m=1}^{\infty}\sum_{n=0}^{\infty} k_x B^{(1)}_{mn} \cos k_x x \sin k_y y \cos k^{(1)}_z z . \end{aligned}$$

After appropriate substitutions and some manipulation we may write

$$\begin{aligned} \frac{\partial G^{(1)}_{xx}}{\partial z} - \frac{\partial G^{(1)}_{xz}}{\partial x} &= -\sum_{m=1}^{\infty}\sum_{n=0}^{\infty} \frac{\varphi_n \tan k^{(2)}_z(h-c)}{ab\, d_{1mn} d_{2mn} \cos k^{(1)}_z h} \\ &\cdot \left\{ k^{(1)}_z k^{(2)}_z \epsilon^*_r \tan k^{(2)}_z (h-c) - \left[(k^{(1)}_z)^2 + k^2_x(1-\epsilon^*_r) \right] \tan k^{(1)}_z h \right\} \\ &\cdot \cos k_x x \sin k_y y \cos k^{(1)}_z z \cos k_x x' \sin k_y y' . \end{aligned} \tag{G.3}$$

Similarly, substitution from (2.38) and (2.39) leads to

$$\frac{\partial G_{xx}^{(2)}}{\partial z} - \frac{\partial G_{zz}^{(2)}}{\partial x} = \sum_{m=1}^{\infty}\sum_{n=0}^{\infty} \frac{\varphi_n \tan k_z^{(1)}h}{ab\, d_{1mn}d_{2mn} \cos k_z^{(2)}(h-c)}$$
$$\cdot \left\{ k_z^{(1)}k_z^{(2)} \tan k_z^{(1)}h - \left[(k_z^{(2)})^2\epsilon_r^* - k_x^2(1-\epsilon_r^*)\right] \tan k_z^{(2)}(h-c)\right\}$$
$$\cos k_x x \sin k_y y \cos k_z^{(2)}(z-c) \cos k_x x' \sin k_y y' \,. \tag{G.4}$$

We are now ready to evaluate the y-component of the magnetic field. Substitution from (G.3) into (G.1) yields

$$H_{qy}^{(1)} = -\sum_{m=1}^{\infty}\sum_{n=0}^{\infty} \frac{\varphi_n \tan k_z^{(2)}(h-c)}{ab\, d_{1mn}d_{2mn} \cos k_z^{(1)}h}$$
$$\cdot \left\{ k_z^{(1)}k_z^{(2)}\epsilon_r^* \tan k_z^{(2)}(h-c) - \left[(k_z^{(1)})^2 + k_x^2(1-\epsilon_r^*)\right] \tan k_z^{(1)}h\right\}$$
$$\cdot \cos k_x x \sin k_y y \cos k_z^{(1)}z \,\left[\mathcal{I}_{qmn}\right] \tag{G.5}$$

Replacement of $\mathcal{I}_{qmn}$ with the expression from Appendix F, yields

$$H_{qy}^{(1)} = \frac{\zeta_q K l_x^2}{4ab \sin K l_x} \sum_{m=1}^{\infty}\sum_{n=0}^{\infty} \frac{\varphi_n \tan k_z^{(2)}(h-c)}{d_{1mn}d_{2mn} \cos k_z^{(1)}h}$$
$$\cdot \left\{ k_z^{(1)}k_z^{(2)}\epsilon_r^* \tan k_z^{(2)}(h-c) - \left[(k_z^{(1)})^2 + k_x^2(1-\epsilon_r^*)\right] \tan k_z^{(1)}h\right\}$$
$$\cdot \cos k_x x_q \,\mathrm{Sinc}\left[\frac{1}{2}(k_x+K)l_x\right] \mathrm{Sinc}\left[\frac{1}{2}(k_x-K)l_x\right] \sin k_y Y_0 \, J_0(k_y \frac{W}{2})$$
$$\cdot \cos k_x x \sin k_y y \cos k_z^{(1)}z \,. \tag{G.6}$$

Similarly, substitution from (G.4) into (G.1) and again making use of (F.27) yields

$$H_{qy}^{(2)} = \frac{-\zeta_q K l_x^2}{4ab \sin K l_x} \sum_{m=1}^{\infty}\sum_{n=0}^{\infty} \frac{\varphi_n \tan k_z^{(1)}h}{d_{1mn}d_{2mn} \cos k_z^{(2)}(h-c)}$$
$$\cdot \left\{ k_z^{(1)}k_z^{(2)} \tan k_z^{(1)}h - \left[(k_z^{(2)})^2\epsilon_r^* - k_x^2(1-\epsilon_r^*)\right] \tan k_z^{(2)}(h-c)\right\}$$
$$\cdot \cos k_x x_q \,\mathrm{Sinc}\left[\frac{1}{2}(k_x+K)l_x\right] \mathrm{Sinc}\left[\frac{1}{2}(k_x-K)l_x\right] \sin k_y Y_0 \, J_0(k_y \frac{W}{2})$$
$$\cdot \cos k_x x \sin k_y y \cos k_z^{(2)}(z-c) \,. \tag{G.7}$$

We now proceed to the evaluation of H_{qz}^i.

EVALUATION OF THE $z-$ COMPONENT OF THE MAGNETIC FIELD

With the use of (2.36), we can write

$$\begin{aligned}
\frac{\partial G_{xx}^{(1)}}{\partial y} &= \sum_{m=1}^{\infty}\sum_{n=0}^{\infty} k_y A_{mn}^{(1)} \cos k_x x \cos k_y y \sin k_z^{(1)} z \\
&= -\sum_{m=1}^{\infty}\sum_{n=0}^{\infty} \frac{\varphi_n k_y \tan k_z^{(2)}(h-c)}{ab\, d_{1mn} \cos k_z^{(1)} h} \\
&\quad \cdot \cos k_x x \cos k_y y \sin k_z^{(1)} z \cos k_x x' \sin k_y y' \,. \qquad \text{(G.8)}
\end{aligned}$$

Similarly, from (2.38)

$$\begin{aligned}
\frac{\partial G_{xx}^{(2)}}{\partial y} &= \sum_{m=1}^{\infty}\sum_{n=0}^{\infty} k_y A_{mn}^{(2)} \cos k_x x \cos k_y y \sin k_z^{(2)}(z-c) \\
&= -\sum_{m=1}^{\infty}\sum_{n=0}^{\infty} \frac{\varphi_n k_y \tan k_z^{(1)} h}{ab\, d_{1mn} \cos k_z^{(2)}(h-c)} \\
&\quad \cdot \cos k_x x \cos k_y y \sin k_z^{(2)}(z-c) \cos k_x x' \sin k_y y' \,. \qquad \text{(G.9)}
\end{aligned}$$

Substitution from (G.8) into (G.2) and using (F.27) yields

$$\begin{aligned}
H_{qz}^{(1)} &= \frac{\zeta_q K l_x^2}{4ab \sin K l_x} \sum_{m=1}^{\infty}\sum_{n=0}^{\infty} \frac{\varphi_n k_y \tan k_z^{(2)}(h-c)}{d_{1mn} \cos k_z^{(1)} h} \\
&\quad \cdot \cos k_x x_q \,\text{Sinc}\left[\frac{1}{2}(k_x+K)l_x\right] \text{Sinc}\left[\frac{1}{2}(k_x-K)l_x\right] \\
&\quad \cdot \sin k_y Y_0\, J_0(k_y \frac{W}{2}) \cos k_x x \cos k_y y \sin k_z^{(1)} z \qquad \text{(G.10)}
\end{aligned}$$

Likewise, substitution from (G.9) in (G.2) yields

$$\begin{aligned}
H_{qz}^{(2)} &= \frac{\zeta_q K l_x^2}{4ab \sin K l_x} \sum_{m=1}^{\infty}\sum_{n=0}^{\infty} \frac{\varphi_n k_y \tan k_z^{(1)} h}{d_{1mn} \cos k_z^{(2)}(h-c)} \\
&\quad \cdot \cos k_x x_q \,\text{Sinc}\left[\frac{1}{2}(k_x+K)l_x\right] \text{Sinc}\left[\frac{1}{2}(k_x-K)l_x\right] \\
&\quad \cdot \sin k_y Y_0\, J_0(k_y \frac{W}{2}) \cos k_x x \cos k_y y \sin k_z^{(2)}(z-c) \qquad \text{(G.11)}
\end{aligned}$$

In summary, the $\hat{y}$ and $\hat{z}$ components of the magnetic field anywhere in the cavity may be expressed as follows:

$$H_{qy}^{(1)} = H_{q0} \sum_{m=1}^{\infty}\sum_{n=0}^{\infty} c_{nq} c_{ymn}^{(1)} \cos k_x x \sin k_y y \cos k_z^{(1)} z \qquad \text{(G.12)}$$

$$H_{qz}^{(1)} = H_{q0} \sum_{m=1}^{\infty} \sum_{n=0}^{\infty} c_{nq} c_{zmn}^{(1)} \cos k_x x \cos k_y y \sin k_z^{(1)} z \quad \text{(G.13)}$$

$$H_{qy}^{(2)} = H_{q0} \sum_{m=1}^{\infty} \sum_{n=0}^{\infty} c_{nq} c_{ymn}^{(2)} \cos k_x x \sin k_y y \cos k_z^{(2)}(z-c) \quad \text{(G.14)}$$

$$H_{qz}^{(2)} = H_{q0} \sum_{m=1}^{\infty} \sum_{n=0}^{\infty} c_{nq} c_{zmn}^{(2)} \cos k_x x \cos k_y y \sin k_z^{(2)}(z-c) \quad \text{(G.15)}$$

where

$$H_{q0} = \frac{\zeta_q K l_x^2}{4ab \sin K l_x}$$

$$c_{nq} = \cos k_x x_q \,\mathrm{Sinc}\left[\frac{1}{2}(k_x + K) l_x\right] \mathrm{Sinc}\left[\frac{1}{2}(k_x - K) l_x\right]$$

and

$$c_{ymn}^{(1)} = \frac{c_{zmn}^{(1)}}{k_y d_{2mn}} \Big\{ k_z^{(1)} k_z^{(2)} \epsilon_r^* \tan k_z^{(2)}(h-c) - \left[(k_z^{(1)})^2 + k_x^2 (1 - \epsilon_r^*) \right] \tan k_z^{(1)} h \Big\} \quad \text{(G.16)}$$

$$c_{zmn}^{(1)} = \frac{\varphi_n k_y \tan k_z^{(2)}(h-c)}{d_{1mn} \cos k_z^{(1)} h} \sin k_y Y_0 \, J_0(k_y \frac{W}{2}) \quad \text{(G.17)}$$

$$c_{ymn}^{(2)} = \frac{c_{zmn}^{(2)}}{k_y d_{2mn}} \Big\{ k_z^{(1)} k_z^{(2)} \tan k_z^{(1)} h - \left[(k_z^{(2)})^2 \epsilon_r^* - k_x^2 (1 - \epsilon_r^*) \right] \tan k_z^{(2)}(h-c) \Big\} \quad \text{(G.18)}$$

$$c_{zmn}^{(2)} = \frac{\varphi_n k_y \tan k_z^{(1)} h}{d_{1mn} \cos k_z^{(2)}(h-c)} \sin k_y Y_0 \, J_0(k_y \frac{W}{2}) \,. \quad \text{(G.19)}$$

APPENDIX H

MICROSTRIP CONNECTION REPEATABILITY STUDY

This appendix includes a description of the microstrip connection repeatability study carried out by the author while at Hughes Aircraft Company. In this study, key repeatability issues related to the measurement of microstrip discontinuities with the TSD (thru-short-delay) technique [44,49], are explored experimentally. These include the repeatability of coax/microstrip connections, microstrip/microstrip interconnects, microstrip line fabrication and substrate mounting, and the electrical characteristics of coax-to-microstrip transitions (launchers). Each of these issues has been explored experimentally and the results are presented for two types of coaxial-to-microstrip test fixtures: one usable to 18GHz, and the other to 40GHz.

The objectives met by this study are two-fold. First, trade-offs were explored for choosing between different connection alternatives for de-embedding in microstrip with the (TSD) technique Secondly, data was obtained to assess the uncertainties in microstrip fixture measurements due to the non-repeatability of various microstrip connections.

Finite measurement uncertainties, due to the repeatability issues described above, are inherent in each fixture measurement made on the TSD standards (during fixture characterization), and the D.U.T.. The measurements described next illustrate how experimentation can be used to determine the magnitudes of

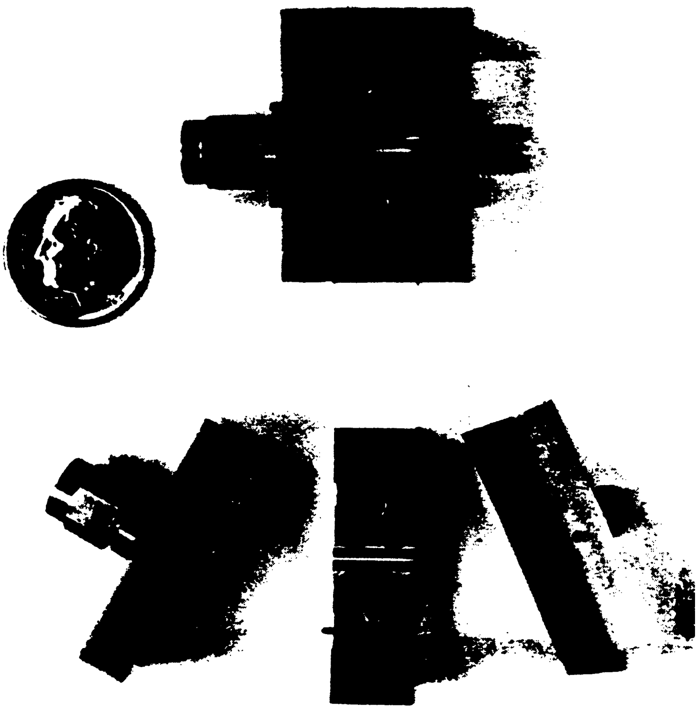

Figure H.1: K-connector (2.9mm) coaxial/microstrip test fixture.

these uncertainties.

DESCRIPTION OF CONNECTION REPEATABILITY EXPERIMENTS

Two types of coaxial test fixtures were used in the experiments. The first, usable to 18 GHz, consists of a pair of 7mm "Eisenhart" launchers [57]. The test circuit used here consists of a 1″ section of 50 ohm microstrip line on an alumina (h = .025″) substrate (Figure 4.4). The other fixture , operable to 40 GHz, uses a pair of Wiltron K-connector (2.9mm) launchers and a .40″ section of 50 ohm microstrip line on a quartz (h = .01″) substrate (Figure H.1).

The repeatability experiments performed are summarized in Table 1. For our purposes, "cycling" a connection refers to disconnecting and reconnecting both the input and output connections simultaneously and repeating the measurement. For the coax/coax repeatability experiment, each fixture was connected to and

Table H.1: SUMMARY OF REPEATABILITY EXPERIMENTS

EXPERIMENT	NUMBER OF TRIALS	FREQUENCY RANGE	DESCRIPTION
1. COAX/COAX			
A) 7 mm FIXTURE	20	0.045-18 GHz	CYCLED CONNECTIONS AT 7 mm COAXIAL MEASUREMENT PORTS
B) K-CONN. FIXTURE	20	0.045-26.5 GHz	CYCLED CONNECTIONS AT K-CONN. COAXIAL MEASUREMENT PORTS
2. COAX/MICROSTRIP			
A) 7 mm FIXTURE	10	0.045-18 GHz	CYCLED PRESSURE CONTACT MADE FROM LAUNCHER TO MICROSTRIP LINE
B) K-CONN. FIXTURE	10	0.045-40 GHz	CYCLED GAP WELD CONNECTION MADE FROM TAB ON K-CONN. SLIDING CONTACT TO MICROSTRIP
3. MICROSTRIP/MICROSTRIP			
K-CONN. FIXTURE	5	0.045-40 GHz	CYCLED TWO GAP WELDED RIBBONS USED TO CONNECT THREE MICROSTRIP LINES TOGETHER
4. MICROSTRIP FABRICATION/ MOUNTING			
K-CONN. FIXTURE	5	0.045-40 GHz	MEASURED FIVE SEPARATE MICROSTRIP LINES WITH SAME LAUNCHERS
5. LAUNCHER-TO-LAUNCHER UNIFORMITY			
A) 7 mm FIXTURE	4	0.045-18 GHz	MEASURED SAME LINE WITH DIFFERENT PAIRS OF 7 mm LAUNCHERS
B) K-CONN. FIXTURE	3	0.045-26.5 GHz	MEASURED SAME LINE WITH DIFFERENT PAIRS OF K-CONN. LAUNCHERS

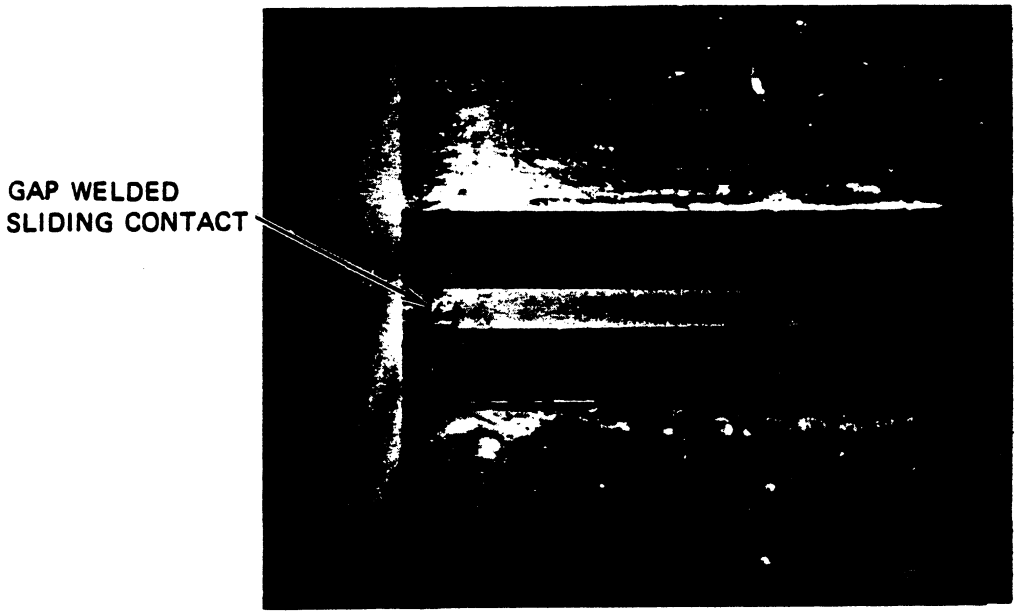

Figure H.2: Coax/microstrip connection technique used with K-connector (2.9mm) launchers.

removed from the coaxial measurement terminals several times, taking care not to disturb the coax/microstrip connection. The 7mm coax/microstrip connection test was performed by cycling pressure contacts made between the wedge shaped center conductors on the Eisenhart launchers, and the microstrip line. For the K-conn. fixture, gap welds used to connect the .018″ tab on the K-conn. "sliding contact" (a small gold plated tab with a sleeve that fits over the launcher's center conductor) to the microstrip line (Figure H.2) were cycled. In order to preserve the microstrip metalization, the minimum amount of weld voltage and pressure needed to secure the tab was used. This made it possible to use the same microstrip line and sliding contacts for all 10 trials.

A similar connection approach was used for the microstrip/microstrip interconnects. Two .020" $\times$ .025″ Gold ribbon straps were gap welded across the connection interfaces between three microstrip lines (Figure H.3). To cycle this connection,

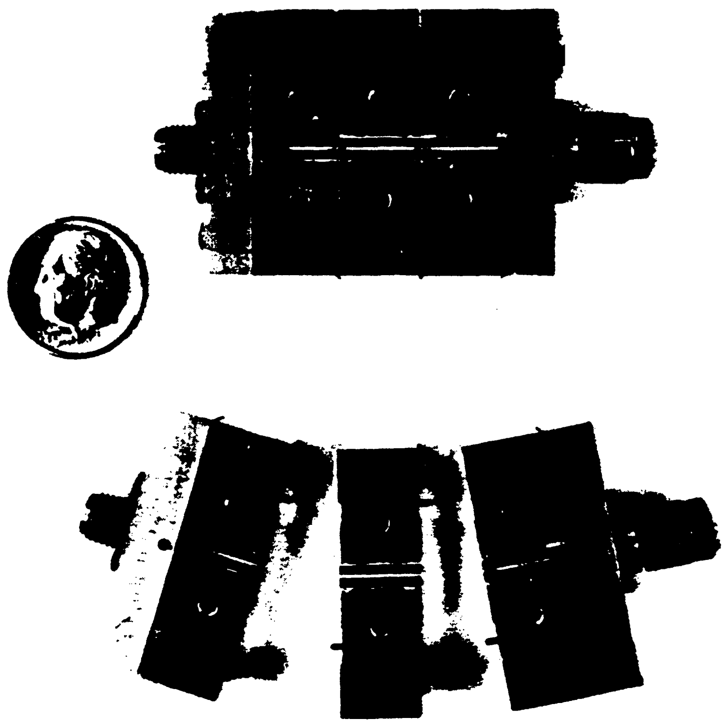

Figure H.3: K-connector multi-line test fixture used for testing microstrip/microstrip interconnects.

the straps were removed and then replaced with new ones. A minimum amount of weld voltage and pressure were used.

Note that none of the repeatability cycling could be performed without removing the fixture from the coaxial measurement ports; hence, coax/coax connection uncertainties are included in all the results. In the microstrip fabrication/mounting experiment, three uncertainty factors are present simultaneously: coax/coax connections, coax/microstrip connections, and the variations in the carrier mounted microstrip lines.

Two automatic network analyzers were employed for the testing; an HP8510 ANA for .045 to 26.5 GHz measurements, and an HP8409 ANA with an in-house frequency extension system for Ka-Band (26.5 to 40GHz) measurements. The HP8510 ANA was operated in step mode with 201 calibration points, and the Ka-Band ANA was operated in phase-locked mode with 51 calibration points.

Calibration was achieved using either 7mm or K-conn. coaxial standards, depending on the fixture. After testing, the S-parameters for each of the measurement trials were stored in separate files so that data processing could be carried out later.

DISCUSSION OF RESULTS

Due to the large volume of data generated, only a sample of the results can be presented. Therefore, we will limit the discussion to the uncertainties in S_{21} (the forward transmission coefficient) due to the repeatability issues discussed above.

Figure H.4a shows the coax/microstrip repeatability measurements made with the 7mm test fixture. At a glance this connection looks very repeatable, yet with some data processing we can get a closer look. A program was written that allows for statistical computations to be made using the data stored on file. With this program, an average set of S-parameters was computed for each experiment. Figure H.4b shows the results of normalizing the S_{21} data to the average S-parameters for the coax/microstrip test. This was achieved by performing a complex division between the S-parameters from each trial and the average S-parameters. After normalization, it is easy to see the variations in phase and magnitude resulting from the repeated connections. For the 7mm coax/microstrip connection, the repeatability in S_{21} is quite good and can be held to within a range of .1dB(+/-.05dB) in amplitude and 1 degree (+/-.5deg.) in phase.

Standard deviation data for each experiment was also computed as a function of frequency. This was done separately for the magnitude and phase angles of the S-parameters using the following formula:

$$\text{Std.Deviation} = s = \sqrt{\frac{\sum x_i^2 - \frac{(\sum x_i)^2}{N}}{N-1}} \qquad \text{(H.1)}$$

where

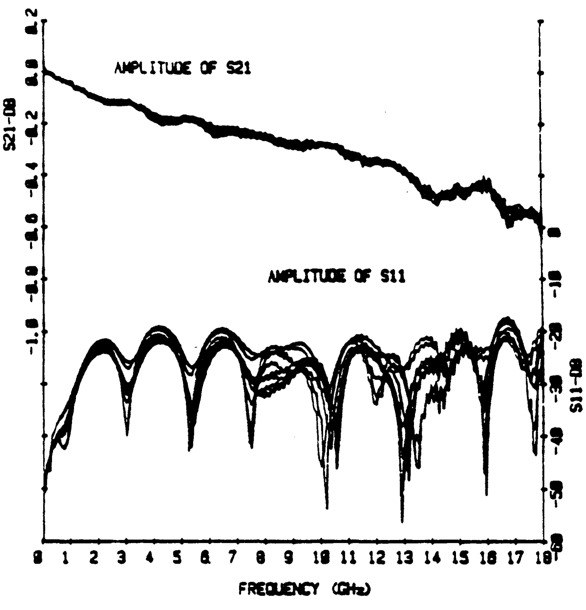

a) Amplitude measurements

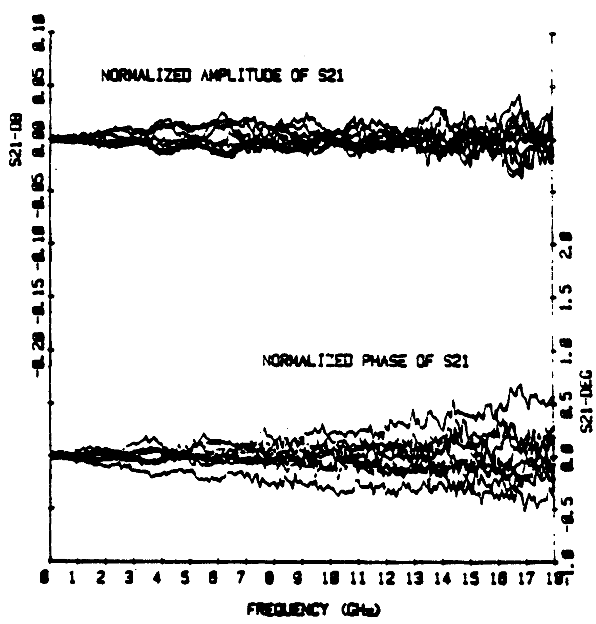

b) S_{21} results normalized to average S-parameters.

Figure H.4: 7mm Coax/microstrip connection repeatability measurements.

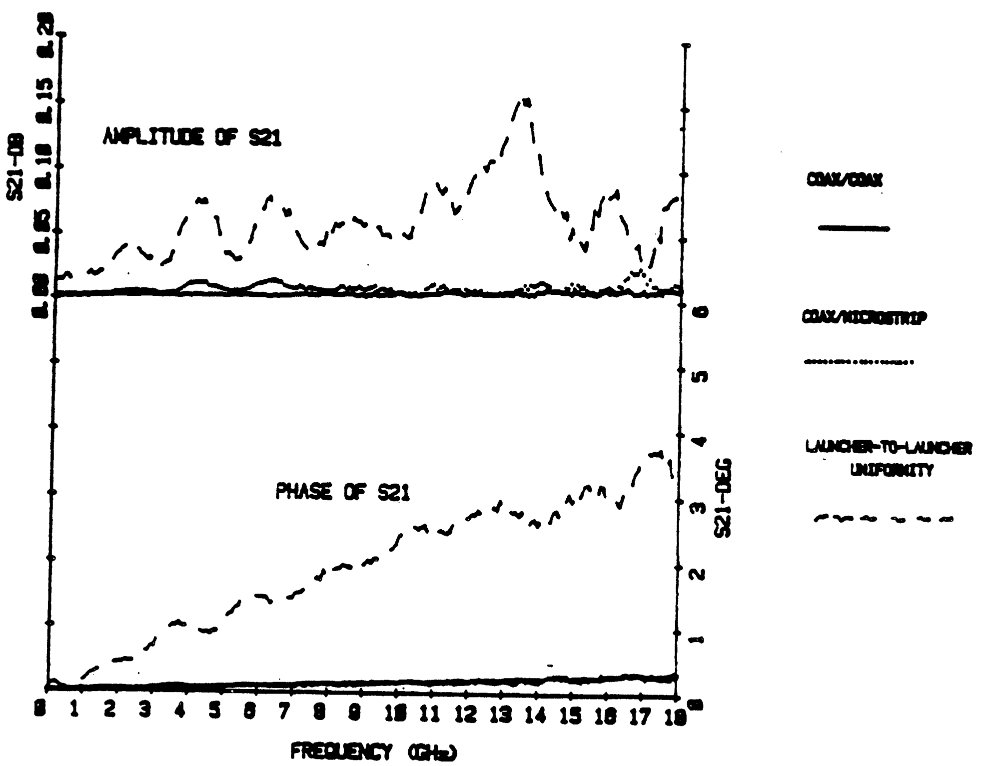

Figure H.5: Standard deviation data for experiments with 7mm fixture

N = number of trials

x_i = magnitude or phase of a particular S-parameter (at a given frequency) for trial i

The standard deviation data on S_{21} for the three experiments performed with the 7mm fixture(Figure H.5), shows clearly that electrical variations between Eisenhart launchers can be significant. This is not surprising, since the center pin on each is individually tuned to achieve good performance. On the other hand, the standard deviation resulting from the coax/microstrip test was almost as good as that from the coax/coax test; thus, the uncertainty contribution to S_{21} caused by the 7mm coax/microstrip connection errors is finite but minimal.

The normalized S_{21} data for the k-connector coax/microstrip experiment (Figure H.6) displays similar repeatability performance to the 7mm coax/microstrip connection to 18 GHz. The approximate range in amplitude is .1dB to 26.5 GHz and .2dB to 40 GHz, and the range in phase is 2 degrees to 26.5 GHz, and 8 degrees to 40GHz. For the microstrip fabrication/mounting experiment (Figure H.7) the amplitude and phase deviation were about the same if one ,apparently erroneous, measurement in the .045 to 26.5GHz band is neglected. The connection repeatability of the microstrip/microstrip interconnects (Figure H.8) was considerably worse than the coax/microstrip connections, with ranges in amplitude of .5dB to 26.5 GHz and .6dB to 40 GHz, and in phase of 10 degrees to 26.5 GHz and as much as 15 degrees to 40 GHz.

A good summary of the K-conn. fixture repeatability experiments is provided by the standard deviation plots of Figure H.9. Admittedly, some of the results (e.g. launcher-to-launcher uniformity) are not entirely conclusive due to the limited number of trials performed, however, some definite trends are apparent.

The erroneous measurement in the fabrication/mounting experiment (Figure H.7) caused the standard deviation in phase below 26.5 GHz to appear much worse than it should. This is supported by the comparatively good standard deviation observed in the 26.5 to 40 GHz band, which follows the coax/microstrip repeatability curve closely. Hence, the measurement uncertainties due to microstrip fabrication/mounting variations are not believed to be a major concern. On the other hand, although the K-conn. launchers are not individually tuned, Figure H.9 indicates significant deviations in S_{21} between the three sets of launchers tested. Consequently, for accurate de-embedding work, launcher-to-launcher uniformity should not be assumed. The standard deviation data for the coax/microstrip and microstrip/microstrip experiments reinforces the S_{21} data of Figures H.6 and H.8. In terms of the TSD connection alternatives discussed in Section 5.3 these results clearly favor an approach relying on repeatable coax/microstrip connections rather

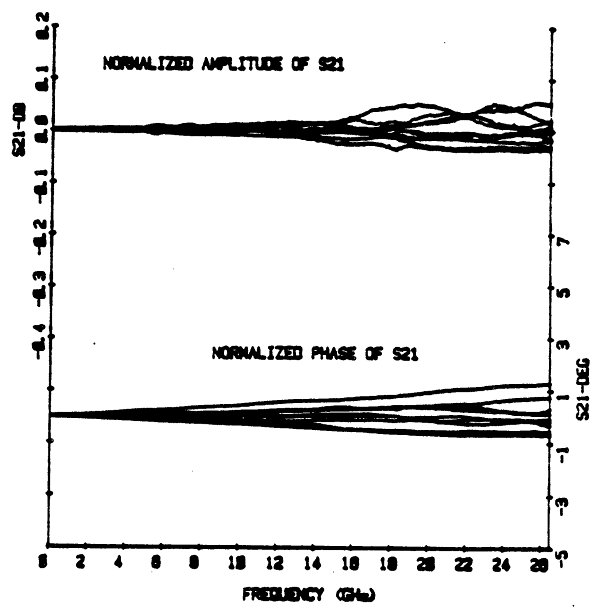

a) Measurements from .045-26.5 GHz

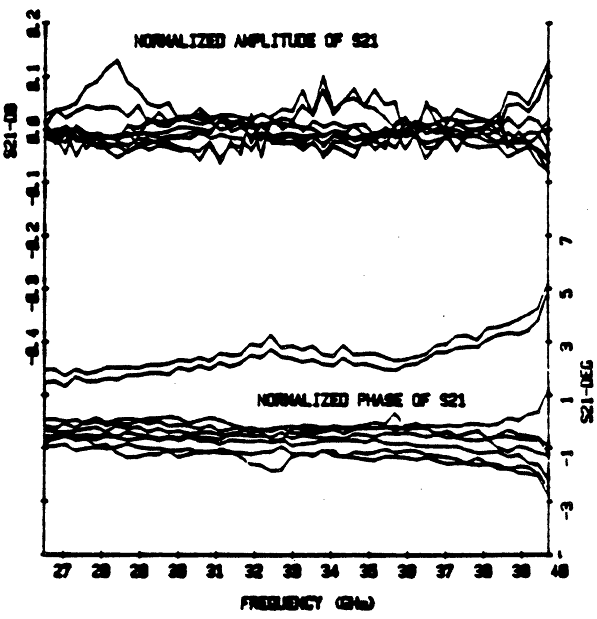

b) Measurements from 26.5-40 GHz

Figure H.6: K-connector coax/microstrip repeatability measurements normalized to average.

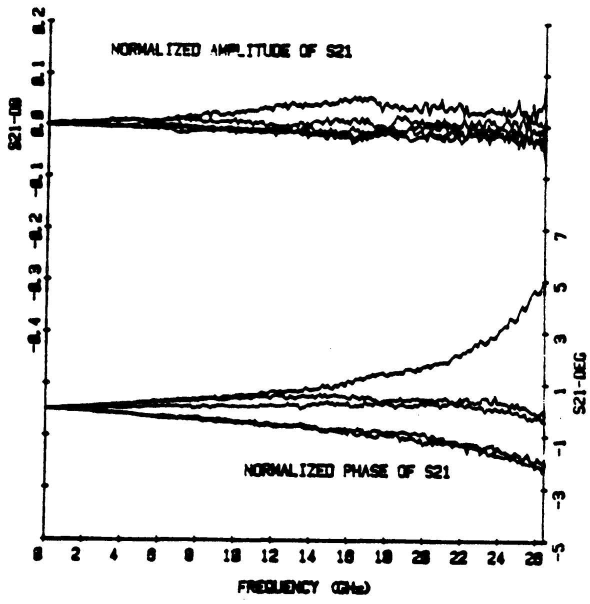

a) Measurements from .045-26.5 GHz

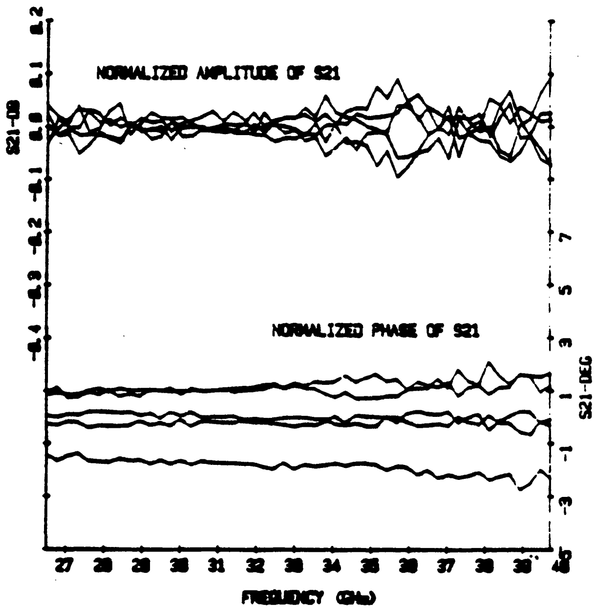

b) Measurements from 26.5-40 GHz

Figure H.7: Microstrip fabrication/mounting repeatability measurements normalized to average.

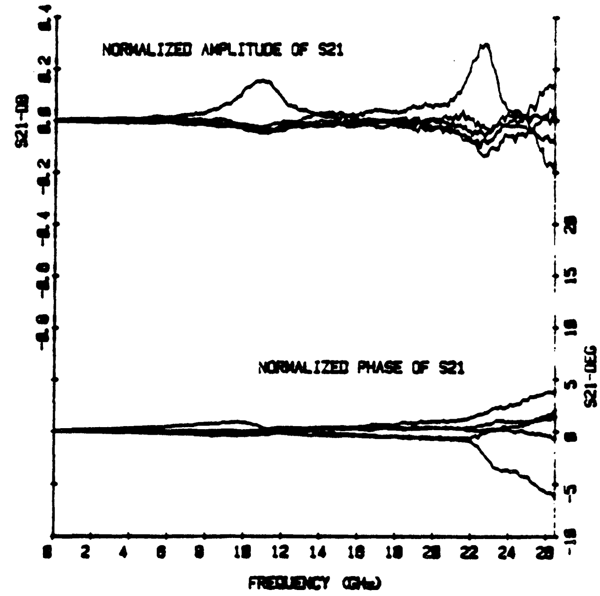

a) Measurements from .045-26.5 GHz

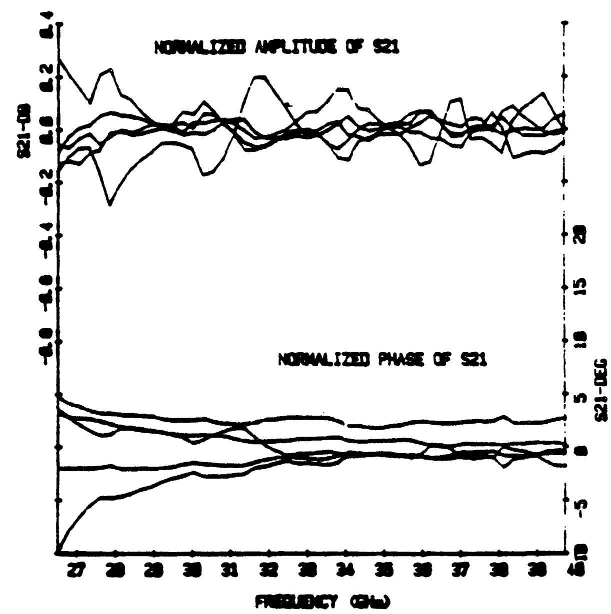

b) Measurements from 26.5-40 GHz

Figure H.8: Microstrip/microstrip interconnect repeatability measurements normalized to average.

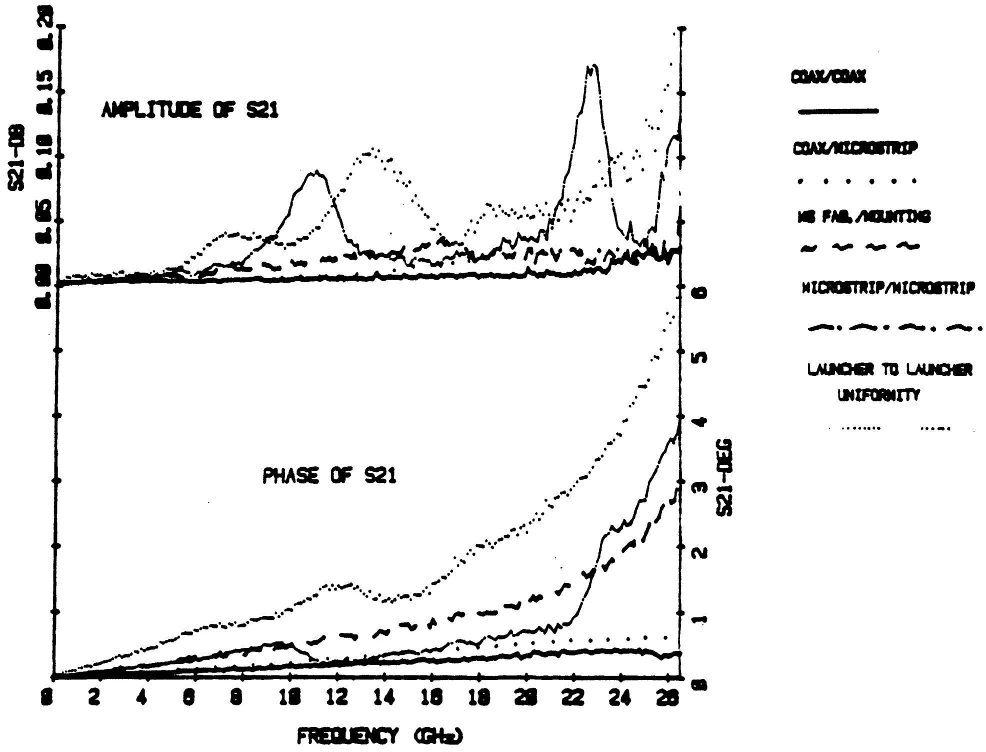

a) Results for experiments conducted from .045-26.5 GHz

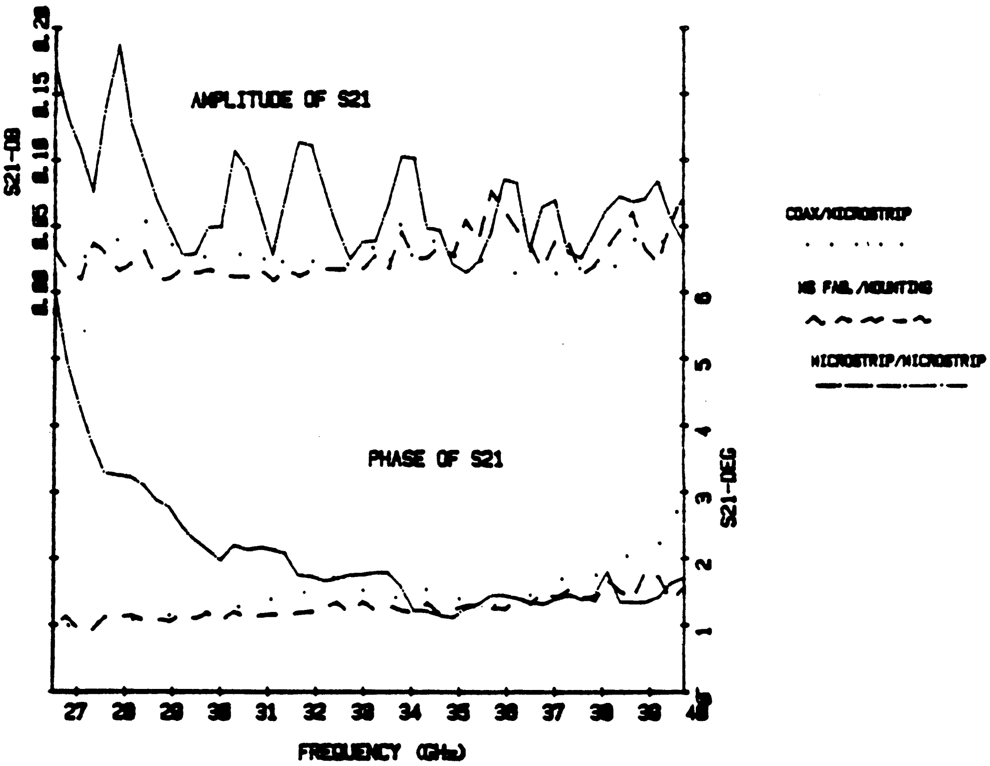

b) Results for experiments conducted from 26.5-40 GHz

Figure H.9: Standard deviation data for experiments with K-connector fixture.

than microstrip/microstrip interconnects for the hardware tested.

BIBLIOGRAPHY

BIBLIOGRAPHY

[1] T.C. Edwards, *Foundations for Microstrip Circuit Design*, John Wiley and Sons, 1981.

[2] K. C. Gupta, R. Garg, and I. J. Bahl, *Microstrip Lines and Slotlines*, Artech House, 1979.

[3] K. C. Gupta, R. Garg, R. Chadha,*Computer-Aided Design of Microwave Circuits*, Artech House, 1981.

[4] Y. C. Shih, T. S. Chu, and T. Itoh, "Comparative Study of Mode Mode Matching Formulations for Microstrip Discontinuity Problems", *1985 IEEE MTT-S Digest*, pp. 435-438.

[5] P. Katehi and N. Alexopoulos, "Microstrip Discontinuity Modeling For Millimetric Integrated Circuits", *1985 IEEE MTT-S Digest*, pp. 571-573.

[6] P. Katehi and N. Alexopoulos,"Frequency-Dependent Characteristics of Microstrip Discontinuities in Millimeter-wave Integrated Circuits", *IEEE Trans. Microwave Theory Tech.* vol. MTT-33 No. 10, Oct. 1985, pp. 1029-1035.

[7] R. Jansen and N. Koster, "A Unified CAD Basis for the Frequency Dependent Characteristics of Strip, Slot, and Coplanar MIC Components", *11th European Microwave Conference*, 1971 pp. 682-687.

[8] R. Jansen, "Hybrid Mode Analysis of End Effects of Planar Microwave and Millimeter-Wave Transmission Lines", *IEEE Proc.*, Vol 128, April 1981, pp. 77-86.

[9] N. Koster and R. Jansen, "The Equivalent Circuit of the Asymmetrical Series Gap in Microstrip and Suspended Substrate Lines", *IEEE Trans. Microwave Theory Tech.*, August 1982, pp. 1273-1279.

[10] T. Itoh,"Analysis of Microstrip Resonators", *IEEE Trans. Microwave Theory Tech.*, vol MTT-24 1974, pp 946-951.

[11] J. Rautio, *A Time-Harmonic Electromagnetic Analysis of Shielded Microstrip Circuits*, Ph.D. dissertation, Syracuse University, August 1986.

[12] J. Rautio, "An Electromagnetic Time-Harmonic Analysis of Shielded Microstrip Circuits",*IEEE Trans. Microwave Theory Tech.*, vol. MTT-35, No. 8, pp726-729.

[13] N. R. Franzen and R. A. Speciale, "A New Procedure for System Calibration and Error Removal in Automated S-Parameter Measurements", *5th European Microwave Conference*,1975, pp. 69-73.

[14] L. Dunleavy and P. Katehi, "Repeatability Issues for De-embedding Microstrip Discontinuity S-parameter Measurements By the TSD Technique" *Automatic RF Techniques Group (ARFTG) Conf. Dig.* June 1986.

[15] L. Dunleavy and P. Katehi, "Eliminate Surprises When De-embedding Microstrip Launches", *Microwaves & RF* August 1987, pp117-122.

[16] R. Collin, *Field Theory of Guided Waves* McGraw Hill 1960, p287

[17] R. Mittra ed., *Computer Techniques for Electromagnetics*, Pergamon Press 1973.

[18] R.Harrington,*Field Computation by Moment Methods* R. Krieger Publishing 1968.

[19] J. Stratton, *Electromagnetic Theory*, McGraw Hill 1941,p. 250.

[20] J.C. Maxwell, *A Treatise on Electricity and Magnetism* 3rd. ed., vol. 1,New York: Dover 1954 pp 296-297.

[21] E. Denlinger, "A Frequency Dependent Solution for Microstrip Transmission Lines", *IEEE Trans. Microwave Theory Tech.* vol. MTT-19, Jan. 1971, pp30-39.

[22] E. Yamashita, Variational Method for the Analysis of Microstrip-like Transmission Lines" *IEEE Trans. Microwave Theory Tech.*, vol. MTT-16, Aug. 1968, pp529-535.

[23] C.T. Tai, *Dyadic Green's Functions in Electromagnetic Theory* , Intext Educational Publishers 1971.

[24] A. Sommerfeld, *Partial Differential Equations in Physics* vol. VI, Academic Press,.1949, pp257-258.

[25] C. Chi and N. Alexopoulos, "Radiation by a Probe Through a Substrate" *IEEE Trans. Antennas Propagat.* vol. AP-34, Sept. 1986, pp 1080-1091.

[26] R. Harrington, *Time-Harmonic Electromagnetic Fields*, McGraw Hill 1961, pp.111-112.

[27] J. Brews, "Characteristic Impedance of Microstrip Lines", *IEEE Trans. Microwave Theory Tech.* vol. MTT-35, January 1987, pp 30-33.

[28] W. Getsinger, "Measurement and Modeling of the Apparent Characteristic Impedance of Microstrip" *IEEE Trans. Microwave Theory Tech.* vol. MTT-31, August 1983, pp 624-632.

[29] R. Jansen and H. Koster, "New Aspects Concerning the Definition of Microstrip Characteristic Impedance as a Function of Frequency", *1982 IEEE MTT-S Digest*, pp 305-307.

[30] W. Getsinger, "Microstrip Characteristic Impedance", *IEEE Trans. Microwave Theory Tech.* vol. MTT-27, April 1979, p. 293.

[31] B. Bianco et. al., "Some Considerations About the Frequency Dependence of the Characteristic Impedance of Uniform Microstrips", *IEEE Trans. Microwave Theory Tech.* vol. MTT-26, March 1978, pp182-185.

[32] P. Katehi, "A Generalized Method for the Evaluation of Mutual Coupling in Microstrip Arrays", *IEEE Trans. Antennas Propagat.* Vol. AP-35, Feb. 1987, pp 125-133.

[33] A.H. Stroud *Approximate calculation of Multiple Integrals*, Prentice Hall, New Jersey 1971, p255.

[34] C. Gerald, *Applied Numerical Analysis* Adison-Wesley 1978, p 509.

[35] G. Golub and C. Van Loan, *Matrix Computations*, John Hopkins University Press, 1983, pp26-27.

[36] J. Fitzpatrick, "Error Models for Systems Measurement",*Microwave Journal*, May 1978, pp. 63-66.

[37] E. W. Strid and K. R. Gleason, "Calibration Methods for Microwave Wafer Testing", *1984 IEEE MTT-S Digest*, pp. 93-97.

[38] B. Easter,"The Equivalent Circuit of Some Microstrip Discontinuities", *IEEE Trans. Microwave Theory Tech.*, vol. MTT-23, No. 8, August 1975, pp. 655-660.

[39] V. Rizzoli, "A General Approach to the Resonance Measurement of Asymmetric Microstrip Discontinuities", *1980 IEEE MTT-S Digest*, pp. 422-424.

[40] M. Kirschning, R. Jansen, and N. Koster, "Measurement and Computer-Aided Modeling of Microstrip Discontinuities by an Improved Resonator Method", *1983 IEEE MTT-S Digest*, pp. 495-497.

[41] B. Easter, A. Gopinath, and I. Stephenson, "Theoretical and Experimental Methods for Evaluating Discontinuities in Microstrip", *Radio and Elec. Engr.*, Vol. 48, No. 1/2, January/February 1978, pp. 73-84.

[42] H. F. Pues and V. Capelle, "Computer-Aided Experimental Characterization of Microstrip-to-Coaxial Transitions", *14th European Microwave Conference*, 1984, pp. 137-141.

[43] R. Lane, "De-Embedding Device Scattering Parameters", *Microwave Journal*, August 1984, pp. 149-156.

[44] N. R. Franzen and R. A. Speciale, "A New Procedure for System Calibration and Error Removal in Automated S-Parameter Measurements", *5th European Microwave Conference*,1975, pp. 69-73.

[45] B. Bianco et. al. "Launcher and Microstrip Characterization" *IEEE Trans. on Instrum. and Meas.* Vol. IM 25, NO. 4, Dec. 1976, pp. 320-323.

[46] G. Engen and C. Hoer, "Thru-Reflect-Line: An improved Technique for Calibrating the Six-Port Automatic Network Analyzer". *IEEE Trans. Microwave Theory Tech.* vol. MTT-27, No. 12, Dec. 1979, pp 987-993.

[47] M. Maury, S. March, and G. Simpson, "LRL Calibration of Vector Automatic Network Analyzers". *Microwave Journal* May 1987, pp. 387-391.

[48] G. Fillipson, "Characterization of Microstrip Fixtures, A Broad Band Model for a Microstrip Connector", National Defense Research Institute (Linkoping, Sweden), FOA Report no.C30338-E (AD/NASA no. N84-21824/7), Sept. 1983,

[49] D. Brubaker, "Measure S-parameters With the TSD Technique", : *Microwaves & RF*, Nov. 1985, pp. 97-102.

[50] M. Hines and H. Stinehelfer, "Time-Domain Oscillographic Microwave Network Analysis Using Frequency-Domain Data", *mtt* , vol. MTT-22, No.3, March 1974, pp. 276-282.

[51] H.E. Stinehelfer, "Discussion of De-embedding Techniques Using Time-Domain Analysis", *IEEE Proceedings*, Vol. 74, No. 1, Jan 1986. pp 90-94.

[52] E. K. da Silva and M. K. McPhun, "Calibration of an Automatic Network Analyser Using Transmission Lines of Unknown Characteristics Impedance Loss and Dispersion", *Radio and Elec. Engr.*, Vol. 48, No. 5, May 1978, pp. 227-234.

[53] R. Bauer, and P. Penfield, "De-embedding and Unterminating", *IEEE Trans. Microwave Theory Tech.*, Vol. MTT-22, No. 5, March 1974, pp. 310-312.

[54] D.E. Peck and D. F. Peterson,"A Measurement Method for Accurate Characterization and Modeling of MESFET Chips", *1981 IEEE MTT-S Digest*, pp. 310-312.

[55] D.E. Peck,"Measurement Methods for Accurate Microwave Characterization and Modeling of MESFET Chips", Technical Report AFWAL-TR-84-1177, January 1985.

[56] P. R. Shepherd and P. Daly, "Modeling and Measurement of Microstrip Transmission Line Structures", 1985 IEEE MTT-S Digest, pp. 679-682.

[57] R.L. Eisenhart,"A Better Microstrip Connector", *1978 IEEE MTT-S Digest*, pp. 318-320.

[58] E. Hassan "Field Solution, Polarization, and Eigenmodes of Shielded Microstrip Transmission Line", *IEEE Trans. Microwave Theory Tech.*, vol. MTT-34 No. 8, August 1986, pp845-851.

[59] E. Yamashita and K. Atsuki, "Analysis of Microstrip-Like Transmission Lines by Nonuniform Discretization of Integral Equations," *IEEE Trans. Microwave Theory Tech.*, vol. MTT-24, pp. 195-200.

[60] L. Pincherle, "Electromagnetic Waves in Metal Tubes Filled Longitudinally with Two Dielectrics,"' *Phys. Rev*, 66, No. 5, pp. 118-130, 1944.

[61] T. Weller, University of Michigan, Personal Communication March 2, 1988.

[62] Mr. Jim Schellenberg, Hughes Aircraft Company, Personal communication June 14, 1987.

[63] J. Snook, "Substrates for Hybrid Microelectronic Applications", *Microwave System News and Comm. Tech.*, February 1988, pp26-31.

[64] R. Jansen, and H. Koster, "Accurate Results on the End Effect of Single and Coupled Lines for Use in Microwave Circuit Design " *A.E.U.* Band 34 1980, pp 453-459.

[65] G.N Watson,*A Treatise on the Theory of Bessel Functions* 2nd ed., Cambridge University Press 1980, p21.

A NEW METHOD FOR DISCONTINUITY ANALYSIS IN SHIELDED MICROSTRIP

L.P. Dunleavy and P.B. Katehi

The Radiation Laboratory

University of Michigan, Ann Arbor, MI

Abstract-. A new integral equation method is described for the accurate full-wave analysis of shielded microstrip discontinuities. The integral equation is derived by an application of reciprocity theorem, then solved by the method of moments. Numerical and experimental results are presented for open-end and series gap discontinuities, and a coupled line filter.

I. INTRODUCTION

The development of more accurate microstrip discontinuity models, based on full-wave analyses, is key to improving microwave and millimeter-wave circuit simulations and reducing lengthy design cycle costs. In most applications, radiation and electromagnetic interference are avoided by enclosing microstrip circuitry in a shielding cavity (or housing) as shown in Figure 1. The effect of the shielding is significant, and requires accurate modeling, at high frequencies. Shielding effects are not adequately accounted for in the discontinuity models used in most available microwave CAD software.

To address these inadequacies, a new method was developed for the full-wave analysis of discontinuities in shielded microstrip [2]. This method accurately takes into account the effect of the shielding enclosure. The theoretical contribution, as compared to previous work [3]-[5], is in the novel way that reciprocity theorem, the method of moments, and transmission line theory are combined to solve for discontinuity parasitics. As illustrated in Figure 2, the coaxial feed is modeled using an equivalent magnetic "frill" current [6,7]. To the authors' knowledge, this is the first time that the frill current approach has been applied to microstrip circuit problems.

To demonstrate the method, numerical results are presented for open-end and series gap discontinuities, and a four resonator coupled line filter. These results are compared to other full-wave analyses, to data from *Super Compact* and *Touchstone* [1], and to measurements. The measurements were performed using a variation of the TSD de-embedding technique [8,9].

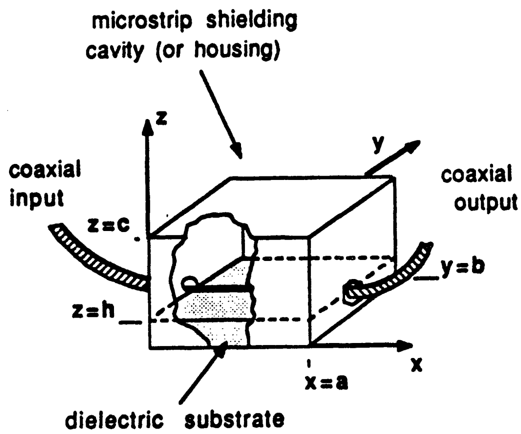

Figure 1: In most practical designs, microstrip circuitry is enclosed in a shielding cavity whose effects must be accurately modeled at high frequencies.

II. SUMMARY OF THEORETICAL METHOD

In the theoretical derivation [2], an application of reciprocity theorem results in an integral equation relating the magnetic current source $\bar{M}_s$, and the electric current on the conducting strips $\bar{J}_s$, to the electromagnetic fields inside the cavity. A Galerkin's implementation of the method of moments is employed by first dividing the strips into N_s subsections. The current is then expanded according to [1]

$$\bar{J}_s = \psi(y) \sum_{p=1}^{N_s} I_p \alpha_p(x)\,\hat{x}\,. \tag{1}$$

[1] *Super Compact* and *Touchstone* are microwave CAD software packages available from Compact Software and EESOF respectively.

0149-645X/88/0000-0701$01.00 © 1988 IEEE

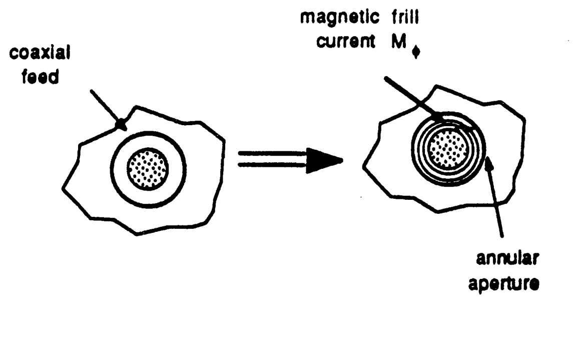

Figure 2: The coaxial feed is represented by an equivalent magnetic frill current $\bar{M}_s = M_\phi \hat{\phi}$; this is used as the excitation mechanism for computing the microstrip current.

where $\psi(y)$ describes the variation of the longitudinal current in the transverse (i.e. y) direction, and $\alpha_p(x)$ are sinusoidal subsectional basis functions.

The resulting equation may be expressed as

$$\sum_{p=1}^{N_s} \left[\int\int_{S_p} \bar{E}_q(x = h) \cdot \psi(y)\, \alpha_p(x)\, \hat{x} ds \right] I_p = \int\int_{S_f} \bar{H}_q \cdot \bar{M}_s ds \qquad (2)$$

where S_p is the surface area of the p^{th} subsection, S_f is the surface of the coaxial aperture, and $\bar{E}_q, \bar{H}_q$ are the electric and magnetic fields respectively, associated with a test current $\bar{J}_q$ existing over the q^{th} strip subsection.

We may express (2) by the matrix equation

$$[\mathbf{Z}]\,[\mathbf{I}] = [\mathbf{V}] \ . \qquad (3)$$

Here, [Z] is the impedance matrix, [V] is the excitation vector and [I] is the unknown current vector comprised of the complex coefficients I_p.

Finally, after evaluating the elements of [Z] and [V], the matrix equation is solved to compute the current distribution. Based on the current, transmission line theory is used to derive scattering parameters, and (if desired) an equivalent circuit model, to characterize the discontinuity [1,2].

III. RESULTS

An open-end can be represented by an effective length extension L_{eff}, by a shunt capacitance c_{op}, or by the associated reflection coefficient Γ_{op} (= S_{11}). The plot of Figure 3 compares L_{eff} results to those of Jansen et. al. [3] and Itoh [4]. Also shown is the cut-off frequency f_c, which is defined as the lowest frequency where non-evanescent waveguide modes can exist within the cavity. The new results are almost identical to those obtained by Jansen et. al. for frequencies above 8 GHz, but show a reduced value for lower frequencies.

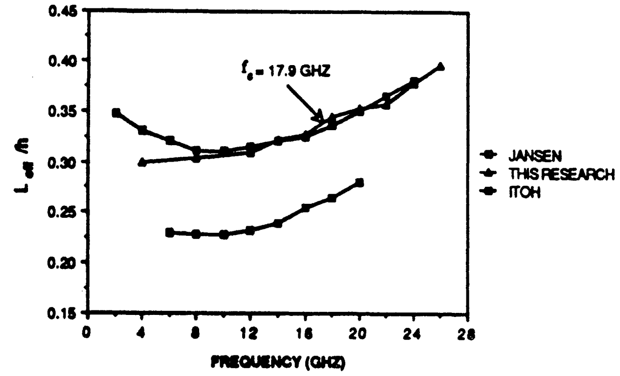

Figure 3: Effective length extension of a microstrip open-end discontinuity, as compared to results from other full-wave analyses (ϵ_r = 9.6, W/h = 1.57, b = .305″, c = .2″, h = .025″).

The results shown in Figure 4 illustrate that shielding effects are significant at high frequencies. The normalized open-end capacitance c_{op} is plotted for three different cavity sizes. The results show that reducing the cavity size raises f_c (as expected), and it lowers the value of c_{op}. For comparison, data obtained from *Super Compact* and *Touchstone* are included.

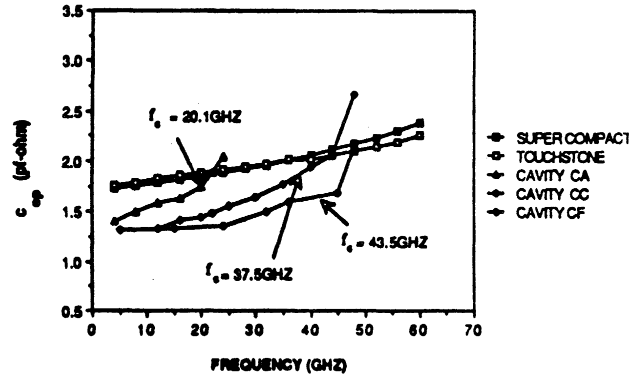

Figure 4: A comparison of the normalized open-end capacitance for three different cavity sizes shows that shielding effects are significant at high frequencies (ϵ_r = 9.7, $W = h$ = .025″; cavity CA: b = c = .25″, cavity CC: b = c =.01″, cavity CF: b = c =.075″).

In the remaining examples, numerical results from the new method are compared to measurements. Figure 5 shows results for the angle of S_{11} of an open-end, and Figure 6 contains results for the magnitude of the transmission coefficient ($/S_{21}/$) for a series gap discontinuity. In both cases, the agreement between the numerical and experimental data is very good.

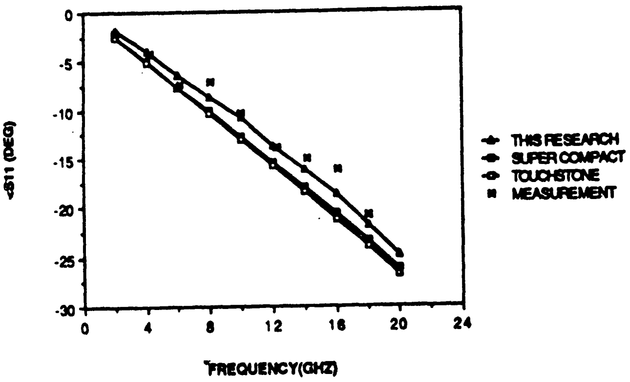

Figure 5: Numerical and measured results show good agreement for the angle of S11 of an open circuit (ϵ_r = 9.7, W = h =.025", b = c =.25").

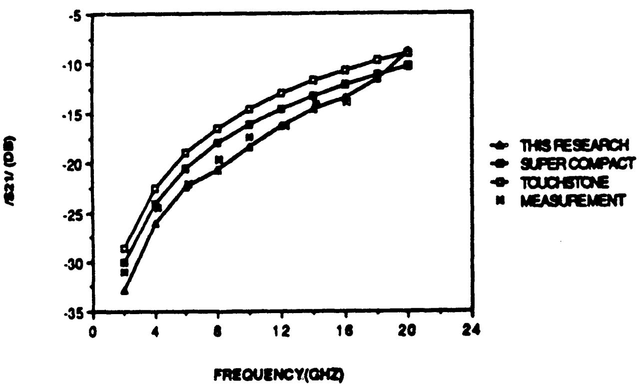

Figure 6: Good agreement with measurements has also been obtained for series gap discontinuities. Shown here is the magnitude of S_{21} for a series gap with a 9 mil gap spacing (ϵ_r = 9.7,W = h = .025", b = c =.25").

Finally, consider the four resonator filter of Figure 7. Numerical results for the magnitude and phase of S_{21}, shown in Figure 8, demonstrate excellent agreement with measurements for frequencies below the cutoff frequency f_c. Above cutoff, the filter measurement is distorted due to waveguide moding within the test fixture.

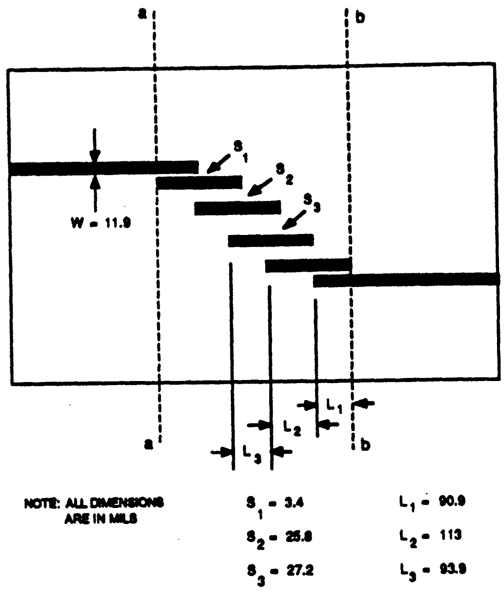

Figure 7: Numerical and experimental results are compared below for this 4 resonator filter (ϵ_r = 9.7, h = .025", b = .4", c = .25").

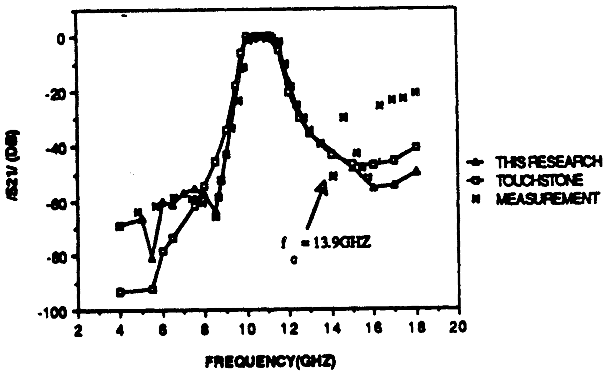

a. Amplitude of S_{21}

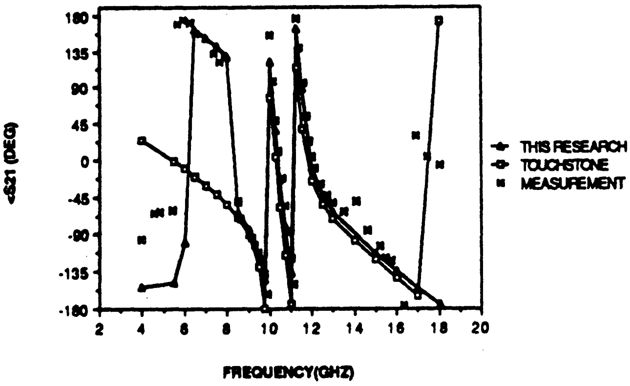

b. Phase of S_{21}

Figure 8: Results for transmission coefficient S_{21} of 4 resonator filter.

IV. CONCLUSIONS

A new analysis method has been described for shielded microstrip discontinuities. Results from this method have demonstrated good agreement with measurements and other numerical results. This method is useful for the evaluation of existing discontinuity models, for the analysis of cases where existing solutions fail –such as when shielding effects are significant–, and for the development of new discontinuity models with improved accuracy for high frequency applications.

ACKNOWLEDGEMENTS

The authors thank Mr. Ed Watkins, Mr. Jim Schellenberg, and Mr. Marcel Tutt for their contributions to this work. This work was primarily sponsored by The National Science Foundation (Contract. No. ECS -8602530). Partial sponsorship was also provided by the Army Research Office (Contract No. DAAL03-87-K-0088) and the Microwave Products Division of Hughes Aircraft Co.

REFERENCES

[1] P. Katehi and N. Alexopoulos,"Frequency Dependent Characteristics of Microstrip Discontinuities in Millimeter-wave Integrated Circuits", *IEEE Trans. Microwave Theory Tech.* Vol. MTT-33 No. 10, Oct. 1985, pp. 1029-1035.

[2] L. Dunleavy and P. Katehi, "A New Method for Discontinuity Analysis in Shielded Microstrip: Theory and Computational Considerations", In preparation.

[3] R. Jansen, and N. Koster, "Accurate Results on the End Effect of Single and Coupled Lines for Use in Microwave Circuit Design " *A.E.U.* Band 34 1980, pp 453-459.

[4] T. Itoh,"Analysis of Microstrip Resonators", *IEEE Trans. Microwave Theory Tech.*, Vol Mtt-24 1974, pp 946-951.

[5] J. Rautio, "An Electromagnetic Time-Harmonic Analysis of Shielded Microstrip Circuits",*IEEE Trans. Microwave Theory Tech.*, Vol. MTT-35, No. 8, pp726-729.

[6] C. Chi and N. Alexopoulos, "Radiation by a Probe Through a Substrate" *IEEE Trans. Antennas Propagat.* vol. AP-34, Sept. 1986, pp 1080-1091.

[7] R. Harrington, *Time-Harmonic Electromagnetic Fields*, McGraw Hill 1961, pp.111-112.

[8] N. Franzen and R. Speciale, "A New Procedure for System Calibration and Error Removal in Automated S-Parameter Measurements", *5th European Microwave Conference*, pp. 69-73.

[9] L. Dunleavy and P. Katehi, "Repeatability Issues for De-embedding Microstrip Discontinuity S-parameter Measurements By the TSD Technique" *Automatic RF Techniques Group (ARFTG) Conf. Dig.* June 1986.

Shielding Effects in Microstrip Discontinuities

Submitted to IEEE Trans. on Microwave Theory and Tech. - April 1988

L.P. Dunleavy* and P.B. Katehi
Radiation Laboratory
Dept. of Electrical Engineering and Computer Science
The University of Michigan
1301 Beal Avenue
Ann Arbor, MI 48109-2122

Abstract-.

As an application of the theoretical method described in a companion paper, numerical and measured results are presented for open-end and series gap discontinuities, and a coupled line filter. Comparisons are also made to commercially available CAD package predictions. The results verify the accuracy of the new theoretical method and demonstrate the effects of shielding on discontinuity behavior. The experimental techniques used, which involve the thru-short-delay de-embedding approach, are also explained.

* L.P. Dunleavy is now with Hughes Aircraft Company.

I. INTRODUCTION

This is the second of two papers concerned with the study of shielding effects in microstrip discontinuities. The companion paper [1] develops a new theoretical method for the full-wave analysis of shielded microstrip discontinuities. The effects of shielding are important in two situations. The first is when the frequency approaches or is above the cutoff frequency for higher order mode propagation. The second occurs when the metal enclosure (Figure 1) is physically close to the circuitry (proximity effects). These effects have not been adequately studied in the past, and are not accounted for in the discontinuity models in most available CAD packages.

In addition to improved theoretical methods, there is a great need for experimental data. Published experimental data on microstrip discontinuites is very limited, especially for high microwave (above X-band) and millimeter-wave frequencies. Such measurements are not trivial, but are essential for verification of the theoretical method. This need motivated the experimental study discussed here.

This paper uses the previously described method [1] to study the effects of the shielding cavity on the behavior of one- and two-port discontinuities including open-ends, series gaps and parallel coupled line filters. Comparisons are made to measurements, to available data from other full-wave analyses, and to commercially available CAD packages.

II. EXPERIMENTAL TECHNIQUES

Measured data on microstrip discontinuities is very limited, particularly at higher frequencies (above 10GHz). This is due to the difficulties involved with performing accurate microstrip measurements. In order to measure a microstrip circuit, it is generally mounted in a test fixture with either coax-to-microstrip or waveguide-to-microstrip transitions. The main difficulties associated with such measurements are the separation of test fixture parasitics from measurements, called de-embedding and the non-repeatability of microstrip connections.

This section explains the experimental techniques used for this study, and addresses the connection repeatability issues that pertain to the measurements.

A. De-embedding Approach

The measurement approach of this study employs Automatic Network Analyzer (ANA) techniques in conjunction with the thru-short-delay (TSD) method for de-embedding the effects of the test fixture from the measurements. The test fixture that was used is shown in Figure 2. The fixture employs a pair of 7mm "Eisenhart" coax-to-microstrip transitions [2]. The shielding is provided by placing U-shaped covers on top of the microstrip carriers. This forms a cavity similar to Figure 1. The instrumentation used for the measurements was an HP8510 ANA.

The test fixture invariably introduces unwanted parasitics and a reference plane shift to the measurements. These effects must be accurately accounted for and removed from the measurements, or incorporated into the ANA system error model. Conventional ANA calibration, which uses a short circuit, an open circuit, and a matched load is not easily performed in microstrip since these calibration standards are much more difficult to realize in microstrip.

The process for removing test fixture effects is called de-embedding and consists of two steps: 1) fixture characterization, and 2) the extraction of fixture parasitics. Through de-embedding, the effective calibration reference planes are moved from the coaxial or waveguide ANA test ports to microstrip test ports within the fixture.

A comparison of various de-embedding techniques [3] lead to the choice of the TSD technique for the experimental study. This approach was selected over the alternatives considered because the standards used for fixture characterization are the easiest to realize in microstrip, and because the connections to these standards can be made in the same way as the connections made to discontinuity test circuits. In the TSD technique, two-port measurements made on a thru (zero length delay) line, a "short" circuit, and a delay line provide enough information to characterize the fixture. Since the original paper [4], it has been pointed out that the "short" implied in TSD, need not be perfect. In fact, any highly reflecting standard may be used in its place [5,6]. The only requirement is that the same reflection coefficient Γ_s must be presented to both microstrip test ports.

This measurement approach provides for the measurement of the effective dielectric constant, the reflection coefficient of open-end discontinuities, and the two-port scattering parameters of series gaps and coupled line filters. In the present implementation of TSD de-embedding, an open-ended microstrip line is used in place of the short as the reflection standard. Measurements of microstrip effective dielectric constant ϵ_{eff}, and the reflection coefficient of the open-end Γ_{op} are obtained as byproducts of the fixture characterization procedure. Once the fixture is characterized, the de-embedded S-parameter measurements of two-port discontinuities are obtained by extracting the fixture parasitics mathematically.

B. Connection Repeatability Issues

One drawback to the TSD technique is that good microstrip connection repeatability is important for accuracy. Microstrip connections are much harder to make, and less repeatable than connections in coax and waveguide. This is a key limiting factor to the accuracy of microstrip measurements at higher frequencies. To address this issue, a microstrip connection repeatability study was carried out [7]. The results of this study were used to decide on the best connection approach to use and to estimate the associated measurement uncertainties.

There are three basic connection alternatives for TSD characterization of a coaxial fixture. Each of these must rely on at least one of the following assumptions:

1. repeatability of connections made from the coax-to-microstrip transition to the microstrip line

2. repeatability of microstrip-to-microstrip interconnects

3. uniformity of electrical characteristics between different transitions (launcher-to-launcher uniformity).

The results of the repeatability study favor a connection approach relying on repeatable coax/microstrip connections, and this was the approach adopted for the present work.

As part of this work, a method was developed to approximate the uncertainties in de-embedded results arising from connection repeatability errors [3]. The analysis consists of perturbing the S-parameters of the TSD standards and the D.U.T. with a set of experimentally derived error vectors that are representative of the variations of each S-parameter (S_{11}, S_{12} etc.) measurement with repeated connections. Software was written to allow processing the perturbed S-parameter data in the same way as the measurement data is processed during the TSD de-embedding procedure discussed above. This perturbation analysis, shows approximately how connection errors —which are inevitable— propagate through the TSD mathematics and limit the precision of the final results.

III. NUMERICAL AND EXPERIMENTAL RESULTS

In this section, the numerical and experimental results of the present research are presented for the network parameters of shielded microstrip discontinuities. Included here are results for the effective dielectric constant, open-end and series gap discontinuities, and coupled line filters. Where possible, comparisons are made to results generated from the commercially available CAD packages *Super Compact* and *Touchstone*[1].

The CAD models used in these packages are based on a combination of different theoretical techniques, most often embodied in simplified closed form solutions, curve fit expressions, or look-up tables. These models do not adequately account for the effects of the shielding box (Figure 1). Further, in simulating a circuit containing many discontinuities, the analysis of these packages assume that the discontinuities are independent of one another and the matrix representations for each discontinuity are simply cascaded together mathematically.

[1] *Super Compact* and *Touchstone* are microwave CAD software packages available from Compact Software and EESOF respectively.

In contrast, the full-wave solution presented in Part I accurately treats the entire geometry of the shielded microstrip circuit as a boundary value problem. The interactions between the discontinuity structure, adjacent microstrip conductors, and the shielding cavity are automatically included in the analysis. Because of this, the method is expected to provide better accuracy than CAD model predictions.

A. Cutoff Frequency and Higher Order Modes

One case where shielding effects are noticeable is when the frequency approaches the cutoff frequency f_c for the first higher order shielded microstrip mode. The nature of higher order modes in shielded microstrip is quite different from that in open microstrip. In open microstrip, higher order modes occur in the form of surface waves and radiation modes. The first surface wave mode has a cutoff frequency of zero. In shielded microstrip, the higher order modes take the form of waveguide modes [8]. As a consequence, below the waveguide cutoff frequency, only the dominant microstrip mode can exist.

For the present work, the f_c for the shielded microstrip geometry of Figure 1, is approximated by considering the dielectric-loaded waveguide formed by removing the strip conductors and the walls at $x = 0$, and a. The cutoff frequencies so derived have been found to give a good prediction of where higher order effects are first observed in the computed current distributions. As an example, Figure 3 shows the current distribution on an open-ended line operating below the cutoff frequency. For the indicated geometry, f_c is about 17.9 GHz. As the frequency is raised above the cutoff frequency, the current becomes more and more distorted as shown in Figure 4. The distortion is due to the interactions between the dominant mode and the first higher order waveguide-like mode inside the cavity.

B. Effective Dielectric Constant

Figure 5 shows ϵ_{eff} for a 25 mil thick alumina substrate where the cross sectional shielding dimensions, b and c, are ten times the substrate thickness (h). The numerical results are compared to measurements, and to CAD package predictions. Note that *Super Compact* allows only the cover height to be varied while the calculation provided by *Touchstone* neglects shielding effects. For the shielding geometry used here, it is seen that the difference between the numerical and CAD package results are within experimental error. However, interestingly enough, better agreement between the CAD results and the numerical results is observed at higher frequencies. This may be due to the fact that the side walls, which are not included in the CAD package analysis are electrically closer to the strip at low frequencies.

The measured data is obtained as a byproduct of the TSD fixture characterization procedure as discussed above. The data shown represents the average of ten separate procedures conducted over a period of time with four different sets TSD standards. The error bars shown in Figure 5 represent the standard deviation ($\pm s$) of the different measurements. This data is shown here in lieu of the result from a single measurement, since it gives a more representative view of the involved measurement uncertainty. In this case the error bars shown represent the combined effect of connection errors, variations in ϵ_r, and other factors. The major error source in this case is believed to be the variations in ϵ_r which can be significant

Table 1: CAVITY NOTATION USED TO DENOTE DIFFERENT GEOMETRY AND SUBSTRATE PARAMETERS

CAVITY	ϵ_r	W (in)	h (in)	b (in)	c (in)	f_c (GHz)
CA	9.7	.025	.025	.250	.250	21.8
CC	9.7	.025	.025	.100	.100	37.5
CF	9.7	.025	.025	.075	.075	41.7
QCB	3.82	.0157	.010	.122	.080	45.8
QCE	3.82	.0157	.010	.100	.100	73.0
QCG	3.82	.0157	.010	.050	.05	102.5

for alumina substrates [9][2].

To see how ϵ_{eff} varies with shielding, consider the plot of Figure 6. This plot compares numerical and *Super Compact* results for three different shielding geometries. The notation used to describe different shielding and substrate geometries is explained in Table 1.

In all cases, as the shielding is brought closer to the microstrip a reduction in ϵ_{eff} is predicted. The case for cavity CA is the same as that of Figure 5. For the other two cases, where the shielding is closer to the microstrip, the *Super Compact* shows a smaller effect than the present integral equation method predicts.

The effect of shielding on ϵ_{eff} for a quartz substrate is displayed in Figure ??. In this case the *Super Compact* analysis is seen to give good results for both of the two larger shielding geometries . However, the numerical results again show a larger reduction in ϵ_{eff} as the size of the shielding is decreased further.

The reduction of the effective dielectric constant, relative to *Super Compact*,

[2]This error reflects the uncertainty of not knowing the exact value of ϵ_r to use in the theoretical simulations.

can be explained as follows. For a larger shielding geometry, the field distribution on the microstrip more closely resembles the open microstrip case, with most of the electric field concentrated in the substrate. In this case, most of the electric field lines originate on the microstrip conductors and terminate on the ground plane below. As the cavity size is reduced, the ground planes of the top and side-walls are brought closer to the microstrip lines. The electric field distribution is now less concentrated in the substrate, as more field lines can terminate on the top and side walls. As a result, a proportionally larger percentage of the energy propagating down the line does so in the air region, and the dielectric constant is reduced.

C. Open-end Discontinuity

As discussed in [1], an open-end discontinuity can be represented by an effective length extension L_{eff}, or by a shunt capacitance c_{op}. Both of these representations will be used in this section.

The plot of Figure 8 compares L_{eff} results to those of Jansen et al. [10] and Itoh [11]. In this case, the dimensions of the shielding cavity are large with respect to the substrate thickness. The results from this research are almost identical to those obtained by Jansen et al. for frequencies above 8 GHz, but show a reduced value for lower frequencies.

The case of Figure 8 was chosen to compare the coaxial and gap generator excitation methods used in the method of moments solution. Table 2 shows that the results computed for this case by the two methods are equivalent. This equivalence also holds for the two-port scattering parameters for the structures considered herein. Hence, as far as computing network parameters is concerned either

Table 2: COMPARISON OF L_{eff}/h COMPUTATION FOR THE TWO TYPES OF EXCITATION METHODS

f (GHz)	4	8	12	14	16	18	20
GAP GENERATOR	.298	.305	.309	.321	.324	.344	.353
COAXIAL EXCITATION	.299	.304	.309	.322	.327	.344	.352

method gives good results. Since the coaxial method is more realistically based, this conclusion lends validity to the use of the gap generator method.

The results shown in Figure 9 illustrate the effect of shielding on the open-end discontinuity. The normalized open-end capacitance c_{op} is plotted for three different cavity sizes. The results show that reducing the cavity size raises f_c (as expected), and it lowers the value of c_{op}. For comparison, data obtained from *Super Compact* and *Touchstone* and measurements (see Section 4.3) are included. The errors bars on the measurements represent the estimated standard deviation ($\pm s$) of the connection errors associated with this measurement[3].

Similar shielding effects are observed for an open-end on a quartz substrate as shown in Figure 10. In this case it is seen that the *Super Compact* result gives a good value for low frequencies, and where the frequency is well below the cutoff frequency for a given shielding size. These results show that shielding effects due to wall proximity are less important than shielding effects due to the onset of higher order modes.

[3]The other error sources indicated for the effective dielectric constant measurement are not considered to be as significant for this measurement.

D. Series Gap Discontinuities

Numerical and experimental results have been obtained for series gap discontinuities of three different gap widths [3]. Results for one of these gaps are presented here.

Numerical results for the magnitude of S_{21} of a series gaps with a 15mil gap width are shown plotted in Figure 11. For comparison, results obtained using *Super Compact*, and *Touchstone* are also shown plotted along with measured data. The numerical results are seen to be in very good agreement with the measurements. The test substrate and shielding dimensions used for the measurements are those for cavity CA (Table 1). The error bars associated with the connection errors, are on the order of $\pm.5$dB and are too small to show on the plots.

Results for the angle of S_{21} and S_{11} for the 15 mil series gap are shown in Figures 12 and 13. The error bars in these charts represent the estimated standard deviation from the perturbation analysis[4]. Although the measurements tend to favor the numerical results, the phase differences are not too significant since it is suspected that the measurement may be in error by more than that attributed to connection errors alone. The phase of the S-parameters for the other two gaps behave in a similar way as that for the 15 mil gap and have been omitted from this treatment.

These results are seen to further verify the theory developed in Part I. For the large shielding dimensions used for the measurements ($b, c \gg h$) the CAD models are also seen to give reasonable predictions. The behavior of series gaps

[4]The analysis was carried out at 10GHz, and it is assumed that the connection errors are approximately the same at the other measurement frequencies.

for different shielding dimensions was not studied, instead emphasis was placed on obtaining results for coupled line filters since their behavior is more complicated and therefore more interesting.

E. Four Resonator Coupled Line Filter

The last results to be presented are for the four resonator coupled line filter of Figure 14. For brevity, only the amplitude and phase of S_{21} will be discussed.

Numerical and measured results of this research are compared along with CAD model predictions in Figure 15. The CAD package analysis for coupled line filters is performed by cascading two different types of discontinuity elements together: coupled microstrip lines, and open-end discontinuities. Neither of the packages studied here account for shielding in the open-end discontinuity model, however, *Super Compact* does include the effect of the cover height in the model for coupled lines.

The numerical results shown in Figure 15 demonstrate excellent agreement with measurements up to the cutoff frequency. The cutoff frequency f_c for the shielding geometry of the filter is approximately 13.9GHz. Above this frequency, the measurements are distorted because of the enhanced electromagnetic coupling between the feed apertures. This coupling is due to the excited waveguide modes within the test fixture.

The results of Figure 15 show that even for large shielding dimensions discrepancies are apparent in the CAD model predictions, whereas the numerical results follow the measurements closely, both in amplitude and phase. As can be seen from the amplitude response (Figure 15a), the CAD models give a good prediction in the pass band, but fail to predict the filter response in the rejection band. This is also seen from the phase response (Figure 15b), where the CAD models display a large error compared to measurements between about 6 and 8.5GHz, while the numerical results track the measured amplitude and phase very well.

Below about 5.5GHz, the measured phase is seen to be different from the predictions of both the CAD models and the numerical results. This is most likely due to a phase error in the measurements. In the TSD technique, the delay line for the measurements should ideally be $\frac{\lambda_g}{4}$ at the measurement frequency [5]. When the electrical length becomes either too short or too close to a multiple of $\frac{\lambda_g}{2}$, phase ambiguities can result. A good rule of thumb is for the delay line to be between $\frac{\lambda_g}{8}$ and $\frac{3\lambda_g}{8}$. At 5.5GHz the delay line used for the measurements is slightly less than $\frac{\lambda_g}{8}$; hence, this is most likely the source of the phase error in the measurements below this frequency.

We will now examine what happens as the top cover is brought closer to the circuitry. Figure 16a shows *Super Compact* predictions for the four resonator filter with two different cover heights. These predictions indicate that lowering the cover height should significantly narrow the pass band, and reduce the amplitude in the rejection band.

A significantly different prediction is observed in the numerical results for this case presented in Figure 16b. A narrowing of the pass band response is also observed in the numerical predictions, but not by nearly as much as *Super Compact* predicts. More importantly, the amplitude in the rejection band is seen to increase

[5] Multiple lines are needed for broadband measurements.

instead of decrease.

To prove that the numerical prediction is indeed the correct one, an additional measurement was made of the filter for the low cover height case. As can be seen from Figure 16b the agreement between measured data and the numerical predictions from this research is excellent.

IV. SUMMARY

In this paper theoretical and experimental results were presented for the network parameters of one- and two-port discontinuities. For the measurements, the TSD de-embedding approach was used. Connection repeatability errors were considered in detail and a perturbation analysis was developed to approximate their effect on the precision of the final de-embedded results.

The effects of shielding on microstrip behavior were studied. It was demonstrated that the computed current distribution becomes distorted above the cutoff frequency f_c for the first higher order shielded microstrip mode. On the other hand, as long as the cavity size is such that the frequency is below f_c, the current is uniform and undistorted regardless of how thick the substrate is.

Only one of the CAD packages studied takes shielding into account for the effective dielectric constant (ϵ_{eff}) calculation, and then only cover effects are considered. A comparison of the CAD package predictions with the numerical results of this research for ϵ_{eff} showed that good agreement is obtained when the shielding dimensions are large with respect to the substrate thickness, while for small shielding dimensions, the difference between the different results becomes significant.

For the open-end discontinuity, good agreement with other full-wave solutions and with measurements has been demonstrated. A comparison of open-end capacitance for different cavity sizes showed that, as the cutoff frequency is approached, the capacitance increases in each case. Choosing a small cavity with a high cut-off frequency extends the region where the capacitance is relatively constant.

Good agreement between numerical and measured results was also demonstrated for series gap discontinuities and a four resonator coupled line filter. For the filter, reducing the cover height was seen to narrow the pass band response and raise the amplitude of the filter's rejection band response. The numerical results of this research give an excellent prediction of this effect, whereas discrepancies are apparent in the CAD model predictions.

ACKNOWLEDGEMENTS

The authors thank Mr. Ed Watkins, Mr. Jim Schellenberg, and Mr. Marcel Tutt for their contributions to this work. This work was primarily sponsored by The National Science Foundation (Contract. No. ECS -8602530). Partial sponsorship was also provided by the Army Research Office (Contract No. DAAL03-87-K-0088) and the Microwave Products Division of Hughes Aircraft Co.

References

[1] L.P. Dunleavy and P.B. Katehi, "A New Integral Equation Method for Analyzing Shielded Microstrip Discontinuities", Accepted for publication in *IEEE Trans. Microwave Theory Tech.*.

[2] R.L. Eisenhart,"A Better Microstrip Connector", *1978 IEEE MTT-S Digest*, pp. 318-320.

[3] L.P. Dunleavy, "Discontinuity Characterization in Shielded Microstrip: A Theoretical and Experimental Study", Ph.D. dissertation, University of Michigan, April 1988.

[4] N. R. Franzen and R. A. Speciale, "A New Procedure for System Calibration and Error Removal in Automated S-Parameter Measurements", *5th European Microwave Conference*,1975, pp. 69-73.

[5] B. Bianco et. al. "Launcher and Microstrip Characterization" *IEEE Trans. on Instrum. and Meas.* Vol. IM 25, NO. 4, Dec. 1976, pp. 320-323.

[6] G. Engen and C. Hoer, "Thru-Reflect-Line: An improved Technique for Calibrating the Six-Port Automatic Network Analyzer". *IEEE Trans. Microwave Theory Tech.* vol. MTT-27, No. 12, Dec. 1979, pp 987-993.

[7] L. Dunleavy and P. Katehi, "Repeatability Issues for De-embedding Microstrip Discontinuity S-parameter Measurements By the TSD Technique" *Automatic RF Techniques Group (ARFTG) Conf. Dig.* June 1986.

[8] E. Yamashita and K. Atsuki, "Analysis of Microstrip-Like Transmission Lines by Nonuniform Discretization of Integral Equations," *IEEE Trans. Microwave Theory Tech.*, vol. MTT-24, pp. 195-200.

[9] J. Snook, "Substrates for Hybrid Microelectronic Applications", *Microwave System News and Comm. Tech.*, February 1988, pp26-31.

[10] R.H. Jansen, and N.H.L. Koster, "Accurate Results on the End Effect of Single and Coupled Lines for Use in Microwave Circuit Design " *A.E.U.* vol. 34, pp 453-459, 1980.

[11] T. Itoh,"Analysis of Microstrip Resonators", *IEEE Trans. Microwave Theory Tech.*, vol MTT-22, pp 946-951, 1974.

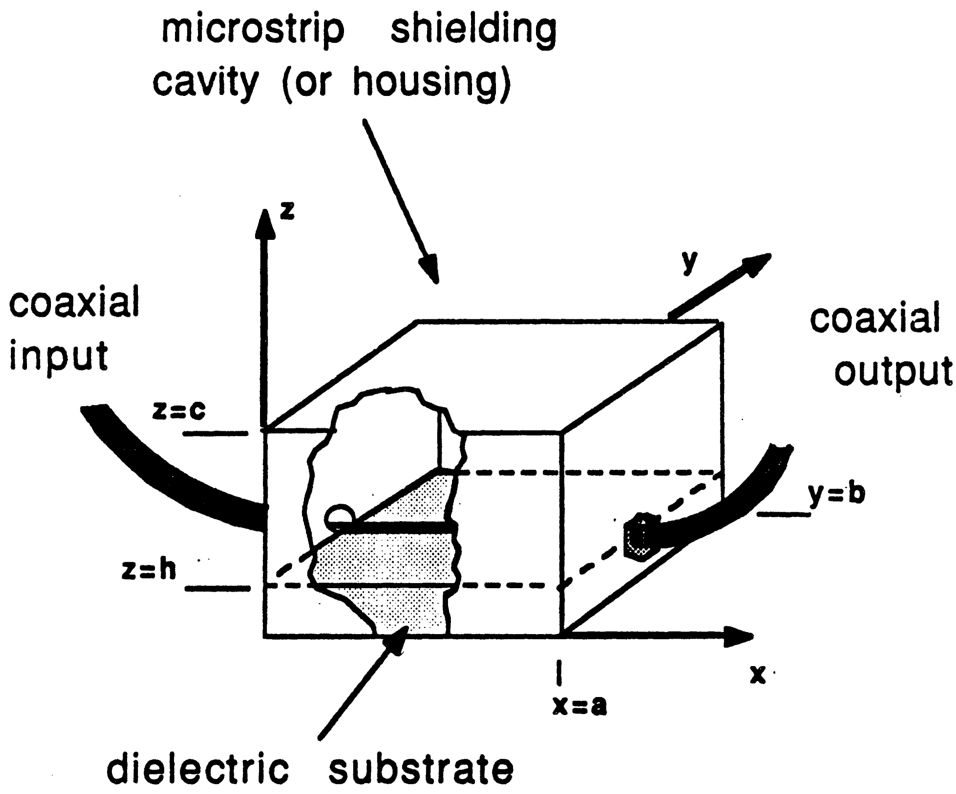

Figure 1: Basic geometry for the shielded microstrip cavity problem.

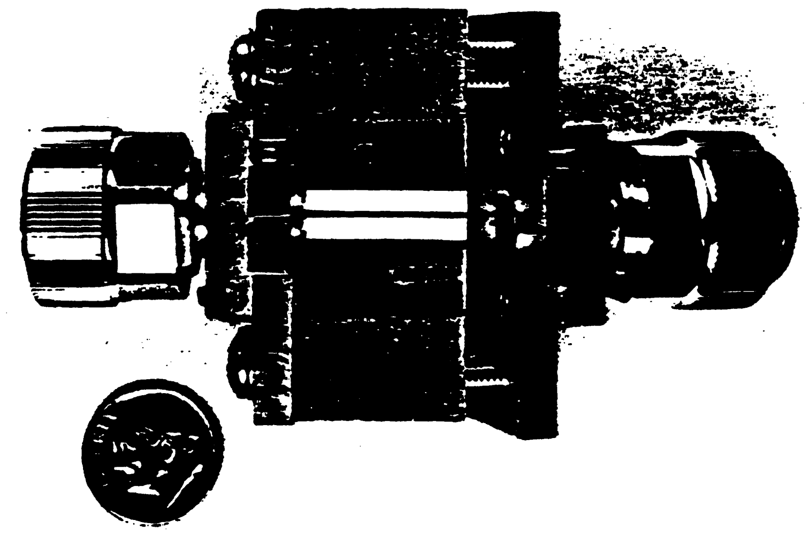

Figure 2: 7mm coaxial/microstrip test fixture (partially disassembled) used for measurements.

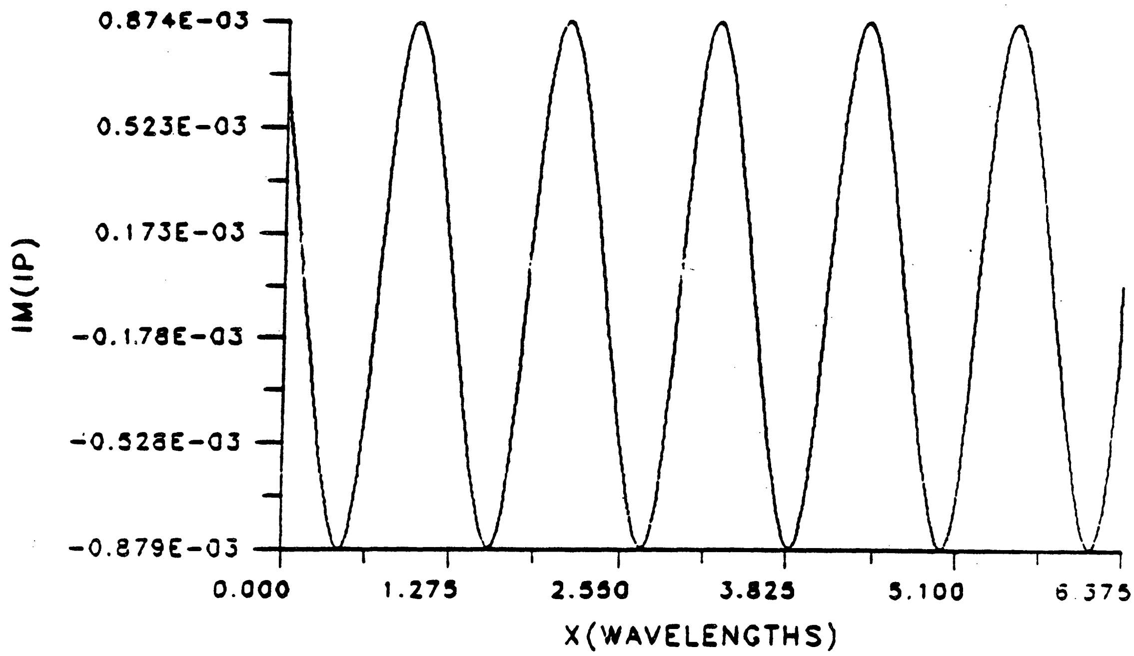

Figure 3: Imaginary part of current on open-ended line below the cutoff frequency f_c (f = 16GHz,$\epsilon_r = 9.7, W/h = 1.57, h = .025", b = c = .275''$).

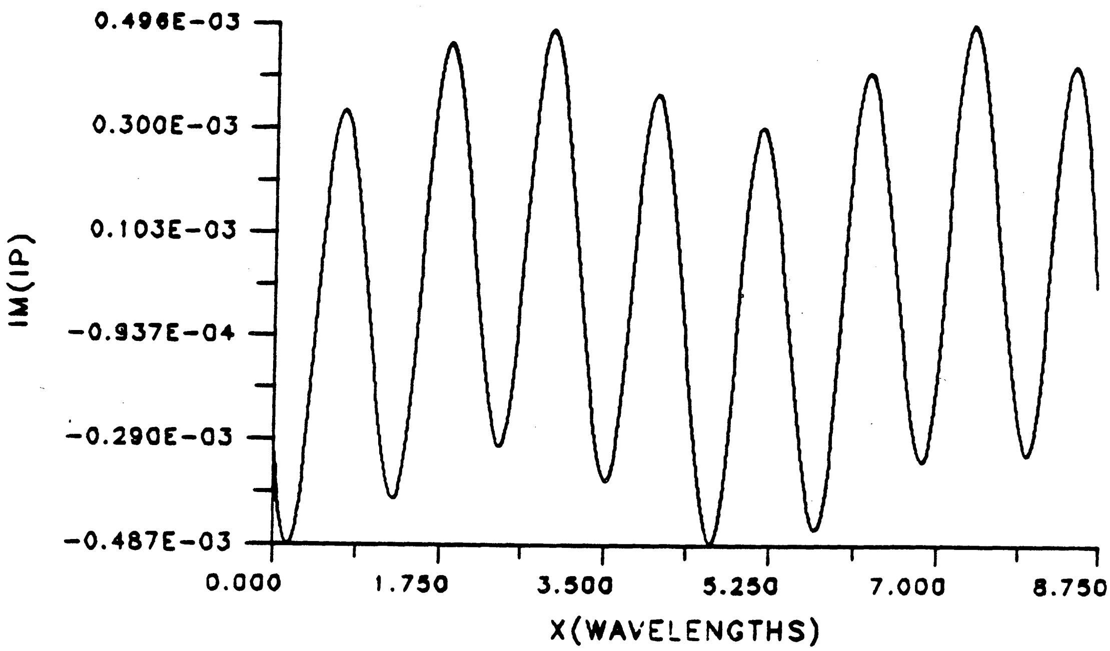

Figure 4: Open-ended microstrip current above f_c (f = 22GHz, ϵ_r = 9.7, W/h = 1.57, h = .025", $b = c = .275''$).

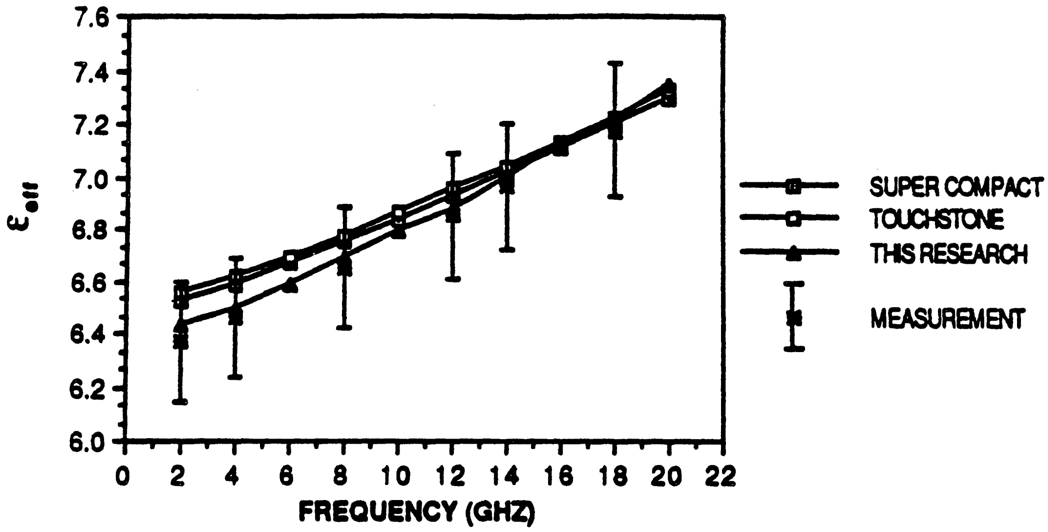

Figure 5: Numerical results for ϵ_{eff} compared with measurements and CAD package predictions ($\epsilon_r = 9.7, h = .025'', b = c = .25''$).

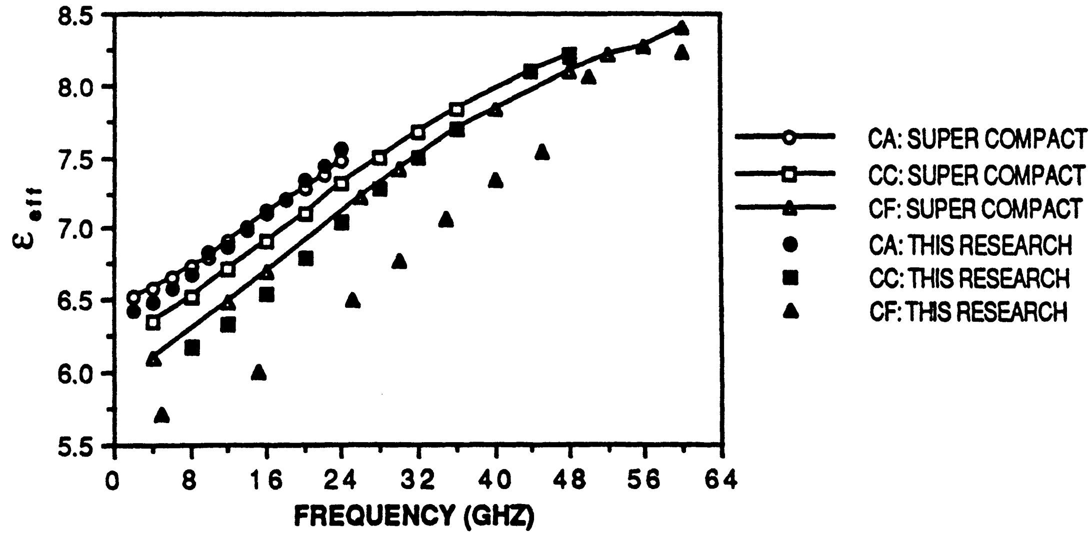

Figure 6: Shielding effects on ϵ_{eff} for an alumina substrate (see Table 5.1 for geometry).

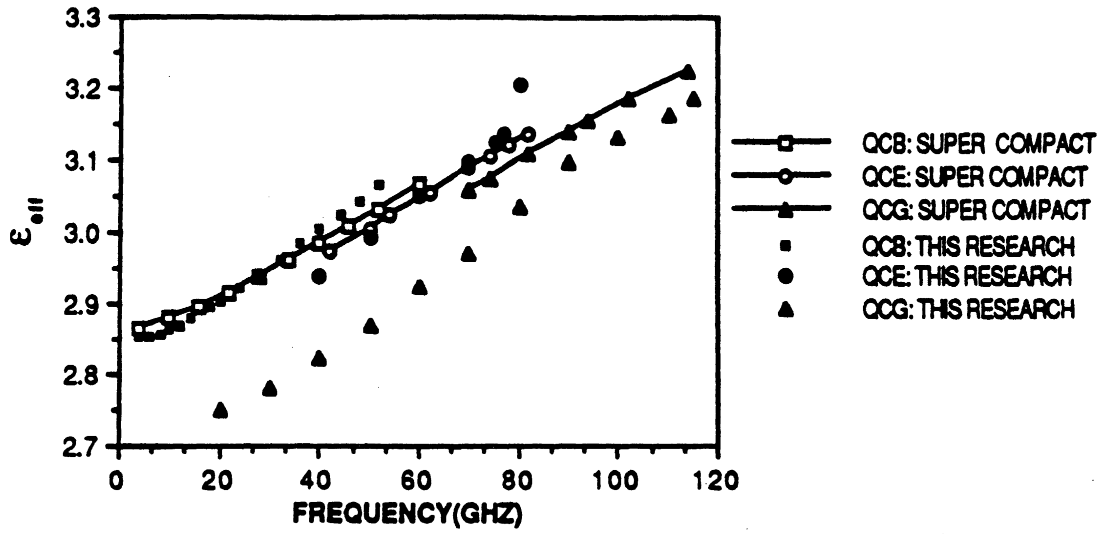

Figure 7: Shielding effects on ϵ_{eff} for a quartz substrate (see Table 5.1 for geometry).

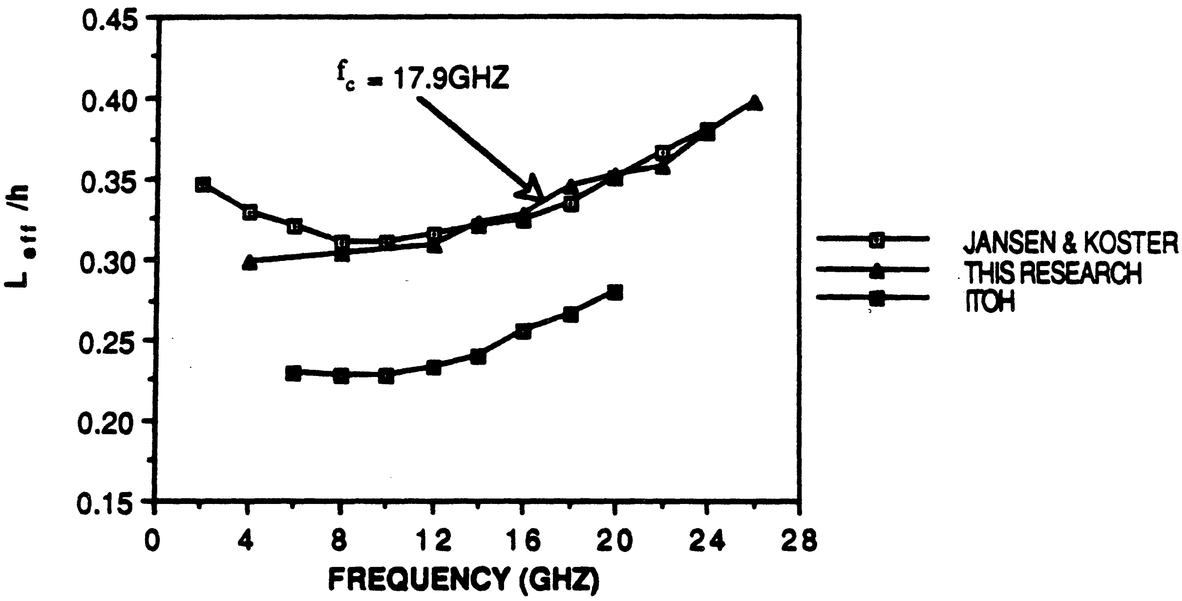

Figure 8: Numerical results compared to those from other full-wave analyses (ϵ_r = 9.6, W/h = 1.57, $b = .305''$, $c = .2''$, $h = .025''$).

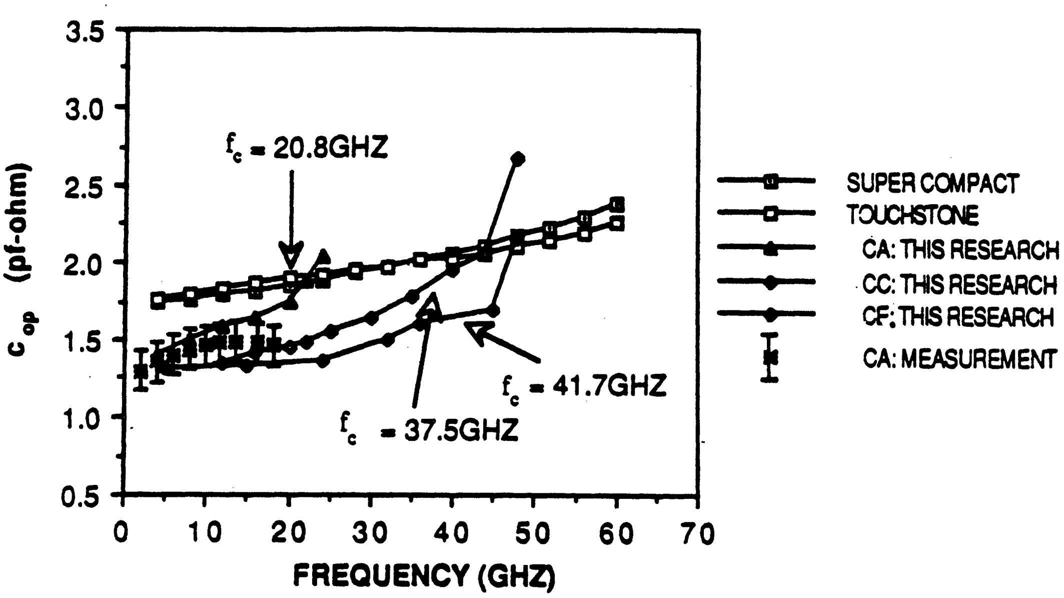

Figure 9: Comparison of the normalized open-end capacitance for three different cavity sizes. This shows that shielding effects are dominated by the onset of higher order modes rather than by proximity effects (see Table 5.1 for cavity geometries).

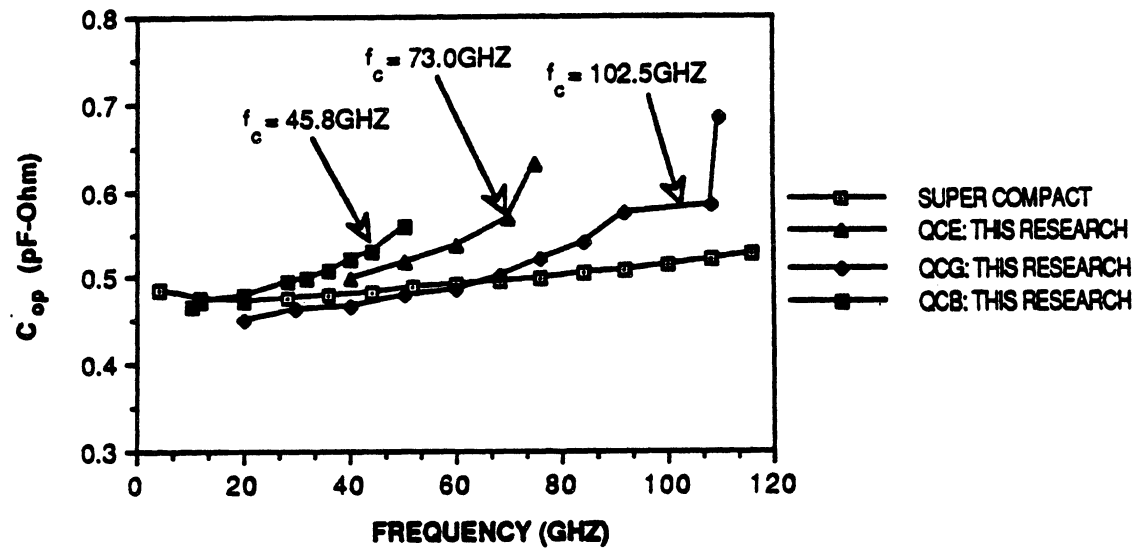

Figure 10: Normalized open-end capacitance for three different cavity sizes for a quartz substrate. These results also show the strong dependence of the capacitance on f_c (see Table 5.1 for cavity geometries).

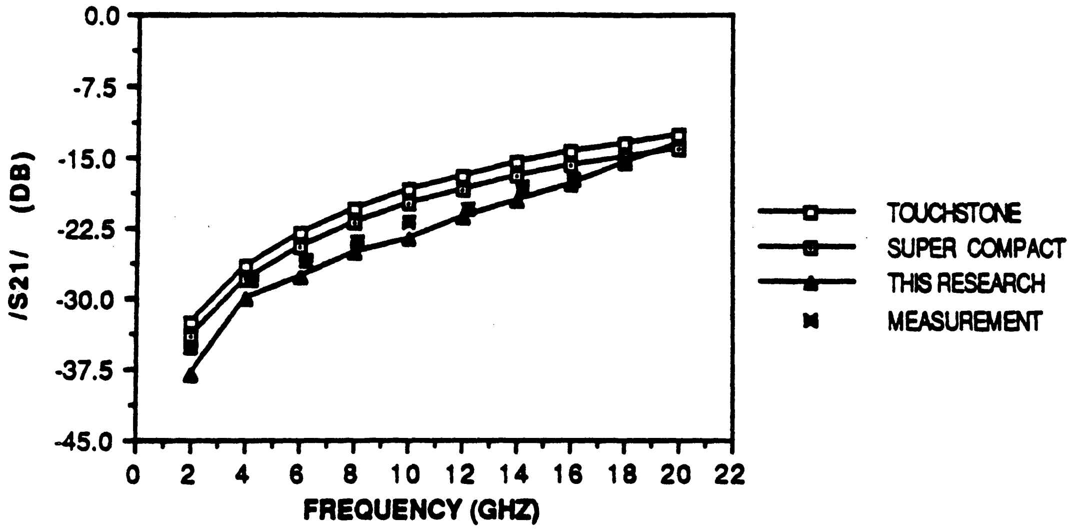

Figure 11: Results for the magnitude of S_{21} for a 15 mil series gap.

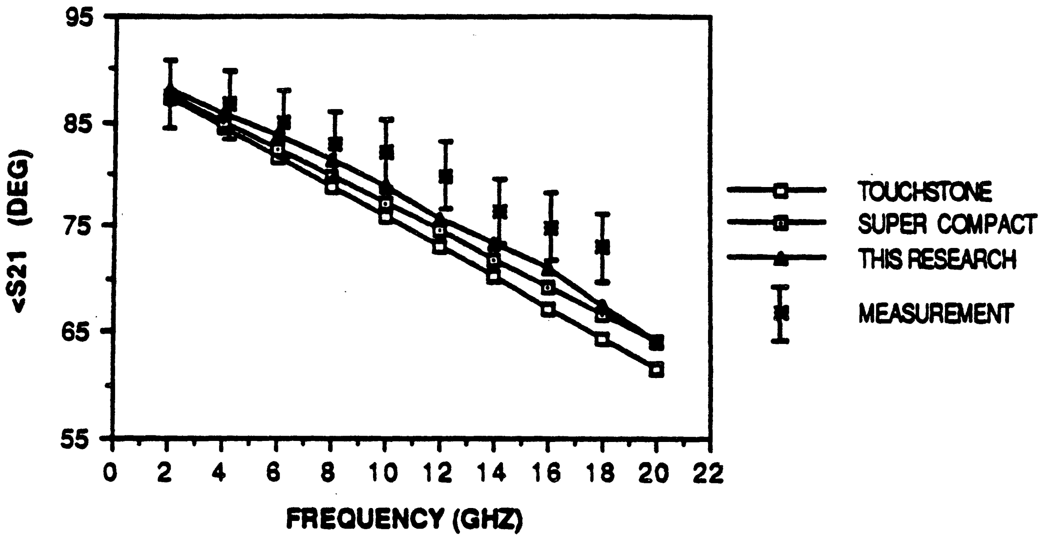

Figure 12: Results for the angle of S_{21} for a 15 mil series gap.

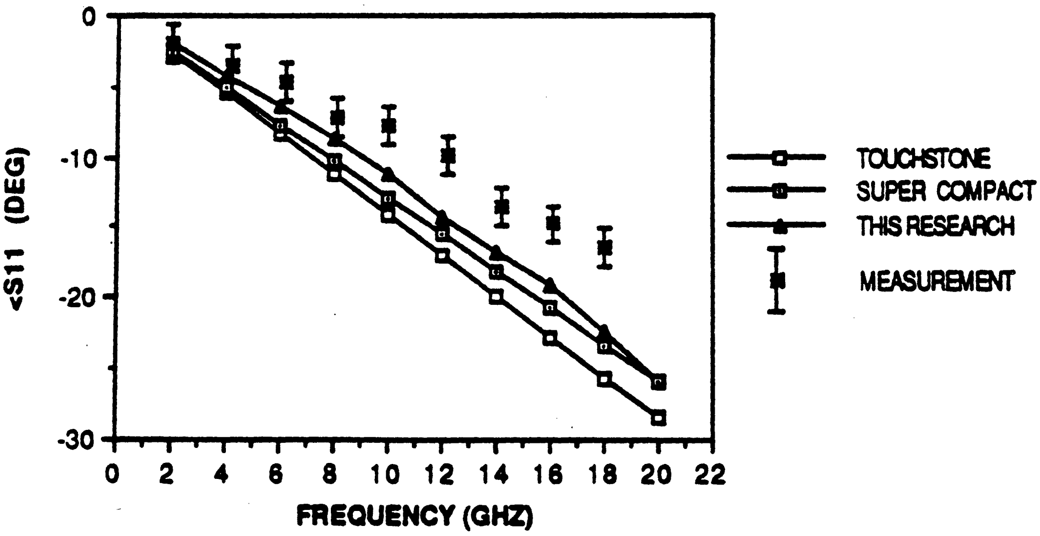

Figure 13: Results for the angle of S_{11} for a 15 mil series gap.

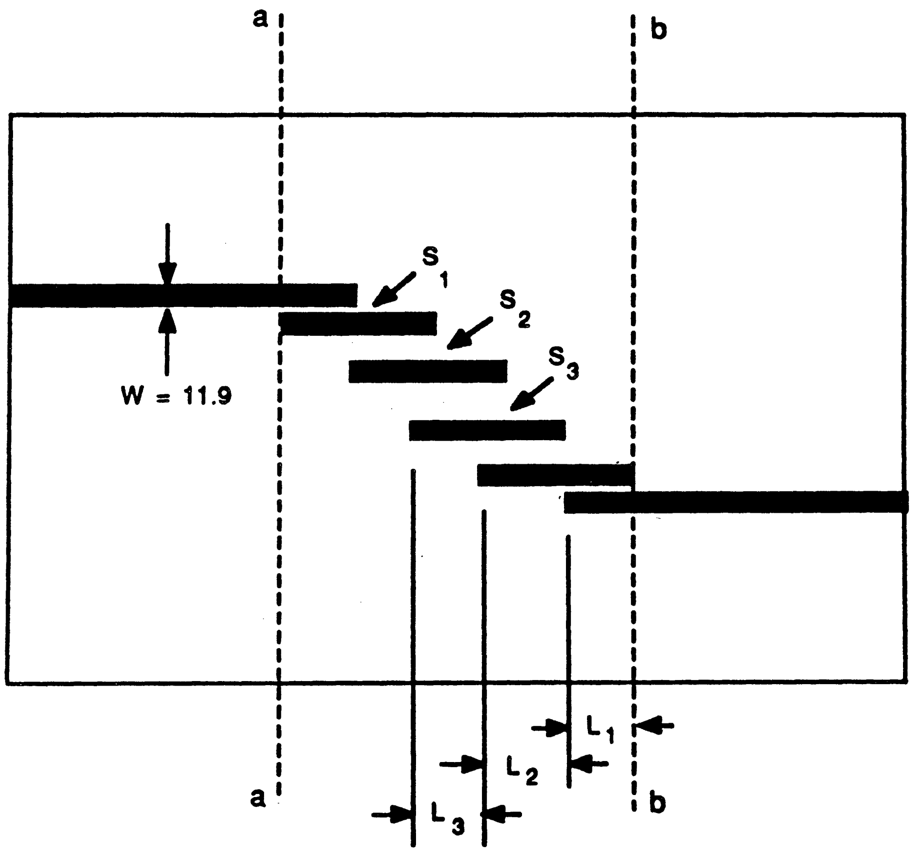

Figure 14: Sketch of four resonator coupled line filter studied here (ϵ_r = 9.7, h = .025″, b = .4″, c = .25″).

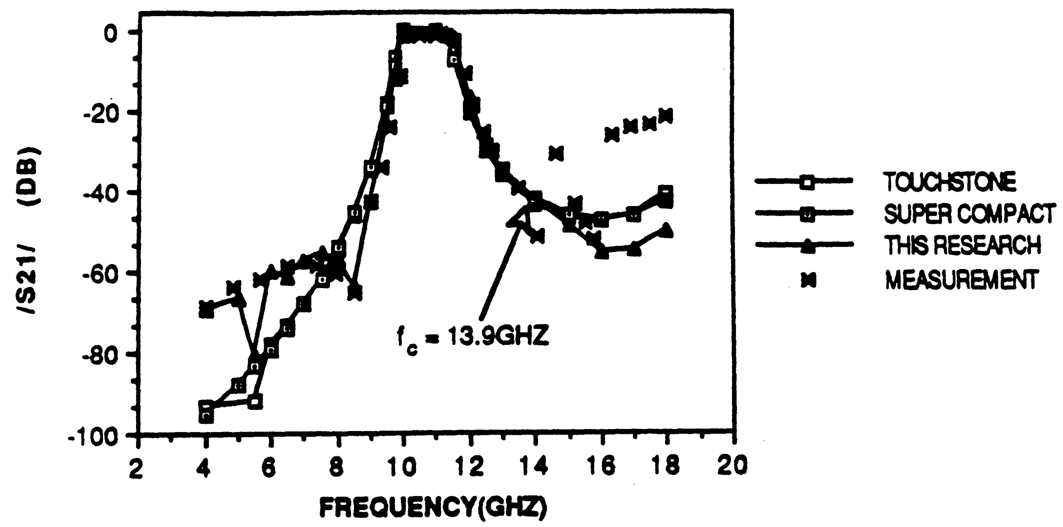

a. Amplitude of S_{21}

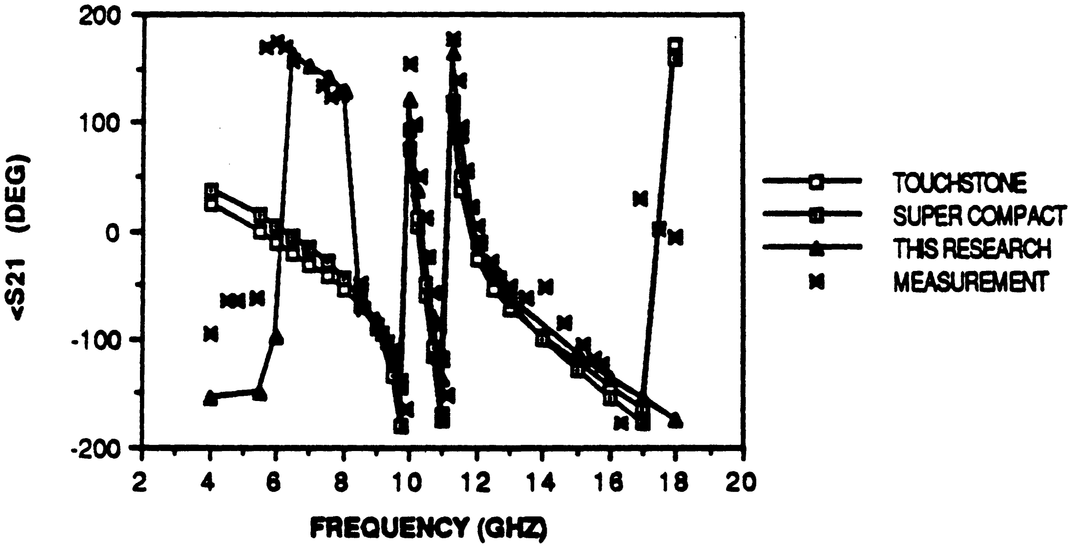

b. Phase of S_{21}

Figure 15: Results for transmission coefficient S_{21} of four resonator filter ($\epsilon_r = 9.7, W = .012''$, $h = .025''$; $b = .4''$, $c = .25''$).

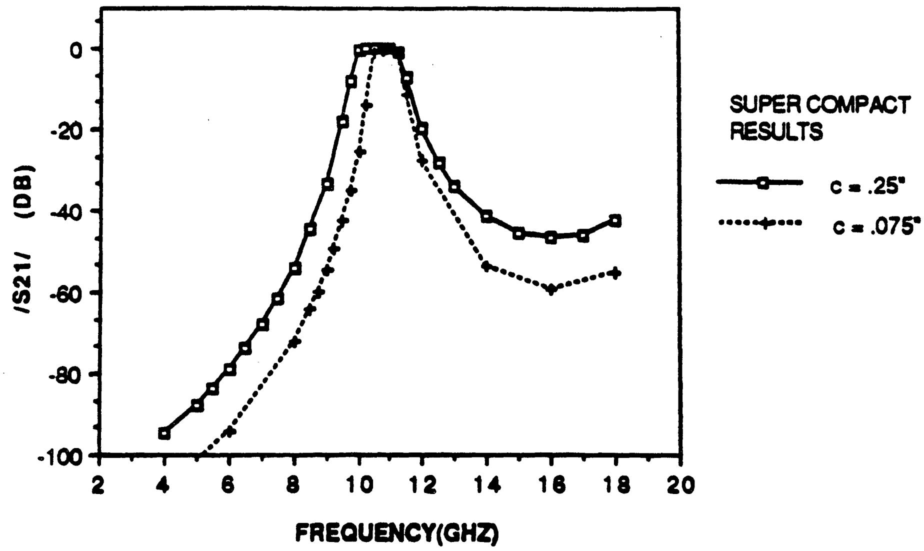

a. Super Compact predictions

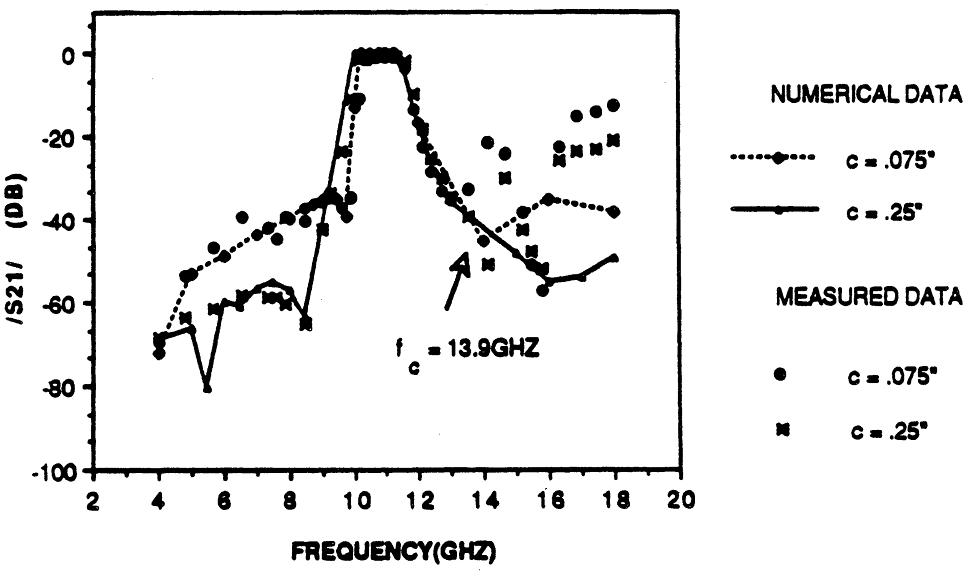

b. Numerical results of this research compared to measurements

Figure 16: Results for lowering the shielding cover on the amplitude response of four resonator filter ($\epsilon_r = 9.7, W = .012'', h = .025''; b = .4''$).

NSF-023827-5-T

HIGH-FREQUENCY CHARACTERIZATION OF OPEN MICROSTRIP JUNCTIONS

W. Harokopus and P.B. Katehi

Radiation Laboratory
Department of Electrical Engineering and Computer Science
The University of Michigan
Ann Arbor, MI 48109

June 1988

Contents

1 Introduction

A method which accurately characterizes open microstrip discontinuities and microstrip antennas has been developed by using a full dynamic analysis [2]. The method accounts for substrate effects, electromagnetic coupling, radiation losses, and surface wave excitation. The method considers a two-dimensional current distribution in the plane of the microstrip, and can therefore accurately characterize microstrip bends, T-junctions, and steps. Also, because the formulation is for an open microstrip geometry, this analysis is also valid for radiating elements such as patches, or travelling wave antennas. The method will also be used to compute the power radiated, and launched into surface waves for discontinuities, and the ratio of radiated power to surface wave power in antenna.

In the formulation of the problem, an integral equation is used which relates the electric field to the current on the microstrip conductor. This integral equation contains the Green's function for the dielectric coated conductor geometry. Method of Moments is used to generate a system of linear equations from the integral equation. This system can then be solved to determine the current on the microstrip conductor, and subsequently the scattering parameters and radiated fields.

2 Pocklington's Integral Equation

This section provides a summary of the formulation for the full-wave analysis of a microstrip element in the spatial domain. For a more detailed summary refer to "Computer Modeling of Microstrip Elements and Discontinuities," [1].

The electric field from the current on a microstrip structure as shown in figure 1 is given by Pocklington's Integral Equation [4]

$$\vec{E} = -\frac{j}{\omega\epsilon\mu}\int\int(k^2\bar{\bar{I}} + \vec{\nabla}\vec{\nabla})\bar{\bar{G}}(\vec{r},\vec{r}')\bar{J}(\vec{r}') \quad (1)$$

Where $\bar{\bar{I}}$ is the unit dyad

$$\bar{\bar{I}} = \hat{x}\hat{x} + \hat{y}\hat{y} + \hat{z}\hat{z} \quad (2)$$

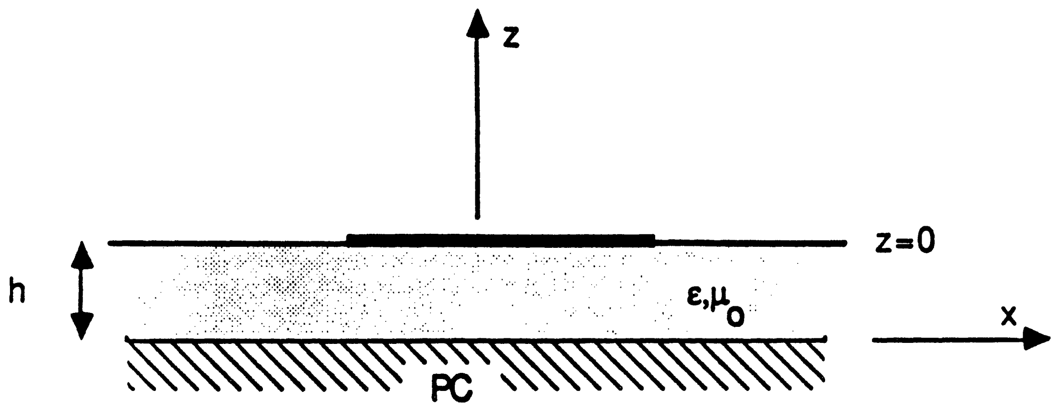

Figure 1: Cross Section of Microstrip Geometry

Also, $\bar{J}$ is the unknown current, and $\bar{\bar{G}}$ is the dyadic Green's function for the dielectric coated conductor and satisfies the wave equation for an infinitesimal point source

$$(\vec{\nabla}\vec{\nabla} + k^2)\bar{\bar{G}}(\vec{r},\vec{r}') = -\mu\bar{\bar{I}}\delta(\vec{r}-\vec{r}') \tag{3}$$

The derivation of the Green's function for an x-directed hertzian dipole above a grounded dielectric slab was done by Sommerfeld [3]. He demonstrated that in the presence of a dielectric-air interface, the Green's function requires both an x and z component making it a dyadic. When both x and y directed currents are considered, as in the case of a bend, the Green's function has four components.

$$\bar{\bar{G}}(\vec{r}/\vec{r}') = G_{xx}\hat{x}\hat{x} + G_{zx}\hat{z}\hat{x} + G_{yy}\hat{y}\hat{y} + G_{zy}\hat{z}\hat{y} \tag{4}$$

Where

$$G_{xx} = -\frac{j\omega\mu_0}{4\pi k_0^2}\int_0^\infty J_0(\lambda\rho)(e^{-u_0|z-d|} - e^{-u_0|z+d|} + 2u_0\frac{\sinh uh}{f_1(\lambda,h)}e^{-u_0|z+d|})\frac{\lambda}{u_0}d\lambda \tag{5}$$

$$G_{zx} = -2\frac{j\omega\mu_0}{4\pi k_0^2}(1-\epsilon_r)\cos\phi\int_0^\infty J_1(\lambda\rho)e^{-u_0|z+d|}\frac{\sinh uh\cosh uh}{f_1(\lambda,h)f_2(\lambda,h)}\lambda^2 d\lambda \tag{6}$$

$$G_{yy} = G_{xx} \tag{7}$$

$$G_{zy} = \tan\phi G_{zx} \tag{8}$$

With

$$f_1(\lambda, h) = u_0 \sinh uh + u \cosh uh \tag{9}$$

$$f_2(\lambda, h) = \epsilon_r u_0 \cosh uh + u \sinh uh \tag{10}$$

$$\rho = \sqrt{(x - x')^2 + (y - y')^2} \tag{11}$$

$$uo = \sqrt{\lambda^2 - k_0^2} \tag{12}$$

$$u = \sqrt{\lambda^2 - k^2} \tag{13}$$

$$\cos\phi = \frac{x - x'}{\rho} \tag{14}$$

3 Method of Moments

Pocklington's Integral Equation (equation 1) cannot be solved analytically. To solve for the unknown current, the integral equation can be used to generate a system of simultaneous linear equations. One method of doing this is entitled Method of Moments [5]. The unknown current is expanded into a finite series of basis functions and unknown coefficients. These series are substituted into 1. To create the system of linear equations, the boundary condition on the electric field at the microstrip conductor is enforced, and Galerkin's method is applied for minimization of the error. The resulting system of linear equations can be solved for the unknown current coefficients.

Assume we wish to find the unknown current on the microstrip bend shown in figure 2. The bend is partitioned into overlapping squares as shown in figure 3. The two directions of current are then expanded into series of the form

$$J_x = \sum_{n=1}^{N+1} \sum_{n=1}^{M+1} I_{nm}^{x} j_{nm}^{x}(x', y') \tag{15}$$

$$J_y = \sum_{n=1}^{N+1} \sum_{n=1}^{M+1} I_{nm}^{y} j_{nm}^{y}(x', y') \tag{16}$$

The current is considered separable with respect to x' and y'. The choice of basis functions are overlapping sub-domain. Each term in the series is non-zero only over a small portion of the bend.

Microstrip Bend

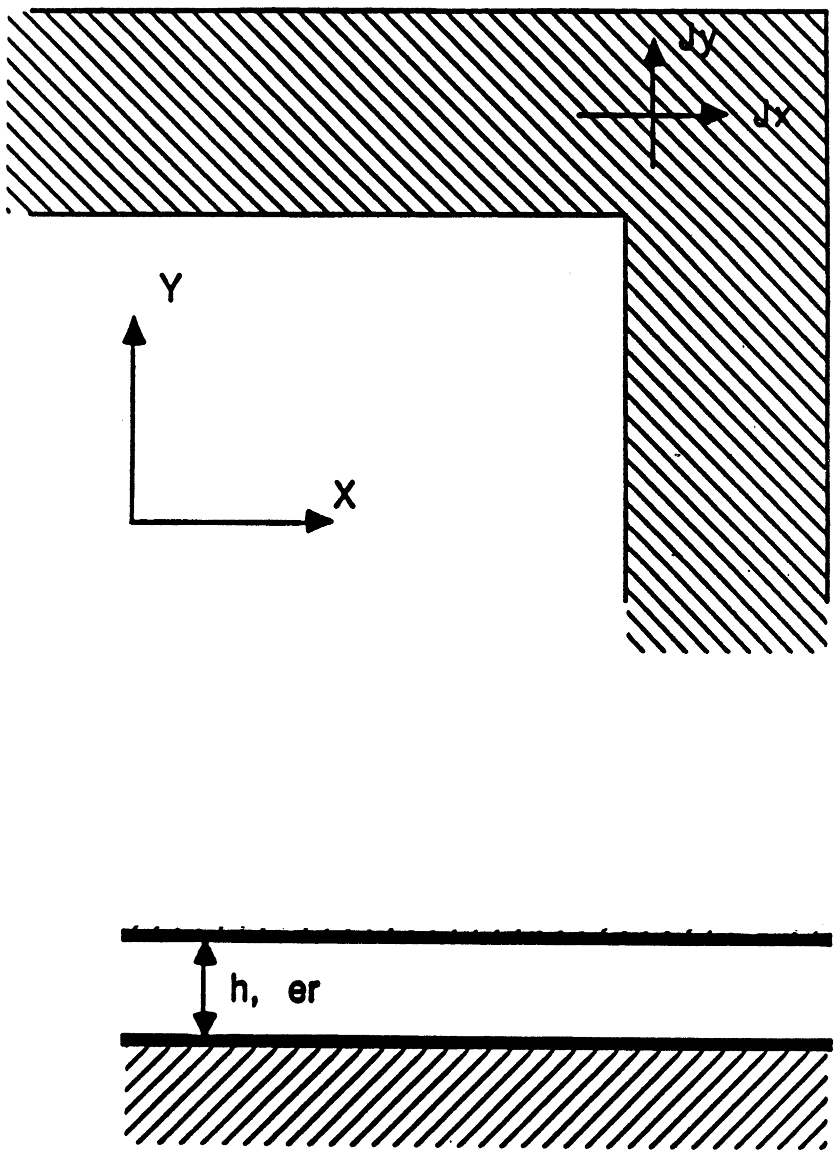

Figure 2: Microstrip Bend

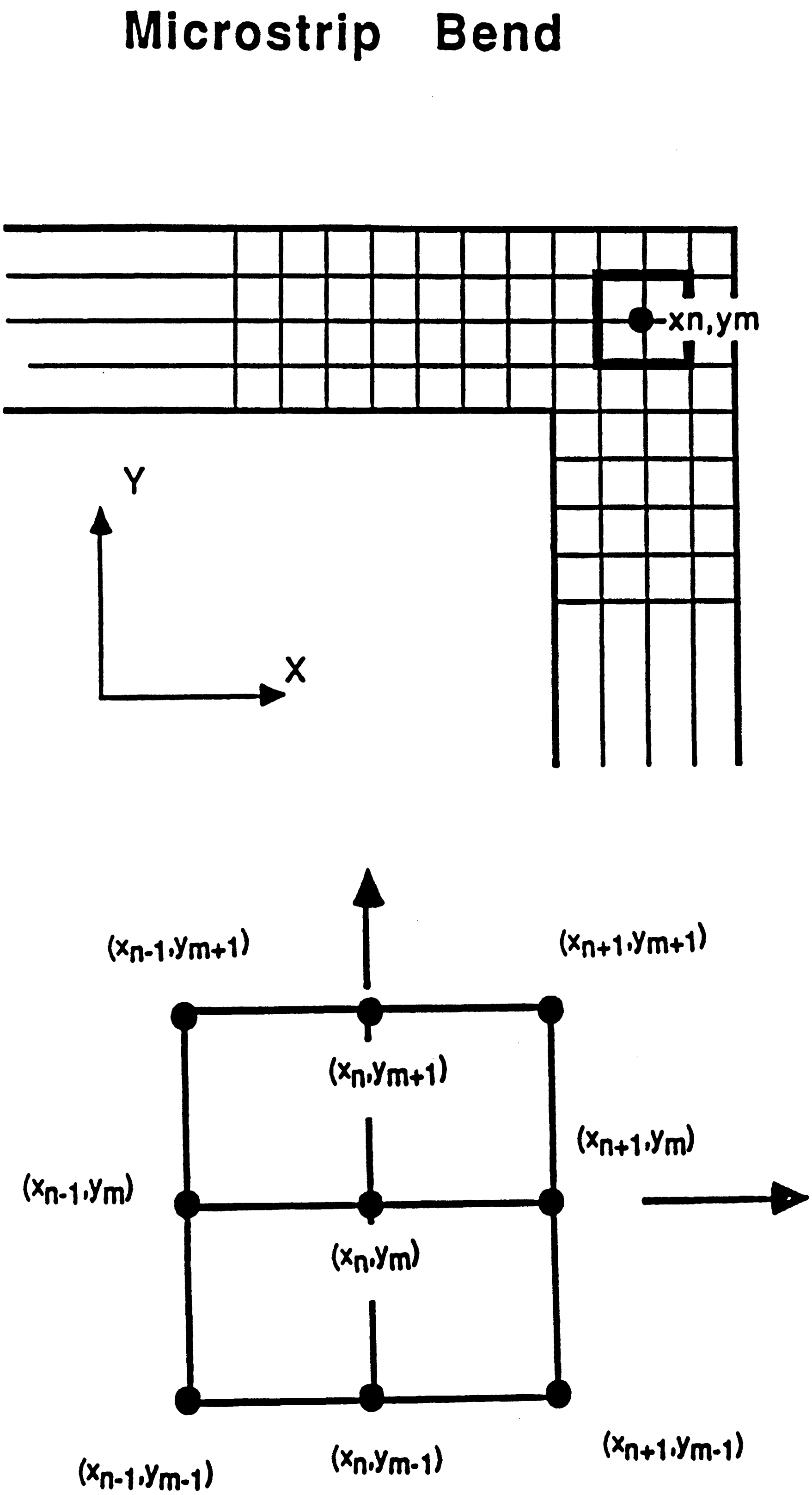

Figure 3: Sub-divided Microstrip Bend

For instance, the (n,m) element is centered at x_n and y_m and is zero out of the square shown in figure 3. The functions overlap so that the sum of the series, once the unknown coefficients are determined, can give an accurate representation of the true current. The basis functions chosen are rooftop, and can be represented mathematically as

$$j^x_{n,m}(x',y') = [f_n(x')g_m(y')] \tag{17}$$

$$j^y_{n,m}(x',y') = [g_n(x')f_m(y')] \tag{18}$$

With

$$f_n(x') = \begin{cases} \frac{\sin k(x_{n+1}-x')}{\sin kl_x} & x_n \le x' \le x_{n+1} \\ \frac{\sin k(x'-x_{n-1})}{\sin kl_x} & x_{n-1} \le x' \le x_n \end{cases}$$

And

$$g_m(y') = \begin{cases} 1 & y_{m-1} \le y' \le y_{m+1} \end{cases}$$

where $l_x = x_{n+1} - x_n$. Functions $f_m(y')$ and $g_n(x')$ are given by the above with $y', y_{n-1}, y_{n+1}, l_y$ substituting for $x', x_{n-1}, x_{n+1}, l_x$.

Substitution of this into Pocklington's Integral equation and expansion of the dyadics results in an expression for the electric field

$$E_x + \Delta E_x = -\frac{j\omega\mu_0}{4\pi k_0^2} 2 \sum_{n=1}^{N+1} \sum_{n=1}^{M+1} I^x_{nm} \int\int_s dx'dy' \mathcal{L}_{xx}(J_0(\lambda\rho)) j_{nm}(x',y') \tag{19}$$

$$- \frac{j\omega\mu_0}{4\pi k_0^2} 2 \sum_{n=1}^{N+1} \sum_{n=1}^{M+1} I^y_{nm} \int\int_s dx'dy' \mathcal{L}_{xy}(J_0(\lambda\rho)) j_{nm}(x',y') \tag{20}$$

And

$$E_y + \Delta E_y = -\frac{j\omega\mu_0}{4\pi k_0^2} 2 \sum_{n=1}^{N+1} \sum_{n=1}^{M+1} I^x_{nm} \int\int_s dx'dy' \mathcal{L}_{yx}(J_0(\lambda\rho)) j_{nm}(x',y') \tag{21}$$

$$- \frac{j\omega\mu_0}{4\pi k_0^2} 2 \sum_{n=1}^{N+1} \sum_{n=1}^{M+1} I^y_{nm} \int\int_s dx'dy' \mathcal{L}_{yy}(J_0(\lambda\rho)) j_{nm}(x',y') \tag{22}$$

With ΔE_x and ΔE_y being the errors introduced by the truncation of the series in 15 and 16. The integro-differential operators, $\mathcal{L}_{xx}, \mathcal{L}_{yy}, \mathcal{L}_{xy}$, and $\mathcal{L}_{yx}$ are

$$\mathcal{L}_{xx} = \int_0^\infty d\lambda \{F_1(\lambda)(k_0^2 + \frac{\partial^2}{\partial x^2}) - F_2(\lambda)\frac{\partial^2}{\partial x^2}\} \tag{23}$$

$$\mathcal{L}_{yy} = \int_0^\infty d\lambda\{F_1(\lambda)(k_0^2 + \frac{\partial^2}{\partial y^2}) - F_2(\lambda)\frac{\partial^2}{\partial y^2}\} \quad (24)$$

$$\mathcal{L}_{xy} = \int_0^\infty d\lambda(F_1(\lambda) - F_2(\lambda))\frac{\partial^2}{\partial x \partial y} \quad (25)$$

$$\mathcal{L}_{xy} = \mathcal{L}_{yx} \quad (26)$$

The functions $F_1(\lambda)$ and $F_2(\lambda)$ are singular functions of λ given by

$$F_1(\lambda) = -\frac{j\omega\mu_0}{4\pi k_0^2}2(e^{-u_0|z-d|} - e^{-u_0|z+d|} + 2u_0\frac{\sinh uh}{f_1(\lambda,h)}e^{-u_0|z+d|})\frac{\lambda}{u_0} \quad (27)$$

$$F_2(\lambda) = -2\frac{j\omega\mu_0}{4\pi k_0^2}(1-\epsilon_r)\cos\phi\int_0^\infty J_0(\lambda\rho)e^{-u_0|z+d|}\frac{\sinh uh \cosh uh}{f_1(\lambda,h)f_2(\lambda,h)}\lambda^2 \quad (28)$$

3.1 Galerkin's Method

The previous section outlined the method of moments procedure. The above equations could be used to arrive at a simultaneous system of linear equations by applying the boundary condition on the strip conductor at $(N+1)(M+1)$ different points, or in other words, by setting ΔE_x and ΔE_y to zero. A stronger condition for the minimization of the error is the definition of the inner product

$$V_{\nu\mu}^x = \langle j_{\nu\mu}(\vec{r}), \Delta E_x\rangle = 0 \quad (29)$$

$$V_{\nu\mu}^y = \langle j_{\nu\mu}(\vec{r}), \Delta E_y\rangle = 0 \quad (30)$$

With

$$\langle j_{\nu\mu}(\vec{r}), \Delta E_x\rangle = \int\int_s dx'dy' j_{\nu\mu}(\vec{r})\Delta E_x \quad (31)$$

When the testing functions, $j_{\nu\mu}(\vec{r})$, are chosen to be the same as the basis functions $f_{nm}(\vec{r}')$ the method is called Galerkin's method. Equations for $\nu = 1, \ldots$ N+1 and $\mu = 1, \ldots.$ M+1 generate a system of linear equations of the form

$$V_{\nu\mu}^x = \sum_{n=1}^{N+1}\sum_{n=1}^{M+1} I_{nm}^x Z_{xx}(\nu,\mu;n,m) + \sum_{n=1}^{N+1}\sum_{n=1}^{M+1} I_{nm}^y Z_{xy}(\nu,\mu;n,m) \quad (32)$$

$$V_{\nu\mu}^y = \sum_{n=1}^{N+1}\sum_{n=1}^{M+1} I_{nm}^x Z_{yx}(\nu,\mu;n,m) + \sum_{n=1}^{N+1}\sum_{n=1}^{M+1} I_{nm}^y Z_{yy}(\nu,\mu;n,m) \quad (33)$$

Where

$$Z_{ij}(\nu,\mu;n,m) = -\frac{j\omega\mu_0}{4\pi k_0^2}2\langle j_{\nu\mu}(\vec{r}), \mathcal{L}_{ij}\{J_0(\lambda\rho)\}, j_{nm}(\vec{r}')\rangle \quad (34)$$

3.2 Impedance Matrix Evaluation

The impedance matrix above contains elements which are very difficult to evaluate. Much care was taken to reduce the impedance matrix elements to a form which would be computationally efficient. The system of equations can be written in matrix form as

$$\begin{bmatrix} ZXX_{nm}^{\nu\mu} & ZXY_{nm}^{\nu\mu} \\ ZXX_{nm}^{\nu\mu} & ZYY_{nm}^{\nu\mu} \end{bmatrix} \begin{bmatrix} I_x^{nm} \\ I_y^{nm} \end{bmatrix} = \begin{bmatrix} V_x^{\nu\mu} \\ V_y^{\nu\mu} \end{bmatrix}$$

We now split the integro-differential operators $\mathcal{L}_{ij}$ defined in the previous section into two parts

$$\mathcal{L}_{ij}\{\} = \mathcal{L}_{ij}^{A}\{\} + \mathcal{L}_{ij}^{\infty}\{\} \qquad (35)$$

In the operator $\mathcal{L}_{ij}^{A}$, the λ-integration extends from zero to A, and in $\mathcal{L}_{ij}^{\infty}$ extends from A to infinity. A is chosen to be a large number such that

$$\tanh\sqrt{A^2 - k^2} \doteq 1 \qquad (36)$$

Beyond A an asymptotic expansion can be used for the Green's function.

Substitution of 36 into $\mathcal{L}_{ij}^{\infty}\{J_0(\lambda\rho)\}$, results in the following expression.

$$\mathcal{L}_{ij}^{\infty}\{J_0(\lambda\rho)\} = a_{ij}\frac{1}{\sqrt{\rho^2 + b_{ij}^2}} - \mathcal{L}_{ij}^{\prime A}\{J_0(\lambda\rho)\} \qquad (37)$$

With

$$\mathcal{L}_{xx}^{\prime} = \int\int_a d\lambda\{S_1(\lambda)(k_0^2 + \frac{\partial^2}{\partial x^2}) - S_2(\lambda)\frac{\partial^2}{\partial x^2}\} \qquad (38)$$

$$\mathcal{L}_{yy}^{\prime} = \int\int_a d\lambda\{S_1(\lambda)(k_0^2 + \frac{\partial^2}{\partial y^2}) - S_2(\lambda)\frac{\partial^2}{\partial y^2}\} \qquad (39)$$

$$\mathcal{L}_{xy}^{\prime} = \int\int_a d\lambda\{S_1(\lambda)(k_0^2 + \frac{\partial^2}{\partial x\partial y}) - S_2(\lambda)\frac{\partial^2}{\partial x\partial y}\} \qquad (40)$$

And in view of the above, equation 35 will take the form

$$\mathcal{L}_{ij}\{J_0(\lambda\rho)\} = L_{ij}^{A}\{J_0(\lambda\rho)\} + a_{ij}\frac{1}{\sqrt{\rho^2 + b_{ij}^2}} \qquad (41)$$

With a_{ij} and b_{ij} being constants which depend on A. Also, L_{ij}^{A} is given by 23-25 with $F_1(\lambda) - S_1(\lambda)$ and $F_2(\lambda) - S_2(\lambda)$ substituting for $F_1(\lambda)$ and $F_2(\lambda)$ respectively.

The resulting integration from 0-A $(L^A_{ij}\{J_0(\lambda\rho)\})$ can be partially transformed to reduce computer effort. Refer to "Computer Modeling of Microstrip Elements and Discontinuities," pp. 21-24 [1] for the details. The integration over this range also includes a finite number of singularities which are handled by a singularity extraction technique discussed on pp. 24-25 and 28-30.

The term $a_{ij}\frac{1}{\sqrt{\rho^2+b_{ij}^2}}$, known as the "tail contribution", is computed by a combination of numerical and analytic techniques as discussed in the same report on page 27.

3.3 Excitation Vector

The excitation vector in the matrix equations depends on the type of excitation used. A useful excitation is the delta gap generator. In this case, the electric field on the strip conductor is zero everywhere except at the delta gap. When the testing cell contains the gap the excitation vector will have a value for that element. If the testing cell does not contain the gap, the excitation vector element will be zero. If the gap is assumed to have unit strength and the fields are x-directed in the gap and located at position x_g, y_g ,then

$$V^x_{\nu\mu} = \left\{ \begin{array}{ll} 1 & if \nu = x_g \\ 0 & elsewhere \end{array} \right\}$$

4 Scattering Parameters

For microstrip discontinuities, the aim of this work is to develop equivalent circuits by using the calculated scattering parameters. Once the current is determined as discussed in section 3.2, the scattering parameters must be determined. One method to do this is the even-odd mode excitation scheme.

4.1 Even-Odd Mode Excitation Method

Any two port, as shown in figure 4, can be represented by 2-port impedance parameters

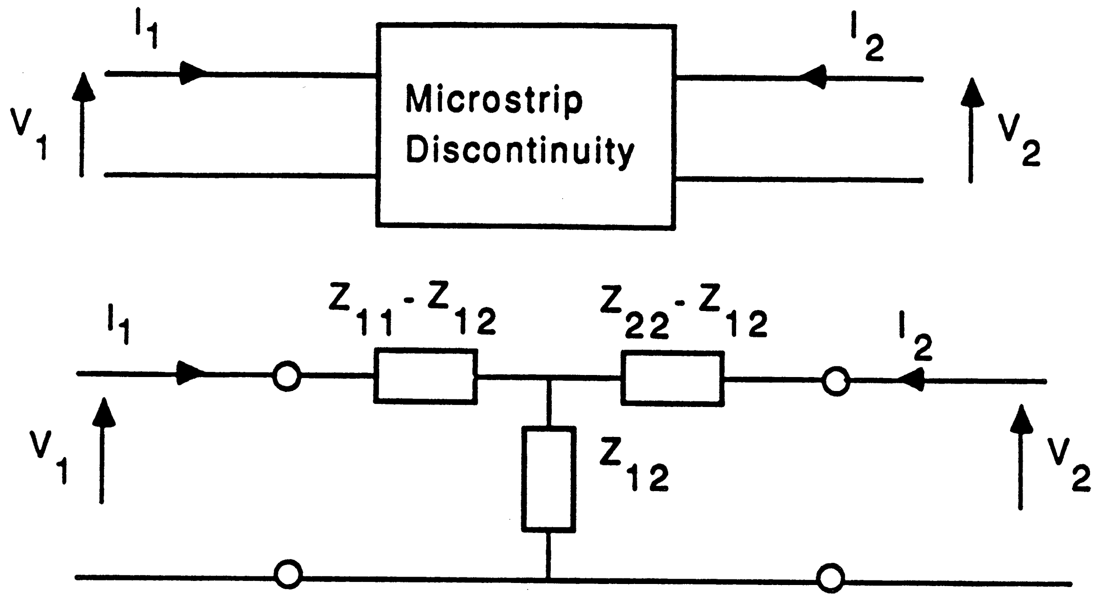

Figure 4: 2-Port Discontinuity

$$\begin{bmatrix} V_1 \\ V_2 \end{bmatrix} = \begin{bmatrix} Z_{11} & Z_{12} \\ Z_{21} & Z_{22} \end{bmatrix} \begin{bmatrix} I_1 \\ I_2 \end{bmatrix}$$

With $Z_{21} = Z_{12}$ due to reciprocity.

To determine these impedance parameters, the even-odd mode excitation method may be used. On each side of the discontinuity, a delta gap generator is placed (V_g^1 and V_g^2) as shown in figure 5. The input impedances $Z_{in}^{1e}, Z_{in}^{2e}, Z_{in}^{1o}$, and Z_{in}^{2o} can be determined at both ports (1,2 superscripts) by the resulting current on the element which is determined as explained in section 3.2 by exciting the discontinuity for the even case $V_g^e = V_g^o$ and the odd case $V_g^e = -V_g^o$. Once these are known, one can construct the Z-matrix from the equations

$$Z_{11} = \frac{1}{2}(Z_{in}^{1e} + Z_{in}^{1o}) \tag{42}$$

$$Z_{22} = \frac{1}{2}(Z_{in}^{2e} + Z_{in}^{2o}) \tag{43}$$

$$Z_{12} = \frac{1}{2}(Z_{in}^{1e} - Z_{in}^{1o}) \tag{44}$$

$$Z_{12} = Z_{21} \tag{45}$$

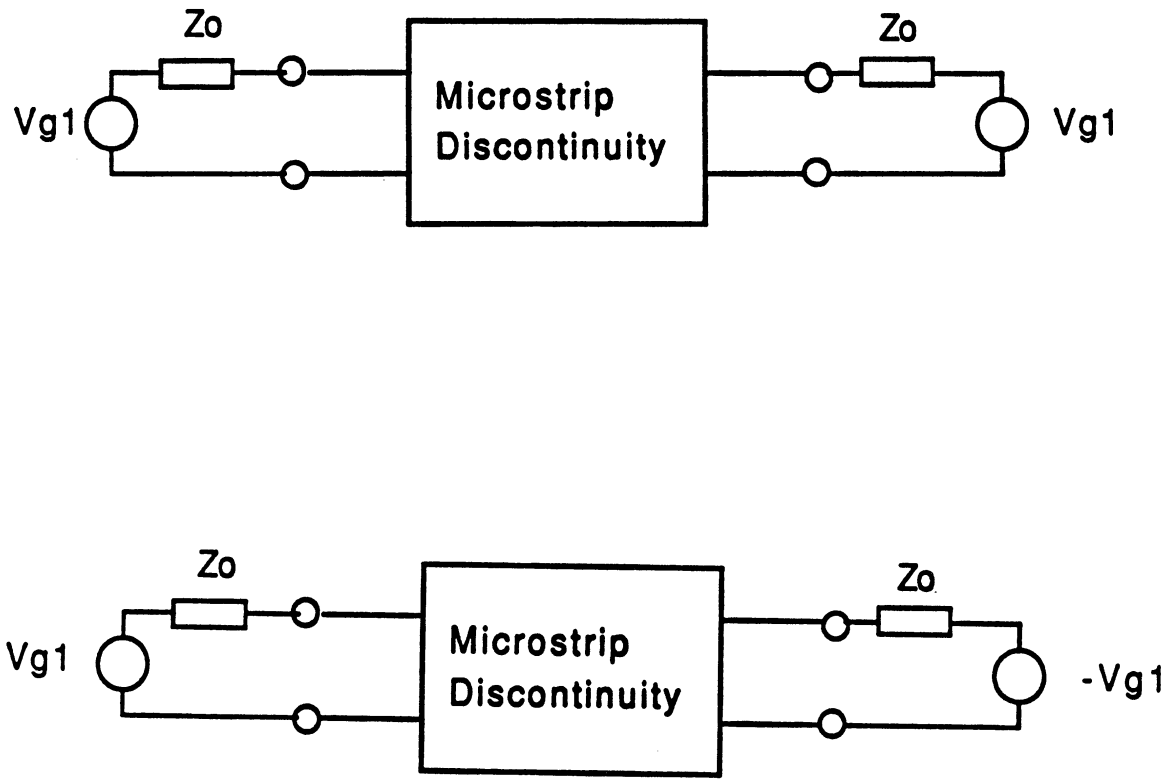

Figure 5: Even and Odd Excitations

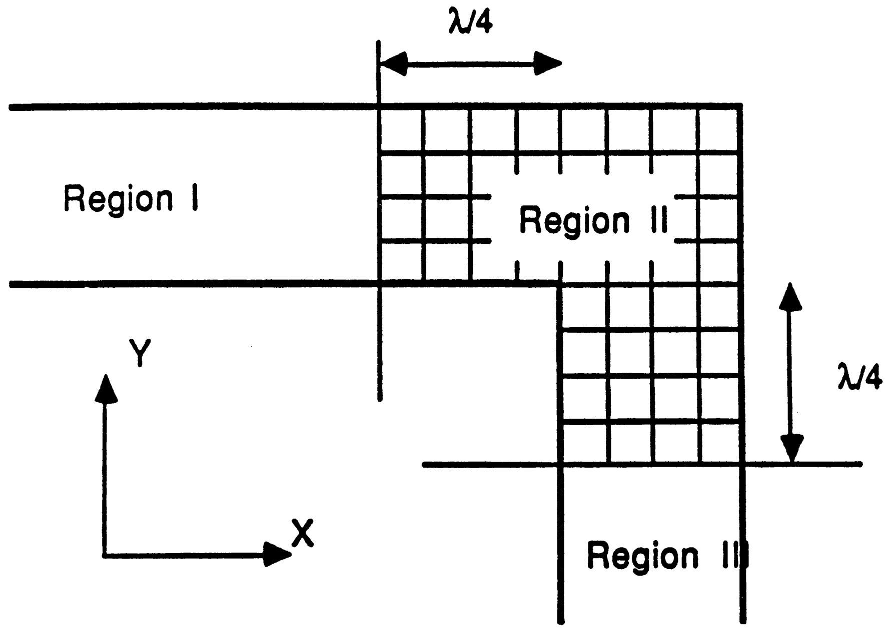

Figure 6: Local Current Model

where the added superscripts refer to the port the input impedances are calculated.

The scattering parameters can then be determined by well known relations between scattering and impedance matrices.

$$S_{11} = \frac{(Z_{11} - 1)(Z_{22} + 1) - Z_{21}^2}{A} \tag{46}$$

$$S_{22} = \frac{(Z_{11} + 1)(Z_{22} - 1) - Z_{21}^2}{A} \tag{47}$$

$$S_{12} = \frac{2Z_{12}}{A} \tag{48}$$

$$A = Z_{11} + 1)(Z_{22} + 1) - Z_{21}^2 \tag{49}$$

4.2 Alternate Method To Calculate Scattering Parameters

Another method of determining the scattering parameters for a microstrip discontinuity is to assume that away from the discontinuity the microstrip propagates the fundamental microstrip mode with propagation constant k_m, which is determined previously for an infinite line [7]. The element can then be divided into 3 regions as shown in figure 6. For the 3 regions assume

i) In region 1, an incident wave of unit magnitude, and a reflected wave with unknown reflection coefficient R is assumed.

ii) Region 2 contains the discontinuity and both x, and y directions of current are expanded by piecewise sinusoidal basis functions as discussed in section 3.2.

iii) In region 3, a transmitted traveling wave with unknown transmission coefficient T is assumed.

By exciting the discontinuity from both directions, one can extract the scattering parameters directly from the solution of the matrix equations ($R = S_{11}$ etc).

5 Surface Waves and Power Radiated

A contribution of this work will be the evaluation of the power radiated and the power launched into surface waves from microstrip discontinuities. These effects are critical at higher frequencies, and must be accounted for in the design of microwave circuits.

5.1 Radiated Power

To calculate the radiation pattern of a microstrip element, the far zone fields above the dielectric-air interface are needed. Once the current is determined as detailed in section 3.2, a numerical integration can be performed with equation 1 to compute the fields, but this is not computationally efficient at large distances from the element. Since only the far fields are needed, the stationary phase method [6] may be used to compute the radiation pattern [2].

The far zone from a printed microstrip element is

$$E_\theta \doteq k_0^2[\cos\theta\cos\phi\pi_x - \sin\theta\pi_z] \tag{50}$$

$$E_\phi \doteq k_0^2[-\sin\phi\pi_x] \tag{51}$$

where

$$\pi_x = -\frac{j\omega\mu_0}{4\pi k_0^2}\int\int_s dx'dy'J(x',y')\int_{-\infty}^{\infty} H_0^{(2)}(\lambda\rho)e^{-u_0 z}\frac{\sinh uh}{f_1(\lambda,h)}\lambda d\lambda \tag{52}$$

$$\pi_z = -\frac{j\omega\mu_0}{4\pi k_0^2}(1-\epsilon_r)\cos\phi\int\int_s dx'dy'J(x',y')\int_{-\infty}^{\infty} H_1^{(2)}(\lambda\rho)e^{-u_0 z}\frac{\sinh uh}{f_1(\lambda,h)}\frac{\cosh uh}{f_2(\lambda,h)}\lambda^2 d\lambda \tag{53}$$

These integrals can be evaluated by the stationary phase method to arrive at the far-field of the microstrip element. From the far field, the pattern or the power lost to radiation can be evaluated.

5.2 Surface Waves

As mentioned, the denominator of the Green's function contains a finite number of singularities along the path of integration. These singularities correspond to TE and TM surface waves which are excited in the dielectric. The characteristic equation for TE surface waves is the function $f_1(\lambda, h)$ in the denominator of the Green's function

$$f_1(\lambda, h) = u_0 \sinh uh + u \cosh uh \tag{54}$$

and for TM

$$f_2(\lambda, h) = \epsilon_r u_0 \cosh uh + u \sinh uh \tag{55}$$

with

$$uo = \sqrt{\lambda^2 - k_0^2} \tag{56}$$

$$u = \sqrt{\lambda^2 - k^2} \tag{57}$$

To evaluate the contribution to the pattern from the surface waves the integrals for the electric field can be evaluated by the saddle point method [6], and the residues corresponding to the TE and TM poles can be evaluated after the contour is deformed. Once the far zone fields in the dielectric are determined, the power launched into surface waves can be found by an integration over a cylindrical region in the dielectric which is in the far-field of the discontinuity.

6 Example-Microstrip Step to Open Circuit Stub

This method has been used to solve for the current on a microstrip step discontinuity to an open circuit stub as shown in figure 7. The computed current on the feeding line is shown in figure 8. As can be seen the current forms a standing wave pattern from which the reflection coefficient can be easily computed as discussed. It should be noted that the standing wave ratio is not infinity because of the losses due to radiation and surface wave excitaion. A two-dimensional plot of the X and Y current on the end of the stub is shown in figures 9 and 10.

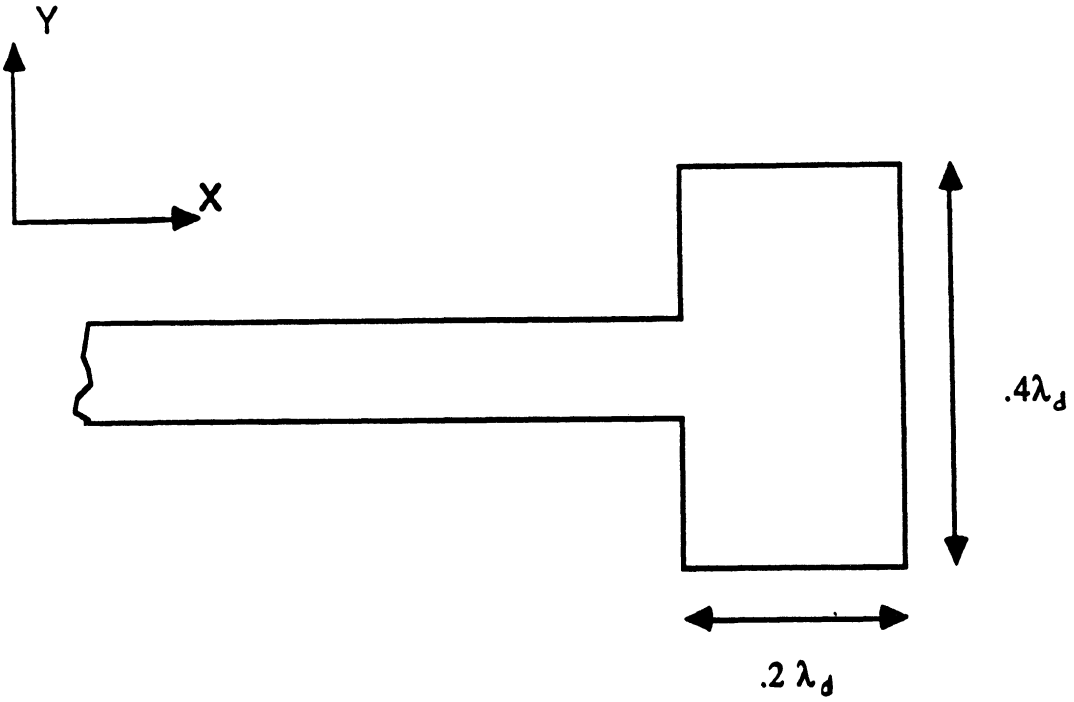

Figure 7: Microstrip Stub

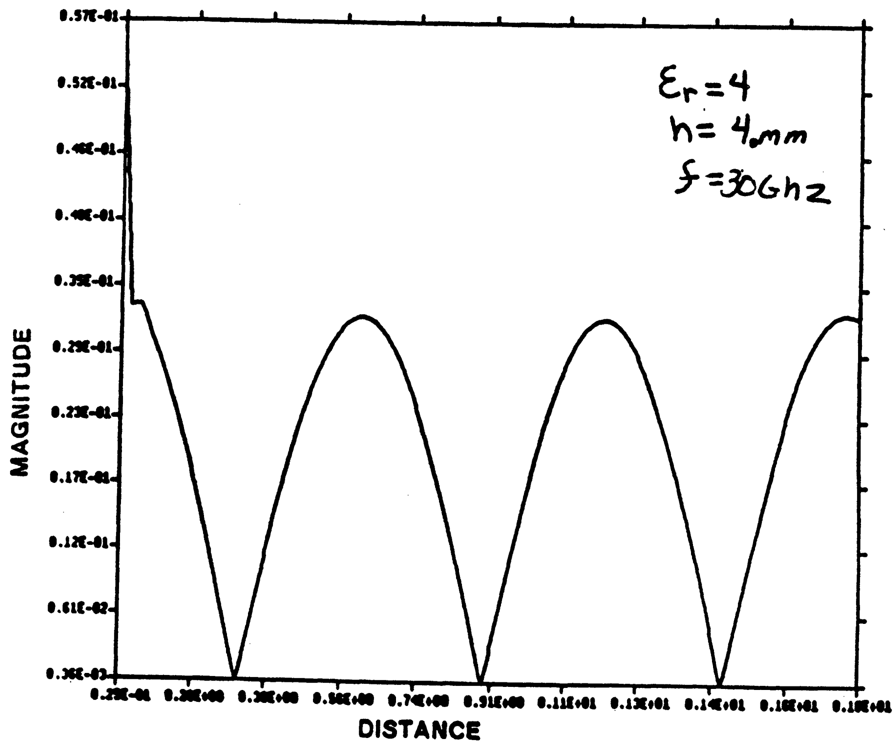

Figure 8: Microstrip Stub Current on Feeding Line

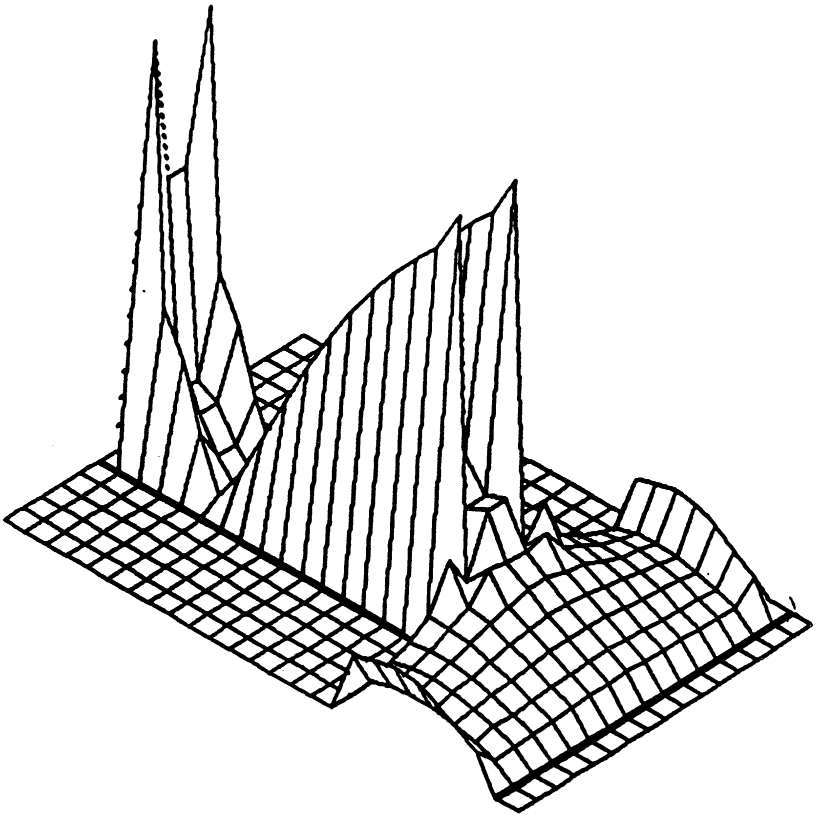

Figure 9: X-Directed Current on Microstrip Stub

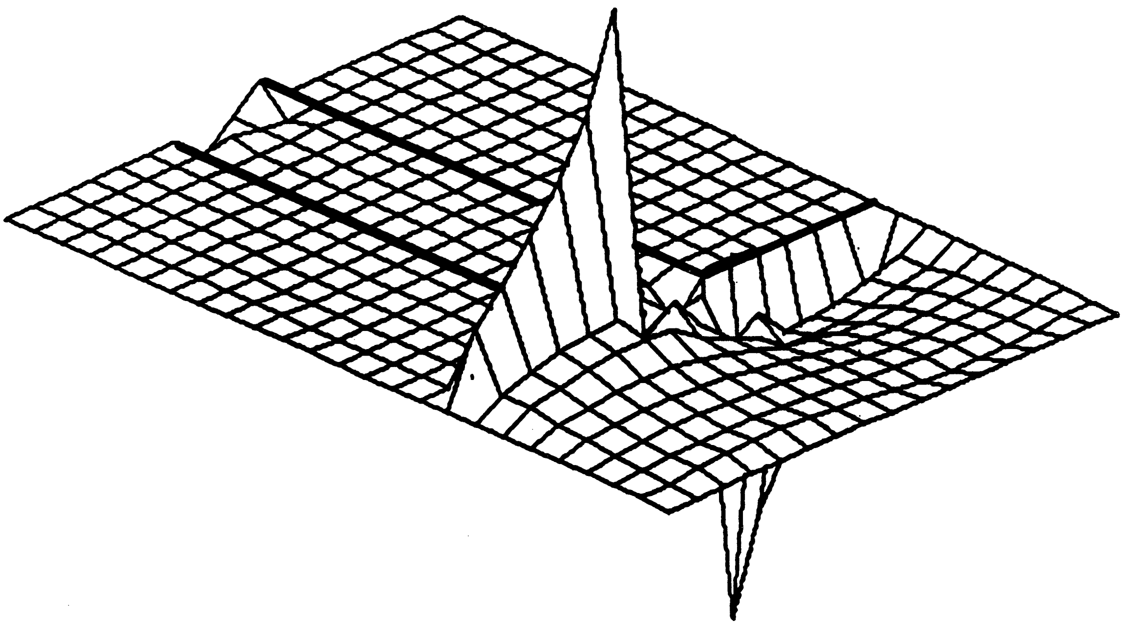

Figure 10: Y-Directed Current on Microstrip Stub

7 Conclusion

A full-wave analysis for open microstrip discontinuities has been developed. The method accounts for dispersion, electromagnetic coupling, radiation losses, and surface wave excitation. At the present time, the method is being used to analyze microstrip circuit discontinuities such as the bend, step and T-junction. The scattering parameters of these discontinuities will be determined, as well as, radiation losses and surface wave excitation. A saddle point method will be used to evaluate the radiation pattern and surface wave losses.

In the future, this method will be used to characterize radiating elements such as the travelling wave antenna.

References

[1] W. P. Harokopus, Jr. and P. B. Katehi Computer Modeling of Microstrip Elements and Discontinuities," Radiation Lab Report, June 1987.

[2] P.B. Katehi, A Generalized Solution to a Class of Printed Circuit Antennas, Dissertation, UCLA, 1984.

[3] A. Sommerfeld, Partial Differential Equations in Physics, New York, N.Y., Academic Press,1949.

[4] R.S. Elliot, "The Green's Function For Electric Dipoles Parallel To and Above or Within a Grounded Dielectric Slab", Hughes Technical Correspondence, 1978.

[5] R. F. Harrington, Field Computation By Moment Methods,Macmillan,N.Y. ,1968.

[6] L.B. Felsen and N. Marcuvitz, "Radiation and Scattering of Waves," Microwave and Fields series, Prentice Hall, Englewood Cliffs, N.J., 1973

[7] R.W. Jackson, and D.M. Pozar,"Full-Wave Analysis of Microstrip Open- End and gap discontinuities," IEEE Microwave Theory and Techniques," VOL. MTT-33, Oct. 1985.

"High-Frequency Characterization of Interconnects on Multilayer Substrates : The Green's Function"

I. INTRODUCTION

Planar transmission line structures such as microstrip line, coplanar line, and finline have been fundamental components of microwave integrated circuits for many years, [1]. More recently, there has been considerable effort devoted to the design and realization of monolithic microwave integrated circuits (MMIC's) for use in the f > 20 GHz region, [2]. In a given MMIC, any number of discontinuities occur such as: i) steps, ii) bends, iii) open ends, and iv) many others. Once fabricated, monolithic circuits are very difficult to tune for optimum performance and this is a major drawback, [2], [3]. Accurate theoretical models of these various discontinuities are required so that their circuit characteristics may be considered in the initial design, thus avoiding a time-consuming and costly production cycle. Research in this direction is ongoing, [4], [5], [6] and much has yet to be done. This paper discusses the theoretical background necessary for the derivation of Green's functions for use in the study of planar discontinuities.

II. ELECTROMAGNETIC VECTOR POTENTIALS

The electromagnetic fields in any region can be derived from appropriate choices of $\bar{A}$ and $\bar{F}$, the magnetic and electric vector potentials, respectively, [7]. For the horizontal electric dipole above a dielectric half-space, Sommerfeld [8], has demonstrated that two components of a magnetic vector potential are necessary to completely represent the electromagnetic fields of this problem. The argument presented in [8] is based on the fact that if only one component of $\bar{A}$ is used to generate the fields in each region, then continuity of tangential electromagnetic field components at the air-dielectric interface requires that the wavenumbers in each region be equal. This contradiction is resolved by considering a second component of $\bar{A}$. Instead of choosing two components of $\bar{A}$ to solve the above mentioned problem, one may use any two components of $\bar{A}$ and/or $\bar{F}$. And thus, although the fields which satisfy a particular boundary value problem are unique, the field generating potentials are not, [9].

In orthogonal coordinate systems it is conventional to denote fields as transverse electric (TE) or transverse magnetic (TM) with respect to coordinate axes. For example, fields derived from $\bar{F} = \hat{x}\ F_x$ are TE to x, or TE_x and so on.

When a rectangular waveguide is loaded with a dielectric layer, modes which are TE or TM with respect to the direction of propagation cannot exist. Instead, modes are designated as LSE and LSM. An LSE mode is said to be TE with respect to the direction that is normal to the air-dielectric interface in the guide. If this is normal is the $\hat{y}$ unit vector, then all waveguide modes can be generated from A_y and F_y. LSE_y and LSM_y modes are orthogonal, [10], and may be solved for separately. Thus, it is suggested that fields in layered cartesian regions be constructed using the components of $\bar{A}$ and $\bar{F}$ that are normal to the layer interfaces. This approach will give electromagnetic fields which decouple and substantially reduce the number of algebraic steps involved. The electromagnetic fields are generated from $\bar{A}$ and $\bar{F}$ as shown in equations (1).

$$\bar{E} = \frac{1}{\varepsilon}\bar{\nabla} \times \bar{F} - j\omega\bar{A} + \frac{1}{j\omega\mu\varepsilon}\bar{\nabla}\bar{\nabla} \bullet \bar{A} \tag{1a}$$

$$\bar{H} = \frac{1}{\mu}\bar{\nabla} \times \bar{A} + j\omega\bar{F} - \frac{1}{j\omega\mu\varepsilon}\bar{\nabla}\bar{\nabla} \bullet \bar{F} \tag{1b}$$

III. THE PRINCIPLE OF SCATTERING SUPERPOSITION

This method was first discussed by Tai, [11], and is conceptually simple. Figure (1a) shows a dipole source within a boundary S_1. A Green's function, $\bar{\bar{G}}$, due to this source is maintained. $\bar{\bar{G}}$ may be analogous to either an electromagnetic field or a vector potential, as long as it satisfies the proper boundary conditions. If another boundary, S_2, is introduced, as shown in Figure (1b), then $\bar{\bar{G}}$ will not satisfy the boundary conditions of this new problem. However, if a composite Green's function, $\bar{\bar{G}}_c$, given by

$$\bar{\bar{G}}_c = \bar{\bar{G}} + \bar{\bar{G}}_s \tag{2}$$

is assumed, then the "scattered" field, $\bar{\bar{G}}_s$, may be determined in such as way that $\bar{\bar{G}}_s$ would satisfy all boundary conditions. For most cases, scattering superposition requires solution in the spectral domain because usually only certain eigenvalues of the original $\bar{\bar{G}}$ are allowed after S_2 is introduced. Initially assuming that the eigenvalues of $\bar{\bar{G}}$ are a continuous spectrum (i.e. by representing $\bar{\bar{G}}_c$ as a fourier integral) allows them to take on their proper values in the spatial domain.

When constructing the scattered Green's function, $\bar{\bar{G}}_s$, for a layered cartesian structure, fewest algebraic steps are required when the components of $\bar{A}$ and $\bar{F}$ which are normal to the boundary, S_2, are used. Consequently, this is the suggested approach.

IV. DERIVATION OF THE TWO-DIMENSIONAL SPATIAL DOMAIN GREEN'S FUNCTION FOR A LAYERED RECTANGULAR WAVEGUIDE

Consider the rectangular waveguide inhomogeneously filled with three dielectrics shown in Figure 2. The dyadic Green's function for an arbitrary current, $\bar{J}(\bar{r}')$, in this waveguide has the form:

$$\bar{\bar{G}}_T(\bar{r}/\bar{r}') = G_{xx}(\bar{r}/\bar{r}')\hat{x}\hat{x} + G_{xy}(\bar{r}/\bar{r}')\hat{x}\hat{y} + G_{xz}(\bar{r}/\bar{r}')\hat{x}\hat{z}$$
$$+ G_{yx}(\bar{r}/\bar{r}')\hat{y}\hat{x} + G_{yy}(\bar{r}/\bar{r}')\hat{y}\hat{y} + G_{yz}(\bar{r}/\bar{r}')\hat{y}\hat{z} \quad (3)$$
$$+ G_{zx}(\bar{r}/\bar{r}')\hat{z}\hat{x} + G_{zy}(\bar{r}/\bar{r}')\hat{z}\hat{y} + G_{zz}(\bar{r}/\bar{r}')\hat{z}\hat{z}$$

where the electric field is obtained from

$$\bar{E}(\bar{r}) = \iiint_{V'} \bar{\bar{G}}_T(\bar{r}/\bar{r}') \bullet \bar{J}(\bar{r}')\, dv' \quad (4)$$

To obtain all nine terms of (3) is an extremely tedious process.

When analyzing planar discontinuities in such a structure, not all terms of the Green's DYAD are required for a rigorous solution. In fact, only four components of (3) are needed. We are interested in the tangential (with respect to the layer interfaces) electric field components (E_y, E_z) due to planar current densities (J_y, J_z). Clearly then, we can write a modified Green's function, appropriate for this analysis, as:

$$\bar{\bar{G}}_M(\bar{r}/\bar{r}') = G_{yy}(\bar{r}/\bar{r}')\hat{y}\hat{y} + G_{yz}(\bar{r}/\bar{r}')\hat{y}\hat{z} + G_{zy}(\bar{r}/\bar{r}')\hat{z}\hat{y} + G_{zz}(\bar{r}/\bar{r}')\hat{z}\hat{z} \quad (5)$$

From this point on, when referring to the Green's function, we mean that given in (5). In this section, the derivation of $G_{zz}(\bar{r}/\bar{r}')$ is outlined and the remaining components of (5) will be given. Note that $G_{zz}(\bar{r}/\bar{r}')$ is merely the $\hat{z}$-component of the electric field due to a $\hat{z}$-directed dipole located at (x', y', z'). We begin by considering the total field generated by the dipole as a superposition of primary and scattered components. The primary fields are generated directly by the source and the scattered fields result when the dielectric boundary layers are introduced. Consequently, the waveguide problem may be considered as a parallel-plate waveguide shorted at x = a which contains a primary field and a scattered field, combined with another parallel-plate waveguide shorted at x = 0, with three dielectric layers stacked on the shorted end, and which contains only scattered fields. These situations are illustrated in Figures (3a) and (3b). Clearly, other structure geometries such as rectangular cavities, may be analyzed by simply modifying the primary and scattered potentials appropriately.

The eigenfunction expansions for the primary fields are obtained from the magnetic vector potential $\bar{A}$, which satisfies the equation:

$$\nabla^2 \bar{A} + k^2 \bar{A} = -\mu_o \bar{J}(\bar{r}') \tag{6}$$

We are looking for $E_z(\bar{r}/\bar{r}')$ due to an infinitesimal $\hat{z}$-directed dipole. Therefore, the appropriate primary field generating function is a solution of

$$\nabla^2 \bar{A} + k^2 \bar{A} = -\hat{z}\,\mu_o\, \delta(x-x')\, \delta(y-y')\, \delta(z-z') \tag{7}$$

subject to the boundary conditions of the parallel plate structure in Figure (3a). It should be pointed out that the primary field will have different x-dependence above and below the source. Above the source is designated as region (0) and below, region (o'). The boundary conditions on $\bar{A}_p$ are obtained from those on the electric field. The necessary relationships are given in equation (1). The expression for $A_{zp}^{(0')}$ for this problem is:

$$A_{zp}^{(0)} = \int_{-\infty}^{\infty} dk_z \sum_m \frac{\varepsilon_{om}\mu_o}{2\pi k_x^{(0)} b} \sin k_x^{(0)} (a-x')\, e^{-jk_x^{(0)}(a-x)}$$

$$\bullet \left[\sin\left(\frac{m\pi y'}{b}\right) \quad \sin\left(\frac{m\pi y}{b}\right)\right] e^{-j k_z (z-z')} \tag{8}$$

where $(k_x^{(0')})^2 + (\frac{m\pi}{b})^2 + k_z^2 = \omega^2\mu_o\varepsilon_o$

The primary electromagnetic fields are obtained from equations (1) with $\bar{F} = 0$. Scattered fields are generated from magnetic and electric vector potentials $\bar{A}$ and $\bar{F}$, respectively. The proper choices are $\bar{A} = \hat{x}\, A_{xs}$ and $\bar{F} = \hat{x}\, F_{xs}$, for reasons discussed earlier. The scattered electromagnetic fields are obtained from equations (1).

By considering the boundary conditions on $\bar{E}_s$ in the parallel-plate structures of Figure 3 we obtain the eigenfunction expansions for the vector potentials $A_{xs}^{(i)}$ and $F_{xs}^{(i)}$ as:

$$A_{xs}^{(0)} = \int_{-\infty}^{\infty} dk_k \sum_m D_m^{(0)} \cos k_x^{(0)} (a-x) \sin (\frac{m\pi y}{b}) e^{-jk_z z} \tag{9a}$$

$$A_{xs}^{(1)} = \int_{-\infty}^{\infty} dk_z \sum_m \left[F_m^{(1)} \sin k_x^{(1)} x + G_m^{(1)} \cos k_x^{(1)} x \right] \sin (\frac{m\pi y}{b}) e^{-jk_z z} \tag{9b}$$

$$A_{xs}^{(2)} = \int_{-\infty}^{\infty} dk_z \sum_m \left[F_m^{(2)} \sin k_x^{(2)} x + G_m^{(2)} \cos k_x^{(2)} x \right] \sin (\frac{m\pi y}{b}) e^{-jk_z z} \tag{9c}$$

$$A_{xs}^{(3)} = \int_{-\infty}^{\infty} dk_z \sum_m D_m^{(3)} \cos k_x^{(3)} x \sin (\frac{m\pi y}{b}) e^{-jk_z z} \tag{9d}$$

$$F_{xs}^{(0)} = \int_{-\infty}^{\infty} dk_z \sum_m A_m^{(0)} \sin k_x^{(0)} (a-x) \cos (\frac{m\pi y}{b}) e^{-jk_z z} \tag{10a}$$

$$F_{xs}^{(1)} = \int_{-\infty}^{\infty} dk_z \sum_m \left[B_m^{(1)} \sin k_x^{(1)} x + C_m^{(1)} \cos k_x^{(1)} x \right] \cos (\frac{m\pi y}{b}) e^{-jk_z z} \tag{10b}$$

$$F_{xs}^{(2)} = \int_{-\infty}^{\infty} dk_z \sum_m \left[B_m^{(2)} \sin k_x^{(2)} x + C_m^{(2)} \cos k_x^{(2)} x \right] \cos (\frac{m\pi y}{b}) e^{-jk_z z} \tag{10c}$$

$$F_{xs}^{(3)} = \int_{-\infty}^{\infty} dk_z \sum_m A_m^{(3)} \sin k_x^{(3)} x \cos (\frac{m\pi y}{b}) e^{-jk_z z} \tag{10d}$$

$$\text{where } (k_x^{(i)})^2 + (\frac{m\pi}{b})^2 + k_z^2 = k_i^2 \tag{11}$$

The scattered fields in regions (0) and (0') are identical.

The electromagnetic fields obtained from (1), (8), (9), and (10) satisfy all boundary conditions in the inhomogeneously filled waveguide except continuity of E_y, E_z, H_y, and H_z at $x = x_{01}$. Imposing these boundary conditions allows us to find exact expressions for the scattered fields. $G_{zz}(\bar{r}/\bar{r}')$ is then obtained. Since only scattered fields exist in the dielectric layers, they must be continuous at each of the interfaces. Consequently, $F_m^{(1)}$ and $G_m^{(1)}$ can both be expressed in terms of $D_m^{(3)}$. Also, $B_m^{(1)}$ and $C_m^{(1)}$ can be expressed in terms of $A_m^{(3)}$. The boundary conditions at $x = x_{01}$ are:

$$E_{yp}^{(0')} + E_{yA}^{(0)} + E_{yF}^{(0)} = E_{yA}^{(1)} + E_{yF}^{(1)}$$

$$E_{zp}^{(0')} + E_{zA}^{(0)} + E_{zF}^{(0)} = E_{zA}^{(1)} + E_{zF}^{(1)} \tag{12}$$

$$H_{yp}^{(0')} + H_{yA}^{(0)} + H_{yF}^{(0)} = H_{yA}^{(1)} + H_{yF}^{(1)}$$

$$H_{zp}^{(0')} + H_{zA}^{(0)} + H_{zF}^{(0)} = H_{zA}^{(1)} + H_{zF}^{(1)}$$

Equations (12) yield two sets of 2x2 equations:

$$\begin{bmatrix} M_{11}^{A} & M_{12}^{A} \\ M_{21}^{A} & M_{22}^{A} \end{bmatrix} \begin{bmatrix} D_m^{(0)} \\ D_m^{(3)} \end{bmatrix} = \begin{bmatrix} S_1^{A} \\ S_2^{A} \end{bmatrix} \tag{13}$$

$$\begin{bmatrix} N_{11}^{F} & N_{12}^{F} \\ N_{21}^{F} & N_{22}^{F} \end{bmatrix} \begin{bmatrix} A_m^{(0)} \\ A_m^{(3)} \end{bmatrix} = \begin{bmatrix} S_1^{F} \\ S_2^{F} \end{bmatrix} \tag{14}$$

Solution of (13) and (14) provides the unknown amplitude coefficients for, respectively, $A_x^{(i)}$ and $F_x^{(i)}$.

To analyze microstrip circuitry enclosed in the structure of Figure 2, the Green's function must be known at the air-dielectric interface because this is where the current carrying strip lies, [5]. From (12) we know that the tangential fields must be continuous at this boundary and, therefore, so is the Green's dyad. Consequently, we can obtain $G_{zz}(\bar{r}/\bar{r}')\,|_{x=x_{01}}$ from E_z in either region (0') or region (1). In the first dielectric region, region (1), the $\hat{z}$-component of the electric field due to a $\hat{z}$-directed current source, from (1a), (9) and (10), is given by:

$$E_z^{(1)} = E_{zA}^{(1)} + E_{zF}^{(1)} \text{ where}$$

$$E_{zA}^{(1)} = \frac{1}{j\omega\mu_o\varepsilon_1} \frac{\partial^2 A_{xs}^{(1)}}{\partial z \partial x} \tag{15}$$

$$E_{zF}^{(1)} = -\frac{1}{\varepsilon_1} \frac{\partial F_{xs}^{(1)}}{\partial y} \tag{16}$$

Substituting (9b) and (10b) into (15) and (16), with the respective amplitude coefficients derived from (13) and (14), yields:

$$E_{zA}^{(1)} = \frac{j\omega\mu_o}{2\pi} \int_{-\infty}^{\infty} dk_k \sum_m \frac{2 \sin k_x^{(0)} (a-x') \, \sin (\frac{m\pi y'}{b}) \, \sin (\frac{m\pi y}{b}) \, e^{-jk_z(z-z')}}{b\left[(\frac{m\pi}{b})^2 + k_z^2 \right]}$$

$$\bullet \left\{ \frac{k_z^2 k_x^{(0)} k_x^{(1)} \left[K_1 \cos k_x^{(1)} x - K_2 \sin k_x^{(1)} x \right]}{k_o^2 \tilde{\Lambda}(k_z^{(i)}, k_z)} \right\} \qquad (17)$$

$$E_{zF}^{(1)} = \frac{-j\omega\mu_o}{2\pi} \int_{-\infty}^{\infty} dk_z \sum_m \frac{2 \sin k_x^{(0)} (a-x') \, \sin (\frac{m\pi y'}{b}) \, \sin (\frac{m\pi y}{b}) \, e^{-jk_z (z-z')}}{b\left[(\frac{m\pi}{b})^2 + k_z^2 \right]}$$

$$\bullet \left\{ \frac{(\frac{m\pi}{b})^2 \left[R_1 \sin k_x^{(1)} x + R_2 \cos k_x^{(1)} x \right]}{\tilde{\Gamma}(k_x^{(i)}, k_z)} \right\} \qquad (18)$$

Specific terms in (17) and (18) will be discussed later. Notice that $E_{zA}^{(1)}$ is associated with a total electromagnetic field which is LSM_x and $E_{zF}^{(1)}$ is associated with a total electromagnetic field which is LSE_x.

The spectral domain form of the Green's function may be used to find dispersion characteristics for the shielded microstrip line shown in figure 4. By convolving a microstrip current distribution which satisfies the edge condition and has axial dependence $e^{-jk_z^{ms} z}$ (k_z^{ms} unknown) with the Fourier domain Green's function, we obtain a quantity which must be zero on the conducting microstrip. Applying the Galerkin's procedure to this integral equation yields an expression having k_z^{ms} as the only unknown. The k_z^{ms} values which are roots to the equation may be obtained efficiently on a P.C. by using the Mueller method with deflation. Preliminary results compare very well with the literature, [12]. Figure 5 shows this comparison where $x_{12} = x_{23} = 0$; $x_{01} = 0.5$mm; $w = 0.5$mm; $a = b = 2.0$cm; $\varepsilon_{r1} = 10$. Notice that lossy substrate lines may be analyzed with this technique.

The remaining task is to complete the inverse fourier transforms of (17) and (18). This will provide us with the desired spatial domain component of the Green's dyad. Both integrals may be evaluated via the calculus of residues since no branch points exist in their respective integrands. For both LSM_x and LSE_x modes, the inversion contour in the k_z-plane is closed in the lower half for $z > z'$, and in the upper half for $z < z'$. Of course, the distribution of poles in the k_z-plane is symmetric about the origin. Completing the inverse transform yields the electric field as

$$E_z^{(1)} = -\sum_n \sum_m \frac{2\omega\mu_o U_{nm}}{\Lambda'(k_{znm})} \sin\left(\frac{m\pi y}{b}\right) \sin\left(\frac{m\pi y'}{b}\right) e^{-jk_{znm}|z-z'|}$$

$$+ \sum_p \sum_m \frac{2\omega\mu_o V_{pm}}{\Gamma'(k_{zpm})} \sin\left(\frac{m\pi y}{b}\right) \sin\left(\frac{m\pi y'}{b}\right) e^{-jk_{zpm}|z-z'|} \qquad (19)$$

where U_{nm} is

$$U_{nm} = \left\{ \frac{k_{znm}^2 k_{xn}^{(0)} k_{xn}^{(1)} (K_1 \cos k_{xn}^{(1)} x - K_2 \sin k_{xn}^{(1)} x)}{k_o^2 b \left[\left(\frac{m\pi}{b}\right)^2 + k_{znm}^2 \right]} \right\} \sin k_{xn}^{(0)} (a-x') \qquad (20)$$

and V_{pm} is

$$V_{pm} = \left\{ \frac{\left(\frac{m\pi}{b}\right)^2 (R_1 \sin k_{xp}^{(1)} x + R_2 \cos k_{xp}^{(1)} x)}{b \left[\left(\frac{m\pi}{b}\right)^2 + k_{zpm}^2 \right]} \right\} \sin k_{xp}^{(0)} (a-x') \qquad (21)$$

Explicit expressions for K_1 and K_2 are given in Appendix A and explicit expressions for R_1 and R_2 in Appendix B. From the residue calculus we know that k_{znm} is a root of $\Lambda(k_x^{(i)}, k_z)$ and corresponds to an allowed LSM_x eigenvalue in the guide. Similarly, we know that k_{zpm} is a root of $\Gamma(k_x^{(i)}, k_z)$ and is an allowed LSE_x eigenvalue of this structure. These eigenvalues may also be determined by the transverse resonance technique, [10]. In our assumed model it required that $x' \geq x_{01}$ and this restriction applies to the field given in equation (18). However, it is not a problem because we are interested in the fields generated in the waveguide due to a source at $x' = x_{01}$. The functions $\Lambda'(k_{znm})$ and $\Gamma'(k_{zpm})$ result from the Taylor series expansions of the denominators of (17) and (18), respectively, and are defined as:

$$\Lambda'(k_{znm}) = \left. \frac{d\Lambda(k_x^{(i)}, k_z)}{dk_z} \right|_{k_z = k_{znm}} \tag{22}$$

$$\Gamma'(k_{zpm}) = \left. \frac{d\Gamma(k_x^{(i)}, k_z)}{dk_z} \right|_{k_z = k_{zpm}} \tag{23}$$

Expressions for $\frac{d\Lambda(k_x^{(i)}, k_z)}{dk_z}$ and $\frac{d\Gamma(k_x^{(i)}, k_z)}{dk_z}$ are given in Appendix A and B respectively.

Equations (17) and (18) also show poles that appear when $k_z = \pm j\left(\frac{m\pi}{b}\right)$. These are non-physical spurious modes which are not orthogonal to the LSM_x and LSE_x modes. Consequently, they need not be discussed any further. The final expression for $G_{zz}(x_{01}, y, z \mid x_{01}, y', z')$ is given in equation (24).

$$G_{zz}(x, x' = x_{01}) = -\sum_n \sum_m \frac{Z\omega\mu_o U_{nm}(x, x' = x_{01})}{\Lambda'(k_{znm})} \sin\left(\frac{m\pi y}{b}\right) \sin\left(\frac{m\pi y'}{b}\right) e^{-jk_{znm}|z-z'|}$$

$$+ \sum_p \sum_m \frac{Z\omega\mu_o V_{pm}(x, x' = x_{01})}{\Gamma'(k_{zpm})} \sin\left(\frac{m\pi y}{b}\right) \sin\left(\frac{m\pi y'}{b}\right) e^{-jk_{zpm}|z-z'|} \tag{24}$$

The remaining three components of the Green's function may be obtained in a completely analogous manner as that used to find G_{ZZ}. For the sake of completeness, all four terms of $\overline{\overline{G}}_m(x, x' = x_{01})$ are given in Appendix C.

V. CONCLUSION

This report has discussed an alternative method for deriving Green's function in layered regions. It has been shown that the usual tedious algebra encountered when working with many layer structures can be reduced to having to solve two 2x2 sets of equations for unknown vector potential amplitude coefficients. To demonstrate the usefulness of this technique, a component of the electric field Green's function was derived for a rectangular waveguide loaded with three isotropic, lossy dielectric slabs.

REFERENCES

[1] T. Itoh, Ed., Planar Transmission Line Structures. New York: IEEE Press, 1987.

[2] R.A. Pucel, "Design Considerations for Monolithic Microwave Circuits," IEEE Trans. on Microwave Theory and Techniques, MTT-29, no. 6, June 1981, pp. 513-534.

[3] R.S. Pengelly, "Hybrid vs. Monolithic Microwave Circuits - A Matter of Cost," Microwave System News, January 1983, pp. 77-114.

[4] R.H. Jansen, "Hybrid Mode Analysis of End Effects of Planar Microwave and Millimetre-Wave Transmission Lines," IEE Proceedings, vol. 128, Pt. H, no. 2, pp. 77-86, April 1981.

[5] P.B. Katehi and N.G. Alexopoulos, "Frequency-Dependent Characteristics of Microstrip Discontinuities in Millimeter-Wave Integrated Circuits," IEEE Trans. on Microwave Theory and Techniques, MTT-33, no. 10, October 1985, pp. 1029-1035.

[6] R.W. Jackson and D.M. Pozar, "Full-Wave Analysis of Microstrip Open-End and Gap Discontinuities," IEEE Trans. on Microwave Theory and Techniques, MTT-33, no. 10, October 1985, pp. 1036-1042.

[7] R.F. Harrington, Time Harmonic Electromagnetic Fields. New York: McGraw-Hill, 1961.

[8] A. Sommerfeld, Partial Differential Equations. New York: Academic Press, 1949.

[9] O. Kellog, Foundations of Potential Theory. New York: Dover, 1953.

[10] R.E. Collin, Field Theory of Guided Waves. New York: McGraw-Hill, 1960.

[11] C.T. Tai, Dyadic Green's Function in Electromagnetic Theory. Scranton: Intext, 1971.

[12] D. Mirshekar-Syahkal, "An Accurate Determination of Dielectric Loss Effect in MMIC's Including Microstrip and Coupled Microstrip Lines," IEEE Trans. on Microwave Theory and Techniques, MTT-31, no. 11, November 1983, pp. 950-954.

APPENDIX A

Expression for K_1, K_2 and $\frac{d\Lambda(k_x^{(i)}, k_z)}{dk_z}$

In Appendix A, primed notation represents the total derivative with respect to k_z.

It is convenient to designate the following functions:

$$\lambda_{01} = \varepsilon_2^2 k_x^{(1)} k_x^{(3)} \sin(k_x^{(3)} x_{23}) \cos(k_x^{(2)} x_{23})$$

$$\lambda_{02} = \varepsilon_2 \varepsilon_3 k_x^{(1)} k_x^{(2)} \cos(k_x^{(3)} x_{23}) \sin(k_x^{(2)} x_{23})$$

$$\lambda_{03} = \varepsilon_1 \varepsilon_3 (k_x^{(2)})^2 \cos(k_x^{(2)} x_{12}) \cos(k_x^{(1)} x_{12})$$

$$\lambda_{04} = \varepsilon_2 \varepsilon_3 k_x^{(1)} k_x^{(2)} \sin(k_x^{(2)} x_{12}) \sin(k_x^{(1)} x_{12})$$

$$\lambda_{05} = \varepsilon_2 \varepsilon_3 k_x^{(1)} k_x^{(2)} \cos(k_x^{(3)} x_{23}) \cos(k_x^{(2)} x_{23})$$

$$\lambda_{06} = \varepsilon_2^2 k_x^{(1)} k_x^{(3)} \sin(k_x^{(3)} x_{23}) \sin(k_x^{(2)} x_{23})$$

$$\lambda_{07} = \varepsilon_2 \varepsilon_3 k_x^{(1)} k_x^{(2)} \cos(k_x^{(2)} x_{12}) \sin(k_x^{(1)} x_{12})$$

$$\lambda_{08} = \varepsilon_1 \varepsilon_3 (k_x^{(2)})^2 \sin(k_x^{(2)} x_{12}) \cos(k_x^{(1)} x_{12})$$

$$\lambda_{09} = \varepsilon_2 \varepsilon_3 k_x^{(1)} k_x^{(2)} \sin(k_x^{(2)} x_{12}) \cos(k_x^{(1)} x_{12})$$

$$\lambda_{10} = \varepsilon_1 \varepsilon_3 (k_x^{(2)})^2 \cos(k_x^{(2)} x_{12}) \sin(k_x^{(1)} x_{12})$$

$$\lambda_{11} = \varepsilon_1 \varepsilon_3 (k_x^{(2)})^2 \sin(k_x^{(2)} x_{12}) \sin(k_x^{(1)} x_{12})$$

$$\lambda_{12} = \varepsilon_2 \varepsilon_3 k_x^{(1)} k_x^{(2)} \cos(k_x^{(2)} x_{12}) \cos(k_x^{(1)} x_{12})$$

$$\lambda_{13} = \varepsilon_{r1} k_x^{(0)} \sin k_x^{(0)} (a - x_{01}) \sin(k_x^{(1)} x_{01})$$

$$\lambda_{14} = k_x^{(1)} \cos k_x^{(0)} (a - x_{01}) \cos(k_x^{(1)} x_{01})$$

$$\lambda_{15} = \varepsilon_{r1} k_x^{(0)} \sin k_x^{(0)} (a - x_{01}) \cos(k_x^{(1)} x_{01})$$

$$\lambda_{16} = k_x^{(1)} \cos k_x^{(0)} (a - x_{01}) \sin(k_x^{(1)} x_{01})$$

Expressions for K_1, K_2 and Λ' are:

$$K_1 = (\lambda_{01} + \lambda_{02})\ (\lambda_{03} + \lambda_{04}) + (\lambda_{05} - \lambda_{06})\ (\lambda_{07} - \lambda_{08})$$

$$K_2 = (\lambda_{01} + \lambda_{02})\ (\lambda_{09} - \lambda_{10}) + (\lambda_{05} - \lambda_{06})\ (\lambda_{11} + \lambda_{12})$$

$$\begin{aligned}\Lambda' = {} & (\lambda'_{13} - \lambda'_{14})\ \tilde{K}_1 + (\lambda'_{15} + \lambda'_{16})\ \tilde{K}_2 \\ & + (\lambda_{13} - \lambda_{14}) \Big[(\lambda'_{01} + \lambda'_{02})\ (\lambda_{03} + \lambda_{04}) + (\lambda_{01} + \lambda_{02})\ (\lambda'_{03} + \lambda'_{04}) \\ & \qquad + (\lambda'_{05} - \lambda'_{06})\ (\lambda_{07} - \lambda_{08}) + (\lambda_{05} - \lambda_{06})\ (\lambda'_{07} - \lambda'_{08}) \Big] \\ & + (\lambda_{15} + \lambda_{16}) \Big[(\lambda'_{01} + \lambda'_{02})\ (\lambda_{09} - \lambda_{10}) + (\lambda_{01} + \lambda_{02})\ (\lambda'_{09} - \lambda'_{10}) \\ & \qquad + (\lambda'_{05} - \lambda'_{06})\ (\lambda_{11} + \lambda_{12}) + (\lambda_{05} - \lambda_{06})\ (\lambda'_{11} + \lambda'_{12}) \Big]\end{aligned}$$

APPENDIX B

Expressions for R_1, R_2 and $\dfrac{d\,\Gamma\,(k_x^{(i)}, k_z)}{dk_z}$

In Appendix B primed notation represents the total derivative with respect to k_z. It is convenient to designate the following functions:

$$\delta_{01} = k_x^{(1)} k_x^{(2)} \sin (k_x^{(3)} x_{23}) \sin (k_x^{(2)} x_{23})$$

$$\delta_{02} = k_x^{(1)} k_x^{(3)} \cos (k_x^{(3)} x_{23}) \cos (k_x^{(2)} x_{23})$$

$$\delta_{03} = k_x^{(1)} k_x^{(2)} \sin (k_x^{(2)} x_{12}) \sin (k_x^{(1)} x_{12})$$

$$\delta_{04} = (k_x^{(2)})^2 \cos (k_x^{(2)} x_{12}) \cos (k_x^{(1)} x_{12})$$

$$\delta_{05} = k_x^{(1)} k_x^{(2)} \sin (k_x^{(3)} x_{23}) \cos (k_x^{(2)} x_{23})$$

$$\delta_{06} = k_x^{(1)} k_x^{(3)} \cos (k_x^{(3)} x_{23}) \sin (k_x^{(2)} x_{23})$$

$$\delta_{07} = k_x^{(1)} k_x^{(2)} \cos (k_x^{(2)} x_{12}) \sin (k_x^{(1)} x_{12})$$

$$\delta_{08} = (k_x^{(2)})^2 \sin (k_x^{(2)} x_{12}) \cos (k_x^{(1)} x_{12})$$

$$\delta_{09} = k_x^{(1)} k_x^{(2)} \cos (k_x^{(1)} x_{12}) \sin (k_x^{(2)} x_{12})$$

$$\delta_{10} = (k_x^{(2)})^2 \cos (k_x^{(2)} x_{12}) \sin (k_x^{(1)} x_{12})$$

$$\delta_{11} = k_x^{(1)} k_x^{(2)} \cos (k_x^{(1)} x_{12}) \cos (k_x^{(2)} x_{12})$$

$$\delta_{12} = (k_x^{(2)})^2 \sin (k_x^{(1)} x_{12}) \sin (k_x^{(2)} x_{12})$$

$$\delta_{13} = k_x^{(0)} \cos k_x^{(0)} (a-x_{01}) \sin (k_x^{(1)} x_{01})$$

$$\delta_{14} = k_x^{(1)} \sin k_x^{(0)} (a-x_{01}) \cos (k_x^{(1)} x_{01})$$

$$\delta_{15} = k_x^{(0)} \cos k_x^{(0)} (a-x_{01}) \cos (k_x^{(1)} x_{01})$$

$$\delta_{16} = k_x^{(1)} \sin k_x^{(0)} \; (a\text{-}x_{01}) \; \sin (k_x^{(1)} \, x_{01})$$

Expressions for R_1, R_2 and Γ are:

$$R_1 = (\delta_{01} + \delta_{02}) \; (\delta_{03} + \delta_{04}) + (\delta_{05} - \delta_{06}) \, (\delta_{07} - \delta_{08})$$

$$R_2 = (\delta_{01} + \delta_{02}) \; (\delta_{09} - \delta_{10}) + (\delta_{05} - \delta_{06}) \, (\delta_{11} + \delta_{12})$$

$$\begin{aligned}
\Gamma = {} & (\delta'_{13} + \delta'_{14}) \; \tilde{R}_1 + (\delta'_{15} - \delta'_{16}) \, \tilde{R}_2 \\
& + (\delta_{13} + \delta_{14}) \; \Big[(\delta'_{01} + \delta'_{02}) \; (\delta_{03} + \delta_{04}) + (\delta_{01} + \delta_{02}) \; (\delta'_{03} + \delta'_{04}) \\
& \qquad + (\delta'_{05} - \delta'_{06}) \; (\delta_{07} - \delta_{08}) + (\delta_{05} - \delta_{06}) \; (\delta'_{07} - \delta'_{08}) \Big] \\
& + (\delta_{15} + \delta_{16}) \; \Big[(\delta'_{01} + \delta'_{02}) \; (\delta_{09} + \delta_{10}) + (\delta_{01} + \delta_{02}) \; (\delta'_{09} + \delta'_{10}) \\
& \qquad + (\delta'_{05} - \delta'_{06}) \; (\delta_{11} - \delta_{12}) + (\delta_{05} - \delta_{06}) \; (\delta'_{11} - \delta'_{12}) \Big]
\end{aligned}$$

APPENDIX C

$$\bar{\bar{G}}_M (x, x' = x_{01}) = G_{yy} (x, x' = x_{01}) \hat{y} \hat{y} + G_{yz} (x, x' = x_{01}) \hat{y} \hat{z}$$

$$+ G_{zy} (x, x' = x_{01}) \hat{z} \hat{y} + G_{zz} (x, x' = x_{01}) \hat{z} \hat{z}$$

It is convenient to reproduce the following functions:

$$U_{nm} (x, x' = x_{01}) = \frac{k_{znm}^2 k_{x_n}^{(0)} k_{x_n}^{(1)} (K_1 \cos k_{x_n}^{(1)} x_{01} - K_2 \sin k_{x_n}^{(1)} x_{01}) \sin k_{x_n}^{(0)} (a-x_{01})}{k_0^2 b \left[(\frac{m\pi}{b})^2 + k_{znm}^2 \right]}$$

$$V_{pm} (x, x' = x_{01}) = \frac{(\frac{m\pi}{b})^2 (R_1 \sin k_{xp}^{(1)} x_{01} + R_2 \cos k_x^{(1)} x_{01}) \sin k_{xp}^{(0)} (a-x_{01})}{b \left[(\frac{m\pi}{b})^2 + k_{zpm}^2 \right]}$$

$$G_{yy} (x, x' = x_{01}) = -\sum_n \sum_m \frac{\varepsilon_{om} \omega\mu_o (\frac{m\pi}{b})^2 U_{nm} (x, x' = x_{01})}{k_{znm}^2 \Lambda' (k_{znm})} \cos (\frac{m\pi y}{b}) \cos(\frac{m\pi y'}{b}) e^{-jk_{znm} |z-z'|}$$

$$+ \sum_p \sum_m \frac{\varepsilon_{om} \omega\mu_o k_{zpm}^2 V_{pm} (x, x' = x_{01})}{(\frac{m\pi}{b})^2 \Gamma(k_{zpm})} \cos (\frac{m\pi y}{b}) \cos (\frac{m\pi y'}{b}) e^{-jk_{zpm} |z-z'|}$$

$$G_{yz}(x, x' = x_{01}) = -\sum_n \sum_m \frac{j\varepsilon_{om} \omega\mu_o (\frac{m\pi}{b}) U_{nm}(x, x' = x_{01})}{k_{znm} \Lambda' (k_{znm})} \cos (\frac{m\pi y}{b}) \sin(\frac{m\pi y'}{b}) e^{-jk_{znm} |z-z'|}$$

$$-\sum_p \sum_m \frac{j\varepsilon_{om} \omega\mu_o k_{zpm} V_{pm}(x, x' = x_{01})}{(\frac{m\pi}{b}) \Gamma'(k_{pm})} \cos(\frac{m\pi y}{b}) \sin(\frac{m\pi y'}{b}) e^{-jk_{zpm} |z-z'|}$$

$$G_{zy}(x, x' = x_{01}) = \sum_n \sum_m \frac{jz\omega\mu_o (\frac{m\pi}{b}) U_{nm}(x, x'=x_{01})}{k_{znm} \Lambda'(k_{znm})} \sin(\frac{m\pi y}{b}) \cos(\frac{m\pi y'}{b}) e^{-jk_{znm} |z-z'|}$$

$$+ \sum_p \sum_m \frac{jz\omega\mu_o k_{zpm} V_{pm}(x, x' = x_{01})}{(\frac{m\pi}{b}) \Gamma(k_{zpm})} \sin(\frac{m\pi y}{b}) \cos(\frac{m\pi y'}{b}) e^{-jk_{zpm} |z-z'|}$$

$$G_{zz}(x, x' = x_{01}) = -\sum_{n}\sum_{m}\frac{z\omega\mu_o U_{nm}(x, x' = x_{01})}{\Lambda'(k_{znm})}\sin(\frac{m\pi y}{b})\sin(\frac{m\pi y'}{b})e^{-jk_{znm}|z-z'|}$$

$$+\sum_{p}\sum_{m}\frac{z\omega\mu_o V_{pm}(x, x' = x_{01})}{\Gamma'(k_{zpm})}\sin(\frac{m\pi y}{b})\sin(\frac{m\pi y'}{b})e^{-jk_{zpm}|z-z'|}$$

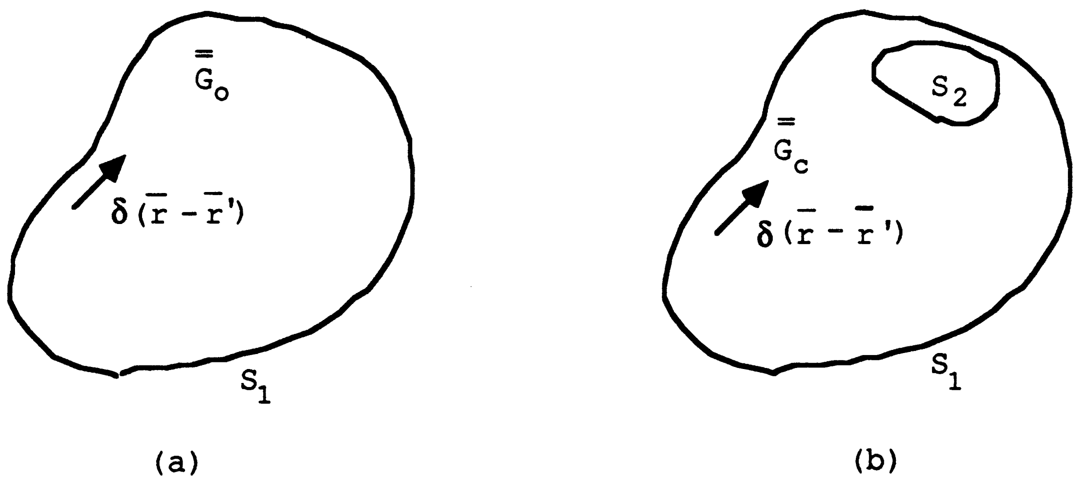

Figure 1. (a) Dipole maintaining $\bar{\bar{G}}$ within boundary S_1.

(b) Dipole maintaining $\bar{\bar{G}}_c$ and boundary S_2 within boundary S_1.

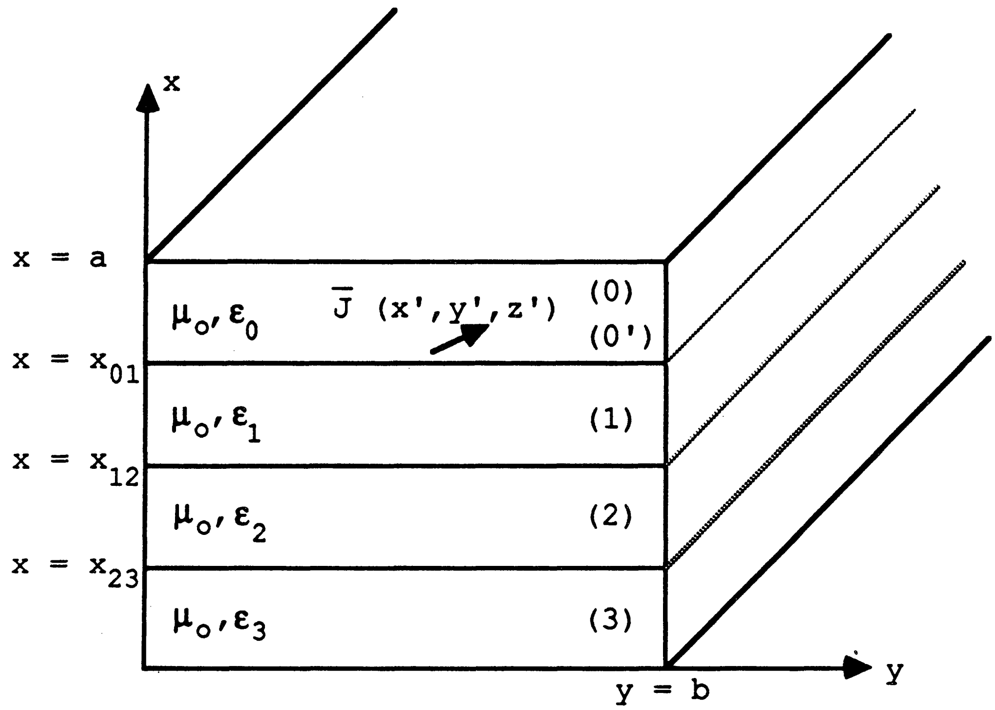

Figure 2. Rectangular waveguide inhomogeneously filled with three dielectrics, excited by current source $\bar{J}(x', y', z')$.

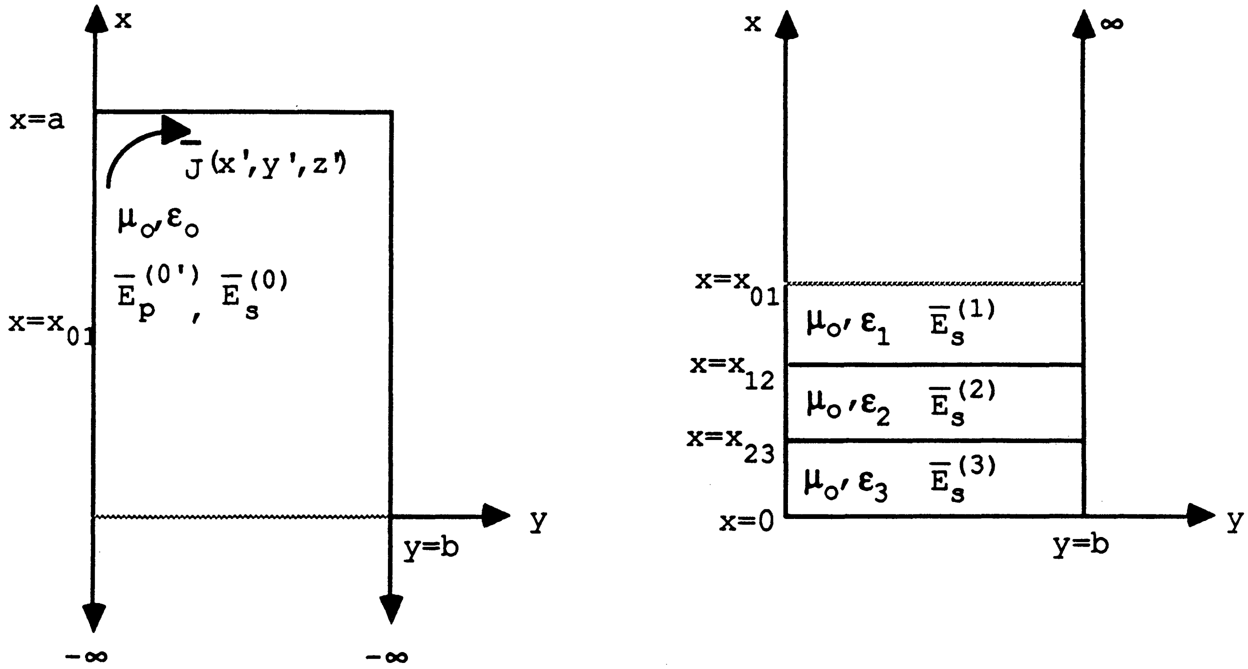

Figure 3. Decomposition of dielectric-loaded waveguide of Figure 2 into equivalent superposition of parallel-plate structures.

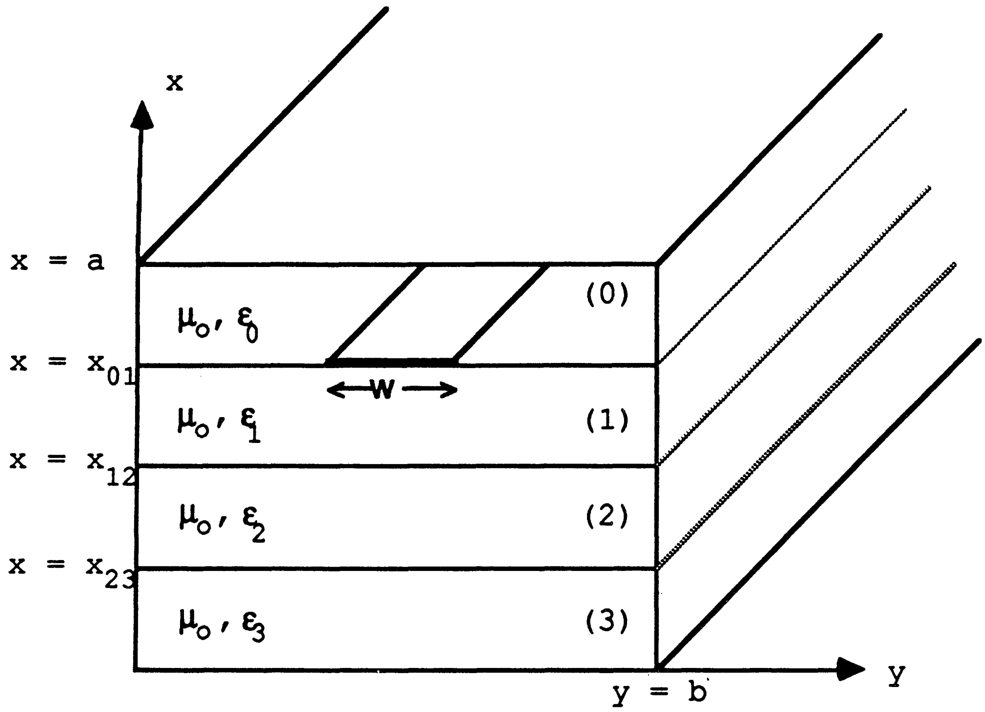

Figure 4. Shielded, layered, microstrip transmission line.

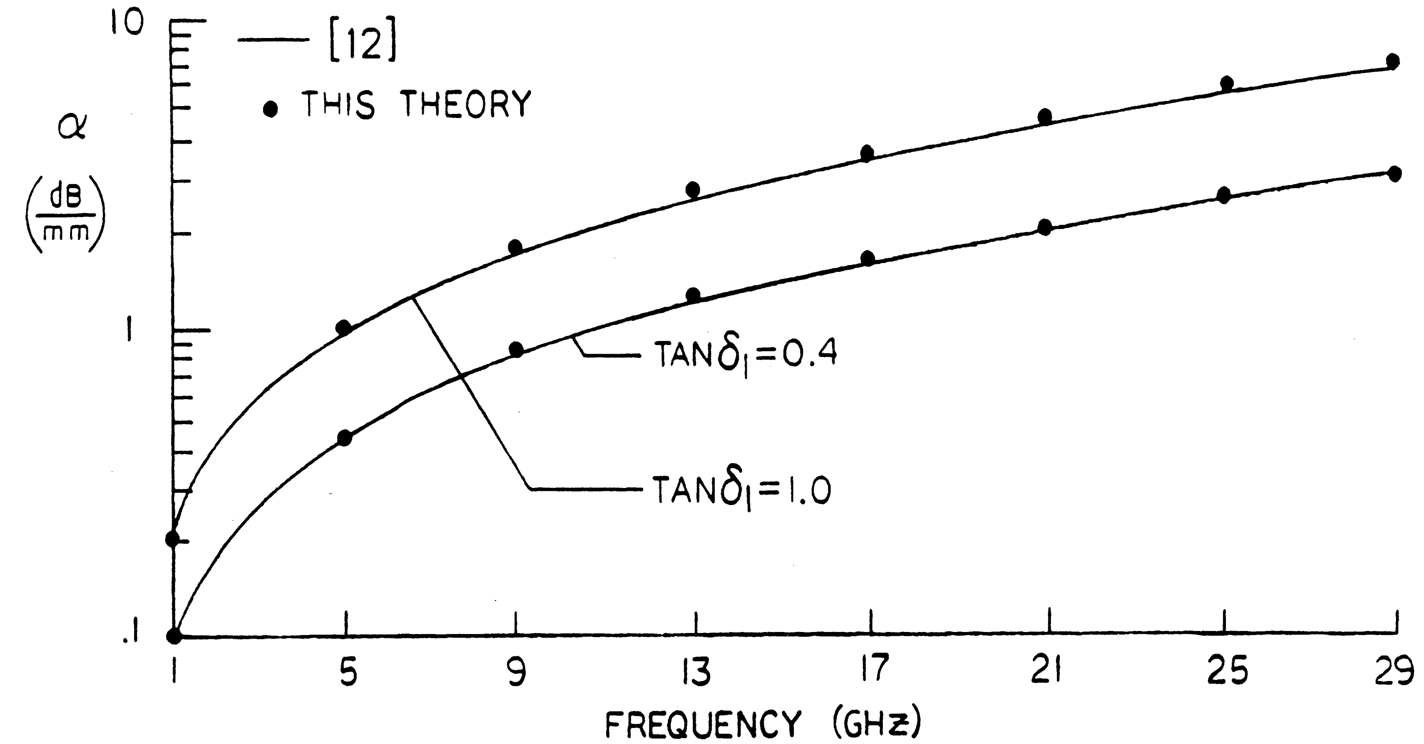

(a)

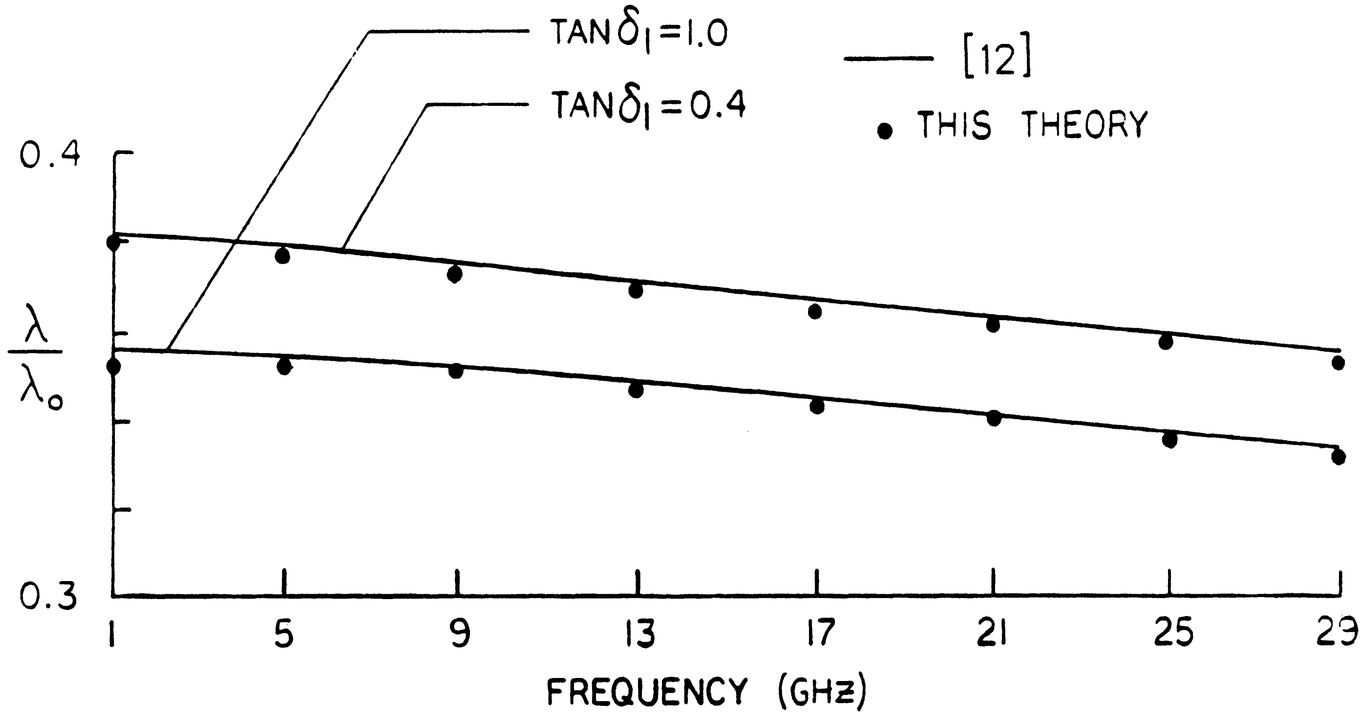

(b)

Figure 5. Comparison of attenuation and normalized wavelength with literature for various values of substrate loss tangent.

(x_{01} = 0.5mm; $x_{12} = x_{23} = 0$; a = b = 2.0cm; w = 0.5mm; $\varepsilon_r = 10$)

NSF-023827-3-T

THE EFFECT OF SEMI-INSULATING, SEMI-CONDUCTING MATERIALS ON THE PROPAGATION CHARACTERISTICS OF DIELECTRIC LOADED WAVEGUIDES

T. Weller and P.B. Katehi
Radiation Laboratory
Department of Electrical Engineering and Computer Science
The University of Michigan
Ann Arbor, MI 48109

April 1988

I. INTRODUCTION

The need for more accurate microstrip circuit simulations has become apparent with the recent interest in millimeter-wave and near millimeter-wave frequencies. The development of more accurate microstrip discontinuity models is very important in improving high frequency circuit simulations. In most applications, the circuits are enclosed in a shielding cavity as shown in Figure 1. This cavity may be considered as a section of a waveguide terminated at both ends. The presence of the shielding cavity affects the performance of the circuit (shielding effects) and has to be taken into consideration.

It has been shown [1] - [2] that one condition where shielding effects are significant is when the frequency approaches the cut-off frequency of the waveguide's dominant mode. In most cases, microstrip circuits including active devices are printed on multilayer structures which consist of a combination of dielectric and semi-conducting materials. The existance of these conducting layers can affect the characteristicts of the loaded cavity and, therefore, of the printed circuits. As it has been pointed out by many authors [3] - [5], the propagation characteristics of higher-order shielded-microstrip modes are very similar to those of the shielding cavity. Consequently, a good understanding of how microstrip modes propagate may be gained by just studying the dielectric-slab loaded waveguide.

In this report we consider the case of a single semi-conducting layer with a dopping density N_D which varies from

10^{14} to 10^{16} and we study the effect of this variation on the cutoff frequencies of the waveguide modes. Conclusions drawn from this study show a very interesting behavior in the propagation characteristics of the modes and may be extended to the case of the shielded microstrip.

II. THEORETICAL FORMULATION

Figure 1 in Appendix I shows a basic description of the loaded waveguide. The modes excited in this structure are LSE and LSM and their characteristic equations which may be derived by applying the transverse resonance condition [6] are shown below:

$$\frac{k_{x1}}{\varepsilon_1} \tan (k_{x1} h) = - \frac{k_{x2}}{\varepsilon_2} \tan \left[k_{x2} (a-h)\right] \qquad \text{LSM} \tag{1}$$

$$\frac{k_{x1}}{\mu_1} \cot (k_{x1} h) = - \frac{k_{x2}}{\mu_2} \cot \left[k_{x2} (a-h)\right] \qquad \text{LSE} \tag{2}$$

The eigenvalues k_{x1} and k_{x2} are given by

$$k_{x1}^2 + k_y^2 + k_z^2 = \omega^2 \varepsilon_1 \mu_1 \tag{3}$$

$$k_{x2}^2 + k_y^2 + k_z^2 = \omega^2 \varepsilon_2 \mu_2 \tag{4}$$

with

$$k_y = \frac{n\pi}{b}$$

$$\varepsilon_1 = \varepsilon_1' \, (1 - j\tan\delta_1) \tag{5}$$

$$\varepsilon_2 = \varepsilon_2' \, (1 - j\tan\delta_2) \tag{6}$$

and

$$\tan\delta_2 = 0$$

$$\tan\delta_1 = \frac{eN_D}{w\varepsilon_1'} \quad . \tag{7}$$

In equation (7), e is the charge of an electron and N_D is the doping density of the material. For the case a perfect dielectric layer, cut-off is defined by k_z=0. However, when $\tan\delta$ is different than zero, the cut-off condition is modified to the following

$$\mathrm{Re}\ (k_z) = 0 \tag{8}$$

This condition imposed on equations (3), (4) can give:

$$k_{x1}^2 = \omega^2\varepsilon_1'\mu_1\ (1 - j\tan\delta_1) - a_z^2 - k_y^2 \tag{9}$$

and

$$k_{x2}^2 = \omega^2\varepsilon_2\mu_2 - a_z^2 - k_y^2 \tag{10}$$

By substracting equation (9) from (10) we can derive a relation between k_{x1} and k_{x2} which does not include the eigenvalue k_y and the attenuation constant at cut-off a_z:

$$k_{x1}^2 - k_{x2}^2 = \omega^2 \left[\varepsilon_1'\mu_1\ (1 - j\tan\delta_1) - \varepsilon_2\mu_2\right] \tag{11}$$

The solution of the sets ((1),(11)) or ((2),(11)) can be performed only numerically and results in infinite many but descrete eigenvalue pairs $(k_{x1}, k_{x2})_m$ which vary with ω and n. The frequency which satisfies (8) for a given pair $(k_{x1}, k_{x2})_m$ and $k_y = n\pi/b$ is the cut-off frequency of the mn mode. This procedure is rather complicated and requires extensive computation. To avoid this shortcoming the cut-off condition is modified to

$$k_z = 0 \tag{12}$$

Equation (12) together with (3) and (4) transforms the characteristic equation into a complex equation for ω resulting in complex cut-off frequencies. The real part of this cut-off frequency will be exactly equal to the one that condition (8) would give. However, the imaginary part which, in general, is about an order of magnitude smaller than the real, compensates for the neglected attenuation at cut-off and is disregarded. The results derived during this study are based on the second condition.

III. NUMERICAL SOLUTION

Numerical solution of the characteristic equation was achieved with Muller's Method [7] which is iterative in nature and requires a good initial guess for fast convergence. Furthermore, when solving for cut-off frequencies there may be a number of solutions to the characteristic equation in a relatively narrow frequency space. To overcome this problem, a method was developed to track a given mode through increasting doping densities. That is, the solution for the cut-off for a given mode is determined first for no losses where zeros are spread further apart and this solution is used as the initial guess as the tanδ is slightly increased. The numerical solution for the lossless case proved to be much more simple than the lossy one. The characteristic equation was solved with the bistatic method [7].

IV. RESULTS AND CONCLUSION

The results derived using the technique described above are plotted in figures (1) - (34) and are for the waveguide geometries of Table 1 in Appendix II. From these results it can be concluded that the effect of the conductivity in the dielectric layer can be tremendous. In some cases, as the doping density increases from 10^{14} to 10^{16} there seems to be a switching of dominant modes. That is, higher order modes tend to exhibit a lower cut-off than the mode which was dominant at lower N_D resulting in much lower cut-off frequencies. In addition, for other geometries, increasing conductivity seems to have an opposite effect.

Presently, we are trying to investigate the effect of the presence of semi-conducting materials on the modes of a shielded microstrip printed on single, as well as multi-layer substrates.

APPENDIX I

Computation of the cut-off frequencies for the case of a non-conducting layer:

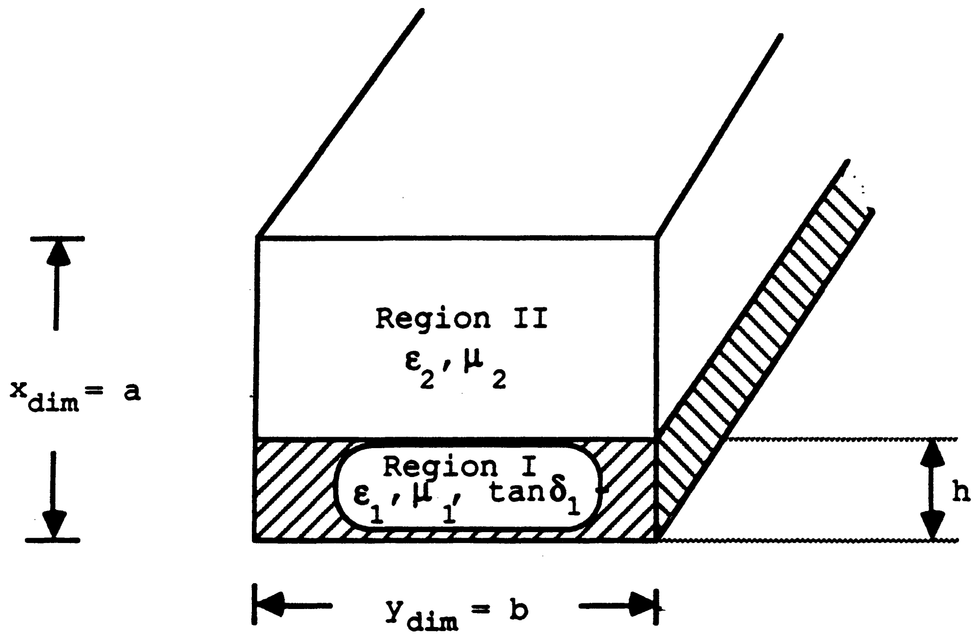

$d = a-h$

$$k_{x1}^2 + k_y^2 + k_z^2 = \omega^2 \varepsilon_1 \mu_1$$

$$k_{x2}^2 + k_y^2 + k_z^2 = \omega^2 \varepsilon_2 \mu_2$$

For LSM, LSE k_z is set to zero to determine the cut-off frequency.

The dominant LSM mode corresponds to TE_{01} $\therefore$ $k_y = \pi/b$

The dominant LSE mode corresponds to TE_{10} $\therefore$ $k_y \triangleq 0.0$

Determining the next higher order mode:

LSM: Interation begins assuming a lower bound which was the cut-off frequency for the dominant mode.

Two possibilities are tested:

(i) $M = 0, \quad N = 2$
(i.e., $k_y = 2\pi/b$)

(ii) $M = 1, \quad N = 1$
(i.e., $k_y = \pi/b$)

whichever case yields the lowest f_c is taken as the next higher mode.

LSE: Similar to the above, using instead the following two cases:

(i) $M = 2, \quad N = 0$
(i.e., $k_y = 0.0$)

(ii) $M = 1, \quad N = 1$
(i.e., $k_y = \pi/b$)

Iteration for dominant mode solution:
(Lossless dielectric)

LSM: A lower bound is determined by the following:

$F_{o_{01}} = c/Zb \triangleq TE_{01}$ cut-off for air-filled WG.

with c the velocity of light in free space.

$F_{d_{01}} = \dfrac{F_{o_{01}}}{\sqrt{\varepsilon_{r1}}} \triangleq TE_{01}$ cut-off for completely filled WG.

$F_{d_{01}}$ is used as the lower bound.

LSE: Similar to the above, using

$F_{o_{01}} = c/Za \triangleq TE_{10}$ cut-off for air-filled WG.

APPENDIX II

Group A Plots

Symbol definition:

Symbol	Mode
	LSM1
*	LSM2
Δ	LSE1
+	LSE2

TABLE 1

Waveguide Parameters:			Substrate Parameters	
Plot #	a (in)	b (in)	h (in)	ε_{r1}
1	.305	.305	.15	3.0
2	.305	.305	.08	3.0
3	.305	.305	.025	3.0
4	.305	.305	.025	12.0
5	.305	.305	.025	16.0
6	.25	.305	.08	3.0
7	.25	.305	.08	12.0
8	.25	.305	.08	16.0
9	.305	.25	.08	3.0
10	.305	.25	.08	12.0
11	.305	.25	.08	16.0

GROUP A

"Cut-off frequencies vs. $\tan\delta$ for LSE and LSM modes"

20:11:15

CUTØFF FREQUENCY .VS. LØSS TANGENT #1

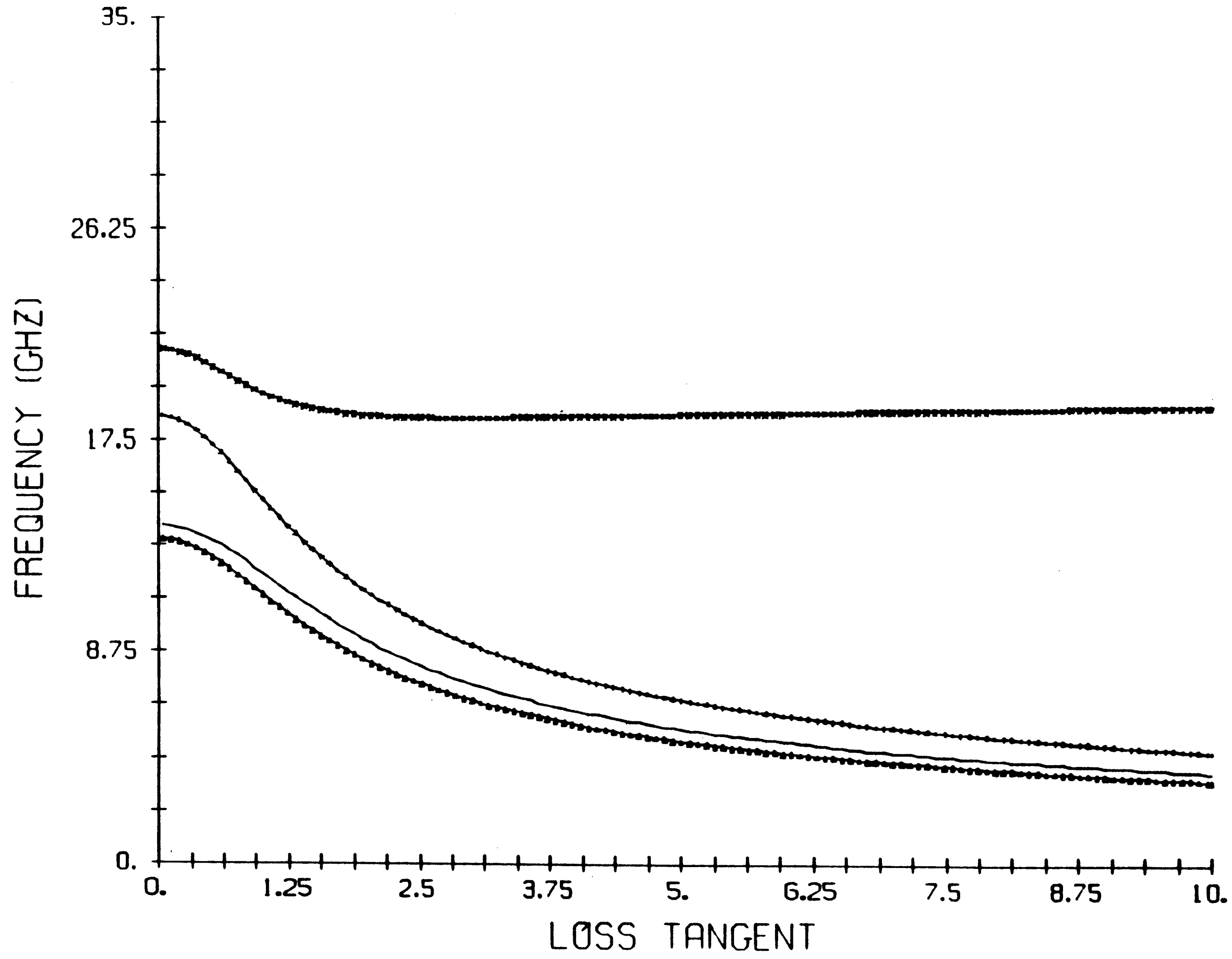

CUTOFF (REAL AND IMAG) .VS. LOSS TANGENT FOR LSM #1

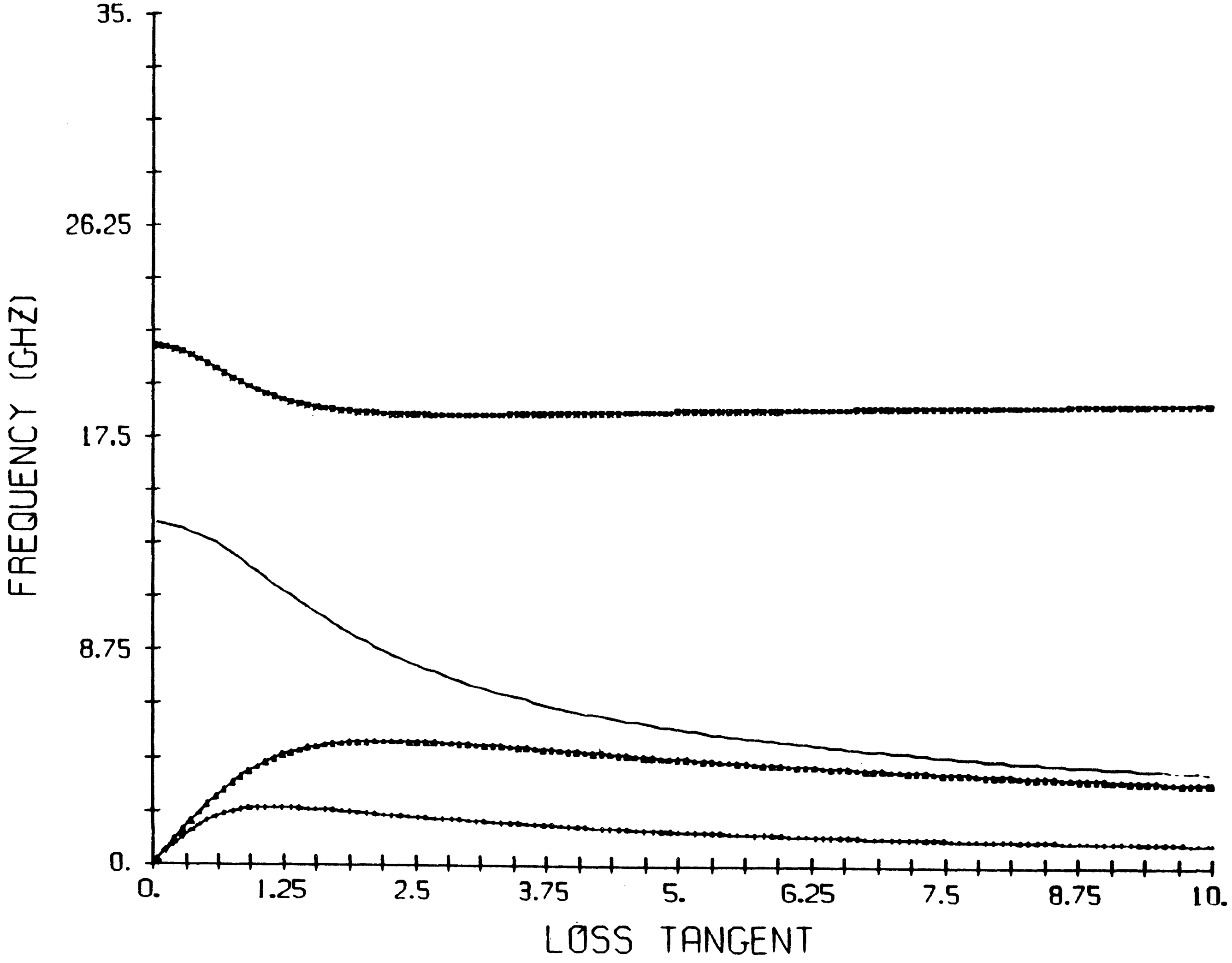

20:11:52

CUTOFF (REAL AND IMAG) .VS. LOSS TANGENT FOR LSE #1

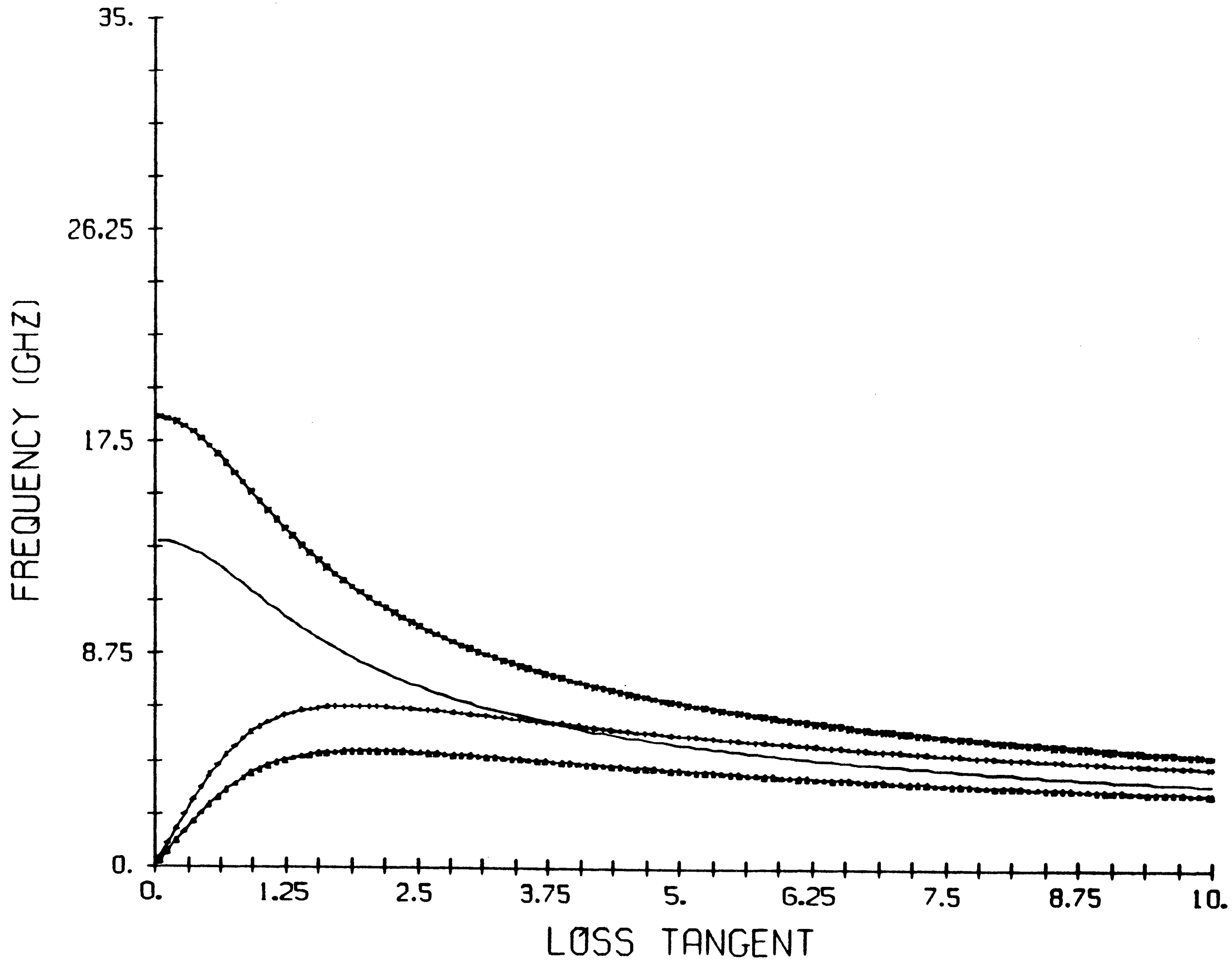

CUTOFF FREQUENCY .VS. LOSS TANGENT #2

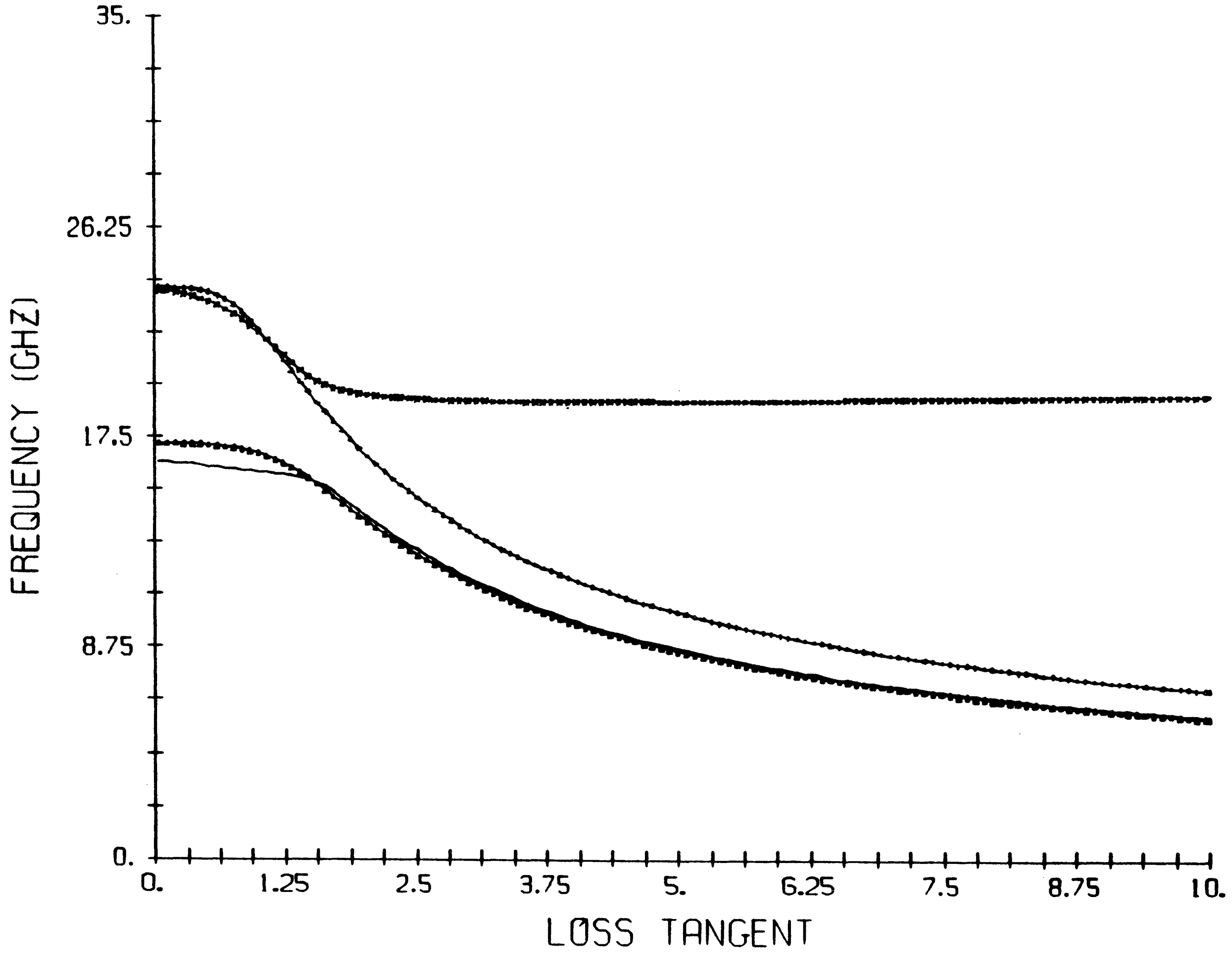

20:19:10

CUTØFF (REAL AND IMAG) .VS. LØSS TANGENT FØR LSM #2

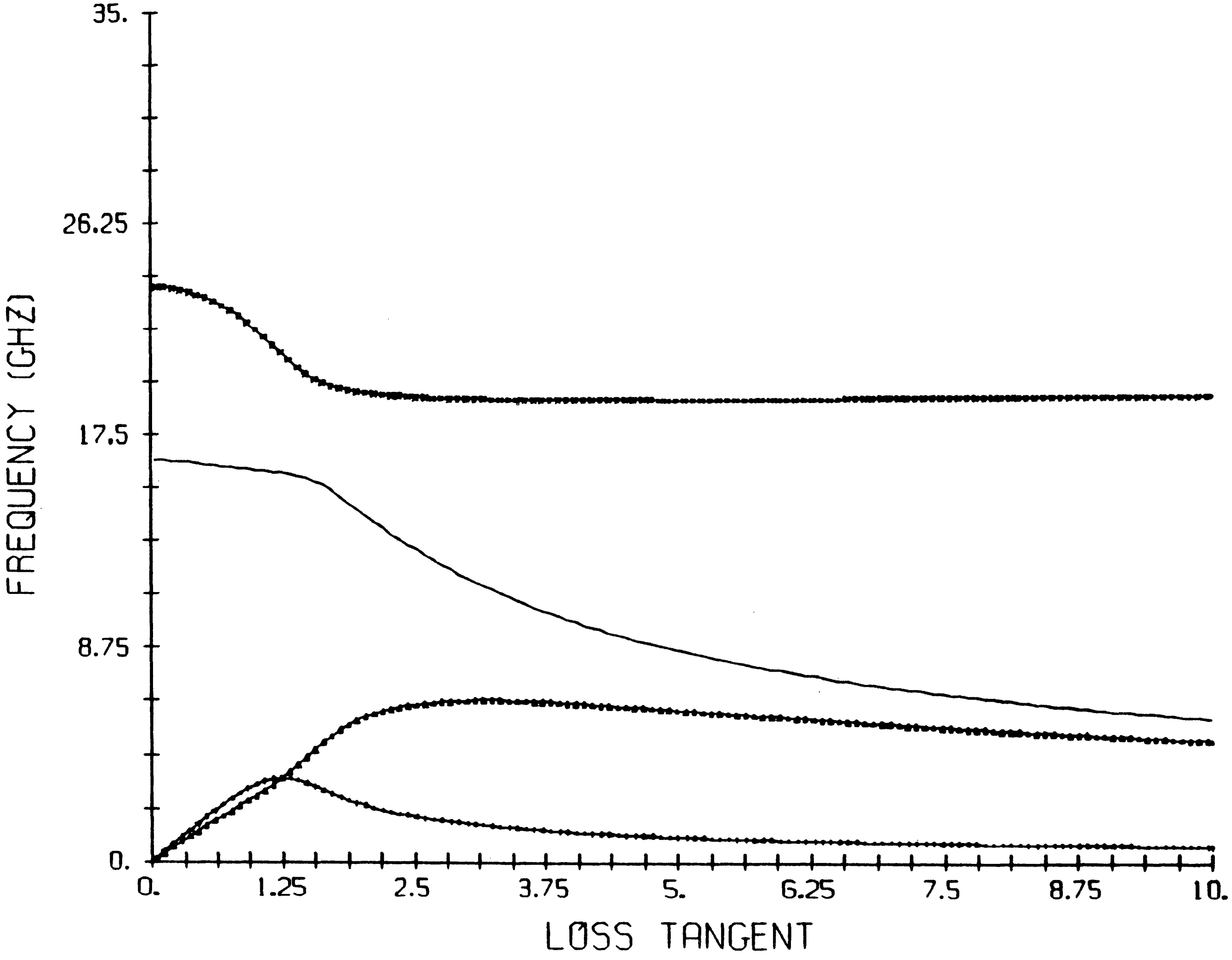

CUTOFF (REAL AND IMAG) .VS. LOSS TANGENT FOR LSE #2

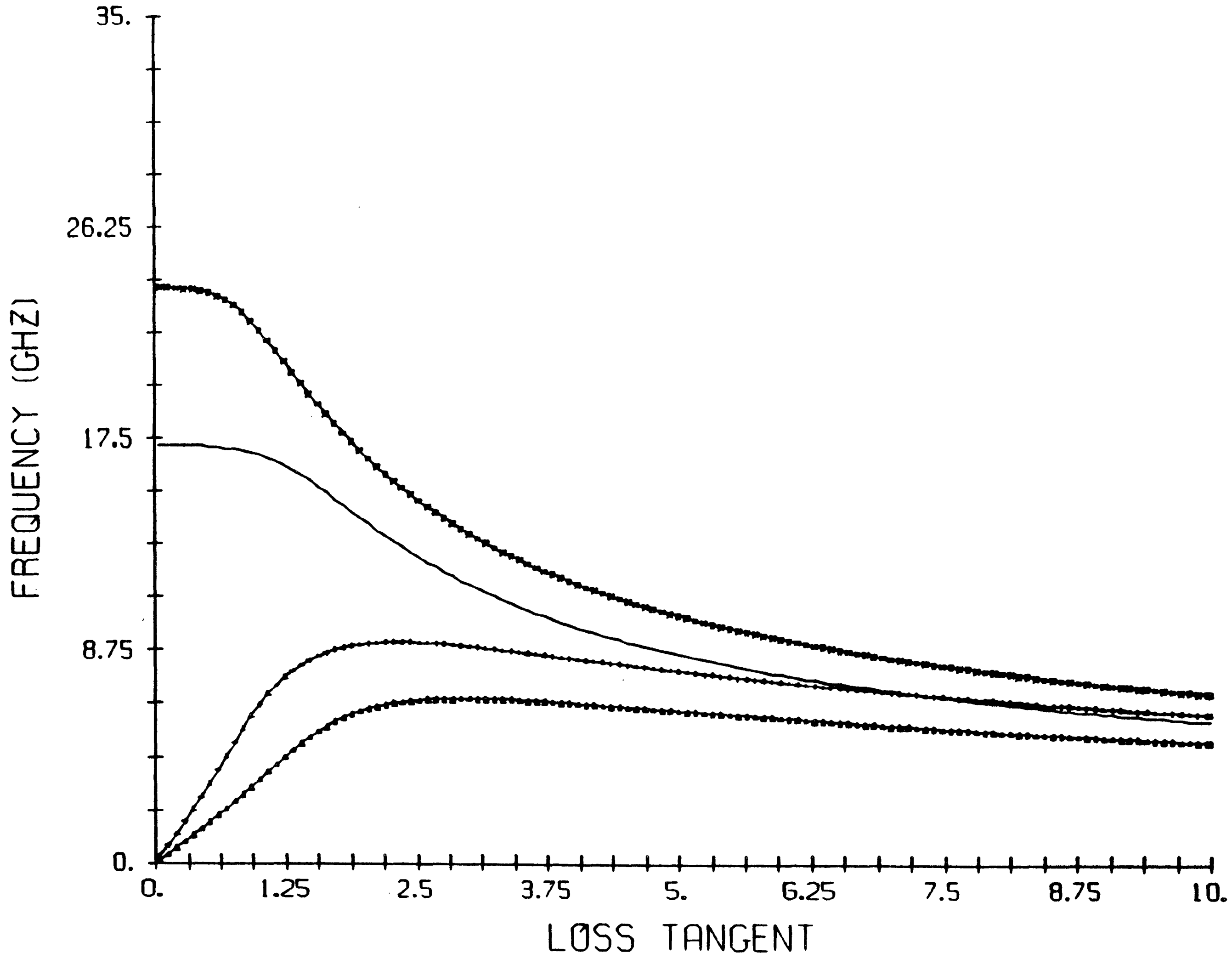

20:21:45

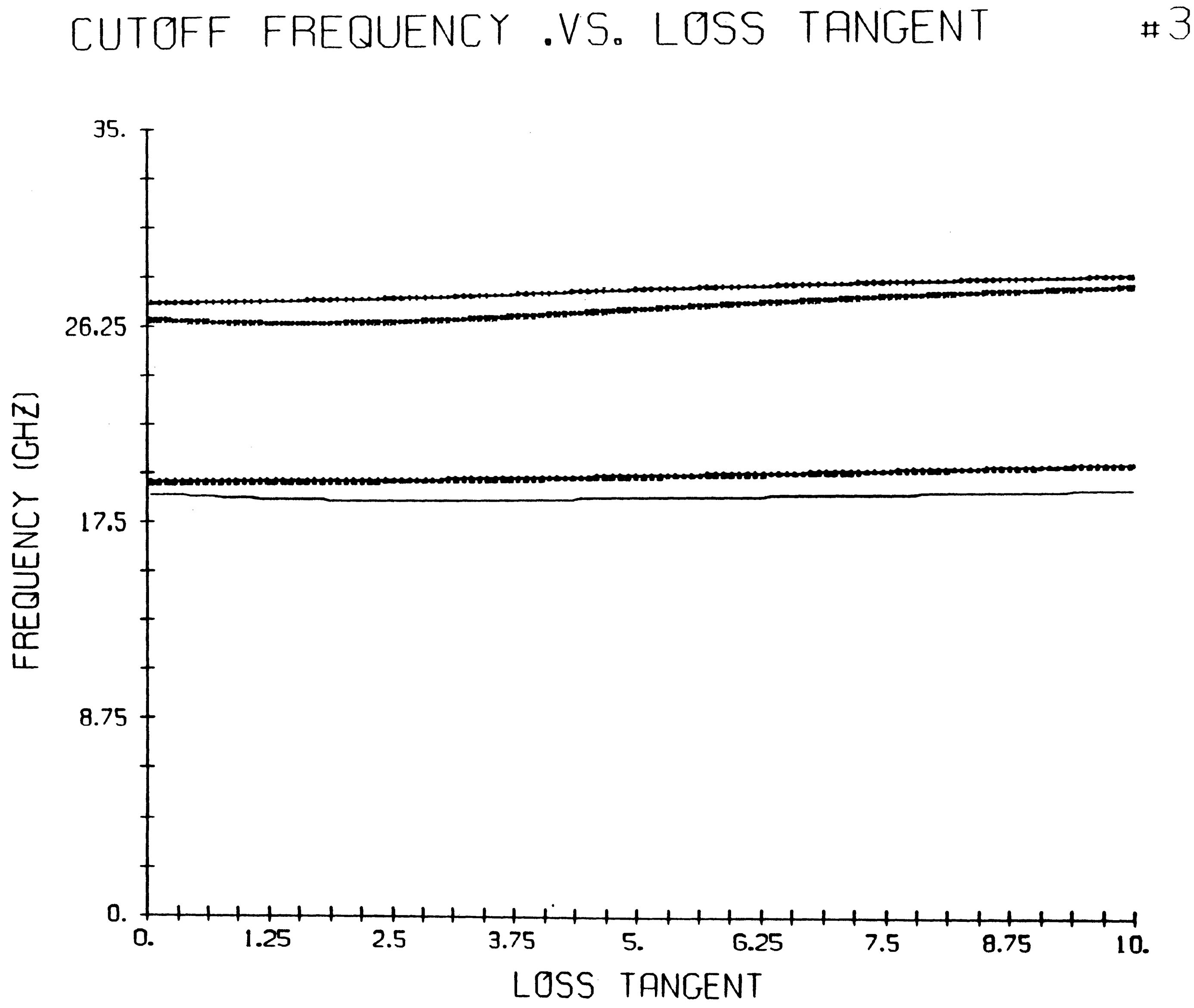
CUTOFF FREQUENCY .VS. LOSS TANGENT
#3
35.
26.25
17.5
8.75
0.
FREQUENCY (GHZ)
0.
1.25
2.5
3.75
5.
6.25
7.5
8.75
10.
LOSS TANGENT

CUTØFF (REAL AND IMAG) .VS. LØSS TANGENT FØR LSM #3

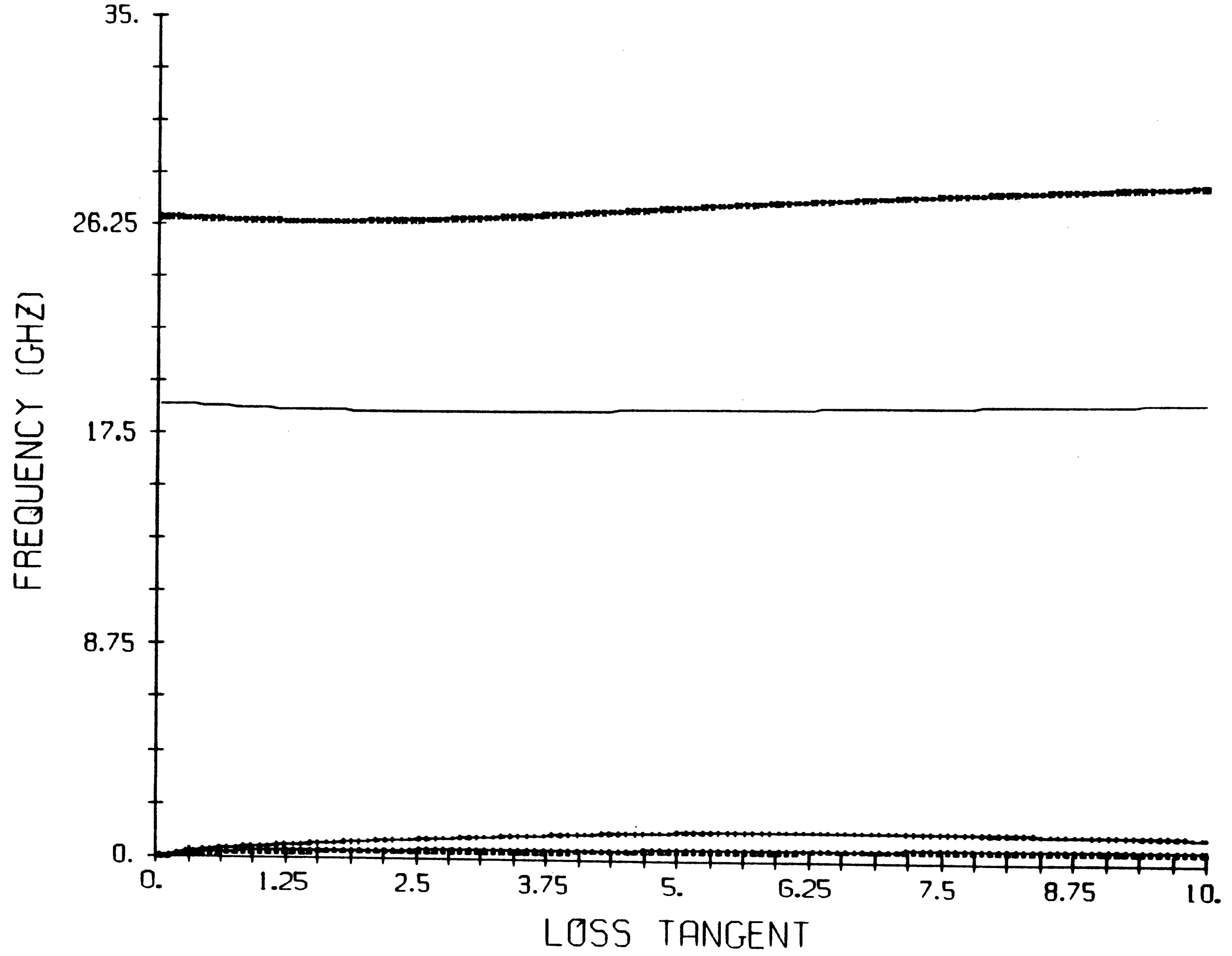

20:22:11

CUTOFF (REAL AND IMAG) .VS. LOSS TANGENT FOR LSE #3

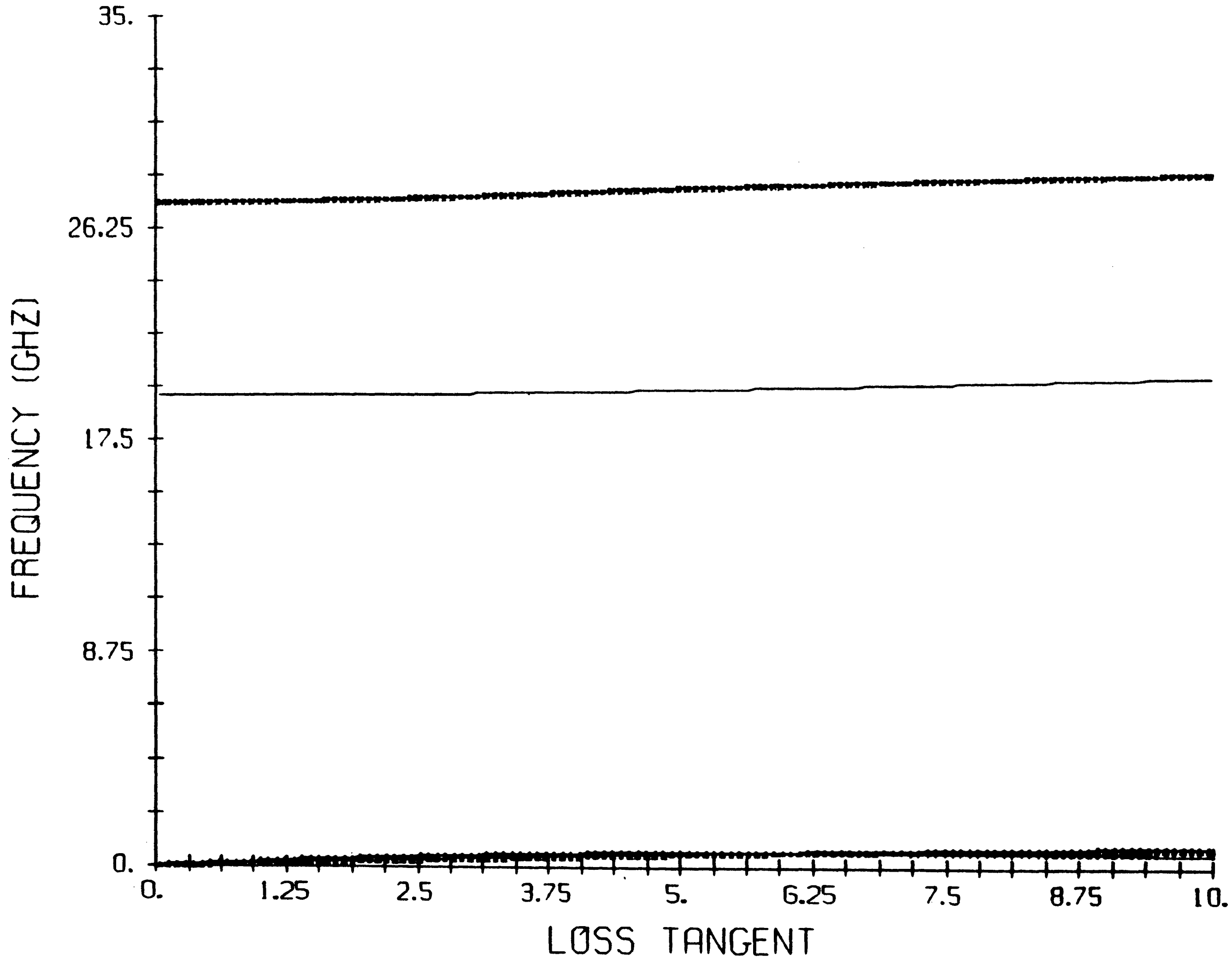

CUTOFF FREQUENCY .VS. LOSS TANGENT #4

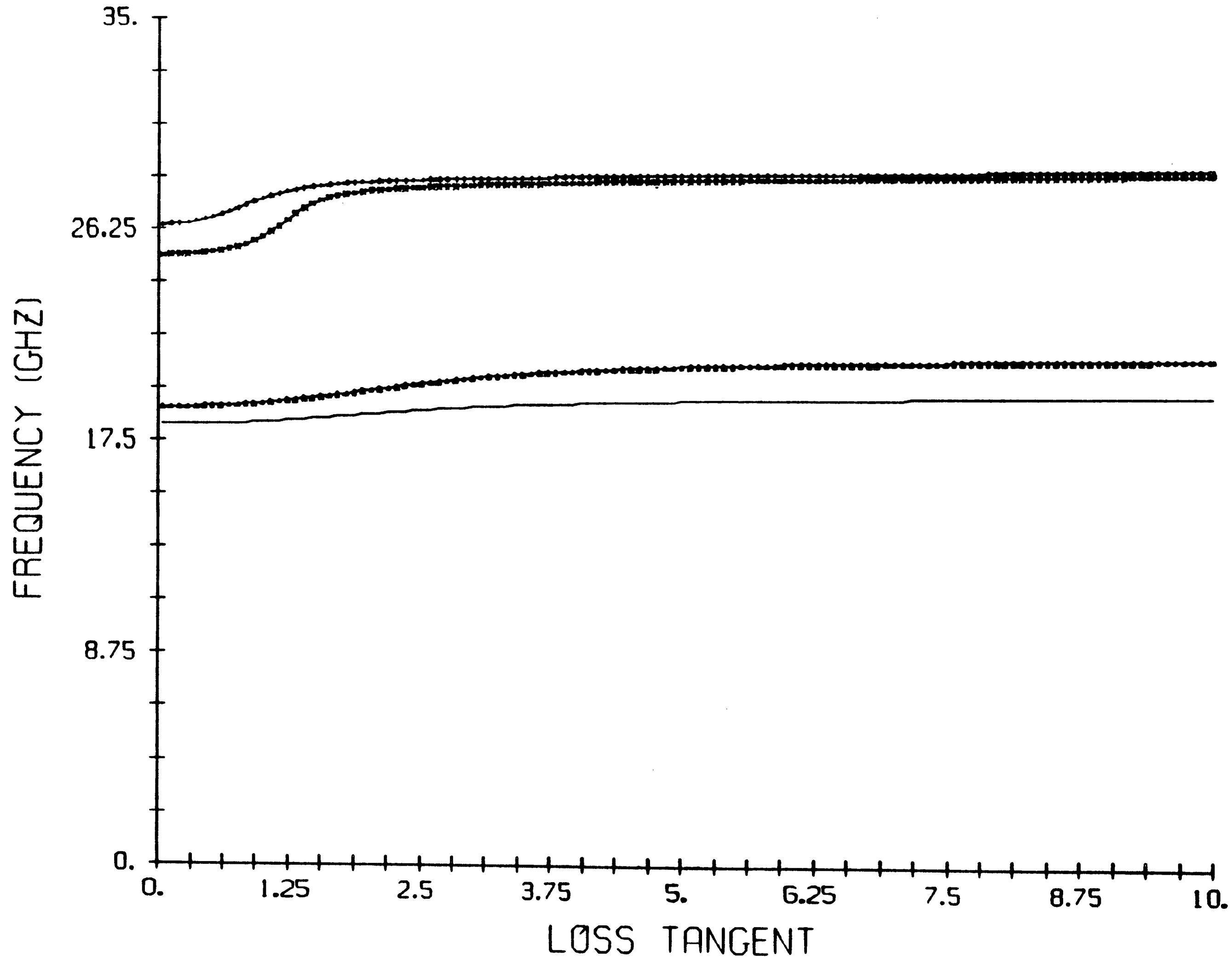

20:25:32

CUTØFF (REAL AND IMAG) .VS. LØSS TANGENT FØR LSM #4

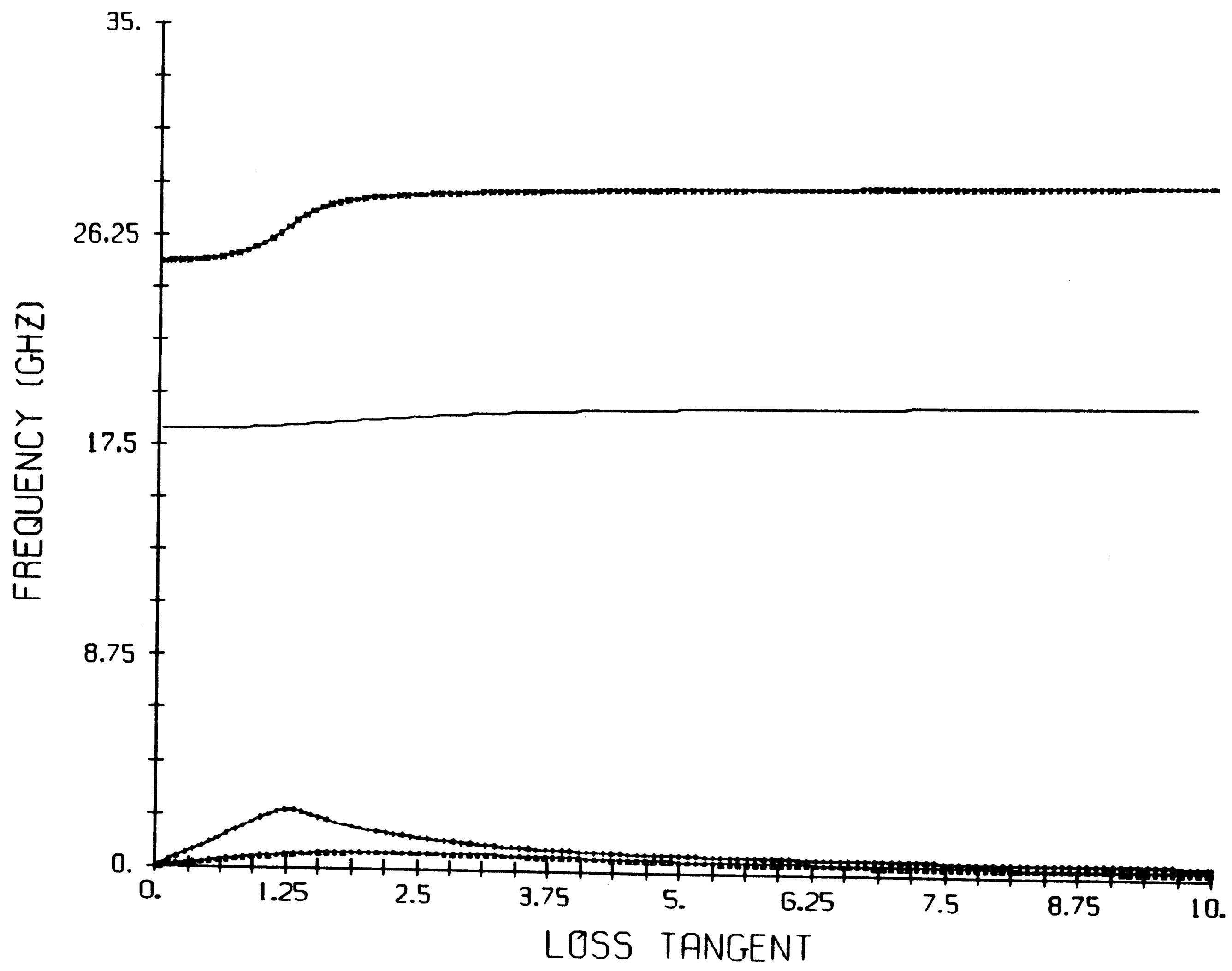

CUTØFF (REAL AND IMAG) .VS. LØSS TANGENT FØR LSE #4

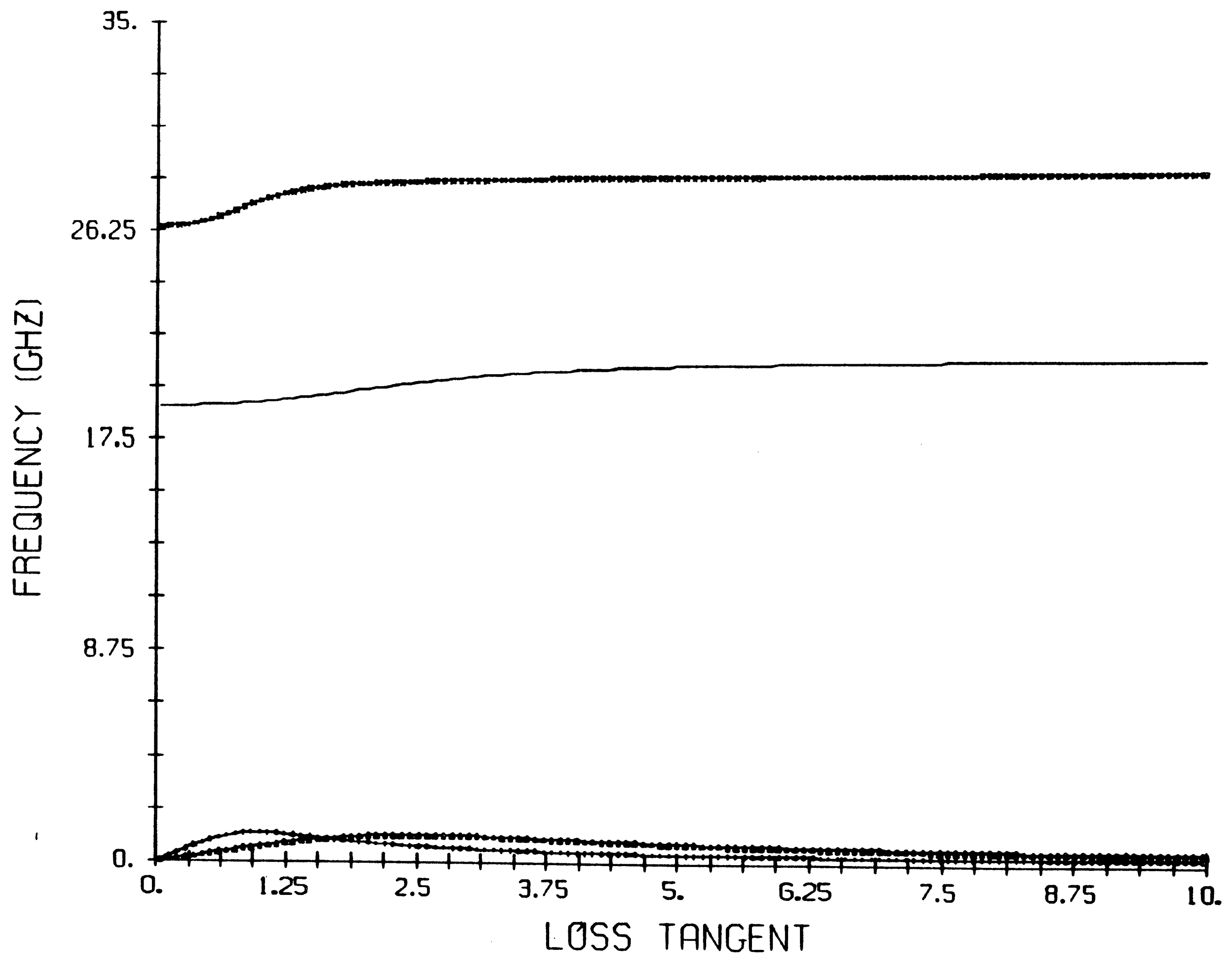

19:50:42

CUTOFF FREQUENCY .VS. LOSS TANGENT #5

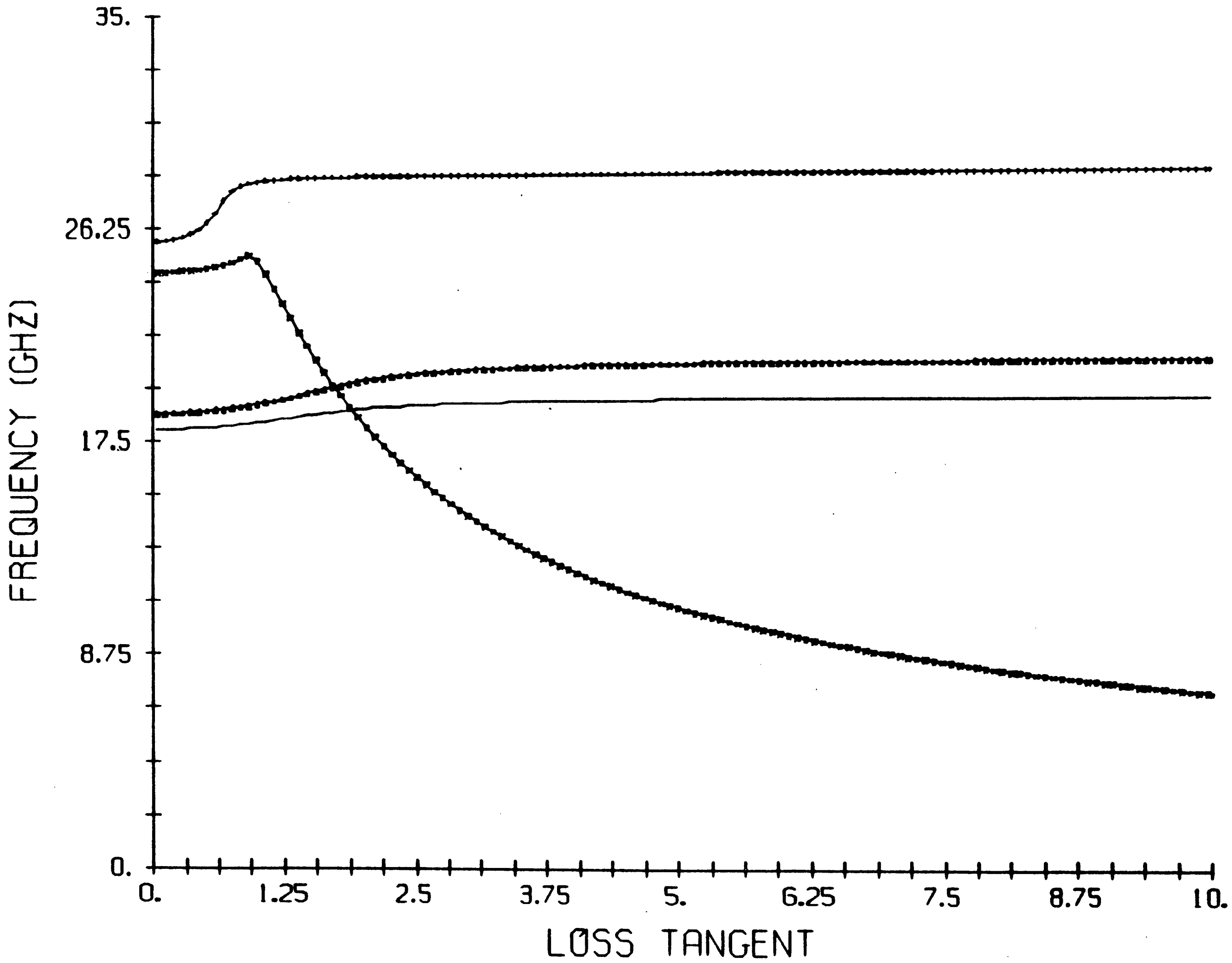

CUTOFF (REAL AND IMAG) .VS. LOSS TANGENT FOR LSM #5

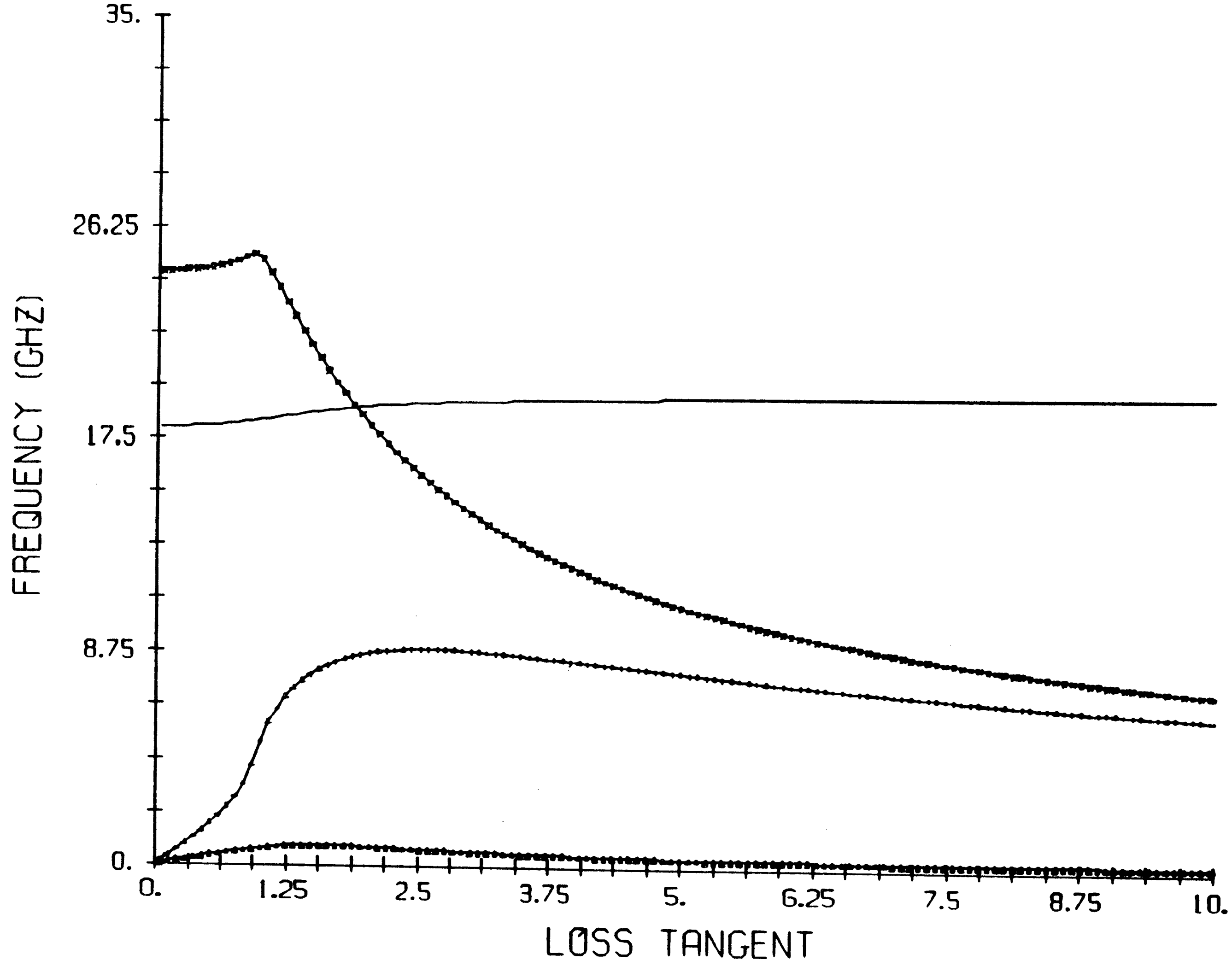

19:58:26

CUTØFF (REAL AND IMAG) .VS. LØSS TANGENT FØR LSE #5

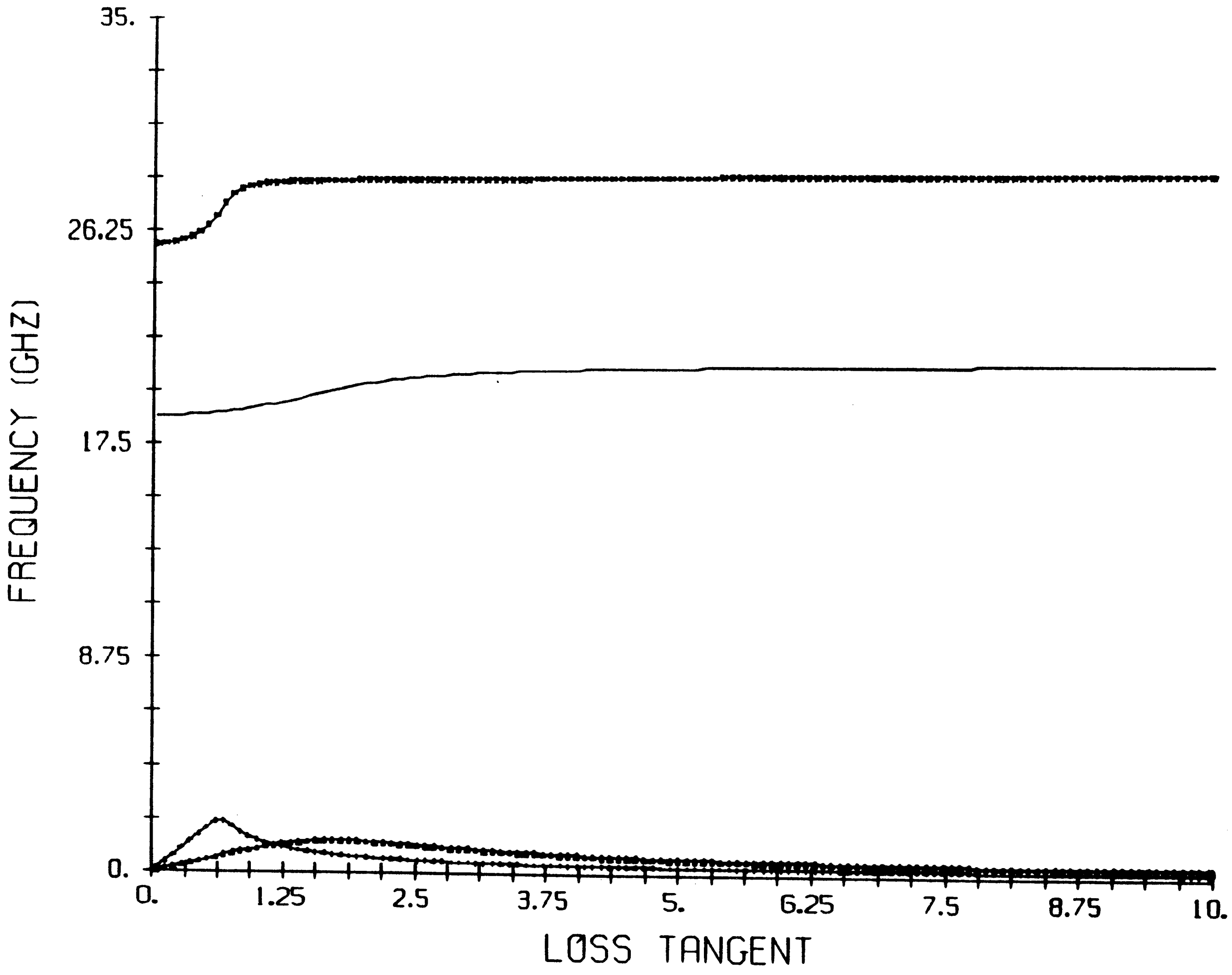

CUTØFF FREQUENCY .VS. LØSS TANGENT #6

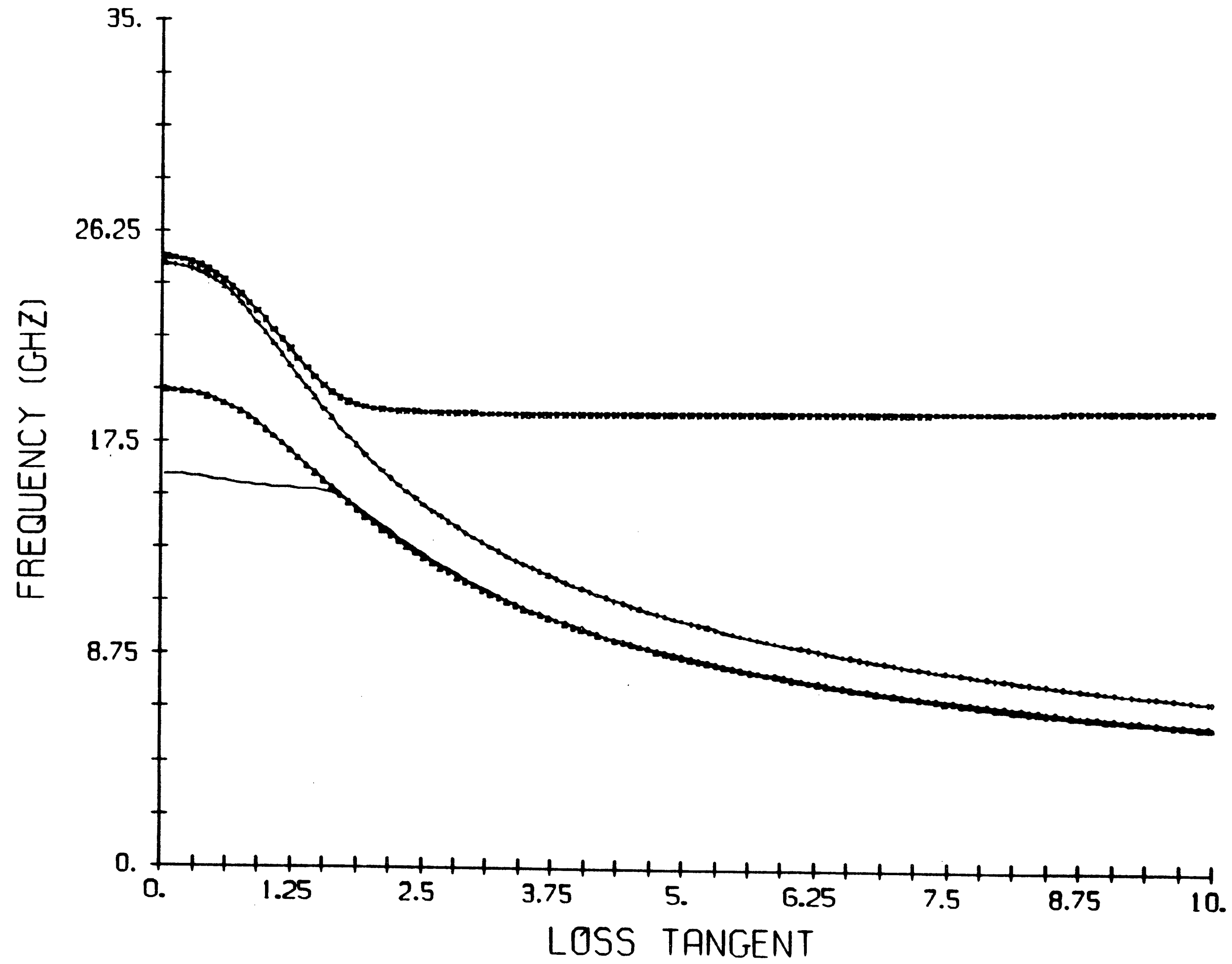

23:24:46

CUTOFF (REAL AND IMAG) .VS. LOSS TANGENT FOR LSM #6

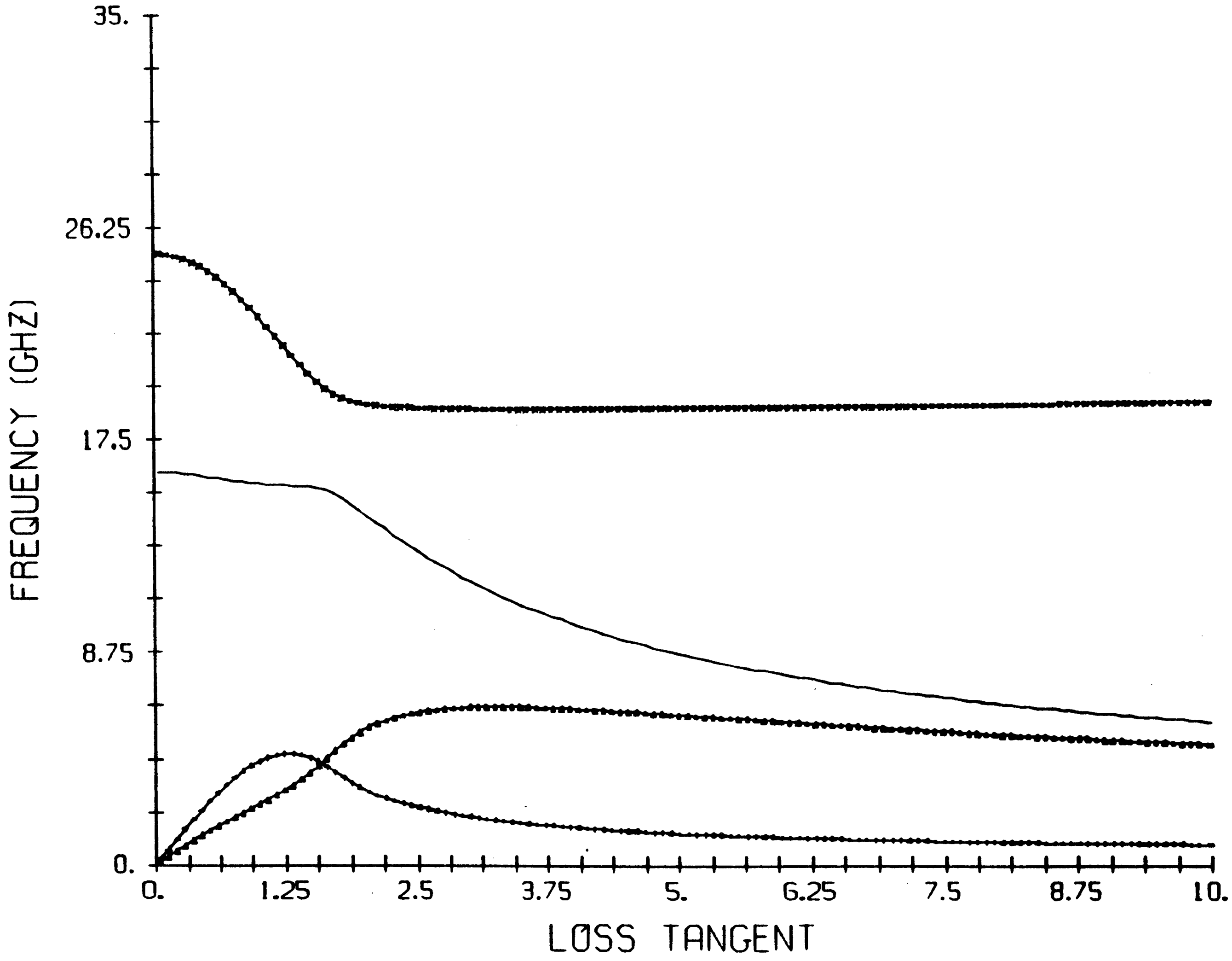

CUTØFF (REAL AND IMAG) .VS. LØSS TANGENT FØR LSE #6

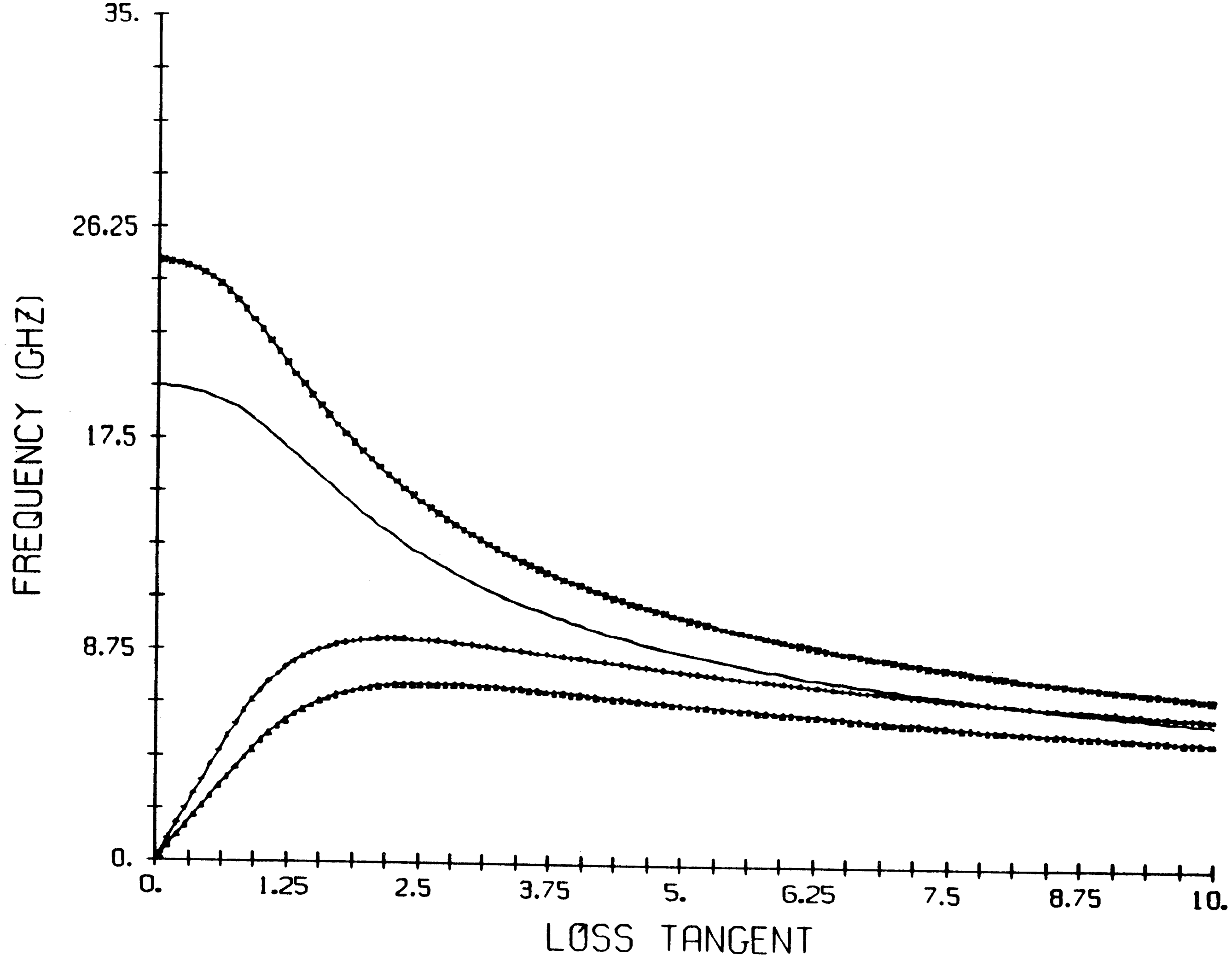

23:32:42

CUTØFF FREQUENCY .VS. LØSS TANGENT #7

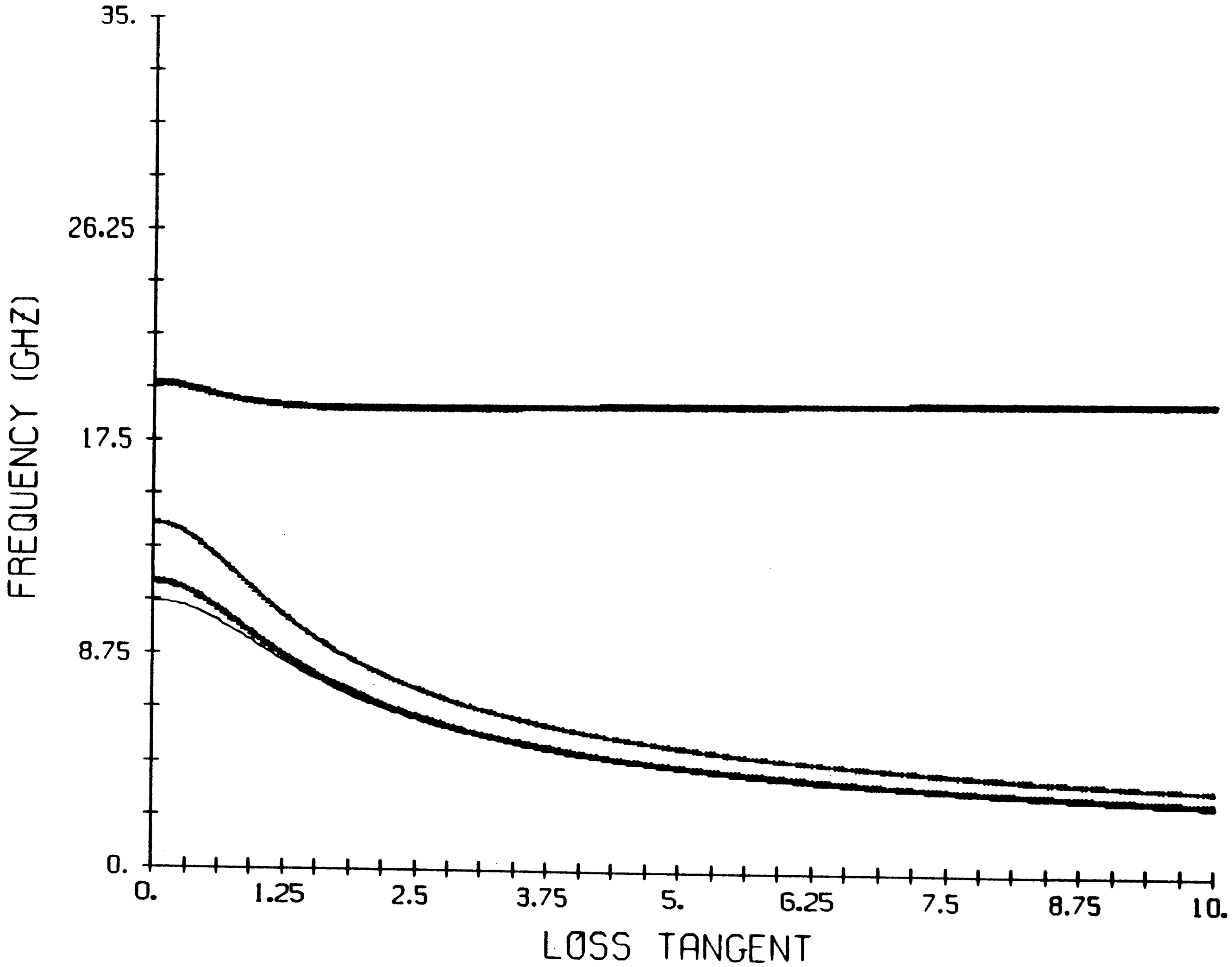

CUTOFF (REAL AND IMAG) .VS. LOSS TANGENT FOR LSM #7

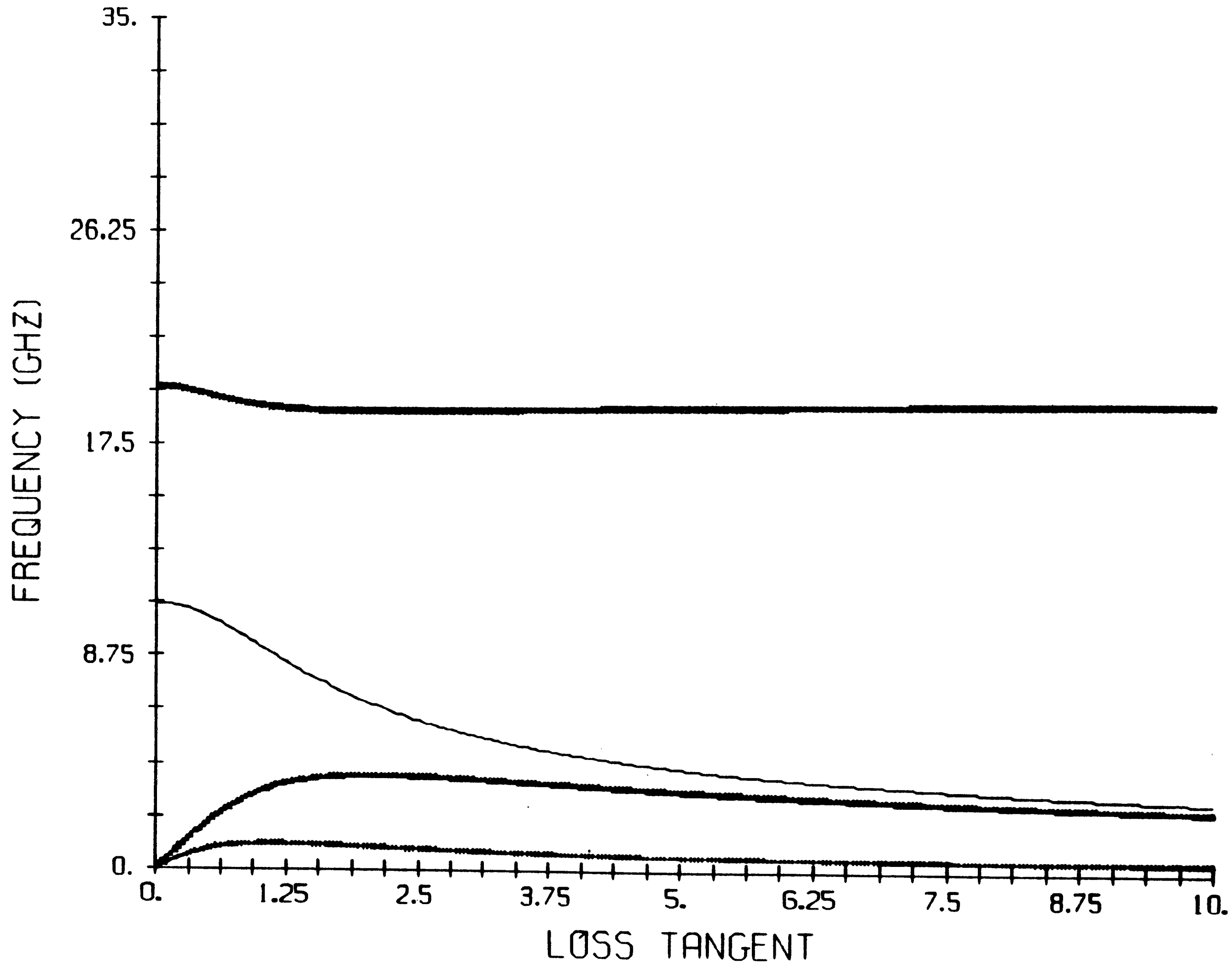

23:33:04

CUTØFF (REAL AND IMAG) .VS. LØSS TANGENT FØR LSE #7

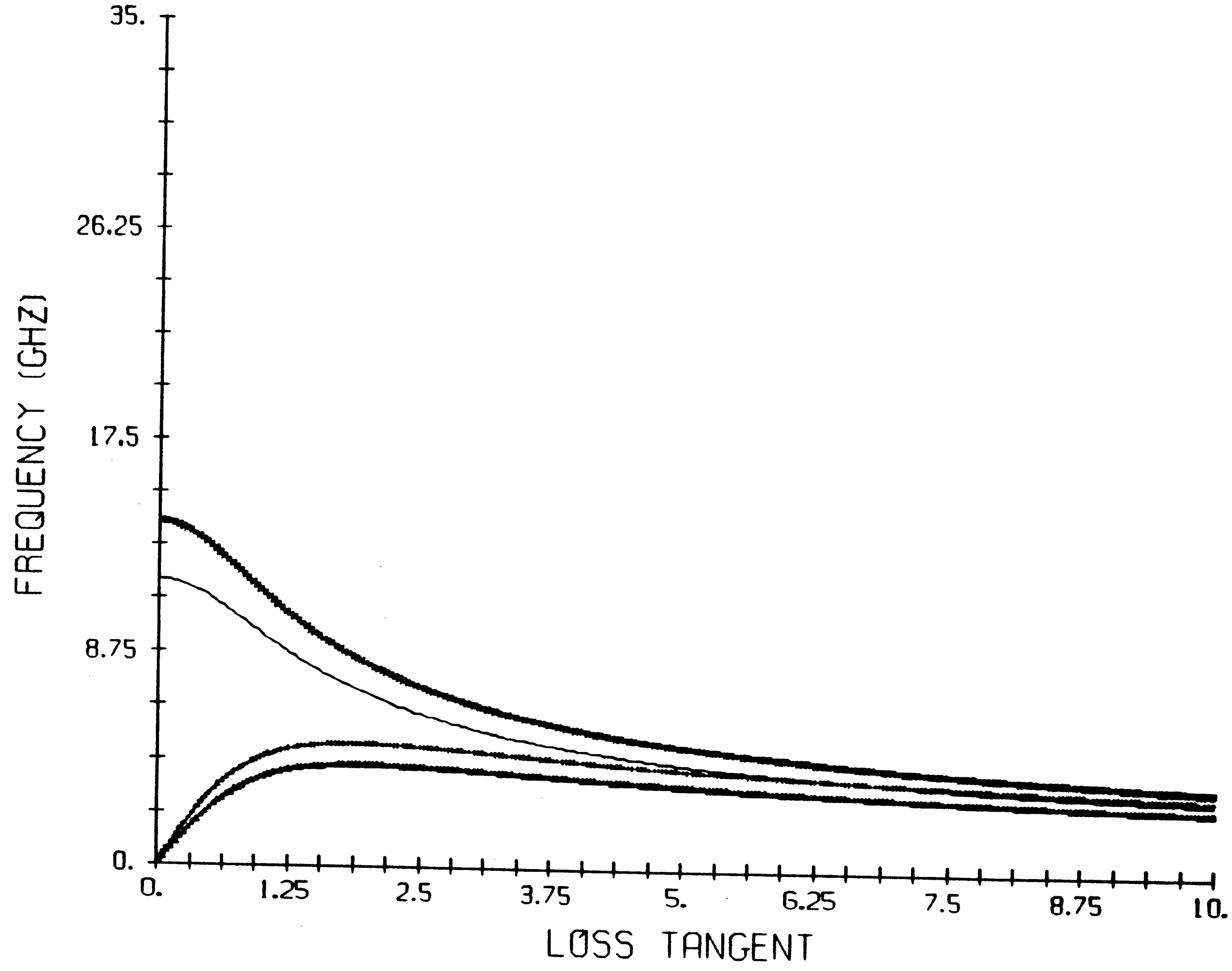

CUTØFF FREQUENCY .VS. LØSS TANGENT #8

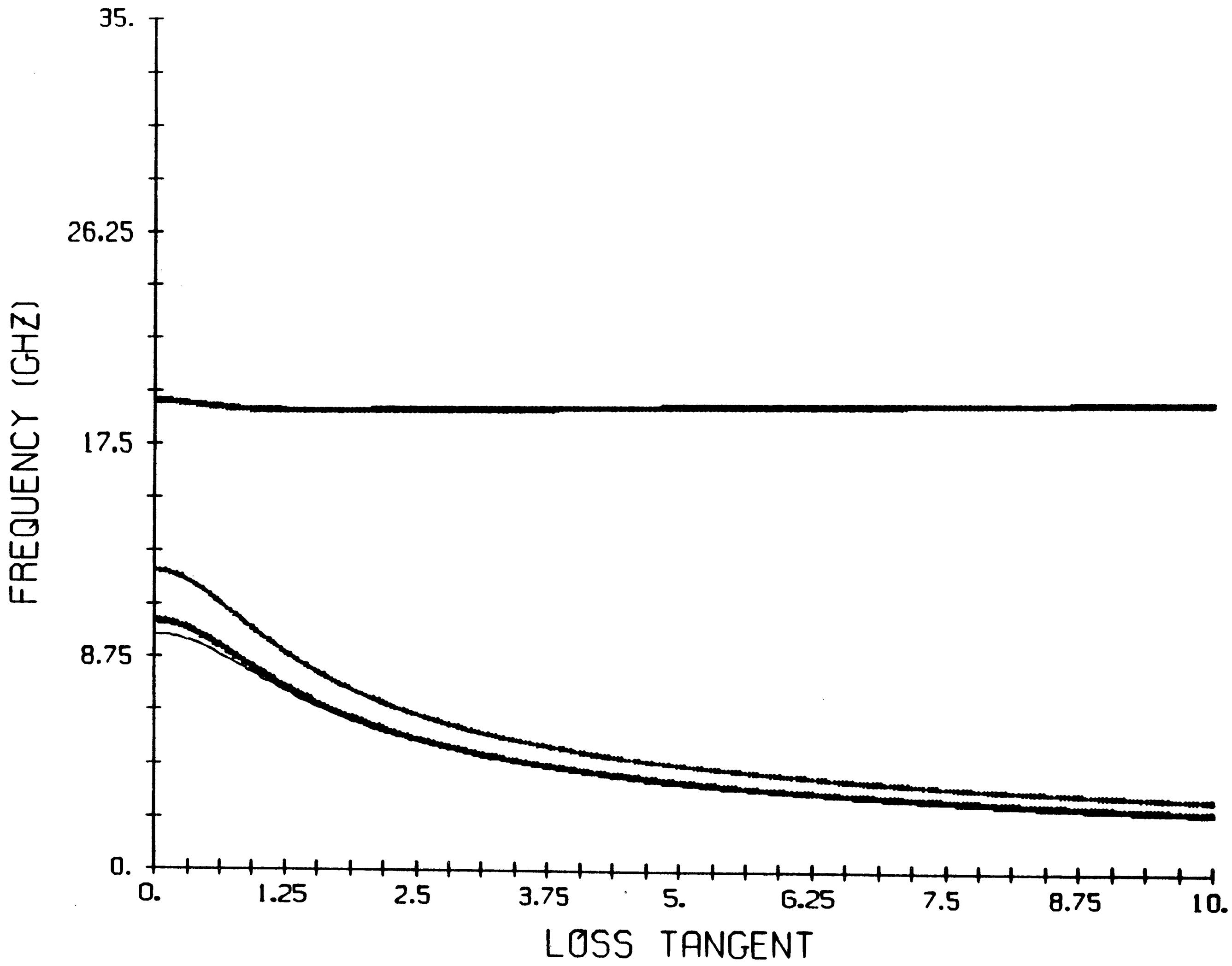

23:44:07

CUTOFF (REAL AND IMAG) .VS. LOSS TANGENT FOR LSM #8

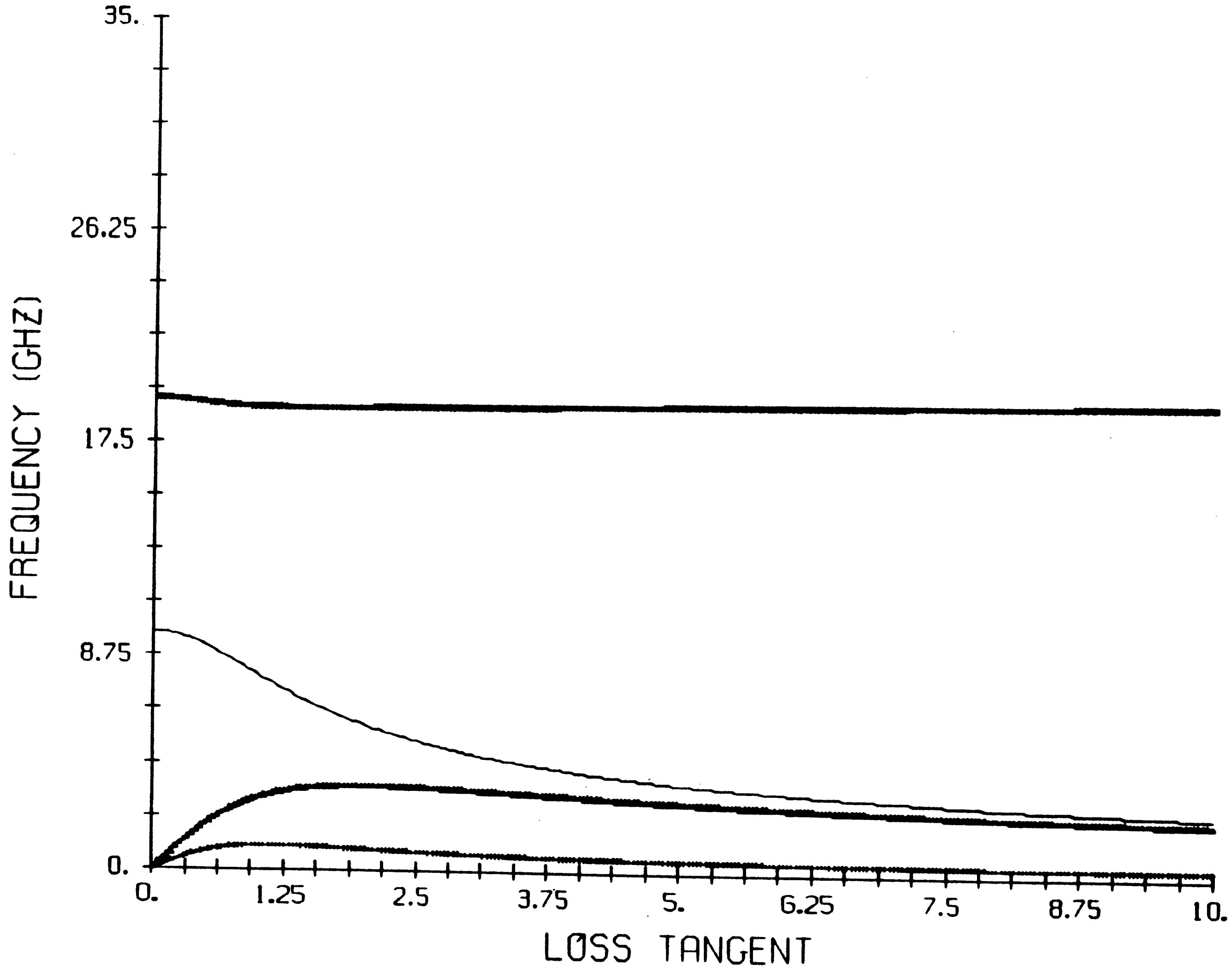

CUTOFF (REAL AND IMAG) .VS. LOSS TANGENT FOR LSE #8

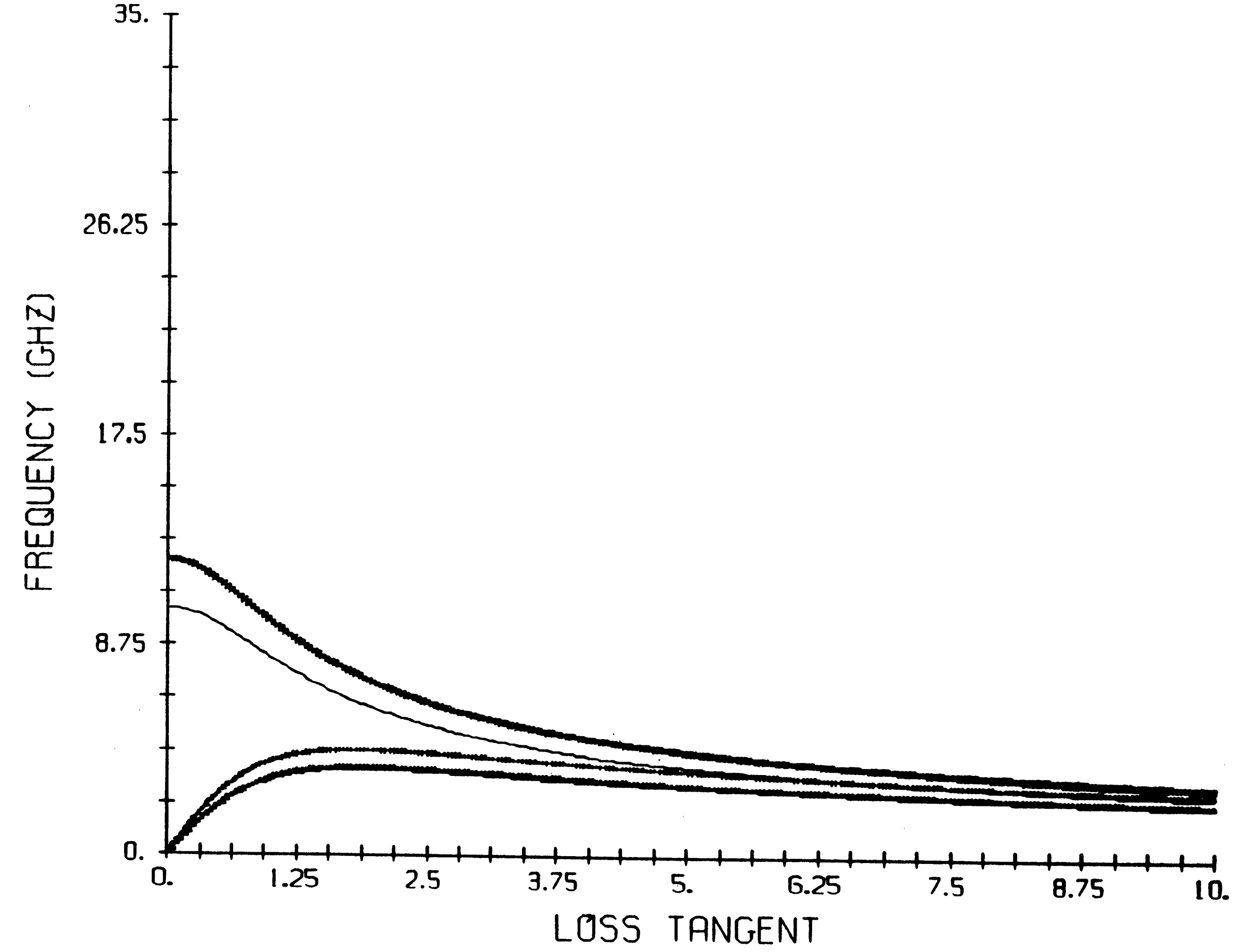

00:13:16

CUTOFF FREQUENCY .VS. LOSS TANGENT #9

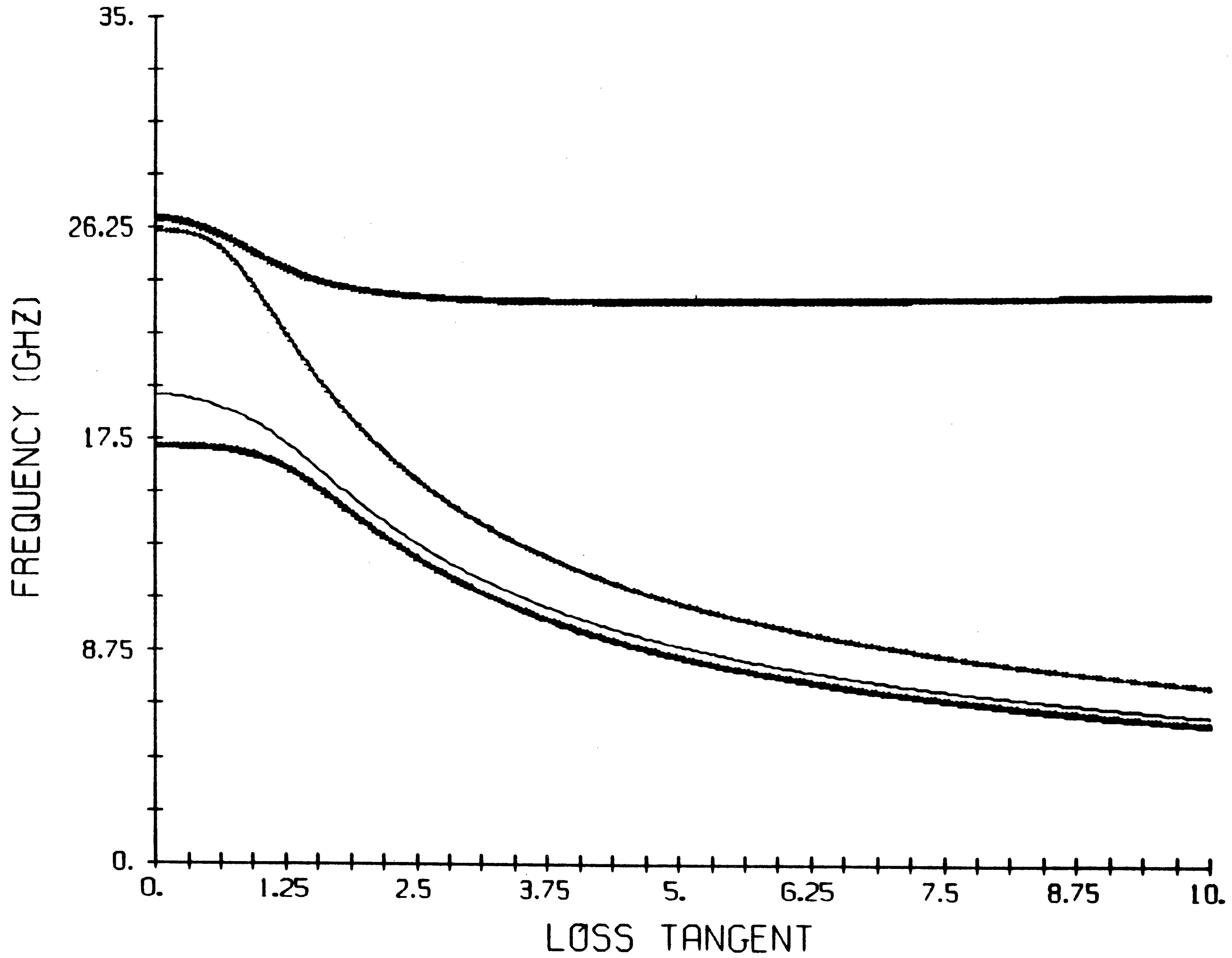

CUTØFF (REAL AND IMAG) .VS. LØSS TANGENT FØR LSM #9

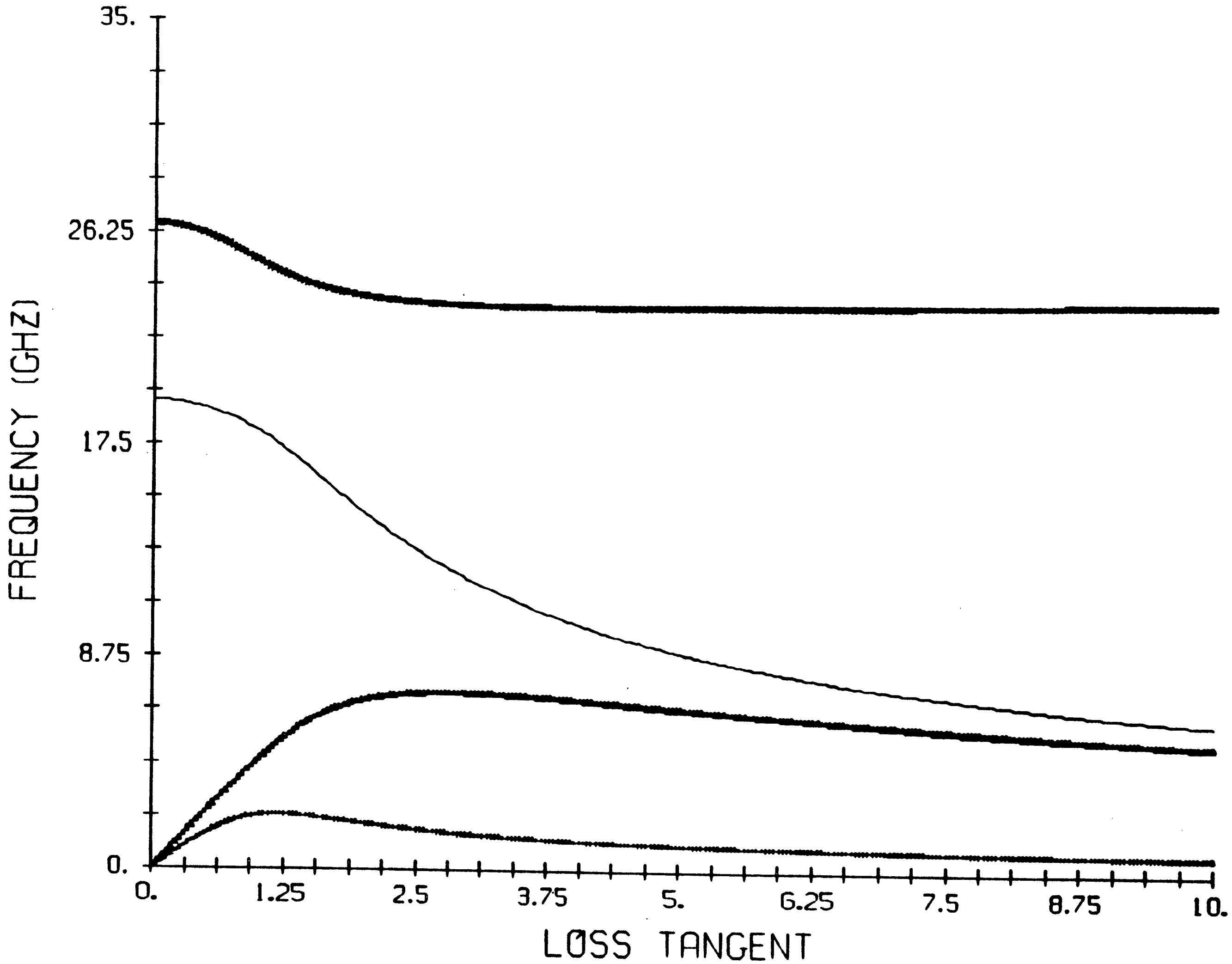

00:13:35

CUTOFF (REAL AND IMAG) .VS. LOSS TANGENT FOR LSE #9

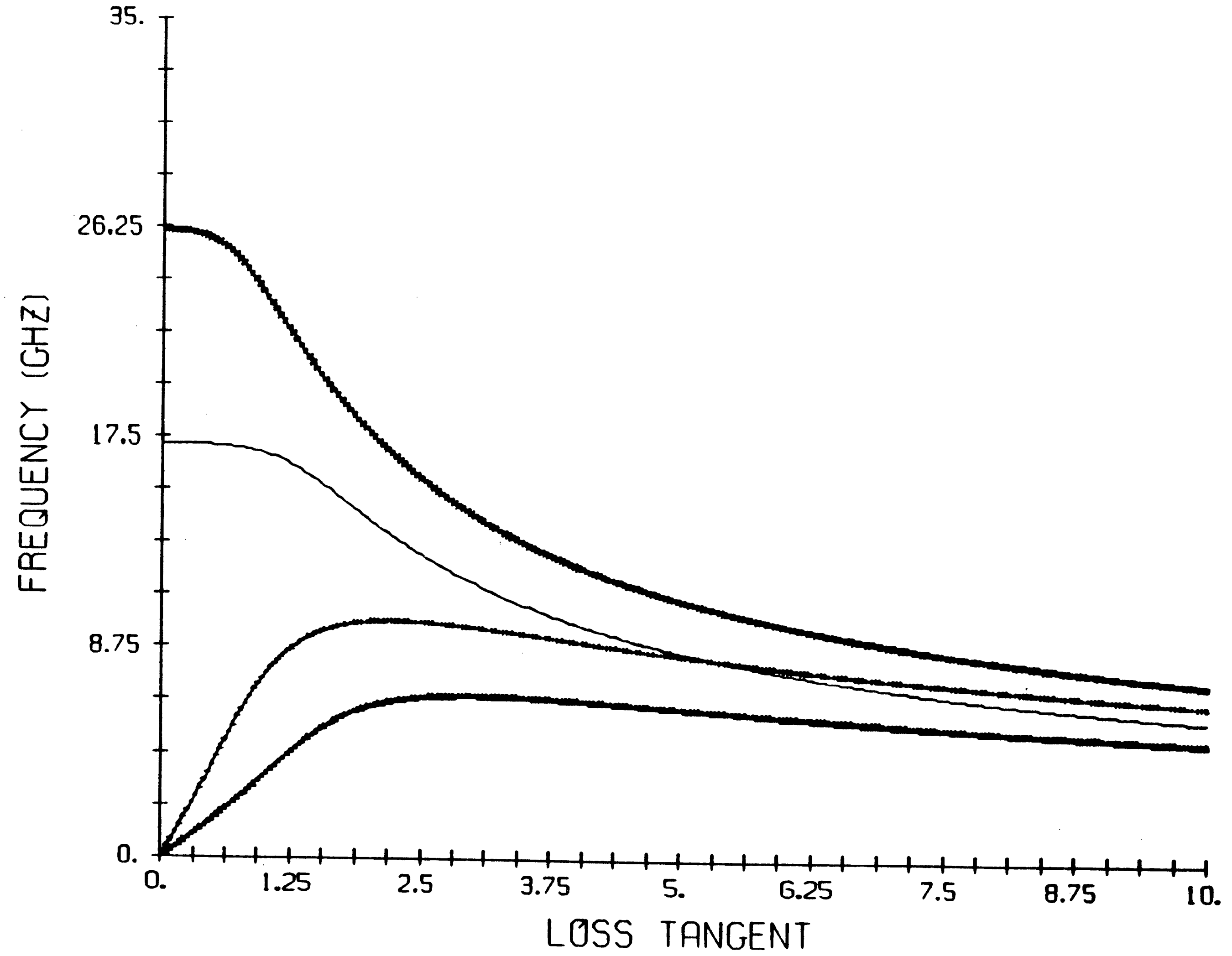

CUTOFF FREQUENCY .VS. LOSS TANGENT #10

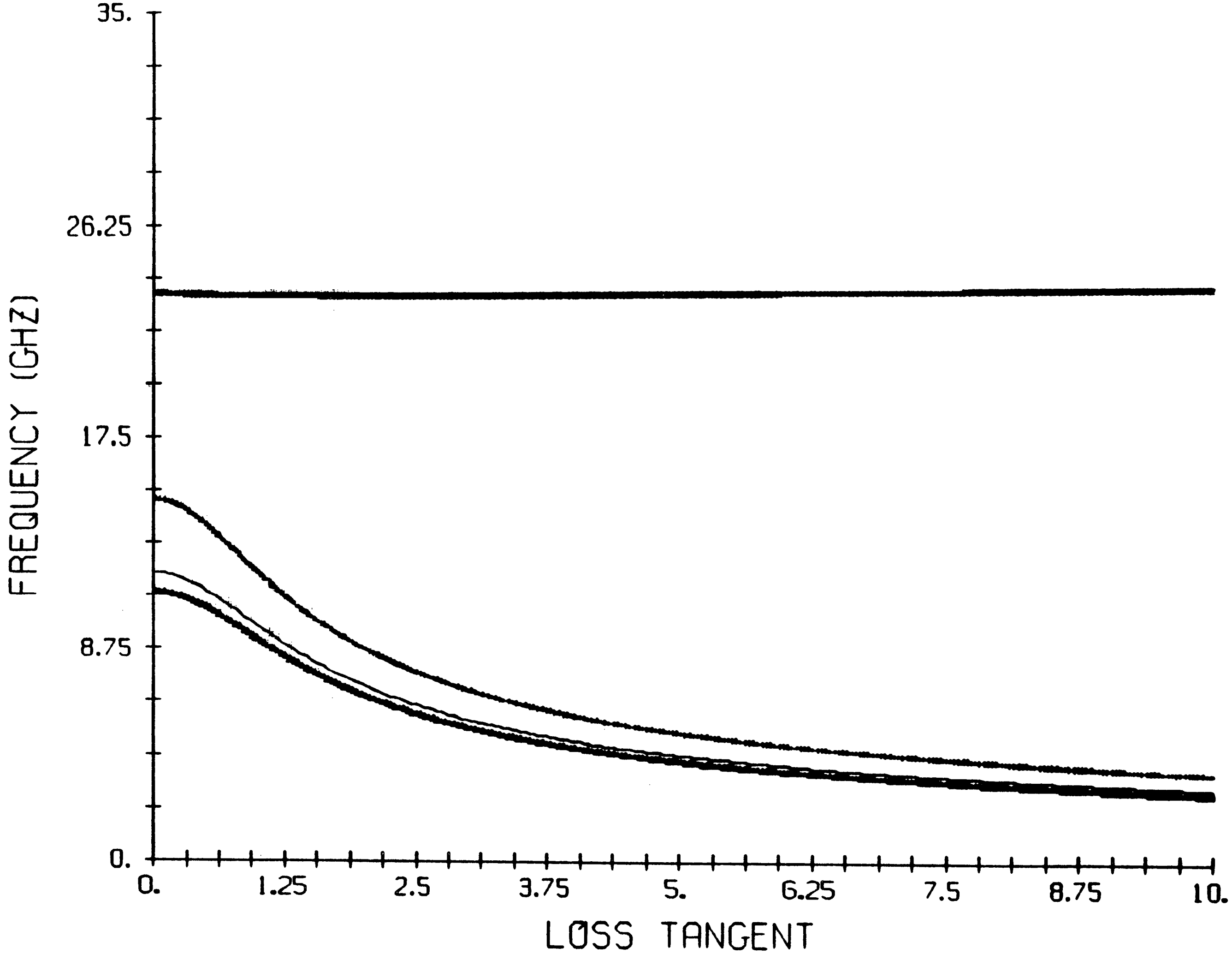

00:18:39

CUTØFF (REAL AND IMAG) .VS. LØSS TANGENT FØR LSM #10

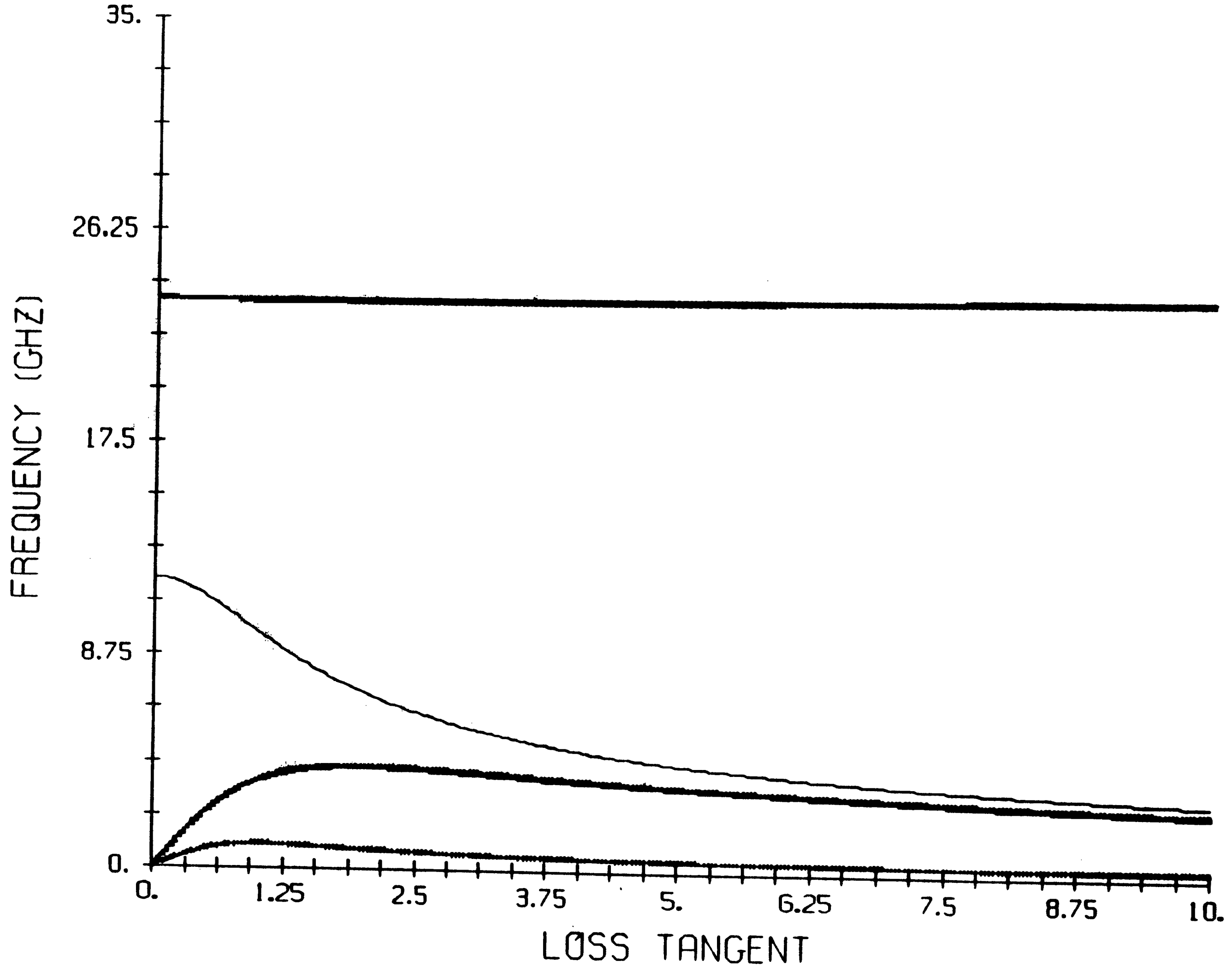

CUTØFF (REAL AND IMAG) .VS. LØSS TANGENT FØR LSE #10

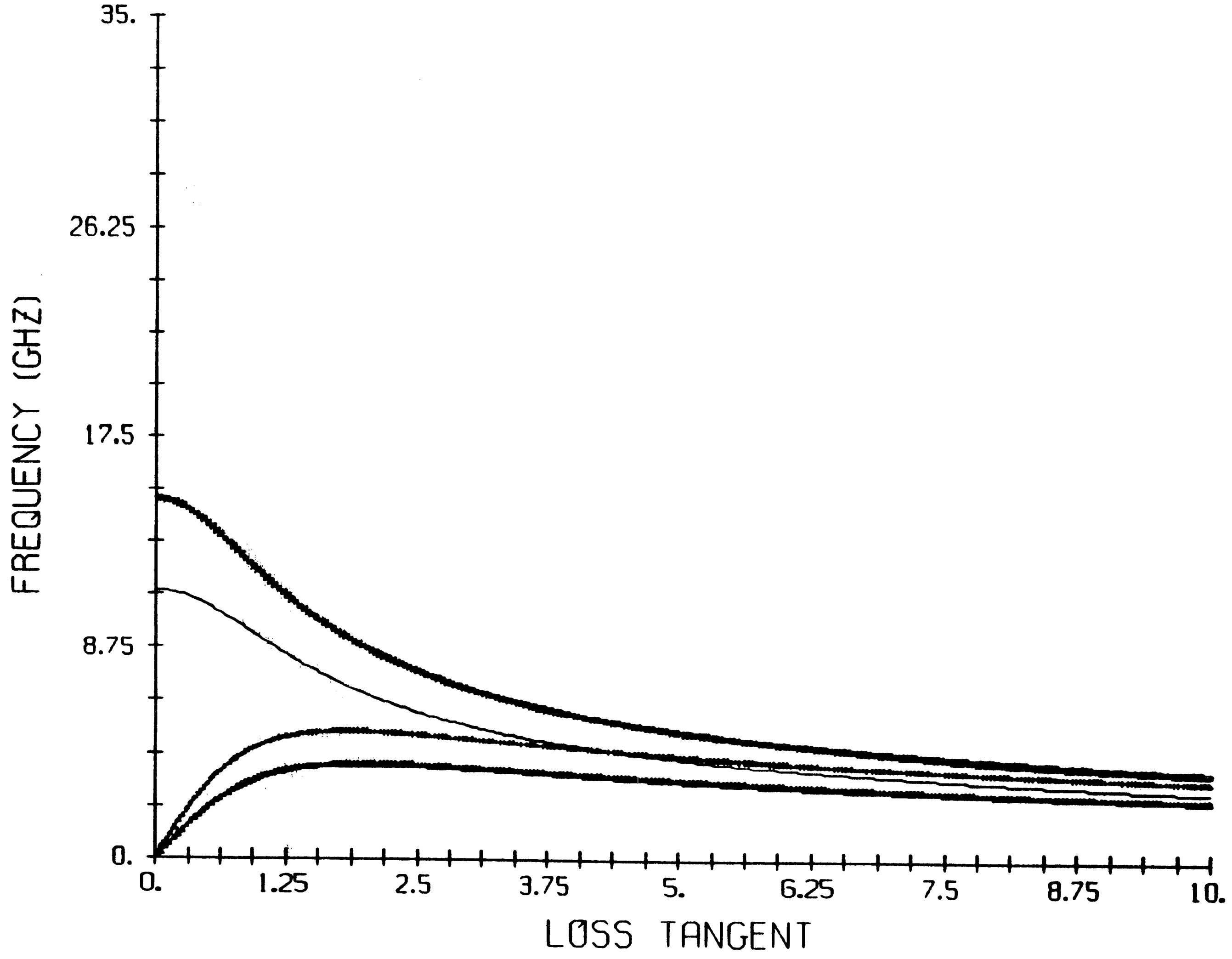

00:21:02

CUTØFF FREQUENCY .VS. LØSS TANGENT #11

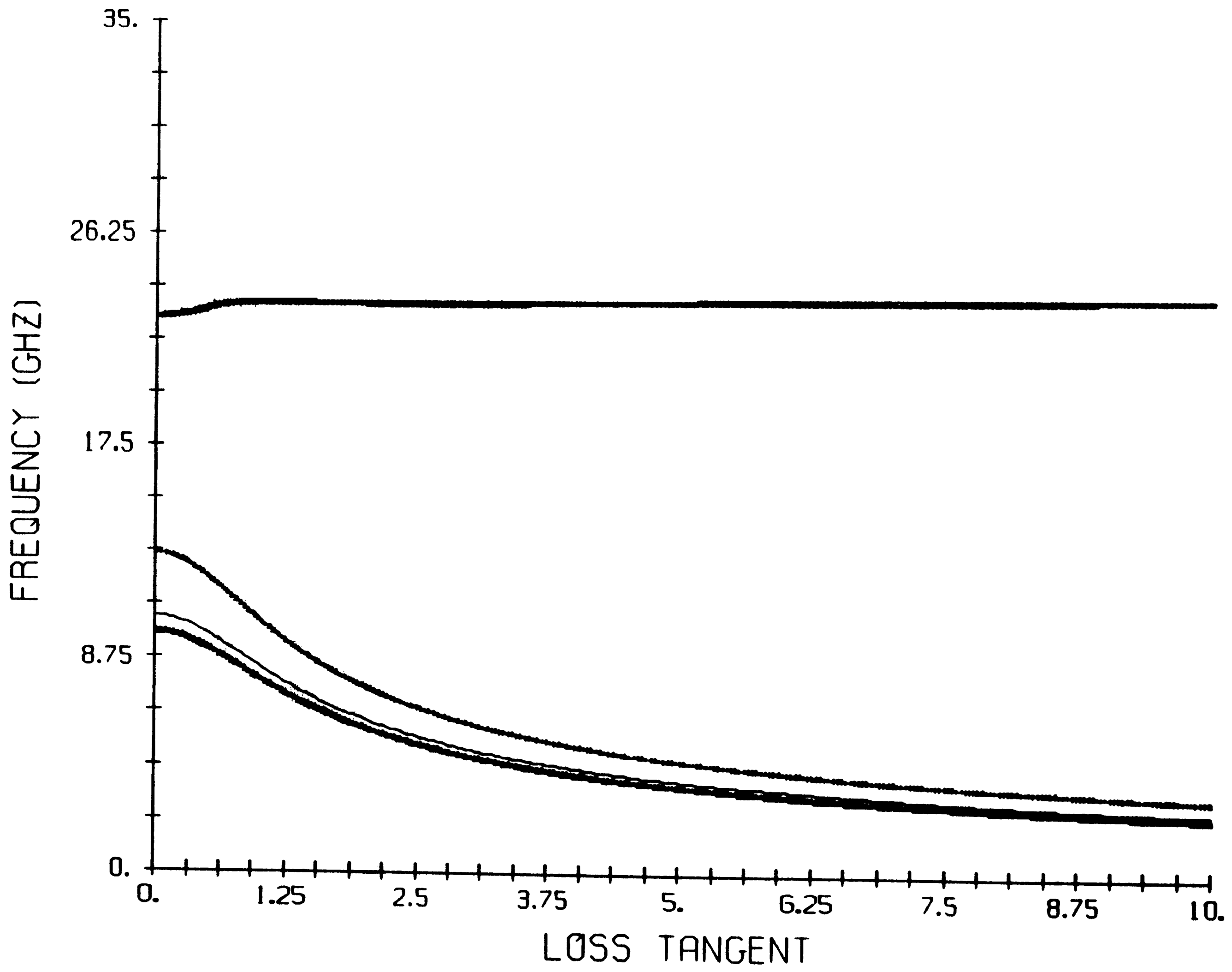

CUTØFF (REAL AND IMAG) .VS. LØSS TANGENT FØR LSM #11

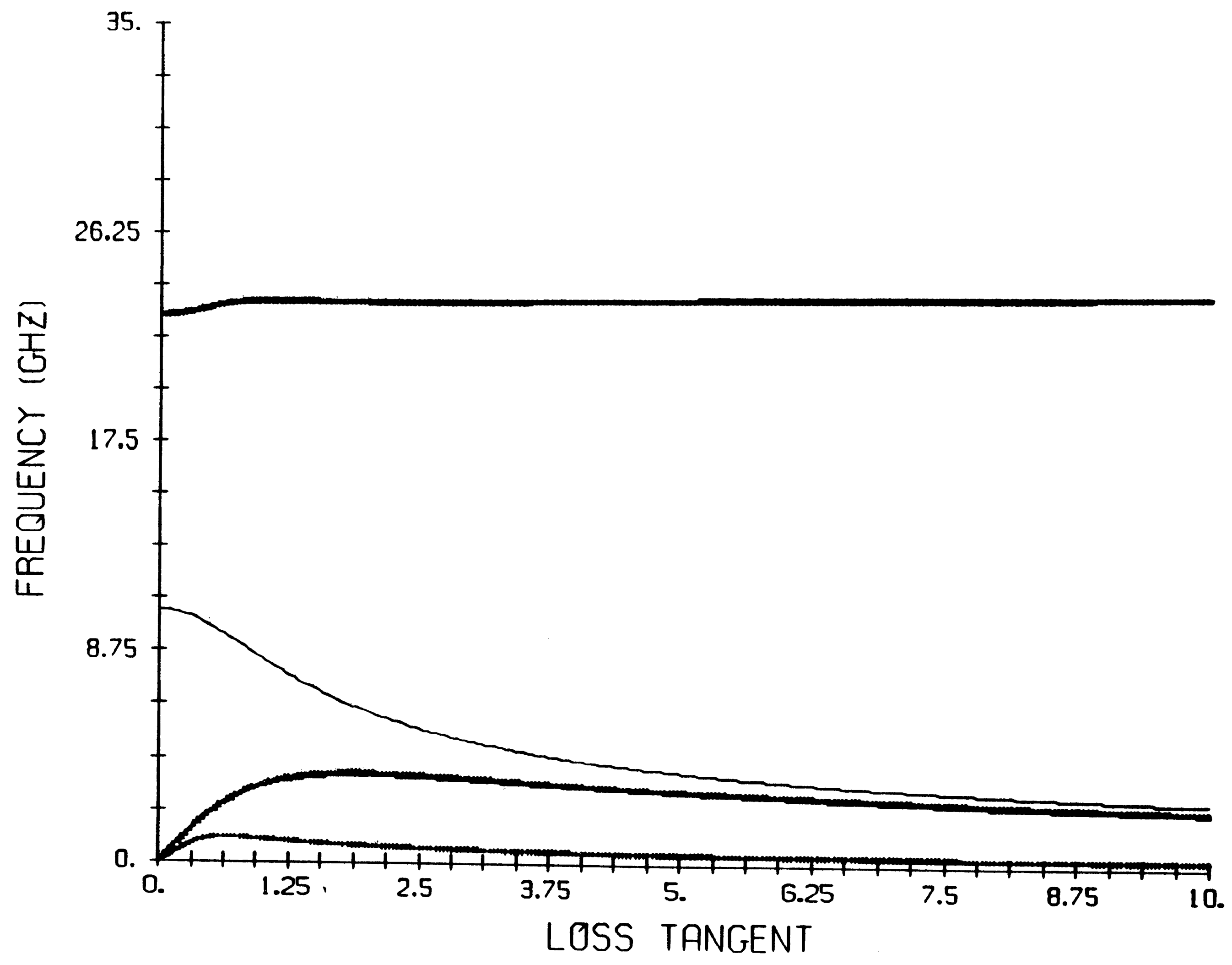

00:21:27

CUTØFF (REAL AND IMAG) .VS. LØSS TANGENT FØR LSE #11

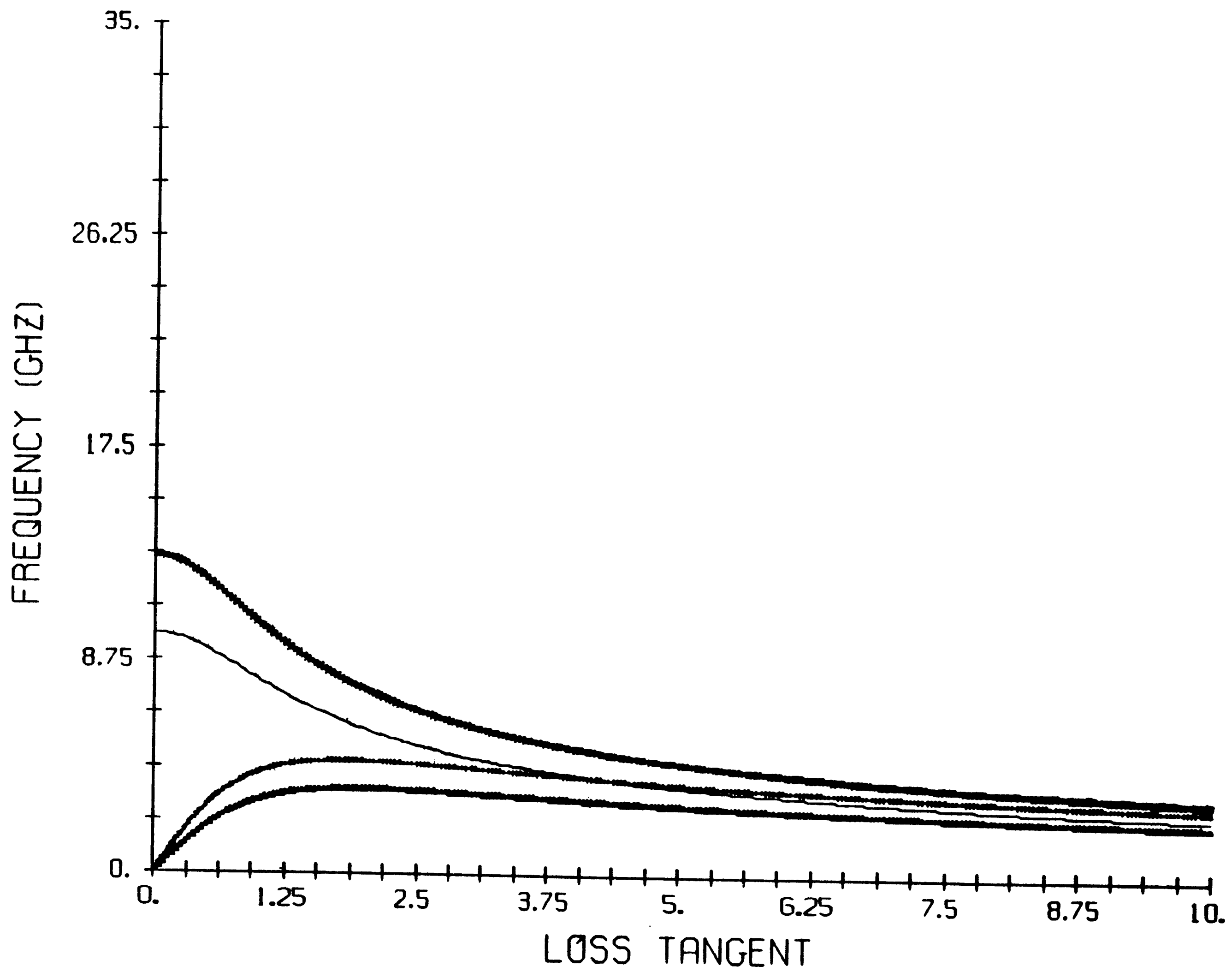

GROUP B

Comments

In this group there are two plots which served as a motivation for generating the plots of groups C-F.

These plots demonstrate the interchange of the mode order (Figure B.1) and the sensitivity of Muller's method to initial guesses (x_i, x_{i-1}, x_{i-2}) (Figure B.2).

21:32:36

CUTOFF (REAL AND IMAG) VS. LOSS TANGENT #5,4

use xi-z values

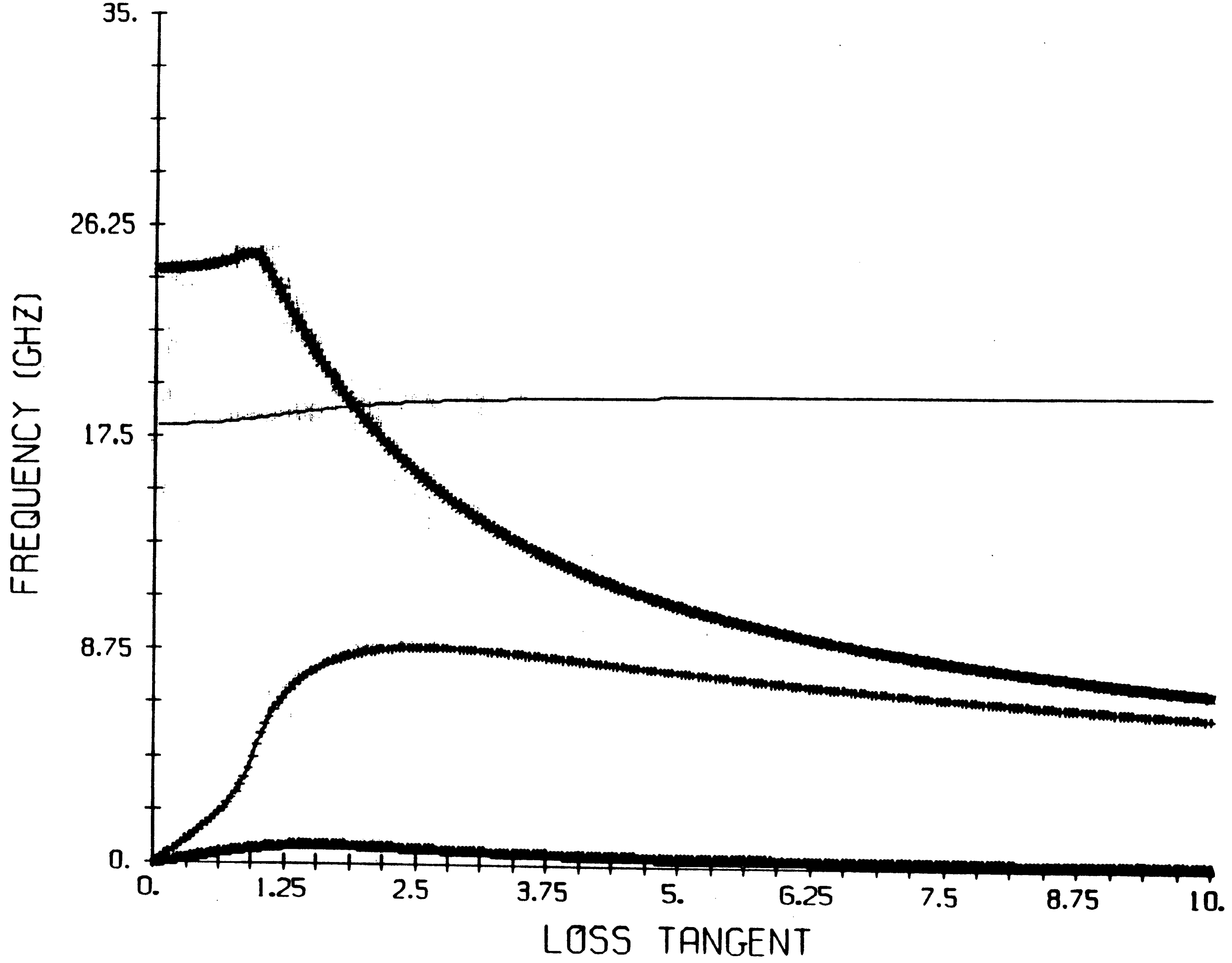

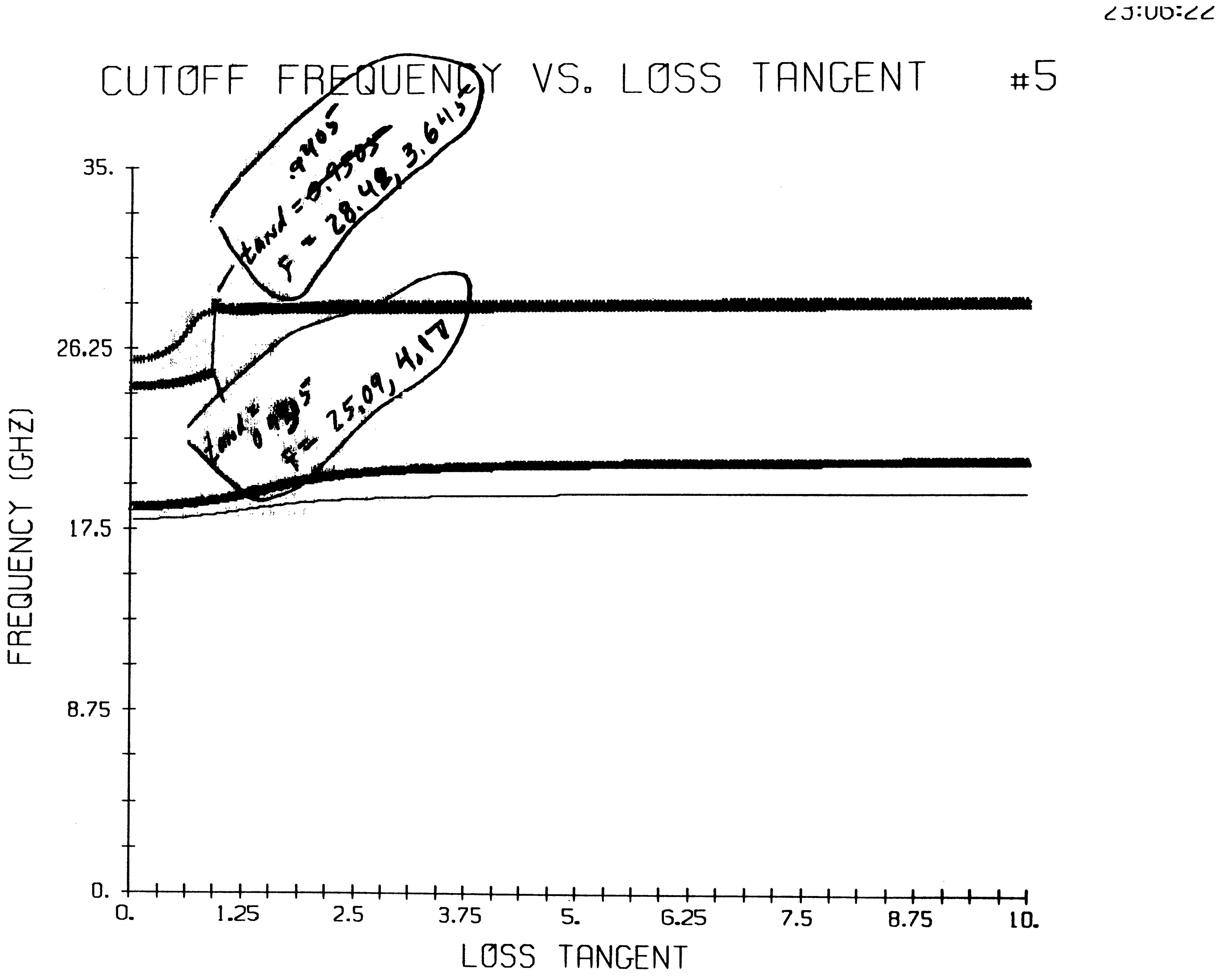

23:06:22
CUTOFF FREQUENCY VS. LOSS TANGENT #5
FREQUENCY (GHZ)
35.
26.25
17.5
8.75
0.
0.
1.25
2.5
3.75
5.
6.25
7.5
8.75
10.
LOSS TANGENT

GROUP C

Specs:

Type of Mode = LSM

$k_y = \pi/b$
h = 0.025"
a = 0.305"
b = 0.305"
$\varepsilon_r = 16.0$

Observations:

- It is obvious that there are two LSM modes very close together.
- As tand increases, one can see that the original 2nd order mode has moved to become the dominant.

Equation for Epsr=0.930

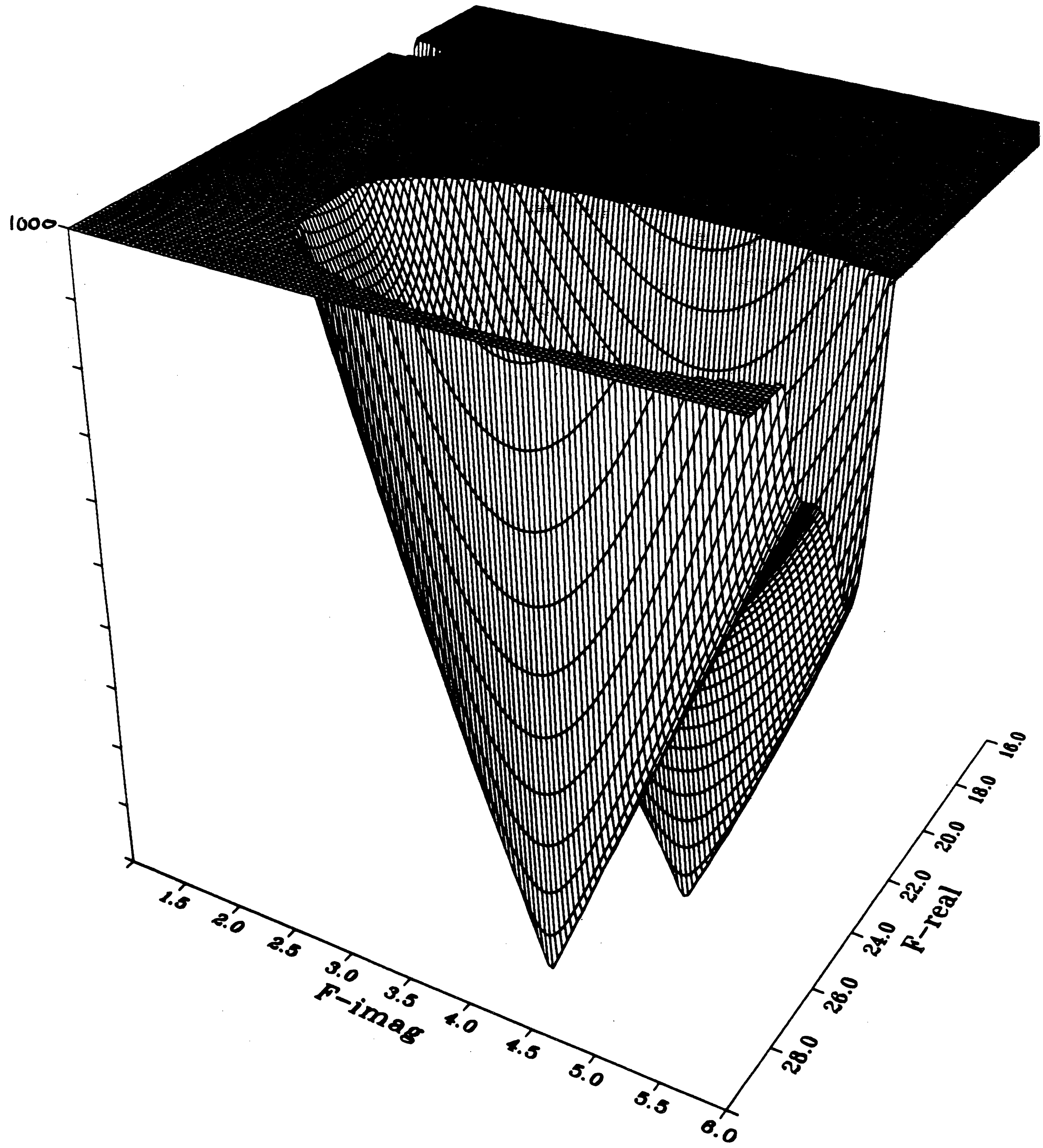

Equation for Epsr=0.9405

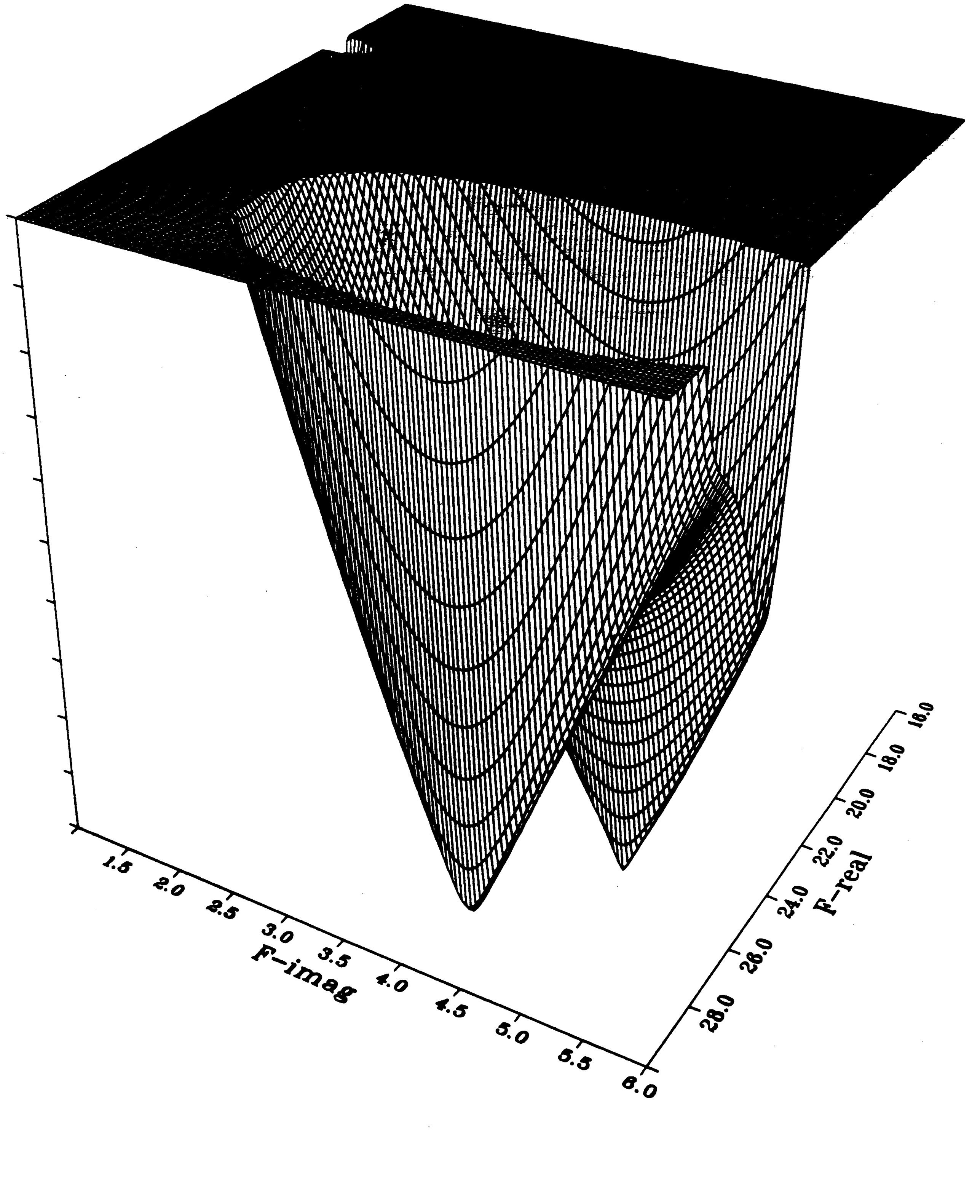

Equation for Epsr=0.940

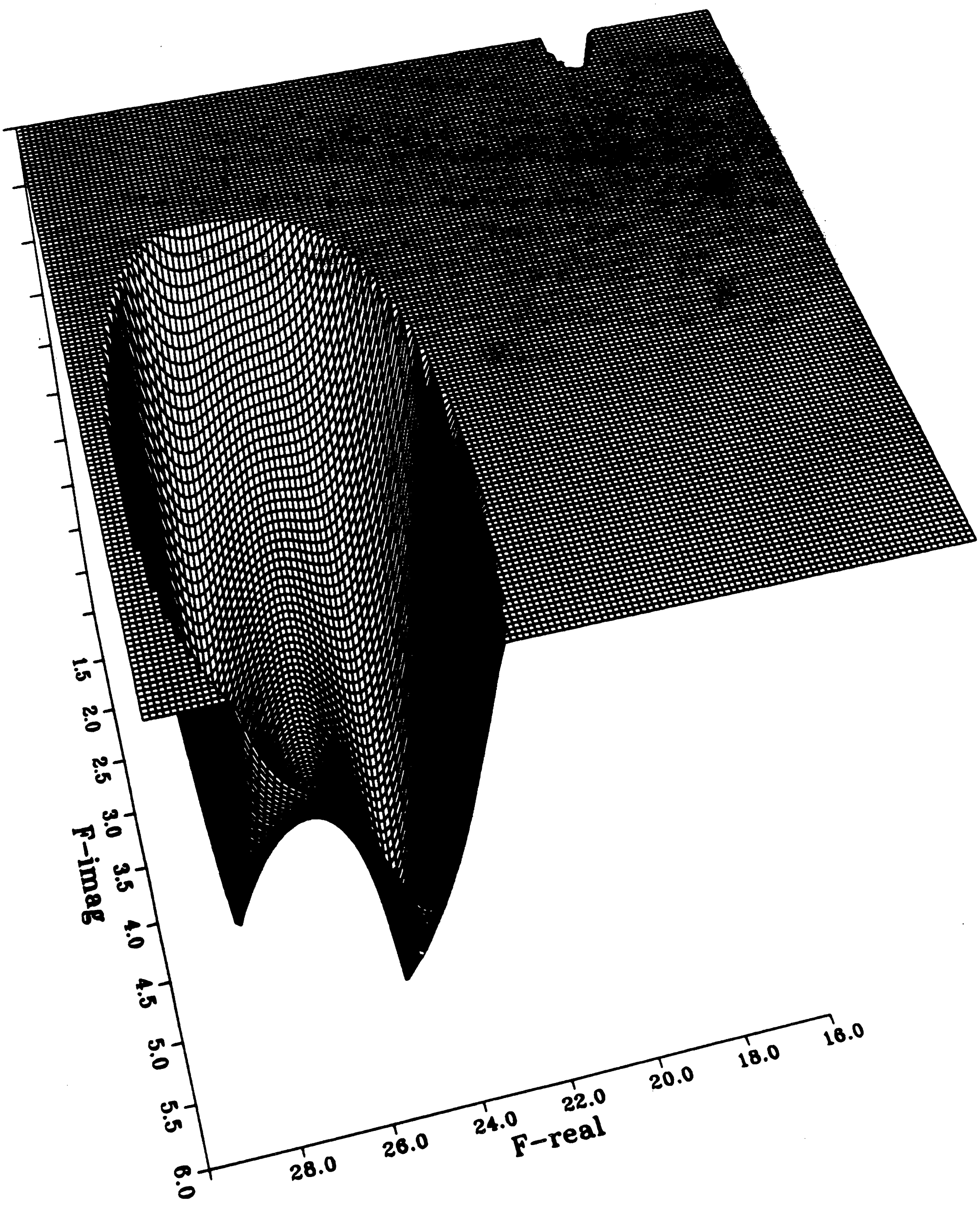

Equation for tand = 0.5

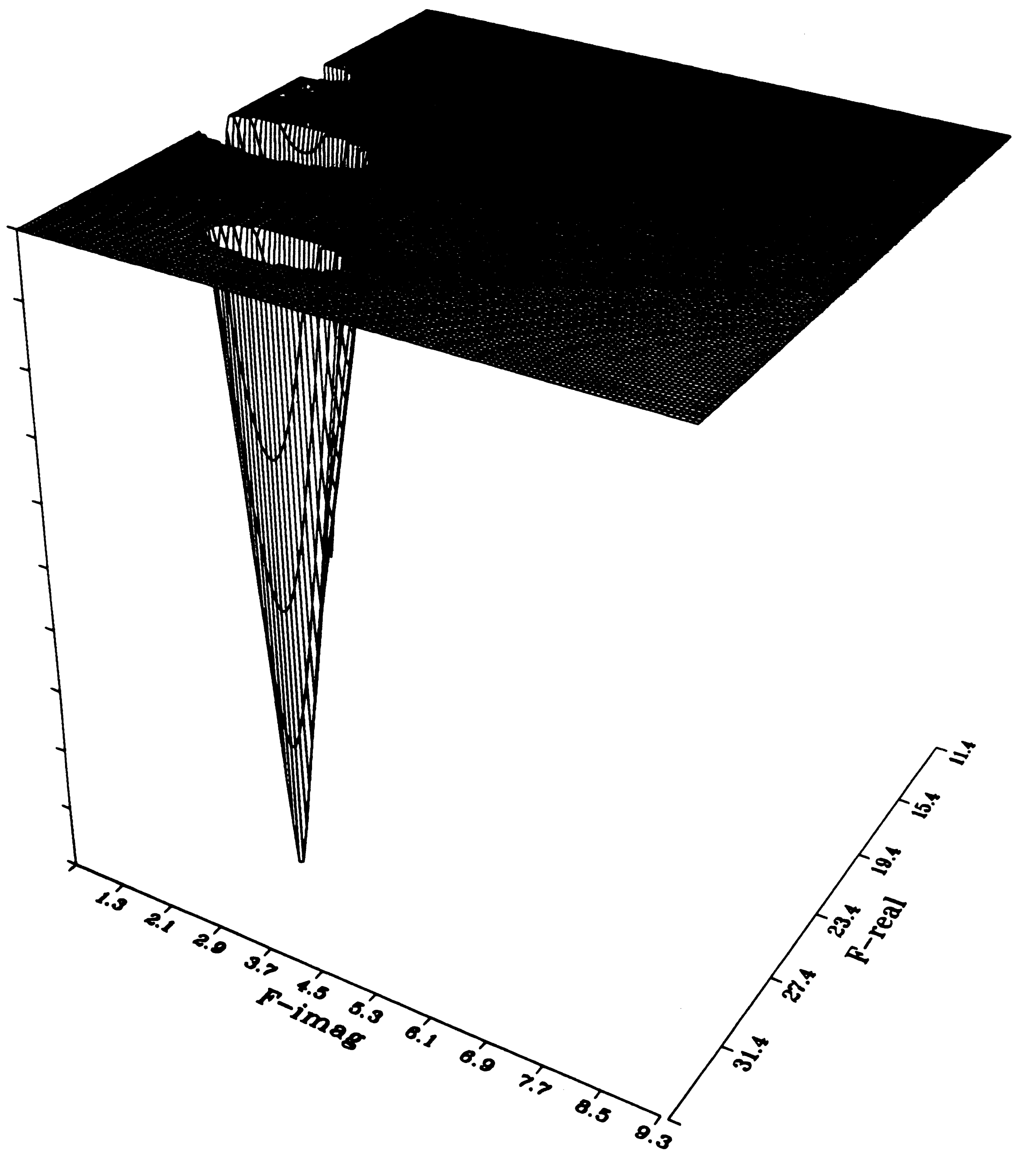

Equation for Epsr=0.5

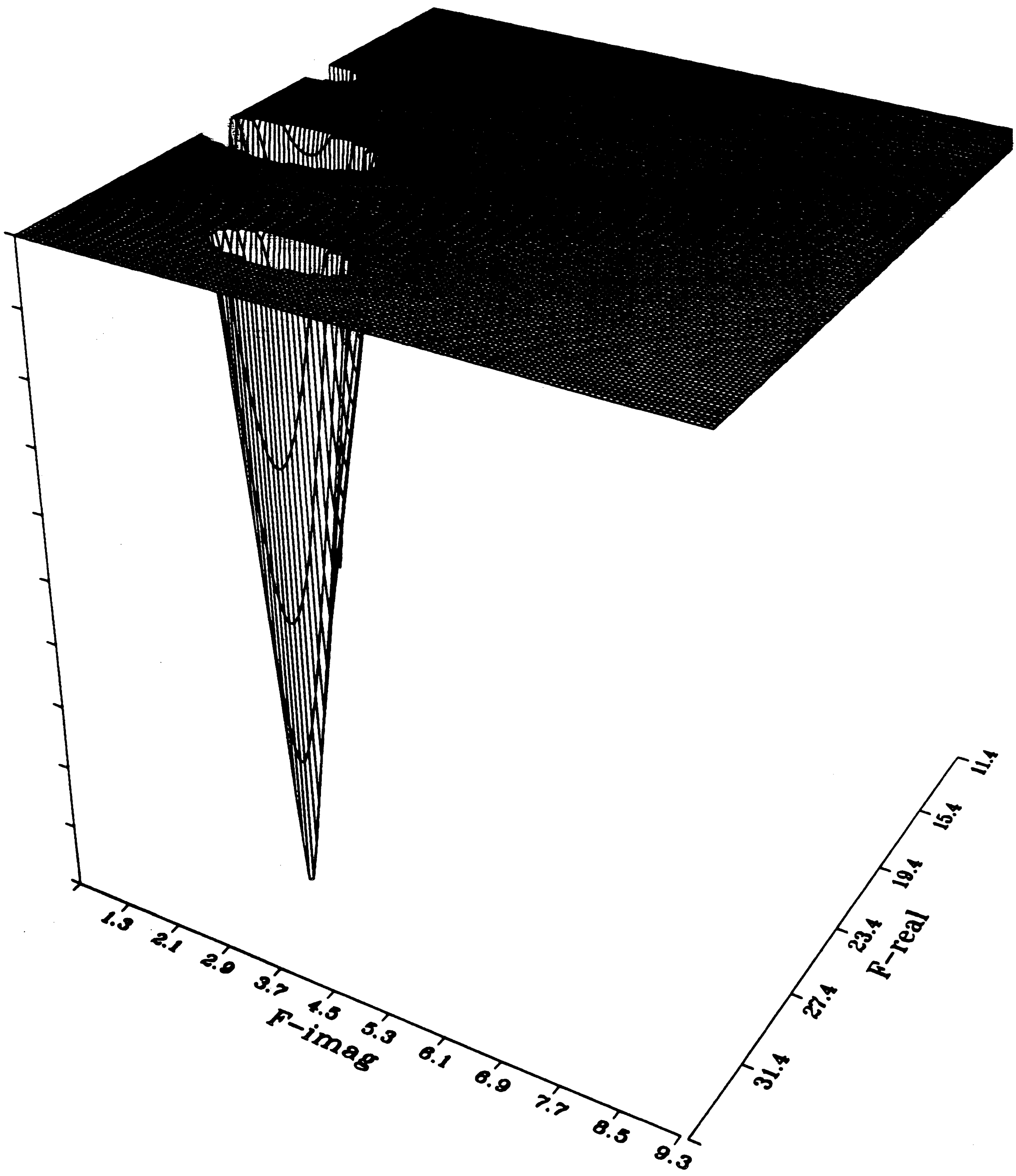

Equation for Epsr=1.0

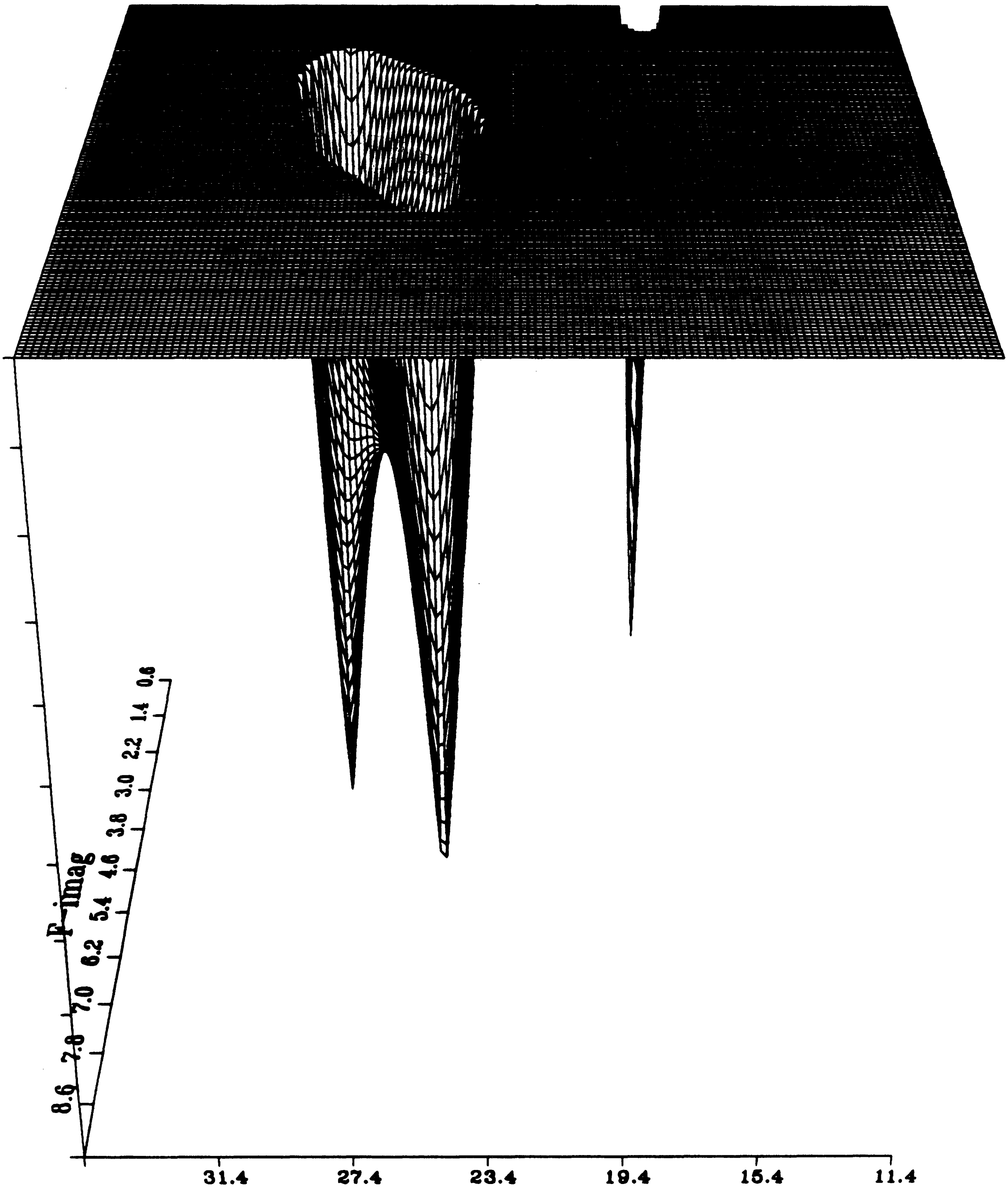

Equation for Epsr=1.5

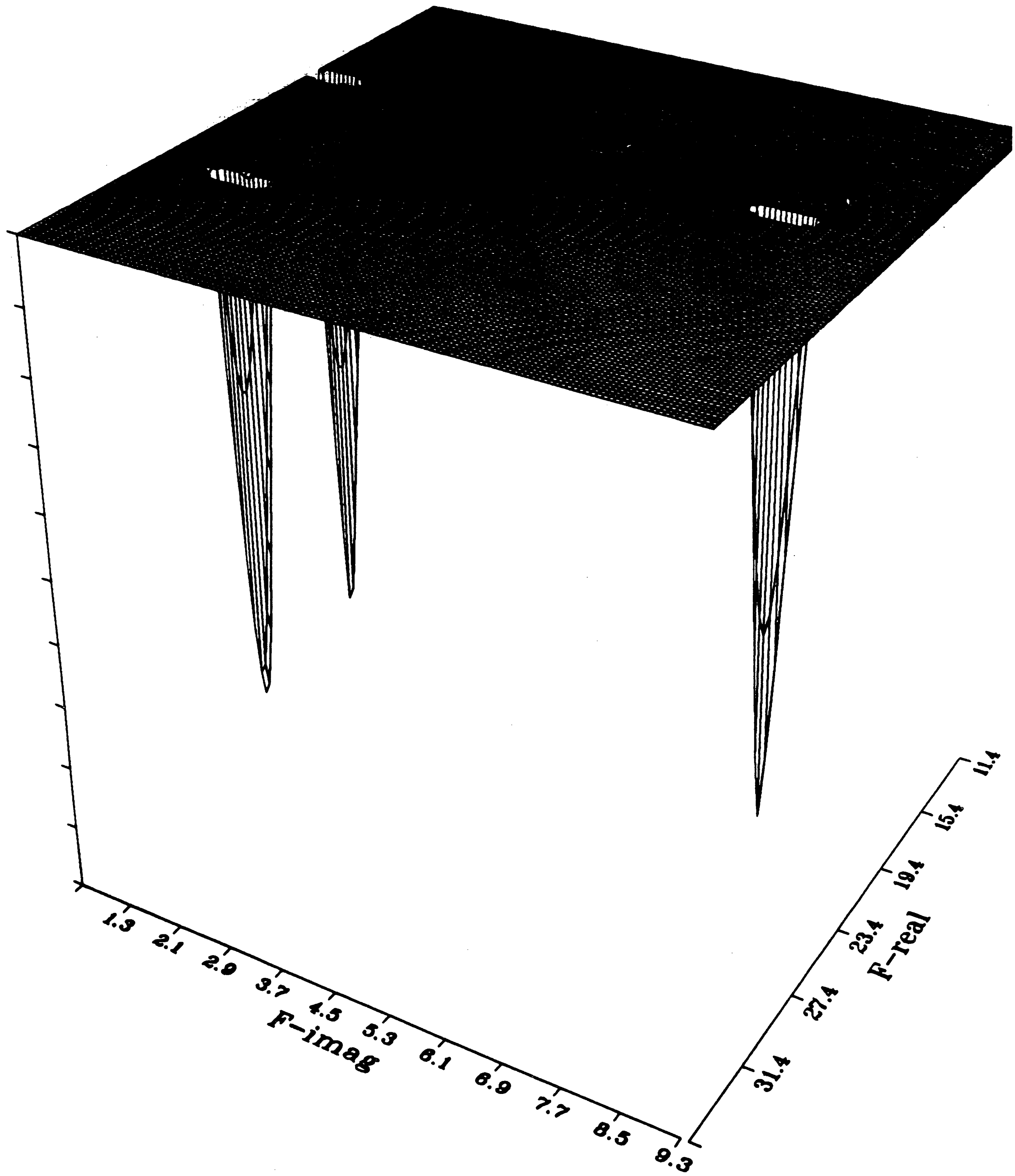

Equation for Epsr=2.0

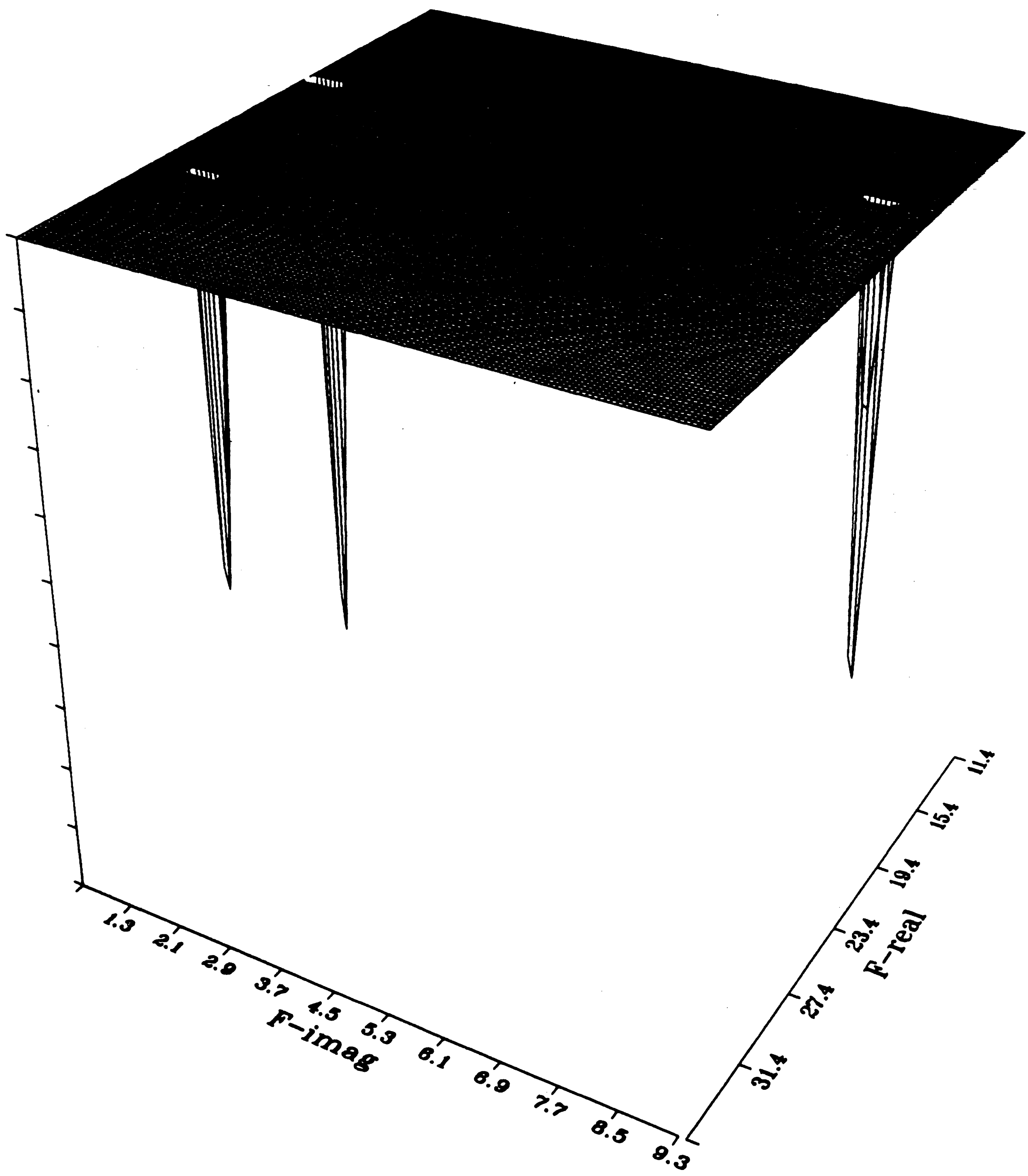

Equation for Epsr=2.5

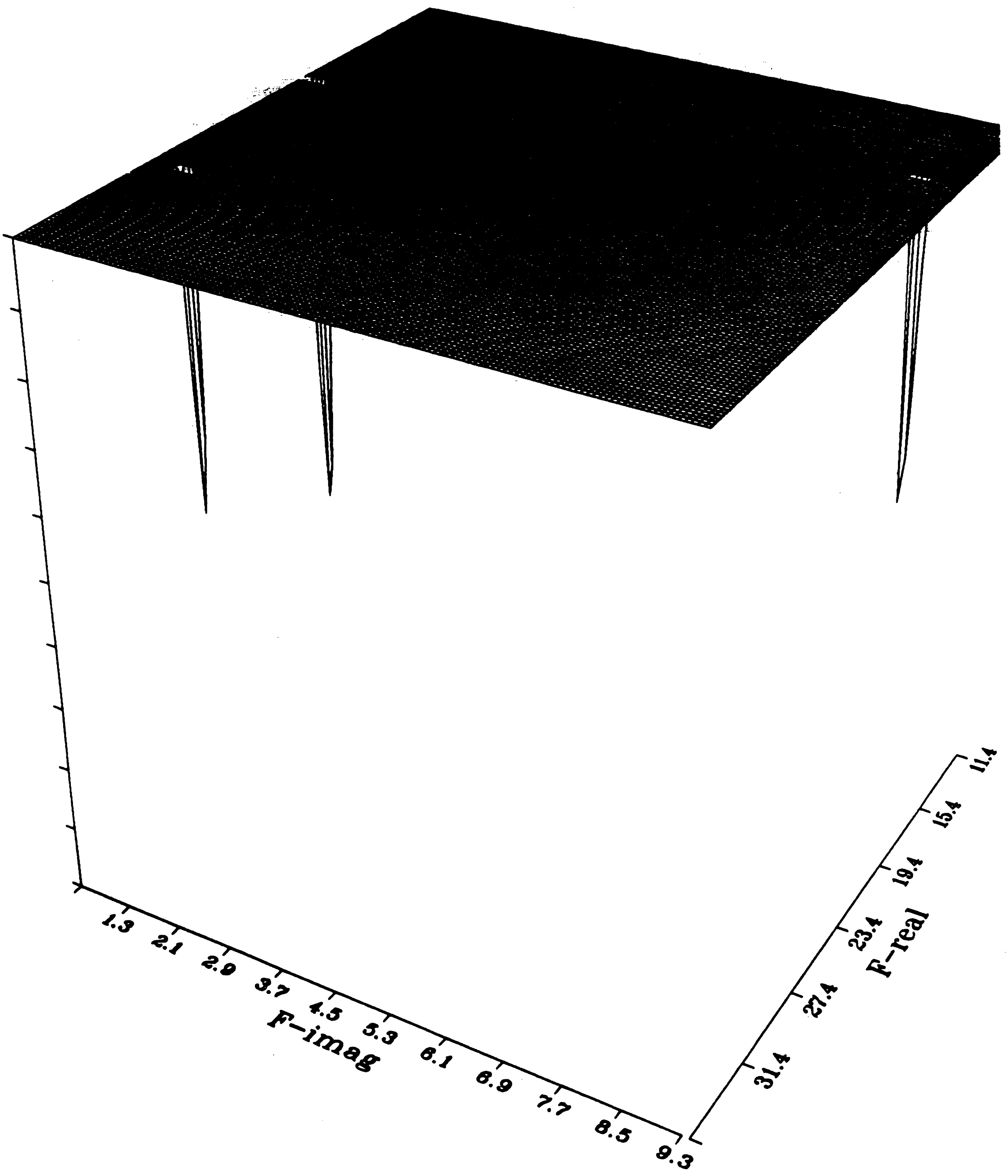

GROUP D

Specs:

Type of Mode = LSE

k_y = 0.0
a = 0.305"
b = 0.305"
ε_r = 16.0
h = 0.025"

Observations:

- At first glance, one might sense a problem with these plots. The specs are nearly the same with those of Group A, #5 which shows no mode crossover. Yet it is clear from these plots that the dominant LSE mode is replaced as tand is increased.
- The difference between this curve and the corresponding one in Group A is in k_y.

Equation for tand=0.005 (I

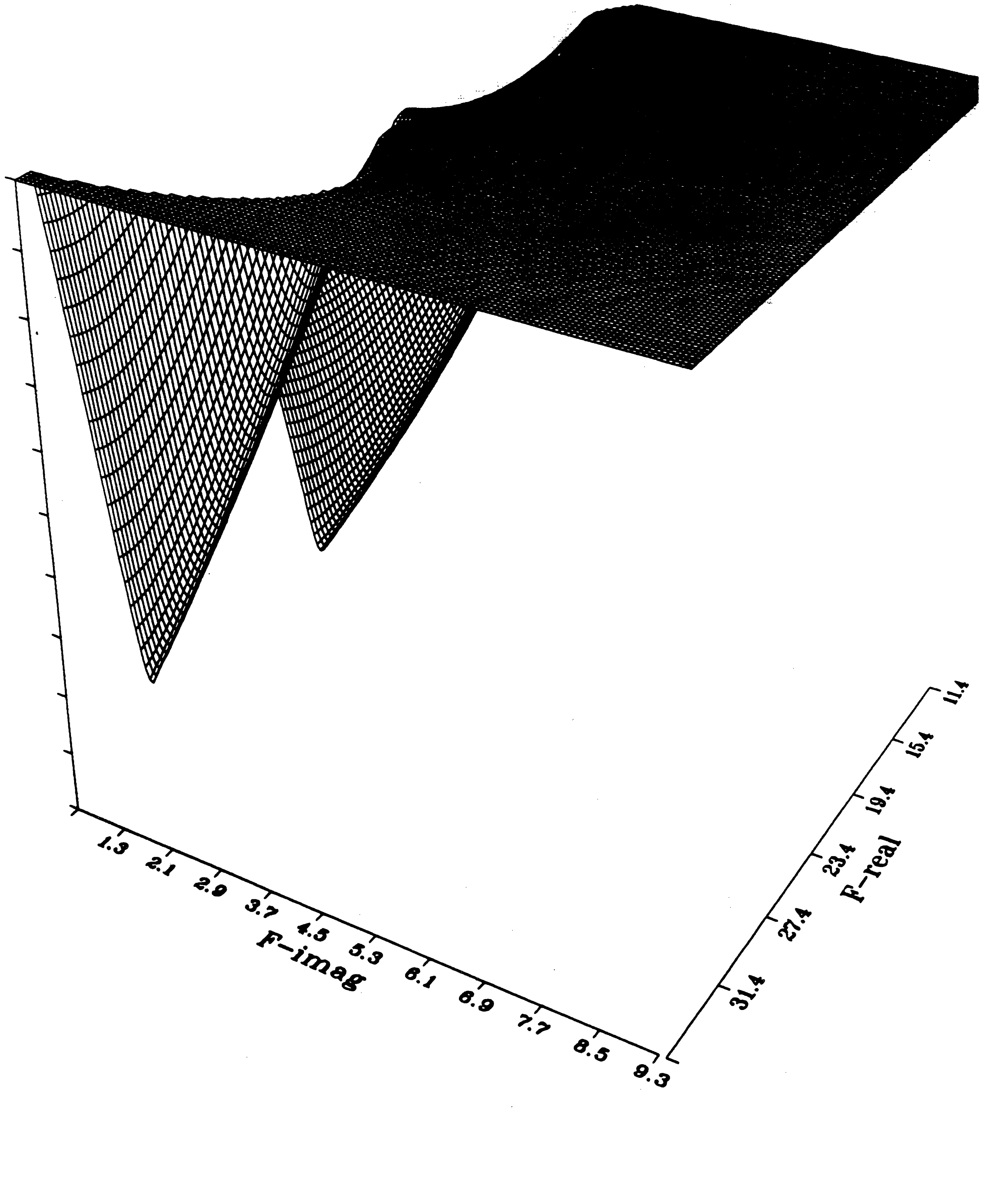

Equation for tand=0.01 (LSE

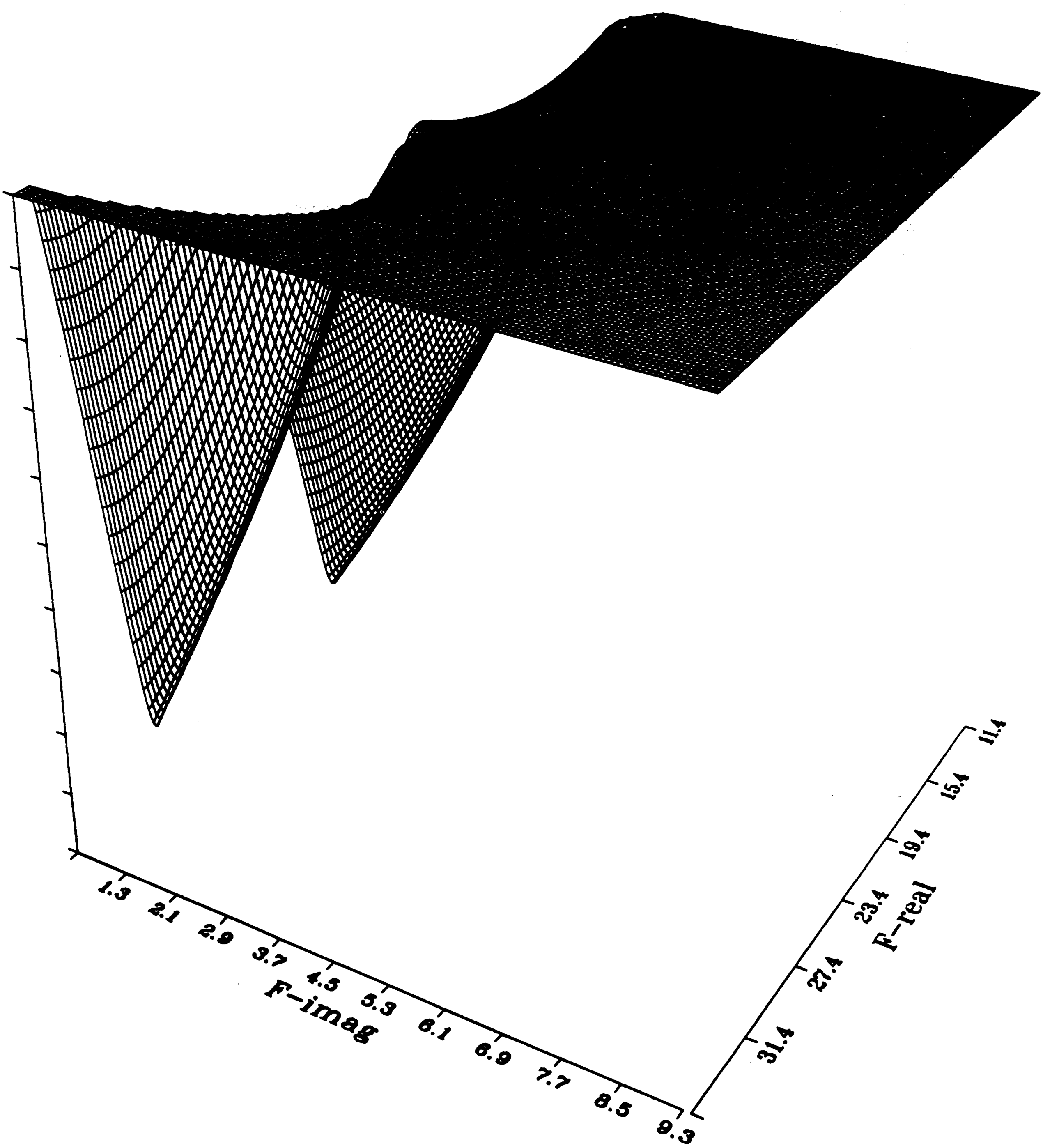

Equation for tand=0.05 (L

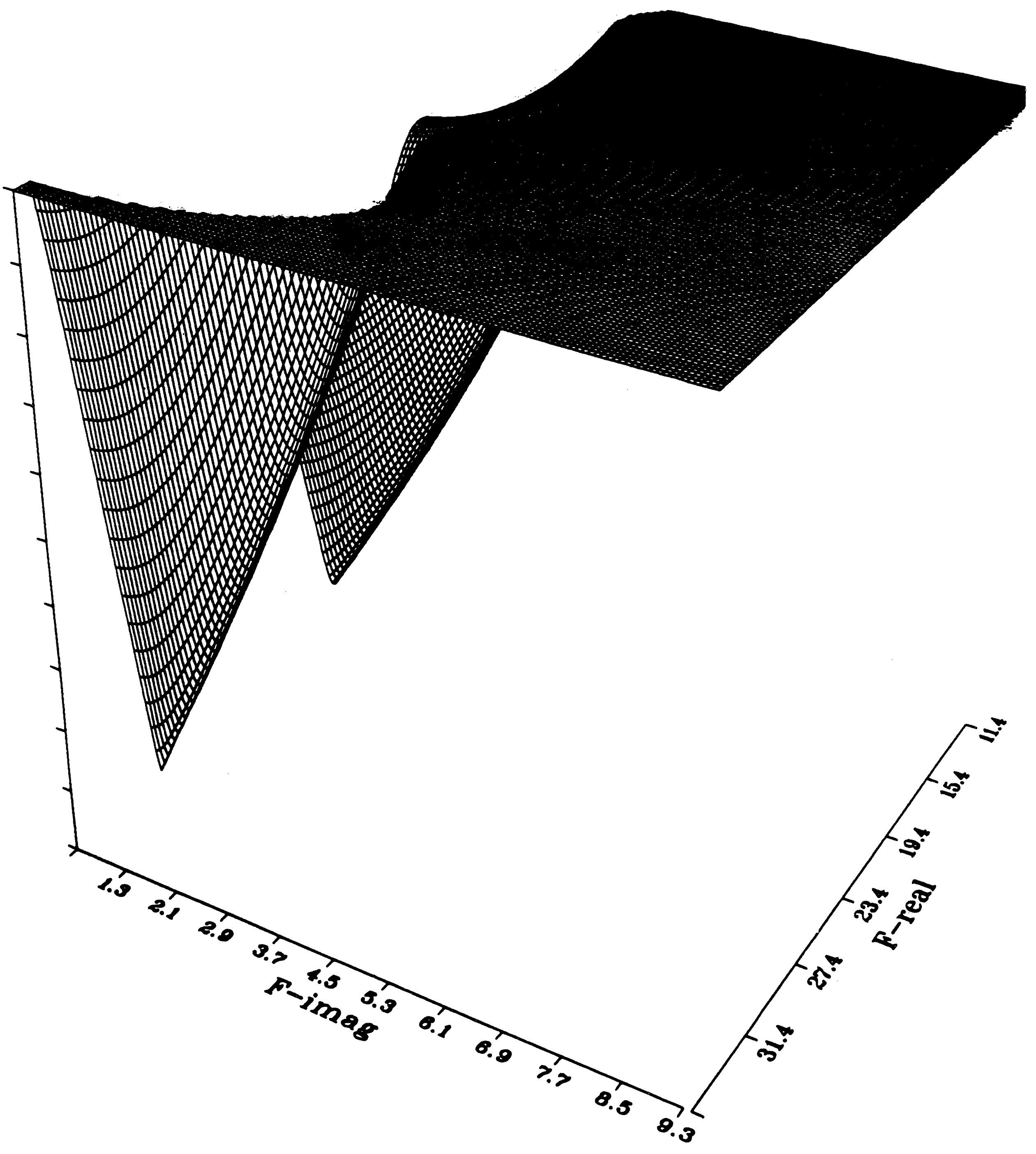

Equation for tand=0.1 (LSE

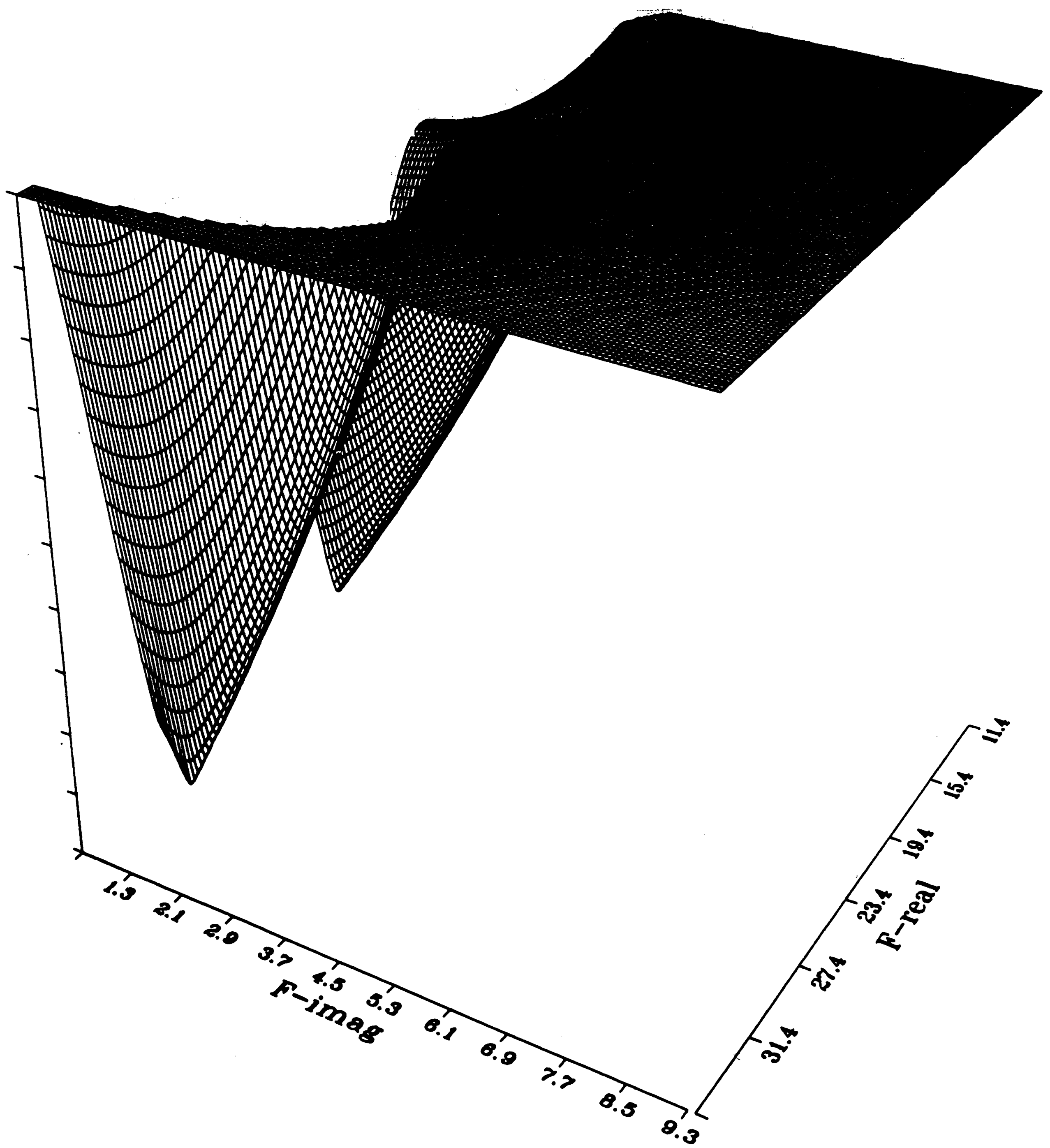

Equation for tand=0.3 (LS

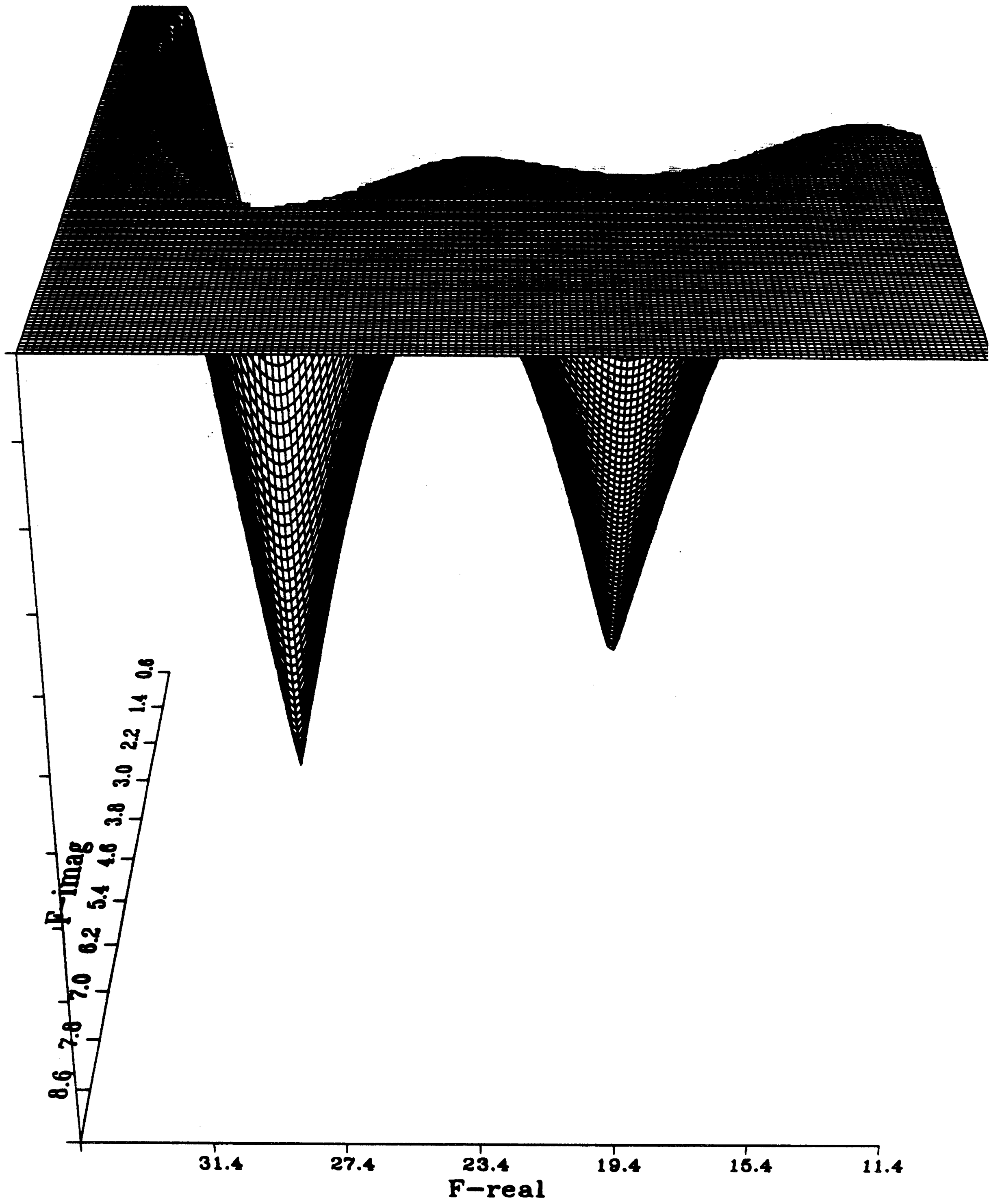

Equation for tand=0.5

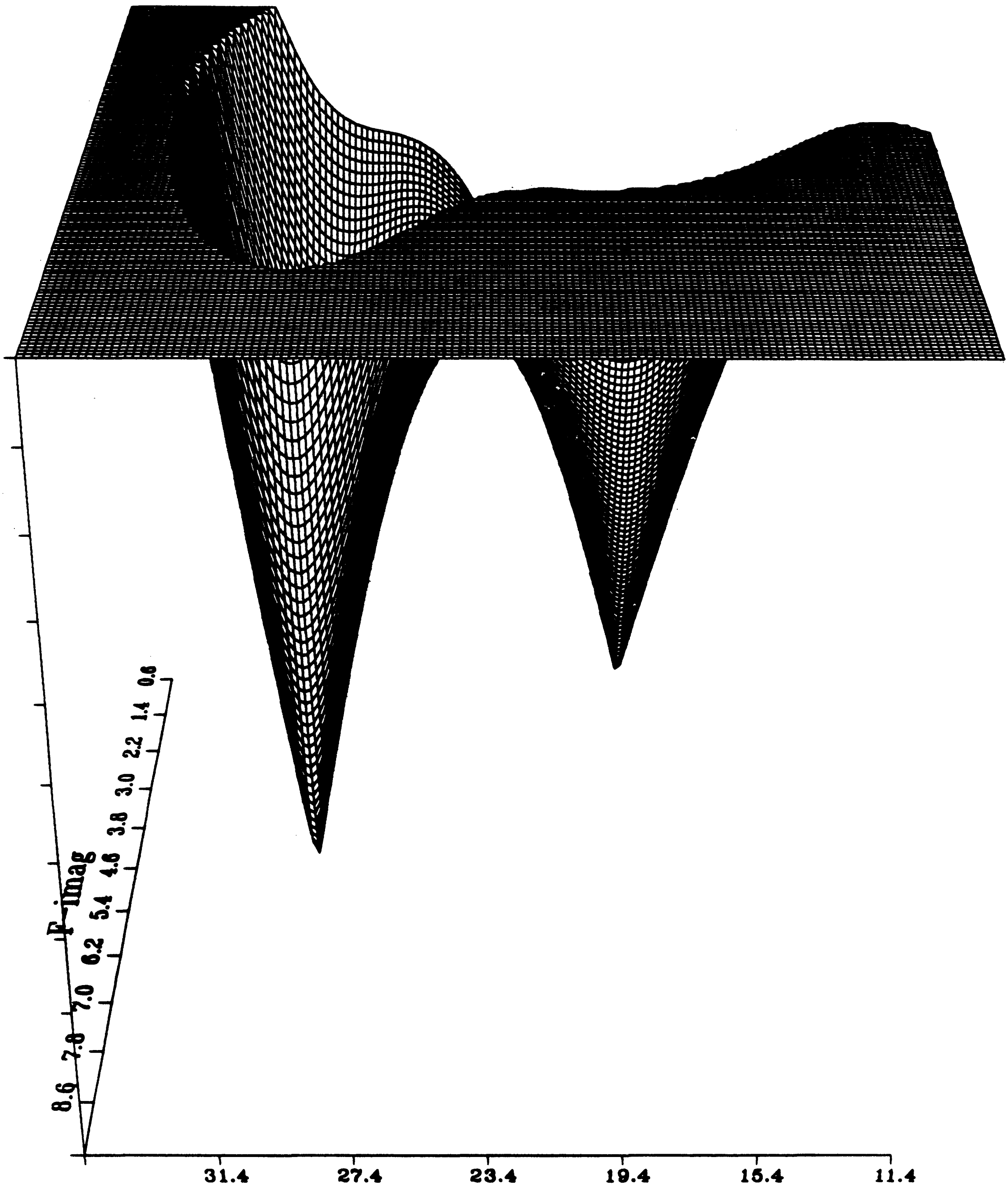

Equation for tand=1.0

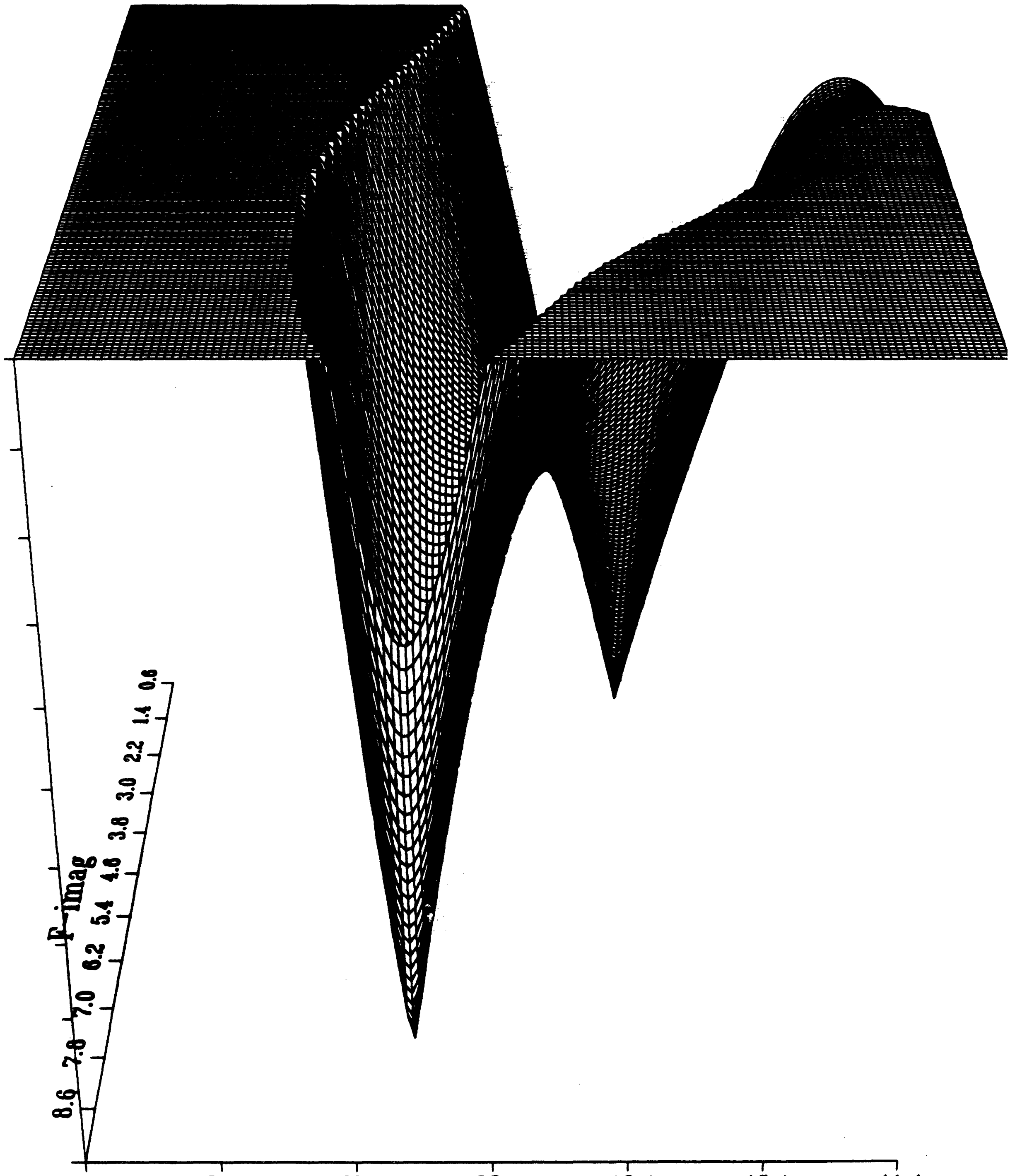

Equation for tand=1.5

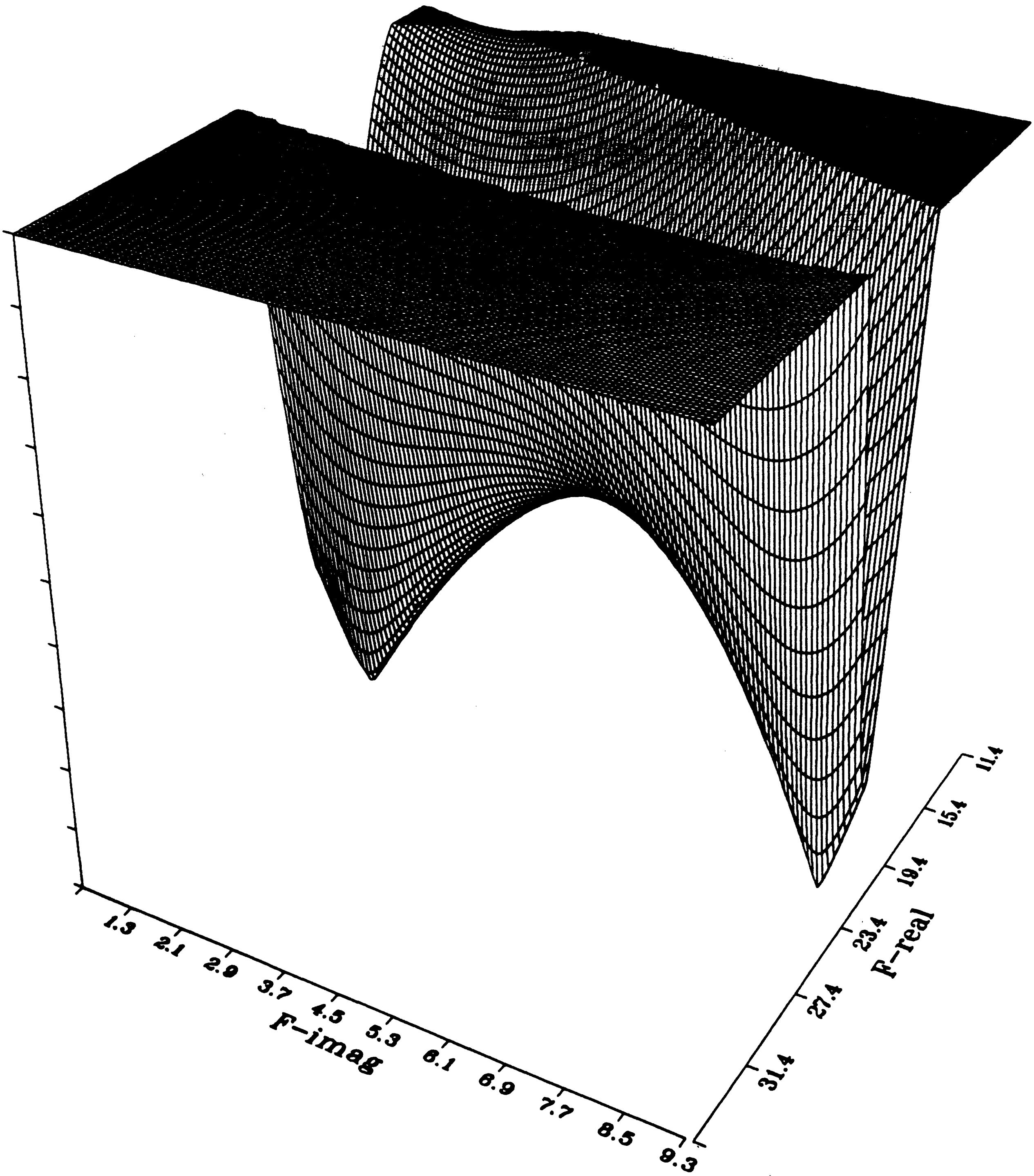

Equation for tand=2.0

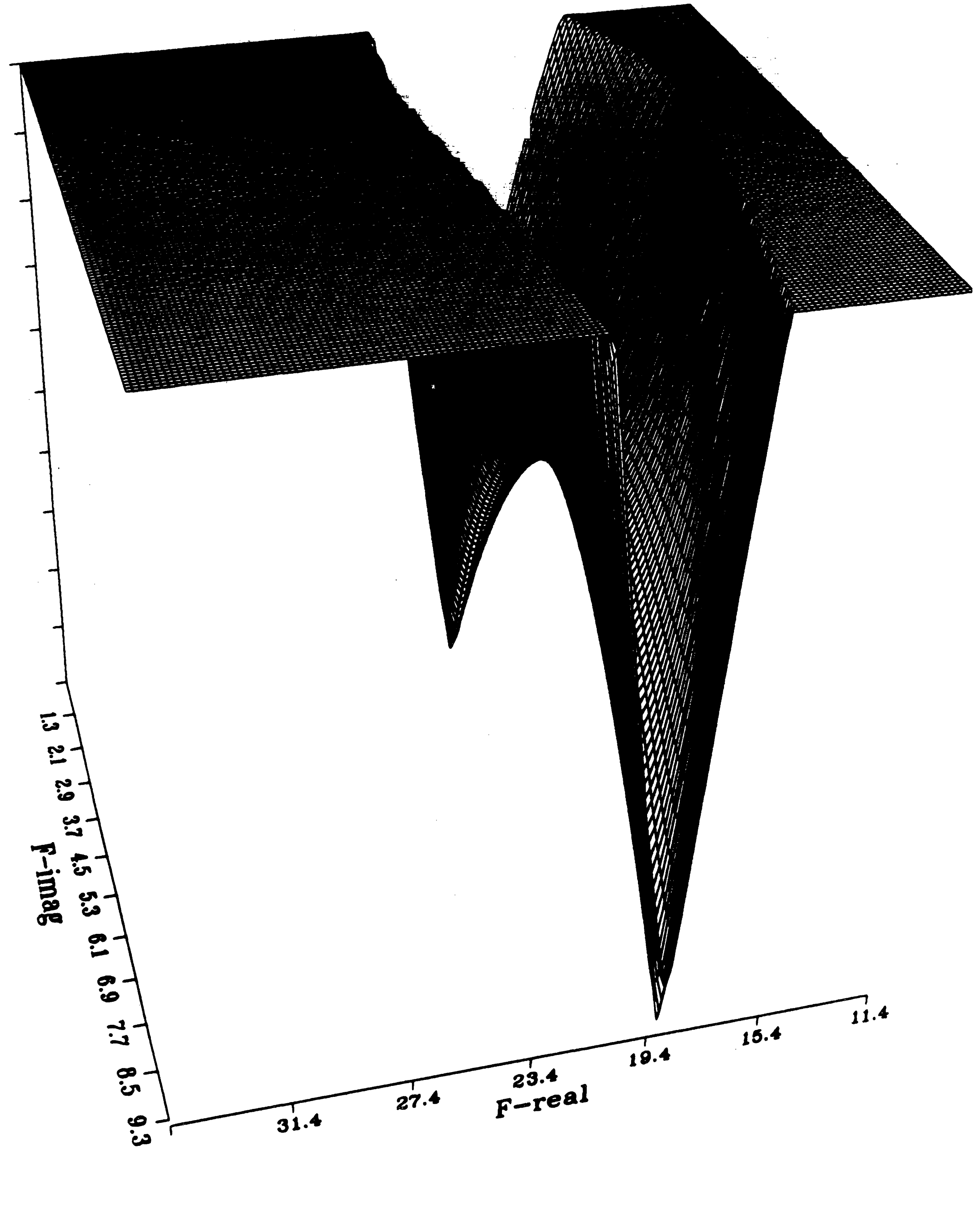

GROUP E

Specs:

Type of Mode = LSE

$k_y = \pi/b$
a = 0.305"
b = 0.305"
ε_r = 16.0
h = 0.025"

Observations:

- Following the progression of these plots, it is clear that there is a mode which remains nearly fixed for increasing tand. This would be the LSE_2 mode which appears in #5 from Group A. It also appears that another higher order mode is cutting across.

Equation for tand=0.1 (LS

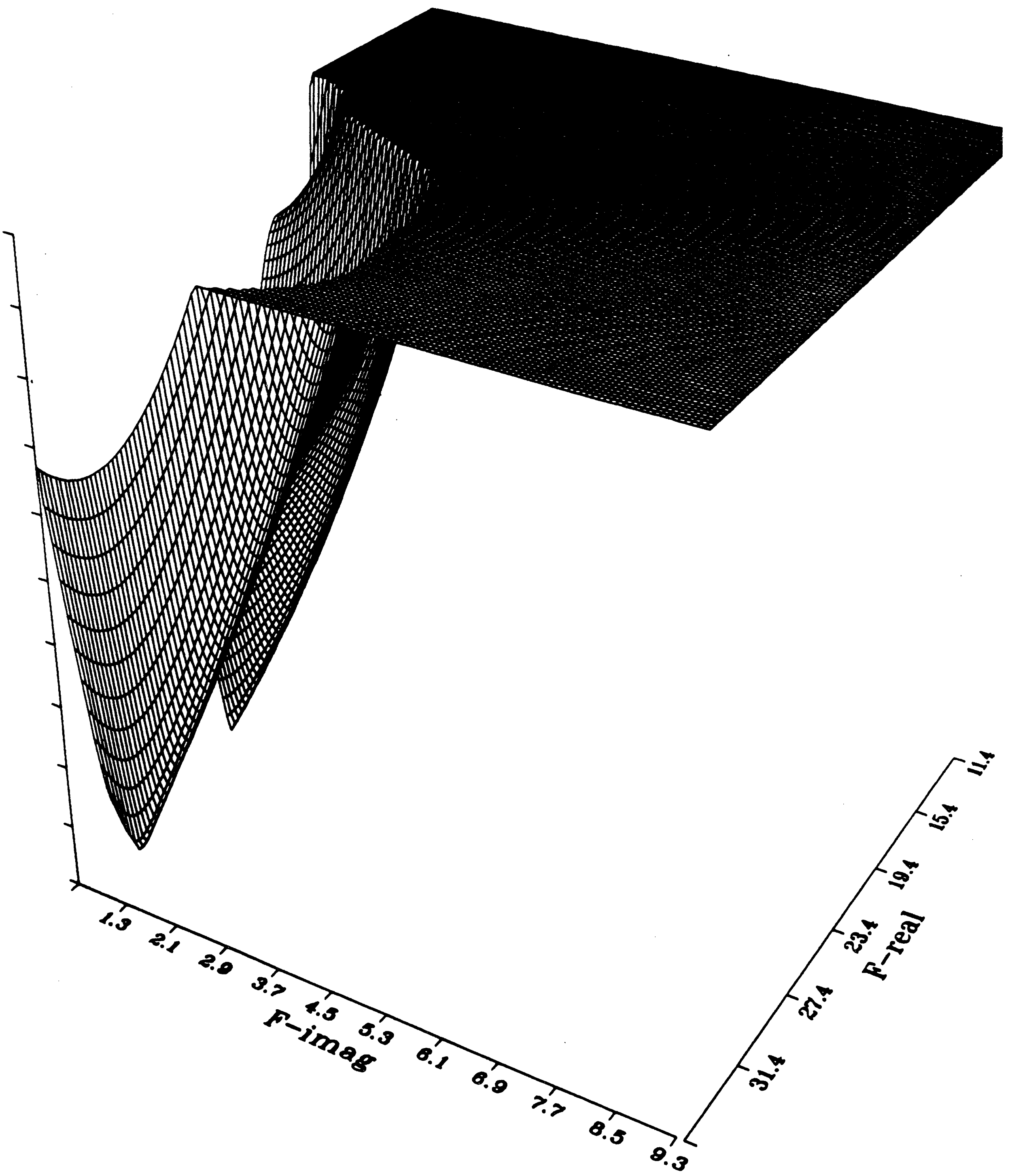

Equation for tand=0.5 (LSE

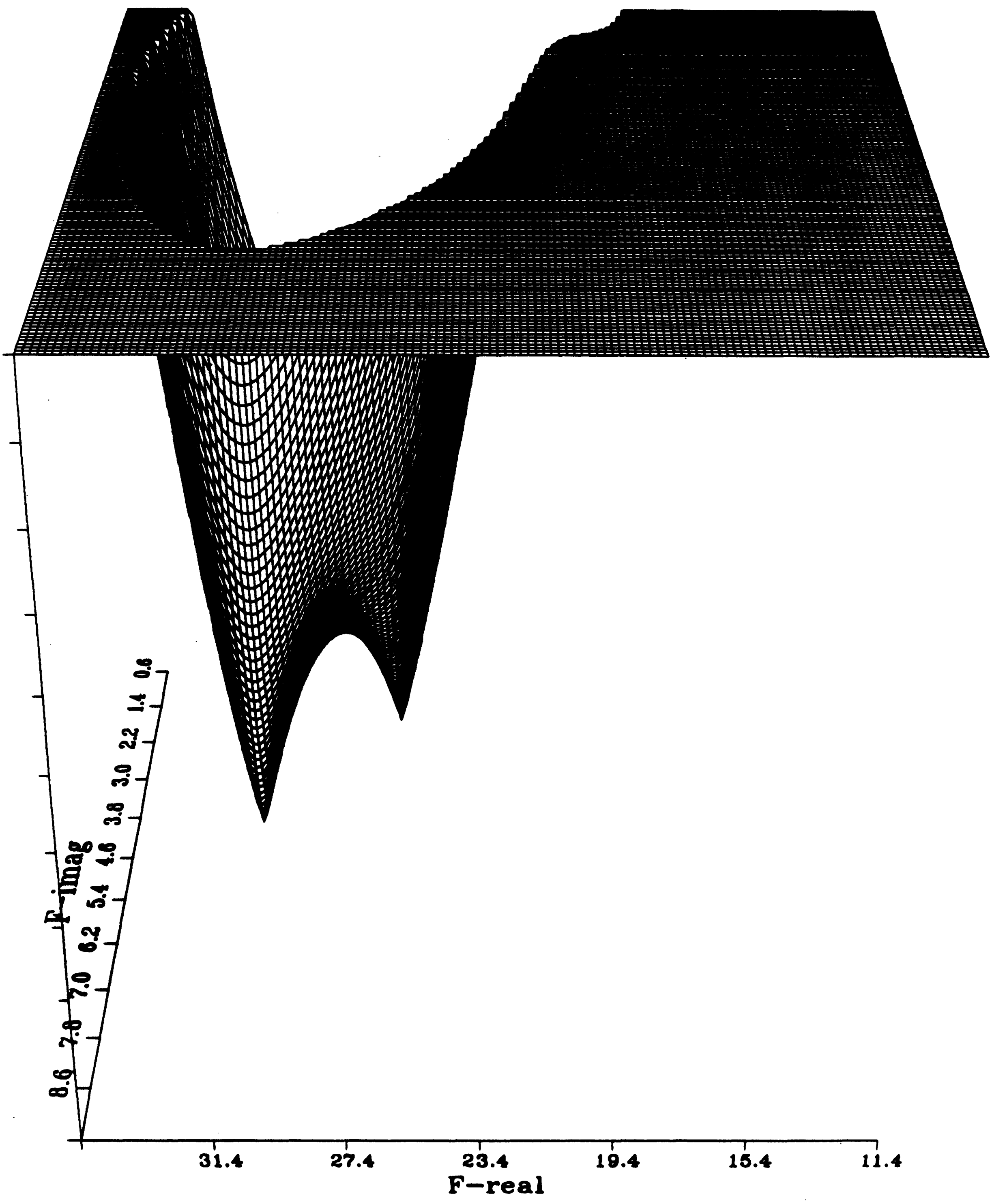

Equation for tand=1.0 (LS

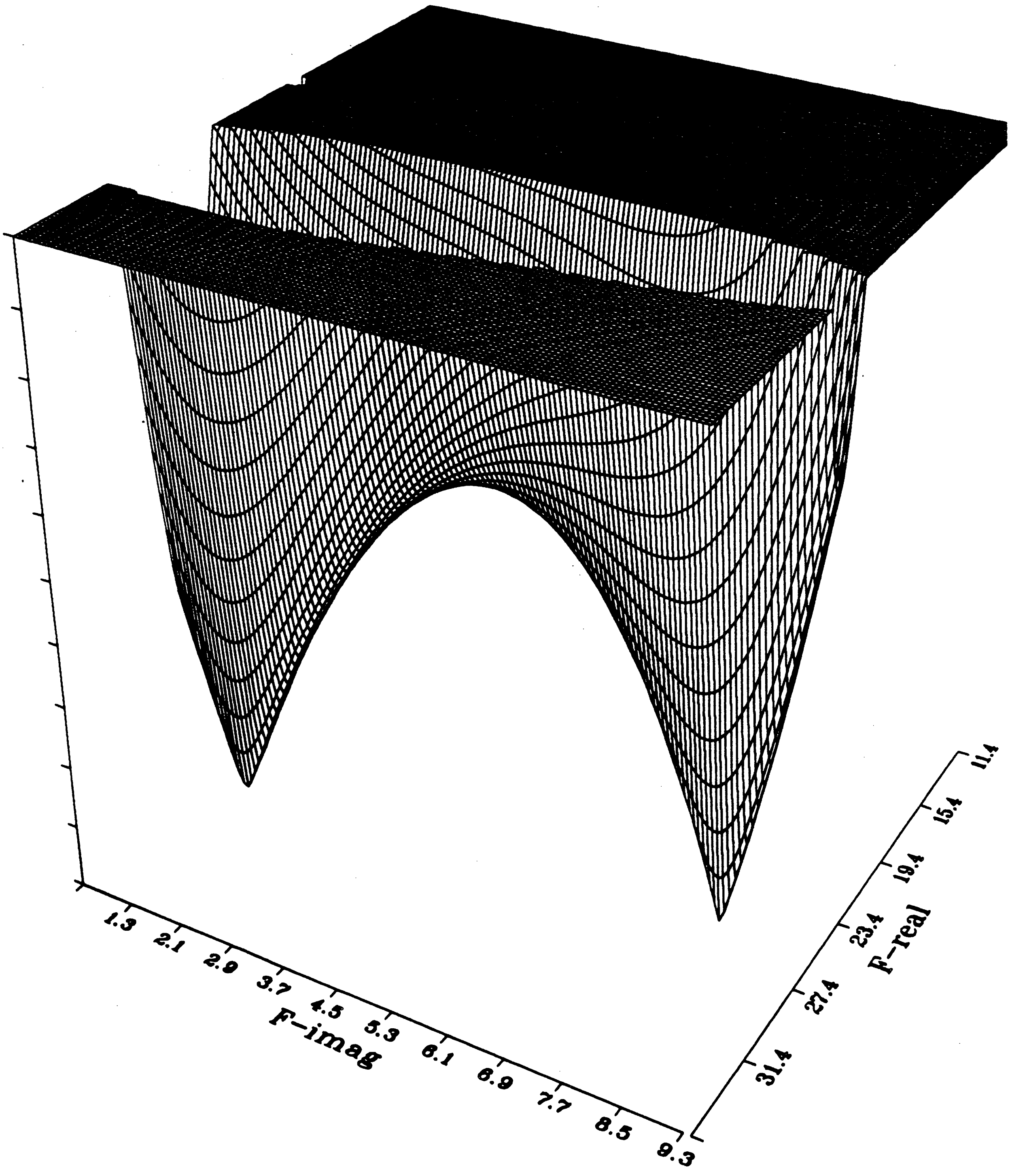

Equation for tand=1.5 (LSE)

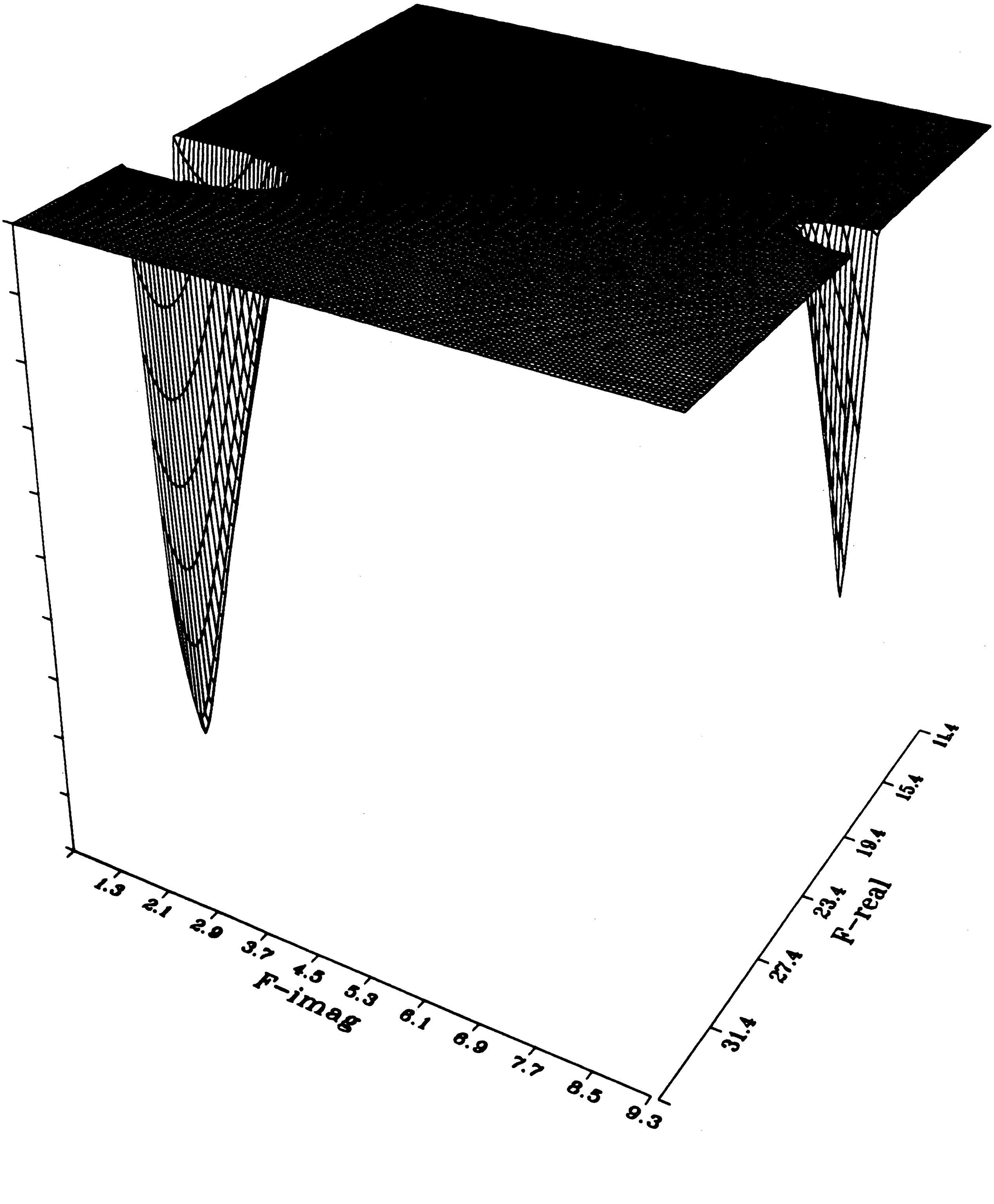

Equation for tand=2.0 (LS

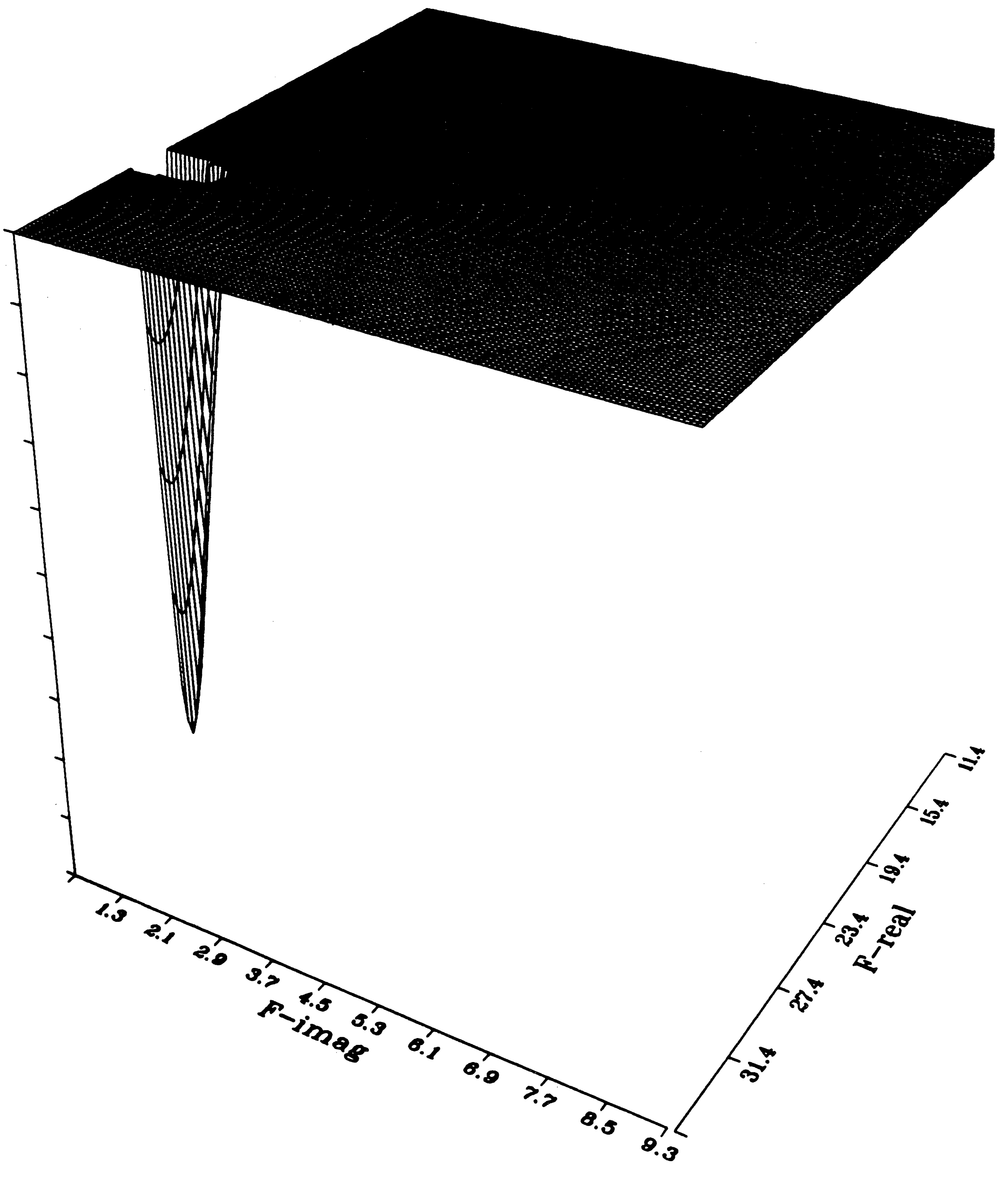

GROUP F

Specs:

Type of mode = LSM

$k_y = \pi/b$
a = 0.305"
b = 0.305"
h = 0.025"
$\varepsilon_r = 12.0$

Observations:

- By changing ε_r from 16.0 to 12.0 we can observe much greater stability in the relationship between LSM_1 and LSM_2. Note, however, that a higher order mode is still seen to be moving to the dominant position.

Equation for tand=0.5 (LS

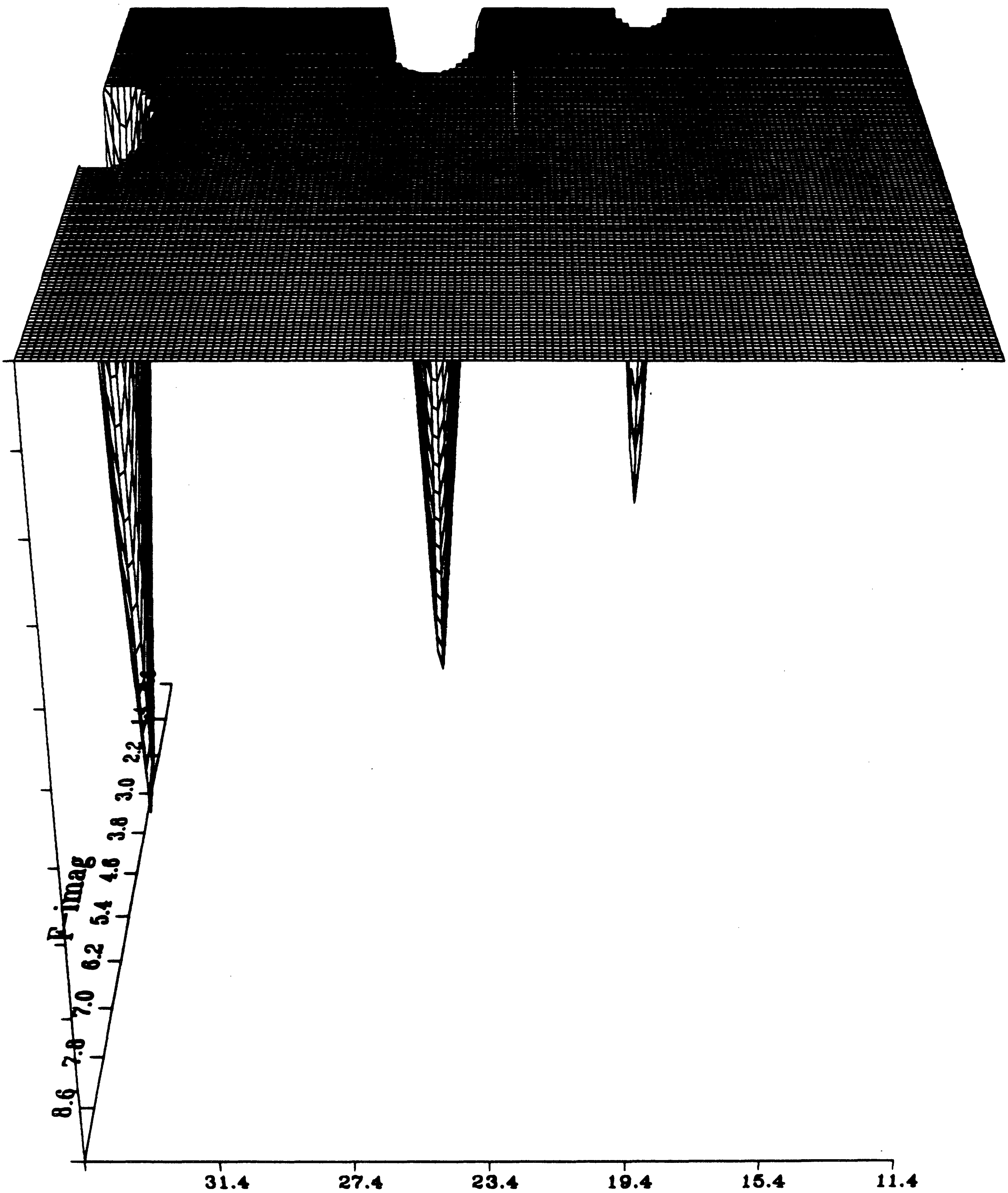

Equation for tand=1.0 (LSM

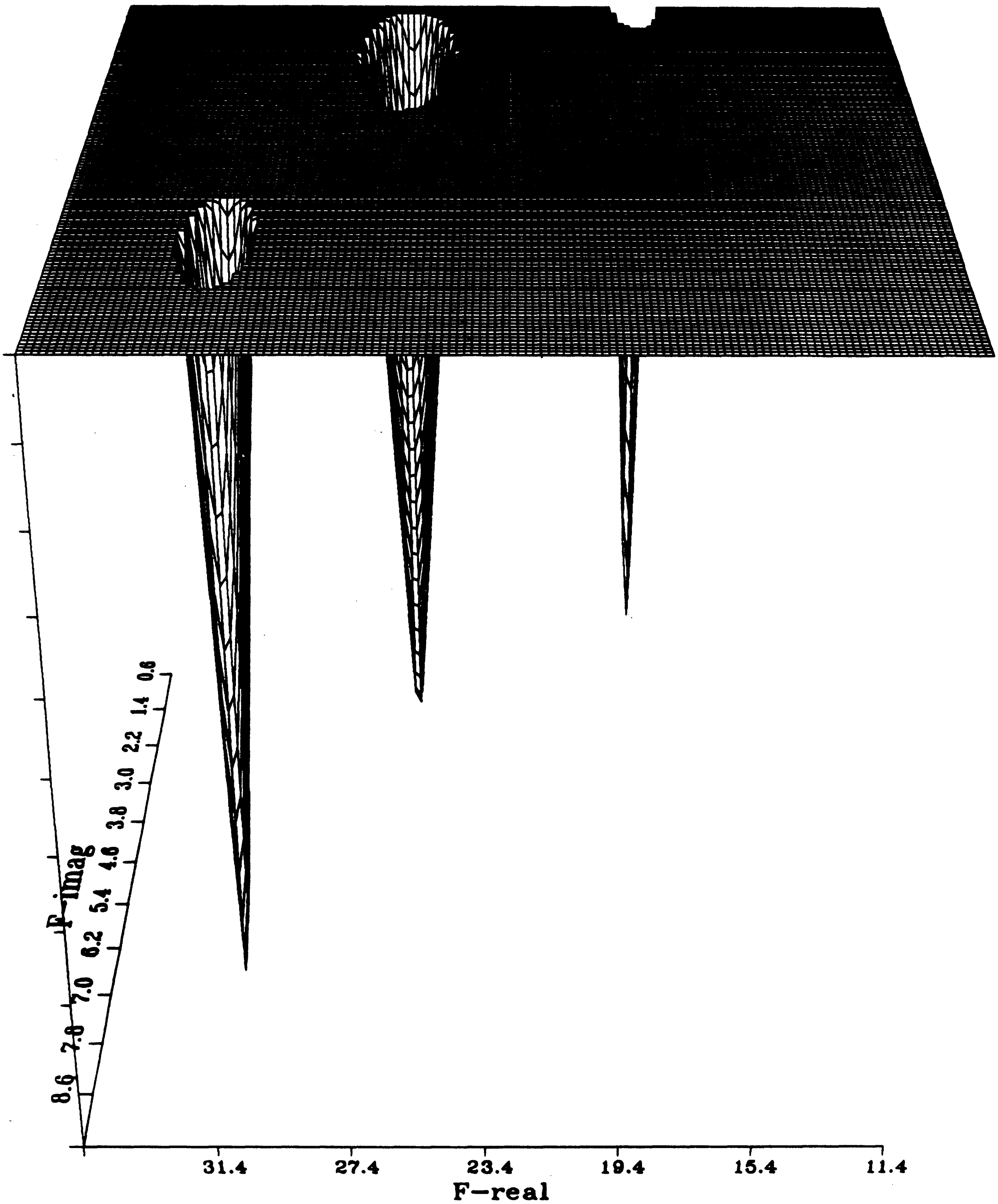

Equation for tand=1.5 (LS

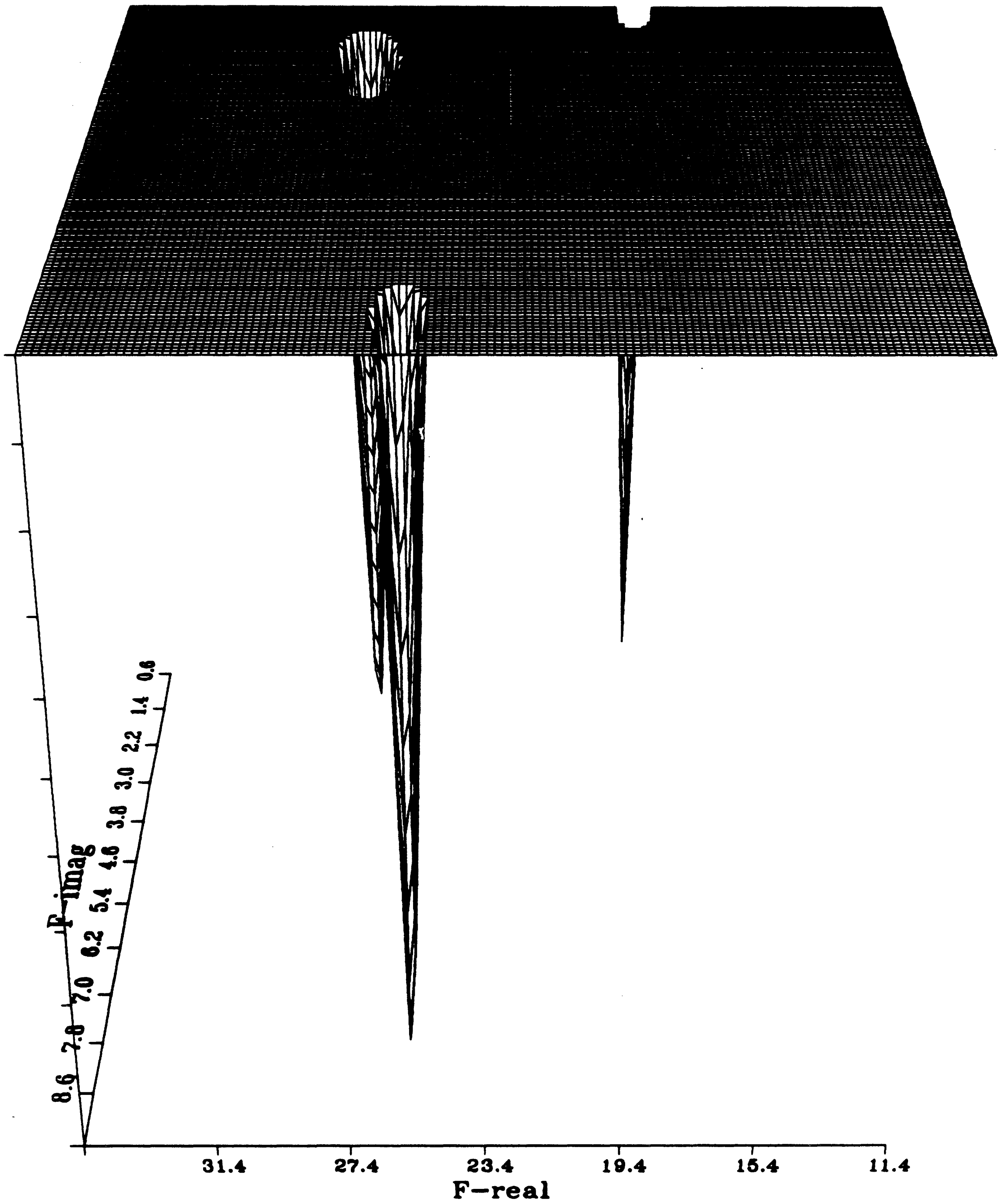

Equation for tand=2.0 (LSM

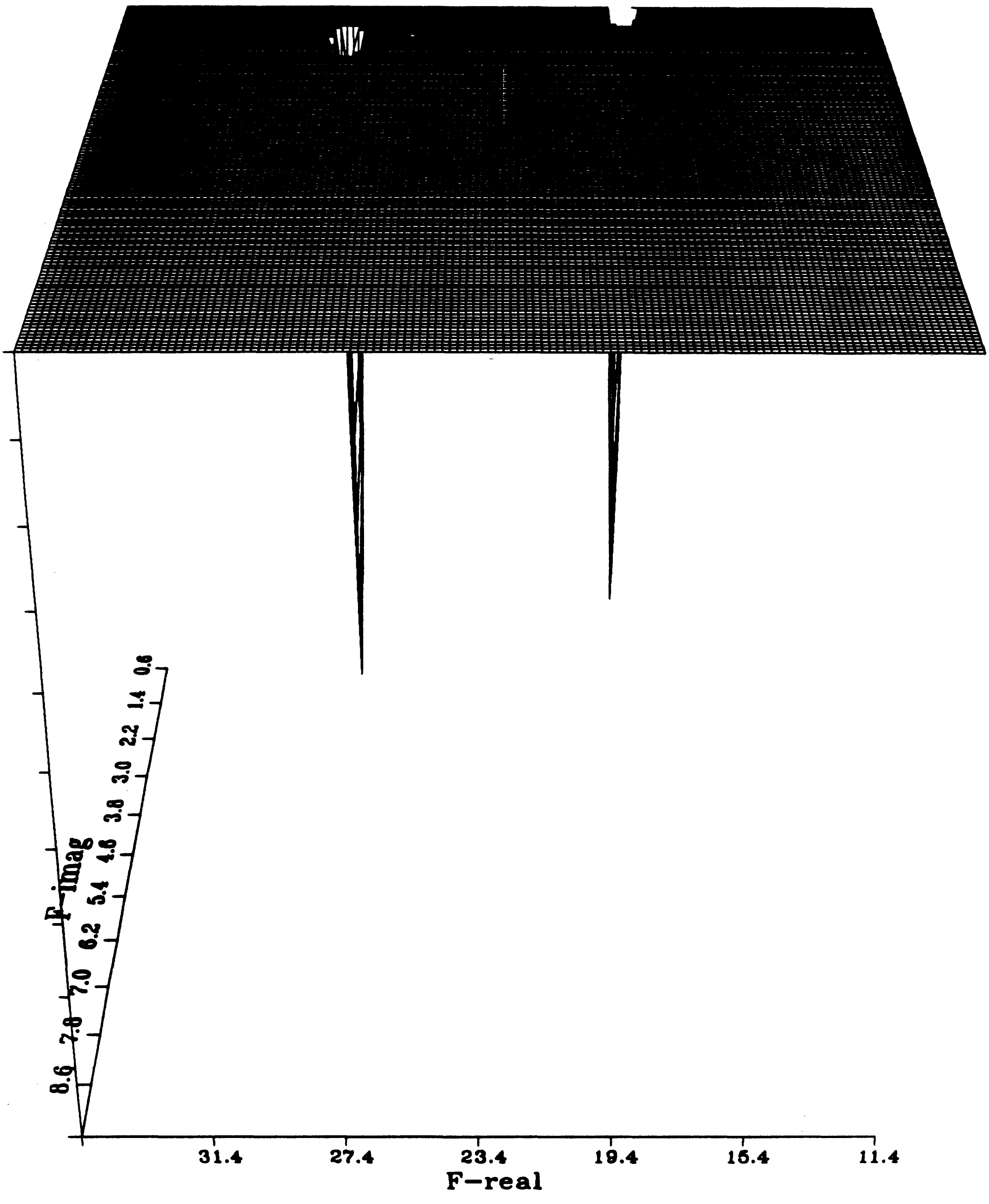

REFERENCES

1. L.P. Dunleavy and P.B. Katehi, "Shielding Effects in Microstrip Discontinuities - Part I: Theory." It has been submitted for publication in IEEE Trans. on Microwave Theory and Techniques.

2. L.P. Dunleavy and P.B. Katehi, "Shielding Effects in Microstrip Discontinuities - Part II: Applications." It has been submitted for publication in IEEE Trans. on Microwave Theory and Techniques.

3. E. Yamashita and K. Atsuki, "Analysis of Microstrip-Like Transmission Lines by Nonuniform Discretization of Integral Equations." IEEE Trans. Microwave Theory and Techniques, vol. MTT-24, No. 4, pp. 195-200, April 1976.

4. M. Hashimoto, "A Rigorous Solution for Dispersive Microstrip." IEEE Trans. on Microwave Theory and Techniques, vol. MTT-33, pp. 1131-1137, Nov. 1985.

5. C.J. Railton and T. Rozzi, "Complex Modes in Boxed Microstrip." IEEE Trans. on Microwave Theory and Techniques, vol. MTT-366, pp. 865-874, May 1988.